

Dissertation zur Erlangung des Doktorgrades
der Fakultät für Chemie und Pharmazie
der Ludwig-Maximilians-Universität München

Multifunctional mesoporous nanoparticles for drug delivery

Stefan Datz

aus

Traunstein, Deutschland

2017

Erklärung

Diese Dissertation wurde im Sinne von § 7 der Promotionsordnung vom 28. November 2011 von Herrn Prof. Dr. Thomas Bein betreut.

Eidesstattliche Versicherung

Diese Dissertation wurde eigenständig und ohne unerlaubte Hilfe bearbeitet.

München, den 21.06.2017

Stefan Datz

Dissertation eingereicht am 15.05.2017

1. Gutachter: Prof. Dr. Thomas Bein
2. Gutachter: Prof. Dr. Christoph Bräuchle

Mündliche Prüfung am 14.06.2017

Danksagung

Zuallererst möchte ich mich sehr herzlich bei meinem Doktorvater Prof. Dr. Thomas Bein für die Möglichkeit bedanken, in seiner Arbeitsgruppe auf diesem interessanten Forschungsgebiet zu arbeiten. Ich bin äußerst dankbar für die großen Freiheiten, die ich während der Bearbeitung der verschiedenen Forschungsprojekte erfahren habe. Außerdem möchte ich mich für die Möglichkeit bedanken, viele verschiedene nationale und internationale Konferenzen besuchen zu können. Der mehrwöchige Forschungsaufenthalt an der University of California, Los Angeles in der Arbeitsgruppe von Dr. Jeffrey I. Zink stellte dabei ein außerordentliches Highlight dar, das ich mit größtem Dank angenommen habe.

Desweiteren möchte ich mich bei Prof. Dr. Christoph Bräuchle für die erfolgreichen Kooperationen und für die Erstellung des Zweitgutachtens bedanken.

Ich möchte meinen weiteren Kooperationspartnern danken, mit denen viele verschiedene Projekte sehr erfolgreich zum Abschluss gekommen sind. Daher möchte ich mich zuallererst bei Dr. Silke Meiners, Dr. Sabine van Rijt und vor allem Deniz Bölükbas vom Comprehensive Pneumology Center für die erfolgreiche und sehr spannende Zusammenarbeit in den letzten vier Jahren bedanken. Außerdem bei Michael Gattner und Prof. Dr. Thomas Carell für die exzellente Zusammenarbeit beim Carboanhydrase-Projekt. Vielen Dank auch an Dr. Jeffrey I. Zink von der UCLA für die gute Zusammenarbeit und den mehrwöchigen spannenden Aufenthalt in seiner Gruppe. Danke auch an Dr. Veronika Weiss, Dr. Adriano Torrano und Dr. Annika Hermann für die tollen Projekte, die wir zusammen bearbeiten durften.

Mein großer Dank gilt der gesamten MesoBio-Subgroup (Alex, Cindy, Dodo, Hanna, Karin, Stefan, Basti, Christian, Noggi, Flo, Berni, Andi, Patrick) für die tolle Unterstützung, mit der die letzten Jahre wie im Flug vergingen. Besonders möchte ich mich bei Christian bedanken, bei dem ich sowohl mein F-Praktikum, als auch meine Masterarbeit angefertigt habe und der mich während der ersten Jahre meiner Promotion perfekt unterstützt hat. Auch für die wundervolle Zeit in den USA möchte ich ihm danken. Dabei gilt mein besonderer Dank auch Basti, der uns toll unterstützt hat, vor allem in Sachen Visa und Wohnung und mit dem am Ende auch das Forschungsprojekt sehr erfolgreich abgeschlossen werden konnte. Dir, Noggi, will ich danken, dass du mich in dein spannendes Projekt mit aufgenommen hast, das wir hoffentlich in Zukunft mit Christian weiter verfolgen können. Auch Hanna möchte ich sehr

für die gute Zusammenarbeit danken und die tolle Supervision, du machst das sehr gut und hast uns viel geholfen! Dir, liebe Dodo, möchte ich auch für alles danken. Ganz besonders möchte ich mich auch bei meinen Bürokollegen bedanken (Andi B., Noggi, Andi Z., Sabrina), mit denen es nie langweilig wurde und die für die nötige Ablenkung sorgten. Ich danke auch meinen Praktikanten Linh Nguyen und Michael Gaziano.

Insbesondere möchte ich mich bei Regina Huber, Tina Reuther, Dr. Markus Döblinger und Dr. Steffen Schmidt bedanken, ohne deren tatkräftige Unterstützung diese Arbeit nie so einfach möglich gewesen wäre. Dir, Regina, möchte ich vor allem dafür danken, dass du immer den Überblick behalten hast, alles perfekt organisiert hast und stets ein offenes Ohr für berufliche wie private Angelegenheiten hattest. Für die tolle Arbeitsatmosphäre möchte ich mich beim gesamten AK Bein bedanken, auch für die vielen Grillfeiern, Stammtische und Kaffeepausen, die die Promotionszeit deutlich unterhaltsamer gemacht haben.

Ich möchte mich auch herzlich bei meinen engsten Freunden bedanken, außerhalb und innerhalb der Uni, die für den nötigen Ausgleich gesorgt haben und stets für jeden Spaß zu haben sind. Besonders bei Obi, Schielei, Tom, Chri, Fex, Mike, Obi sen., Marty, Annette, Michi, Martina, Andi, Simone, Michi, Lisa, Tommy, Babsi, Robin und dem gesamten PIC Team (Ursi, Tobi, Andi, Matze, Fipsi).

Der größte Dank gilt meiner Familie, meinen Eltern, meinem kleinen Bruder und meiner Freundin Sabrina. Ich bin euch unendlich dankbar für eure Unterstützung in jeglicher Hinsicht. Ganz besonders möchte ich mich bei dir, liebe Brini, bedanken, dass du mir immer zur Seite standest, mit mir tapfer durchgehalten hast und dich immer mit mir gefreut hast, wenn es was zu feiern gab. Ohne dich hätte ich das alles nicht erreichen können. Zuletzt bleibt nur noch meinen Eltern für die Unterstützung in allen Lebenslagen zu danken, die immer kompromisslos hinter mir standen und mich immer motiviert haben, diesen langen Weg durchzuziehen. Ohne Euch wäre das alles nicht möglich gewesen!

Abstract

One of the most intriguing fields of research in this century is the development of controllable and effective drug delivery systems for targeted cancer therapy. This goal is closely connected to the development of suitable and innovative nanomaterials. In addition to the design of completely new nanoparticles, the properties of already existing materials, such as mesoporous silica nanoparticles, can be improved and modified by investigating new stimuli-responsive release mechanisms and different cancer cell targeting strategies. Cancer nanotherapeutics is a rapidly progressing and growing research field, with conventional drug delivery systems already bypassing limitations of classical chemotherapy such as nonspecific biodistribution and targeting, lack of water solubility and poor bioavailability. The design of tailor-made nanoparticles of differing sizes and surface characteristics offers the ability to increase their circulation time in the bloodstream. Additionally, they are able to carry their loaded active cargo selectively to cancer cells and release the drugs after applying specific internal or external stimuli. By using the unique pathophysiology of tumors, such as their enhanced permeability and retention (EPR) effect and the difference in vascularity of the tumor microenvironment compared to healthy tissue, passive tumor targeting can be exploited. In addition to this passive targeting mechanism, active targeting strategies using ligands or antibodies on the external surface of nanocarriers can lead to enhanced specific receptor-mediated cancer cell uptake. Hence, emerging multifunctional nanoscale drug delivery systems can improve current cancer treatment strategies to close the gap to specific and personalized chemotherapy.

This thesis is focused on the synthesis and modification of nanomaterials for targeted drug delivery applications. Effective tailoring of mesoporous silica nanoparticles (MSN) is described to further develop their great potential as multifunctional drug delivery

nanocarriers. The requirements for an efficient stimuli-responsive and thus controllable release of cargo molecules into cancer cells and the design principles for smart and autonomous nanocarriers are discussed. The possibility to spatially and temporally control the release of cargo molecules is shown. Different innovative stimuli-responsive release mechanisms were investigated and demonstrated in several *in vitro* and *in vivo* environments. The coating of the nanoparticles with different organic moieties on the external particle surface improves their biocompatibility, it can be utilized for the effective encapsulation of cancer therapeutics, and it facilitates attachment of targeting ligands for specific cellular recognition. The use of specific ligands for active cancer cell targeting is discussed in detail. The biocompatibility and toxicity of functionalized nanoparticles was tested *in vitro* and *in vivo*. Additionally, new silica-reduced and non-silica based nanomaterials for biomedical applications were synthesized and used for cellular delivery approaches.

The first part of this thesis describes an enzyme-responsive release system on MSNs. These nanoparticles allow for controlled and targeted drug delivery to diseased tissues and therefore bypass systemic side effects. Spatio-temporal control of drug release can be achieved by these nanocarriers that respond to elevated levels of disease-specific enzymes. For example, matrix metalloproteinase 9 (MMP9) enzymes are overexpressed in tumors, are known to enhance the metastatic potency of malignant cells, and have been associated with poor prognosis of lung cancer. Here, the used MSNs are tightly capped by avidin molecules via MMP9 sequence-specific linkers to allow for site-selective drug delivery in high MMP9-expressing tumor areas. We provide proof-of-concept evidence for successful MMP9-triggered drug release from MSNs in human tumor cells and in mouse and human lung tumors using the novel technology of *ex vivo* 3D lung tissue cultures. This technique allows for translational testing of drug delivery strategies in diseased mouse and human tissue. Using this method we show MMP9-mediated release of cisplatin, which induced apoptotic cell death only in lung tumor

regions of Kras mutant mice, without causing toxicity in tumor-free areas or in healthy mice. The MMP9 responsive nanoparticles also allowed for effective combinatorial drug delivery of cisplatin and the proteasome inhibitor bortezomib, which had a synergistic effect on the toxicity. Importantly, we demonstrate the feasibility of MMP9 controlled drug release in human lung tumors (Chapter 3).

Another stimuli-responsive capping system is described in Chapter 4, where a novel thermoresponsive snaptop for stimulated cargo release from superparamagnetic iron oxide core – mesoporous silica shell nanoparticles based on a [2+4] cycloreversion reaction (retro-Diels Alder reaction) is presented. The non-invasive external actuation through alternating magnetic fields makes this material a promising candidate for future applications in externally triggered drug delivery.

In a joint project with Prof. Bräuchle, Prof. Carell, and co-workers, a third stimuli-responsive release mechanism on MSNs is presented (Chapter 5). Here, we describe a novel enzyme-based cap system for mesoporous silica nanoparticles (MSNs) that is directly combined with a targeting ligand via bio-orthogonal click chemistry. The capping system is based on the pH-responsive binding of an aryl-sulfonamide-functionalized MSN and the enzyme carbonic anhydrase (CA). An unnatural amino acid (UAA) containing a norbornene moiety was genetically incorporated into CA. This UAA allowed for the site-specific bio-orthogonal attachment of even very sensitive targeting ligands such as folic acid and anandamide. This leads to specific receptor-mediated cell and stem cell uptake. We demonstrate the successful delivery and release of the chemotherapeutic agent Actinomycin D to KB cells. This novel nanocarrier concept provides a promising platform for the development of precisely controllable and highly modular theranostic systems.

In order to show the biocompatibility and explore the toxicity of functionalized MSNs in the lung, we investigated the bioresponse of avidin-coated MSNs (MSN-AVI), as well as aminated (uncoated) MSNs, after direct application into the lungs of mice (Chapter 6). We quantified MSN distribution, clearance rate, cell-specific uptake, and inflammatory responses to MSNs within one week after instillation. We show that amine-functionalized (MSN-NH₂) particles are not taken up by lung epithelial cells, but induced a prolonged inflammatory response in the lung and macrophage cell death. In contrast, MSN-AVI co-localized with alveolar epithelial type 1 and type 2 cells in the lung in the absence of sustained inflammatory responses or cell death, and showed preferential epithelial cell uptake in *in vitro* co-cultures. Further, MSN-AVI particles demonstrated uniform particle distribution in mouse lungs and slow clearance rates. Thus, we provide evidence that avidin functionalized MSNs (MSN-AVI) have the potential to serve as versatile biocompatible drug carriers for lung-specific drug delivery. These MSNs were subsequently used for active targeting studies in the upcoming section.

Specific receptor-mediated cancer cell targeting with functionalized MSNs was evaluated in Chapter 7. Targeting of tumor cells typically involves functionalization of nanoparticles with ligands for receptors that are specific for or overexpressed in cancer cells. Combination therapy with distinctly functionalized nanocarriers can be employed to target several cancer cell types. Here, we investigated the targeting efficiencies of EGFR- or CCR2-targeted mesoporous silica nanoparticles (MSNs) *in vitro* and *in vivo* for lung cancer therapy with cellular resolution. Nanoparticles functionalized with the artificial peptides GE11- or ECL1i- for EGFR- or CCR2-targeting, respectively, were specifically taken up by receptor overexpressing cell lines of the lung *in vitro*. In contrast, systemically applied GE11-functionalized nanoparticles failed to accumulate in EGFR-overexpressing flank or lung tumors of mice, but accumulated in the liver or tissue-resident macrophages regardless of

their functionalization and the flank tumor type. Moreover, both EGFR- and CCR2-functionalized MSNs did not target lung tumor tissue but were efficiently taken up by resident alveolar macrophages in tumorous but also tumor-free regions of the lungs upon local intratracheal administration to Kras-mutant transgenic mice. In conclusion, in vitro validated nanoparticle-mediated targeting of receptors on tumor and immune cells can fail in vivo in two distinct biological environments, i.e. the blood and the lung lining fluid. These findings suggest that nanoparticle-bound targeting ligands can be effectively shielded by the distinct biological environment in the serum and the lining fluid of the lung and redirected to phagocytosing mononuclear cells. Novel strategies that overcome this natural defense mechanism of the organism to foreign materials are thus required to establish efficient cell-specific nanoparticle-mediated delivery of drugs for tumor therapy.

The final parts of this thesis mainly focus on the development of new nanomaterials for cellular delivery applications. In Chapter 8 we describe a novel inorganic-organic hybrid material with a strikingly high organic content of almost 50 wt%. The colloidal periodic mesoporous organosilica (PMO) nanoparticles synthesized in this section consist entirely of curcumin and ethane derivatives serving as constituents that are crosslinked by siloxane bridges, without any added silica. These mesoporous curcumin nanoparticles (MCNs) exhibit very high surface areas (over 1000 m²/g), narrow particle size distribution (around 200 nm) and a strikingly high stability in simulated biological media. Additionally, the MCNs showed high autofluorescence and were used as a cargo delivery system in live-cell experiments. A supported lipid bilayer (SLB) efficiently seals the pores and releases Rhodamin B as model cargo in HeLa cells.

Another innovative multifunctional nanomaterial that is applied in controlled drug delivery comprises cyclodextrin-based nanoparticles. In Chapter 9 we report on the synthesis of a

novel biocompatible material, entirely consisting of covalently crosslinked organic molecules. The β -cyclodextrin structures were crosslinked with a rigid organic linker molecule to obtain small (~150 nm) and highly water-dispersable nanoparticles. The nanoparticles can be covalently labeled with dye molecules to effectively track them in *in vitro* cell experiments. Very fast cell-uptake kinetics were observed on HeLa cells revealing particle uptake within less than an hour due to sugar-receptor mediated endocytosis. Additionally, the particles can be loaded with different cargo molecules showing pH-responsive release behavior. Successful nuclei staining with Hoechst 33342 and effective cell killing with doxorubicin as cargo molecules were shown in live-cell experiments, respectively.

In summary, different novel stimuli-responsive release mechanisms (enzyme-responsive, temperature-responsive, pH-responsive) were investigated for MSNs and proven in *in vitro*, *ex vivo* and *in vivo* experiments. Additional toxicity studies and targeting approaches reveal the great potential as well as possible pitfalls of this family of nanomaterials in future drug delivery applications. We also established two new nanoparticle systems with reduced silica-content or completely silica-free chemistry to expand the repertoire of powerful multifunctional nanocarrier systems.

Table of contents

1	Introduction.....	1
1.1	Introduction to Nanotechnology.....	1
1.2	Introduction to Porous Nanomaterials and their Biomedical Application.....	3
1.3	Multifunctional Drug Delivery Systems.....	9
1.3.1.	Mesoporous Silica Nanoparticles.....	9
1.3.2.	Periodic Mesoporous Organosilica.....	20
1.3.3.	Magnetic Nanocomposites.....	27
1.3.4.	Supramolecular Nanoparticles.....	31
1.4	References.....	37
2	Characterization.....	50
2.1	Dynamic light scattering (DLS).....	50
2.2	Zeta potential.....	53
2.3	Nitrogen sorption.....	56
2.4	X-ray diffraction (XRD).....	60
2.5	Electron microscopy.....	62
2.6	Infrared spectroscopy.....	66
2.7	Raman spectroscopy.....	67
2.8	Thermogravimetric analysis.....	69
2.9	Fluorescence spectroscopy.....	70
2.10	UV/VIS spectroscopy.....	72
2.11	Fluorescence microscopy.....	73
2.12	Nuclear magnetic resonance spectroscopy.....	77
2.13	Superconducting quantum interference device.....	79
2.14	References.....	81
3	Protease mediated release of chemotherapeutics from mesoporous silica nanoparticles to <i>ex vivo</i> human and mouse lung tumors.....	83
3.1	Introduction.....	84
3.2	Results and Discussion.....	86
3.3	Conclusion.....	104
3.4	Experimental Part.....	104

3.5	References	112
3.6	Appendix	118
4	A molecular nanocap activated by superparamagnetic heating for externally stimulated cargo release.....	135
4.1	Introduction	136
4.2	Results and Discussion.....	139
4.3	Conclusion.....	146
4.4	Experimental Part.....	147
4.5	References	157
4.6	Appendix	160
5	Genetically designed biomolecular capping system for mesoporous silica nanoparticles enables receptor-mediated cell uptake and controlled drug release.....	166
5.1	Introduction	167
5.2	Results and Discussion.....	170
5.3	Conclusion.....	181
5.4	Experimental Part.....	182
5.5	References	197
5.6	Appendix	200
6	Applicability of avidin protein coated mesoporous silica nanoparticles as drug carriers in the lung	205
6.1	Introduction	206
6.2	Results and Discussion.....	210
6.3	Conclusion.....	225
6.4	Experimental Part.....	227
6.5	References	234
6.6	Appendix	237
7	Cellular resolution is essential for validation of active targeting of nanoparticles in vivo.....	247
7.1	Introduction	248
7.2	Results and Discussion.....	250
7.3	Conclusion.....	261
7.4	Experimental Part.....	263
7.5	References	266
7.6	Appendix	270

8	Lipid bilayer-coated curcumin-based mesoporous organosilica nanoparticles for cellular delivery	290
8.1	Introduction	291
8.2	Results and Discussion.....	293
8.3	Conclusion.....	300
8.4	Experimental Part.....	301
8.5	References	307
8.6	Appendix	313
9	Biocompatible β -cyclodextrin nanoparticles as multifunctional carriers for cellular delivery	318
9.1	Introduction	319
9.2	Results and Discussion.....	321
9.3	Experimental Part.....	331
9.4	Conclusion.....	330
9.5	References	336
9.6	Appendix	341
10	Conclusion and Outlook	345
11	Curriculum Vitae	350
12	Publications and Presentations.....	352
12.1	Publications	352
12.2	Presentations.....	354

1 Introduction

1.1 Introduction to nanotechnology

In December 1959 Richard Feynman, an American theoretical physicist, gave a lecture in front of an audience at the California Institute of Technology in Pasadena which is now considered to be the founder's charta of modern nanotechnology.

“But I am not afraid to consider the final questions to whether - in the great future - we can arrange the atoms the way we want; the very atoms, all the way down! What would happen if we could arrange the atoms one by one the way we want them. [...] Atoms on small scale behave like nothing on a large scale, for they satisfy the laws of quantum mechanics. So, as we go down and fiddle around with the atoms down there, we are working with different laws, and we can expect to do different things.”¹

His ideas of denser computer circuitry, better electron microscopes and adapting concepts of small, but complex, biological systems later led to the invention of groundbreaking microscopy techniques, e.g. scanning tunneling microscopy (STM) and atomic force microscopy (AFM), and high-performance storage systems like *Millipede* which were invented by IBM researchers.^{2,3} In a general definition, nanomaterials are objects with at least one dimension being smaller than 100 nm, leading to drastically different properties compared to bulk materials. The change in optical, electrical or magnetic properties is partially due to the drastic increase in surface atoms with decreasing size compared to the total number of atoms in a material.⁴ As one of the first researchers recognizing the huge scientific and application potential of nanotechnology, in 1974 Norio Taniguchi characterized it as the separation, deformation or formation of materials formed from few atoms or molecules.⁵ The field of nanoscience experienced another big push in the late eighties and early nineties with

the discovery of carbon-based nanomaterials.⁶⁻⁸ The groundbreaking work of Harry Kroto and Sumio Iijima on fullerenes and single- and multi-walled carbon nanotubes provided materials with possible applications in power engineering, semiconductor industry and usage for biological and medical purposes. With the continuous improvement of characterization and imaging techniques it is possible to develop and characterize nanomaterials in less and less time and with greatly increasing information content, e.g., high-resolution transmission electron microscopy allows for the direct imaging of the atomic structure of a material.⁹ Far-field optical nanoscopy methods, such as stimulated emission depletion (STED) or photoactivated localization microscopy (PALM), provides lateral resolution in the nanometer range even for fluorophore-labeled living cells.^{10, 11} This toolbox of Nobel prize – awarded characterization techniques in combination with proper preparation approaches made nanotechnology one of the most dynamic growing fields in scientific and industrial research.

In general, two preparation approaches can be used to synthesize nanomaterials and fabricate nanostructures, namely top-down or bottom-up.¹² The bottom-up approach includes the self-assembly of components at the atomic level (atoms, molecules, clusters) to complex and stable nanostructures. Typical examples are the formation of nanoparticles from colloidal dispersions or quantum dot formation during epitaxial growth. In contrast, the top-down approach starts with larger initial structures that are then reduced to nanoscale with externally controlled processes. Photolithography, electron-beam lithography, etching or ball milling are just a few examples for top-down approaches that are used to achieve the synthesis of stable nanostructures, with great structural control in the case of lithography. In comparison to bottom-up synthesis of nanoparticles, top-down milling processes often lead to nanomaterials with more inhomogenous morphologies and broader particle size distributions, whereas more homogenous nanoobjects can be synthesized following the bottom-up approach.

One of the most demanding and most promising fields in nanotechnology in the next century will be the development of effective and controllable nanosystems for targeted cancer therapy. Since cancer is a widespread disease with almost half a million new cases in Germany per year alone and a high general mortality rate, the demand for innovative therapies is enormous.¹³ The following introduction guides the reader through different preparation methods for silica- and non-silica-based mesoporous nanoparticles and describes different applications of these materials in conventional drug delivery, imaging, sensing and for general biomedical purposes.

1.2 Introduction to porous nanomaterials and their biomedical application

According to the International Union of Applied Chemistry (IUPAC) notation, porous materials are classified into three general categories depending on their pore size. Microporous materials exhibit pore sizes less than 2 nm in diameter and macroporous materials have pore sizes bigger than 50 nm, whereas mesoporous materials lie in between (from 2 to 50 nm).¹⁴ Due to their corresponding difference in optical, electrical, adsorption and physiological properties porous nanomaterials have an emerging variety of possible applications in energy conversion and storage, biomedicine and microelectronics, just to name a few.¹⁵ Prominent representatives in the class of porous materials are zeolites, metal-organic frameworks (MOFs), covalent organic frameworks (COFs), mesoporous silica nanoparticles (MSNs) and supramolecular nanoparticles (SNPs).

In general, zeolites are crystalline porous aluminosilicate materials consisting of corner-sharing MO_4 tetrahedra ($M = Si, Al, P, \text{etc.}$), which are being used at large industrial scale for separation, ion exchange and catalysis applications.¹⁶⁻¹⁸ These microporous crystals recently reached the nanoscale with colloidal stability and particle sizes under 200 nm, which brings

along unique properties and expands the area of zeolite applications towards optoelectronics, chemical sensing, and medicine.¹⁹ The size-controlled synthesis of nanozeolites can be achieved via controlled hydrothermal conditions in a water/surfactant/organic solvent mixture (emulsion method).²⁰ The hydrophilic/hydrophobic properties of these nanomaterials can be finely tuned by changing the framework composition or adjusting the applied synthesis conditions. A recent example for nanozeolites used in biomedical applications was shown by the group of de Cola where PEGylated and antibody-modified L-Zeolite nanocrystals exhibited fast and targeted cancer cell uptake.²¹ However, some limitations of zeolite materials such as the sensitivity to deactivation by irreversible adsorption, as well as their limited pore size and structural rigidity and limited tunability, encouraged scientists to focus on the investigation of other porous materials for biomedical applications.²²

MOFs are another prominent representative of microporous materials, which attract increasing scientific interest over the past decade. MOFs are framework structures consisting of inorganic metal ions and organic linker molecules. This new class of crystalline materials with exceptionally high surface areas and high thermal stability was first introduced by Omar M. Yaghi in 1995.²³ Another great advantage of MOFs is the finely tunable composition and structure due to their versatile coordination chemistry, which makes them attractive for different applications such as gas storage, catalysis and separations.²⁴

The chemical tailorability and the structural diversity of MOFs are based on the nearly infinite number of combination possibilities for metal ions with specific functionalized organic molecules that are connected via molecular linkers using coordinative bonds. This leads to the creation of a well-ordered crystalline framework and provides the possibility to adjust pore sizes and structures, to design the shape of the material and to implement different functionalities within the material (Figure 1-1).

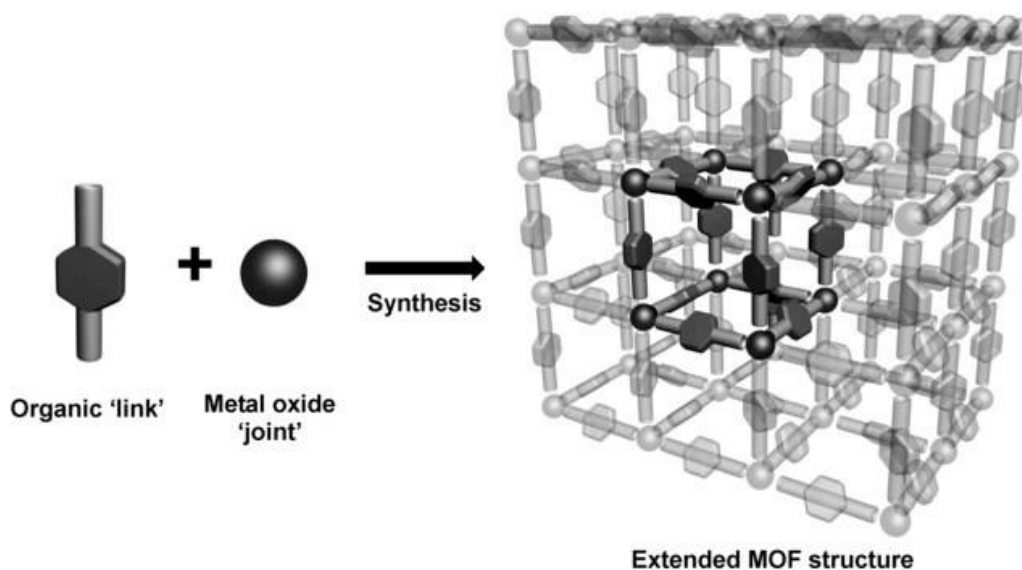


Figure 1-1. Schematic illustration of a MOF synthesis strategy.²⁵

In recent years different groups have focused on scaling down the bulk materials to the nanometer length scale, which offers new application fields for MOFs with the obvious advantages of nanomaterials for biomedical purposes.²⁶⁻²⁸

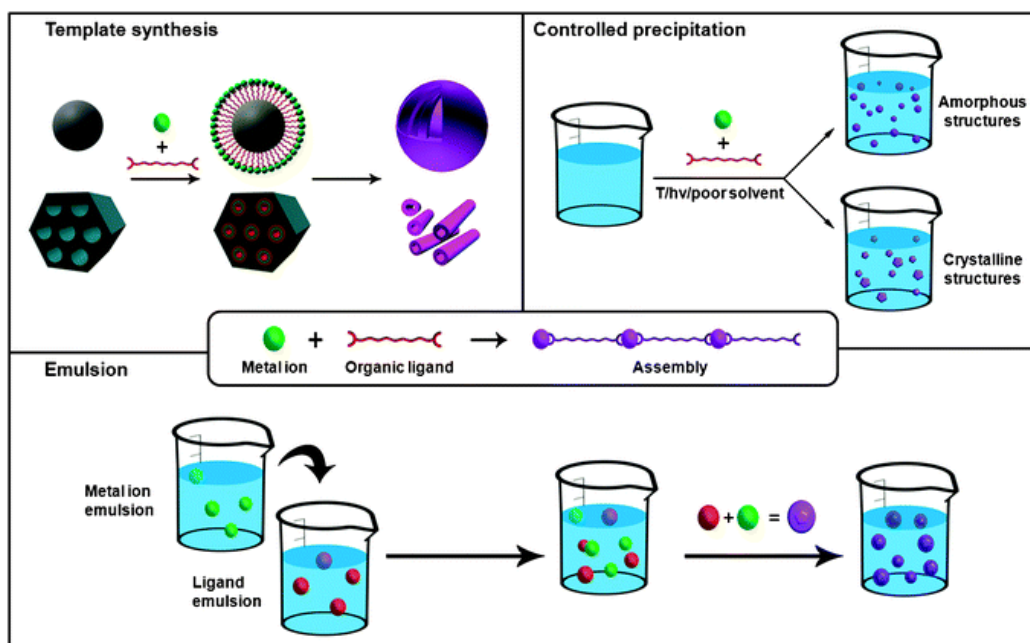


Figure 1-2: Schematic illustration of different synthesis strategies to achieve MOF nanostructures.²⁷

The different bottom-up approaches used for the synthesis of MOF nanoparticles are shown in Figure 1-2 including template-assisted synthesis, controlled solvothermal precipitation and microemulsion techniques.

Much effort was then put in the functionalization of the outer surface and the enhancement of the specific drug loading capacity of the synthesized MOF nanoparticles, leading to uptake in cancer cells and controlled drug release behavior.²⁹⁻³³ The bridge to achieve mesoporosity with large pore sizes of up to 20 nm in the formerly microporous MOFs was closed during the last few years. This makes these materials even more promising for the delivery of larger therapeutic agents.³⁴⁻³⁶

Mesoporous silica-based materials are another important class of porous nanoparticles for biomedical applications and basic scientific investigations. The whole research area of synthesizing mesoporous silica systems started back in 1991, when scientists from the American Mobil Oil Company successfully investigated the M41S systems.³⁷ These were the first structured mesoporous silica systems synthesized via a basic-catalyzed sol-gel process. Three different mesoporous representatives were synthesized through a self-assembled liquid crystal templating mechanism: the most-studied hexagonal MCM41 (Figure 1-3 a), the cubic MCM48 (b), and the lamellar MCM50 (c).

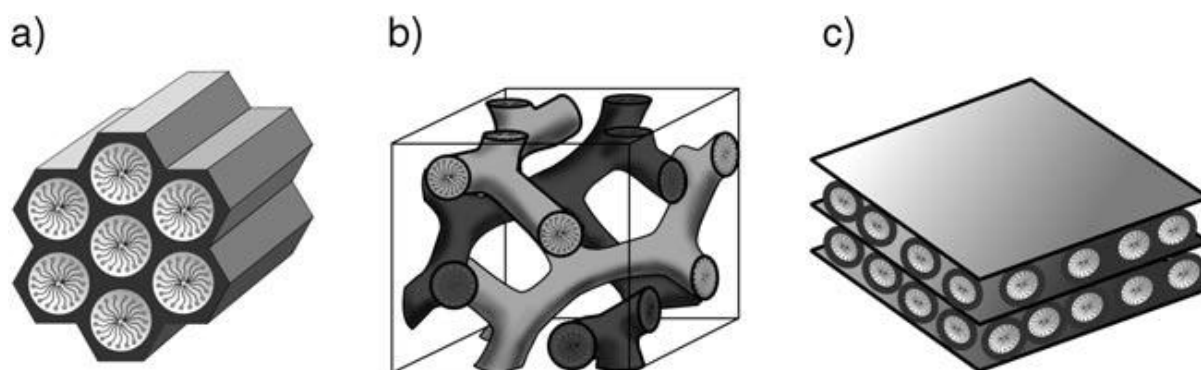


Figure 1-3: Structures of mesoporous silica systems: MCM41 (a), MCM48 (b), MCM50 (c).³⁸

The down-sizing of these materials to the nanoscale led to the synthesis of mesoporous silica nanoparticles (MSNs) with high colloidal stability, which quickly attracted growing attention as drug delivery systems for targeted cancer therapy and as bioimaging devices.³⁹⁻⁴¹ MSNs can feature a well-defined and tunable porosity, tunable pore sizes and pore shapes, high loading capacity, good control over synthesis and introduction of core-shell functionalization, and the possibility to attach different functionalizations for targeting and entering different types of cells.⁴² Generally, the synthesis of MSNs used in this work follows a base-catalyzed hydrolysis and condensation of the silica source in the presence of an organic template. The organic template forms micelles in the aqueous reaction medium and strongly influences the resulting pore diameter and shape.⁴³ Depending on reaction parameters such as temperature, pH value and surfactant to solution ratio the micelles form lamellar ($g = 1$), spherical ($g = 1/3$) or cylindrical ($g = 1/2$) structures. For this purpose, the characteristic parameter g is defined as the surfactant packing parameter.⁴⁴

$$g = \frac{2V}{ad}$$

Equation 1-1. g = surfactant packing parameter, V = Volume of the micelles of the organic template, a = surface interface of micelles, d = micelle diameter.

Figure 1-4 shows schematically the self-assembly of ionic surfactants and amphiphilic block-copolymer molecules into micelles acting as structure directing agents (SDA) for the synthesis of ordered porous nanostructures. Body centered cubic (bcc) packed spheres (BCC), hexagonally ordered cylinders (HEX), gyroids ($Ia\bar{3}d$), hexagonally perforated layers (HPL), modulated lamellae (MLAM), lamellae (LAM), cylindrical micelles (CYL), and spherical micelles (MIC) are common structures that can be formed by organic template molecules.

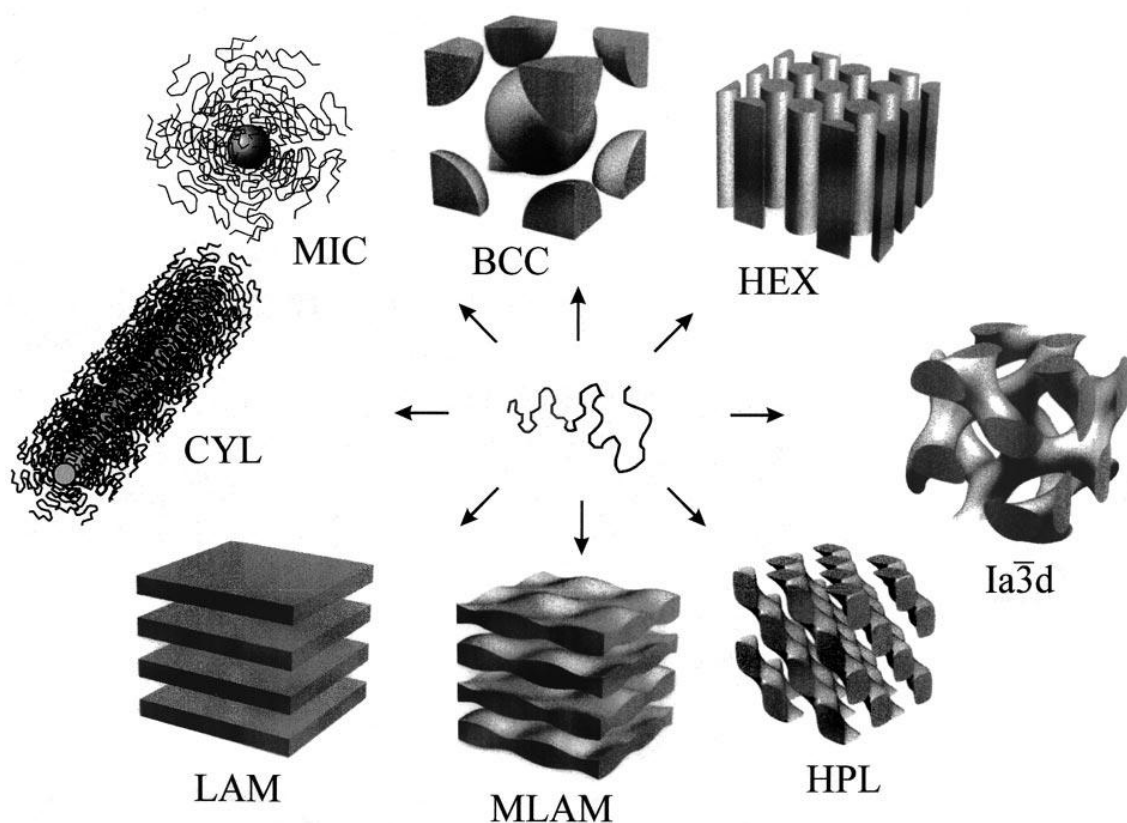


Figure 1-4: Schematic illustration of different template shapes of ionic surfactants and amphiphilic block-copolymers.⁴⁵

In case of a common MSN synthesis, the positively charged headgroups of the surfactant molecules are attracted to the anionic groups of the hydrolyzed silica precursor (usually tetraethyl ortho silicate, TEOS) by Coulomb forces. Subsequently, the silica source condenses and forms Si-O-Si bridges around the micellar template. In a subsequent step the

condensation proceeds and the silica framework is built around the surfactant micelles.⁴⁶ To slow down the reaction rate of the condensation process, and therefore controlling the particle size, the complexing agent triethanolamine (TEA) can be added to the reaction mixture.⁴⁷ In cooperation with a small amount of ammonium fluoride this leads to particles that are well-defined and controlled in size and shape. The mesoporous system is generally made accessible upon template extraction in boiling organic solvents or calcination at high temperatures (Figure 1-5).

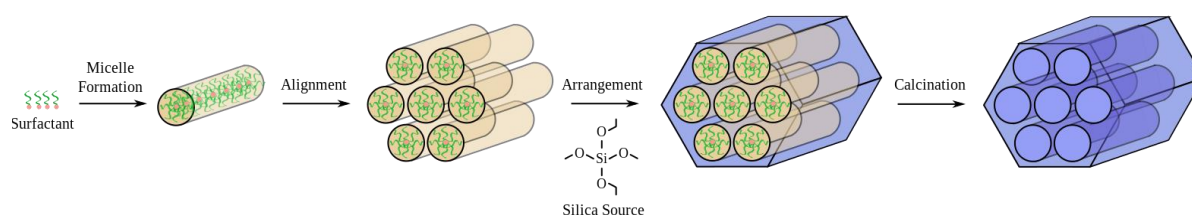


Figure 1-5. Illustration of a template-assisted MCM41 synthesis procedure.⁴⁸

Because of their favourable particle size, the exceptional pore parameters and the possibility to specifically functionalize their inner and outer surface, these MSNs are prominent representatives for nanoparticles in biomedical applications. In the following chapters, different materials classes, such as MSNs, periodic mesoporous organosilica nanoparticles (PMOs), superparamagnetic hybrid nanoparticles and supramolecular structures for high-performance multifunctional drug delivery and biomedical imaging and sensing are presented in detail.

1.3 Multifunctional drug delivery systems

1.3.1. Mesoporous silica nanoparticles

Mesoporous silica nanoparticles (MSNs) are widely studied for possible applications in targeted drug delivery because of their exceptional materials properties such as porosity,

biocompatibility and favorable particle sizes.^{49,50} However, the possibility to site-specifically functionalize MSNs makes them even more attractive for further investigations and applications in biomedicine and host-guest chemistry. Especially, the delayed co-condensation approach developed in our group leads to controlled and spatially segmented distribution of different functionalization of the pores and the external surface of MSNs (Figure 1-6).⁵¹ In a first step of the synthesis procedure, an organosilane precursor (green) and tetraethyl orthosilicate (TEOS) are mixed in an aqueous template solution containing the basic catalyst. This leads to the formation of a functionalized nanoparticle core. The nanoparticle growth is continued in a second step by the addition of a specific amount of pure TEOS (blue) resulting in an unfunctionalized silica shell around the functionalized core. With the addition of a second organotriethoxysilane (RTES, R represents an organic moiety, red) and TEOS the external surface with a different functionality is formed.

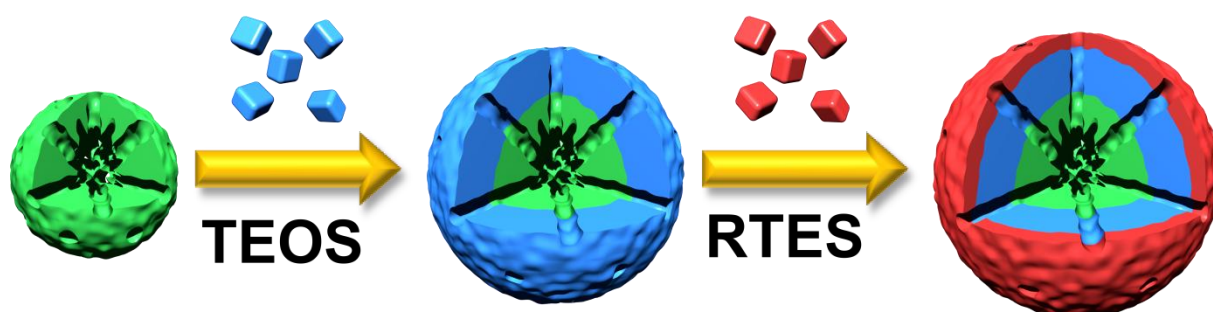


Figure 1-6: Delayed co-condensation approach for the synthesis of core-shell functionalized MSNs.

The introduced functionalization can be used for various applications. The functionalization of the internal pore structure can lead to controlled and well-defined interactions between the pore walls and the corresponding cargo molecules, e.g. to trigger the release only at the desired spot. The functionalization of the external surface can increase colloidal stability, and with varying the surface charge the interaction with living cells and other biological substrates

can be influenced. Different stimuli-responsive capping systems can be attached on the external particle surface by introducing specific organic moieties. The capping systems can open and close the pore system of the nanoparticles by using well-defined and controlled trigger mechanisms. Additionally, the external surface can be modified with specific targeting ligands that are able to recognize overexpressed receptors at cancer cell surfaces to release the cargo efficiently and to discriminate between healthy and cancerous cells with more efficient uptake kinetics.⁴² With the great advantages of all the aforementioned functionalization and the additional high storage capacity, MSNs can be developed as site-specific vehicles with the possibility to adjust properties to requirements. Figure 1-7 shows schematically the illustration of MSNs containing the necessary features for a stimuli-responsive controlled release of the loaded cargo into the cytosol of a targeted cell.

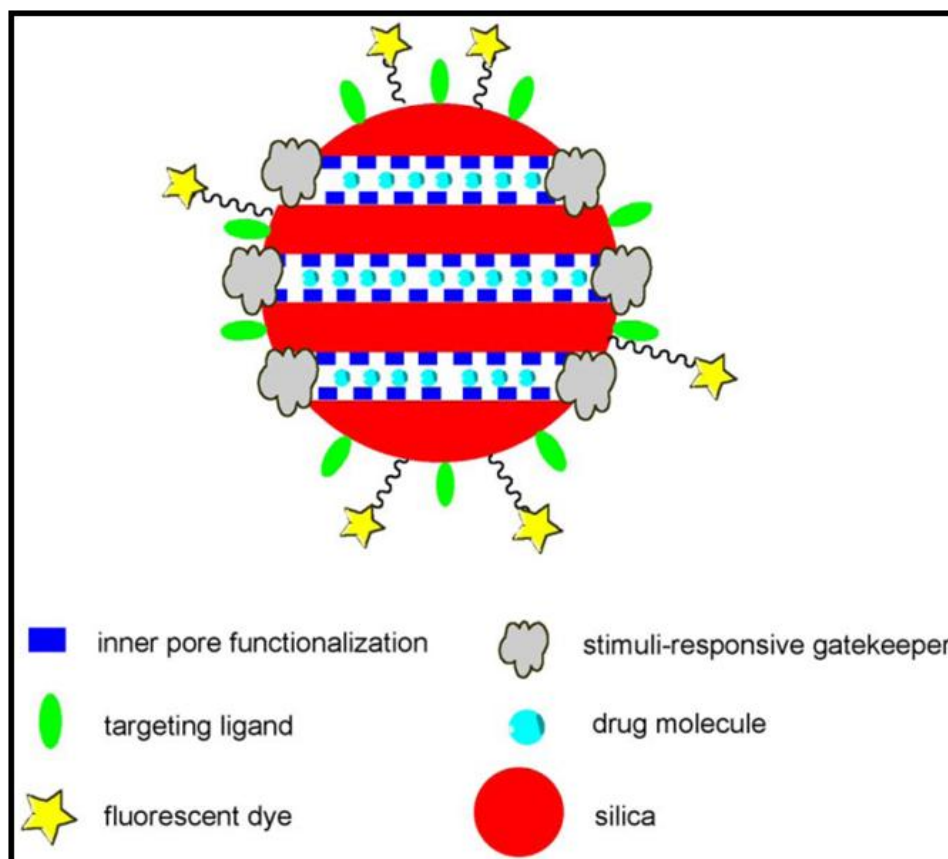


Figure 1-7: MSNs as highly functionalized drug delivery vehicles.

The stimuli-responsive gates can be specifically cleaved by either external (light, temperature, magnetic, ultrasound) or internal stimuli (pH, redox, enzyme) to release the cargo from the particles at the desired site. The fluorescent dye attached to the outer surface of the particle allows for monitoring the cellular uptake by using different fluorescence microscopy methods. The advantages of such a complex drug delivery system compared to common chemotherapeutic approaches include controllable release of the cargo and potential reduction of side-effects by specific attack of cancer tissue. Therefore, in principle the damage of healthy tissue by highly toxic chemotherapeutics can be avoided.

In the last decade, various studies were published using different capping and trigger strategies to achieve controlled drug delivery with MSNs, which are schematically shown in Figure 1-8. A few selected examples are described in the following.

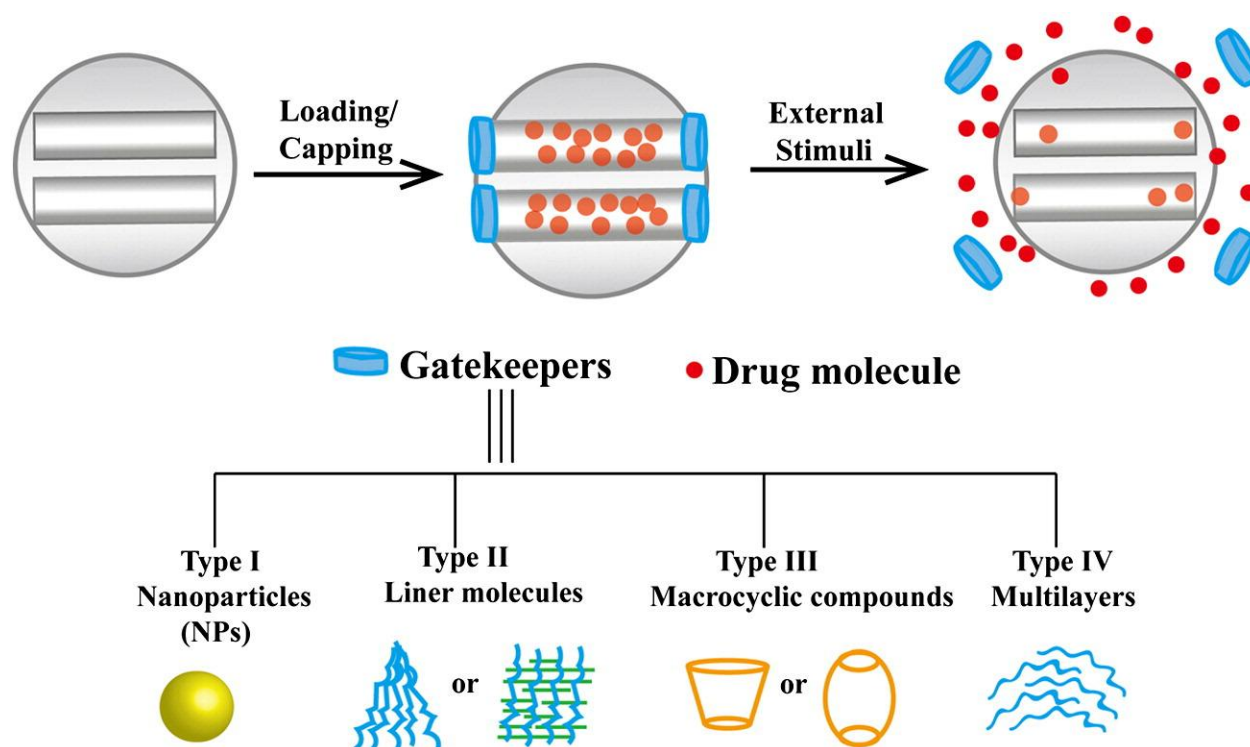


Figure 1-8: Different gatekeeper strategies on the pore outlets of MSNs for controlled drug delivery.⁵²

Different nanoparticles, such as Fe_3O_4 , Au, CdS or ZnO, can be covalently bound to the external particle surface and can be used to block the pore entrances of MSNs before being removed by applying specific external or internal triggers.⁵³⁻⁵⁵ An early example was shown by Lin *et al.* where iron oxide nanoparticles, covalently bound to the surface via redox-responsive cleavable disulfide linkers, could be removed from the pore entrances by applying external magnetic fields in combination with the cell-internal reductive milieu to achieve controlled cargo release.⁵⁶ In a similar redox-responsive mechanism CdS nanoparticles were used to release neurotransmitters and drug molecules.⁵⁷

In a second type of gatekeepers, linear molecules like polymers are often used to achieve efficient and controllable pore closure. A pH-responsive and reversible capping system was introduced by covalently attaching poly(2-vinylpyridine) (PVP) which uses the change in hydrophobicity upon protonation in the endosomal cell compartments to open the pore system.⁵⁸ Moreover, high colloidal stability was achieved due to an additionally coupled PEG

shell which offers the ability to covalently attach a wide variety of dyes, targeting ligands and other functionalities at the outer periphery. Other polymers like poly(N-isopropylacrylamide) (PNIPAM) were used as a temperature-sensitive capping system on MSNs.⁵⁹ These nanoparticle-polymer composites show temperature-dependent uptake and release of different cargos. The response is correlated to the lower critical solution temperature (LCST) of the polymer and its corresponding phase transition from a random coil to a globular structure at reduced temperatures. Ultrasound can also be used as an external trigger for polymer-grafted MSNs, exploiting the change in hydrophobicity of the corresponding polymer and therefore effectively controlling the cargo release upon the action of remote stimuli.⁶⁰

In another general type of capping systems macrocyclic compounds such as cyclodextrins, crown ethers, cucurbit[6]urils or proteins are attached to the pore outlets of MSNs through covalent or non-covalent interactions that can be cleaved by certain stimuli, thereby clearing the pore entrances.⁶¹⁻⁶⁸ Cyclodextrins were developed as a prominent representative for macrocyclic gatekeepers on MSNs and combined with various external or internal triggers. The groups of Fraser Stoddart, Jeffrey Zink *et al.* developed different pH-responsive systems usually consisting of a layer of β -cyclodextrin (β -CD) rings positioned selectively around the orifices of the mesopores of silica nanoparticles. Under neutral conditions even large cargo molecules (e.g. rhodamine) could be stored effectively in the porous system whereas under slightly acidic conditions the cargo was released upon removal of the cyclodextrin.⁶⁹⁻⁷¹ Another cyclodextrin-based pH-responsive capping system was investigated by Kim *et al.* who post-synthetically functionalized MSNs with polyethylenimine (PEI).⁷² This surface was subsequently complexed with cyclodextrines. By slight acidification (pH ~ 5) afterwards, the PEI backbone gets positively charged and the cyclodextrine caps are detached from the surface. As an early example for protein-coated MSNs, an enzyme-mediated capping system

based on the well-studied biotin-avidin complex was developed by Schlossbauer et al.. Herein, biotin-functionalized MSNs with encapsulated cargo molecules were capped by the bulky protein avidin from egg white via noncovalent interactions with the biotin molecules on the external particle surface. After addition of the protease trypsin, simulated as a cell-internal trigger, the linkage between biotin and avidin was cleaved and the cargo could be released.⁷³

Figure 1-8 shows a fourth general type of pore blockers, which is multilayers such as supported lipid bilayers (SLB) or layered double hydroxides.⁷⁴⁻⁷⁸ Recently, Bein and co-workers could demonstrate different systems consisting of MSNs coated with an SLB and equipped with different external trigger mechanisms. The SLB was shown to seal the pores and to prevent premature release of the loaded cargo. Upon activation of an incorporated photosensitizer with red light, the subsequent generation of reactive oxygen species initiated cargo release due to rupture of the SLB. Photosensitizers are promising components of nanocarrier systems for efficient drug delivery because they can simultaneously cause endosomal escape and controlled cargo release in combination with SLB-coated MSNs.

In order to effectively trigger efficient cargo release within the cancerous tissue, targeting of cancer cells with nanoparticles is viewed as a promising approach to avoid unwanted side effects observed with classic chemotherapeutics. Especially in anticancer chemotherapy, the limited selectivity of the clinically used cytostatic agents towards tumor cells is responsible for many undesired side effects. Nonspecific toxicity to normal cells can cause these severe side effects and prevents an effective killing of malignant cells requiring a higher drug dose.^{79,80} Nanoparticles with sizes smaller than 500 nm are often taken up via endocytosis where they are engulfed by the cell membrane and transferred as intracellular endosomal or lysosomal vesicles.^{81, 82} A passive targeting approach based on nanoparticles relies on the enhanced permeability and retention (EPR) effect, which is described as the tendency of particles (in the nanometer size range), such as nanoparticles, liposomes, or macromolecular

drugs, to preferentially accumulate in tumor tissue.⁸³ Tumorous and inflamed tissues typically reveal increased permeable vascularities and are lacking effective lymphatic drainage. Additionally, a lack of cell-specific interactions might affect the therapeutic efficiency and induce multiple drug resistance (MDR).⁸⁴⁻⁸⁷ The cellular uptake kinetics are strongly dependent on the size of the applied nanoparticles *in vitro* as well as *in vivo*. It was shown that the cellular uptake of specific nanoparticles *in vitro* on HeLa cells is highly size-dependent in the order 50 nm > 30 nm > 110 nm > 280 nm > 170 nm.^{88, 89}

In order to overcome the pitfall of unspecific cell uptake and to enhance the specificity achieved by the EPR effect, different targeting ligands, like folic acid or the epidermal growth factor (EGF), can be employed in order to exploit the overexpression of certain receptors on tumor cell surfaces which will lead to enhanced binding to tumor cells and subsequent interaction with targeting ligands. Figure 1-9 shows an overview of different overexpressed cell membrane receptors on cancer cells used in preclinical investigations of cancer treatment. This active targeting can promote specific nanocarrier binding and cancer-cell uptake. In particular, active nanoparticle-based targeting of tumor cells has emerged as a potential therapeutic approach to increase drug doses within the tumor while reducing systemic toxicity.^{90, 91} Cell-specific targeting can be achieved by engineering of nanoparticles with defined ligands on their surface that bind to receptors which are specifically overexpressed on cancer cells. One prominent example is nanoparticles that target the epidermal growth factor receptor (EGFR). This receptor is overexpressed in several types of cancer including breast carcinoma, colon carcinoma, and lung cancer.⁹² Nanoparticles are often functionalized with EGFR ligands and designed to deliver either silencing agents against defined oncogenes or chemotherapeutic drugs.⁹³ These nanoparticles are then preferentially recognized and bound by tumor cells overexpressing EGFR, and are rapidly taken up into the cell by receptor-

mediated endocytosis where the drug is released intracellularly to specifically kill the tumor cell.⁹⁴

Major receptor type	Specific receptor(s)	Overexpression in cancer cell types
G protein coupled receptors (GPCRs)	<i>Bombesin receptor (BnR)</i>	Lung, prostate, breast, pancreatic, head/neck, colon, uterine, ovarian, renal cell, glioblastomas, neuroblastomas, gastrointestinal carcinoids, intestinal carcinoids, and bronchial carcinoids.
	<i>Somatostatin receptors (SSTRs)</i>	Small cell lung, neuroendocrine tumor, prostate cancer, breast cancer, colorectal carcinoma, gastric cancer, hepatocellular carcinoma
	<i>Endothelin receptors (ETRs)</i>	Melanoma tissues
Integrins	<i>$\alpha v\beta 3$ is of particular interest in selective drug targeting</i>	Activated endothelial cells and tumor cells (such as U87MG glioblastoma cells), ovarian cancer cells.
Folate receptors (FRs)	<i>FRα, FRβ and FRγ</i>	Most tissues including breast cancer cells.
Transferrin receptors (TfRs)	<i>Two types of receptors only have been described so far</i>	Breast, ovary, and brain cancers such as glioma and glioblastomas.
Epidermal growth factor receptor (EGFR)	<i>EGFR (or ErbB1, HER1), ErbB2 (HER2, neu in rodents), ErbB3 (HER3) and ErbB4 (HER4)</i>	Lung, breast, bladder, and ovarian cancers.
Fibroblast growth factors (FGFRs)	<i>A hallmark of FGFRs is the presence of an acidic, serine-rich sequence</i>	Breast, prostate, bladder, and gastric cancer
Sigma receptors (SRs)	<i>S1R and S2R</i>	Non-small cell lung carcinoma, prostate cancer, melanoma, and breast cancer.
Others	<i>Follicle stimulating hormone receptors (FSHRs)</i>	Ovarian surface epithelium
	<i>Biotin receptors (BRs)</i>	Leukemia
	<i>C-type lectin receptors (CLRs).</i>	Hepatocytes, dendritic cells, macrophages
	<i>NRP-1</i>	Human vascular cells

Figure 1-9. Summary of overexpressed cell membrane receptors on different cancer cells.⁹⁵

Another prominent ligand used on mesoporous silica nanoparticles is the small molecule folic acid (FA), which has been widely investigated and has shown a notable enhancement in uptake efficiency and kinetics of MSN nanocarriers on different cancer cell types.^{58, 96-98} In general, the attachment of targeting ligands onto the external surface of spherical MSNs is

often achieved by using long spacer molecules, such as PEG chains or other linear or branched polymers. This linkage provides high flexibility to obtain efficient binding of the targeting ligands to the cell membrane receptors. In another example, the group of Wilner *et al.* exploited the overexpression of transferrin receptors on breast cancer cells and glioblastoms by synthesizing specific aptamers via a modified stable nucleic acid lipid particle (SNALP) protocol which led to enhanced cancer cell uptake in various cell lines.⁹⁹

In obvious contrast to the ever-growing number of sophisticated nanoparticle-based cell-targeting strategies that effectively target tumor cells *in vitro*, only few studies showed successful tumor-cell specific targeting and controlled cancer cell killing *in vivo*. Even fewer nanoformulations have found their way into clinical studies and practice.¹⁰⁰ This translational gap is partly due to insufficient data on cell-specific targeting *in vivo* and the lack of physiologically and clinically relevant animal models.^{101, 102} Although the main research interest in the nanoparticle field lies on the investigation of effective active targeting approaches, one of the few clinically relevant examples so far is DOXIL[®], a PEGylated doxorubicin formulation, which is exploiting exclusively passive targeting pathways via the EPR effect.¹⁰³ Active tumor targeting without nanoparticles is shown by HERCEPTIN[®] from Roche, a humanized monoclonal antibody that can bind effectively to the HER2 receptors which are overexpressed on breast cancer cells.

Another important bioapplication of MSNs is *in vitro* and *in vivo* imaging. With the possibility to functionalize MSNs specifically with different dye molecules or to combine them with other materials the field of application ranges from optical microscopy to magnetic resonance imaging, and to ultrasonic imaging, near infrared imaging and other techniques.^{104,105} To investigate cellular internalization of the nanoparticles, MSNs can be covalently modified by the conjugation with fluorescent dye molecules, such as FITC or

RITC. He *et al.* used fluorescein-modified MSNs in order to investigate the particle shape and size on the uptake kinetics in A375 cancer cells (Figure 1-10).¹⁰⁶

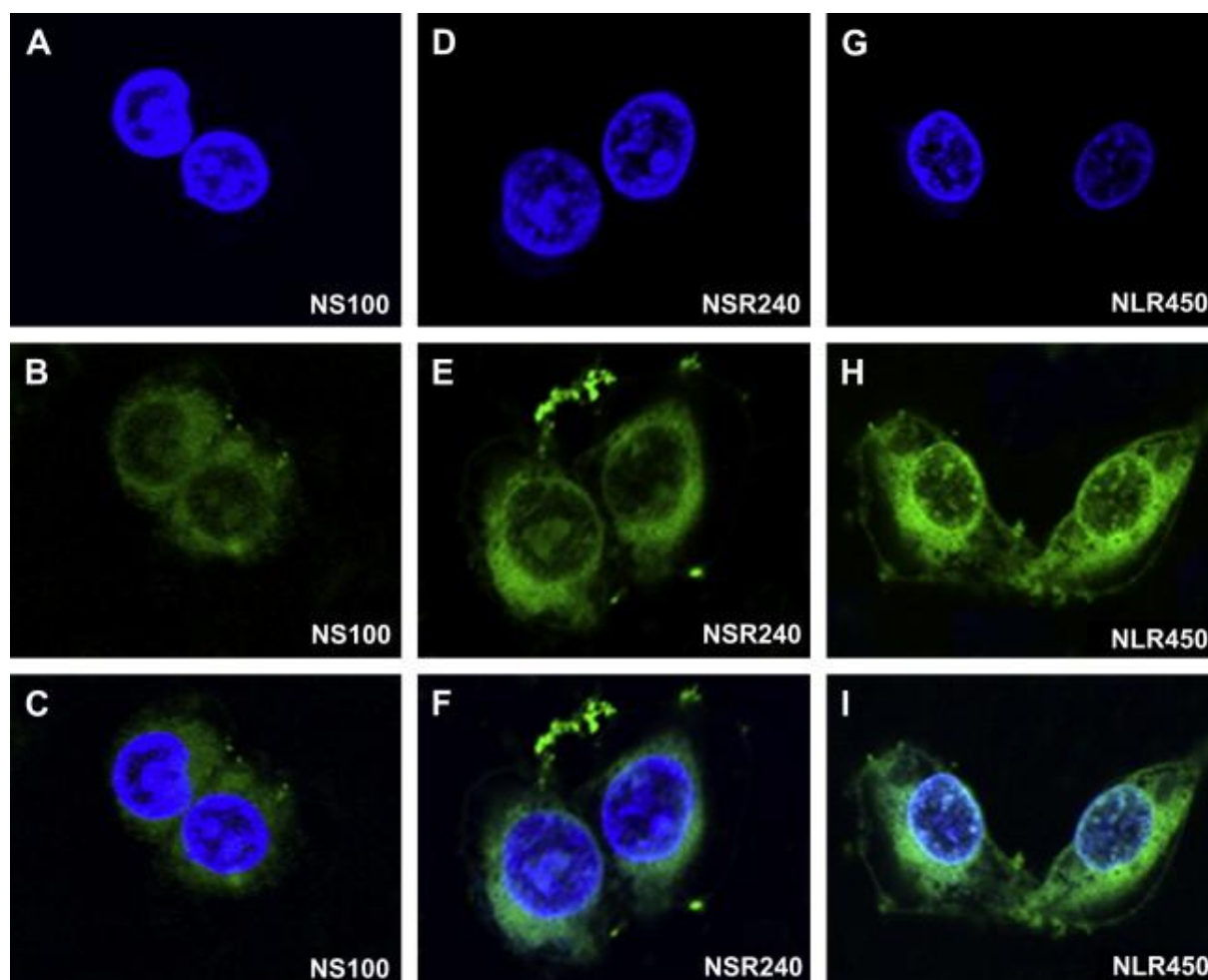


Figure 1-10. Confocal microscopy images of A375 cells after 4 h incubation at 37 °C with MSN nanoparticles with different functionalization. Fluorescent images of the cell nucleus (A, D, G), images of MSN-FITC fluorescence in cells (B, E, H), image of MSN-FITC fluorescence superimposed on the nucleus (C, F, I).¹⁰⁶

Mesoporous silica nanoparticles were successfully equipped with different functionalities to become excellent bimodal imaging probes for intracellular labeling and *in vivo* magnetic resonance imaging (MRI) contrast agents. Mou *et al.* showed the first *in vivo* application of magnetic-MSN hybrids via direct injection into mice for MRI experiments.¹⁰⁷ Yang *et al.* synthesized theranostic nanoparticles that can act as an effective MRI/NIRF bimodal imaging probe and operate in combination with an effective drug delivery system that shows great

potential in cancer diagnosis and therapy.¹⁰⁸ By functionalizing MSNs specifically with near-infrared (NIRF) dyes, such as Cy7, in combination with an incorporated iron oxide core this platform can be used for NIRF and magnetic resonance imaging of tumorous tissue *in vivo* (Figure 1-11).

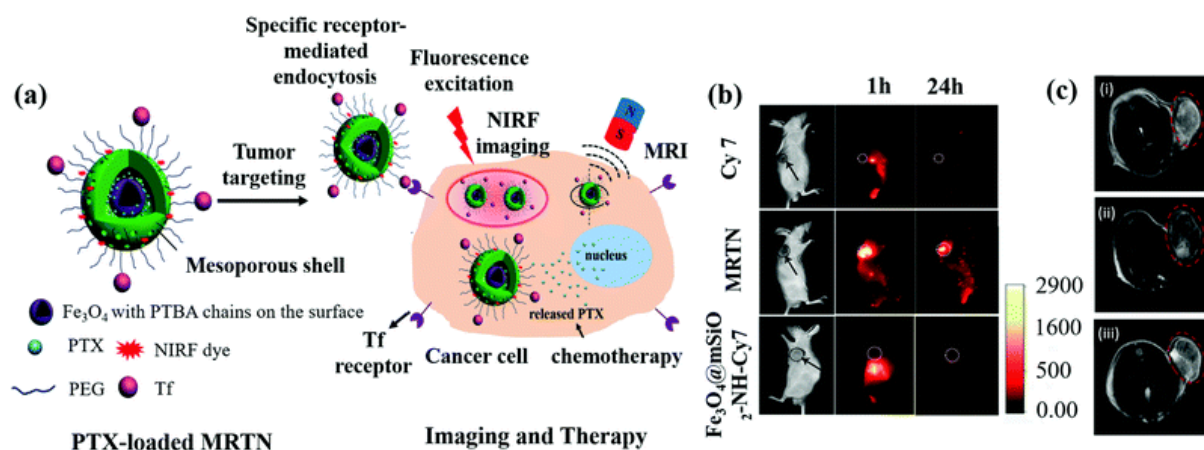


Figure 1-11. (a) Schematic representation of PTX-loaded $Fe_3O_4@mSiO_2$ NPs for tumor targeting, MRI, fluorescence imaging and chemotherapy. (b) In vivo NIRF imaging of the pure NIRF dye (Cy7), MRTN and $Fe_3O_4@mSiO_2-NH-Cy7$ in A549 lung cancer tumor-bearing mice (marked with a circle) at 1 and 24 h post injection. The first column shows the bright field images of the tumor-bearing mice. (c) In vivo MRI of a tumor-bearing mouse (SW620 tumor, marked with the circle) without injection (i), and at 1 h post injection of MRTN (ii) and $Fe_3O_3@mSiO_2$ nanorattle (iii).¹⁰⁸

1.3.2. Periodic mesoporous organosilica

In recent years, periodic mesoporous organosilica materials (PMO) have attracted much attention for biomedical applications. Since this class of inorganic-organic hybrid materials offers a wide variety of tunable mesopores and an almost unlimited diversity in the chemical nature of the walls, it holds great promise in a variety of fields such as chemical sensing,¹⁰⁹⁻¹¹⁵ catalysis¹¹⁶⁻¹²⁰ and biomedical applications.¹²¹⁻¹²³ Since the independent discovery of this new class of mesoporous materials in the groups of Inagaki, Stein and Ozin in 1999,¹²⁴⁻¹²⁶ PMO materials, synthesized by using bridged silsesquioxanes as precursors, have recently been

prepared at the nanoscale.¹²⁷⁻¹²⁹ Figure 1-12 shows the schematic synthesis route of mesoporous and non-porous organosilica materials with or without the presence of TEOS as silica source. These different types of organosilica composite nanomaterials can be distinguished in the following four categories: mesoporous organosilica, non-porous organosilica, periodic mesoporous organosilica, and non-porous silsesquioxane NPs.

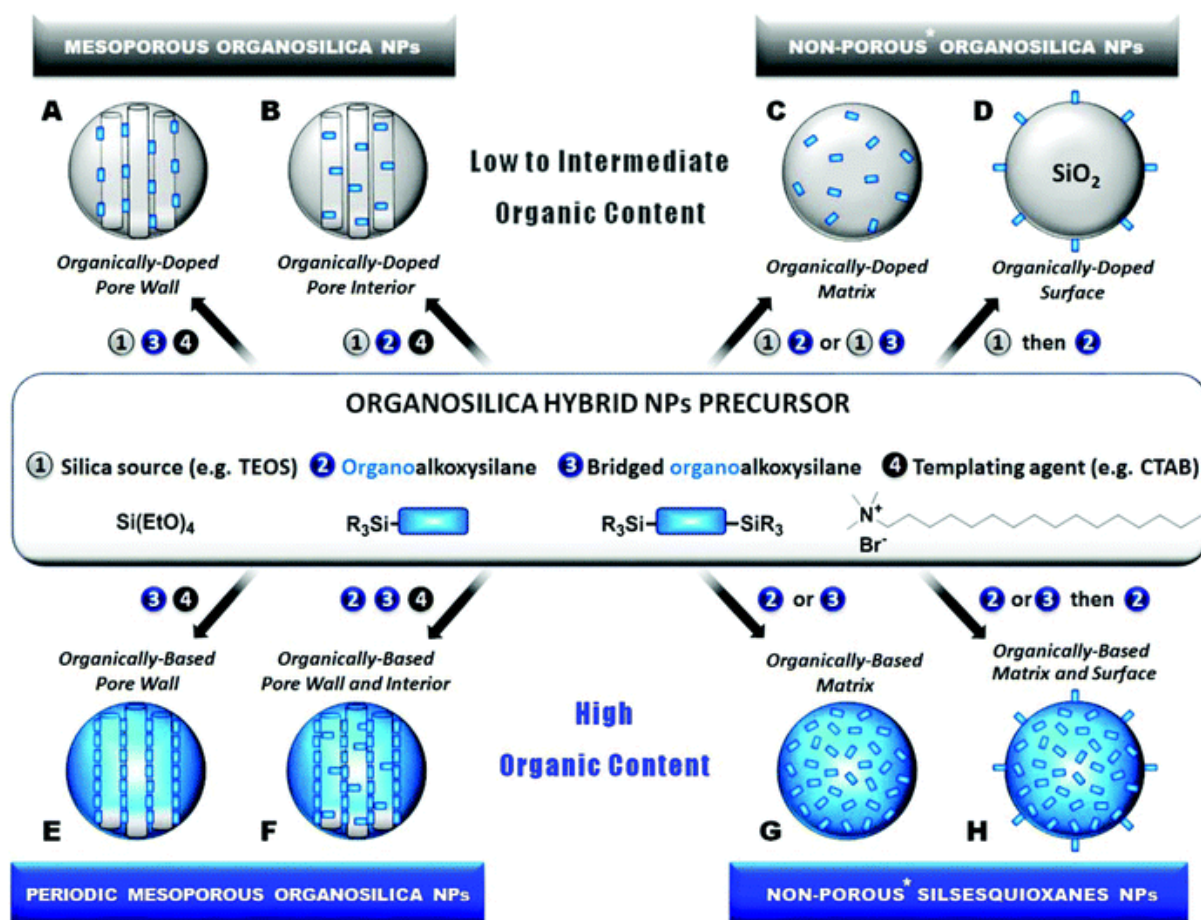


Figure 1-12. Structures and synthetic pathways of various organosilica nanocomposites: organically-doped mesoporous silica NPs (A and B), organically-doped (C) and surface-functionalized (D) non-porous silica NPs, periodic mesoporous organosilica NPs (E and F),* and non-porous silsesquioxane NPs with or without surface functionalization (H and G respectively). Cetyltrimethylammonium bromide (CTAB) is a typical surfactant in sol–gel processes. Organoalkoxysilane and bridged organoalkoxysilane precursors can possess ethoxy or methoxy R groups. *Not sensu stricto but generally with a disorganized low micro or mesoporosity.¹³¹

The PMO structures are based only on silsesquioxanes, which implies that the synthesis must be performed in the absence of a silica source (e.g. tetraethoxysilane), and that there is sufficient porosity to be considered a mesoporous material, which is often a major synthetic challenge.¹³⁰ Mesoporous organosilica NPs could be prepared by co-condensation of a silica source (e.g. tetraethoxysilane (TEOS)) with a mono or a bridged organoalkoxysilane in a templated aqueous solution which leads to nanoparticles with functional pores (Figure 1-12

A, B). A template-assisted sol-gel synthesis route with bridged organoalkoxysilanes without additional TEOS as the silica source affords particles with much higher organic wall content (Figure 1-12 E, F). Without using any template during the synthesis procedure, non-porous organosilica or silsequioxane particles can be prepared (Figure 1-12 C, D, G, H). Different approaches were used to synthesize PMO nanoparticles with simple, low-molecular-weight organosilane bridging groups. In a sol-gel process using Pluronic P123 as the template, Landskron *et al.* synthesized rodlike nanoparticles with adjustable aspect ratios.¹³² Using cetyltrimethylammonium bromide (CTAB) as the micellar template and an ammonia-catalyzed sol-gel reaction, Huo *et al.* prepared highly ordered and dispersible PMO nanoparticles with methane, ethane, ethylene and benzene organic bridging groups within the pore walls (Figure 1-13).¹³³

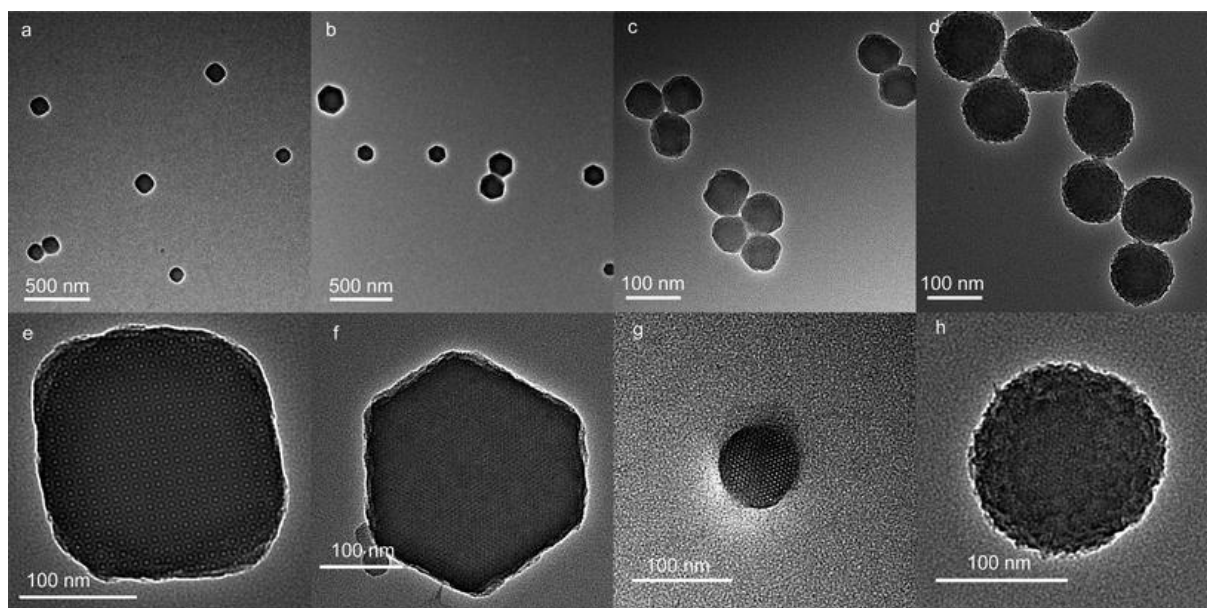


Figure 1-13. TEM images of ethylene- (a, b), methylene- (c, d), ethynylene- (e, f), and phenylene-bridged PMO NPs (g, h) at low and high magnification.¹³³

In another approach, the group of Shi *et al.* used silica-etching chemistry to obtain hollow PMO nanoparticles that were used for nano-biomedical applications for the first time.¹³⁴

Recently, the group of Durand reported the synthesis of biodegradable PMO nanospheres and

nanorods with a disulfide-containing organic bridging group. The morphology and size of these nanostructures was controlled by adjusting the ratio of bis(triethoxysilyl)ethane and bis(3-triethoxysilyl-propyl)-disulfide (Figure 1-14).¹³⁵ These mixed PMO nanospheres and rods were used as a biodegradable nanocarrier for doxorubicin in breast cancer cell lines. In the group of Kashab *et al.*, enzymatically degradable silsesquioxane nanoparticles were synthesized and used as fluorescent nanoprobe for *in vitro* imaging of cancer cells.¹³⁶ Zink and co-workers developed different light-activatable and pH-responsive hybrid materials for drug delivery applications.¹³⁷⁻¹³⁹

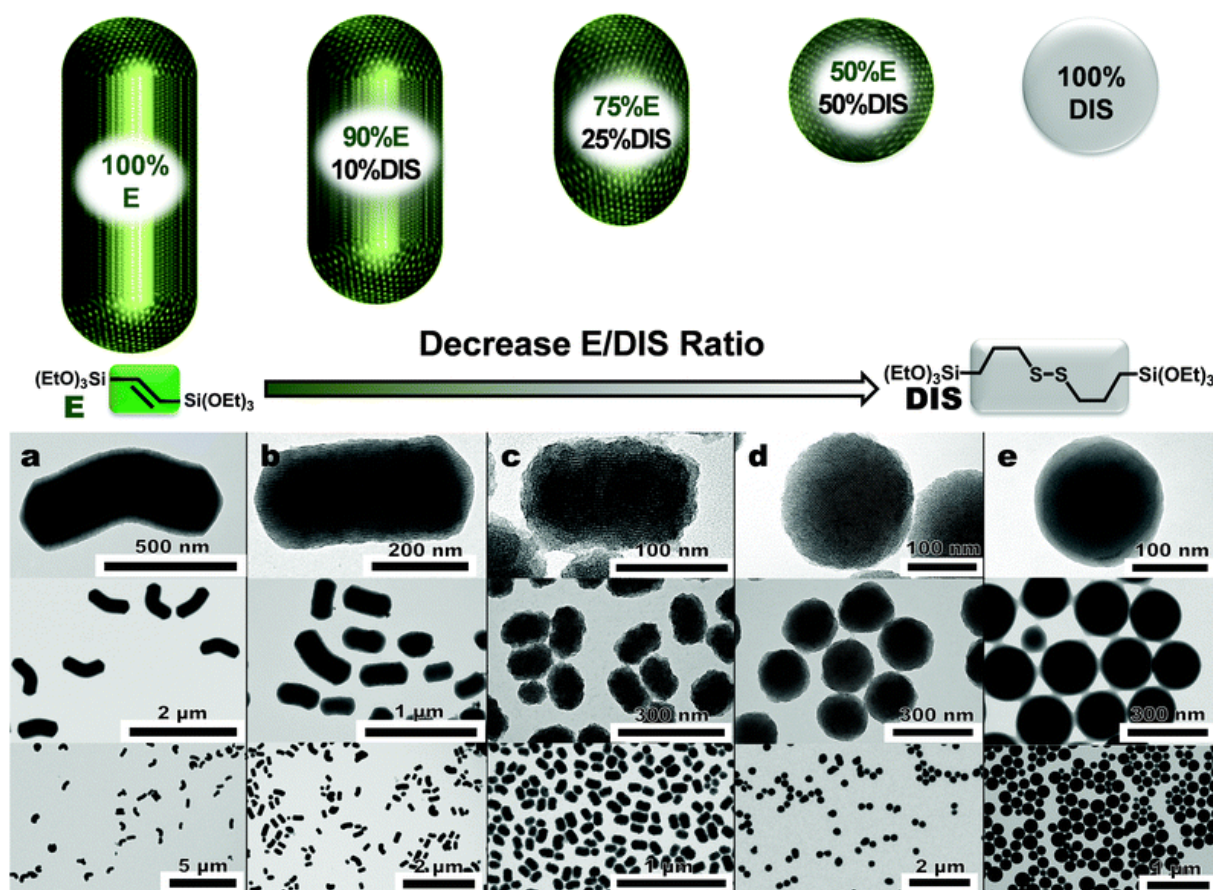


Figure 1-14. Schematic representation of the size and morphology control in ethynylene-bridged PMO (a), ethynylene-bis(propyl)disulfide-bridged PMO (b-d), and non-porous bis(propyl)disulfide bridged silsesquioxane NPs (e) by the variation of the E/DIS precursor ratio in the reaction media. TEM images of NPs obtained from E/DIS ratios of 100/0, 90/10, 75/25, 50/50, and 0/100 (a-e respectively).¹³⁵

Besides the described drug delivery applications, PMO nanoparticles were also investigated as bioimaging tools in *in vitro* and *in vivo* experiments. Due to the great variety of organic components that could be incorporated into organosilica nanostructures, several strategies have been explored to endow the particles with imaging capabilities. The first approach of bioimaging via PMO nanoparticles involved the synthesis of a hybrid material consisting of Nile red dyes and a large conjugated molecule as the main organic components. This structure was used to generate Förster resonance energy transfer (FRET) upon two-photon-excited fluorescence-imaging in the near-infrared range and allowed for successful *in vitro* particle tracking.¹⁴⁰ Another important aspect of bioimaging was successfully investigated in the group of Lin. By synthesizing a biodegradable polysilsequioxane with an extremely high incorporation of paramagnetic Gd(III) centers, this material was explored as an efficient contrast agent for magnetic resonance imaging (MRI).¹⁴¹ Herein, a disulfide-containing Gd(III) diethylenetriamine pentaacetate (Gd-DTPA) silane precursor was reacted in a base-catalyzed reverse microemulsion experiment to form biodegradable nanoparticles. The Gd(III)-containing nanoparticles showed high T_1 -weighted sensitivity and were demonstrated in *in vitro* MR imaging of human lung and pancreatic cancer cells. With the ability to incorporate additional specific photosensitizers into the organosilica wall material of PMO nanoparticles, these structures can also be used in photodynamic therapy (PDT). Upon appropriate laser irradiation, photosensitizers can generate reactive oxygen species, such as singlet oxygen (1O_2).^{142, 143} Hayashi and co-workers recently reported one of the most advanced PDT studies in *in vivo* therapy by using organosilica NPs consisting of porphyrin building blocks as well as iodopropyl silanes as the main organic components (Figure 1-15 A, B).¹⁴⁴ The synthesized monodisperse 50 nm spherical particles combine photodynamic and photothermal therapy (PTT) to effectively treat tumor-bearing mice. The relative quantum yield of the production of singlet oxygen in these particles was enhanced via the external

heavy atom effect of the incorporated iodine affording a higher yield (0.85) than that of photosensitizers currently used in clinics and clinical trials (0.3 to 0.77).¹⁴⁵ With laser irradiation at 650 nm the nanoparticle-treated mice showed a tumor growth ten times lower than the control group and survived the complete experimental time of ten weeks (Figure 1-15 C, D).

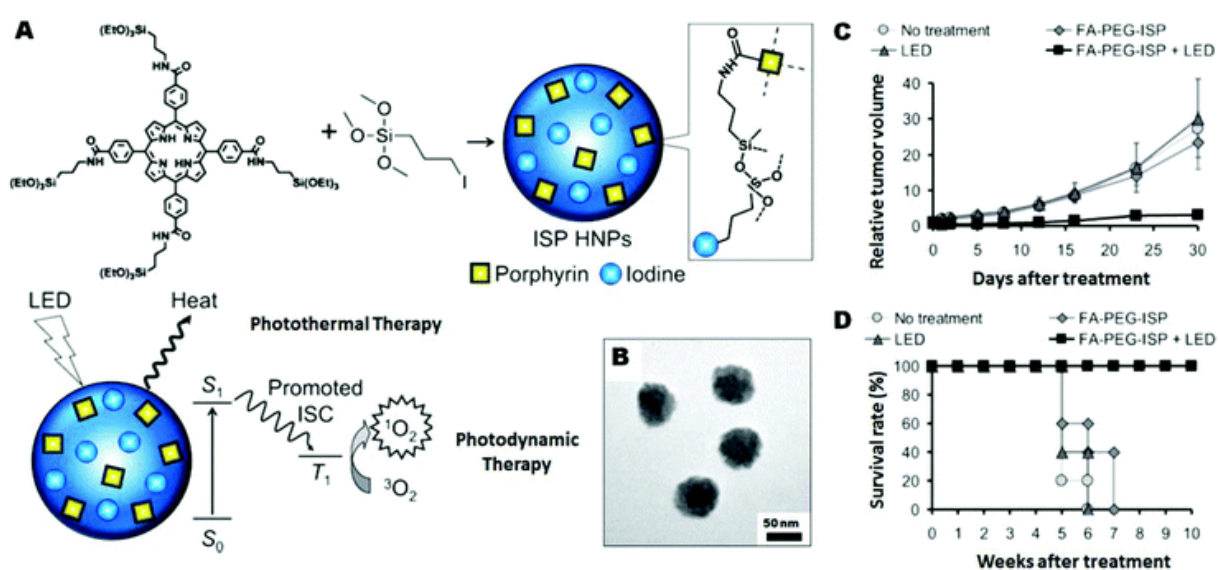


Figure 1-15. Synthesis of iodine-porphyrin containing organosilica hybrid nanoparticles and their PDT/PTT combination therapy by the enhancement of $^1\text{O}_2$ generation via the heavy atom effect and the conversion of the energy absorbed from photons into heat (A). TEM image of the as-synthesized nanoparticles (B). Tumor growth behavior (C) and the survival period of mice (D) (circle: mice without treatment, diamond: mice injected with nanoparticles, triangle: mice exposed to LED light, square: mice exposed to LED light after injection of nanoparticles).¹⁴⁴

Due to their unique capability of introducing an almost unlimited number of organic constituents into the wall structure of porous nanoparticles, PMO nanomaterials constitute a very promising new area of research in the following decade. The remarkable control of the synthesis and composition of such particles offer a wide variety of possible application fields.

1.3.3. Magnetic nanocomposites

Nanocomposites with a magnetically responsive core and a functional outer shell have attracted increasing attention because of their unique functionality and separability.¹⁴⁶ Especially the coating of superparamagnetic iron oxide nanocrystals with a multifunctional mesoporous silica shell has opened up a wide range of applications including magnetic resonance imaging (MRI), hyperthermia treatment, applications in toxin removal, waste remediation, catalysis, reactive sorbents, and targeted drug delivery, since they combine different advantageous properties in one multifunctional nanocomposite.¹⁴⁷⁻¹⁵⁰ The first step in the exploration of these nanocomposites is the synthesis of small and stable magnetic nanoparticles (NPs).

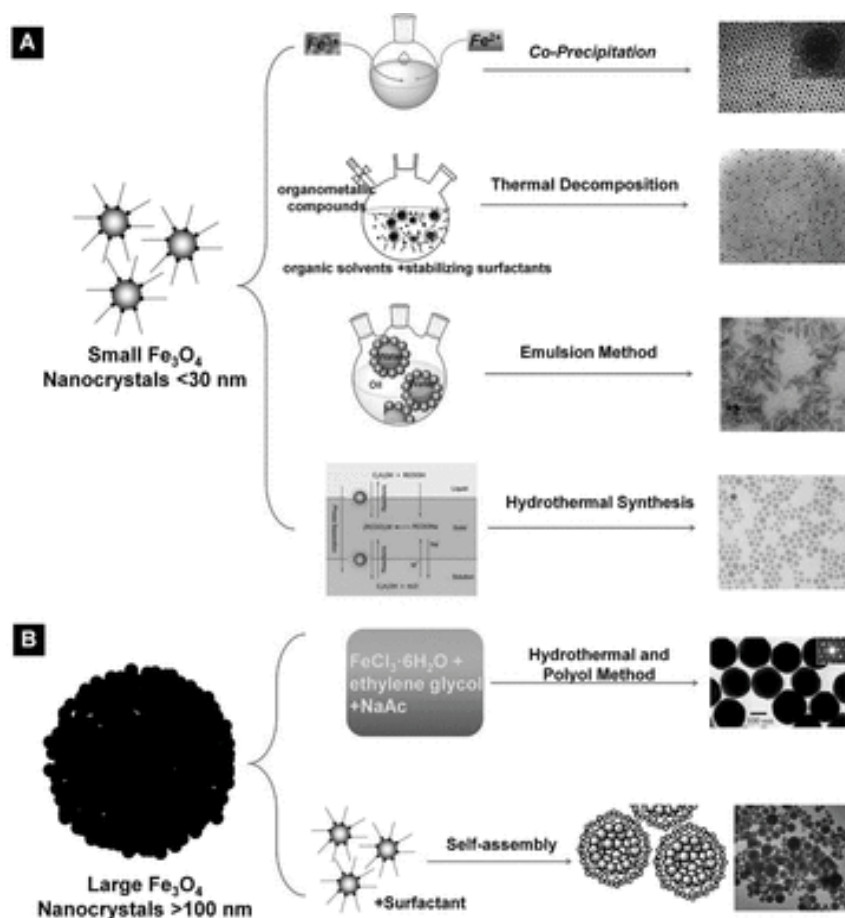


Figure 1-16. Schematic illustration of different methods for preparation of magnetic nanoparticles: A) synthesis of magnetic NPs smaller than 30 nm, and B) synthesis of magnetic NPs larger than 100 nm.¹⁵¹

Magnetic NPs can be synthesized with a number of different compositions and phases including pure iron oxides such as magnetite (Fe_3O_4) and maghemite ($\gamma\text{-Fe}_2\text{O}_3$), or alloys such as FePt, as well as spinel-type ferromagnets such as NiFe_2O_4 . Using different synthesis approaches, such as co-precipitation, thermal decomposition, the emulsion method or hydrothermal synthesis small and stable high-quality magnetic nanocrystals can be prepared (Figure 1-16 A).¹⁵²⁻¹⁵⁵ Because of their exceptional stability under a large range of conditions, the most common method for the production of magnetic NPs with particle diameters below 30 nm is the chemical co-precipitation of iron salts. The polyol method and different self-assembly approaches are generally adapted for the synthesis of magnetic nanoparticles with a particle size larger than 100 nm

(Figure 1-16 B). Nano-sized magnetic NPs with particle diameters smaller than 20 nm exhibit superparamagnetic properties without a permanent magnetic moment but just one single crystal domain, which allows for targeting of biological samples by exposure to an external magnetic field.^{156, 157}

Due to their hydrophobic exterior after the synthesis, magnetic NPs consisting of iron oxide can aggregate rapidly into large clusters and thus lose their unique properties associated with the presence of single particles. In order to prevent this behavior, the magnetic NPs have to be coated with different materials to prevent them from irreversible aggregation. This can be achieved by generating a core-shell structure with the magnetic nanocrystal as the inner part and an outer, more hydrophilic mesoporous silica shell built around it.

Hyeon and coworkers were the first who reported back in 2008 the synthesis of magnetic NPs coated with fluorescently labeled mesoporous silica shells that were utilized as drug nanocarriers.¹⁵⁸ With the usage of cetyltrimethylammonium bromide (CTAB) as the surfactant different tasks in this specific synthesis approach were addressed. The surfactant

molecules transfer the as-synthesized hydrophobic iron oxide NPs to the aqueous phase via a ligand-exchange process. Additionally, the surfactant molecules can act as a template for the following sol-gel reaction of the silica source creating core-shell particles with a magnetic core and a mesoporous silica shell after subsequent template extraction (Figure 1-17).

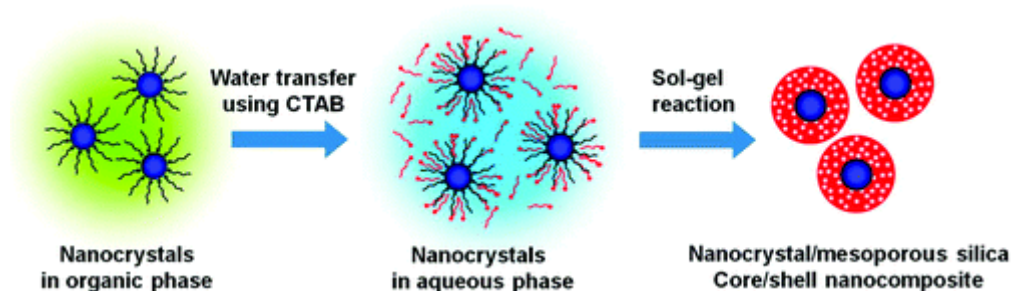


Figure 1-17. Synthesis scheme for the coating of hydrophobic magnetic nanoparticles with a mesoporous silica shell.¹⁵⁰

The obtained nanocomposites feature high surface areas and pore volumes in addition to the ability to react to externally applied magnetic fields, which makes these vehicles promising candidates for targeted drug delivery.^{159, 160}

Zink and co-workers showed an early example of successful *in vitro* drug release by using a magnetic-silica hybrid nanomaterial.¹⁶¹ These nanoparticles featured a nanovalve that remained closed at physiological temperature and opened when heated as a result of external magnetic heating procedures. The material demonstrated successful doxorubicin release in the breast cancer cell line MDA-MB-231 in the presence of the oscillating magnetic field (Figure 1-18). The local heating caused by the incorporated nanocrystals facilitated the release of doxorubicin from the silica pores, inducing effective apoptosis in the *in vitro* experiments. In contrast, non-loaded particles showed less toxicity due to hyperthermia effects only. Thus,

both hyperthermia and drug delivery contributed to cell death and the nanoparticles showed a synergistic effect.

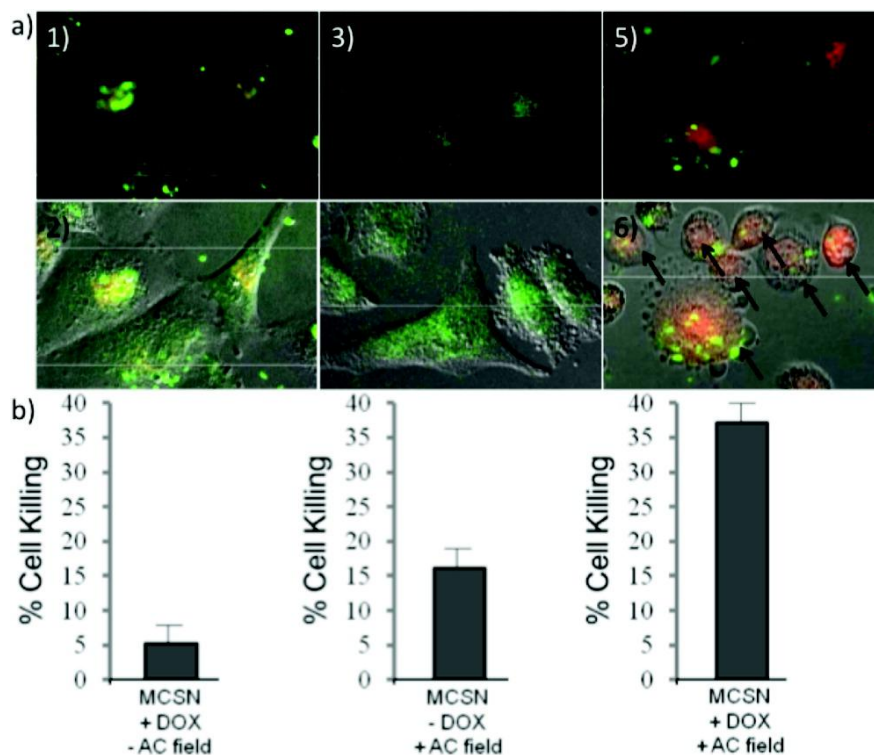


Figure 1-18. Results of MDA-MB-231 cancer cells exposure to magnetic mesoporous silica nanoparticles. Color scheme: green, fluorescently labeled nanoparticles; red, doxorubicin (DOX); yellow, merged green and red. Nanoparticles containing DOX were taken up into the cells, but before the AC field was applied, no drug release (images 1 and 2) and negligible cell death [$\sim 5\%$; panel (b), left bar] occurred. Images 3 and 4 show the effects of the magnetic field on nanoparticles without DOX in the pores. Heating of the particles accounted for 16% of the cell killing [panel (b), middle bar]. Images 5 and 6 demonstrate DOX release after a 5 min AC field exposure, which caused 37% of the cell death [panel b, right bar].¹⁶¹

Another approach was investigated by Kim *et al.* who reported on the dual function of a silica–iron oxide hybrid nanoparticle combined with a stimulus responsive gatekeeper attached to the external surface of the nanomaterial.¹⁶² The gatekeeper can be stimuli-responsively cleaved in the presence of increased reductive milieu, as it is present in the cytosol of cancer cells. Figure 1-19 shows images of the hybrid material with incorporated iron oxide cores and the response of A549 cancer cells towards doxorubicin-loaded

nanoparticles. In this case the magnetic cores were used as an additional MR imaging probe featuring significant reduction of the transverse relaxation time T_2 .

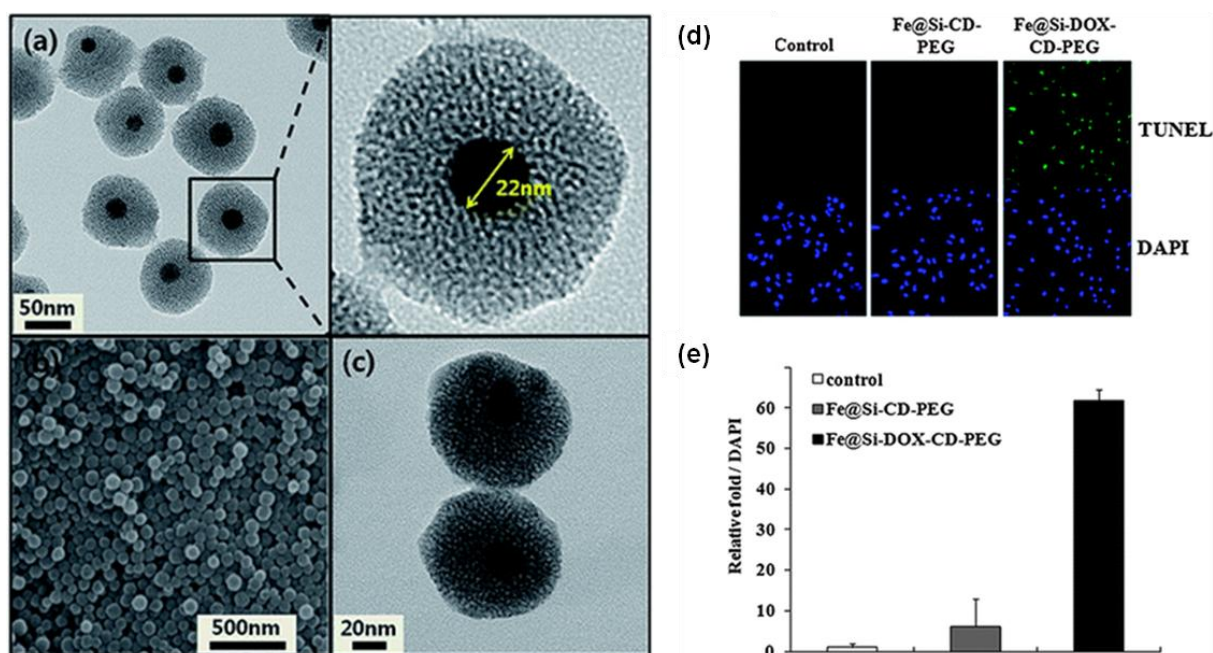


Figure 1-19. TEM (a, c) and SEM (b) images of mesoporous silica nanoparticles with a magnetic core of 22 nm. Representative photomicrographs of A549 cells after treatment with plain nanoparticles and doxorubicin-loaded nanoparticles (d). Cell-viability study where relative fluorescence intensities were quantified and normalized to the fluorescence intensity of DAPI (e).¹⁶²

In summary, magnetic nanocomposites with well-defined mesoporous structures, shapes, and tailored properties are of growing scientific and technological interest. Because of their chemical and physical stability, and the functional and magnetic properties provided by magnetic cores, these nanocomposites hold promise as important drug nanocarrier systems. Moreover, they can additionally serve as imaging agents for magnetic resonance and fluorescence imaging.

1.3.4. Supramolecular nanoparticles

Supramolecular nanoparticles (SNPs) have increasingly attracted attention as drug delivery systems and non-viral gene vectors in preclinical studies and even in clinical trials.¹⁶³⁻¹⁶⁶

SNPs are particles in which different building blocks are brought together by non-covalent interactions resulting in the controlled assembly of larger structures.¹⁶⁷ The assembly is either based on electrostatic interactions or hydrophobic host-guest interactions.^{168, 169} In contrast to conventional chemical synthesis, which is capable of forming and breaking covalent bonds, the formation of supramolecular complexes requires the combination of several elemental noncovalent interactions and an additional geometric fitting within the interaction structure. Prominently used host molecules in supramolecular chemistry are pillararenes, crown ethers, polypeptides, calixarenes, cucurbiturils, and different metallo structures.¹⁷⁰⁻¹⁷⁴

The most widely used host entity family in the formation of SNPs by far is cyclodextrin. Cyclodextrins (CDs) are cyclic oligosaccharides composed of six, seven, or eight D(+)-glucose units linked by α -1,4-linkages, which are named α -, β -, and γ -CD, respectively (Figure 1-20).¹⁷⁵ These different oligosaccharides are frequently used in the medical field because of their biocompatibility and their low toxicity.¹⁷⁶⁻¹⁷⁹

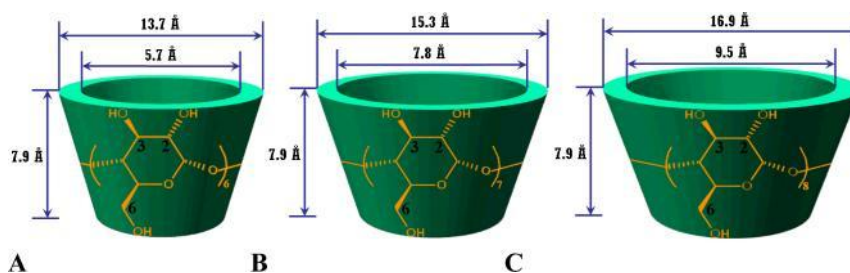


Figure 1-20. Molecular structures and dimensions of various CDs: A, α -CD; B, β -CD; and C, γ -CD.¹⁸⁰

CDs have a hydrophilic exterior and a hydrophobic cavity inside the oligosaccharide rings, which can be used to encapsulate different kinds of guest and cargo molecules.¹⁸¹⁻¹⁸⁴ The encapsulation is based on supramolecular host-guest interactions, such as hydrogen bonding, van-der-Waals forces or hydrophobic interactions, and is used in various application fields such as biomedicine, catalysis, environmental protection and separation processes.¹⁸⁵ The

hydrophobic cavity in β -CD can form inclusion complexes with several guest moieties (adamantane, azobenzene, ferrocene, cholesterol, etc.) to form nanostructures through a controlled self-assembly process.¹⁸⁶ Wang and co-workers introduced a controlled self-assembly process of supramolecular nanoparticles that is achieved by adjusting the molar ratio of polymer to β -CD. This self-assembly approach is termed the “bricks and mortar” strategy in which Ad-PEG and Ad-PAMAM with the guest adamantyl groups serve as the bricks while the PEI- β -CD polymer bearing the host functionality serves as the mortar (Figure 1-21). The size of the structures can be controlled via modifying the polymer length and polymer to cyclodextrin ratio.¹⁸⁷

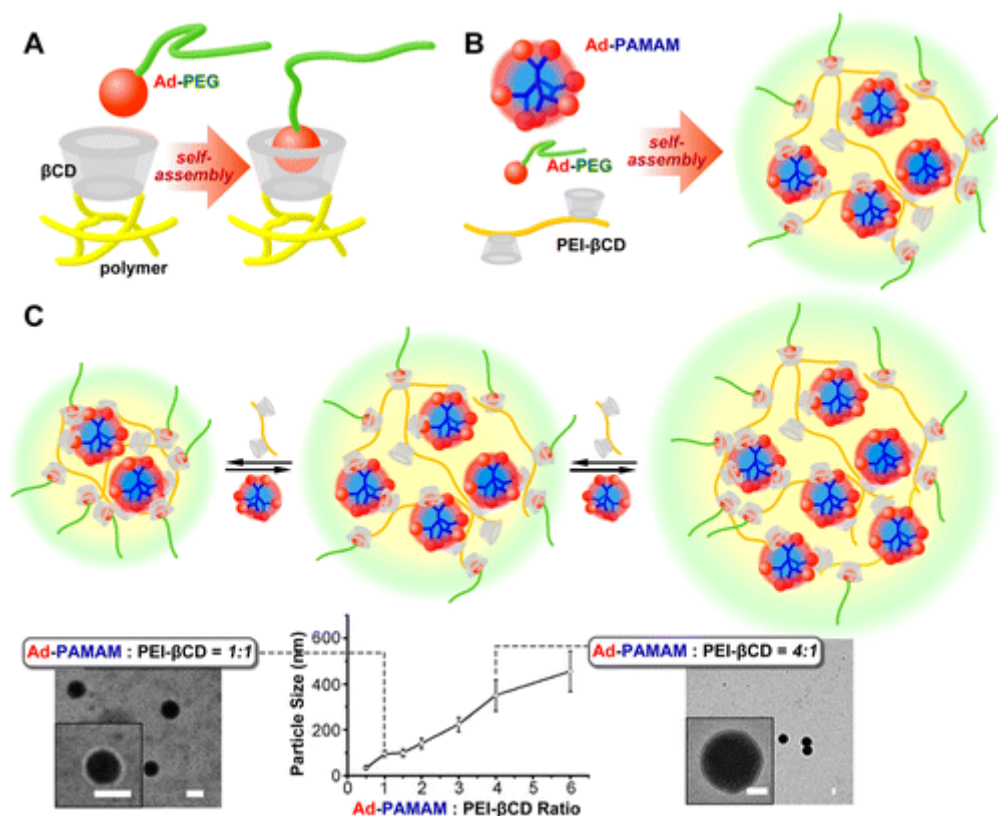


Figure 1-21. (A) General PEGylation on β -CD-grafted polymer mediated by adamantyl PEG (Ad-PEG). (B) Synthesis, and (C) size control of supramolecular nanoparticles assembled by PEI- β CD, Ad-PEG, and Ad-PAMAM with the “bricks and mortar” strategy, presented by electron microscopy with scale bar = 100 nm.¹⁸⁷

A prominent example for supramolecular structures already reaching clinical trials is given by Eliasof *et al.*, where the cyclodextrin-poly(ethylene glycol) copolymer conjugated to camptothecin, a classic hydrophobic cytostatic agent, is investigated for the therapy of pancreatic cancer, non small-cell lung cancer, breast cancer and colorectal cancer.¹⁸⁸ The drug-cyclodextrin-PEG conjugates self-assembled into nanoparticles that are called CRLX101 (Figure 1-22).

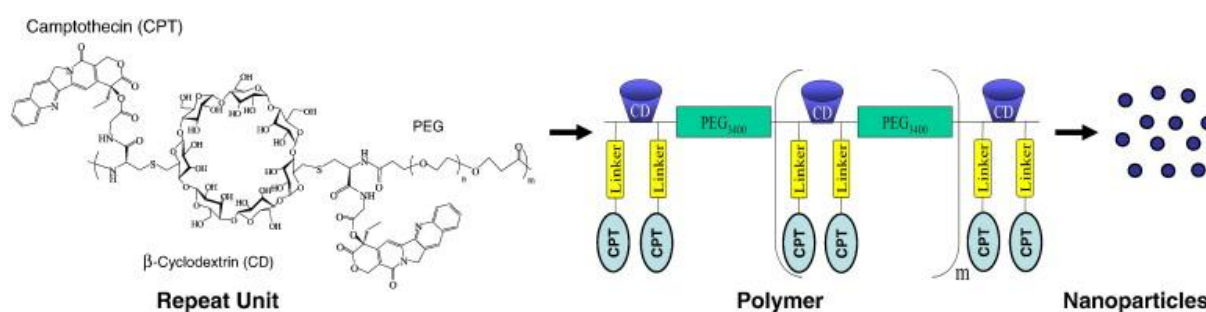


Figure 1-22. Schematic synthesis of CRLX101, a nanopharmaceutic comprised of camptothecin conjugated to a linear, cyclodextrin-poly(ethylene glycol) (CD-PEG) copolymer and formulated into nanoparticles.¹⁸⁸

Camptothecin is known to be a potent inhibitor of topoisomerase 1 (Topo 1), which is an important and validated drug target for cancer therapy today. Topo 1 remains a highly attractive drug target because it is essential for basic cellular processes including DNA replication, recombination, and transcription, which are particularly up-regulated in rapidly dividing tumor cells.¹⁸⁹

The supramolecular assembly CRLX101 was successfully investigated using a lymphoma xenograft model *in vivo* featuring efficient therapy and prolonged animal survival rates

compared to the control group and simultaneously applied irinotecan, a conventional lymphoma drug (Figure 1-23).¹⁹⁰

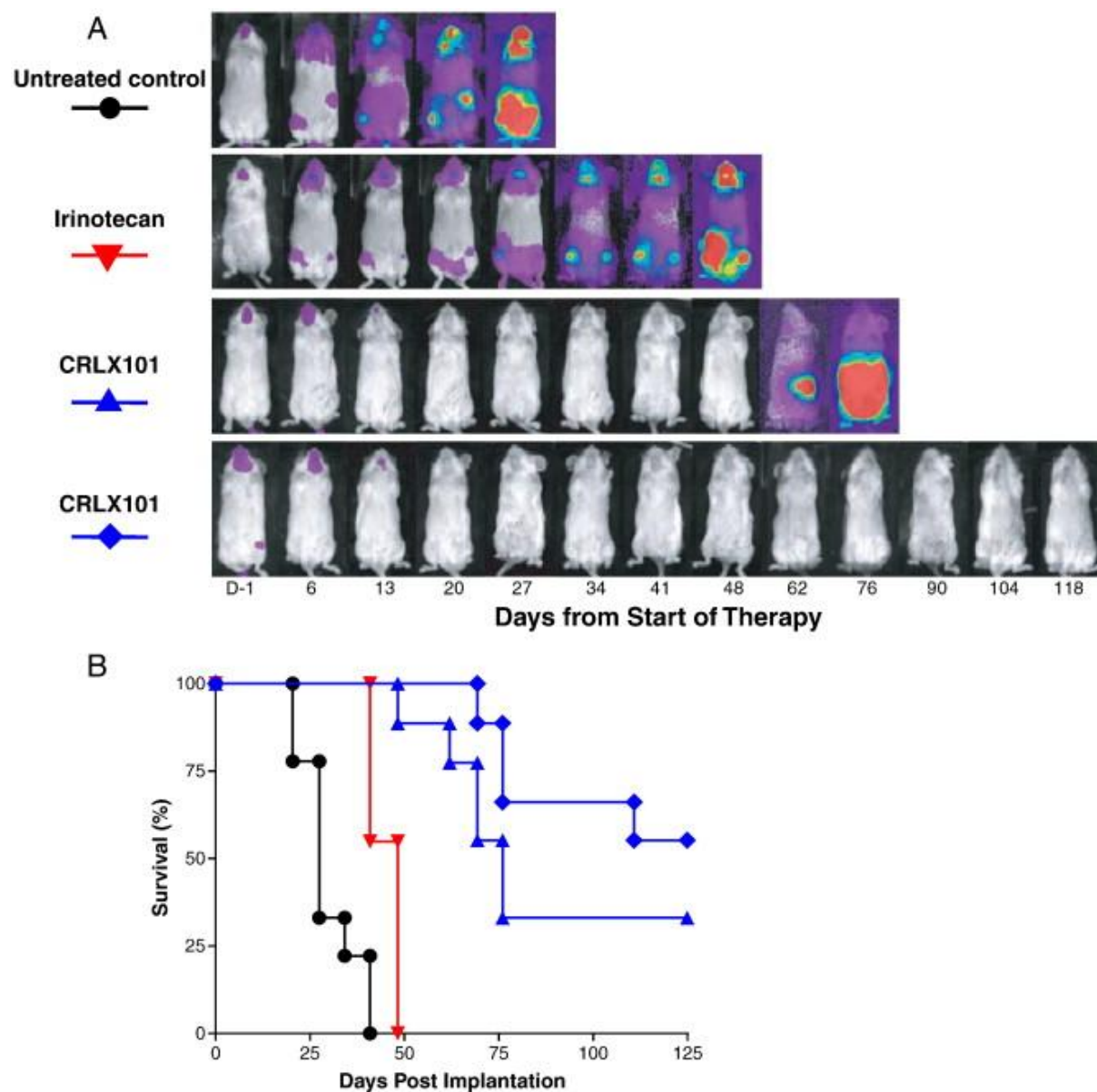


Figure 1-23. Efficacy study of CRLX101 compared to irinotecan using a lymphoma xenograft in mice. A) bioluminescence study using luciferase activity of the incorporated tumors. Weekly dosing $\times 3$ at 100 mg/kg (irinotecan), 5 mg/kg (CRLX101, triangles), and 10 mg/kg (CRLX101, diamonds). B) corresponding survival graphs. CRLX101 achieved 55.6% complete tumor response at Day 125 post-treatment at the 10 mg/kg dose, while no complete tumor responses were observed in irinotecan-treated mice and the control group.¹⁹⁰

Even though there are examples of successful applications of SNPs in the biomedical field, the non-covalent interactions could limit their use for drug delivery applications, since they might degrade easily before they reach their target, and any new guest molecule that is

incorporated or loaded into the particle needs to be optimized in its interactions with the particle structure. Thus, covalently crosslinked cyclodextrin materials could facilitate their breakthrough for drug delivery applications. Recently, different approaches were used to prepare covalently crosslinked CD molecule-containing materials. One is through crosslinking α -CD-poly-ethyleneglycol (PEG) inclusion complexes by using epichlorohydrin. The nanomaterial was obtained after extracting the PEG chains that penetrated the hydrophobic cavity.¹⁹¹

In another approach, Dichtel *et al.* polymerized β -CD in a nucleophilic aromatic substitution reaction with tetrafluoro terephthalonitrile and obtained a mesoporous bulk material that was used to rapidly remove organic micropollutants from waste water.¹⁹² In chapter 9 the successful synthesis of covalently crosslinked cyclodextrin nanoparticles is shown in detail, which makes this innovative and biocompatible nanocarrier concept a promising platform for the development of controllable and efficient theranostic systems.

1.4 References

1. R. P. Feynman, *Engineering and Science*, 1960, **23**, 22-36.
2. P. Vettiger, M. Despont, U. Drechsler, U. Durig, W. Haberle, M. I. Lutwyche, H. E. Rothuizen, R. Stutz, R. Widmer and G. K. Binnig, *IBM Journal of Research and Development*, 2000, **44**, 323-340.
3. G. Binnig and H. Rohrer, *IBM J. Res. Dev.*, 1986, **30**, 355-369.
4. C. N. R. Rao, A. Müller and A. K. Cheetham, *The Chemistry of Nanomaterials: Synthesis, Properties and Applications*, John Wiley & Sons, New York, 2006.
5. N. Taniguchi, *On the Basic Concept of "Nano-Technology"*, Proc. Intl. Conf. Prod. Eng., Tokyo, 1974.
6. H. W. Kroto, J. R. Heath, S. C. O'Brien, R. F. Curl and R. E. Smalley, *Nature*, 1985, **318**, 162-163.
7. S. Iijima, *Nature*, 1991, **354**, 56-58.
8. S. Iijima and T. Ichihashi, *Nature*, 1993, **363**, 603-605.
9. C. Kisielowski, B. Freitag, M. Bischoff, H. van Lin, S. Lazar, G. Knippels, P. Tiemeijer, M. van der Stam, S. von Harrach, M. Stekelenburg, M. Haider, S. Uhlemann, H. Müller, P. Hartel, B. Kabius, D. Miller, I. Petrov, E. A. Olson, T. Donchev, E. A. Kenik, A. R. Lupini, J. Bentley, S. J. Pennycook, I. M. Anderson, A. M. Minor, A. K. Schmid, T. Duden, V. Radmilovic, Q. M. Ramasse, M. Watanabe, R. Erni, E. A. Stach, P. Denes and U. Dahmen, *Microscopy and Microanalysis*, 2008, **14**, 469-477.
10. S. W. Hell, *Science*, 2007, **316**, 1153-1158.
11. E. Betzig, G. H. Patterson, R. Sougrat, O. W. Lindwasser, S. Olenych, J. S. Bonifacino, M. W. Davidson, J. Lippincott-Schwartz and H. F. Hess, *Science*, 2006, **313**, 1642-1645.
12. G. A. Ozin, A. Arsenault and L. Cademartiri, *Nanochemistry : A Chemical Approach to Nanomaterials*, RSC Publishing, London, 2008.
13. Robert-Koch-Institut, *Gesellschaft der epidemiologischen Krebsregister in Deutschland e.V.* , 2012.

14. J. Rouquerol, D. Avnir, C. W. Fairbridge, D. H. Everett, J. M. Haynes, N. Pernicone, J. D. F. Ramsay, K. S. W. Sing and K. K. Unger, *Pure and Applied Chemistry*, 1994, **66**, 1739.
15. M. E. Davis, *Nature*, 2002, **417**, 813-821.
16. J. E. Naber, K. P. de Jong, W. H. J. Stork, H. P. C. E. Kuipers and M. F. M. Post, in *Studies in Surface Science and Catalysis*, eds. H. G. K. H. P. J. Weitkamp and W. Hölderich, Elsevier, 1994, vol. Volume 84, pp. 2197-2219.
17. J. A. Rabo, in *Zeolites: Science and Technology*, eds. F. R. Ribeiro, A. E. Rodrigues, L. D. Rollmann and C. Naccache, Springer Netherlands, Dordrecht, 1984, DOI: 10.1007/978-94-009-6128-9_11, pp. 291-316.
18. I. E. Maxwell and W. H. J. Stork, in *Studies in Surface Science and Catalysis*, eds. E. M. F. H. van Bekkum and J. C. Jansen, Elsevier, 1991, vol. Volume 58, pp. 571-630.
19. L. Tosheva and V. P. Valtchev, *Chemistry of Materials*, 2005, **17**, 2494-2513.
20. T. Tago, H. Konno, Y. Nakasaka and T. Masuda, *Catalysis Surveys from Asia*, 2012, **16**, 148-163.
21. R. Marega, E. A. Prasetyanto, C. Michiels, L. De Cola and D. Bonifazi, *Small*, 2016, DOI: 10.1002/sml.201601447, n/a-n/a.
22. G. Perot and M. Guisnet, *Journal of Molecular Catalysis*, 1990, **61**, 173-196.
23. O. M. Yaghi, G. Li and H. Li, *Nature*, 1995, **378**, 703-706.
24. H. K. Chae, D. Y. Siberio-Perez, J. Kim, Y. Go, M. Eddaoudi, A. J. Matzger, M. O'Keeffe and O. M. Yaghi, *Nature*, 2004, **427**, 523-527.
25. C. Doonan, <https://blog.csiro.au/botox-of-plastic-to-freeze-power-costs/>.
26. K. Liu, Z.-R. Shen, Y. Li, S.-D. Han, T.-L. Hu, D.-S. Zhang, X.-H. Bu and W.-J. Ruan, *Scientific Reports*, 2014, **4**, 6023.
27. A. Carne, C. Carbonell, I. Imaz and D. Maspoch, *Chemical Society reviews*, 2011, **40**, 291-305.
28. R. C. Huxford, J. D. Rocca and W. Lin, *Current opinion in chemical biology*, 2010, **14**, 262-268.
29. S. Wuttke, S. Braig, Prei, A. Zimpel, J. Sicklinger, C. Bellomo, J. O. Radler, A. M. Vollmar and T. Bein, *Chemical communications*, 2015, **51**, 15752-15755.

30. A. Zimpel, T. Preiß, R. Röder, H. Engelke, M. Ingrisch, M. Peller, J. O. Rädler, E. Wagner, T. Bein, U. Lächelt and S. Wuttke, *Chemistry of Materials*, 2016, **28**, 3318-3326.
31. S. Rojas, F. J. Carmona, C. R. Maldonado, P. Horcajada, T. Hidalgo, C. Serre, J. A. R. Navarro and E. Barea, *Inorganic Chemistry*, 2016, **55**, 2650-2663.
32. C. Orellana-Tavra, E. F. Baxter, T. Tian, T. D. Bennett, N. K. H. Slater, A. K. Cheetham and D. Fairen-Jimenez, *Chemical communications*, 2015, **51**, 13878-13881.
33. X.-G. Wang, Z.-Y. Dong, H. Cheng, S.-S. Wan, W.-H. Chen, M.-Z. Zou, J.-W. Huo, H.-X. Deng and X.-Z. Zhang, *Nanoscale*, 2015, **7**, 16061-16070.
34. I. Senkowska and S. Kaskel, *Chemical communications*, 2014, **50**, 7089-7098.
35. L. Song, J. Zhang, L. Sun, F. Xu, F. Li, H. Zhang, X. Si, C. Jiao, Z. Li, S. Liu, Y. Liu, H. Zhou, D. Sun, Y. Du, Z. Cao and Z. Gabelica, *Energy & Environmental Science*, 2012, **5**, 7508-7520.
36. L. Peng, J. Zhang, Z. Xue, B. Han, X. Sang, C. Liu and G. Yang, *Nat Commun*, 2014, **5**.
37. C. T. Kresge, M. E. Leonowicz, W. J. Roth, J. C. Vartuli and J. S. Beck, *Nature*, 1992, **359**, 710-712.
38. F. Hoffmann, M. Cornelius, J. Morell and M. Froba, *Angewandte Chemie-International Edition*, 2006, **45**, 3216-3251.
39. Slowing, II, J. L. Vivero-Escoto, C. W. Wu and V. S. Lin, *Advanced drug delivery reviews*, 2008, **60**, 1278-1288.
40. J. L. Vivero-Escoto, Slowing, II, B. G. Trewyn and V. S. Lin, *Small*, 2010, **6**, 1952-1967.
41. M. Vallet-Regi, A. Rámila, R. P. del Real and J. Pérez-Pariente, *Chemistry of Materials*, 2001, **13**, 308-311.
42. C. Argyo, V. Weiss, C. Bräuchle and T. Bein, *Chemistry of Materials*, 2014, **26**, 435-451.
43. J. W. F. Schüth, *Handbook of porous materials*, Wiley & Sons, 2 edn., 2002.
44. J. Israelachvili, *Intermolecular and Surface Forces*, Harcourt Brace & Company, 2 edn., 1998.
45. S. Förster and M. Antonietti, *Advanced materials*, 1998, **10**, 195-217.

46. A. Monnier, F. Schuth, Q. Huo, D. Kumar, D. Margolese, R. S. Maxwell, G. D. Stucky, M. Krishnamurty, P. Petroff, A. Firouzi, M. Janicke and B. F. Chmelka, *Science*, 1993, **261**, 1299-1303.
47. K. Möller, J. Kobler and T. Bein, *Advanced Functional Materials*, 2007, **17**, 605-612.
48. M. Reichinger, Dissertation, Ruhr-Universität Bochum, 2007.
49. Slowing, II, J. L. Vivero-Escoto, C. W. Wu and V. S. Y. Lin, *Advanced Drug Delivery Reviews*, 2008, **60**, 1278-1288.
50. S. Radin, G. El-Bassyouni, E. J. Vresilovic, E. Schepers and P. Ducheyne, *Biomaterials*, 2005, **26**, 1043-1052.
51. V. Cauda, A. Schlossbauer, J. Kecht, A. Zürner and T. Bein, *J. Am. Chem. Soc.*, 2009, **131**, 11361-11370.
52. Y. Wang, Q. Zhao, N. Han, L. Bai, J. Li, J. Liu, E. Che, L. Hu, Q. Zhang, T. Jiang and S. Wang, *Nanomedicine: Nanotechnology, Biology and Medicine*, 2015, **11**, 313-327.
53. Y. Zhao, J. L. Vivero-Escoto, I. I. Slowing, B. G. Trewyn and V. S. Y. Lin, *Expert Opinion on Drug Delivery*, 2010, **7**, 1013-1029.
54. R. Liu, Y. Zhang, X. Zhao, A. Agarwal, L. J. Mueller and P. Feng, *Journal of the American Chemical Society*, 2010, **132**, 1500-1501.
55. J. Zhang, D. Wu, M.-F. Li and J. Feng, *ACS Applied Materials & Interfaces*, 2015, **7**, 26666-26673.
56. S. Giri, B. G. Trewyn, M. P. Stellmaker and V. S. Y. Lin, *Angewandte Chemie International Edition*, 2005, **44**, 5038-5044.
57. C.-Y. Lai, B. G. Trewyn, D. M. Jęftinija, K. Jęftinija, S. Xu, S. Jęftinija and V. S. Y. Lin, *Journal of the American Chemical Society*, 2003, **125**, 4451-4459.
58. S. Niedermayer, V. Weiss, A. Herrmann, A. Schmidt, S. Datz, K. Müller, E. Wagner, T. Bein and C. Brauchle, *Nanoscale*, 2015, **7**, 7953-7964.
59. Y.-Z. You, K. K. Kalebaila, S. L. Brock and D. Oupický, *Chemistry of Materials*, 2008, **20**, 3354-3359.
60. J. L. Paris, M. V. Cabañas, M. Manzano and M. Vallet-Regí, *ACS Nano*, 2015, **9**, 11023-11033.
61. M. Xue, X. Zhong, Z. Shaposhnik, Y. Qu, F. Tamanoi, X. Duan and J. I. Zink, *Journal of the American Chemical Society*, 2011, **133**, 8798-8801.

62. E. Aznar, C. Coll, M. D. Marcos, R. Martínez-Máñez, F. Sancenón, J. Soto, P. Amorós, J. Cano and E. Ruiz, *Chemistry – A European Journal*, 2009, **15**, 6877-6888.
63. C. Park, K. Oh, S. C. Lee and C. Kim, *Angewandte Chemie International Edition*, 2007, **46**, 1455-1457.
64. G.-F. Luo, W.-H. Chen, Y. Liu, Q. Lei, R.-X. Zhuo and X.-Z. Zhang, *Scientific Reports*, 2014, **4**, 6064.
65. J. Croissant and J. I. Zink, *Journal of the American Chemical Society*, 2012, **134**, 7628-7631.
66. Q. Yuan, Y. Zhang, T. Chen, D. Lu, Z. Zhao, X. Zhang, Z. Li, C.-H. Yan and W. Tan, *ACS nano*, 2012, **6**, 6337-6344.
67. A. Schlossbauer, J. Kecht and T. Bein, *Angewandte Chemie International Edition*, 2009, **48**, 3092-3095.
68. K. K. Coti, M. E. Belowich, M. Liong, M. W. Ambrogio, Y. A. Lau, H. A. Khatib, J. I. Zink, N. M. Khashab and J. F. Stoddart, *Nanoscale*, 2009, **1**, 16-39.
69. Y.-L. Zhao, Z. Li, S. Kabehie, Y. Y. Botros, J. F. Stoddart and J. I. Zink, *Journal of the American Chemical Society*, 2010, **132**, 13016-13025.
70. M. Xue, D. Cao, J. F. Stoddart and J. I. Zink, *Nanoscale*, 2012, **4**, 7569-7574.
71. H. Meng, M. Xue, T. Xia, Y.-L. Zhao, F. Tamanoi, J. F. Stoddart, J. I. Zink and A. E. Nel, *Journal of the American Chemical Society*, 2010, **132**, 12690-12697.
72. C. Park, K. Oh, S. C. Lee and C. Kim, *Angewandte Chemie-International Edition*, 2007, **46**, 1455-1457.
73. A. Schlossbauer, J. Kecht and T. Bein, *Angewandte Chemie*, 2009, **48**, 3092-3095.
74. V. Cauda, H. Engelke, A. Sauer, D. Arcizet, C. Brauchle, J. Radler and T. Bein, *Nano letters*, 2010, **10**, 2484-2492.
75. S. A. Mackowiak, A. Schmidt, V. Weiss, C. Argyo, C. von Schirnding, T. Bein and C. Bräuchle, *Nano letters*, 2013, **13**, 2576-2583.

76. A. Schloßbauer, A. M. Sauer, V. Cauda, A. Schmidt, H. Engelke, U. Rothbauer, K. Zolghadr, H. Leonhardt, C. Bräuchle and T. Bein, *Advanced Healthcare Materials*, 2012, **1**, 316-320.
77. M. P. Dobay, A. Schmidt, E. Mendoza, T. Bein and J. O. Rädler, *Nano letters*, 2013, **13**, 1047-1052.
78. Q. Zheng, Y. Hao, P. Ye, L. Guo, H. Wu, Q. Guo, J. Jiang, F. Fu and G. Chen, *Journal of Materials Chemistry B*, 2013, **1**, 1644-1648.
79. A. E. Nel, L. Mädler, D. Velegol, T. Xia, E. M. Hoek, P. Somasundaran, F. Klaessig, V. Castranova and M. Thompson, *Nature materials*, 2009, **8**, 543-557.
80. M. Ferrari, *Nature Reviews Cancer*, 2005, **5**, 161-171.
81. J. Liu, A. Stace-Naughton and C. J. Brinker, *Chemical communications*, 2009, 5100-5102.
82. H. Meng, S. Yang, Z. Li, T. Xia, J. Chen, Z. Ji, H. Zhang, X. Wang, S. Lin and C. Huang, *ACS nano*, 2011, **5**, 4434-4447.
83. H. Maeda, J. Wu, T. Sawa, Y. Matsumura and K. Hori, *Journal of controlled release*, 2000, **65**, 271-284.
84. J. Fang, H. Nakamura and H. Maeda, *Advanced drug delivery reviews*, 2011, **63**, 136-151.
85. H. Maeda, H. Nakamura and J. Fang, *Advanced drug delivery reviews*, 2013, **65**, 71-79.
86. H. Maeda, *Bioconjugate chemistry*, 2010, **21**, 797-802.
87. Y. H. Bae and K. Park, *Journal of Controlled Release*, 2011, **153**, 198.
88. Q. He, Z. Zhang, F. Gao, Y. Li and J. Shi, *Small*, 2011, **7**, 271-280.
89. F. Lu, S. H. Wu, Y. Hung and C. Y. Mou, *Small*, 2009, **5**, 1408-1413.
90. J. D. Byrne, T. Betancourt and L. Brannon-Peppas, *Advanced drug delivery reviews*, 2008, **60**, 1615-1626.
91. D. Peer, J. M. Karp, S. Hong, O. C. Farokhzad, R. Margalit and R. Langer, *Nature nanotechnology*, 2007, **2**, 751-760.
92. N. Normanno, A. De Luca, C. Bianco, L. Strizzi, M. Mancino, M. R. Maiello, A. Carotenuto, G. De Feo, F. Caponigro and D. S. Salomon, *Gene*, 2006, **366**, 2-16.
93. A. Wicki, D. Witzigmann, V. Balasubramanian and J. Huwyler, *Journal of Controlled Release*, 2015, **200**, 138-157.

94. F. M. Mickler, L. Möckl, N. Ruthardt, M. Ogris, E. Wagner and C. Bräuchle, *Nano letters*, 2012, **12**, 3417-3423.
95. M. J. Akhtar, M. Ahamed, H. A. Alhadlaq, S. A. Alrokayan and S. Kumar, *Clinica chimica acta*, 2014, **436**, 78-92.
96. V. Lebret, L. Raehm, J.-O. Durand, M. Smaïhi, M. H. Werts, M. Blanchard-Desce, D. Méthy-Gonnod and C. Dubernet, *Journal of biomedical nanotechnology*, 2010, **6**, 176-180.
97. J. M. Rosenholm, V. Mamaeva, C. Sahlgren and M. Lindén, *Nanomedicine*, 2012, **7**, 111-120.
98. V. Mamaeva, C. Sahlgren and M. Lindén, *Advanced drug delivery reviews*, 2013, **65**, 689-702.
99. S. E. Wilner, B. Wengerter, K. Maier, M. d. L. B. Magalhães, D. S. Del Amo, S. Pai, F. Opazo, S. O. Rizzoli, A. Yan and M. Levy, *Molecular Therapy—Nucleic Acids*, 2012, **1**, e21.
100. T. Lammers, F. Kiessling, W. E. Hennink and G. Storm, *Journal of controlled release*, 2012, **161**, 175-187.
101. D. A. Bölükbas and S. Meiners, *Nanomedicine*, 2015, **10**, 3203-3212.
102. A. Salvati, A. S. Pitek, M. P. Monopoli, K. Prapainop, F. B. Bombelli, D. R. Hristov, P. M. Kelly, C. Åberg, E. Mahon and K. A. Dawson, *Nature nanotechnology*, 2013, **8**, 137-143.
103. V. Torchilin, *Advanced drug delivery reviews*, 2011, **63**, 131-135.
104. M. D. K. Glasgow and M. B. Chougule, *Journal of biomedical nanotechnology*, 2015, **11**, 1859-1898.
105. W. Q. Lim, S. Z. F. Phua, H. V. Xu, S. Sreejith and Y. Zhao, *Nanoscale*, 2016, **8**, 12510-12519.
106. X. Huang, X. Teng, D. Chen, F. Tang and J. He, *Biomaterials*, 2010, **31**, 438-448.
107. S.-H. Wu, Y.-S. Lin, Y. Hung, Y.-H. Chou, Y.-H. Hsu, C. Chang and C.-Y. Mou, *ChemBioChem*, 2008, **9**, 53-57.
108. Y. Jiao, Y. Sun, X. Tang, Q. Ren and W. Yang, *Small*, 2015, **11**, 1962-1974.
109. B. Xiao, J. Zhao, X. Liu, P. Wang and Q. Yang, *Microporous Mesoporous Mater.*, 2014, **199**, 1-6.

110. V. K. Rana, M. Selvaraj, S. Parambadath, S.-W. Chu, S. S. Park, S. Mishra, R. P. Singh and C.-S. Ha, *J. Solid State Chem.*, 2012, **194**, 392-399.
111. X. Qiu, S. Han, Y. Hu, M. Gao and H. Wang, *J. Mater. Chem. A*, 2014, **2**, 1493-1501.
112. S. C. Nunes, V. de Zea Bermudez, J. Cybinska, R. A. Sá Ferreira, J. Legendziewicz, L. D. Carlos, M. M. Silva, M. J. Smith, D. Ostrovskii and J. Rocha, *J. Mater. Chem. A*, 2005, **15**, 3876.
113. Y. Li, F. Auras, F. Lobermann, M. Doblinger, J. Schuster, L. Peter, D. Trauner and T. Bein, *J. Am. Chem. Soc.*, 2013, **135**, 18513-18519.
114. D. Herault, G. Cerveau, R. J. Corriu and A. Mehdi, *Dalton transactions*, 2011, **40**, 446-451.
115. M. Gao, S. Han, X. Qiu and H. Wang, *Microporous Mesoporous Mater.*, 2014, **198**, 92-100.
116. T. Seki, K. McEleney and C. M. Crudden, *Chem. Comm.*, 2012, **48**, 6369.
117. M. Waki, Y. Maegawa, K. Hara, Y. Goto, S. Shirai, Y. Yamada, N. Mizoshita, T. Tani, W. J. Chun, S. Muratsugu, M. Tada, A. Fukuoka and S. Inagaki, *J. Am. Chem. Soc.*, 2014, **136**, 4003-4011.
118. M. W. A. MacLean, T. K. Wood, G. Wu, R. P. Lemieux and C. M. Crudden, *Chem. Mater.*, 2014, **26**, 5852-5859.
119. E. De Canck, I. Dosuna-Rodríguez, E. Gaigneaux and P. Van Der Voort, *Materials*, 2013, **6**, 3556-3570.
120. A. Corma, D. Das, H. Garcia and A. Leyva, *J. Catal.*, 2005, **229**, 322-331.
121. M. Santha Moorthy, S.-S. Park, D. Fuping, S.-H. Hong, M. Selvaraj and C.-S. Ha, *J. Mater. Chem.*, 2012, **22**, 9100.
122. S. Parambadath, V. K. Rana, D. Zhao and C.-S. Ha, *Microporous Mesoporous Mater.*, 2011, **141**, 94-101.
123. S. Parambadath, V. K. Rana, S. Moorthy, S.-W. Chu, S.-K. Park, D. Lee, G. Sung and C.-S. Ha, *J. Solid State Chem.*, 2011, **184**, 1208-1215.
124. B. T. H. Brian J. Melde, Christopher F. Blanford, and Andreas Stein, *Chem. Mater.*, 1999, **11**, 3302-3308.
125. S. G. S. Inagaki, Y. Fukushima, T. Ohsuna, O. Terasaki, *J. Am. Chem. Soc.*, 1999, **121**, 9611-9614.
126. M. J. M. T. Asefas, N. Coombs, G. A. Ozin, *Nature*, 1999, **402**, 867-871.

127. V. Rebbin, M. Jakubowski, S. Pötz and M. Fröba, *Microporous Mesoporous Mater.*, 2004, **72**, 99-104.
128. M. Mandal and M. Kruk, *Chem. Mater.*, 2012, **24**, 123-132.
129. J. Croissant, X. Cattoen, M. Wong Chi Man, P. Dieudonne, C. Charnay, L. Raehm and J. O. Durand, *Adv. Mater.*, 2014, **27**, 145.
130. J. G. Croissant, X. Cattoen, M. Wong Chi Man, J.-O. Durand and N. M. Khashab, *Nanoscale*, 2015, **7**, 20318-20334.
131. J. G. Croissant, X. Cattoen, J.-O. Durand, M. Wong Chi Man and N. M. Khashab, *Nanoscale*, 2016, **8**, 19945-19972.
132. P. Mohanty and K. Landskron, *Nanoscale research letters*, 2009, **4**, 1524-1529.
133. B. Guan, Y. Cui, Z. Ren, Z. A. Qiao, L. Wang, Y. Liu and Q. Huo, *Nanoscale*, 2012, **4**, 6588-6596.
134. Y. Chen, P. Xu, H. Chen, Y. Li, W. Bu, Z. Shu, Y. Li, J. Zhang, L. Zhang, L. Pan, X. Cui, Z. Hua, J. Wang, L. Zhang and J. Shi, *Adv. Mater.*, 2013, **25**, 3100-3105.
135. J. Croissant, X. Cattoen, M. W. Man, A. Gallud, L. Raehm, P. Trens, M. Maynadier and J. O. Durand, *Adv. Mater.*, 2014, **26**, 6174-6180.
136. Y. Fatieiev, J. Croissant, K. Julfakyan, L. Deng, D. H. Anjum and N. M. Khashab, *Nanoscale*, 2015, DOI: 10.1039/C5NR03065J.
137. J. Croissant, M. Maynadier, A. Gallud, H. Peindy N'Dongo, J. L. Nyalosaso, G. Derrien, C. Charnay, J.-O. Durand, L. Raehm, F. Serein-Spirau, N. Cheminet, T. Jarrosson, O. Mongin, M. Blanchard-Desce, M. Gary-Bobo, M. Garcia, J. Lu, F. Tamanoi, D. Tarn, T. M. Guardado-Alvarez and J. I. Zink, *Angewandte Chemie International Edition*, 2013, **52**, 13813-13817.
138. J. Croissant, A. Chaix, O. Mongin, M. Wang, S. Clément, L. Raehm, J.-O. Durand, V. Hugues, M. Blanchard-Desce, M. Maynadier, A. Gallud, M. Gary-Bobo, M. Garcia, J. Lu, F. Tamanoi, D. P. Ferris, D. Tarn and J. I. Zink, *Small*, 2014, **10**, 1752-1755.
139. C. Théron, A. Gallud, C. Carcel, M. Gary-Bobo, M. Maynadier, M. Garcia, J. Lu, F. Tamanoi, J. I. Zink and M. Wong Chi Man, *Chemistry – A European Journal*, 2014, **20**, 9372-9380.

140. S. Kim, H. Huang, H. E. Pudavar, Y. Cui and P. N. Prasad, *Chemistry of Materials*, 2007, **19**, 5650-5656.
141. J. L. Vivero-Escoto, W. J. Rieter, H. Lau, R. C. Huxford-Phillips and W. Lin, *Small*, 2013, **9**, 3523-3531.
142. P. K. Frederiksen, M. Jørgensen and P. R. Ogilby, *Journal of the American Chemical Society*, 2001, **123**, 1215-1221.
143. I. E. Kochevar and R. W. Redmond, *Methods in enzymology*, 2000, **319**, 20-28.
144. K. Hayashi, M. Nakamura, H. Miki, S. Ozaki, M. Abe, T. Matsumoto, T. Kori and K. Ishimura, *Advanced Functional Materials*, 2014, **24**, 503-513.
145. A. Kearvell and F. Wilkinson, *Molecular Crystals*, 1968, **4**, 69-81.
146. M. Arruebo, R. Fernández-Pacheco, M. R. Ibarra and J. Santamaría, *Nano today*, 2007, **2**, 22-32.
147. J. Liu, S. Z. Qiao and Q. H. Hu, *Small*, 2011, **7**, 425-443.
148. P. Wu, J. Zhu and Z. Xu, *Advanced Functional Materials*, 2004, **14**, 345-351.
149. A. Guerrero-Martínez, J. Pérez-Juste and L. M. Liz-Marzán, *Advanced materials*, 2010, **22**, 1182-1195.
150. J. E. Lee, N. Lee, T. Kim, J. Kim and T. Hyeon, *Accounts of chemical research*, 2011, **44**, 893-902.
151. X. Wang, J. Zhuang, Q. Peng and Y. Li, *Nature*, 2005, **437**, 121-124.
152. S. Peng and S. Sun, *Angewandte Chemie International Edition*, 2007, **46**, 4155-4158.
153. S. Sun, C. B. Murray, D. Weller, L. Folks and A. Moser, *Science*, 2000, **287**, 1989-1992.
154. A. Bee, R. Massart and S. Neveu, *Journal of Magnetism and Magnetic Materials*, 1995, **149**, 6-9.
155. T. Hyeon, S. S. Lee, J. Park, Y. Chung and H. B. Na, *Journal of the American Chemical Society*, 2001, **123**, 12798-12801.
156. J. H. Park, G. von Maltzahn, L. Zhang, M. P. Schwartz, E. Ruoslahti, S. N. Bhatia and M. J. Sailor, *Advanced materials*, 2008, **20**, 1630-1635.
157. H. Zeng, J. Li, J. P. Liu, Z. L. Wang and S. Sun, *Nature*, 2002, **420**, 395-398.
158. J. Kim, H. S. Kim, N. Lee, T. Kim, H. Kim, T. Yu, I. C. Song, W. K. Moon and T. Hyeon, *Angewandte Chemie International Edition*, 2008, **47**, 8438-8441.

159. S. Giri, B. G. Trewyn, M. P. Stellmaker and V. S. Y. Lin, *Angewandte Chemie International Edition*, 2005, **44**, 5038-5044.
160. E. Ruiz-Hernández, A. López-Noriega, D. Arcos, I. Izquierdo-Barba, O. Terasaki and M. Vallet-Regí, *Chemistry of Materials*, 2007, **19**, 3455-3463.
161. C. R. Thomas, D. P. Ferris, J.-H. Lee, E. Choi, M. H. Cho, E. S. Kim, J. F. Stoddart, J.-S. Shin, J. Cheon and J. I. Zink, *Journal of the American Chemical Society*, 2010, **132**, 10623-10625.
162. J. Lee, H. Kim, S. Kim, H. Lee, J. Kim, N. Kim, H. J. Park, E. K. Choi, J. S. Lee and C. Kim, *Journal of Materials Chemistry*, 2012, **22**, 14061-14067.
163. J. Li, C. Yang, H. Li, X. Wang, S. H. Goh, J. L. Ding, D. Y. Wang and K. W. Leong, *Advanced materials*, 2006, **18**, 2969-2974.
164. R. Kumar, M.-H. Chen, V. S. Parmar, L. A. Samuelson, J. Kumar, R. Nicolosi, S. Yoganathan and A. C. Watterson, *Journal of the American Chemical Society*, 2004, **126**, 10640-10644.
165. M. E. Davis, J. E. Zuckerman, C. H. J. Choi, D. Seligson, A. Tolcher, C. A. Alabi, Y. Yen, J. D. Heidel and A. Ribas, *Nature*, 2010, **464**, 1067-1070.
166. Y. Chen, X.-H. Pang and C.-M. Dong, *Advanced Functional Materials*, 2010, **20**, 579-586.
167. L. G. Suárez, W. Verboom and J. Huskens, *Chemical communications*, 2014, **50**, 7280-7282.
168. S. Yu, Y. Zhang, X. Wang, X. Zhen, Z. Zhang, W. Wu and X. Jiang, *Angewandte Chemie International Edition*, 2013, **52**, 7272-7277.
169. M. E. Davis, *Molecular pharmaceuticals*, 2009, **6**, 659-668.
170. S. B. Nimse and T. Kim, *Chemical Society reviews*, 2013, **42**, 366-386.
171. K. Kim, N. Selvapalam, Y. H. Ko, K. M. Park, D. Kim and J. Kim, *Chemical Society reviews*, 2007, **36**, 267-279.
172. S. T. Meek, J. A. Greathouse and M. D. Allendorf, *Advanced materials*, 2011, **23**, 249-267.
173. M. Xue, Y. Yang, X. Chi, Z. Zhang and F. Huang, *Accounts of Chemical Research*, 2012, **45**, 1294-1308.
174. S. Dong, Y. Luo, X. Yan, B. Zheng, X. Ding, Y. Yu, Z. Ma, Q. Zhao and F. Huang, *Angewandte Chemie International Edition*, 2011, **50**, 1905-1909.

175. J. Szejtli, *Chemical reviews*, 1998, **98**, 1743-1754.
176. F. Acartürk and N. Çelebi, *Cyclodextrins in pharmaceuticals, cosmetics, and biomedicine: current and future industrial applications*, 2011, 45-64.
177. H. Arima, K. Motoyama and T. Irie, *Cyclodextrins in pharmaceuticals, cosmetics, and biomedicine: Current and future industrial applications*, 2011, 91-122.
178. E. Bilensoy, *Cyclodextrins in pharmaceuticals, cosmetics, and biomedicine: current and future industrial applications*, John Wiley & Sons, 2011.
179. A. A. Hincal, H. Eroğlu and E. Bilensoy, *Cyclodextrins in Pharmaceuticals, Cosmetics, and Biomedicine: Current and Future Industrial Applications*, 2011, 123-130.
180. J. Zhang and P. X. Ma, *Advanced drug delivery reviews*, 2013, **65**, 1215-1233.
181. T. Auletta, M. R. de Jong, A. Mulder, F. C. J. M. van Veggel, J. Huskens, D. N. Reinhoudt, S. Zou, S. Zapotoczny, H. Schönherr, G. J. Vancso and L. Kuipers, *Journal of the American Chemical Society*, 2004, **126**, 1577-1584.
182. W. C. Cromwell, K. Bystrom and M. R. Eftink, *The Journal of Physical Chemistry*, 1985, **89**, 326-332.
183. M. R. Eftink, M. L. Andy, K. Bystrom, H. D. Perlmutter and D. S. Kristol, *Journal of the American Chemical Society*, 1989, **111**, 6765-6772.
184. B. V. K. J. Schmidt, M. Hetzer, H. Ritter and C. Barner-Kowollik, *Progress in Polymer Science*, 2014, **39**, 235-249.
185. E. M. Del Valle, *Process biochemistry*, 2004, **39**, 1033-1046.
186. G. Chen and M. Jiang, *Chemical Society reviews*, 2011, **40**, 2254-2266.
187. H. Wang, S. Wang, H. Su, K.-J. Chen, A. L. Armijo, W.-Y. Lin, Y. Wang, J. Sun, K.-i. Kamei, J. Czernin, C. G. Radu and H.-R. Tseng, *Angewandte Chemie International Edition*, 2009, **48**, 4344-4348.
188. S. Svenson, M. Wolfgang, J. Hwang, J. Ryan and S. Eliasof, *Journal of Controlled Release*, 2011, **153**, 49-55.
189. F. M. Muggia, I. Dimery and S. G. Arbuck, *Annals of the New York Academy of Sciences*, 1996, **803**, 213-223.
190. T. Numbenjapon, J. Wang, D. Colcher, T. Schluep, M. E. Davis, J. Durringer, L. Kretzner, Y. Yen, S. J. Forman and A. Raubitschek, *Clinical Cancer Research*, 2009, **15**, 4365-4373.
191. W. Zhu, K. Zhang, Y. Chen and F. Xi, *Langmuir*, 2013, **29**, 5939-5943.
-

192. A. Alsaiee, B. J. Smith, L. Xiao, Y. Ling, D. E. Helbling and W. R. Dichtel, *Nature*, 2015.

2 Characterization

Various techniques have been used to characterize the synthesis, functionalization and applications of the investigated nanomaterials. The size and the agglomeration behavior of the nanoparticles in different solvents can be investigated by Dynamic Light Scattering (DLS) measurements. By measuring Zeta potential, the surface charge of the different nanomaterials can be determined. The porous structure and morphological parameters can be investigated with nitrogen sorption measurements, X-ray Diffraction (XRD), Transmission Electron Microscopy (TEM) and Scanning Electron Microscopy (SEM). Vibrational spectroscopy (infrared and Raman spectroscopy) and solid-state nuclear magnetic resonance spectroscopy (ssNMR) are necessary to characterize different functional groups and organic compounds attached to the nanoparticles. The amount of attached or incorporated organic moieties was evaluated by thermo gravimetric analysis (TGA). By means of fluorescence and UV/VIS spectroscopy the loading capacity and stimuli-responsive release of fluorescence dyes from the porous nanocarriers can be explored. Temperature- and pH-responsive sensing of nanoparticles was also investigated with fluorescence spectroscopy. Different fluorescence microscopy techniques were used in live-cell imaging. Nuclear magnetic resonance (NMR) spectroscopy of liquids and mass spectroscopy are helpful tools to investigate the successful synthesis of organic compounds. Superconducting quantum interference device (SQUID) measurements were used to explore the superparamagnetic behavior of hybrid nanoparticles.

2.1 Dynamic light scattering

Hydrodynamic radii of nanoparticles in colloidal solutions and their degree of agglomeration in different solvents can be investigated with dynamic light scattering (DLS) measurements.

Typical reliable values of measured diameters of colloidal nanomaterials lie in the range between 1 and 1000 nm. The theoretical background of this method is based on the Brownian motion of nanoparticles. The Brownian motion is the movement of particles due to temperature > 0 K and the deflection is due to random collision with molecules in a colloidal solution surrounding the particle.¹ Usually, a DLS setup is composed of a laser source, a sample holder with thermostat, a photodetector and an autocorrelation software. Figure 2-1 shows a schematic illustration of a DLS measurement setup. By illuminating the sample with a laser beam, the scattering of this beam is correlated with the collision of the particles. A monochromatic laser beam is directed through the cuvette filled with a diluted suspension of nanoparticles and the scattered light is collected and analyzed with a photomultiplier and a photo detector system.

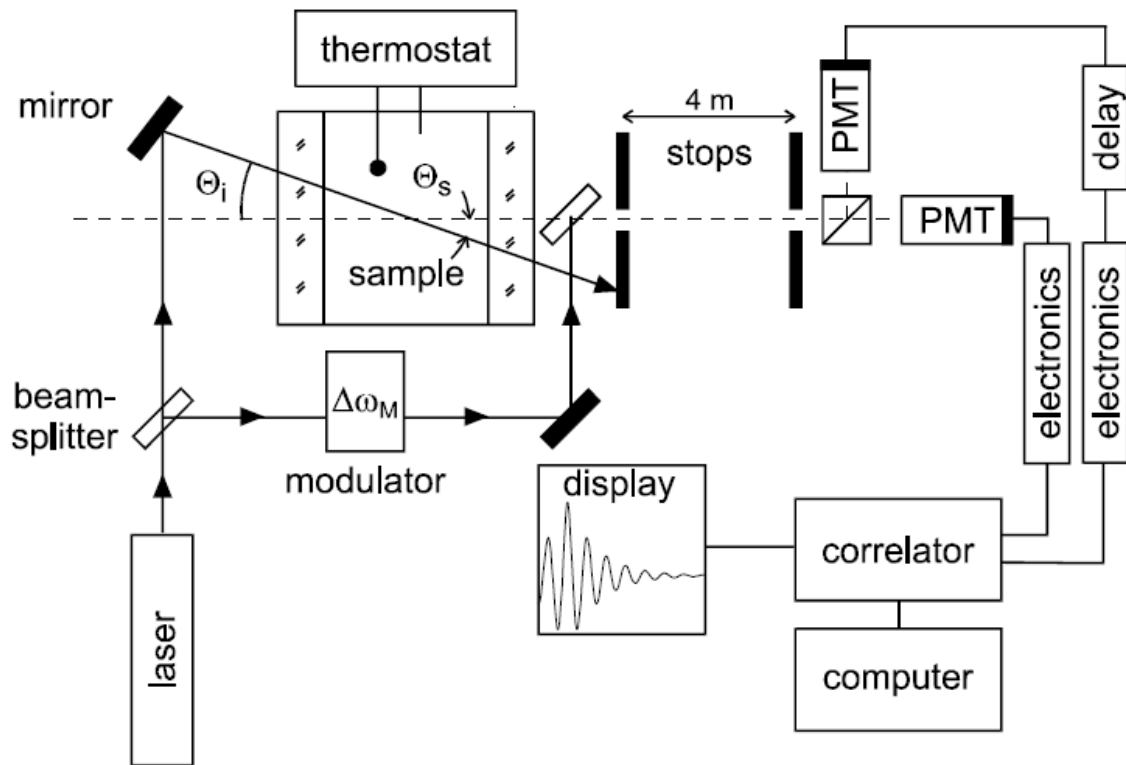


Figure 2-1. Schematic illustration of a DLS measurement setup.²

If the size of the particles is small compared to the wavelength of the light source, Rayleigh scattering occurs equally in all directions. The constructive and destructive interference of the scattered light gives intensity fluctuations, a so-called speckle pattern. This pattern contains information about the movement of the scatterers, i.e. the nanoparticles in the measured solution. The resulting detected size is always the hydrodynamic radius rather than the real size of the objects. The changes in the speckle pattern are analyzed with the help of a digital correlator and the fluctuations in intensity are correlated over time with a second order autocorrelation function:

$$g^2(q; \tau) = \frac{\langle I(t)I(t + \tau) \rangle}{\langle I(\tau) \rangle^2} \quad 2-1.$$

Equation 2-1: 2nd order autocorrelation function; q : wave detector, τ : delay time, I : Intensity.

This function decays exponentially towards long delay times and can be related to a first order autocorrelation function g^1 :

$$g^2(q; \tau) = 1 + \beta [g^1(q; \tau)]^2 \quad 2-2.$$

Equation 2-2: 1st order autocorrelation function; q : wave detector, τ : delay time, β : correction factor.

The diffusion coefficient D can be obtained from a single exponential function when assuming a monodisperse dilute dispersion of nanoparticles:

$$g^1(q; \tau) = e^{-q^2 D \tau} \quad 2-3.$$

Equation 2-3: D : Diffusion coefficient.

The Stokes-Einstein equation gives the relation between this diffusion coefficient and the hydrodynamic diameter of spherical particles:

$$D = \frac{kT}{3\pi\eta d} \quad 2-4.$$

Equation 2-4: Stokes-Einstein equation; k : Boltzmann constant, T : temperature, η : solvent viscosity, d : hydrodynamic diameter.

If the measured solution contains polydisperse nanoparticles, size distribution effects have to be taken into account by the application of Mie theory or Rayleigh scattering. While Rayleigh scattering is used to describe the elastic interaction of unpolarized light with particles smaller than the wavelength of the light, Mie theory describes the scattering of larger particles:

$$I = I_0 \frac{1 + \cos^2 \theta}{2 R^2} \left(\frac{2\pi}{\lambda} \right)^4 \left(\frac{n^2 - 1}{n^2 + 2} \right)^2 \left(\frac{d}{2} \right)^6 \quad 2-5.$$

Equation 2-5: Scattering intensity; I_0 : intensity of incoming light, θ : scattering angle, R : distance to the particle, λ : wavelength of incoming light, n : refractive index of the material, d : diameter of particles.

Since the scattering intensity is proportional to d^6 , big particles contribute much more to the scattering intensity as compared to small ones. This effect leads to an over-estimation of the size in polydisperse samples and thus needs to be considered in data evaluation. To solve this issue, the intensity-based measurement data of the DLS can also be presented as volume-weighted (d^3) or number-weighted (d) distributions, giving the real size distribution of polydisperse samples. Dynamic light scattering (DLS) measurements in this work were carried out on diluted suspensions using a Malvern Zetasizer-Nano instrument with a 4 mW He-Ne laser ($\lambda = 633$ nm) and an avalanche photo detector.

2.2 Zeta potential

The charge of the outer surface of nanoparticles can be investigated by measuring the Zeta potential. For this purpose, the electrostatic potential of the sample is measured depending on changing pH values of the surrounding medium. Nanoparticles in an aqueous dispersion feature a zeta potential, which is the electrokinetic potential difference between a stationary layer of ions in a liquid attached to the dispersed particles and the liquid medium in the surroundings.³ Particles in these aqueous colloidal suspensions can exhibit surface charges that either originate from the adsorption of charged species, ionization of functional groups at the external particle surface, or differential loss of charged species from the particle. The charged particle surfaces affect the distribution of ions in the dispersion medium, generating

2.2. Zeta potential

layers of counter ions close to the surface. The resulting electrical double layer which exists around individual particles is shown

Figure 2-2.

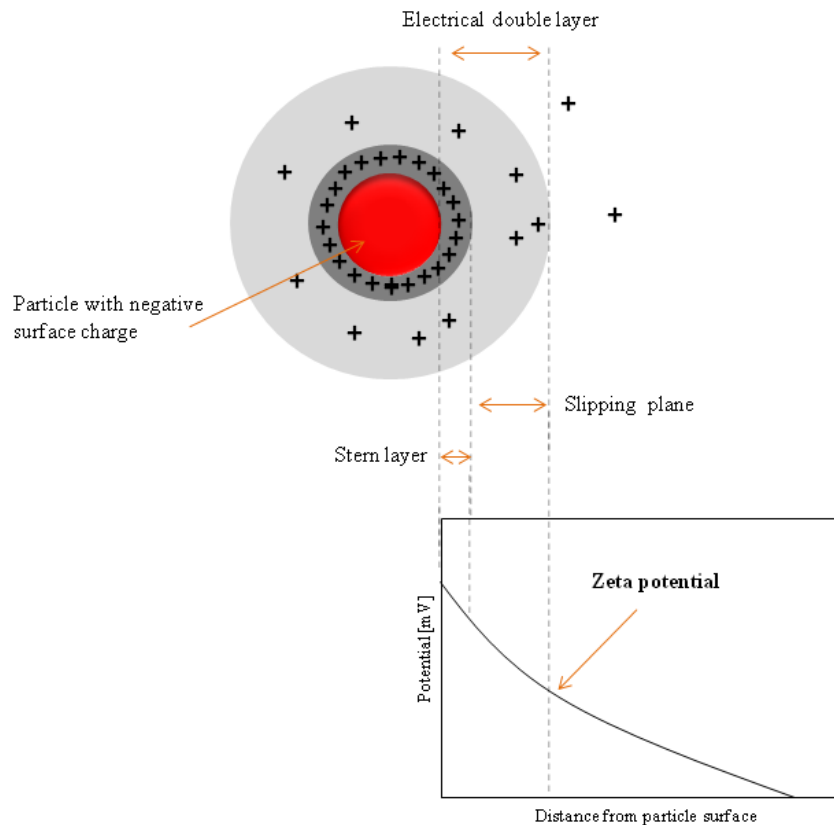


Figure 2-2. Negatively charged particle surrounded by an electric double layer.

Both layers consist of ions that are charged oppositely to the nanoparticle. The outer boundary (of the double layer) is called slipping plane and the inner layer with more densely packed counter ions is called Stern layer. The Stern layer as well as the slipping plane is very sensitive towards pH changes of the surrounding medium. The zeta potential is measured indirectly by determination of the electrophoretic mobility. In order to measure the zeta potential of a sample, an electric field is applied across a capillary cell containing the particle suspension and the electrophoretic mobility is observed. Particles inside the dispersion that possess a specific zeta potential will migrate towards the electrode of opposite charge

whereby the migration velocity is proportional to the magnitude of the zeta potential. Using the technique of Laser Doppler Velocimetry (LDV), this velocity within the dispersion is measured. The frequency shift of the laser light ($\lambda = 633 \text{ nm}$) caused by the different migration velocities of nanoparticles is recorded as the particle mobility. This mobility is transformed into zeta potential by the application of an appropriate theory together with the input of the dispersant's viscosity. The Henry equation describes the relation between the electrophoretic mobility and the zeta potential.

$$U_e = \frac{2\varepsilon f(k\alpha)}{3\eta} \zeta \quad \text{2-6.}$$

Equation 2-6: Henry equation; U_e = electrophoretic mobility, ε = dielectric constant of the sample, $f(k\alpha)$ = Henry function, η = viscosity, ζ = zeta potential.

With low electrical fields and small particles (diameter < 200 nm) the Henry function becomes approximately 1, which leads to the Hückel-Onsager approximation that was finally used to calculate the zeta potential of particles in colloidal solutions.⁴ The Smoluchowski approximation is suitable for particles larger than 200 nm in diameter and for suspensions containing more than 1 mM salt concentrations. A typical plot shows the zeta potential of the sample depending on the set pH value. At the isoelectric point the zeta potential equals zero. Zeta potential measurements in this work were carried out on diluted suspensions (0.1 mg/mL) using a Malvern Zetasizer-Nano instrument with a 4 mW He-Ne laser ($\lambda = 633 \text{ nm}$), an avalanche photo detector and an MPT-2 titration system.

2.3 Nitrogen sorption

Nitrogen sorption experiments of a gas adsorbate on a porous adsorbent give information about the specific surface area, the pore volume and the size and shape of the corresponding

pore system of a material.^{5, 6} The weak interactions occurring during physisorption (physical adsorption) measurements are mainly van-der-Waals forces such as dipole-dipole interactions, London forces or hydrogen bonding. Chemisorption (chemical adsorption), however, involves the formation of covalent chemical bonds between the adsorbate and the surface. This process is thus less preferred for the determination of porosity parameters. Herein, nitrogen gas was used as the adsorbate because it is not reacting with the analyzed sample material. The amount of the adsorbed nitrogen gas at different pressures and at a constant temperature near its boiling point (77 K) is used to generate sorption isotherms in typical physisorption measurements (Figure 2-3). The increase in the adsorbed gas volume by the substrate is measured as a function of the partial pressure. During the measurement an equilibrium state is established between the adsorptive gas and the adsorbate depending on the relative pressure p/p_0 .

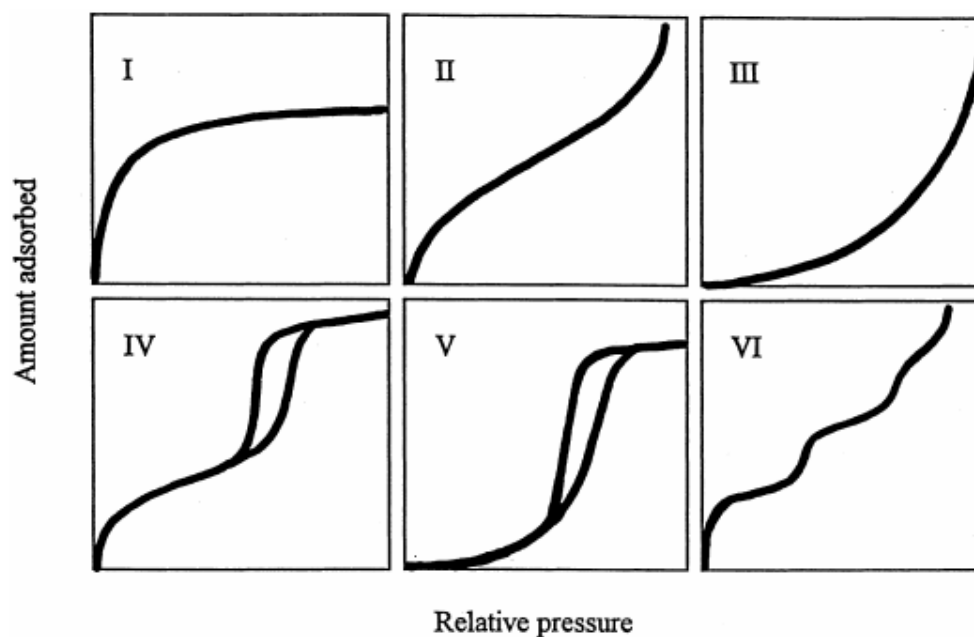


Figure 2-3. Six major types of sorption isotherms defined by the IUPAC.

The equilibrium isotherms are obtained by plotting the adsorbed volume as a function of p/p_0 . The IUPAC classifies six major types of adsorption isotherms (Figure 2-3, Table 2-1), each type being characteristic for materials with certain pore structures.

Isotherm type	Interpretation for corresponding material
I	Chemisorption isotherm or physisorption in microporous materials, where a plateau is reached after filling of the micropores
II	Nonporous and macroporous materials with high energies of adsorption
III	Nonporous and macroporous materials with low energies of adsorption
IV	Mesoporous materials with high energies of adsorption, often contain hysteresis loops attributed to mesoporosity
V	Mesoporous materials with low energies of adsorption, often contain hysteresis loops attributed to mesoporosity
VI	Several possibilities, including multiple pores sizes and multiple distinct energies of adsorption

Table 2-1. Major types of sorption isotherms classified by IUPAC.

High surface area materials with microporous systems (pore sizes up to 2 nm) like metal organic frameworks (MOFs), covalent organic frameworks (COFs) or zeolites exhibit type I isotherms with a very steep increase in adsorbed gas volume at low relative pressures, corresponding to the pore filling of the micropores of the material. These materials can reach

surface areas of over 7000 m²/g material.⁷ Most of the particles obtained in this work exhibit type IV isotherms, which are typical for mesoporous materials (pore sizes between 2 and 50 nm). In contrast to microporous materials, the sorption behavior in mesoporous materials is also depending on the attractive interactions between the fluid molecules. This leads to the occurrence of multilayer adsorption and capillary condensation in the pores of the material at relative pressures above $p/p_0 \approx 0.2$. The pore walls are covered by a multilayer adsorbed film at the onset of the pore condensation.⁸ Due to resulting van-der-Waals forces during the measurement more energy has to be applied to remove the adsorbed gas molecules from the solid when the external pressure p is reduced during the desorption process. Hence, adsorption and desorption curves typically do not completely overlap when the pores are bigger than 4 nm in diameter. Generally, a wide variety of shapes for hysteresis loops is known corresponding to different pore shapes. The type of hysteresis loop formed by adsorption/desorption isotherms is determined by different mechanisms of condensation and evaporation and depends upon the size and the shape of pores.⁹ The most common ones are depicted in Figure 2-4.

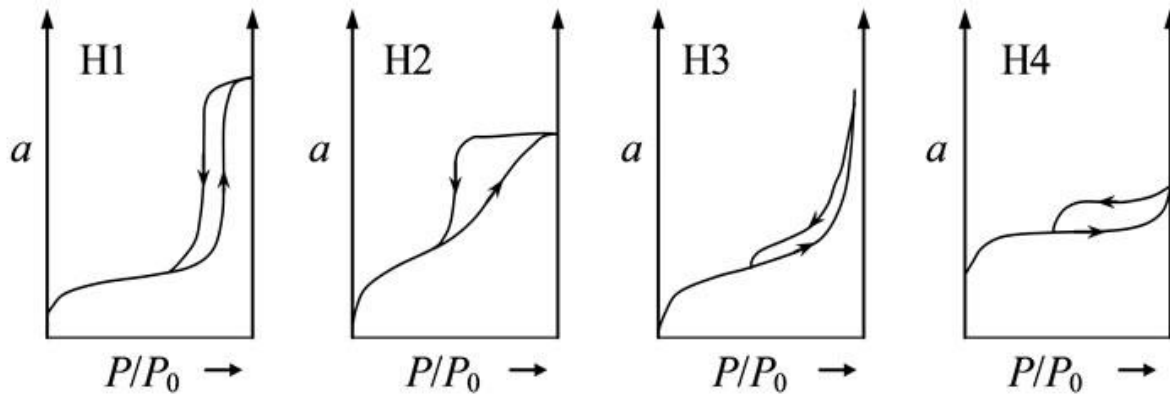


Figure 2-4. Different types of hysteresis loops corresponding to different pore shapes.¹⁰

There are many mathematical methods to calculate the porosity of particles. The most commonly used models are the Langmuir, Freundlich or Brunauer-Emmett-Teller (BET, Equation 2-7: BET equation; n = amount of the adsorbate at a relative pressure $\frac{p}{p_0}$, n_m = capacity of a single monolayer, C = BET constant, p = equilibrium pressure, p_0 = saturation vapor pressure of the sample.) approaches.^{11 12 13} Besides simple approximations like a uniform surface and equal binding sites, the used BET approach also includes multilayer adsorption.

$$\frac{n}{n_m} = \frac{C \frac{p}{p_0}}{\left(1 - \frac{p}{p_0}\right) \left(1 + C - \frac{p}{p_0}\right)} \quad 2-7.$$

Equation 2-7: BET equation; n = amount of the adsorbate at a relative pressure $\frac{p}{p_0}$, n_m = capacity of a single monolayer, C = BET constant, p = equilibrium pressure, p_0 = saturation vapor pressure of the sample.

The BET plot of $(p/p_0)/[n(1-p/p_0)]$ versus p/p_0 gives a linear relationship with a slope of $(C-1)/n_m C$ and intercept $1/n_m C$. Based on these data and the required space of one adsorbed molecule on the surface of the particle, the specific surface area of the adsorbent material can be calculated. To calculate the pore size distribution, density functional theory (DFT) or Monte-Carlo based simulations are the most accurate models.¹⁴ Nitrogen sorption

measurements in this work were either performed on Quantachrome Instruments NOVA 4000e or Autosorb at 77 K. For the measurements a minimum of 5 mg of the dried sample were used. Sample outgassing was usually performed at 120 °C and 10 mTorr for 12 hours. For enzyme-containing or temperature-sensitive samples, the outgassing temperature was set to room temperature. The corresponding pore volumes and pore sizes were calculated with a NLDFT equilibrium model for N₂ on silica or carbon with cylindrical pores. To estimate the specific surface areas of the different samples, a BET model was used.

2.4 X-ray diffraction

X-ray diffraction (XRD) is a common non-destructive technique in materials science that is widely used for the investigation of crystalline materials, providing information on phase composition, lattice parameters, unit cell dimensions, and size of crystalline domains. Additionally, XRD can be used for the characterization of periodically ordered mesostructures, e.g., mesoporous silica or organosilica nanoparticles show specific reflections in small-angle X-ray diffraction (SAXS), which can be used to calculate the pore-to-pore distance within the amorphous material.¹⁵ In general, X-ray diffraction is based on the scattering of a monochromatic X-ray beam by atoms in a periodic three-dimensional structure having a periodicity similar to the X-ray wavelengths. Herein, the scattered X-rays interfere constructively and give the diffraction pattern when the material is periodically structured. The used X-rays are generated in a cathode ray tube by heating a filament to produce electrons. These electrons are accelerated towards a target anode (typically Cu, Mo or Co) using high voltage. The collision of the accelerated electrons with the anode material leads to the emission of a continuous radiation (Bremsstrahlung) and characteristic X-ray radiation. By knocking out inner shell electrons from the anode atoms and electrons from higher energy

levels filling up the resulting vacancies, characteristic X-ray photons are emitted. The generated X-ray beam is filtered through a monochromator and directed onto the sample. A copper anode is the most commonly used target material with a resulting wavelength of Cu $K\alpha$ radiation of 1.5418 Å. Constructive interference occurs when the interaction of the incident X-rays with the sample satisfies the Bragg equation:

$$2d \sin \theta = n\lambda \quad 2-8.$$

Equation 2-8: Bragg's equation; d =lattice spacing, θ = scattering angle, n =order of reflexes, λ = wavelength.

Figure 2-5 shows a graphic illustration of Bragg's law:

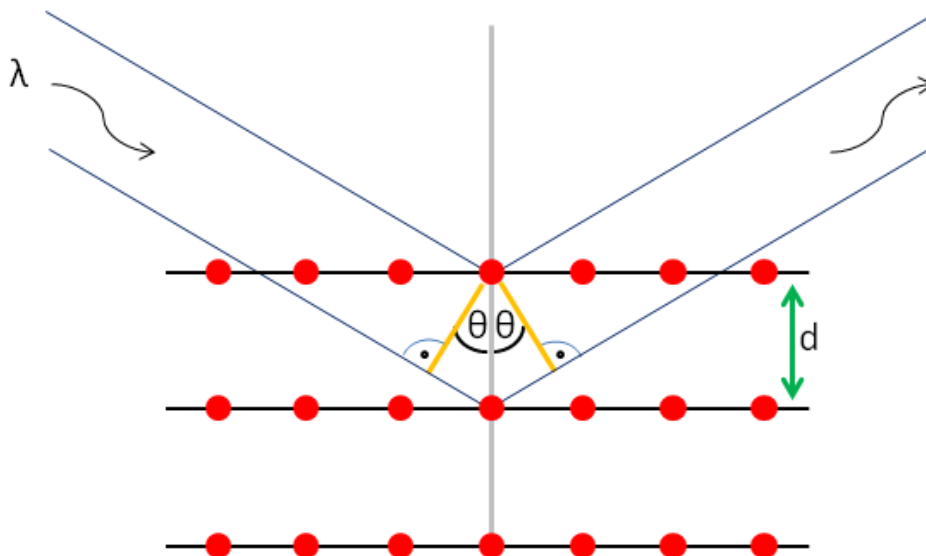


Figure 2-5. Illustration of the Bragg relation; Constructive interference occurs when the path difference is a multiple integer of the wavelength of the X-rays.

The distances between the atoms in the material analyzed correspond to the wavelength of the X-rays, so that the crystalline structure can be determined. The crystallite sizes can be

calculated by using the broadening of the reflections in the diffraction pattern. For this purpose, the Scherrer equation is used:

$$D = \frac{K\lambda}{\beta \cos\theta} \quad \text{2-9.}$$

Equation 2-9: Scherrer equation; D = mean size of the crystalline domains, K = dimensionless shape factor with a typical value of around 0.9 for spherical particles, β = full width at half maximum (FWHM) of the reflection corrected for the intrinsic instrumental broadening, λ = wavelength, θ = diffraction angle.

Because of the pore walls consisting of amorphous silica for most of the materials synthesized in this work and due to the small domain sizes and limited periodicity the observable reflexes appear quite broad.¹⁶ The moderately ordered wormlike channels of the mesoporous system of the nanoparticles studied here are responsible for receiving only first order reflections in the small angle range ($2\theta < 10^\circ$). X-Ray diffraction patterns were investigated on a Bruker D8 Discovery diffractometer in θ/θ Bragg-Brentano scattering geometry using Ni-filtered Cu- K_α radiation with $\lambda = 1.5406 \text{ \AA}$. Small-angle experiments were performed to analyze the mesoporous structure of the samples. Wide-angle experiments and diffraction patterns on a STOE Stadi MP with Mo- K_α radiation with $\lambda = 0.7118 \text{ \AA}$ were performed to investigate the metal oxide phases.

2.5 Electron microscopy

Electron microscopy is a very important technique to characterize materials concerning their structure and composition on the nanoscale. Optical microscopes using wavelengths of roughly 400 – 800 nm have a resolution limit due to the Abbe restriction with a maximum resolution of about 250 nm. In order to image very small features (smaller than about half the wavelength of visible light), an electron microscope can be used.¹⁷ Since the achievable

resolution in microscopy is directly proportional to the wavelength of the electromagnetic waves used to image a specimen, waves of short wavelengths are needed. These short wavelengths in electron microscopy are produced by accelerating electrons to very high kinetic energies. Primary electrons are accelerated by an anode and then focused by several electromagnetic coils onto the specimen. In general, thermal emission or field emission is used to generate electrons from a tungsten filament. These electrons are then accelerated by an anode to energies of up to 400 keV and focused by condenser lenses.

$$\lambda = \frac{h}{\sqrt{2m_e E_{kin}}} \quad \text{2-10.}$$

Equation 2-10: Equation to calculate the wavelength of the electrons; λ = wavelength; h = Planck constant, m_e = mass of the electron, E_{kin} = acceleration energy.

Atomic resolution can be obtained with the generated small wavelength of the electrons, which makes electron microscopy predestined for studying cell parameters, pore dimensions and morphologies of nanomaterials. Different processes can occur when the electron beam hits the surface of the specimen. Accelerated electrons can undergo elastic scattering or can be inelastically scattered. Others just pass through the sample without interaction (Figure 2-6). Typical signals used for imaging include transmitted electrons in TEM applications and secondary electrons (SE) and backscattered electrons (BSE) in SEM mode. Cathodoluminescence, Auger electrons and characteristic X-rays are used for quantitative and semiquantitative analyses of materials as well as element mapping. Bremsstrahlung (continuum) radiation is a continuous spectrum of X-rays from zero to the energy of the electron beam and produces a large background signal. To obtain the characteristic X-rays for analysis this background has to be removed.

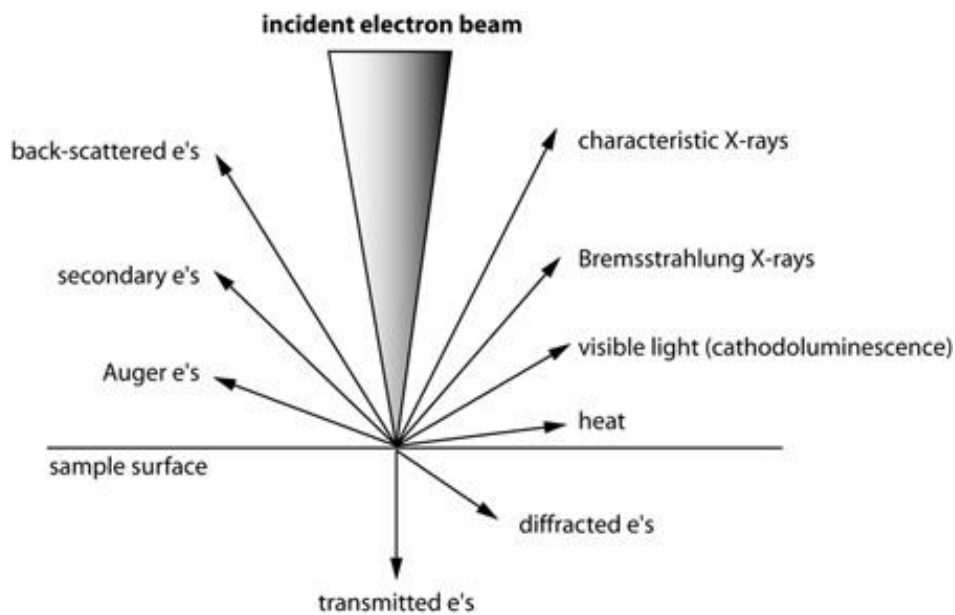


Figure 2-6. Electron beam-specimen interactions leading to different processes.¹⁸

For TEM investigations the specimen has to be very thin, because only transmitted electrons are detected on the CCD detector. Electron radiation is ionizing and therefore can interact in many different ways with the analyzed sample. This can lead to radiolysis where chemical bonds within the sample structure are destroyed. Further limiting factors in the usage of electron microscopy are spherical aberrations, chromatic aberrations and astigmatism.^{19 20} The spherical aberration is limiting the level of details by bending electrons more strongly which are further away from the optical axes. For this reason, a point is imaged as a disc. The chromatic aberration creates the same effect by bending electrons with higher energy more strongly than others. These aberration errors can be reduced with a special arrangement of concave lenses and a monochromator. Figure 2-7 shows schematic constructions and beam paths of a transmission electron microscope and a scanning electron microscope.

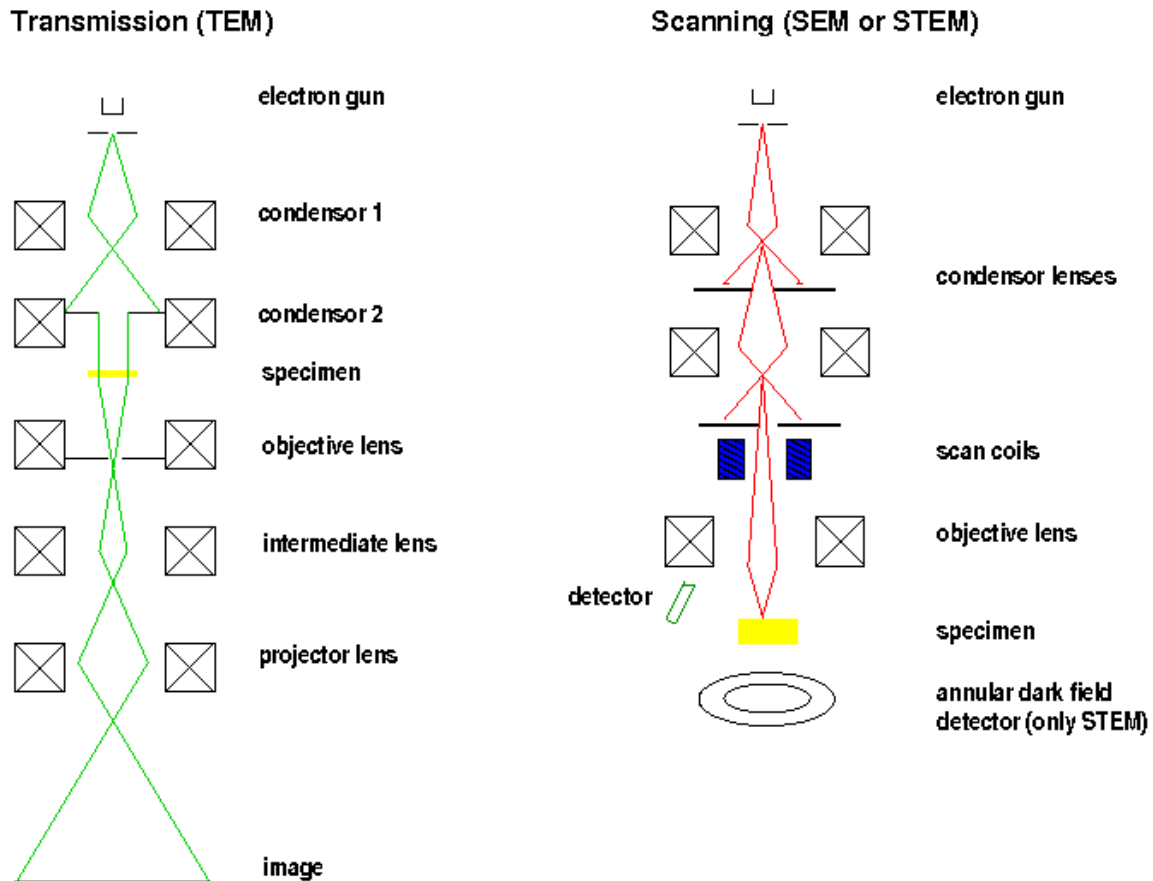


Figure 2-7. Schematic construction of a transmission electron microscope and a scanning electron microscope.²¹

Besides imaging, a TEM can also be used to create an electron diffraction pattern. Electrons are negatively charged, which can lead to strong interactions with the subject matter and therefore they are diffracted by electron density and atomic nuclei. By inserting an aperture between the sample holder and the detector into the beam path of the TEM column, selected area electron diffraction (SAED) patterns can be obtained. Furthermore, both TEM and SEM can be used to analyze the chemical and electronic structure of a sample. For this purpose, energy dispersive X-ray (EDX) analysis or electron energy loss spectroscopy (EELS) in TEM mode can be carried out. The TEM measurements were either performed on a Jeol JEM-2010 operating at 200 kV and a basic CCD detection system or with a FEI Titan 80-300 equipped with a field emission gun operated at 80 kV. SEM images were obtained with a JEOL JSM-6500F scanning electron microscope equipped with a field emission gun operated at 2.5 kV.

2.6 Infrared spectroscopy

Infrared (IR) spectroscopy is an extremely powerful analytical method for both qualitative and quantitative analysis of nanomaterials. Here, the sample is illuminated with infrared light (range of 400 – 4000 cm^{-1}) to excite vibrational energy states:

$$E = hc\nu^* \quad \text{2-11.}$$

Equation 2-11: Equation for exciting energy states; h = Planck constant, c = velocity of the light, ν^* = wavenumber.

In general, molecules possessing an electric dipole that changes during vibrational excitation are IR active.²² The frequency of the incident light has to match the frequency of the oscillating bonds of the irradiated molecule. The energetic difference between two vibrational states is often characteristic for a specific bond or functional group. In the near infrared (NIR) region (0.8 μm to 2.5 μm , 12 800 cm^{-1} to 4000 cm^{-1}), usually higher harmonics of vibrations can be found. In the mid infrared (MIR) region (2.5 μm to 50 μm , 4000 cm^{-1} to 200 cm^{-1}) fundamental vibrations occur, and the far infrared (FIR) region (50 μm to 1000 μm , 200 cm^{-1} to 10 cm^{-1}) usually features rotational or phonon modes. By absorbing energy from infrared light illumination, molecules can be stimulated to excited vibrational and rotational states. The quantum mechanical model of the anharmonic oscillator is used to describe the transitions between different vibrational states (Figure 2-8).

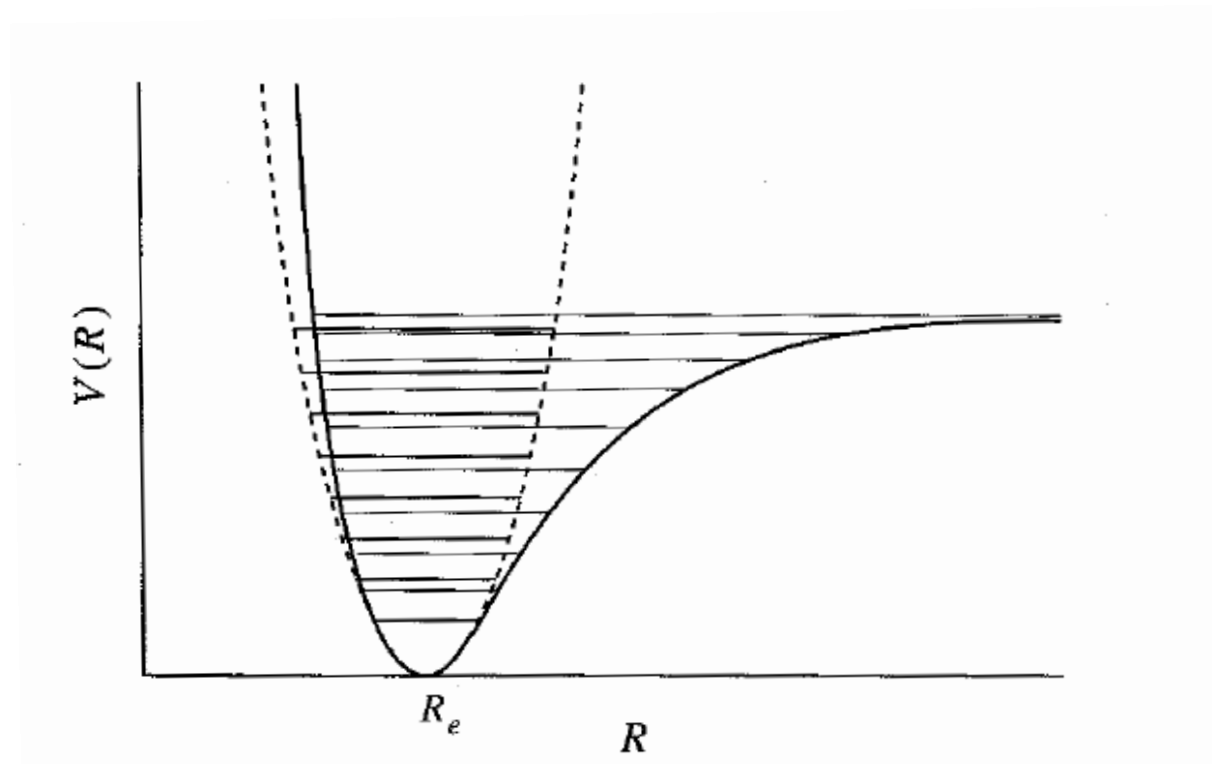


Figure 2-8. Potential of the harmonic (dashed line) and anharmonic (full line) oscillator.²³

By analyzing the characteristic vibrational modes of different functional groups, it is possible to obtain information about the chemical bonding within the molecules and the structure in the specimen. The intensity of the transmitted or scattered light is measured. IR measurements in this work were performed with small amounts of sample on a ThermoScientific Nicolet iN10 IR microscope in absorption mode with a liquid nitrogen-cooled MCT-A detector.

2.7 Raman spectroscopy

In contrast to IR spectroscopy, a molecule is Raman-active when the activated vibrations create a change in polarizability (deformation in the electron cloud).²⁴ When light is scattered from a molecule, most photons are elastically scattered, which means that they have the same energy as the incident photons. However, a small fraction of light (approximately 1 in 10^7 photons) is inelastically scattered (usually lower frequencies compared to the incident photons) leading to the Raman effect. Raman scattering can occur with a change in

vibrational, rotational or electronic energy of a molecule. To characterize a sample with Raman spectroscopy, usually monochromatic light generated by a laser is used. The interaction between light and the electron shell of molecules causes scattering radiation that is measured, and the intensity of scattered light is plotted versus the energy difference in a Raman spectrum. Rayleigh, Stokes or Anti-Stokes scattering can be observed in a Raman experiment (Figure 2-9), depending on absorbing or desorbing energy from the laser beam.

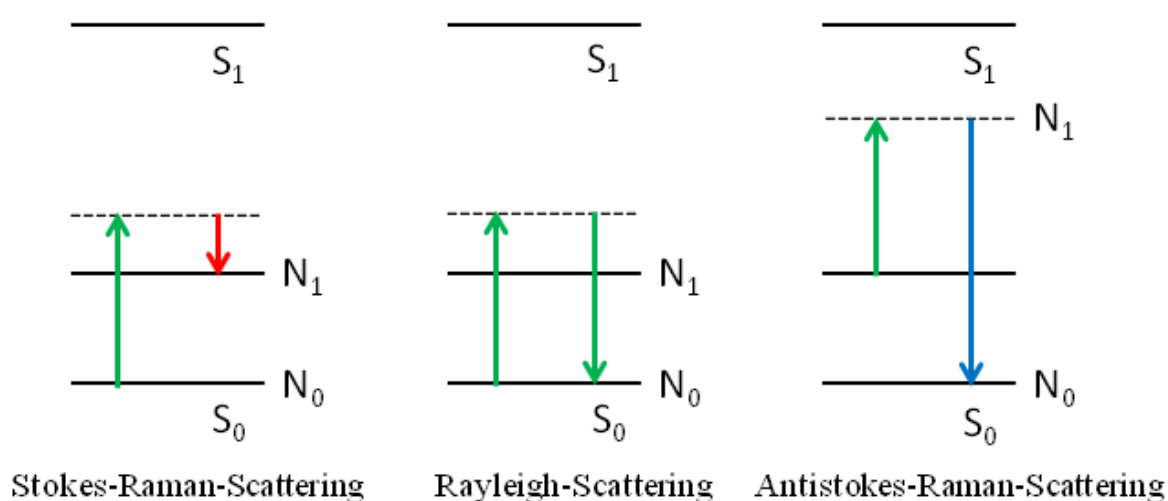


Figure 2-9. Raman excitation and relaxation processes.

Since the elastic Rayleigh scattering shows no change in frequency, it is not of interest for the analysis of a molecule's excitation processes. In inelastic Raman scattering the scattered light can either be shifted to lower frequencies (Stokes Raman) or higher frequencies (Anti-Stokes Raman) with respect to the incident frequency of photons. Because of its higher intensity, Stokes scattering is mostly used for the analysis. Comparable to IR spectroscopy, different functional groups show characteristic scattering frequencies which can be used to determine information about the chemical environment in the sample analyzed.²⁵ The nanomaterials in this work were measured on a Raman spectrometer equipped with a He-Ne laser ($\lambda=633$ nm).

A confocal LabRAM HR UV/VIS (HORIBA Jobin Yvon) Raman microscope (Olympus BX 41) with a SYMPHONY CCD detection system was used. In this case, the dried samples were directly measured on a glass plate. Raman spectra were also measured on a Bruker Equinox 55 FTIR/FTNIR, set in Raman mode, with a laser power of 100 mW.

2.8 Thermogravimetric analysis

Thermogravimetric analysis (TGA) is used to determine the mass loss of a sample related to the temperature of a heating ramp. With temperatures up to 900 °C, attached organic moieties or adsorbed guest molecules can be gravimetrically measured and quantitatively analyzed. Besides other reactions, pyrolysis and evaporation of the attached molecules take place. By controlling the atmosphere during the measurement process with inert gas or synthetic air, oxidation of the sample can be controlled. The probe is heated with a constant temperature ramp and sample weight is measured depending on the applied temperature.²⁶ The obtained thermograms include quantitative information about the amount of organic moieties attached to the analyzed materials. Additional differential scanning calorimetry (DSC) experiments can be carried out simultaneously with the TGA measurement. In DSC, the temperature of the sample is increased and the amount of required heat is compared to that of an inert reference material. With this information a weight loss step observed in TGA can either be attributed to an endothermic or an exothermic process. Therefore, the temperature stability of materials as well as exothermic (weight losses connected to combustion) or endothermic (desorption) processes can be investigated. Thermogravimetric analysis (TGA) of approximately 10 mg of dried bulk powder was performed on a Netsch STA 440 C TG/DSC. The measurements proceed at a heating rate of 10 K/min up to 900 °C in a stream of synthetic air or nitrogen of about 25 mL/min.

2.9 Fluorescence spectroscopy

By means of fluorescence spectroscopy the fluorescence of samples can be investigated. Upon excitation of electronic ground states with applied laser light, non-radiative deactivation takes place, according to Franck-Condon's rule. The subsequent emission of a photon with lower energy than the incident laser beam by reaching the electrical ground-state is called fluorescence.²⁷ This process includes different stages as can be seen in Figure 2-10.

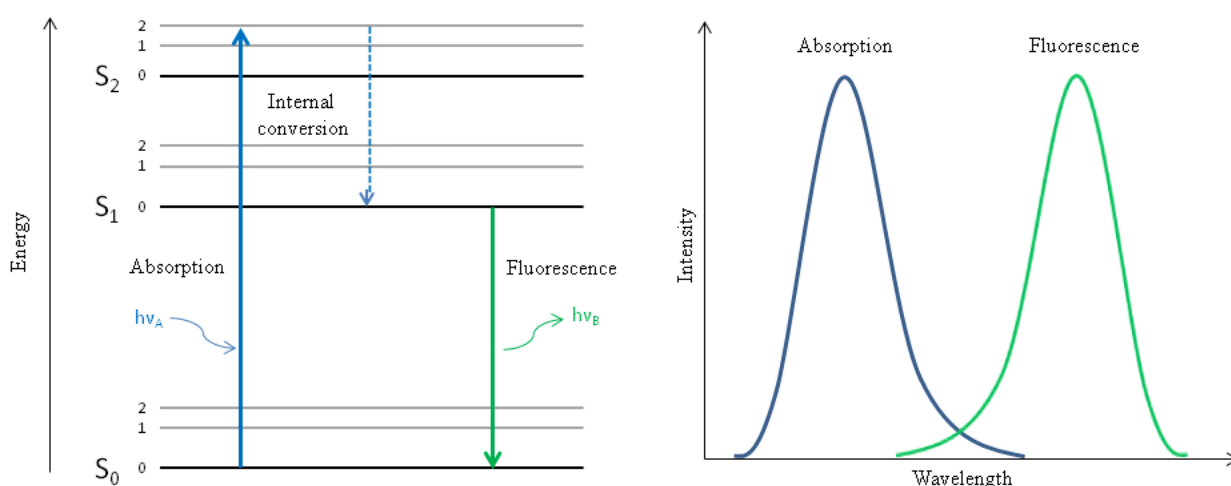


Figure 2-10. Mechanism of the fluorescence process.

In a first absorption step, a photon A of certain energy ($h\nu_A$) is generated by an external source (incandescent lamp or laser light) and absorbed by the fluorophore material. This can result in an excitation of the electron from the electronic ground state (S_0) to an excited electronic state (S_2). This process is very fast, taking place within femtoseconds. Subsequently, a process called internal-conversion takes place usually within 1 – 10 ns. This non-radiative transition of the electron from the excited state (S_2) to the relaxed excited state (S_1) is caused by vibrational relaxation of the fluorophores. In the last step, the excited electron falls back to the ground state (S_0) while emitting a photon B with lower energy ($h\nu_B$) than in the absorption process. This is the reason why fluorescence leads to a red-shift of the

emitted wavelength in comparison with the incident photons. The difference between the corresponding maxima of absorption and emission spectra (Figure 2-11) is called bathochromic Stokes-shift and is due to the previously described energy loss in the non-radiative deactivation process.²⁸

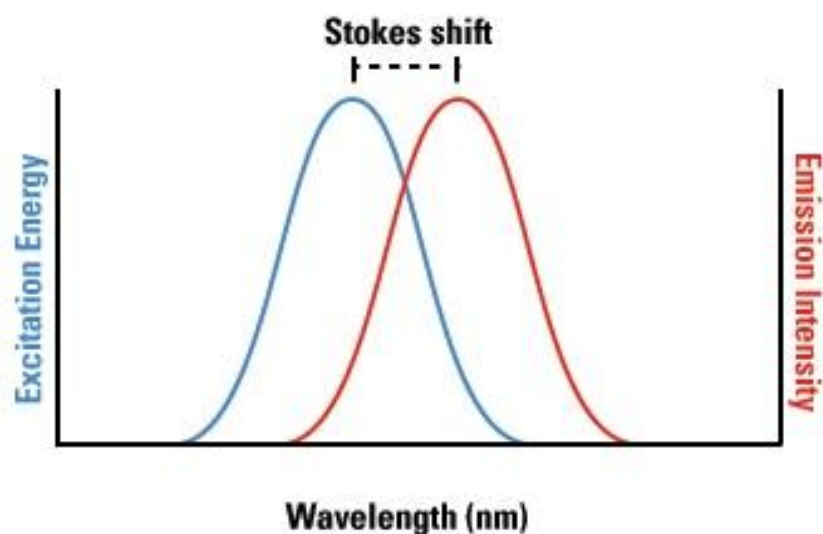


Figure 2-11. Schematic absorption and emission spectra of a fluorescence dye.²⁹

In addition to fluorescence, other relaxation processes can occur that cause a fall-back of the excited electrons to the ground state or into other related states, e.g. quenching, photobleaching, fluorescence energy transfer and intersystem crossing, which leads to phosphorescence. Fluorescence spectra in this work were recorded on a PTI spectrofluorometer with a xenon short arc lamp (UXL-75XE USHIO) and a photomultiplier detection system (model 810/814). For the release experiments a ROTH Visking type 8/32 dialysis membrane with a molecular cut-off of 14000 g/mol was used.

2.10 UV/VIS spectroscopy

In UV/VIS spectroscopy electromagnetic waves in the visible and the ultraviolet range are used to illuminate molecules in solutions or solids. The absorption of light of a specific wavelength leads to excitation of valence electrons to higher energy states. The energy of the absorbed photons by the molecules corresponds to the energy difference of the states and can give information about the electronic properties of the analyzed sample. The concentration of an analyte in the absorbing species can be determined using Lambert-Beer's law:

$$A = -\log \frac{I}{I_0} = \epsilon cl \quad \text{2-12.}$$

Equation 2-12: Lambert-Beers law; A= Absorbtion, I_0 = Intensity of incident light, I =Intensity of transmitted light, ϵ = Molar extinction coefficient, c = Concentration of the analyte, l = Path length through the cuvette.

An UV/VIS spectrometer setup usually exists of a light source (deuterium lamp for UV range, tungsten lamp for visible range), a monochromator, a detector and a cuvette holder for the analyte (Figure 2-12).

UV/VIS measurements in the following work were performed on a Perkin Elmer Lambda 1050 spectrophotometer with a deuterium arc lamp and a tungsten filament. The detector was a standard CCD system. Small sample amounts were measured on a NanoDrop 2000c spectrophotometer from Thermo Fisher Scientific.

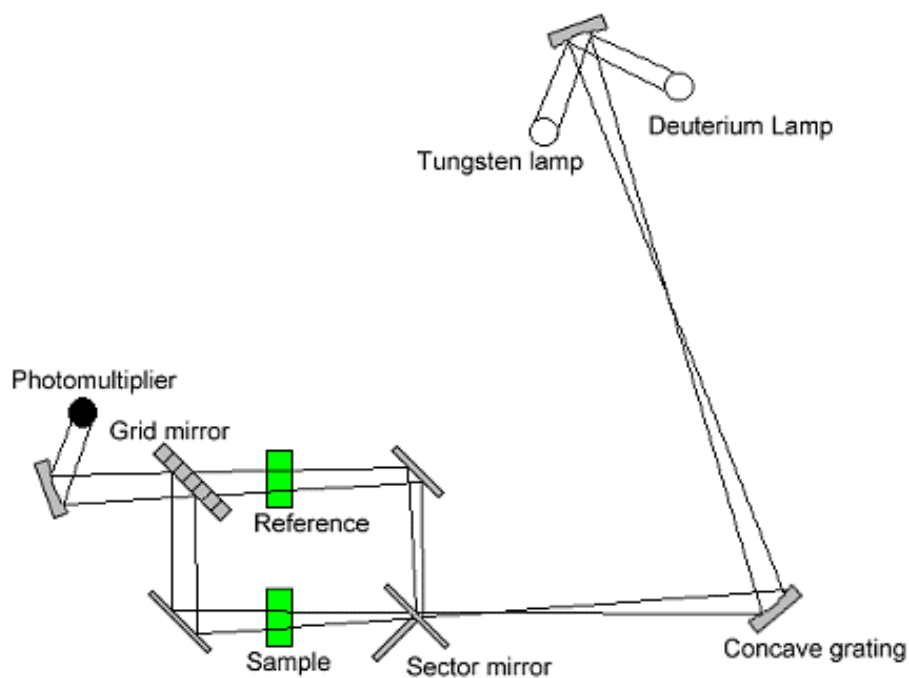


Figure 2-12. Schematic UV/VIS setup.³⁰

2.11 Fluorescence microscopy

Fluorescence microscopy is a powerful method in nanosciences to detect and investigate cell-particle-interactions. The instrument is capable of imaging the distribution of single molecular species based solely on fluorescence emission. With fluorescence microscopy, the precise location of intracellular components labeled with specific fluorophores and additional labeled nanoparticles can be monitored.

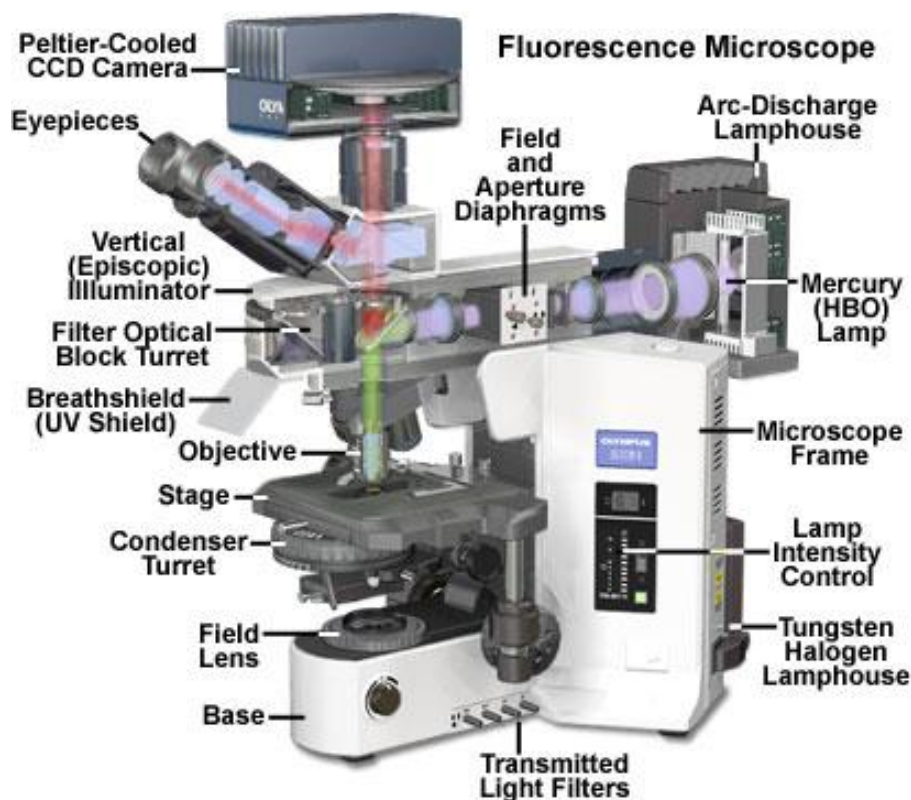


Figure 2-13. Schematic setup of a basic upright fluorescence microscope.³¹

High spatial resolution in 3D and a high time resolution is crucial to gain proper information. In general, fluorescence microscopy can also be used to investigate environmental parameters such as pH, viscosity, refractive index, ionic concentrations, membrane potential, and solvent polarity in living cells and tissues. Figure 2-13 shows a schematic setup of a basic fluorescence microscope with incident reflected light illumination. The microscope usually consists of a trinocular observation head that is coupled to a cooled charge-coupled device (CCD) camera system. Two illumination sources are used, one for transmitted light and the other for the excitation of fluorescence processes (tungsten-halogen for UV range and mercury arc-discharge for visible range, respectively). Alternatively, lasers can also be used for illumination.

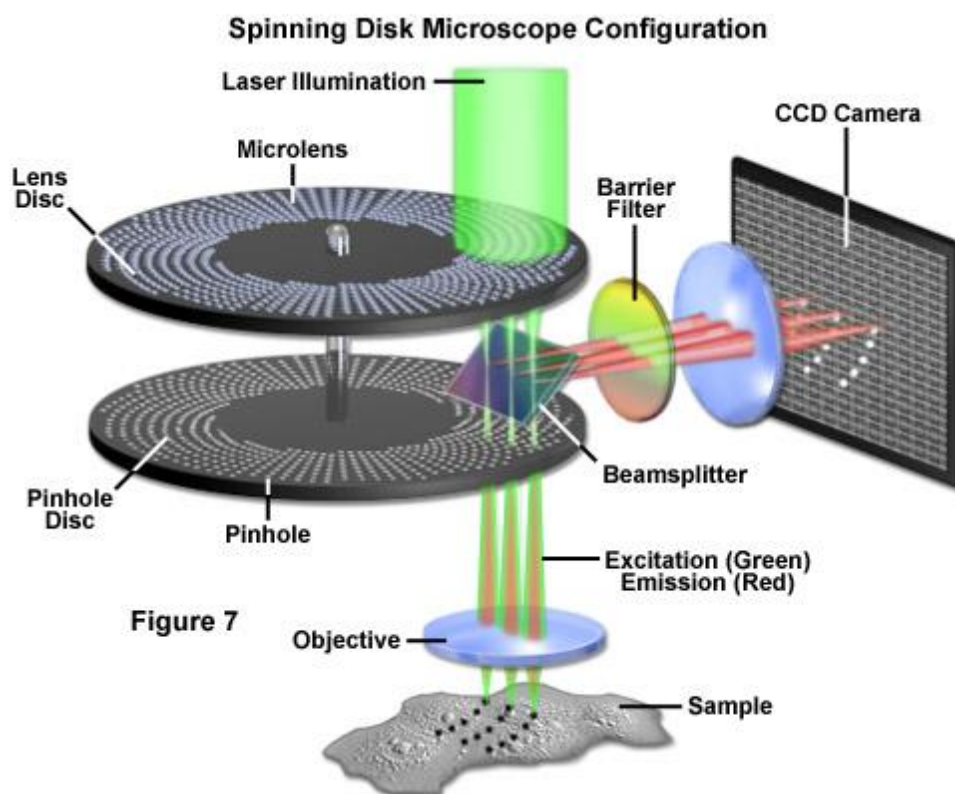


Figure 2-14. Schematic illustration of spinning disc microscope.³²

Different optical excitation filters are needed to isolate one specific wavelength for the excitation of fluorophores in the sample. It is possible to separate excitation and emission light in the same pathway optically via a dichroic mirror. This is due to the previously described Stokes shift of excitation and emission wavelength. In this case, only the emission light is collected by the objective and an additional emission filter helps to suppress unwanted background light. To study living cells and cell-particle interactions in this work, a spinning disc microscope was used. Figure 2-14 shows schematically the setup of such a spinning disc microscope. A confocal microscope is improved in comparison to a simple fluorescence microscope by introducing pinholes in the excitation and detection pathway to block the out-of-focus fluorescence. Thereby, especially the axial resolution is increased, which is given by the Rayleigh criterion:

$$d_{axial} = \frac{2n\lambda}{N.A.} \quad \text{2-13.}$$

Equation 2-13: Axial resolution of confocal microscope. d_{axial} = axial resolution, n = refractive index, λ = wavelength, $N.A.$ = numerical aperture.

Spinning disc confocal microscopes are further improved confocal microscopes. Herein, the usual pinholes are substituted with a spinning disk unit consisting of two fast rotating discs. One disc contains multiple lenses that are concentrically arranged. On the other disc there are pinholes that allow for multiple simultaneous scans. With the combination of these fast rotating discs many confocal spots can be screened over the sample. This leads to a faster imaging compared to a scanning confocal microscope and to a significant increase in time resolution. However, strong lasers are needed when using this method because much light gets lost while passing through the pinholes. Confocal microscopy for live-cell imaging in this work was performed on a setup based on the Zeiss Cell Observer SD utilizing a Yokogawa spinning disk unit CSU-X1. The system was equipped with a 1.40 NA 100x Plan apochromat oil immersion objective or a 0.45 NA 10x air objective from Zeiss. For all experiments the exposure time was 0.1 s and z-stacks were recorded. DAPI and Hoechst 33342 dyes were imaged with approximately $0,16 \text{ W/mm}^2$ of 405 nm, GFP and the caspase-3/7 reagent were imaged with approximately 0.48 W/mm^2 of 488 nm excitation light. Atto 633 was excited with 11 mW/mm^2 at 639 nm. In the excitation path a quad-edge dichroic beamsplitter (FF410/504/582/669-Di01-25x36, Semrock) was used. For two-color detection of GFP/caspase-3/7 reagent or DAPI/Hoechst 33342 and Atto 633, a dichroic mirror (560 nm, Semrock) and band-pass filters 525/50 and 690/60 (both Semrock) were used in the detection path. Separate images for each fluorescence channel were acquired using two separate electron multiplier charge coupled device (EMCCD) cameras (Photometrics Evolve™).

2.12 Nuclear magnetic resonance spectroscopy

Nuclear magnetic resonance (NMR) spectroscopy is frequently used as an indispensable physical method to analyze the behavior of certain nuclei in external magnetic fields. Fast and precise analysis of organic reaction products, determination of molecular structures in solids and liquids, as well as the study of dynamics in organic, inorganic, and biological systems can be obtained with a small amount of sample. Only isotopes with an intrinsic nuclear spin \vec{s} unequal to zero and therefore containing a magnetic moment $\vec{\mu}$ can be measured:

$$\vec{\mu} = \gamma \vec{s} \quad \text{2-14.}$$

Equation 2-14: Magnetic moment; $\vec{\mu}$ = magnetic moment; γ = gyromagnetic constant, \vec{s} = nuclear spin.

By applying an external magnetic field these magnetic moments spin towards the applied direction. With the resulting angular momentum a resonance frequency (Larmour frequency) is obtained:

$$\vec{\omega} = -\gamma \vec{H}_0 \quad \text{2-15.}$$

Equation 2-15: Larmour frequency; $\vec{\omega}$ = Larmour frequency; γ = gyromagnetic constant, \vec{H}_0 = external magnetic field.

In an external magnetic field these spin states are not degenerate and split into certain energy levels. The difference in energy between the two states is given by:

$$\Delta E = \frac{h}{2\pi} \omega \quad \text{2-16.}$$

Equation 2-16: ΔE = Different energy levels, h = Planck constant, $\vec{\omega}$ = Larmour frequency.

The resonance frequencies and therefore the energy transitions are influenced by the individual chemical and magnetic environment of the different nuclei. Because of this property, NMR spectroscopy can be used to investigate the electronic environment and chemical structure of a molecule. In solid-state NMR (ssNMR) the internuclear dipole-dipole interactions and the anisotropy of the chemical shift result in the broadening of the signals in the corresponding spectrum. These anisotropic interactions can be eliminated by using magic-angle spinning (MAS) during the measurement (Figure 2-15). To this end, the sample holder is rotated at a very high frequency (usually between 1 and 100 kHz) at the magic angle of $54^{\circ}74''$ with respect to the direction of the applied magnetic field.

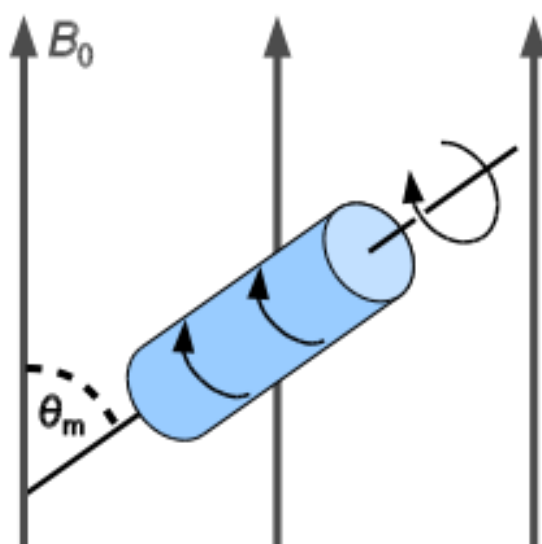


Figure 2-15. Schematic illustration of the sampleholder rotating at the "magic angle" of 54.74 degrees with respect to the direction of the magnetic field.³³

In this work, approximately 100 mg of ssNMR samples were measured on a Bruker Avance III-500 (500 MHz, 11.74 T) instrument. Liquid NMR samples were dissolved in the corresponding deuterated solvent and measured either on a Bruker or a JEOL 400 MHz instrument.

2.13 Superconducting quantum interference device

A superconducting quantum interference device (SQUID) was used to measure the magnetization of nanoparticles and to investigate their possible superparamagnetic behavior. Figure 2-16 shows schematically the setup of such devices: two Josephson junctions can split a superconducting path while sustaining a maximum supercurrent. With a magnetic material, and therefore a certain amount of magnetic flux piercing through the loop, the amplitude of the electrical current is modulated and can be monitored. This modulation is used to determine the properties of magnetic materials.

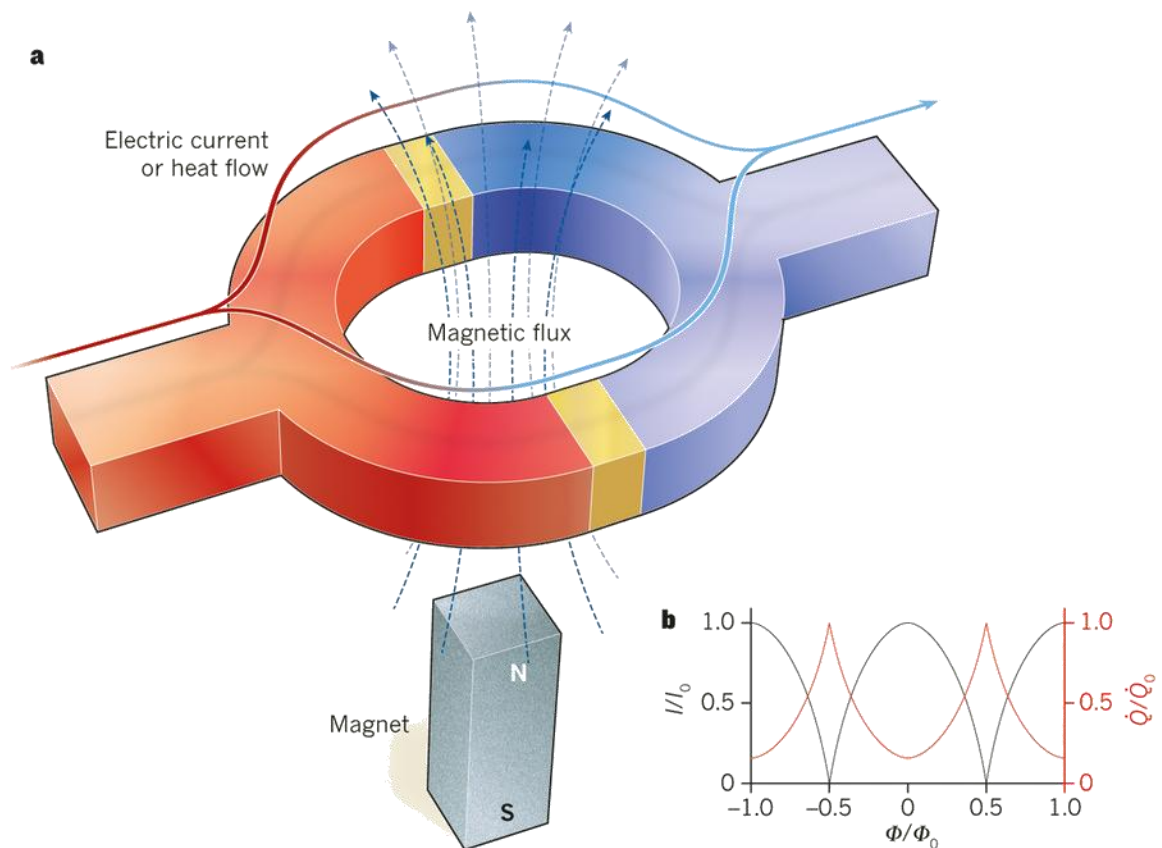


Figure 2-16. a) Schematic illustration of a SQUID containing two Josephson junctions. b) The maximum electrical current (I , black, left axis) flowing through the device from left to right can be fully modulated by the amount of magnetic flux (Φ) passing through the loop.³⁴

Magnetic nanomaterials in this work were examined in a Quantum Design MPMS XL5 SQUID-magnetometer (Superconducting QUantum Interference Device) operating in a temperature range between 1.8 K and 380 K and with magnetic fields from -50 kOe to +50 kOe. The homogenized samples were weighed out in gelatine capsules with familiar diamagnetic properties and subsequently fixed in a plastic straw. Measurements were accomplished via the software MPMS MultiVu, whereas the program SQUID Processor was used to convert and correct the data. Origin was used to process the output data files.

2.14 References

1. A. Einstein, *Annalen der Physik*, 1905, **322**, 549-560.
2. A. L. Andreas P. Fröba, *diffusion-fundamentals*, 2005, **2**, 63.61-63.25.
3. J. D. Clogston and A. K. Patri, in *Characterization of Nanoparticles Intended for Drug Delivery*, ed. E. S. McNeil, Humana Press, Totowa, NJ, 2011, DOI: 10.1007/978-1-60327-198-1_6, pp. 63-70.
4. K. G. Hans-Jürgen Butt, Michael Kappl *Physics and Chemistry of Interfaces*, Wiley, 2006.
5. M. Thommes, *Chemie Ingenieur Technik*, 2010, **82**, 1059-1073.
6. M. D. Donohue and G. L. Aranovich, *Advances in Colloid and Interface Science*, 1998, **76–77**, 137-152.
7. O. K. Farha, I. Eryazici, N. C. Jeong, B. G. Hauser, C. E. Wilmer, A. A. Sarjeant, R. Q. Snurr, S. T. Nguyen, A. Ö. Yazaydın and J. T. Hupp, *Journal of the American Chemical Society*, 2012, **134**, 15016-15021.
8. M. Thommes, R. Köhn and M. Fröba, *Applied Surface Science*, 2002, **196**, 239-249.
9. M. Thommes, B. Smarsly, M. Groenewolt, P. I. Ravikovitch and A. V. Neimark, *Langmuir*, 2006, **22**, 756-764.
10. W. Wang, P. Liu, M. Zhang, J. Hu and F. Xing, *Open Journal of Composite Materials*, 2012, **Vol.02No.03**, 9.
11. I. Langmuir, *Journal of the American Chemical Society*, 1916, **38**, 2221-2295.
12. H. Freundlich and G. Losev, *Zeitschrift Fur Physikalische Chemie--Stoichiometrie Und Verwandtschaftslehre*, 1907, **59**, 284-312.
13. S. Brunauer, P. H. Emmett and E. Teller, *Journal of the American Chemical Society*, 1938, **60**, 309-319.
14. J. E. S. S. Lowell, M.A. Thomas, M. Thommes, *Characterization of Porous Solids and Powders: Surface Area, Pore Size and Density*, Kluwer Academic Publishers, Netherlands, 16 edn., 2004.
15. L. A. Chiavacci, K. Dahmouche, C. V. Santilli, V. de Zea Bermudez, L. D. Carlos, V. Briois and A. F. Craievich, *Journal of Applied Crystallography*, 2003, **36**, 405-409.
16. H. F. Poulsen, J. Neuefeind, H. B. Neumann, J. R. Schneider and M. D. Zeidler, *Journal of Non-Crystalline Solids*, 1995, **188**, 63-74.

17. C. R. Brundle, C. A. E. Jr. and S. Wilson, *Encyclopedia of materials characterization: Surfaces, interfaces, thin films*, Butterworth-Heinemann Limited, 1992.
18. http://serc.carleton.edu/research_education/geochemsheets/electroninteractions.html.
19. C. B. C. D.B. Williams, *Transmission electron microscopy – A textbook for material science*, Springer Science + Business Media, 2009.
20. J. M. H. B. Fultz, *Transmission electron microscopy and diffractometry of materials*, Springer Verlag, Berlin, 2008.
21. L. Reimer, *Transmission electron microscopy: Physics of image formation*, Springer, 2008.
22. H. U. G. H. Günzler, *IR-Spektroskopie: Eine Einführung*, Wiley VCH, Weinheim, 2003.
23. <http://www.files.chem.vt.edu>.
24. B. Schrader, *Infrared and Raman Spectroscopy*, VCH Publishers Inc, New York, 1995.
25. H. M. M. Hesse, B. Zeeh, *Spektroskopische Methoden in der organischen Chemie*, Georg Thieme Verlag, Leipzig, 2005.
26. G. R. G. W. Ehrenstein, P. Trawiel, *Thermal analysis of plastics*, Hanser Gardner Publications, Cincinnati, 2005.
27. P. W. Atkins, *Physikalische Chemie*, Wiley-VCH, Weinheim, 2001.
28. J. R. Lackowicz, *Principles of Fluorescence Spectroscopy*, Plenum Press., 1983.
29. <http://www.piercenet.com>.
30. <http://teaching.shu.ac.uk/hwb/chemistry/tutorials/molspec/dbspec2.gif>.
31. <http://www.olympusmicro.com/primer/techniques/fluorescence/bx51fluorescence.html>.
32. <http://zeiss-campus.magnet.fsu.edu/articles/livecellimaging/techniques.html>.
33. <https://de.wikipedia.org/wiki/Magic-Angle-Spinning>.
34. R. W. Simmonds, *Nature*, 2012, **492**, 358-359.

3 Protease mediated release of chemotherapeutics from mesoporous silica nanoparticles to *ex vivo* human and mouse lung tumors

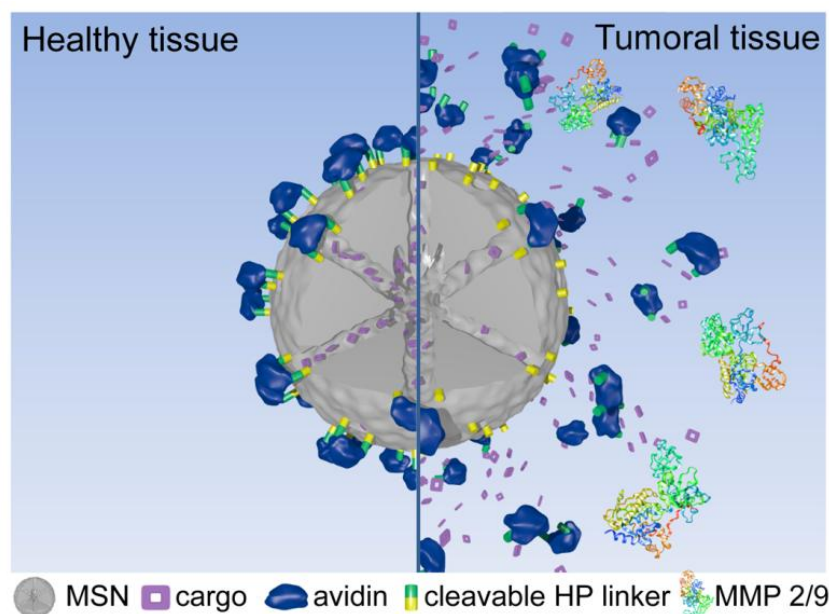
This chapter is based on the following publication:

Sabine H. van Rijt, Deniz A. Bölükbas, Christian Argyo, Stefan Datz, Michael Lindner, Oliver Eickelberg, Melanie Königshoff, Thomas Bein, and Silke Meiners, *ACS Nano* **2015**, *9*, 2377-2389.

Abstract

Nanoparticles allow for controlled and targeted drug delivery to diseased tissues and therefore bypass systemic side effects. Spatio-temporal control of drug release can be achieved by nanocarriers that respond to elevated levels of disease-specific enzymes. For example, matrix metalloproteinase 9 (MMP9) are overexpressed in tumors, are known to enhance the metastatic potency of malignant cells, and have been associated with poor prognosis of lung cancer. Here, we report the synthesis of mesoporous silica nanoparticles (MSNs) tightly capped by avidin molecules *via* MMP9 sequence-specific linkers to allow for site-selective drug delivery in high expressing MMP9 tumor areas. We provide proof-of-concept evidence for successful MMP9-triggered drug release from MSNs in human tumor cells and in mouse and human lung tumors using the novel technology of *ex vivo* 3D lung tissue cultures. This technique allows for translational testing of drug delivery strategies in diseased mouse and human tissue. Using this method we show MMP9-mediated release of cisplatin, which induced apoptotic cell death only in lung tumor regions of *Kras* mutant mice, without causing toxicity in tumor-free areas or in healthy mice. The MMP9 responsive nanoparticles also

allowed for effective combinatorial drug delivery of cisplatin and proteasome inhibitor bortezomib, which had a synergistic effect on the toxicity. Importantly, we demonstrate the feasibility of MM9 controlled drug release in human lung tumors.



3.1 Introduction

In the past decade, the use of nanoparticles as inert carriers for therapeutics has revolutionized the field of drug delivery. Such nanocarrier systems have shown advantageous features resulting in improved accumulation of active drugs at disease sites, and have contributed to reduced systemic toxicity.¹ However, release systems of many drug carriers rely on spontaneous degradation of the nanoparticle *in vivo* (e.g., hydrolysis), and do not allow for controlled drug release. Controlled drug delivery can be achieved by exploiting the (patho)physiologic characteristics of biological microenvironments, such as reducing conditions, changes of pH (e.g., acidic endosomal compartments), or altered levels of disease-specific enzymes. For example, matrix metalloproteinases 2 and 9 (MMP2 and MMP9) are overexpressed in advanced stages of cancer including lung cancer, whereas they are

minimally expressed in healthy tissue.² Indeed, elevated levels of MMP9 in the tumor microenvironment enhance the metastatic potency of malignant cells and correlate with tumor progression, angiogenesis, or metastasis.³ In particular, increased expression of MMP9 has been associated with poor prognosis of lung cancer.^{4, 5} Specific peptide sequences can be exploited as protease-sensitive linkers⁶ to allow for controlled release of chemotherapeutics from nanoparticles, as recently shown by the use of MMP2/9 sensitive peptides for drug delivery.⁷⁻¹³ Consequently, the use of MMP2/9 responsive nanoparticles represents a promising strategy for local treatment of aggressive lung cancer.

Multifunctional mesoporous silica nanoparticles (MSNs) are attractive carriers for drug delivery.¹⁴ They offer unique properties such as tunable pore sizes and pore volumes for high drug loading capacity, and efficient encapsulation of a wide variety of cargo molecules.¹⁵ Additionally, these carriers can be selectively functionalized at specific sites within the nanoparticle.¹⁶ For example, an outer shell functionalization enables the attachment of external functions exclusively on the outer surface of the particle, which do not interfere with the pore environment. This can be exploited to create stimuli-responsive pore sealing for controlled drug release.¹⁷⁻²¹ For example, MSN pore closing can be achieved by utilizing biotin-avidin complexation, which serves as a bulky biomolecule-based valve blocking the entrances of the MSN pores.²²

In this work, we developed avidin-capped MSNs functionalized with linkers that are specifically cleaved by MMP9, thereby allowing for controlled release of chemotherapeutics from the MSNs in high MMP9 expressing lung tumor areas. We demonstrate efficient protease sequence-specific release of the incorporated chemotherapeutic cisplatin (CP), as well as combination treatment with proteasome inhibitor, bortezomib (Bz), in two lung cancer cell lines. To assay therapeutic effectiveness in diseased tissue, we established a novel experimental set-up using 3D lung tissue cultures (3D-LTC) of mouse lung cancer tissue. This

technique allows for spatio-temporal resolution and quantification of nanoparticle-mediated drug delivery in the preserved 3D environment of diseased mouse and human lung tissue. We here demonstrate MMP9-mediated tumor-site selective drug release and tumor cell death in mouse and human lung tumors revealing the feasibility of MMP9 controlled drug site-selective delivery for treatment of lung cancer.

3.2 Results and Discussion

Synthesis and characterization of MMP9 responsive MSNs. According to previous reports, the MSNs were synthesized by a sol-gel procedure.^{16, 23} In the present work, the external surface of the MSNs was coated with a heptapeptide (HP) linker (MSN_{HP}) consisting of a biotin functionality on the periphery (for detailed synthesis procedure, refer to SI). This HP sequence is selectively recognized by MMP9 for proteolysis (RSWM**GLP**, cutting sequence shown in bold).²⁴ As a negative control, MSNs containing a non-cleavable heptapeptide (NHP) attached to the outer surface of the particles were synthesized (MSN_{NHP}). In this NHP-biotin linker, the specific cleavage site for MMP9 is lost due to an exchange of a single amino acid (RSW**MLLP**, exchanged amino acid shown in bold). After dye/drug uptake into the mesopores of both particle types, the glycoprotein avidin (66 kDa, av. diameter ~8 nm) was attached to the outer surface of the particles *via* non-covalent linkage to the biotin groups. The particles have been termed throughout the script as cMSN (MMP9-cleavable linkers) or ncMSN (MMP9 non-cleavable linkers). Avidin shows high affinity to biotin, and therefore acts as a bulky gatekeeper to block the mesopores of the silica nanoparticles. The complete synthesis strategy and characterization of the particles is depicted in Figure 3-1. Comprehensive characterization of the synthesized MSNs involved a range of physiochemical methods; thermogravimetric analysis, zeta potential, dynamic light scattering, nitrogen sorption, and infrared (IR) spectroscopy (Figure 3-1B–F, respectively), all of which

confirmed the successful synthesis of cMSN or ncMSN. See also Table 3-1 and SI for additional information. From these data, we conclude that the attachment of the avidin gatekeepers *via* short heptapeptide-biotin linkers (cleavable and non-cleavable for MMP9) to the external surface of MSNs was successful. In order to prove the MMP9-specific release behavior of our nanoparticle system, release experiments with fluorescein were performed as previously reported.²² Only upon the addition of recombinant MMP9 to the particle suspension, an increase in fluorescence intensity over time was observed reaching a plateau after about 16 h. Importantly, no release of the preloaded fluorescein was observed for MSNs containing a non-cleavable heptapeptide linker (ncMSN) (Figure 3-1G). Furthermore, MMP2 was also able to induce fluorescein release from the particles, but with slower kinetics, compared to MMP9 (Figure S 3-1D). This is not surprising as MMP2 has differential enzyme kinetics compared to MMP9, and has been shown to degrade several substrates that are not degraded by MMP9 and vice versa.²⁵ For this reason, we chose to continue with MMP9 in the *in vitro* studies. However, it is important to note that both enzymes are overexpressed in lung cancer and so we expect a cumulative effect on cargo release *in vivo*.^{4, 5} The cMSN particles could uptake the drug cisplatin very efficiently (0.44 ± 0.02 mg/mg cMSN) and showed specific release of cisplatin when incubated with recombinant MMP9, whereas no release of cisplatin could be detected in the absence of MMP9 (Table 3-3). Furthermore, the avidin capped particles preloaded with fluorescein (cMSN-fluorescence) showed stability of the capping system for up to 16 h (Figure S 3-1F). Colloidal stability of our particles was retained for up to 7 days (168 hours), after which time agglomeration of the MSNs could be observed in solution (Figure S 3-1G). In addition, long-term cargo release experiments of fluorescein loaded cMSN in HBSS buffer solution (no MMP9) showed that the particles were stable for at least 28 days (Figure S 3-1H), similar to what we previously observed for related MSNs with

organic coatings.^{26, 27} Consequently, above experiments validate highly specific release behavior of fluorescein and cisplatin from cMSNs by recombinant MMP2/9 enzymes.

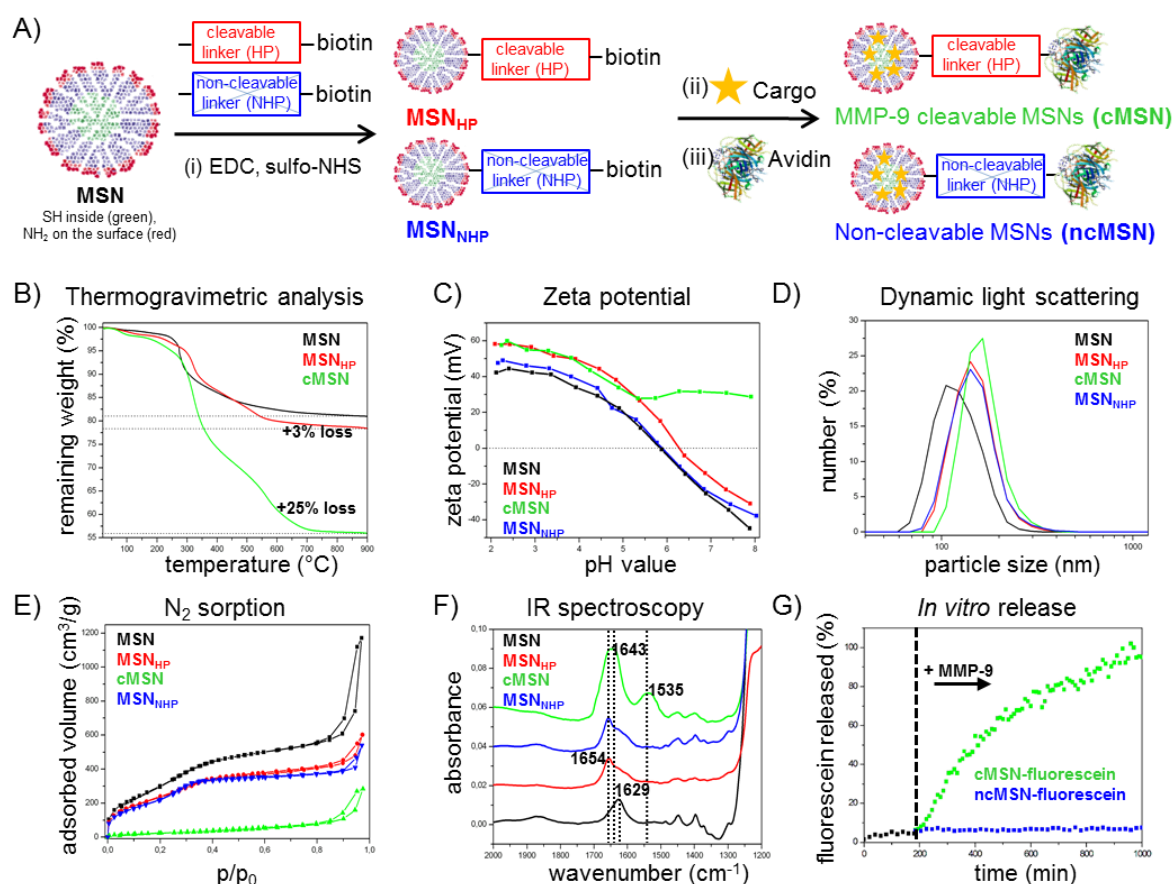


Figure 3-1. Synthesis and characterization of MMP9 responsive mesoporous silica nanoparticles. **A)** Synthesis scheme of core (green, thiol groups) shell (red, amino groups) functionalized mesoporous silica nanoparticles (MSN). (i) EDC amidation of amino groups with carboxy groups of the MMP9 cleavable HP (HP, red) or the MMP9 non-cleavable HP-biotin linker (NHP, blue) results in a covalent attachment to the external particle surface (MSN_{HP} , MSN_{NHP}). (ii) After cargo incorporation (cisplatin (CP) or bortezomib combination treatment (CT), yellow star), (iii) the strong binding affinity of biotin to avidin leads to blocking of the mesopores for MSNs with MMP9 cleavable linkers (cMSN) and MMP9 non-cleavable linkers (ncMSN). Characterization of MSNs. **B)** Thermogravimetric analysis, **C)** zeta potential measurements, **D)** dynamic light scattering, **E)** nitrogen sorption isotherms, and **F)** infrared spectroscopy (all curves are shifted by a value of 0.02 along the y-axis for clarity) of MSN (black), MSN_{HP} (red), MSN_{NHP} (blue), and cMSNs (green). **G)** Release kinetics of fluorescein from the MSNs before and after MMP9 administration.

3. Protease mediated release of chemotherapeutics from mesoporous silica nanoparticles to ex vivo human and mouse lung tumors

Sample	Particle size ^a (nm)	BET surface area (m ² /g)	Pore volume ^b (cm ³ /g)	DFT pore size ^c (nm)
MSN	106 ±9	1150	0.67	3.6 ±0.1
MSN _{HP}	142 ±13	882	0.55	3.6 ±0.1
cMSN	164 ±15	90	0.05	- ±0
MSN _{NHP}	142 ±17	825	0.52	3.6 ±0.1

Table 3-1. Structural parameters of functionalized MSNs.

^aParticle size refers to the peak value of the size distribution derived from DLS measurements.

^bPore volume was calculated up to a pore size of 8 nm to remove the contribution of inter-particle textural porosity. ^cDFT pore size refers to the peak value of the pore size distribution.

MMP9 responsive release of cargo using lung cancer cells. We next investigated MMP9 mediated release of the chemotherapeutic drug cisplatin in two human lung cancer cell lines (A549 and H1299) as a function of cell viability. MMP9-dose responsive release of cisplatin from the nanoparticles, and subsequent induction of dose-dependent cell death was observed in both cell lines (Figure 3-2A and B).

It is important to note that the MSNs were preloaded by diffusing a defined cisplatin solution into the particles, after which the particles were sealed and washed. In the figures, these loading concentrations are referred to as loaded cisplatin concentrations. However, the amount of cisplatin released from the particles, thus the effective cisplatin concentration the cells or tissue were exposed to, was much lower, as the incorporated amount is lower than the provided amount in the stock solution. Of note, we observed high cisplatin MSN loading of

440 ± 0.02 µg/mg MSN, when diffusing 10 mM cisplatin stock solution into the pores. The cisplatin concentration released from the particles was estimated to be an order of 10 fold less (then the used stock solution), when compared to free cisplatin as determined by a dose-response viability curve of direct cisplatin treatment in A549 and H1299 cells (Figure S 3-2A). To determine if cell-secreted MMP9 was able to open the particle caps, A549 and H1299 cells were transiently transfected with MMP9 cDNA and overexpression of active MMP9 was validated with gelatin zymography (Figure S 3-2B). MMP9 overexpressing cells responded to cisplatin loaded MSNs with pronounced loss of cell viability compared to empty vector transfected control cells. This demonstrates that the cell-secreted concentrations of MMP9 were able to trigger the release of chemotherapeutic drugs from stimuli-responsive MSNs (Figure 3-2C). Importantly, cisplatin-loaded MSNs containing non-cleavable linkers (ncMSN-CP) did not induce any cell death in either cell line (Figure 3-2D) indicating tight sealing of the particles. Importantly, non-loaded MSNs were found to be nontoxic at the dose applied (50 µg/mL) (Figure 3-2E).

Because MSNs can efficiently encapsulate multiple drugs, these carriers offer a unique opportunity for combinatorial drug delivery, which overcomes the problem of acquired drug resistance.²⁸ Proteasome inhibitors are promising combinatorial drugs as suggested by multiple clinical trials, since they effectively inhibit proliferation of tumor cells, sensitize them to apoptosis, and overcome drug resistance.²⁹ Bortezomib (Bz) is FDA-approved for treatment of multiple myeloma and mantle cell lymphoma, and is currently tested in phase II clinical trials for lung cancer.³⁰ In our set-up, nanoparticles loaded with non-toxic doses of cisplatin and Bz when used on their own, induced significant cell death in the presence of MMP9 when applied in combination (Figure 3-2F). Augmented cytotoxicity was largest for the lowest cisplatin dose (2 µM), with an increased cytotoxicity of over 35 % in the presence of Bz. This was a remarkable 5 to 10 fold increase in cytotoxic potency for non-toxic doses of

3. Protease mediated release of chemotherapeutics from mesoporous silica nanoparticles to *ex vivo* human and mouse lung tumors

a single drug. Cells exposed to MSNs loaded with cisplatin and Bz (cMSN-CT) in the absence of MMP9 showed no significant loss in cell viability (Figure 3-2F, white bars) indicating again tight sealing of the particles. These results demonstrated that the combinatorial delivery of cisplatin and Bz *via* nanoparticles induced an additive cytotoxic effect and thus allow for a reduction of drug doses.

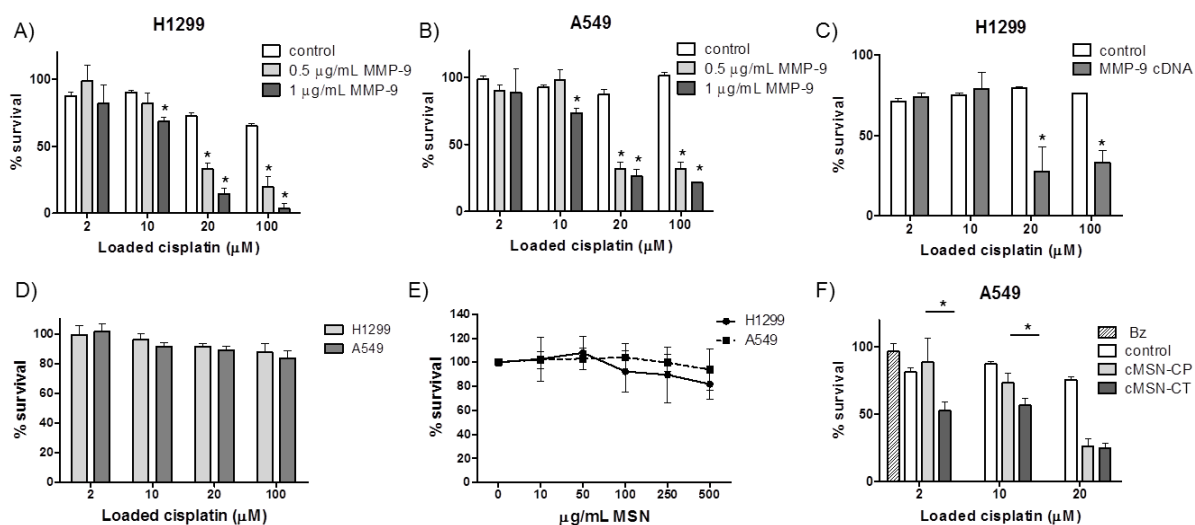


Figure 3-2. MMP9 responsive release in lung cancer cells. Controlled release of cisplatin from cMSN as measured by percent cell survival after 24 h exposure, incubated with; 0 (white bars), 0.5 (light-grey bars), or 1 μg/mL (dark-grey bars) MMP9 for in H1299 (A) and A549 cells (B), or C) with MMP9 cDNA (grey bars) or empty vector transfected cells (white bars) in H1299. D) ncMSN particles encapsulating cisplatin incubated in presence of 1 μg/mL MMP9 for 24 h did not result in significant cytotoxicity in H1299 (light grey bars) and A549 cells (dark grey bars). E) Cytotoxicity of cMSNs determined by WST-1 assay in H1299 and A549 lung cancer cell lines after 24 h of exposure. F) Controlled release of cMSN loaded with cisplatin alone (CP, light grey bars) and in combination with 1 μM bortezomib (CT, dark grey bars) in MMP9 cDNA transfected A549 cells, in comparison to empty vector transfected A549 cells (white bars). Untreated cells were set to 100 % survival, * means a significant decrease in percent cell survival compared to control ($p < 0.05$). Values given are average of three independent experiments \pm SD.

Application of 3D lung mouse and human tissue cultures. Having shown the feasibility of MMP9 mediated drug release from the avidin capped MSNs in lung tumor cell lines, we next aimed to validate MMP9 responsive drug release in the complex setting of lung tumor tissue. For that purpose, we made use of a novel 3D *ex vivo* tissue culture method. This technology

involves the preparation of *ex vivo* tissue cultures from healthy and tumoral mouse and human lungs, which can be cultured for up to 7 days (Figure 3-3A). For our purposes, mouse and human lung tissue slices of 200 μm thickness were exposed for 24 to 72 h to MSNs that had been covalently labeled with Atto633 in their core. After treatment, lung tissue slices were fixed and stained using immunofluorescence (Figure 3-3B). As a model for murine lung tumors, we used transgenic mice carrying a spontaneously activated *Kras* mutation, which are highly predisposed to a range of tumor types, however predominantly show early spontaneous development of lung cancer after only a few weeks of age.³¹ This mouse model does not only carry the most common mutation, i.e. *Kras*, observed in human lung cancer patients,³²⁻³⁴ but also closely resembles spontaneous tumor development *via* oncogene activation as seen in humans. Human material was obtained from freshly excised lung tumor tissue from consenting patients. Tumor lesions were clearly detectable in both mouse *Kras* and human patient derived 3D-LTC as characterized by loss of parenchymal lung structure and the appearance of dense cell populations (Figure 3-3B, phalloidin staining). Staining of 3D-LTC with a *Kras* antibody confirmed its overexpression in *Kras* tumor and non-tumor tissue, compared to low expression in 3D-LTC of wild-type (WT) mice. MSNs suspended in culture media distributed evenly and reproducibly in the tissue (Figure S 3-4B). Non-loaded particles were not toxic to the 3D-LTC for up to 72 h of exposure as revealed by the absence of apoptotic caspase-3 activation (Figure S 3-4C). High MMP9 expression was detected in tumor lesions of *Kras* mutant mice and in tumorous human tissue by MMP9 immunofluorescence staining, and by immunohistochemistry of paraffin-embedded lung tissue (see SI). MMP9 expression was highest in early-phase neoplasms and staining was most pronounced at the invading peripheries of the tumors (Figure S 3-4D). These data confirm MMP9 overexpression in *Kras* mouse and human lung tumors, validating this model as suitable for MMP9-mediated drug delivery.

3. Protease mediated release of chemotherapeutics from mesoporous silica nanoparticles to ex vivo human and mouse lung tumors

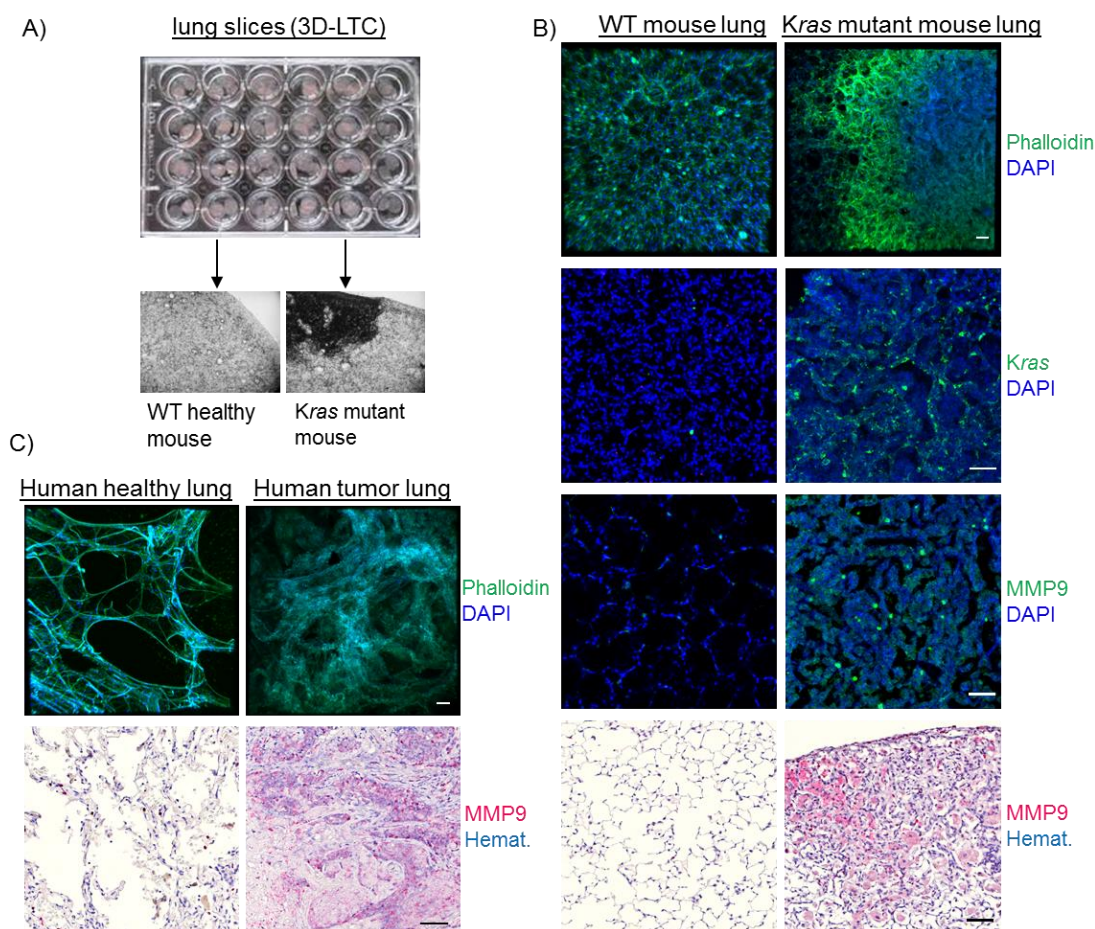


Figure 3-3. 3D human and mouse ex vivo tissue culture. A) 200 µm thick WT and Kras mouse and human lung tissue slices were kept under normal culture conditions, Kras mouse tumors can be easily observed with bright-field microscopy (5x objective). B) Confocal microscopy images of WT mouse and Kras mutant mouse 3D-LTC with (from top to bottom) phalloidin, Kras, and MMP9 staining using immunofluorescence and immunohistochemistry. C) 3D images of tumorous and tumor-free lung tissues from human with (from top to bottom) phalloidin, and MMP9 staining using immunohistochemistry (Hemat. = hematoxylin). The scale bar is 50 µm.

MSN mediated MMP9 responsive drug delivery to Kras mutant mouse lungs. Having established the 3D-LTCs of Kras mouse lung tumor tissue as a powerful tool for MMP9 mediated drug delivery *via* nanoparticles, we next evaluated therapeutic effectiveness of drug release from our functionalized nanoparticles (cMSN). For that, lung tissue slices of Kras mutant mice were exposed to particles that contained different concentrations of cisplatin (cMSN-CP_{low} and cMSN-CP_{high}; 5x higher concentration), or a combination of low doses of

cisplatin with bortezomib (cMSN-CT) for 24 or 48 h. Comparing cell death caused by cisplatin released from the MSNs to that of direct cisplatin administration in our *in vitro* experiments, we estimated that the cisplatin concentration released from the particles is at the order of 10 fold less. Next, we established the dose for direct cisplatin application by exposing the lung tissue slices to various concentrations of the drug. At the reported concentrations we observed a significant amount of apoptosis of approx. 12 % of cells after 24 h and 20 % after 48 h using the higher dose of cisplatin (Figure 3-4D, F), as indicated by a significant amount of caspase-3 positive staining (Figure S 3-6A, B and Figure S 3-7A, B). Based on our *in vitro* findings of about 10fold less encapsulation of cisplatin into the MSNs we encapsulated 10x higher doses of cisplatin solution inside the MSNs to be able to achieve a similar effect and applied those to the lung slices (see Table 3-2 for an overview of used doses). Importantly, a similar induction of tumor cell death was observed for both, the encapsulated drugs and the drugs alone for all tested doses and time-points, showing that the chosen doses were effective and comparable to each other (Figure 3-4C-F).

Strikingly, all nanoparticles containing chemotherapeutic(s) induced apoptosis only in tumor lesions of *Kras* lungs, while not affecting tumor-free regions in the same *Kras* lung tissues (Figure 3-4A). In addition, we observed a dose-dependent therapeutic effect on apoptotic cell death, with the combination therapy (cMSN-CT) being most effective. In contrast, *Kras* mutant mouse 3D-LTC exposed to comparable doses of free (non-encapsulated) drug(s) (CP or CT), resulted in apoptotic cell death that did not discriminate between tumorous and non-tumorous tissue. Of note, MSNs with non-cleavable linkers encapsulating both drugs (ncMSN-CT), did not cause any significant apoptotic cell death in *Kras* tumors or in healthy tissue in *Kras* lungs (Figure 3-4B upper panel). In addition, healthy lungs of WT mice exposed to drug-loaden nanoparticles (cMSN-CT) did not show significant signs of apoptosis, whereas exposure to comparable doses of free (non-encapsulated) drugs caused apoptotic cell

death that distributed evenly in the healthy tissue further proving the selective cytotoxic effect of our MSNs. The dose- and time- dependent therapeutic effects of the MSNs were quantified by counting the number of apoptotic cells versus the total number of cells in lung tissue slices containing tumors of comparable size (see Figure S 3-6 and Figure S 3-7 for the images used for quantification). Of note, cell death in the tumor area was 10 to 25 fold higher compared to the non-tumor area upon nanoparticle-mediated drug delivery. This was even more pronounced after 48 h (Figure 3-4E). The effect was highest for the combination therapy with a 25-fold increase in apoptotic tumor cell death while exposure of *Kras* lung tissue to Bz alone did not cause any significant apoptosis (Figure S 3-8A). In contrast to the nanoparticle-mediated drug delivery, *Kras* lungs exposed to comparable doses of cisplatin ± Bortezomib for 24 h and 48 h showed a similar degree of apoptotic cell death in the tumor and non-tumor areas (Figure 3-4D and F). Only for the highest doses (CP_{high} and CT) a small but significant increase in tumor cell death was observed. This might be attributed to the increased effectiveness of cisplatin towards fast-dividing and ‘leaky’ tumor cells.³⁵

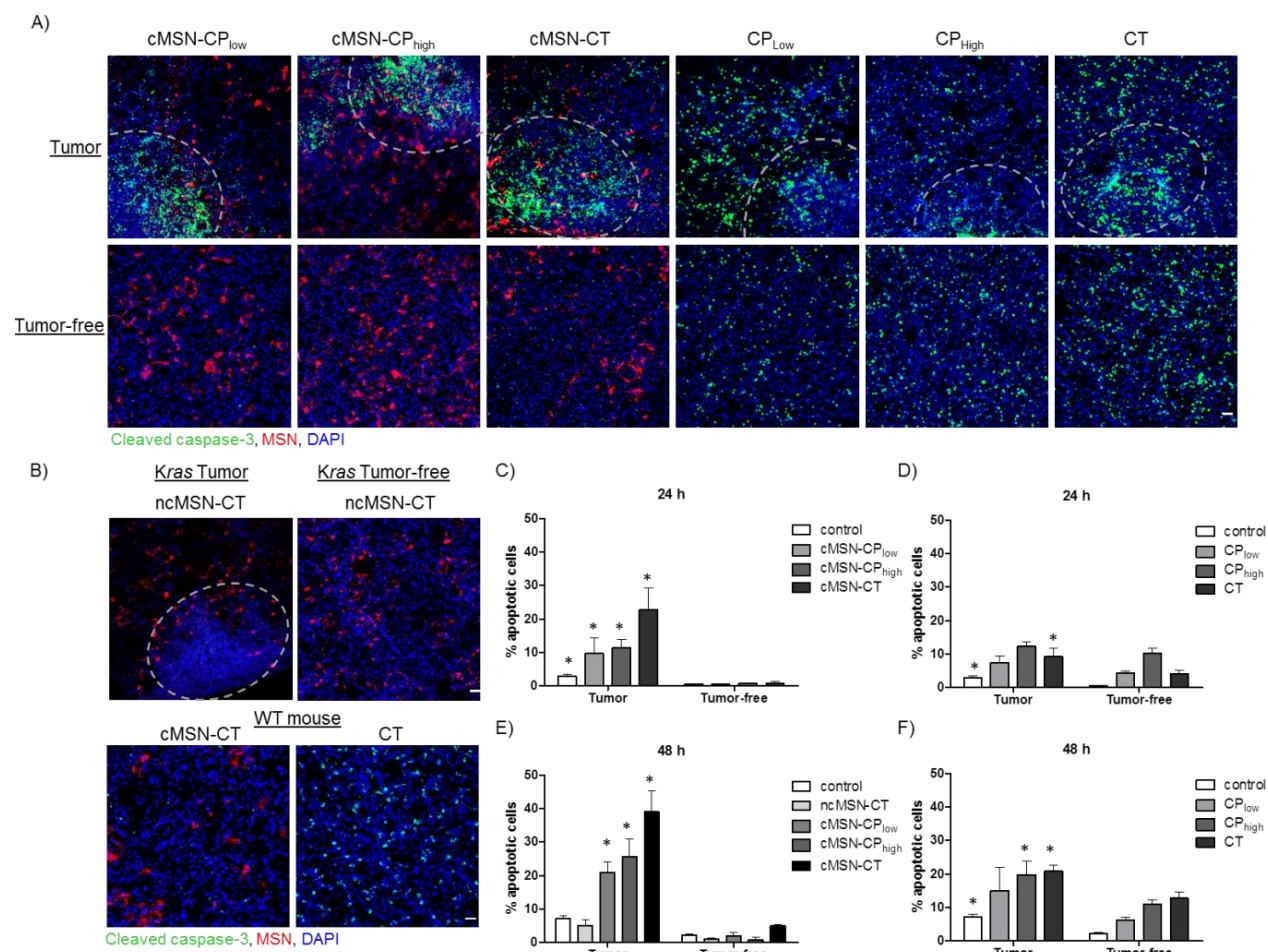


Figure 3-4. Therapeutic efficacy of MMP9 responsive MSNs in *Kras* mutant mouse lungs. A) *Kras* mutant mouse 3D-LTC exposed to MSN particles encapsulating either a low dose of cisplatin (cMSN-CP_{low}), high dose of cisplatin (cMSN-CP_{high}), low dose of cisplatin in combination with Bz (cMSN-CT), or to comparable doses of the free drugs (CP/ CT) for 48 h. B) *Kras* mouse 3D-LTC exposed to MSNs with non-cleavable linkers encapsulating combination treatment (ncMSN-CT) for 48 h (upper panel) and WT mouse 3D-LTC exposed to MSNs with MMP9-cleavable linkers encapsulating combination treatment (cMSN-CT), or free (non-encapsulated) drugs (CT) for 48 h (lower panel). The scale bar is 50 μ m. Comparable sized tumors were chosen for microscopy (indicated by dotted line), tumor-free refers to images that were made in a non-tumor area of a *Kras* 3D-LTC. Nuclear staining (DAPI) is shown in blue, apoptotic marker (cleaved caspase-3 positive) in green and Atto633 labelled MSN particles in red. Images shown are representative for three independent experiments (see also Figure S6, S7). Quantification of apoptotic cells (cleaved caspase-3) per number of counted nuclei (DAPI) in tumor and tumor-free areas in *Kras* 3D-LTC after C, D) 24 h of exposure and E, F) 48 h of exposure to MSN particles encapsulating drugs (cMSN-CP/CT) or free (non-encapsulated) drugs (CP/CT), respectively. Non-treated control slices (white bars) and control MSNs (i.e., ncMSN-CT) (light grey bar, 48 h exposure) were also included in the study. * means a significant increase in apoptosis compared to a non-tumor control area ($p < 0.05$). Values given are average of three independent experiments \pm SD.

3. Protease mediated release of chemotherapeutics from mesoporous silica nanoparticles to ex vivo human and mouse lung tumors

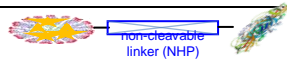
As represented in Fig. 1	Label	(loaded) drug concentrations
	cMSN-CP _{low}	2 mM cisplatin
	cMSN-CP _{high}	10 mM cisplatin
	cMSN-CT	2 mM cisplatin + 1 μM Bortezomib
	ncMSN-CP _{low}	2 mM cisplatin
	ncMSN-CP _{high}	10 mM cisplatin
	ncMSN-CT	2 mM cisplatin + 1 μM Bortezomib
	CP _{low}	0.2 mM cisplatin
	CP _{high}	1 mM cisplatin
	CT	0.2 mM cisplatin + 0.2 μM Bortezomib

Table 3-2. Drug doses used for the mouse lung tissue slices experiments.

Importantly, MSNs induced apoptosis correlated with MMP9 expression in tumor lesions (Figure 3-5A, Figure S 3-8B). Detailed analysis of the 3D-LTC revealed that apoptosis took place throughout the tumor while the particles remained mainly on the top of the tissue, where they associated with the tissue (Figure 3-5B and Figure S 3-8C). This observation suggests that the particles are first immobilized on the tissue and subsequently cleaved by overexpressed MMP9 on the surface of the tissue, and the released chemotherapeutic(s) effectively diffuse into the tissue. A similar distribution of apoptotic cells was observed for 3D-LTC exposed to the drug alone (Figure 3-5B and Figure S 3-8C). This indicates that deep

penetration of nanoparticles into the tumor tissue is not required as the released drugs effectively diffuse throughout the tissue. Moreover, we confirmed that the cytotoxic effects were mainly restricted to epithelial tumor cells by co-staining of 3D-LTCs with cleaved caspase-3 and the epithelial cell type marker E-cadherin (Figure 3-5C Figure S 3-8D). These data clearly demonstrate tumor site-selective drug delivery by our nanoparticles.

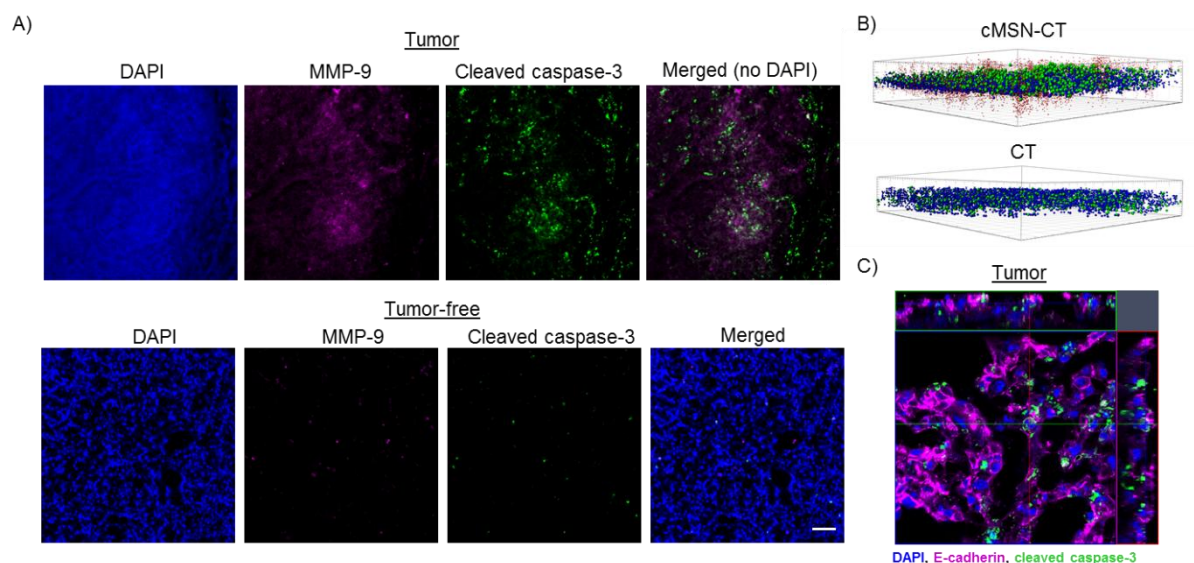


Figure 3-5. A) Kras 3D-LTC exposed to cMSN-CT for 48 h with MMP9 antibody co-staining (magenta, maximum intensity projections of the different channels, white dots in merged image show direct overlay) in tumor (top) and tumor-free (bottom) areas. B) Exposed Kras 3D-LTC, only showing the calculated number of particles, nuclei and apoptotic cells per 3D-LTC tissue slice from the side where tumor tissue is located. Red spots represent the calculated particles, blue spots represent the nuclei, and green spots represent the apoptotic cells in cMSN-CT exposed 3D-LTC (above panel), and CT exposed 3D-LTC (below panel). Original stainings were omitted for clarity. C) Kras 3D-LTC exposed to cMSN-CT for 48 h with E-cadherin antibody co-staining (magenta, orthographic representation using a 63x objective). The nuclear staining (DAPI) is shown in blue, apoptotic marker (cleaved caspase-3) in green. The fluorescence signal originating from Atto 633 labeled MSN particles was omitted from the images for clarity (for A and C). Scale bar is 50 μm .

MMP9 responsive drug delivery to human lung tumors. In a final step, we set out to assess protease responsive drug delivery from our nanoparticles in human lung tumors. For that purpose, we used 3D-LTCs from freshly excised human lung cancer tissue obtained from different donors. Cisplatin-loaded nanoparticles (cMSN-CP_{low}) induced pronounced apoptotic

cell death in human cancer tissue after 72 h of exposure. This correlated well with particle density on the tissue (Figure 3-6A). Furthermore, therapeutic effectiveness of the cMSN-CP was not dependent on the tumor type as apoptotic cell death was induced both in metastatic and primary lung tumors (Figure 3-6A). Untreated control tissue showed only a minor degree of apoptosis which might be attributed to the tissue cutting procedure (Figure 3-6A). Human 3D-LTCs exposed to non-cleavable MSNs (ncMSN-CP) did not show significantly more apoptosis compared to control tissues (Figure 6A, middle panel) confirming MMP9 sequence specific drug release. Importantly, cMSN-CP_{low} particle exposure did not induce any apoptosis in healthy human tissue (Figure 3-6B). MSN induced apoptosis was observed throughout the tumor tissue (Figure S 3-9). The therapeutic effect of the particles was confirmed by quantification of cleaved caspase-3 levels by western blot analysis using whole 3D-LTC homogenates (Figure 3-6C).

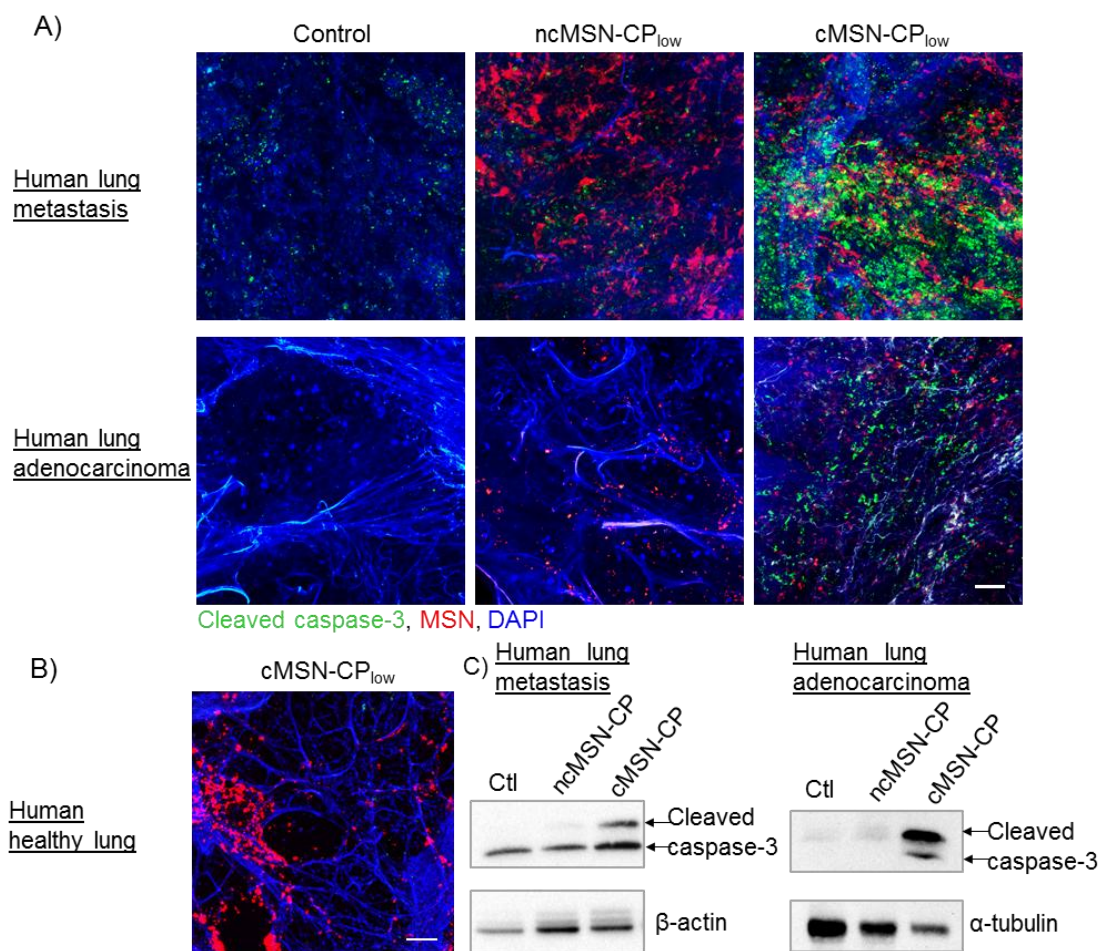


Figure 3-6. Therapeutic effect of MMP9 responsive MSNs in human lungs. A) human lung adenocarcinoma and B) human healthy lung 3D-LTC exposed to cMSN-CP_{low}, or ncMSN-CP_{low} for 72 h. Non-exposed control slices were included in the study. Nuclear staining (DAPI, blue), cleaved caspase-3 (green) and MSNs (red). The scale bar is 50 μ m. Images shown are representative for three different cuts within the tumor (see also Figure S9). C) Western blot analysis of human 3D-LTC exposed to cMSN-CP_{low} and ncMSN-CP_{low} for 72 h.

Nanoparticles as drug delivery carriers have received a lot of attention in the last decades and several formulations have been approved by the FDA and European Medicines Agency for the treatment of cancer.³⁶ Many of these formulations offer improved pharmacodynamics over the free drug by increasing their bioavailability, and tumor delivery efficiency. In addition, nanoparticles such as MSNs can be developed for inhalation therapy³⁷, which is advantageous for treatment of lung cancer as drugs are directly administered in the target organ, bypassing the gastrointestinal tract and the liver, and problems associated with stability throughout blood

circulation become irrelevant. Indeed, our preliminary data indicate that the particles are well distributed in the lungs and have low lung toxicity. The drug release of nanocarriers such as liposomes and polymers is sustained (i.e. slow release of drugs over-time that is not controllable). A promising approach to further increase the tumor-specificity and effectiveness of nanoparticles is the ability to release high concentrations of drugs only in the extracellular matrix in close proximity to the tumor site. Cancer-specific extracellular enzymes can be used to achieve this goal. For example, MMP9 is overexpressed in lung tumors, known to enhance the metastatic potency of malignant cells, and is associated with poor prognosis in lung cancer.²⁻⁵ The feasibility and promise of MMP2/9 responsive drug therapy has previously been demonstrated in *in vivo* mouse xenografts of the pancreas,³⁸ fibrosarcoma,¹¹ glioblastoma (brain),¹² and hepatoma (liver),³⁹ demonstrating that this is a promising technology for treatment of a variety of cancers. No such *in vivo* data for NSCLC lung cancer currently exists.

In the present study, we report the synthesis of novel mesoporous silica nanoparticles containing an MMP9 responsive avidin capping system. MMPs-responsive MSNs were reported only in three studies recently by Singh *et al.*,⁴⁰ Zhang *et al.*,⁴¹ and by Xu *et al.*⁴² However, these studies did not report a MMP9 sequence-specific capping system for controlled drug delivery from the MSNs. In the study by Singh *et al.*, the MSNs were coated with a polymer shell consisting of MMP substrate polypeptides with a degradable sequence. However, need for improvement over control of drug release is required for these nanocarriers. In the study by Zhang *et al.*, MSNs were coated with a polyanion layer preventing particle uptake by healthy cells, which could be removed *via* MMP cleavage in MMP2 expressing colon and squamous cancer cell lines. After (tumor) cell uptake of the particle, cargo release (doxorubicin) was obtained by a redox-driven release mechanism. In

another study by Xu *et al*, gelatin was used both as a gatekeeper and as a degradable substrate for MMPs in gelatin-coated MSNs and showed efficacy in a MMP2 overexpressing colon cancer cell line and a xenograft mouse model. Nevertheless, the efficiency of pore sealing to prevent premature drug release was poor in this system. In contrast, here we showed effective MMP2/9 sequence-specific release of loaded cargo from the biomolecule-capped MSN system in two non-small-cell lung cancer cell lines and in mouse and human lungs. To achieve this, we developed a novel *ex vivo* tissue culture application (3D-LTC) to test our particles. The 3D-LTC technique allows for high resolution and spatio-temporal imaging of the therapeutic effect of nanoparticles in selected areas of interest (e.g. diseased versus healthy areas) within the complex 3D structure of lung (cancer) tissue. While previous reports have used 3D-LTC predominantly for short-term toxicological analysis of nanoparticles,⁴³⁻⁴⁵ we studied the therapeutic effect of nanoparticles in relevant disease models. As a model for murine lung tumors, we used transgenic mice carrying a spontaneously activated *Kras* mutation, which show early spontaneous development of lung cancer after only a few weeks of age. As this model closely reflects the human pathophysiology, we believe that therapeutic strategies that are confirmed in this model are more likely to translate to humans than the commonly used xenograft mouse models. Furthermore, finding therapeutic strategies that work against *Kras* tumors is promising as *Kras* mutations result in aggressive cancers, are generally correlated with poor prognosis, and are associated with reduced responsiveness to many existing therapies.⁴⁶⁻⁴⁸ Additionally, this technique allowed us to confirm our findings also in diseased human tissue, which represents a major advance in closing the gap between drug development and application in the clinics. Using this method, we show that *in vivo* MMP9 concentrations are locally highly expressed in mouse *Kras* tumor and in patient derived explanted tumor tissue compared to healthy mouse and human lung tissue. Because MMP9 expression has been reported as a clinical marker for tumor progression and

metastasis,⁴⁹ it is possible that these highly MMP9 positive tumor areas represent metastasis-prone tumor cells. A link between MMP9 expression and metastasis was also shown in mice where MMP9 deficient mice had a reduced number of metastatic colonies.⁵⁰ MMP9 mediated drug delivery may thus most likely target metastatic tumor cell areas and therefore may effectively reduce tumor invasion and metastasis. Indeed, only MMP9-expressing *Kras* tumor areas were affected by MSN treatment as revealed by spatio temporal high-resolution imaging, whereas healthy lungs from WT mice and healthy areas in tumor-bearing mouse lungs remained unaffected. In contrast, slices exposed to free (non-encapsulated) drugs had an even distribution of apoptosis in tumor, tumor-free and healthy lung tissue. Accordingly, quantification of the therapeutic effect showed that the MSNs were 10 to 25 fold more effective in tumor tissue, whereas the free drug was less than 2-fold more effective in tumor tissue compared to the tumor-free areas in the same tissue slices. Furthermore, our 3D-LTC data proved the synergistic effect of our combinatorial drug delivery strategy and agrees very well with our *in vitro* data where we observed a 5-10 fold increase in cytotoxic potency upon combinatorial drug delivery. Using proteasome inhibitors in combination with a commonly used chemotherapeutic is a novel approach for treatment of cancer in general, and for lung cancer in particular. A phase II clinical trial study with bortezomib in combination with carboplatin (another platinum-based chemotherapeutic) showed promising progression-free and improved overall survival rates for treatment of non-small cell lung cancer (NSCLC).⁵¹ Our report is the first in which nanoparticle-based controlled release of a proteasome inhibitor in combination with cisplatin shows greatly enhanced antitumor activity. Finally, we provide proof that these particles are also effective in human metastasis and adenocarcinoma lung cancer. We show that MMP9 sensitive MSNs encapsulating cisplatin cause significant apoptosis in human lung tumor 3D-LTCs but not in healthy human lung tissue 3D-LTCs. This effect was MMP9 sequence specific as no apoptosis was induced for MSNs containing non-

cleavable linkers encapsulating the same cisplatin concentration. To our knowledge, we are the first to show the effectiveness of MMP9 responsive drug delivery to human patient-derived tissue.

3.3 Conclusion

In summary, this study shows the feasibility of MMP9 mediated drug release in human lung tissue and in an advanced mouse model (Kras mutant mice) that closely reflects the human pathophysiology. Specifically, our novel drug delivery system using MMP9 responsive MSN particles could be used to effectively deliver a combination of two drugs, bortezomib and cisplatin, in a stimuli-controlled manner, and potentiate a synergistic effect selectively to (metastatic) tumors in mouse and human ex vivo tissue slices.

3.4 Experimental Part

Materials. Tetraethyl orthosilicate (TEOS, Fluka, > 98 %), triethanolamine (TEA, Aldrich, 98 %), cetyltrimethylammonium chloride (CTAC, Fluka, 25 % in H₂O), mercaptopropyl triethoxysilane (MPTES, Fluka, > 80 %), aminopropyl triethoxysilane (APTES, Sigma Aldrich, 99 %), ammonium fluoride (NH₄F, Fluka), ammonium nitrate (NH₄NO₃, Fluka), hydrochloric acid (HCl, 37 %), Bio-PLGMWSR (HP-biotin, GenScript, 96.3 %), Bio-PLLMWSR (NHP-biotin, GenScript, 90.1 %), *N*-(3-dimethylaminopropyl)-*N*'-ethylcarbodiimide hydrochloride (EDC, Aldrich), *N*-hydroxysulfosuccinimide sodium salt (sulfoNHS, Aldrich), avidin, egg white (Merck, Calbiochem), fluorescein disodium salt dihydrate (Acros), calcein acetoxymethyl ester (calcein-AM, Sigma Aldrich), cisplatin (Sigma Aldrich), bortezomib (Bz, Velcade, Millennium Pharmaceuticals), cleaved caspase-3 antibody (Asp175) (Cell signaling, 9661), E-cadherin antibody (BD biosciences, 610181), *Kras*

antibody (Santa Cruz, SC30), MMP9 antibody (Millipore, AB19016), β -actin antibody (Cell Signaling), α -tubulin (Genetex) and secondary Alexafluor antibodies (Invitrogen) were used as received. Ethanol (EtOH, Aldrich, absolute), dimethylsulfoxide (DMSO, Aldrich), and HBSS buffer (Gibco) were used as solvents without further purification. Bi-distilled water was obtained from a Millipore system (Milli-Q Academic A10).

Synthesis procedures. Particle synthesis of MSNs containing SH groups in the core particle and NH_2 groups on the particle surface (MSN). A mixture of tetraethyl orthosilicate (TEOS, 1.63 g, 7.82 mmol), mercaptopropyl triethoxysilane (MPTES, 112 mg, 0.48 mmol) and triethanolamine (TEA, 14.3 g, 95.6 mmol) was heated under static conditions at 90 °C for 20 min in a polypropylene reactor. Then, a solution of cetyltrimethylammonium chloride (CTAC, 2.41 mL, 1.83 mmol, 25 wt% in H_2O) and ammonium fluoride (NH_4F , 100 mg, 2.70 mmol) in H_2O (21.7 g, 1.21 mmol) was preheated to 60 °C, and rapidly added to the TEOS solution. The reaction mixture was stirred vigorously (700 rpm) for 20 min while cooling down to room temperature. Subsequently, TEOS (138.2 mg, 0.922 mmol) was added in four equal increments every three minutes. After another 30 min of stirring at room temperature, TEOS (19.3 mg, 92.5 μmol) and aminopropyl triethoxysilane (APTES, 20.5 mg, 92.5 μmol) were added to the reaction. The resulting mixture was then allowed to stir at room temperature overnight. After addition of ethanol (100 mL), the MSNs were collected by centrifugation (19,000 rpm, 43,146 rcf, for 20 min) and re-dispersed in absolute ethanol. The template extraction was performed by heating the MSN suspension under reflux (90 °C, oil bath temperature) for 45 min in an ethanolic solution (100 mL) containing ammonium nitrate (NH_4NO_3 , 2 g), followed by 45 min heating under reflux in a mixture of concentrated hydrochloric acid (HCl, 10 mL) and absolute ethanol (90 mL). The mesoporous silica

nanoparticles were collected by centrifugation and washed with absolute ethanol after each extraction step.

Heptapeptide functionalization (MSN_{HP} and MSN_{NHP}). Bio-PLGMWSR (HP-biotin 96.3 %, 5.1 mg, 4.6 μmol) or Bio-PLLMWSR (NHP-biotin, 90.1 %, 5.0 mg, 4.0 μmol) were dissolved in 100 μL DMSO. The solution was diluted by addition of 400 μL H₂O. Then, EDC (0.8 mg, 5.2 μmol) was added, and the reaction mixture was stirred for 5 min at room temperature. Subsequently, sulfoNHS (1 mg, 5.0 μmol) was added, and the reaction mixture was stirred for another 5 min at room temperature. This mixture was added to a suspension containing 50 mg of MSN-NH₂_{OUT} in a total volume of 8 mL (EtOH:H₂O 1:1). The resulting mixture was then allowed to stir at room temperature overnight. The MSNs were thoroughly washed with EtOH and H₂O (3 times) and finally collected by centrifugation (19,000 rpm, 43,146 rcf, 20 min). The HP-biotin or NHP-biotin functionalized MSNs were stored as colloidal suspension in absolute ethanol.

Cargo loading. 1 mg of MSNs (MSN_{HP} or MSN_{NHP}) were immersed in 500 μL HBSS buffer containing fluorescein disodium salt dihydrate (1 mM), calcein-AM (20 μM or 50 μM), cisplatin (2 μM , 10 μM , 20 μM , or 100 μM), or a combination of cisplatin and Bz (2 μM + 1 μM , 10 μM + 1 μM , or 20 μM + 1 μM) for 2 h at room temperature. Afterwards, the particles were coated with avidin. Fluorescein-loaded particles were washed once by centrifugation and redispersion prior to the addition of avidin. All other samples were coated with avidin without a previous washing procedure.

Avidin capping (cMSN and ncMSN). 1 mg of loaded or non-loaded MSNs (in 500 μL HBSS buffer) were added to 500 μL HBSS buffer containing 1 mg of avidin. The solution was mixed by vortexing for 5 sec and allowed to react for 30 min under static conditions at room temperature. The resulting suspension was then centrifuged (5000 rpm, 2200 rcf, 4 min,

3. Protease mediated release of chemotherapeutics from mesoporous silica nanoparticles to ex vivo human and mouse lung tumors

15 °C) and washed three times with HBSS buffer. The particles were finally re-dispersed in HBSS buffer and used for cuvette release experiments or *in vitro* studies.

For details on characterization of the MSNs, please refer to the Supporting Information.

Cell culture. The human non-small cell lung cancer (NSCLC) cell lines, A549 and H1299, were obtained from ATCC (American Type Culture Collection, Manassas, USA). Both cell lines were maintained in DMEM media (Gibco, Life Technologies). Media were supplemented with 10 % FBS (fetal bovine serum) and 1 % penicillin/streptomycin. All cells were grown at 37 °C in a sterile humidified atmosphere containing 5 % CO₂.

WST-1 assay. Cytotoxicity of the non-loaded MSNs was assessed using the WST-1 assay (Roche). Briefly, 1.5×10^4 cells/well were seeded in 96-well plates. 24 h after seeding, the cells were exposed to MSN_{HPAVI} or MSN_{NH₂} particles for 4 or 24 h. After treatment, 10 µL of WST-1 reagent solution (Roche) was added to each well, and the cells were incubated at 37 °C for 30 min. Absorbance was measured at 450 nm using a Tristar LB 941 plate-reader (Berthold Technologies).

MTT assay. The MTT assay was performed to assess cell viability after cisplatin or Bz release from the particles. Briefly, 1×10^4 cells/well for H1299 and 0.5×10^4 cells/well for A549 were seeded in 96-well plates. 48 h after seeding, cells were exposed to 50 µg/mL MSN particles that had been loaded with solutions of cisplatin with or without Bz, in the presence of 0, 0.5 or 1 µg/mL of recombinant MMP9 (Enzo life sciences) in 50 µL of fresh media. In the case of transfected cells, 24 h after seeding, the cells were transfected with 0.15 µg of MMP9 cDNA (DNASU) or empty vector cDNA per well using SatisFectionTM transfection reagent (Agilent Technologies), according to manufacturer's instructions. 24 h after transfection, the cells were exposed to 50 µg/mL cMSN particles that had been loaded with

solutions of cisplatin, in 50 μL of fresh media. After treatment, 10 μL of freshly prepared solution of 5 mg thiazolyl blue tetrazolium bromide/mL PBS (Sigma) was added to each well, and the cells were incubated at 37 °C for 1 h. The supernatant was then aspirated, and the violet crystals were dissolved in 500 μL isopropanol + 0.1 % Triton X-100. Absorbance was measured at 570 nm, using a Tristar LB 941 plate-reader (Berthold Technologies). Experiments were done in triplicate. Data analyses were performed in Prism graphpad (version 6) software.

Zymography. To assess catalytically active MMP9 expression and transfection efficiency in A549 and H1299 cells, gelatin zymography was performed. In short, collected cell culture supernatants were centrifuged to get rid of cellular debris and then electrophoresed on 10 % SDS-gels containing 1 % gelatin substrate in non-reducing conditions (i.e., no β -mercaptoethanol), so that the proteins could renature afterwards. After electrophoresis, the enzymes were renatured by incubation with 2.5 % Triton-X-100 in developing buffer (50 mM Tris, 200 mM NaCl, 5 mM CaCl_2 , pH 7.5) for 1 h at room temperature, to ensure that the proteins were catalytically active. Afterwards, the gels were incubated in developing buffer at 37 °C for 24 h, to allow for the enzyme reaction to proceed. Thereafter, the gels were stained using PAGE-BlueTM (Fermentas) protein staining, according to the manufacturer's instructions. Gels were analyzed using the ChemiDocTM XRS+ software (BioRad).

Animals. 129S/Sv-*Kras*^{tm3Tyj/J} (K-ras^{LA2}) mutant mice were obtained from The Jackson Laboratory, Bar Harbor, Maine, USA and cross-bred with FVB-NCrl WT females obtained from the Charles River Laboratories, Sulzfeld, Germany for seven generations. Animals were kept in rooms maintained at constant temperature and humidity with a 12/12 h light/dark cycle, and were allowed food and water ad libitum. All procedures were conducted according

to the international guidelines and with the approval of the Bavarian Animal Research Authority in Germany.

Human tissue. The experiments with human tissue were approved by the Ethics Committee of the Ludwig-Maximilians-University Munich, Germany (LMU, project Nr. 455-12). All samples were provided by the Asklepios Biobank for Lung Diseases, Gauting, Germany (Project Nr. 333-10). Written informed consent was obtained from all subjects. Tumor or tumor-free tissue from patients who underwent lung tumor resection was used.

Human and mouse precision cut lung slicing (3D-LTC). The whole procedure was performed under sterile conditions. WT FVB as well as *Kras* mutant mice with lung tumor burden were anaesthetized with a mixture of ketamine and xylazin hydrochloride (bela-pharm, Germany). *Kras* mice of approx. 3 months of age which had several tumor lesions in each lung tissue slice were used. After intubation and diaphragm dissection, lungs were perfused *via* the right ventricle with sodium chloride solution (Braun Vet Care, Germany). Using a syringe pump, airways were filled with warm 2 wt-% low melting agarose solution (Sigma, Germany) prepared in DMEM/F12 (Gibco, Germany) supplemented with 1% penicillin/streptomycin and amphotericin B (Sigma, Germany). Later, tracheae were knotted with a thread to keep the liquid agarose inside the airways. Afterwards, the lungs were excised and transferred into tubes loaded with cultivation medium, left to cool on ice to allow for the solidification of the agarose. Finally, lobes were separated and cut with a vibratome (Hyrax V55, Zeiss, Germany) to a thickness of 200 μm . The 3D-LTC were cultivated for up to three days. The amount of sections per mouse varied between 30 to 50 slices. Directly after cutting, mouse 3D-LTC were exposed to 50 $\mu\text{g}/\text{mL}$ of CP, CT or to Atto 633 labelled MSNs particles containing CP or CT, administered directly into the medium. For human 3D-LTC, tumorous and tumor-free regions excised from lung cancer surgeries were used. Airways at tumor-free

segments were filled up with 3 wt-% agarose dissolved in DMEM/F12 as described above, *via* respective bronchi. Both the tumorous and tumor-free segments were then cut to a thickness of 300 μm with the vibratome. Directly after cutting, mouse and human 3D-LTC were exposed to 50 $\mu\text{g}/\text{mL}$ of MSNs particles containing CP or CT, administered directly into the medium. Human and mouse 3D-LTC were treated for either 24 or 48 h.

Immunofluorescence. 3D-LTC were fixed with acetone/methanol 50/50 vol% solution for 10 min, washed with PBS, blocked for 1 h with Roti®-ImmunoBlock (Carl Roth, Germany) at room temperature, and incubated with primary antibody at 4°C overnight. Afterwards, 3D-LTC were washed with PBS, incubated with secondary antibody for 2 h at room temperature, again washed with PBS and finally stained with DAPI. Stained 3D-LTC were mounted using fluorescence mounting medium (DAKO, USA) and evaluated using confocal microscopy (LSM710, Carl Zeiss, Germany). 3D reconstruction and quantification of cell death in the 3D-LTC were conducted using the IMARISx64 software (version 7.6.4, Bitplane, Switzerland). Maximum intensity projections were made using ZEN2009 software (Carl Zeiss, Germany).

Immunohistochemistry. Lung segments were placed in 4% (w/v) paraformaldehyde after excision and processed for paraffin embedding. 3 μm thick sections on slides were subjected to quenching of endogenous peroxidase activity using a mixture of methanol/ H_2O_2 for 20 min, followed by antigen retrieval in a decloaking chamber. From this step on, the slides were washed with TBST after each incubation with the reagents throughout the procedure. The sections were incubated firstly with Rodent Block M (Zytomed Systems, Germany) for 30 min, and then with the primary antibody, i.e. MMP9 (Millipore, USA) or IgG, control for 1 h. The cuts were then incubated with Rabbit on Rodent AP-Polymer for 30 min which was followed by Vulcan Fast Red, AP substrate solution (both Biocare Medical, Concord, USA) incubation for 10-15 min. The sections were counterstained with hematoxylin (Carl Roth,

Germany) and dehydrated respectively in consecutively grading ethanol and xylene (both AppliChem, Germany) incubations. Dried slides were mounted in entellan (Merck, Germany).

Study design and statistics. The therapeutic effect of the particles was assessed by immunofluorescent stainings using an apoptosis marker (cleaved caspase-3) and was investigated on lung tissue slices from 15 different *Kras* mutant animals that were cut and exposed to the MSNs or free drugs in three independent experiments. Similarly sized tumors were chosen for the imaging from a minimum of 3 different mice per individual staining. In addition, each staining was performed a minimum of 3 times per mouse. Three representative images of 3 different mice were chosen for the quantification as shown in Figure 4. The quantification was done blinded using the IMARISx64 software (version 7.6.4, Bitplane, Switzerland). For the controls, 9 WT FVB mice were cut in 3 independent experiments, and stained and quantified according the same principle. For comparison of two groups, one-way ANOVA analysis was performed. A p-value lower than 0.05 was considered statistically significant

Western Blotting. Human 3D-LTC were lysed in RIPA buffer (50 mM Tris HCl, pH 7.5, 150 mM NaCl, 1% NP40, 0.5% sodiumdeoxycholate, 0.1% SDS) supplemented with protease inhibitor cocktail (CompleteTM, Roche). Protein content was determined in the supernatants using the Pierce BCA protein assay kit (Thermo Scientific). For western blot analysis, equal amounts of protein were subjected to electrophoresis on 12% SDS-PAGE gels and blotted onto PVDF membranes. Membranes were treated with antibodies using standard Western blot techniques. The ECL Plus Detection Reagent (GE Healthcare) was used for chemiluminescent detection and membranes were analyzed with the ChemiDocTM XRS+ (Bio-Rad).

3.5 References

1. Malam, Y.; Lim, E. J.; Seifalian, A. M. Current Trends in the Application of Nanoparticles in Drug Delivery. *Curr. Med. Chem.* **2011**, *18*, 1067-1078.
2. Egeblad, M.; Werb, Z. New Functions for the Matrix Metalloproteinases in Cancer Progression. *Nat. Rev. Cancer* **2002**, *2*, 161-174.
3. Gialeli, C.; Theocharis, A. D.; Karamanos, N. K. Roles of Matrix Metalloproteinases in Cancer Progression and Their Pharmacological Targeting. *FEBS J.* **2011**, *278*, 16-27.
4. Iniesta, P.; Moran, A.; De Juan, C.; Gomez, A.; Hernando, F.; Garcia-Aranda, C.; Frias, C.; Diaz-Lopez, A.; Rodriguez-Jimenez, F. J.; Balibrea, J. L. *et al.* Biological and Clinical Significance of Mmp-2, Mmp-9, Timp-1 and Timp-2 in Non-Small Cell Lung Cancer. *Oncol. Rep.* **2007**, *17*, 217-223.
5. Martins, S. J.; Takagaki, T. Y.; Silva, A. G.; Gallo, C. P.; Silva, F. B.; Capelozzi, V. L. Prognostic Relevance of Ttf-1 and Mmp-9 Expression in Advanced Lung Adenocarcinoma. *Lung Cancer* **2009**, *64*, 105-109.
6. Turk, B. E.; Huang, L. L.; Piro, E. T.; Cantley, L. C. Determination of Protease Cleavage Site Motifs Using Mixture-Based Oriented Peptide Libraries. *Nat. Biotechnol.* **2001**, *19*, 661-667.
7. Li, H.; Yu, S. S.; Miteva, M.; Nelson, C. E.; Werfel, T.; Giorgio, T. D.; Duvall, C. L. Matrix Metalloproteinase Responsive, Proximity-Activated Polymeric Nanoparticles for Sirna Delivery. *Adv. Funct. Mater.* **2013**, *23*, 3040-3052.
8. Chien, M. P.; Carlini, A. S.; Hu, D. H.; Barback, C. V.; Rush, A. M.; Hall, D. J.; Orr, G.; Gianneschi, N. C. Enzyme-Directed Assembly of Nanoparticles in Tumors Monitored by in Vivo Whole Animal Imaging and Ex Vivo Super-Resolution Fluorescence Imaging. *J. Am. Chem. Soc.* **2013**, *135*, 18710-18713.
9. Yamada, R.; Kostova, M. B.; Anchoori, R. K.; Xu, S.; Neamati, N.; Khan, S. R. Biological Evaluation of Paclitaxel-Peptide Conjugates as a Model for Mmp2-Targeted Drug Delivery. *Cancer Biol. Ther.* **2010**, *9*, 192-203.
10. Zhu, L.; Kate, P.; Torchilin, V. P. Matrix Metalloprotease 2-Responsive Multifunctional Liposomal Nanocarrier for Enhanced Tumor Targeting. *ACS Nano* **2012**, *6*, 3491-3498.

11. Chien, M. P.; Thompson, M. P.; Barback, C. V.; Ku, T. H.; Hall, D. J.; Gianneschi, N. C. Enzyme-Directed Assembly of a Nanoparticle Probe in Tumor Tissue. *Adv. Mater.* **2013**, *25*, 3599-3604.
12. Gu, G.; Xia, H.; Hu, Q.; Liu, Z.; Jiang, M.; Kang, T.; Miao, D.; Tu, Y.; Pang, Z.; Song, Q. *et al.* Peg-Co-Pcl Nanoparticles Modified with Mmp-2/9 Activatable Low Molecular Weight Protamine for Enhanced Targeted Glioblastoma Therapy. *Biomaterials* **2013**, *34*, 196-208.
13. Hatakeyama, H.; Akita, H.; Ito, E.; Hayashi, Y.; Oishi, M.; Nagasaki, Y.; Danev, R.; Nagayama, K.; Kaji, N.; Kikuchi, H. *et al.* Systemic Delivery of Sirna to Tumors Using a Lipid Nanoparticle Containing a Tumor-Specific Cleavable Peg-Lipid. *Biomaterials* **2011**, *32*, 4306-4316.
14. Argyo, C.; Weiss, V.; Bräuchle, C.; Bein, T. Multifunctional Mesoporous Silica Nanoparticles as a Universal Platform for Drug Delivery. *Chem. Mater.* **2013**.
15. Li, Z.; Barnes, J. C.; Bosoy, A.; Stoddart, J. F.; Zink, J. I. Mesoporous Silica Nanoparticles in Biomedical Applications. *Chem. Soc. Rev.* **2012**, *41*, 2590-2605.
16. Cauda, V.; Schlossbauer, A.; Kecht, J.; Zurner, A.; Bein, T. Multiple Core-Shell Functionalized Colloidal Mesoporous Silica Nanoparticles. *J. Am. Chem. Soc.* **2009**, *131*, 11361-11370.
17. Sauer, A. M.; Schlossbauer, A.; Ruthardt, N.; Cauda, V.; Bein, T.; Brauchle, C. Role of Endosomal Escape for Disulfide-Based Drug Delivery from Colloidal Mesoporous Silica Evaluated by Live-Cell Imaging. *Nano Lett.* **2010**, *10*, 3684-3691.
18. Zhao, Y. L.; Li, Z.; Kabehie, S.; Botros, Y. Y.; Stoddart, J. F.; Zink, J. I. Ph-Operated Nanopistons on the Surfaces of Mesoporous Silica Nanoparticles. *J. Am. Chem. Soc.* **2010**, *132*, 13016-13025.
19. Giri, S.; Trewyn, B. G.; Stellmaker, M. P.; Lin, V. S. Y. Stimuli-Responsive Controlled-Release Delivery System Based on Mesoporous Silica Nanorods Capped with Magnetic Nanoparticles. *Angew. Chem., Int. Ed.* **2005**, *44*, 5038-5044.
20. Aznar, E.; Mondragon, L.; Ros-Lis, J. V.; Sancenon, F.; Marcos, M. D.; Martinez-Manez, R.; Soto, J.; Perez-Paya, E.; Amoros, P. Finely Tuned

- Temperature-Controlled Cargo Release Using Paraffin-Capped Mesoporous Silica Nanoparticles. *Angew. Chem., Int. Ed.* **2011**, *50*, 11172-11175.
21. Popat, A.; Liu, J.; Lu, G. Q.; Qiao, S. Z. A Ph-Responsive Drug Delivery System Based on Chitosan Coated Mesoporous Silica Nanoparticles. *J. Mater. Chem.* **2012**, *22*, 11173-11178.
 22. Schlossbauer, A.; Kecht, J.; Bein, T. Biotin-Avidin as a Protease-Responsive Cap System for Controlled Guest Release from Colloidal Mesoporous Silica. *Angew. Chem., Int. Ed.* **2009**, *48*, 3092-3095.
 23. Mackowiak, S. A.; Schmidt, A.; Weiss, V.; Argyo, C.; von Schirnding, C.; Bein, T.; Brauchle, C. Targeted Drug Delivery in Cancer Cells with Red-Light Photoactivated Mesoporous Silica Nanoparticles. *Nano Lett.* **2013**, *13*, 2576-2583.
 24. Bae, M.; Cho, S.; Song, J.; Lee, G. Y.; Kim, K.; Yang, J.; Cho, K.; Kim, S. Y.; Byun, Y. Metalloprotease-Specific Poly(Ethylene Glycol) Methyl Ether-Peptide-Doxorubicin Conjugate for Targeting Anticancer Drug Delivery Based on Angiogenesis. *Drugs Exp. Clin. Res.* **2003**, *29*, 15-23.
 25. Bauvois, B. New Facets of Matrix Metalloproteinases Mmp-2 and Mmp-9 as Cell Surface Transducers: Outside-in Signaling and Relationship to Tumor Progression. *Biochim. Biophys. Acta* **2012**, *1825*, 29-36.
 26. Cauda, V.; Schlossbauer, A.; Bein, T. Bio-Degradation Study of Colloidal Mesoporous Silica Nanoparticles: Effect of Surface Functionalization with Organo-Silanes and Poly(Ethylene Glycol). *Microporous Mesoporous Mater.* **2010**, *132*, 60-71.
 27. Cauda, V.; Argyo, C.; Bein, T. Impact of Different Pegylation Patterns on the Long-Term Bio-Stability of Colloidal Mesoporous Silica Nanoparticles. *J. Mater. Chem.* **2010**, *20*, 8693-8699.
 28. Dubey, S.; Powell, C. A. Update in Lung Cancer 2007. *Am. J. Respir. Crit. Care Med.* **2008**, *177*, 941-946.
 29. Davies, A. M.; Lara, P. N., Jr.; Mack, P. C.; Gandara, D. R. Incorporating Bortezomib into the Treatment of Lung Cancer. *Clin. Cancer Res.* **2007**, *13*, s4647-4651.
 30. Besse, B.; Planchard, D.; Veillard, A. S.; Taillade, L.; Khayat, D.; Ducourtieux, M.; Pignon, J. P.; Lumbroso, J.; Lafontaine, C.; Mathiot, C *et al.*

- Phase 2 Study of Frontline Bortezomib in Patients with Advanced Non-Small Cell Lung Cancer. *Lung Cancer* **2012**, *76*, 78-83.
31. Johnson, L.; Mercer, K.; Greenbaum, D.; Bronson, R. T.; Crowley, D.; Tuveson, D. A.; Jacks, T. Somatic Activation of the K-Ras Oncogene Causes Early Onset Lung Cancer in Mice. *Nature* **2001**, *410*, 1111-1116.
 32. Mills, N. E.; Fishman, C. L.; Rom, W. N.; Dubin, N.; Jacobson, D. R. Increased Prevalence of K-Ras Oncogene Mutations in Lung Adenocarcinoma. *Cancer Res.* **1995**, *55*, 1444-1447.
 33. Cancer Genome Atlas Research, N. Comprehensive Molecular Profiling of Lung Adenocarcinoma. *Nature* **2014**, *511*, 543-550.
 34. Clinical Lung Cancer Genome, P.; Network Genomic, M. A Genomics-Based Classification of Human Lung Tumors. *Sci. Trans. Med.* **2013**, *5*, 209ra153.
 35. Dasari, S.; Bernard Tchounwou, P. Cisplatin in Cancer Therapy: Molecular Mechanisms of Action. *Eur. J. Pharmacol.* **2014**, *740C*, 364-378.
 36. Rink, J. S.; Plebanek, M. P.; Tripathy, S.; Thaxton, C. S. Update on Current and Potential Nanoparticle Cancer Therapies. *Curr. Opin. Oncol.* **2013**, *25*, 646-651.
 37. Taratula, O.; Garbuzenko, O. B.; Chen, A. M.; Minko, T. Innovative Strategy for Treatment of Lung Cancer: Targeted Nanotechnology-Based Inhalation Co-Delivery of Anticancer Drugs and Sirna. *J. Drug Targeting* **2011**, *19*, 900-914.
 38. Kulkarni, P. S.; Haldar, M. K.; Nahire, R. R.; Katti, P.; Ambre, A. H.; Muhonen, W. W.; Shabb, J. B.; Padi, S. K.; Singh, R. K.; Borowicz, P. P. *et al.* Mmp-9 Responsive Peg Cleavable Nanovesicles for Efficient Delivery of Chemotherapeutics to Pancreatic Cancer. *Mol. Pharm.* **2014**, *11*, 2390-2399.
 39. Liu, Q.; Li, R. T.; Qian, H. Q.; Yang, M.; Zhu, Z. S.; Wu, W.; Qian, X. P.; Yu, L. X.; Jiang, X. Q.; Liu, B. R. Gelatinase-Stimuli Strategy Enhances the Tumor Delivery and Therapeutic Efficacy of Docetaxel-Loaded Poly(Ethylene Glycol)-Poly(Varepsilon-Caprolactone) Nanoparticles. *Int. J. Nanomed.* **2012**, *7*, 281-295.
 40. Singh, N.; Karambelkar, A.; Gu, L.; Lin, K.; Miller, J. S.; Chen, C. S.; Sailor, M. J.; Bhatia, S. N. Bioresponsive Mesoporous Silica Nanoparticles for Triggered Drug Release. *J. Am. Chem. Soc.* **2011**, *133*, 19582-19585.

41. Zhang, J.; Yuan, Z. F.; Wang, Y.; Chen, W. H.; Luo, G. F.; Cheng, S. X.; Zhuo, R. X.; Zhang, X. Z. Multifunctional Envelope-Type Mesoporous Silica Nanoparticles for Tumor-Triggered Targeting Drug Delivery. *J. Am. Chem. Soc.* **2013**, *135*, 5068-5073.
42. Xu, J. H.; Gao, F. P.; Li, L. L.; Ma, H. L.; Fan, Y. S.; Liu, W.; Guo, S. S.; Zhao, X. Z.; Wang, H. Gelatin-Mesoporous Silica Nanoparticles as Matrix Metalloproteinases-Degradable Drug Delivery Systems in Vivo. *Microporous Mesoporous Mater.* **2013**, *182*, 165-172.
43. Neuhaus, V.; Schwarz, K.; Klee, A.; Seehase, S.; Forster, C.; Pfennig, O.; Jonigk, D.; Fieguth, H. G.; Koch, W.; Warnecke, G. *et al.* Functional Testing of an Inhalable Nanoparticle Based Influenza Vaccine Using a Human Precision Cut Lung Slice Technique. *PLoS One* **2013**, *8*, e71728.
44. Paranjpe, M.; Neuhaus, V.; Finke, J. H.; Richter, C.; Gothsch, T.; Kwade, A.; Buttgenbach, S.; Braun, A.; Muller-Goymann, C. C. In Vitro and Ex Vivo Toxicological Testing of Sildenafil-Loaded Solid Lipid Nanoparticles. *Inhalation Toxicol.* **2013**, *25*, 536-543.
45. Nassimi, M.; Schleh, C.; Lauenstein, H. D.; Hussein, R.; Lubbers, K.; Pohlmann, G.; Switalla, S.; Sewald, K.; Muller, M.; Krug, N. *et al.* Low Cytotoxicity of Solid Lipid Nanoparticles in in Vitro and Ex Vivo Lung Models. *Inhalation Toxicol.* **2009**, *21 Suppl 1*, 104-109.
46. Uberall, I.; Kolar, Z.; Trojanec, R.; Berkovcova, J.; Hajduch, M. The Status and Role of ErbB Receptors in Human Cancer. *Exp. Mol. Pathol.* **2008**, *84*, 79-89.
47. Eberhard, D. A.; Johnson, B. E.; Amler, L. C.; Goddard, A. D.; Heldens, S. L.; Herbst, R. S.; Ince, W. L.; Janne, P. A.; Januario, T.; Johnson, D. H. *et al.* Mutations in the Epidermal Growth Factor Receptor and in Kras Are Predictive and Prognostic Indicators in Patients with Non-Small-Cell Lung Cancer Treated with Chemotherapy Alone and in Combination with Erlotinib. *J. Clin. Oncol.* **2005**, *23*, 5900-5909.
48. Cappuzzo, F.; Varella-Garcia, M.; Finocchiaro, G.; Skokan, M.; Gajapathy, S.; Carnaghi, C.; Rimassa, L.; Rossi, E.; Ligorio, C.; Di Tommaso, L. *et al.* Primary Resistance to Cetuximab Therapy in Egfr Fish-Positive Colorectal Cancer Patients. *Br. J. Cancer* **2008**, *99*, 83-89.

49. Roy, R.; Yang, J.; Moses, M. A. Matrix Metalloproteinases as Novel Biomarkers and Potential Therapeutic Targets in Human Cancer. *J. Clin. Oncol.* **2009**, *27*, 5287-5297.
50. Itoh, T.; Tanioka, M.; Matsuda, H.; Nishimoto, H.; Yoshioka, T.; Suzuki, R.; Uehira, M. Experimental Metastasis Is Suppressed in Mmp-9-Deficient Mice. *Clin. Exp. Metastasis* **1999**, *17*, 177-181.
51. Davies, A. M.; Lara, P. N.; Lau, D. H.; Mack, P. C.; Gumerlock, P. H.; Gandara, D. R.; Schenkein, D.; Doroshow, J. H. The Proteasome Inhibitor, Bortezomib, in Combination with Gemcitabine (Gem) and Carboplatin (Carbo) in Advanced Non-Small Cell Lung Cancer (Nslc): Final Results of a Phase I California Cancer Consortium Study. *J. Clin. Oncol.* **2004**, *22*, 642s-642s.

3.6 Appendix

Materials and Methods. Transmission electron microscopy (TEM) was performed at 300 kV on an FEI Titan 80-300 equipped with a field emission gun. For sample preparation, the colloidal solution of MSNs was diluted in absolute ethanol, and one drop of the suspension was then deposited on a copper grid sample holder. The solvent was allowed to evaporate. Dynamic light scattering (DLS) and zeta potential measurements were performed on a Malvern Zetasizer-Nano instrument equipped with a 4 mW He-Ne laser (633 nm) and an avalanche photodiode detector. DLS measurements were directly recorded in diluted colloidal aqueous suspensions of the MSNs at a constant concentration of 1 mg/mL for all sample solutions. Zeta potential measurements were performed using the add-on Zetasizer titration system (MPT-2), based on diluted NaOH and HCl as titrants. For this purpose, 1 mg of the MSN sample was diluted in 10 mL bi-distilled water. Thermogravimetric analyses (TGA) of the extracted bulk samples (approximately 10 mg) were recorded on a Netzsch STA 440 C TG/DSC. The measurements proceeded at a heating rate of 10 °C/min up to 900 °C, in a stream of synthetic air of about 25 mL/min. Nitrogen sorption measurements were performed on a Quantachrome Instrument NOVA 4000e at -196 °C. Sample outgassing was performed for 12 hours at a vacuum of 10 mTorr at 120 °C. Pore size and pore volume were calculated with an NLDFT equilibrium model of nitrogen on silica, based on the desorption branch of the isotherms. In order to remove the contribution of the interparticle textural porosity, pore volumes were calculated only up to a pore size of 8 nm. A BET model was applied in the range of 0.05 – 0.20 p/p₀ to evaluate the specific surface area. Infrared spectra were recorded on a ThermoScientific Nicolet iN10 IR-microscope in reflection-absorption mode with a liquid-N₂ cooled MCT-A detector. ICP-OES measurements have been performed on a Varian Vista RL (radial) CCD Simultaneous ICP-OES instrument. Time-based fluorescence spectra were recorded on a PTI spectrofluorometer equipped with a xenon short arc lamp (UXL-

75XE USHIO) and a photomultiplier detection system (model 810/814). The measurements were performed in HBSS buffer at 37 °C, to simulate human body temperature. For time-based release experiments of fluorescein, a custom-made container consisting of a Teflon tube, a dialysis membrane (ROTH Visking type 8/32, MWCO 14,000 g/mol), and a fluorescence cuvette were used (Figure S2). The excitation wavelength was set to $\lambda=495$ nm S3 for fluorescein-loaded MSNs. Emission scans (505 – 650 nm) were performed every 5 min. All slits were adjusted to 1.0 mm, bandwidth 8 nm. The release of calcein-AM, hence the staining of the cells from the particles was assessed using confocal microscopy. Freshly prepared calcein-AM containing MSN or MSNctl particles were incubated with 0, 1 or 2 $\mu\text{g/mL}$ recombinant MMP9 (Enzo life sciences) for 2 h at 37 °C in a thermoblock that was shaking mildly at 700 rpm. After the incubation time, the particles were removed by centrifugation, and the cells were incubated with the supernatants for 30 min, so that the released calcein-AM could be taken up by the living cells. Afterwards, the nuclei of the cells were counterstained with Hoechst (Enzo life sciences). Live cell imaging was performed using a confocal microscope (Zeiss LSM 710).

Characterization of the particles. The core-shell functionalized MSNs have been synthesized by a delayed co-condensation approach, resulting in functionalization of the external particle surface with amino groups. Additionally, the inner pore system has been decorated with thiol groups. This additional core functionalization offers a site for covalent attachment of cargo via cleavable linkers, or binding of fluorescent dyes for particle tracking, which are important for particle tracking in in vitro and in vivo studies. Sample MSN consisted of nano-sized mesostructured particles of about 70 nm, as derived from transmission electron microscopy (TEM, Figure S 3-1A). The TEM image shows a spherical particle shape, and the worm-like structure of the mesopores is clearly visible. Dynamic light

scattering (DLS) measurements revealed a mean particle size of 106 nm (Table 3-1) and good colloidal stability. This apparent difference in particle size, compared to TEM, is attributed to the involvement of the hydrodynamic diameter and weak transient agglomeration of a few nanoparticles during the DLS measurements. Importantly, a narrow particle size distribution and no significant agglomeration were observed after each synthesis step (particle size distribution, see Figure 3-1D). After the modification of the MSNs with the short heptapeptide linkers and further attachment of avidin, the mean particle sizes increased, due to these additional organic layers (Table 3-1 and Figure 3-1D). Thermogravimetric analyses showed stepwise additional weight loss for the samples MSN_{HP} and fully functionalized MSNs (MSN), compared to MSN_{naked} , during heating from 150 – 900 °C (Figure 3-1). This confirmed efficient attachment of the short organic heptapeptide linker and the bulky protein avidin (+3 % and +25 % additional weight loss, respectively). The zeta potential measurements showed no significant change in the surface charge at different pH values of the MSN_{HP} and MSN_{NHP} samples, compared to MSN_{naked} , confirming that the quantity of charged groups at the external surface was not increased by the attachment of the heptapeptide linkers (mainly consisting of unprotonable residues). The isoelectric points were around pH = 6. Only after attachment of the avidin ($cMSN$), a drastic change in the surface charge of the coated nanoparticles was observed at around pH = 7 (Figure 3-1C). Avidin-capped MSNs still showed positive surface charge at neutral pH values, which was due to various functional groups in the protein sequence including arginine, lysine, and histidine residues. Nitrogen sorption measurements were performed to gain information about the porosity and the surface area of the functionalized MSNs. Figure 3-1E shows typical type IV isotherms for MSN , MSN_{HP} , and MSN_{NHP} samples with inflection points at around 0.3 p/p_0 , indicating mesoporous structure for these samples. Furthermore, nitrogen sorption isotherms showed a small hysteresis loop at around 0.9 p/p_0 for all samples, which is attributed to

interparticle textural porosity (Figure 3-1E). Relatively high BET surface areas and pore volumes were obtained for the MSN nanoparticles. A summary of the porosity parameters is given in Table 3-1. A reduction in specific surface area and pore volume occurred for the MSNs containing the heptapeptide linkers (MSNHP and MSNNHP, Table 3-1). This reduction in BET surface area and pore volume, compared to unfunctionalized MSN, can be attributed to the increased sample weight by addition of non-porous organic material (HP-biotin and NHP-biotin), and to the blocking of some pores towards the access of nitrogen molecules by frozen organic moieties in the surface layer of the nanoparticles. The narrow pore size distribution, with a maximum at around 3.6 nm, confirmed an accessible porous system even after modification with the heptapeptide linkers (Figure S 3-1B). After the attachment of avidin to the silica nanoparticles (cMSN), we obtained a type II isotherm, indicating loss of specific surface area and pore volume (Figure 3-1E). These data show that the mesopores of the avidin-coated MSNs were blocked for the access of nitrogen molecules, proving that avidin is a suitable gatekeeper to efficiently seal the mesopores of our nanoparticles. Infrared spectroscopy of MSNHP and MSNNHP showed a band at 1654 cm^{-1} (C=O stretching vibration), which can be attributed to the amide bonds of the short heptapeptide linkers (Figure 3-1F, for full spectra see Figure S 3-1C). Subsequently, this band was fully obscured after the modification with avidin (MSN), and typical amide vibration bands of high intensity (amide I: C=O stretching vibration at 1643 cm^{-1} ; amide II: N-H deformation and C-N stretching vibration at 1535 cm^{-1}) were detected, providing evidence for the presence of the avidin protein. Additionally, infrared spectra of all MSN samples showed typical bands of the silica framework (Si-O-Si) between 1000 and 1300 cm^{-1} . Two additional bands at 780 and 900 cm^{-1} were also present (asymmetric stretching and bending vibrations of Si-OH groups).

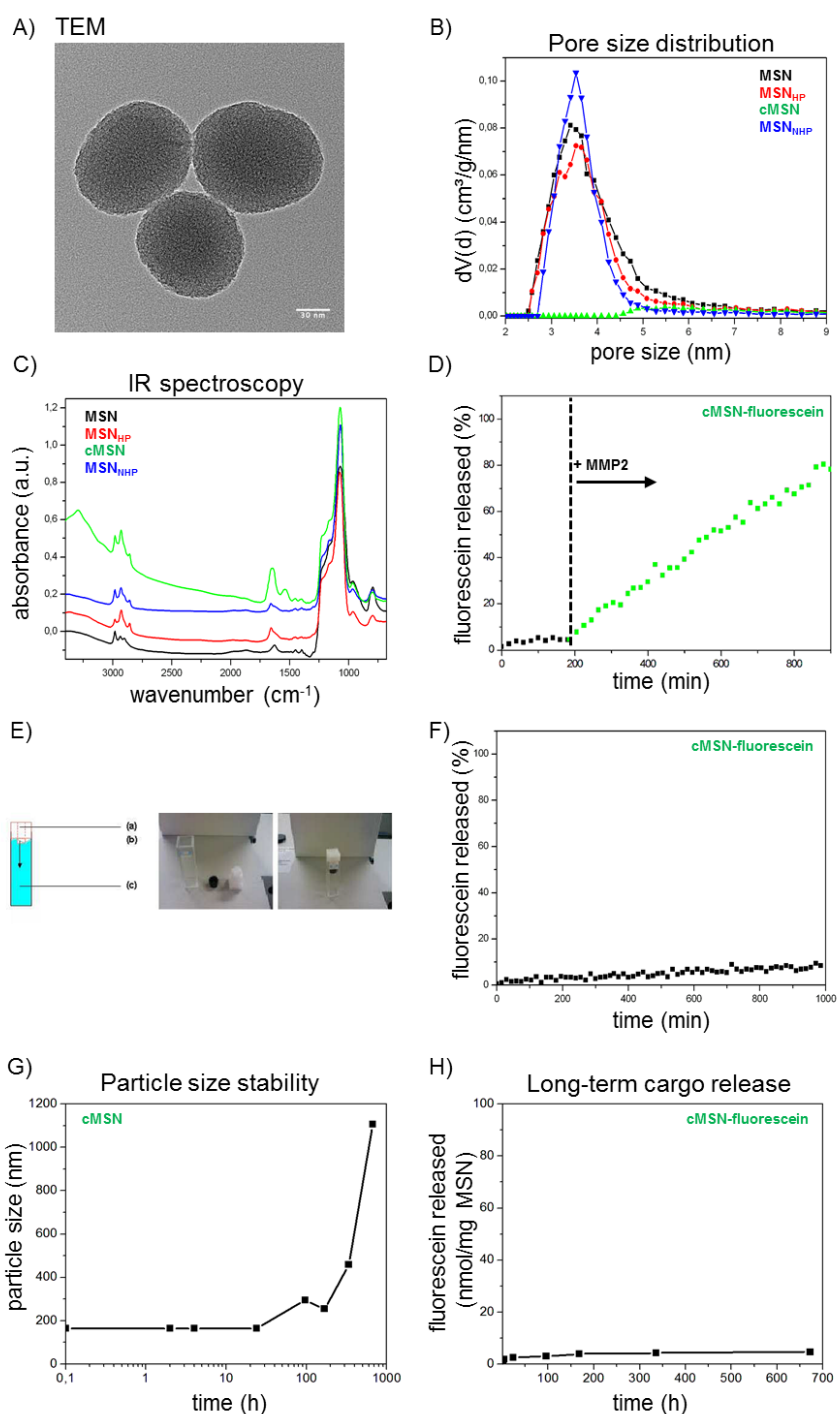


Figure S 3-1. Additional characterization of mesoporous silica nanoparticles. A) Transmission electron micrograph of sample MSN. B) DFT pore size distribution, and D) infrared spectroscopy data (full range) of MSN (black), MSNHIP (red), MSNNHP (blue), and avidin-capped cMSNs (green). D) Release kinetics of fluorescein from the MSNs before (black dots) and after (red dots) MMP2 administration (100% of released fluorescein is defined as the total amount being released from MSN after addition of MMP9). E) Custom-made release setup consists of a reservoir for the particles (Teflon tube) (a), a dialysis membrane (b), and a fluorescence cuvette (c). F) Long-term stability of avidin capping for MSNs (MSN) in the absence of MMP9 (100% of released fluorescein is defined as the total amount being released from cMSN).

3. Protease mediated release of chemotherapeutics from mesoporous silica nanoparticles to ex vivo human and mouse lung tumors

after addition of MMP9). G) Long-term particle size stability assay of cMSN measured by DLS investigating the aggregation behavior in HBSS buffer solution for 28 days. H) Long-term cargo release experiment of fluorescein loaded cMSN in HBSS buffer solution (no MMP-9) for 28 days. The amount of fluorescein released (nmol/mg MSN) has been determined by UV-Vis measurements.

Uptake of CP	440 ± 0.02 µg/mg MSN
Release of CP (+ MMP-9)	7 ± 0.8 µg/mg MSN
Release of CP (- MMP-9)	0 µg/mg MSN*

Table 3-3. Quantification of the uptake and release of cisplatin (CP) by/from cMSN. Release behavior has been investigated in the presence (+) and absence (-) of MMP-9. Data derived by ICP-OES measurements. Values given are average of three independent measurements ± SD. * Values < LOD (Limit of Detection).

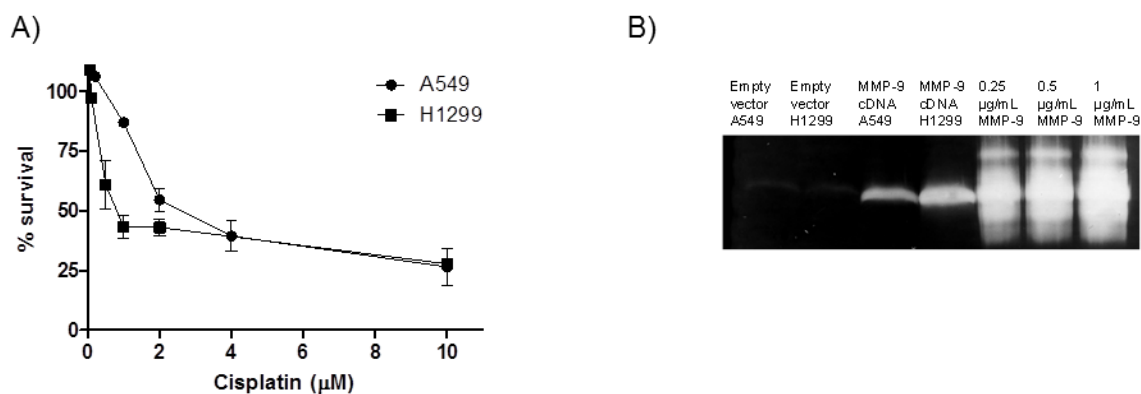


Figure S 3-2. A) Dose-response survival curve of cisplatin (non-encapsulated) in A549 and H1299 cells after 24 h exposure. B) Gelatin zymography, assessing MMP9 activity in cell culture supernatants of empty vector (first two lanes) or MMP9 cDNA (middle two lanes) transfected A549 and H1299 cells, compared to 0.25, 0.5 and 1 µg/mL recombinant MMP9 (outer three lanes).

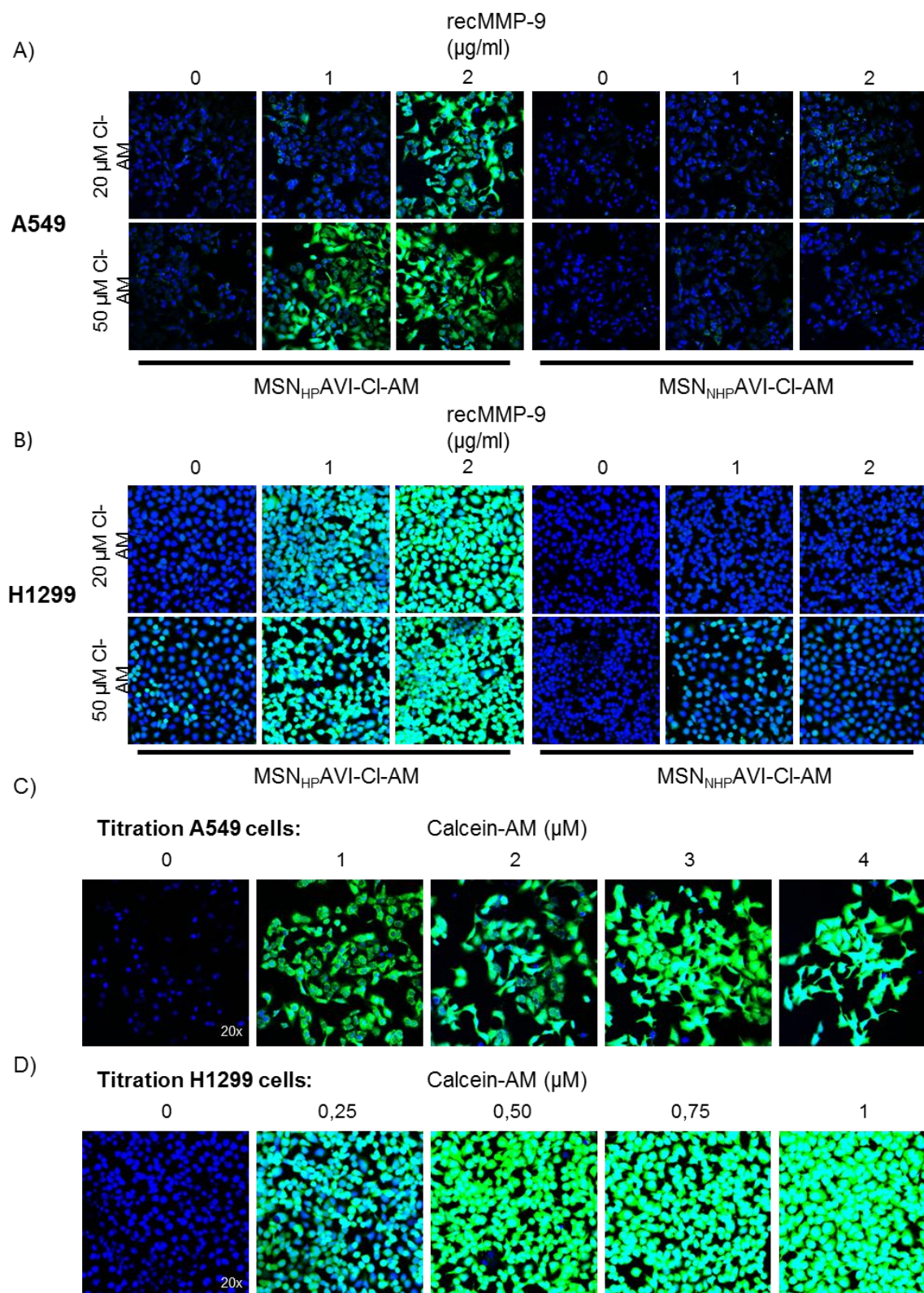


Figure S 3-3. Confocal microscopy images showing A) calcein staining as a result of MMP-9 responsive release of calcein-AM (Cl-AM, green) from MSNs containing MMP-9 cleavable or non-cleavable linkers (MSN_{HP}AVI and MSN_{NHP}AVI), after 2 h incubation with 0, 1, or 2 µg/mL MMP-9 administration in A549 cells and B) in H1299 cells. C) dose-responsive calcein staining (green) as a result of increasing calcein-AM

3. Protease mediated release of chemotherapeutics from mesoporous silica nanoparticles to ex vivo human and mouse lung tumors

concentrations directly administered to A549 and D) H1299 cells. Hoechst was used as a counterstain for nuclei (blue). Pictures show representative micrographs from three independent experiments. Image sizes are 450 x 450 μm .

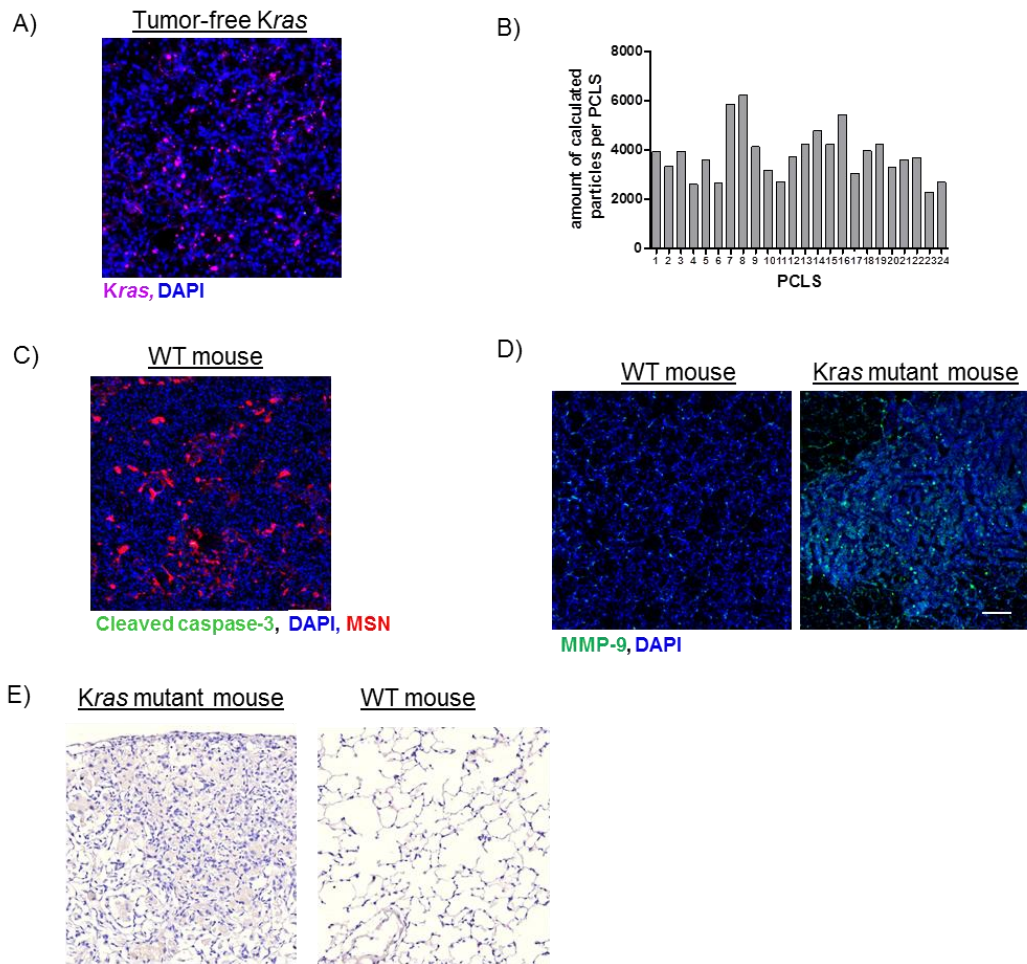


Figure S 3-4. Experimental set-up of precision cut lung slices (3D-LTC) using healthy wild-type (WT) and *Kras* mutant (*Kras*) mice. A) *Kras* 3D-LTC in a tumor-free region stained with *Kras* antibody, B) Calculated amount of particles per 3D-LTC using Imaris software over 24 slices, C) Toxicity of avidin-capped MSNs in WT lung 3D-LTC slices after 72 h of exposure. D) WT and *Kras* 3D-LTC stained with MMP9 antibody. Scale bar is 50 μm . E) IgG control for MMP9 immunohistochemistry in WT and *Kras* mouse tissue.

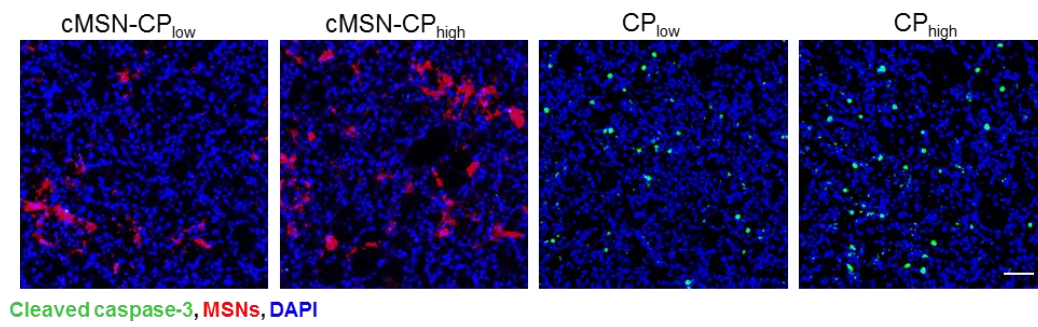
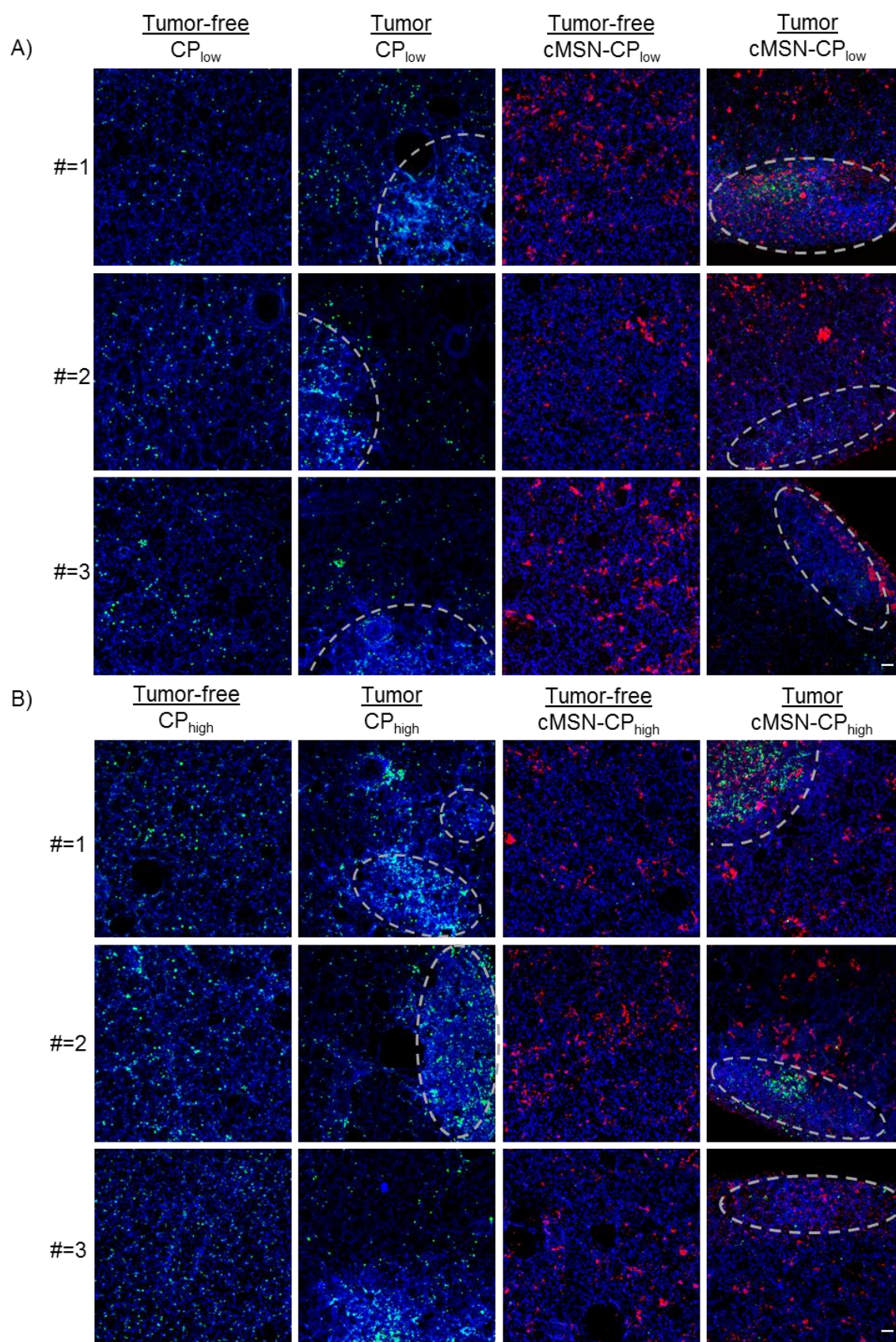


Figure S 3-5. WT 3D-LTC exposed to cMSN-CP_{low}, cMSN-CP_{high} and CP_{low} and CP_{high}. The nuclear staining (DAPI) is shown in blue, apoptotic marker (cleaved caspase-3) in green. Scale bar is 50 μ m.

3. Protease mediated release of chemotherapeutics from mesoporous silica nanoparticles to ex vivo human and mouse lung tumors



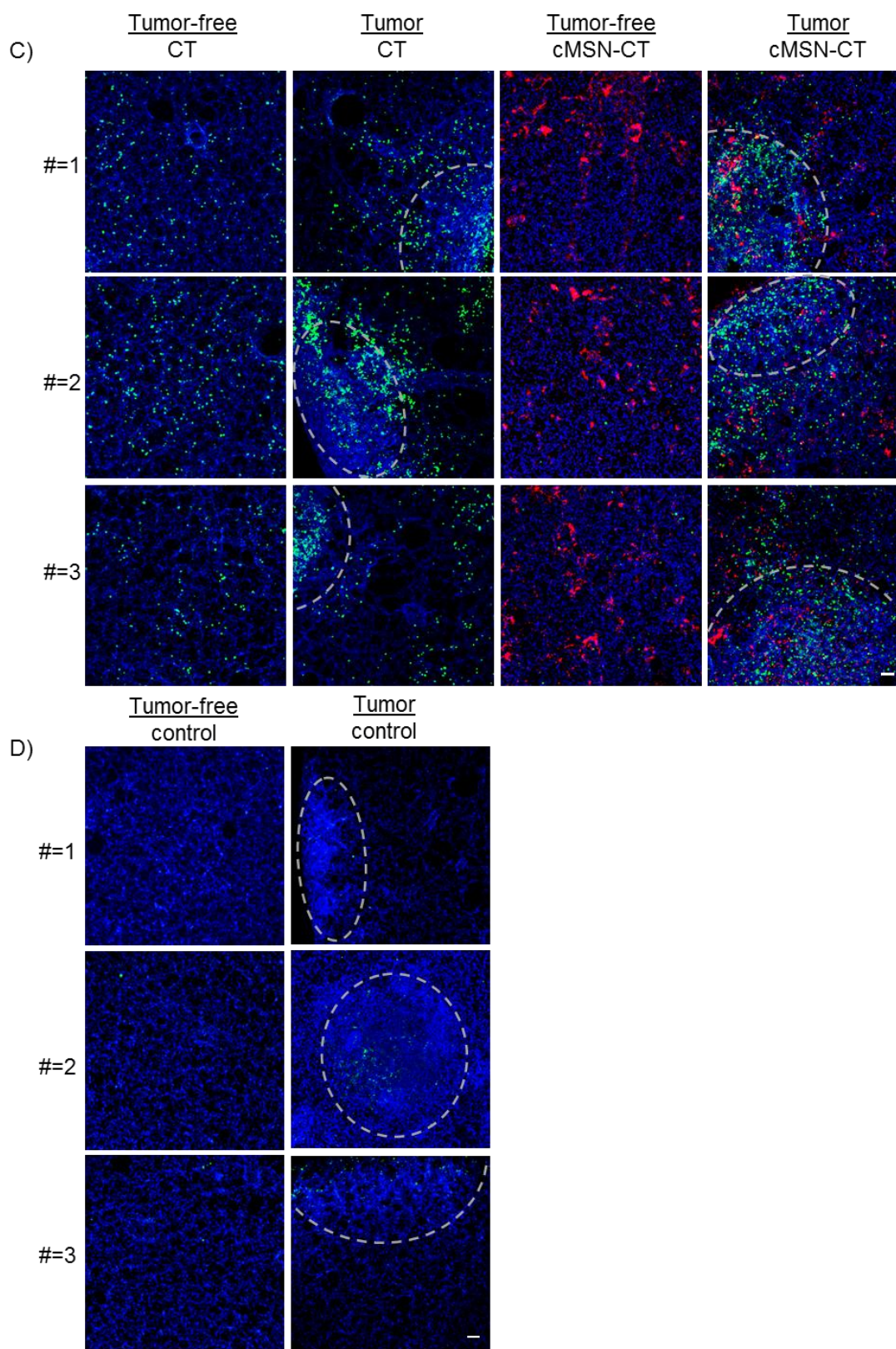
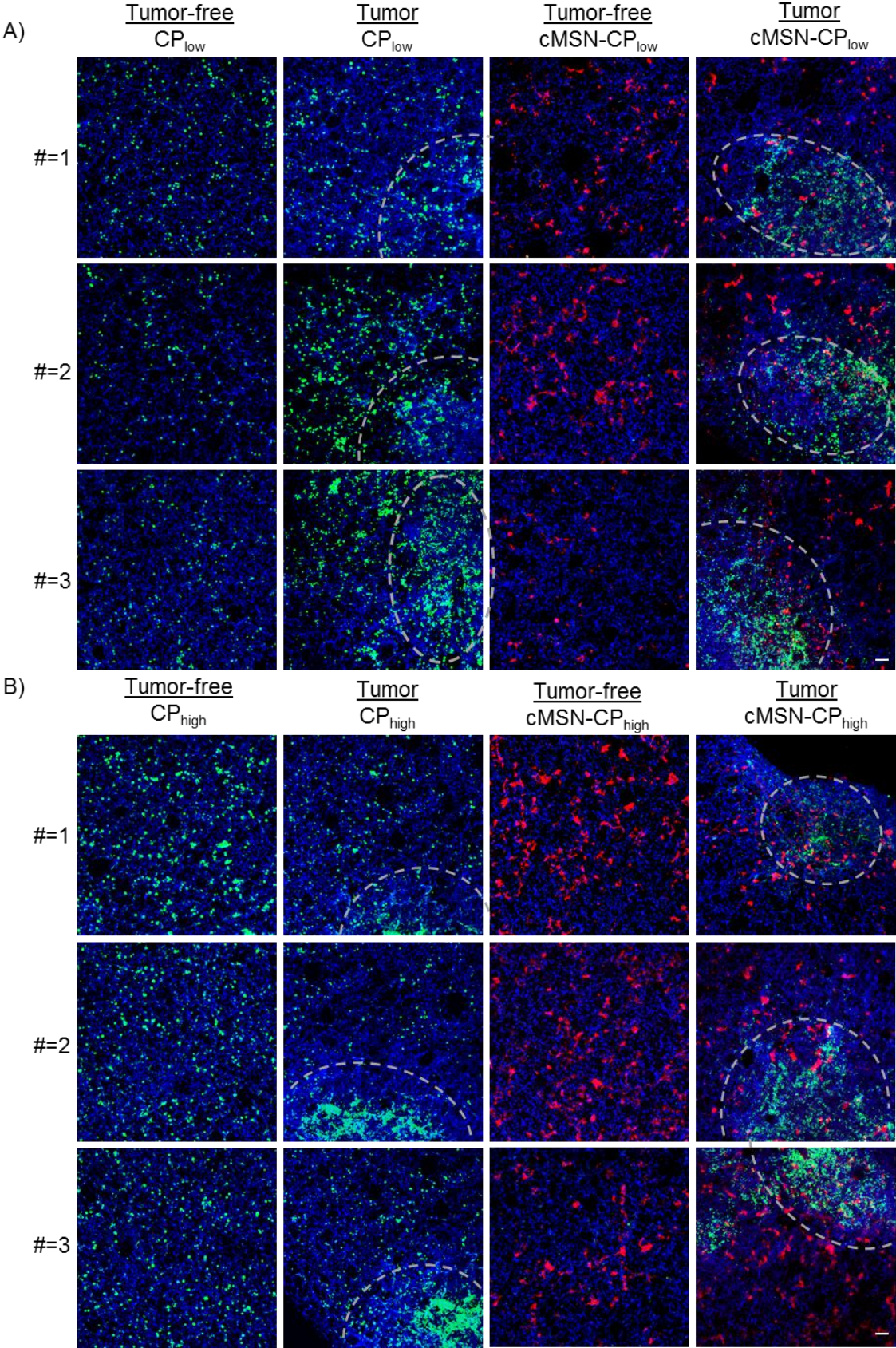


Figure S 3-6. Maximum intensity projections of *Kras* mutant mouse 3D-LTC exposed for 24 h to A) low dose of cisplatin (CP_{low}) and MSN encapsulated CP_{low} (cMSN- CP_{low}) B) high dose of cisplatin (CP_{high}) and cMSN- CP_{high} and C) low dose of cisplatin in combination with Bz (CT) and cMSN-CT D) untreated controls. Comparably sized tumors were chosen for the imaging (indicated by dotted line), tumor-free

3. Protease mediated release of chemotherapeutics from mesoporous silica nanoparticles to ex vivo human and mouse lung tumors

refers to images that were made in a non-tumor area of a Kras 3D-LTC. Nuclear staining (DAPI) is shown in blue, apoptotic marker (cleaved caspase-3) in green and Atto 633 labeled MSN particles in red. Scale bar is 50 μm . Unexposed control slices were included in the study.



3. Protease mediated release of chemotherapeutics from mesoporous silica nanoparticles to ex vivo human and mouse lung tumors

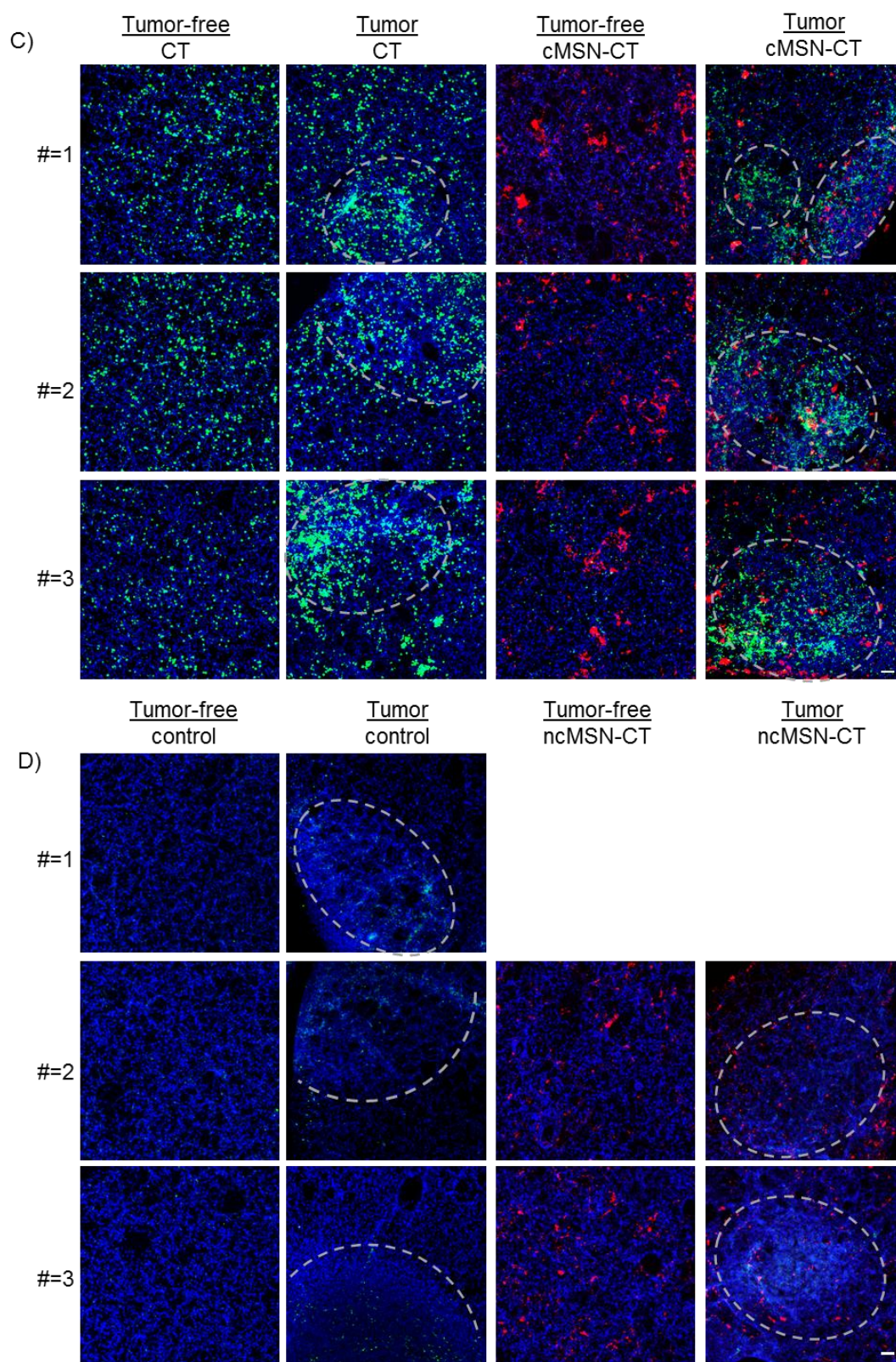


Figure S 3-7. Maximum intensity projections of Kras mutant mouse 3D-LTC exposed for 48 h to A) a low dose of cisplatin (CP_{low}) and cMSN encapsulated CP_{low} (cMSN- CP_{low}), B) a high dose of cisplatin (CP_{high}) and cMSN- CP_{high} , and C) low dose of cisplatin in combination with Bz (CT) and cMSN-CT. D) untreated controls and MSN with non-cleavable linkers encapsulating a low dose of cisplatin in combination with Bz

(cMSN-CT). Comparably sized tumors were chosen for the imaging (indicated by dotted line), non-tumor refers to images that were taken in a non-tumor area of a *Kras* 3D-LTC. Nuclear staining (DAPI) is shown in blue, apoptotic marker (cleaved caspase-3) in green and Atto 633 labeled MSN particles in red. Scale bar is 50 μm .

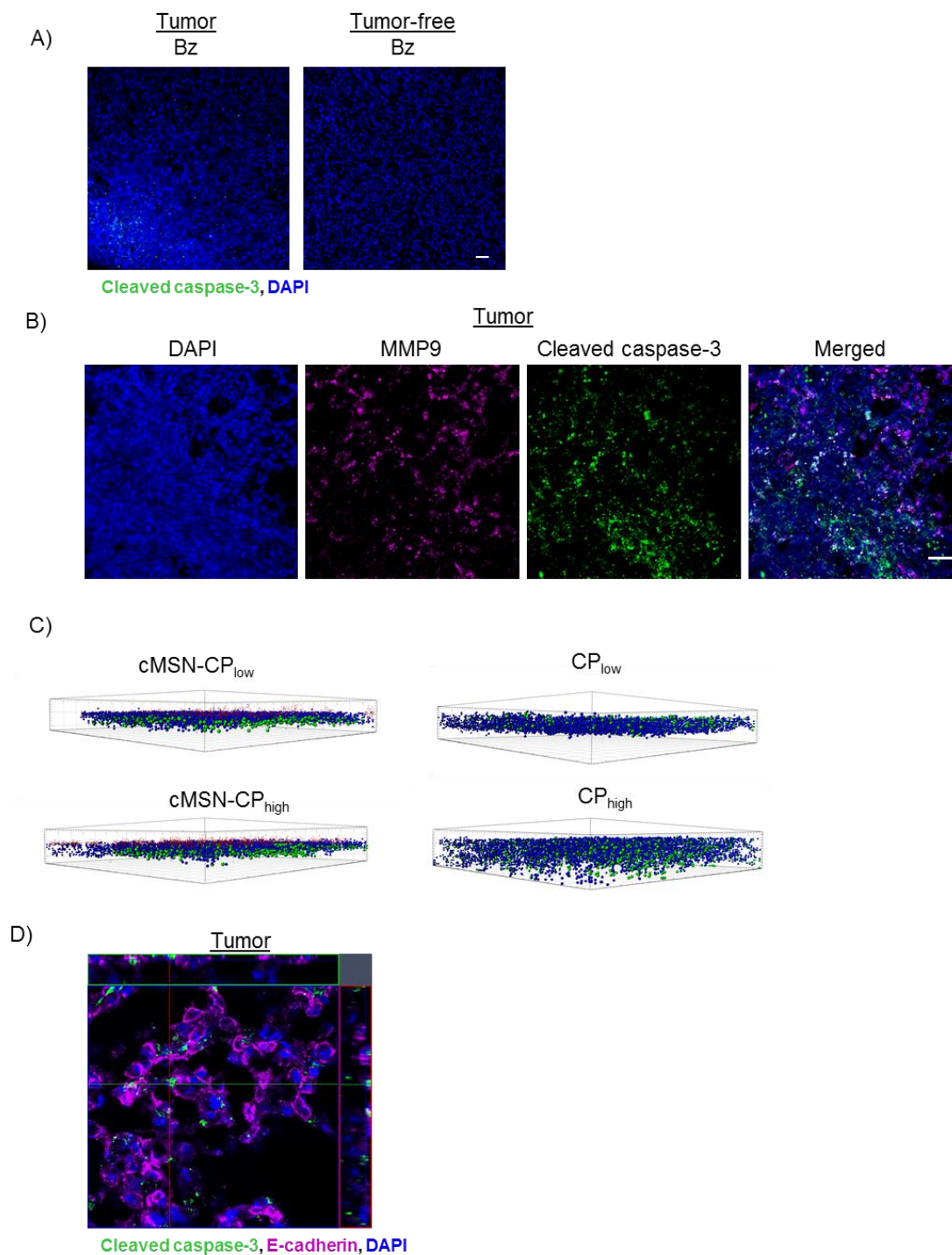


Figure S 3-8. A) *Kras* 3D-LTC exposed to Bz alone. Nuclear staining (DAPI) is shown in blue, apoptotic marker (cleaved caspase-3) in green and Atto 633 labeled MSN particles in red. B) *Kras* 3D-LTC exposed to cMSN-CT for 48 h with MMP9 antibody co-staining (magenta, maximum intensity projections of the

3. Protease mediated release of chemotherapeutics from mesoporous silica nanoparticles to ex vivo human and mouse lung tumors

different channels, white dots in merged image show direct overlay) in tumor area. The calculated number of particles, nuclei and apoptotic cells per 3D-LTC tissue slice is shown from the side where tumor tissue is located. Red spots represent the calculated particles, blue spots represent the nuclei, and green spots represent the apoptotic cells in C) cMSN-CP exposed 3D-LTC and D) CP exposed 3D-LTC. Original stainings were omitted for clarity. D) *Kras* 3D-LTC exposed to cMSN-CT for 48 h with E-cadherin antibody co-staining (magenta, orthographic representation using a 63x objective). The fluorescence signal originating from Atto 633 labeled MSN particles was omitted from the images for clarity. Scale bar is 50 μm . Images are representative of three independent experiments.

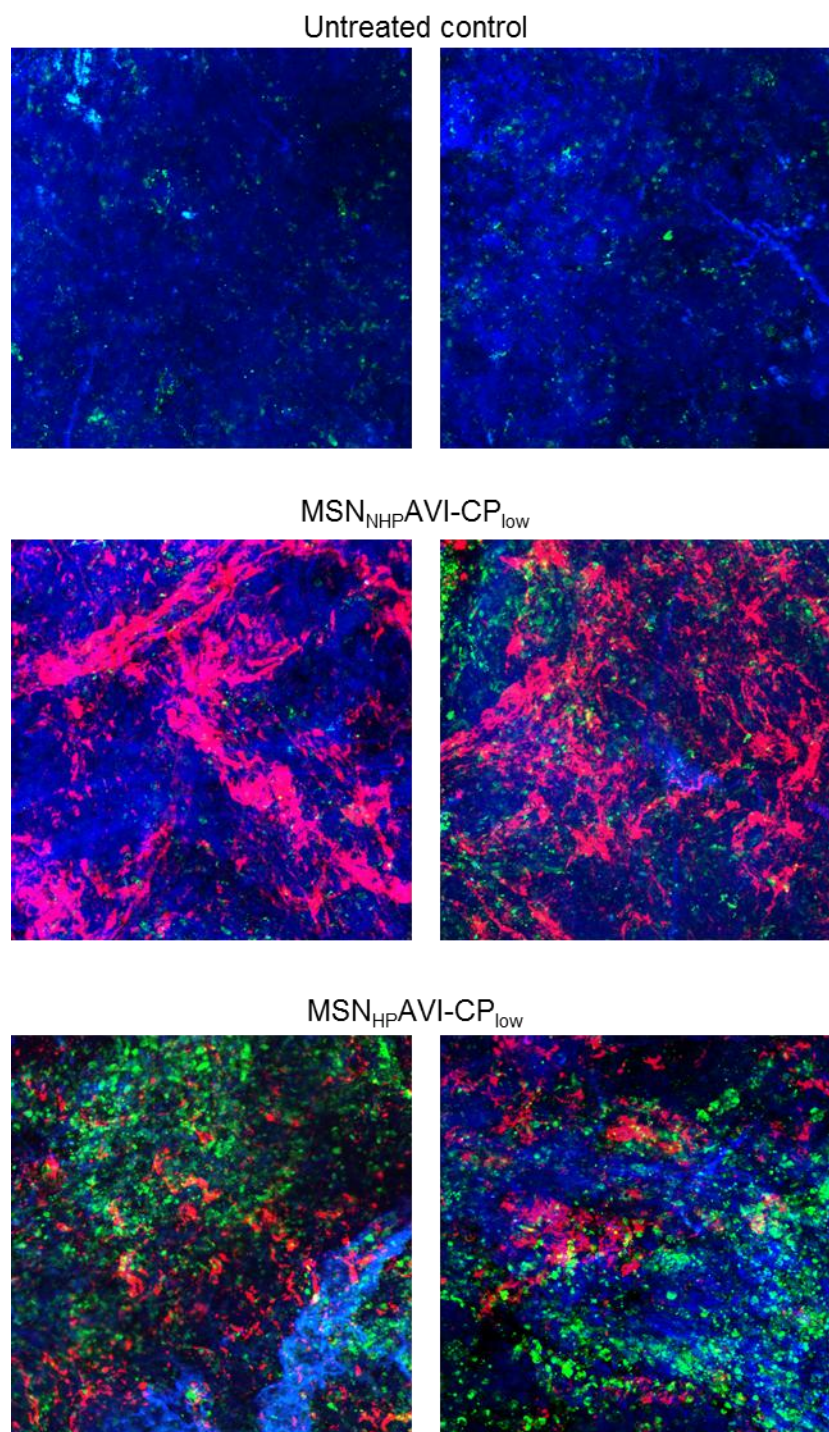


Figure S 3-9. Maximum intensity projections of human carcinoma 3D-LTC exposed to cMSN or ncMSN particles loaded with CP_{low} (cMSN-CP_{low} and ncMSN_{ctl}-CP_{low}, respectively) for 72 h in two different areas in the tumor. Nuclear staining (DAPI) is shown in blue, apoptotic marker (cleaved caspase-3) in green and Atto 633 labeled MSN particles in red. Scale bar is 50 μ m.

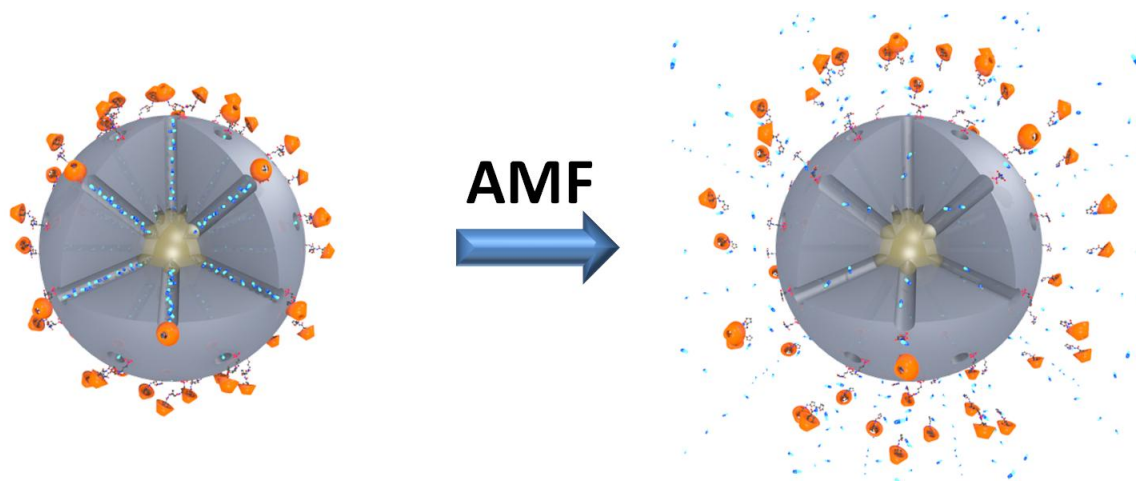
4 A molecular nanocap activated by superparamagnetic heating for externally stimulated cargo release

This chapter is based on the following publication:

Bastian Rühle, Stefan Datz, Christian Argyo, Thomas Bein, Jeffrey I. Zink, *Chem. Comm.* **2016**, 52, 1843-1846.

Abstract

A novel thermoresponsive snaptop for stimulated cargo release from superparamagnetic iron oxide core – mesoporous silica shell nanoparticles based on a [2+4] cycloreversion reaction (retro-Diels Alder reaction) is presented. The non-invasive external actuation through alternating magnetic fields makes this material a promising candidate for future applications in externally triggered drug delivery.



4.1 Introduction

Mesoporous silica nanoparticles (MSNs) have attracted much attention as drug carriers in recent years. Using specific functionalization and design allows for controlled and targeted drug delivery from silica nanocarriers to specific target sites, such as cancer cells.¹⁻⁵ However, there is still a great demand for spatial and temporal control of the release *via* external, non-invasive methods of actuation. Superparamagnetic iron oxide nanoparticles (SPIONs) can generate heat when exposed to an alternating magnetic field (AMF),⁶ and also act as contrast agents in T₂-weighted magnetic resonance imaging, making them an important tool in biomedical applications and theranostics.⁷⁻⁹ These characteristics can even be enhanced when using iron oxide nanoparticles that were doped with other metal ions that increase the magnetization, such as zinc and manganese ions.¹⁰ Combining both materials in a single, multifunctional core-shell nanostructure provides access to the advantages of both materials, i.e. a high loading capacity of various guests into the mesoporous silica shell, as well as localized superparamagnetic heating of the iron oxide core through an external AMF.¹¹ This localized heating has the advantage of spatio-temporal control and activation using a deep tissue penetration stimulus. In consequence, decorating the pore openings of the MSNs with thermosensitive molecular gatekeepers that can act as valves and unblock the pores upon localized heating is a promising concept for developing new, externally controlled, on-demand delivery systems for various cargo molecules.¹² A particularly interesting concept for thermally triggered release of molecules is the cleavage of covalent chemical bonds. While this process often requires high temperatures, it is known that a concerted [2+4] cycloaddition (Diels Alder reaction) and more importantly also the corresponding cycloreversion of maleimide derivatives with furan derivatives can proceed at mild temperatures.¹³⁻¹⁵ It has been demonstrated that the Diels Alder reaction of a maleimide derivative with a furan derivative can be carried out on the surface of Stöber particles.¹⁶ Also, it was shown that the

corresponding cycloreversion of Diels Alder adducts attached directly to the surface of superparamagnetic iron oxide or gold nanoparticles can be triggered by superparamagnetic heating¹⁷ or plasmonic heating,^{18, 19} respectively. However, these examples require that the molecule that should be released features either a furan group or a maleimide group, which is not the case for many biologically or pharmaceutically relevant compounds. Moreover, in these examples each cycloreversion leads to the release of only one cargo molecule. A delivery system based on superparamagnetic iron oxide core – mesoporous silica shell nanoparticles (SPION@MSN) does not suffer from these limitations. The mesoporous silica shell features a high loading capacity for various cargo molecules without the requirement that they have specific functional groups. Additionally, when thermoresponsive gatekeepers are used to block the pore openings of the SPION@MSN and dissociate upon superparamagnetic heating, a single cycloreversion event will result in the release of multiple cargo molecules instead of just one. While there are examples in the literature of thermoresponsive gatekeepers that can be operated through superparamagnetic heating, most of them are based on polymers or phase change materials²⁰⁻²⁴ and there are only few examples of small molecular nanovalves that block individual pores and can be controlled through AMFs.¹² The advantage of these small molecular nanovalves is that the surface of the MSN can be further functionalized with additional functional groups such as targeting ligands, fluorescent probes, or even polymers such as PEG or PEI without affecting the operation of the valves.²⁵ Moreover, because each of the molecular nanovalves is chemically identical, heterogeneities that occur during polymer capping due to the random coiling and entanglement of polymer chains or phase change materials are avoided, resulting in a more well-defined and homogeneous system. In this work, we present a small molecular snaptop²⁶⁻²⁸ which blocks the pores of MSNs by supramolecular interactions between β -cyclodextrin and adamantane,²⁹⁻³² while thermoresponsiveness is implemented by attaching the

adamantane group to maleimide-functionalized silica nanoparticles through a thermally reversible [2+4] cycloaddition of a furan-modified linker (see Figure 4-1). Upon conventional or superparamagnetic heating, the system can undergo a cycloreversion, resulting in the dissociation of the furan-adamantane- β -cyclodextrin moiety from the particle surface, which leads to pore unblocking and cargo release (see Figure 4-1).

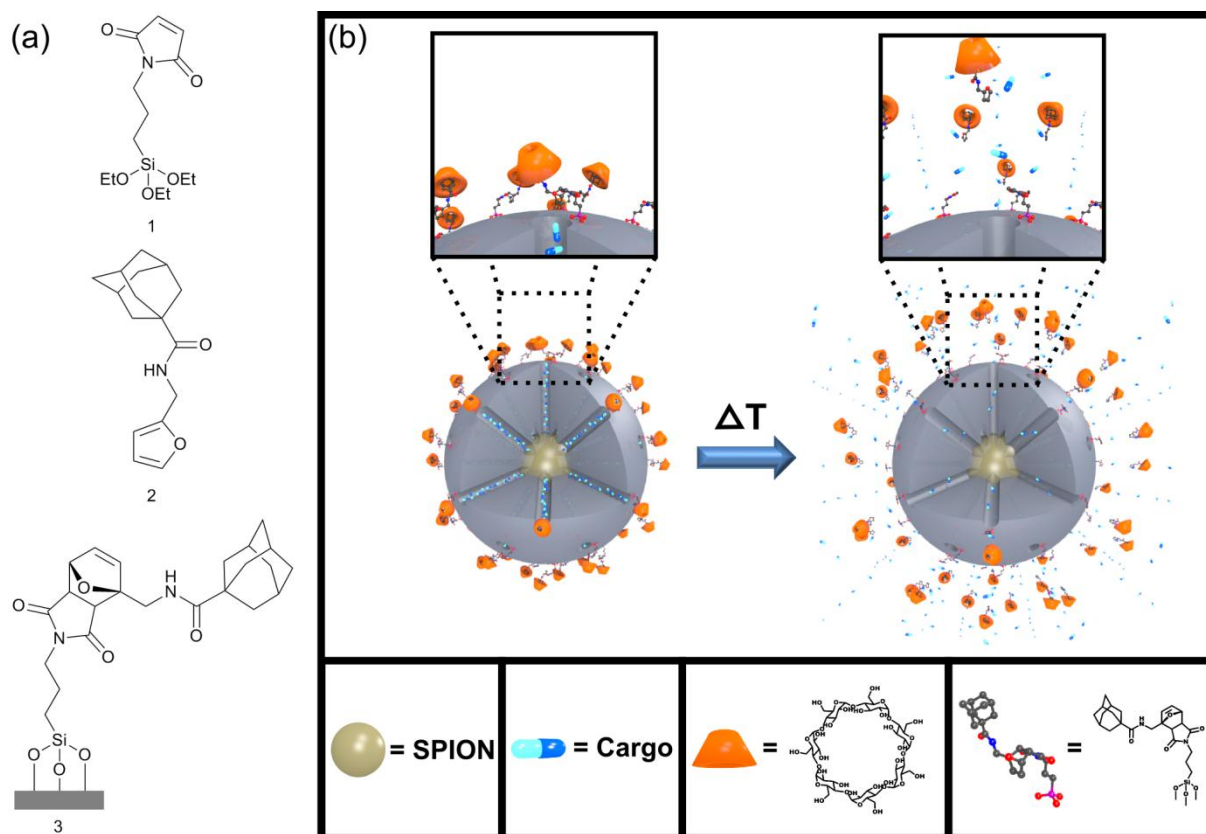


Figure 4-1. (a) Chemical structures of the dienophile (1), the diene (2) and the Diels-Alder cycloaddition product (3). (b) Schematic representation of the operating principle of the thermoresponsive nanovalve. A change in temperature triggers a cycloreversion reaction which leads to a dissociation of the bulky gatekeepers from the silica surface and allows cargo molecules to diffuse out of the mesopores.

4.2 Results and Discussion

Two different kinds of nanoparticles were prepared. Mesoporous silica nanoparticles without an iron oxide core (denoted MSN) that were used in the conventional heating experiments were synthesized under basic conditions with hexadecyltrimethylammonium bromide (CTAB) as the template according to a published procedure.^{33, 34} The particles were grafted with maleimidopropyl triethoxysilane 1 (denoted MSN-Mal), which was synthesized by a two step procedure (see supplementary information). A co-condensation synthesis where maleimidopropyl triethoxysilane and tetraethylorthosilicate were reacted in a one-pot procedure was unsuccessful, probably due to hydrolysis of the maleimide under the basic conditions during MSN synthesis. The zinc and manganese doped superparamagnetic iron oxide nanoparticles (SPIONs) with the formula $(\text{Zn}_{0.4}\text{Mn}_{0.6})\text{Fe}_2\text{O}_4$ were chosen due to the larger magnetization of the doped SPIONs (~200 emu/g, Figure S 4-10) as compared to undoped SPIONs (typically 50-120 emu/g), leading to an enhancement of superparamagnetic heating and MRI contrast.¹⁰ The doped SPION particles were synthesized by a thermal decomposition process of the metal salts in oleic acid/oleylamine/octyl ether according to literature (see also Figure S 4-10).¹⁰ TEM analysis shows that their approximate size is 8-10 nm (see Figure 4-2a and Figure S 4-10). In order to coat them with mesoporous silica, the SPIONs were transferred to the aqueous phase by coating them with CTAC, followed by the addition of triethanolamine, and heating the mixture at 60°C. A stepwise addition of tetraethyl orthosilicate (TEOS) in small portions resulted in mesoporous silica shells in a layer-by-layer manner (see supplementary information for experimental details). After template removal from the sample by solvent extraction, the nanoparticles (denoted SPION@MSN) show a high BET surface area of 1034 m²/g, a total pore volume of 1.23 cc/g, a mesopore volume (pore diameter < 6.5 nm) of 0.81 cc/g, and a pore diameter of 4.3 nm (see Figure 4-2b and

Table 4-1). The particles are about 70-80 nm in diameter (based on TEM observations, see Figure 4-2a), have an effective hydrodynamic diameter of about 110 nm in water at pH=7 (based on DLS measurements, see Figure 4-2c) and a zeta potential at pH=7 of -21 mV (Figure 4-2d). After surfactant extraction, the particles were grafted with maleimidopropyl triethoxysilane 1 (the resulting sample is denoted SPION@MSN-Mal). The maleimide groups on the surfaces of samples MSN-Mal and SPION@MSN-Mal later act as the dienophile component in the Diels Alder reaction. As the diene component, the adamantane-functionalized furan derivative 2 was synthesized in a one step procedure by acylation of furfurylamine with adamantane carbonyl chloride in dry dichloromethane in the presence of triethylamine (see supplementary information for more details).

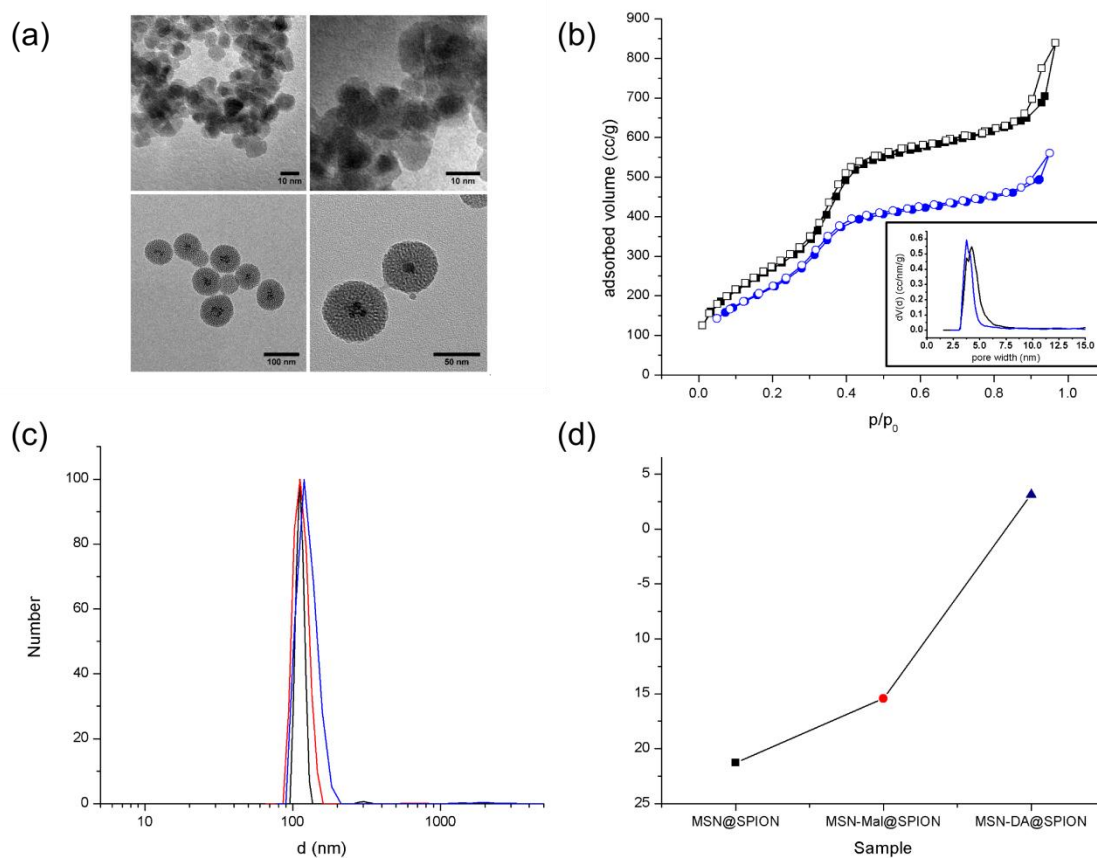


Figure 4-2. (a) TEM images of zinc and manganese doped iron oxide nanoparticles ($(\text{Zn}_{0.4}\text{Mn}_{0.6})\text{Fe}_2\text{O}_4$; top) and SPION@MSN (bottom) at different magnifications; (b) nitrogen adsorption (filled symbols) and desorption (open symbols) isotherms of sample SPION@MSN (black squares) and SPION@MSN-DA (blue circles) (inset: NLDFT pore size distribution); (c) dynamic light scattering of samples SPION@MSN (black), SPION@MSN-Mal (red) and SPION@MSN-DA (blue); (d) zeta potential analysis at pH=7 of samples SPION@MSN (black square), SPION@MSN-Mal (red circle) and SPION@MSN-DA (blue triangle; the line is a guide to the eye).

The Diels Alder reaction of the maleimide groups attached to the silica surface of samples MSN-Mal and SPION@MSN-Mal and the furan-modified adamantane was then carried out in toluene for 3 days at 40 °C, giving samples MSN-DA and SPION@MSN-DA, respectively. The successful attachment of the maleimide and the formation of the Diels Alder cycloaddition product were confirmed by Fourier transform infrared spectroscopy (FTIR, Figure 4-3), thermogravimetric analysis (TGA, Figure S 4-1), and ^{13}C solid state NMR

(ssNMR, Figure S 4-7). The appearance of two bands in the IR spectrum due to carbonyl stretching vibrations at $\nu=1773\text{ cm}^{-1}$ and $\nu=1702\text{ cm}^{-1}$ indicate the presence of maleimide groups attached to the silica particles. This is also supported by newly emerging absorptions at $\nu=1354\text{ cm}^{-1}$ (C-N-C stretching vibration), $\nu=845\text{ cm}^{-1}$ (C-H deformation vibration) and $\nu=697\text{ cm}^{-1}$ (maleimide ring deformation vibration). Additionally, two new characteristic amide absorptions (Amide I and Amide II) appear after the Diels Alder reaction at $\nu=1652\text{ cm}^{-1}$ and $\nu=1539\text{ cm}^{-1}$, respectively. At the same time the sharp band at $\nu=697\text{ cm}^{-1}$ disappears and a new, broader band at $\nu=702\text{ cm}^{-1}$ appears, indicating the successful cycloaddition of the furan derivative to the maleimide groups. Thermogravimetric analysis shows a mass loss of 13%, 16% and 23% for samples SPION@MSN, SPION@MSN-Mal and SPION@MSN-DA after heating in air to $550\text{ }^{\circ}\text{C}$, indicating the presence of organic molecules attached to the silica nanoparticles after the functionalization steps. The increase in weight loss from 16% to 23% after the Diels Alder reaction corresponds well to the theoretical 7% weight gain of the Diels-Alder addition product compared to the maleimidopropyl silane functionalized MSNs. ^{13}C ssNMR of sample MSN-DA shows new peaks at $\delta = 177\text{ ppm}$, 138 ppm , 128 ppm , 90 ppm , 79 ppm and 48 ppm (see green arrows in Figure S 4-7) that can tentatively be assigned to the bicyclic cycloaddition product, while there are no peaks corresponding to the monocyclic ring carbon atoms of maleimide or furan; other signals from both components are however present. A strong shift of the monocyclic ring carbon signals is expected after forming the cycloaddition product, so these findings also indicate that the Diels-Alder reaction was successful and nearly quantitative.

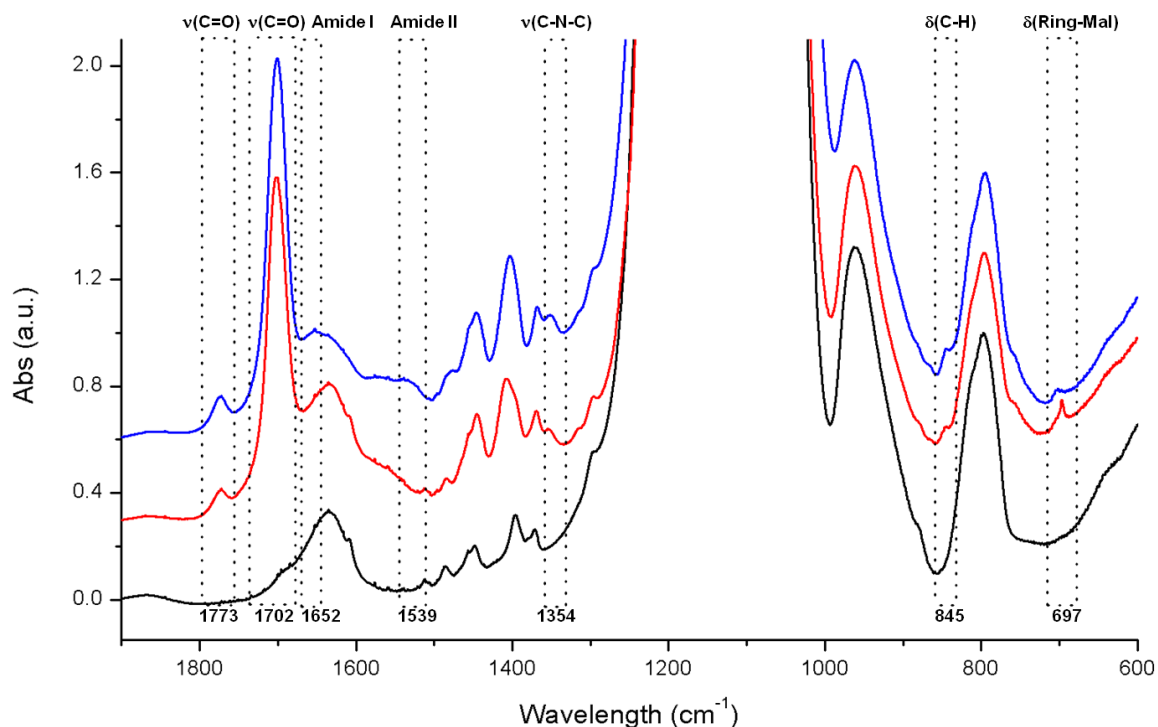


Figure 4-3. IR data for samples SPION@MSN (black), SPION@MSN-Mal (red), and SPION@MSN-DA (blue). The vibrations discussed in the text are highlighted by boxes. Peak assignments are based on literature data.³⁵ For further information and raw spectral data see Fig. S2 in the supplementary information.

Nitrogen sorption indicates a small loss of surface area, pore diameter and total pore volume after the functionalization steps, probably due to some extent of internal pore surface functionalization during silane grafting. However, with a remaining BET surface area of 859 m²/g, a pore diameter of 3.8 nm and a total pore volume of 0.82 cc/g the porosity of the functionalized material is still sufficient for its application as a carrier system (see Figure 4-2b and Table 4-1). As expected, dynamic light scattering does not show a significant change in hydrodynamic diameter of the particles (approximately 110-120 nm) after any of the modification steps (see Figure 4-2c). The zeta potential at pH=7 changes from -21 mV for sample SPION@MSN to -15 mV for sample SPION@MSN-Mal and then to an almost

neutral value of +3 mV for sample SPION@MSN-DA (see Figure 4-2d). This can be explained by the fact that after surface functionalization with maleimide and especially with the hydrophobic adamantane-functionalized furan derivative, the negatively charged silanol groups on the surface of the silica nanoparticles are shielded by the uncharged organic moieties. After attaching the adamantane-functionalized furan to the silica surface, fluorescein cargo was loaded into the mesoporous silica nanoparticles by soaking them in a 1 mM aqueous solution overnight. The pore openings were then blocked by a bulky β -cyclodextrin moiety, which was bound to the adamantane groups through supramolecular interactions (samples MSN-CD and SPION@MSN-CD). Carrying out the cycloaddition first and sealing the pores with a bulky gatekeeper at a later stage has the advantage that the experimental conditions for the loading step can be chosen independently from the reaction conditions for the cycloaddition reaction (i.e., organic solvents such as toluene, 3 days, 40 °C) that might be incompatible with some cargo molecules. In order to confirm that the intended cycloreversion and pore unblocking can be triggered by external heating, fluorescein release from sample MSN-CD was monitored at room temperature, 37 °C and 65 °C, respectively. 0.5 mg of MSN-CD were placed in a reservoir that was separated from an aqueous solution inside a fluorescence cuvette by a 14 kDa MWCO dialysis membrane, which is permeable to fluorescein but impermeable to the silica nanoparticles. The fluorescence intensity of fluorescein released into the cuvette was monitored over time. The temperature was adjusted externally by using a temperature-controlled cuvette holder, and the temperature dependence of fluorescein emission was corrected with the help of calibration curves obtained separately (see Figure S 4-8 and the supplementary information for more details). The data show that there is almost no leakage at room temperature and 37°C, but a strong increase in fluorescein release upon heating from 37 °C to 65 °C (see Figure 4-4a). Encouraged by these findings and by the fact that a similar temperature increase should also be feasible through

4. A molecular nanocap activated by superparamagnetic heating for externally stimulated cargo release

superparamagnetic heating of iron oxide core – silica shell nanoparticles,¹¹ a similar release experiment was performed with sample SPION@MSN-CD in order to confirm that the release can also be triggered by superparamagnetic heating. After monitoring the release every 15 min for 1 h at room temperature, the sample was exposed to an AMF in a five-turn copper coil (5 cm height and diameter) at a power of 5 kW and a frequency of 370 kHz for 30 min, followed again by monitoring the release at room temperature (the bulk solution temperature increased from room temperature to approx. 38 °C directly after the AMF exposure, but cooled back down to room temperature before the next AMF cycle). In total, five such heating/monitoring cycles were performed (see Figure 4-4b).

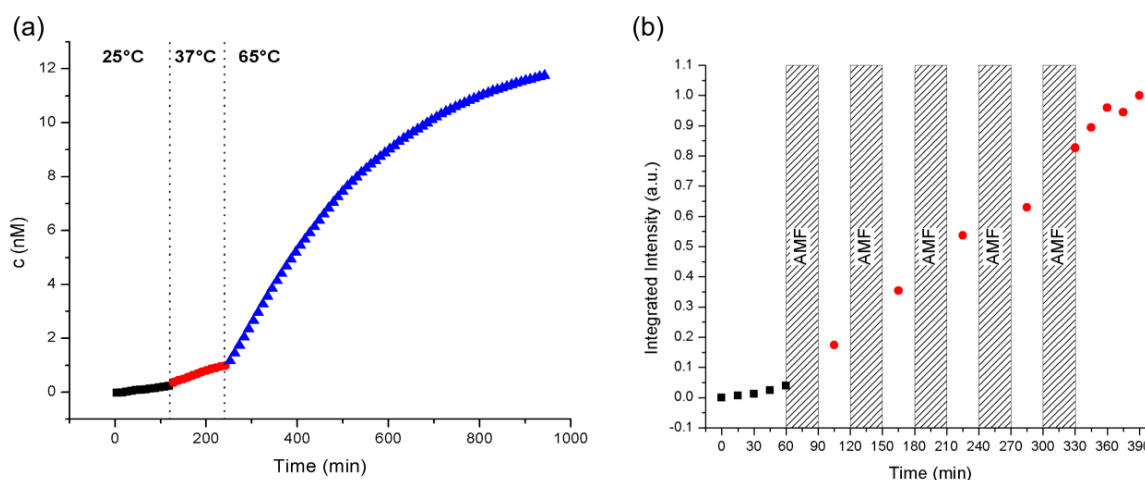


Figure 4-4. Release of the fluorescein cargo from samples (a) MSN-CD and (b) SPION@MSN-CD through (a) bulk solvent heating and (b) local superparamagnetic heating.

The observed rise in fluorescein fluorescence indicates that a displacement of the β -cyclodextrin caps can also be triggered externally by local heating by an AMF. To exclude the possibility that the observed increase in fluorescein release is merely caused by bulk heating

of the solution rather than localized superparamagnetic heating of SPION cores inside the mesoporous silica nanoparticles, a similar release experiment was carried out, but the sample was kept in an ice bath at 0°C at all times (see Figure S 4-9). Under these conditions, the bulk solution temperature stays unchanged, and the heat generation is confined to the core-shell nanoparticles. As expected, the fluorescence intensity still rises after AMF exposure, indicating that indeed localized superparamagnetic heating triggers the release. In conclusion, we have demonstrated that a thermally reversible cycloaddition reaction can be used to construct a molecular snaptop that can trap cargo inside the pores of mesoporous silica nanoparticles. The cycloreversion can be triggered by an externally applied AMF resulting in local particle heating and thus in the detachment of the cap from the pore openings and cargo release.

4.3 Conclusion

This new concept of a molecular nanocap based on a retro-Diels Alder reaction activated through superparamagnetic heating adds to the toolbox of externally controllable, thermally triggered nano-valves. We envision that changing the electronic properties of the diene and dienophile component in the Diels Alder reaction should allow for further fine-tuning of the release properties of such nanovalves. Actuation through an AMF has the advantage of deep tissue penetration and non-invasiveness, making these nanovalves interesting candidates for future applications in drug delivery.

4.4 Experimental Part

Nuclear magnetic resonance spectroscopy was carried out on a Bruker AV400 at room temperature in CDCl₃ at 400.13 MHz and 16 scans (¹H), or at 100.61 MHz and 512 scans (¹³C) for 1D spectra, on a Bruker DRX500 in CDCl₃ at 500.33 MHz and 8 scans for 2D spectra, and on a Bruker Avance III-500 at 125.79 MHz 65272 scans for ssNMR. All FIDs were processed by zero-filling and phase correction, and liquid-state NMR FIDs are calibrated to the solvent signal. FIDs for solid state and 1D ¹³C spectra were processed additionally by applying an exponential window function to the FID before FFT. FIDs of 2D spectra were processed additionally by applying a 0° shifted sine window function to the FID before FFT (LB=0.3 Hz and GF=0.1 Hz in the evolution (F1) domain and LB=0.3 Hz and GF=0.0 Hz in the detection (F2) domain). Peak assignments are based on multiplicity, integrals, HMBC and HMQC spectra. NMR spectra of new compounds are shown in Figure S 4-3 - Figure S 4-7.

Fourier transform infrared spectroscopy (FTIR) was carried out with a JASCO FT/IR-420 spectrometer averaging 128 scans in the range of 4000–400 cm⁻¹ at a resolution of 1 cm⁻¹. KBr discs were prepared by mixing approximately 2 mg of nanoparticles with approximately 200 mg of KBr and forming the disc under pressure. The spectra shown in the main text are background corrected with a linear baseline, normalized to the symmetric Si–O–Si stretching vibration around $\nu = 795 \text{ cm}^{-1}$, and vertically offset by 0.3 units. Raw spectral data are shown in Figure S 4-2.

Transmission electron microscopy (TEM) images were recorded on a Tecnai T12 Quick CryoEM and CryoET (FEI) at an accelerating voltage of 120 kV. A suspension (8 μL) of nanoparticles in ethanol (MSNs) or chloroform (SPIONs) was dropped on a 200 mesh carbon coated copper grid and the solvent was allowed to evaporate at room temperature. Energy-

dispersive x-ray spectroscopy (EDX) and electron diffraction (ED) were carried out at 300 kV using a Titan 80-300 kV microscope and are shown in Figure S 4-10.

Nitrogen adsorption and desorption isotherms were obtained at 77 K using an Autosorb-iQ (Quantachrome Instruments). Sample outgassing was performed for 12 hours at 493 K. Pore size distribution and pore volume were calculated by a NLDFT equilibrium model of N₂ on silica, based on the adsorption branch of the isotherms. BET surface area was calculated over the range of partial pressure between ~0.08–0.23 p/p₀. The mesopore volume was determined from NLDFT calculations for pores smaller than 6.5 nm in diameter.

Zeta-potential analysis and dynamic light scattering (DLS) were carried out on a ZetaSizer Nano (Malvern Instruments Ltd., Worcestershire, U.K.) in DI water for MSNs and in chloroform for SPION nanoparticles.

Fluorescence spectra were recorded on an Acton Spectra Pro 2300i CCD cooled below -120 °C with liquid nitrogen. For excitation, a CUBE 445-40C laser (Coherent Inc., Santa Clara, CA, USA) was used at a wavelength of 448 nm and a power of 2 mW. A 475 nm long pass filter was used to block scattered and stray light. In the experiments with conventional heating, a temperature-controlled cuvette holder (Varian Cary 1x1 Peltier) was used. Spectral calibration curves of the fluorescein emission at different temperatures and concentrations are shown in Figure S7 and a release curve obtained at 0 °C is shown in Figure S 4-8.

Superparamagnetic heating was carried out using a Magnetic Hyperthermia System manufactured by MSI Automation, Inc. The diameter and height of the five-turn copper coil that was used for the experiments was 50 mm, the oscillation frequency was 370 kHz, and the induction power was 5 kW.

Thermogravimetric analysis (TGA) was performed using a Perkin-Elmer Pyris Diamond TG/DTA under air (200 mL/min). Approximately 10-15 mg of sample was loaded into aluminum pans. The sample was held at 50 °C for ten minutes, and then the data were recorded from 50 to 550 °C at a scan rate of 5 °C/min. The plotted values are normalized to the weight at 200 °C. An empty aluminum pan was used as a reference.

Field-dependent magnetization isotherms were recorded with a MPMS-XL superconducting quantum interference device (SQUID) magnetometer (Quantum Design Inc.) at 300 K and are shown in Figure S 4-10.

Chemicals. Tetraethylorthosilicate (TEOS; 99%, Aldrich), cetyltrimethylammonium bromide (CTAB; 98% , Aldrich), sodium hydroxide (99%, Fisher Scientific), maleic anhydride (99%, Aldrich), zinc chloride (anhydrous, 97%, Strem Chemicals), zinc powder (97%, Fisher Scientific), iron(III) acetylacetonate ($\text{Fe}(\text{acac})_3$; 97%, Aldrich), manganese(II) chloride (MnCl_2 ; Merck), octylether (99%, Aldrich), triethanolamine (TEA; 98%, Aldrich), cetyltrimethylammonium chloride (CTAC; 25% in H_2O , Fluka), ammonium nitrate, absolute ethanol (EtOH; Aldrich), chloroform (CHCl_3 ; Aldrich), hexamethyldisilazane (HMDS; 99%, Aldrich), 3-aminopropyl triethoxysilane (APTES; 99%, Aldrich), furfurylamine (99%, Aldrich), 1-adamantanecarbonyl chloride (95%, Aldrich), triethylamine (99.5%, EMD), β -cyclodextrin (β -CD; 95%, TCI) and fluorescein disodium salt (90%, Aldrich) were used as received.

Anhydrous toluene and dichloromethane (DCM) were obtained by distillation from CaH_2 under dry nitrogen.

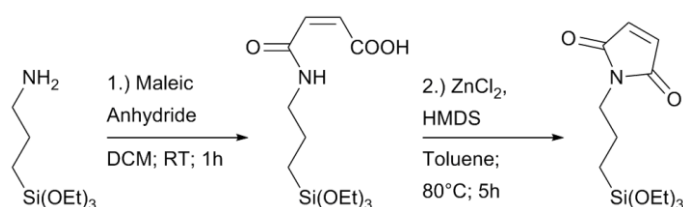
Zinc chloride was purified according to a literature protocol.³⁶ In brief, 10 g of zinc chloride and 1 g of zinc powder were refluxed in 1,4-dioxane for 1 h, the hot solution was filtered

through celite to remove Zn powder, and allowed to cool to room temperature. The white crystalline solid that formed after cooling was recrystallized from 1,4-dioxane.

Oleic acid and oleylamine were distilled under reduced pressure (1 mbar and 167 °C and 1 mbar and 155°C, respectively) prior to use.

All organic reactions were carried out in dried glassware under an inert atmosphere of dry nitrogen using standard Schlenk techniques.

Synthesis of N-((3-Triethoxysilyl)propyl)maleimide (1):



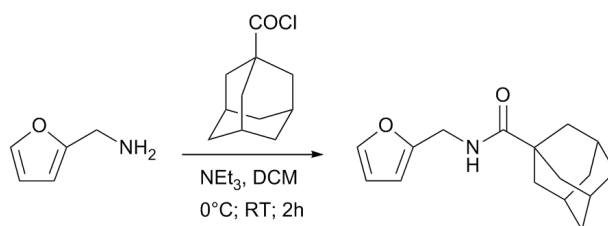
The synthesis was carried out according to a published procedure.^{4, 5} In brief, 1.73 g (17.6 mmol) of maleic anhydride were stirred in 60 mL of anhydrous dichloromethane in a flame-dried 250 mL three neck round bottom flask under nitrogen for 5 minutes. Then, 4.125 mL of 3-aminopropyl triethoxysilane (17.6 mmol) in 20 mL of dry dichloromethane was added slowly under stirring, and the resulting mixture was kept at room temperature for 1 h. After that, volatiles were removed *in vacuo*, and the intermediate maleamic acid derivative was obtained as a white powder, which was directly used in the next step without further purification.

In the next step, the intermediate product was dissolved in 60 mL of dry toluene and stirred under nitrogen. Then, 2.40 g of anhydrous zinc chloride were added at once and the reaction

4. A molecular nanocap activated by superparamagnetic heating for externally stimulated cargo release

mixture was heated to 80 °C. Next, 3.67 mL of hexamethyldisilazane (17.6 mmol) were added, and the mixture was kept at 80 °C for 5 hours. After cooling to room temperature, the solution was filtered to remove zinc chloride and the solvent was removed *in vacuo*, giving the product as a colorless oil. ¹H NMR (400.13 MHz; CDCl₃): δ = 0.53(m, 2H, SiCH₂), 1.16(t, 9H, CH₃CH₂O), 1.64(p, 2H, SiCH₂CH₂), 3.45(t, 2H, CH₂N), 3.75(q, 6H, CH₃CH₂O), 6.63(s, 2H, HC=CH), ¹³C NMR (100.61 MHz; CDCl₃): δ = 7.88(SiCH₂), 18.41(CH₃CH₂O), 22.26(SiCH₂CH₂), 40.55(CH₂N), 58.57(CH₃CH₂O), 134.18(HC=CH), 170.98(C=O).

Synthesis of N-(furan-2-ylmethyl)adamantane-1-carboxamide (2):



In a flame-dried 100 mL round bottom flask, a mixture of 2.0 mL of furfurylamine (22 mmol) and 3 mL of triethylamine were stirred in 45 mL of dry dichloromethane under nitrogen at 0 °C. Then, 4.4 g of 1-adamantane carbonylchloride (22 mmol) in 5 mL of dry dichloromethane was added slowly, and the solution was allowed to warm to room temperature. After stirring for 1 h at room temperature, the solution was washed with 40 mL of an aqueous ammonium chloride solution (saturated) and 40 mL of an aqueous potassium carbonate solution (5%), the organic layer was separated, dried over MgSO₄, filtered, and evaporated to dryness *in vacuo*. The crude product was recrystallized from heptane/EtOAc = 1:1 (v/v) to yield the product as off-white needles (3.15 g, 55%). ¹H NMR (400.13 MHz; CDCl₃):δ =

1.69(m, 6H, CCH₂CHCH₂(Ad)), 1.84(m, 6H, CCH₂CHCH₂(Ad)), 2.02(m, 3H, CCH₂CHCH₂(Ad)), 4.40(d, 2H, CH₂NH), 5.86(bs, 1H, NH), 6.18(dd, 1H, CCHCHCH(Fur)), 6.29(dd, 1H, CCHCHCH(Fur)), 7.33(dd, 1H, CCHCHCH(Fur)) ¹³C NMR (100.61 MHz; CDCl₃): δ = 28.31(CCH₂CHCH₂(Ad)), 36.70(CCH₂CHCH₂(Ad)), 36.70(CH₂NH), 39.41(CCH₂CHCH₂(Ad)), 40.88(CCH₂CHCH₂(Ad)), 107.42(CCHCHCH(Fur)), 110.63(CCHCHCH(Fur)), 142.34(CCHCHCH(Fur)), 151.84(CCHCHCH(Fur)), 177.88(C=O).

Sample MSN. Unfunctionalized mesoporous silica nanoparticles were synthesized according to a published procedure.⁴ In brief, 200 mg of CTAB and 600 μL of sodium hydroxide solution (2 M) were dissolved in 100 mL of water under stirring. The solution was heated at 80 °C for 30 minutes, followed by the addition of 1050 μL of TEOS under vigorous stirring. Stirring was continued for 2 h at 80 °C, and then the solution was allowed to cool to room temperature. The nanoparticles were collected by centrifugation (10 min at 7197 rcf), washed 2x with water (2x 90 mL), 2x with ethanol (2x 90 mL) and 2x with toluene (2x 90 mL), redispersed in 20 mL of dry toluene and directly used for further functionalization.

Sample MSN-Mal. The unfunctionalized mesoporous silica nanoparticles in 20 mL of dry toluene were stirred in a flame-dried 50 mL round bottom flask under nitrogen. Then, 40 μL of N-((3-triethoxysilyl)propyl)maleimide were added, and the resulting mixture was heated to reflux overnight. The nanoparticles were collected by centrifugation (10 min at 7197 rcf), washed 2x with toluene (2x 90 mL) and 2x with ethanol (2x 90 mL). To extract the organic template from the pores, the nanoparticles were dispersed in 90 mL of an ethanolic ammonium nitrate solution (1 mg/50 mL), refluxed for 1 h, collected by centrifugation (10 min at 7197 rcf), washed 1x with ethanol (90 mL), redispersed in 90 mL of a fresh ethanolic

ammonium nitrate solution (1 mg/50 mL), refluxed again for 1 h, collected by centrifugation (10 min at 7197 rcf), washed 2x with ethanol (2x 90 mL) and stored in ethanol.

Sample MSN-DA. 25 mg of MSN-Mal nanoparticles (dispersed in ethanol) were washed 2x with toluene (2x 1.5 mL), and then redispersed in 10 mL of toluene. 80 mg of N-(furan-2-ylmethyl) adamantane-1-carboxamide were added, and the resulting mixture was stirred for 3 days at 40°C. The nanoparticles were collected by centrifugation in a cooled centrifuge (5 min at 20817 rcf and 18°C), washed 2x with toluene (2x 1.5 mL), 2x with ethanol (2x 1.5 mL) and 2x with water (2x 1.5 mL).

Sample MSN-CD. For loading the model drug into the nanoparticles, 0.5 mg of sample MSN-DA were dispersed in 1 mL of an aqueous fluorescein solution (1 mM) and kept on a shaker over night at room temperature. For capping, 15 mg of β -cyclodextrin was added to the solution, and shaking was continued for 1 d at room temperature. The nanoparticles were then collected by centrifugation in a cooled centrifuge (5 min at 20817 rcf and 18 °C), washed 5x with water (5x 1.5 mL), and redispersed in 250 μ L water.

Superparamagnetic zinc and manganese doped iron oxide nanoparticles ($\text{Zn}_{0.4}\text{Mn}_{0.6}\text{Fe}_2\text{O}_4$). Zinc and manganese doped iron oxide nanoparticles were synthesized following a thermal decomposition process as previously described.³⁷ In brief, 0.353 g (1.00 mmol) $\text{Fe}(\text{acac})_3$, 30.0 mg (0.220 mmol) ZnCl_2 and 63.3 mg (0.320 mmol) MnCl_2 were placed in a 50 mL three-neck round bottom flask equipped with a reflux condenser under nitrogen atmosphere. 2.00 mL oleic acid, 4.00 mL oleylamine and 2.06 mL octylether were added and the reaction mixture was heated to 300 °C (SiC bath) for 1 h. The reaction mixture was cooled to room temperature and absolute ethanol was added. The resulting nanoparticles were washed three times with a mixture of chloroform and ethanol (1:10) by centrifugation (10 min, 26892 rcf) and finally redispersed in 10 mL of chloroform.

Sample SPION@MSN. Prior to the sol-gel reaction, the SPIONs were transferred from the organic phase to the aqueous phase. 4.285 mL of a 7 mg/mL SPION dispersion in CHCl_3 (corresponding to 30 mg of SPIONs) were placed in a polypropylene reactor. 21.7 g H_2O and 2.41 mL of aqueous CTAC solution (25 wt%) was added, generating a second phase. The mixture was sonicated for 15 min (60% of continuous power (250 W), frequency 20 KHz) using a probe sonicator and subsequently the chloroform was evaporated at elevated temperature (70 °C) for 2 h. After a second sonication step lasting 15 min, the mixture was added to 14.3 g TEA and stirred (1000 rpm) at 60 °C. The silica source TEOS (10 times 155 μL , 692 μmol) was added stepwise every 10 min over a total time period of 90 min at constant temperature of 60 °C. The synthesis mixture was stirred at 1000 rpm at room temperature for 12 h. After addition of ethanol (100 mL), the SPION@MSNs were separated by centrifugation (43.146 rcf for 20 min) and redispersed in ethanol. The template extraction was performed twice by heating the SPION@MSN suspension under reflux at 90 °C (oil bath) for 45 min in an ethanolic solution (100 mL) containing ammonium nitrate (2 g). The SPION@MSNs were collected by centrifugation and washed with ethanol after each extraction step. The resulting nanoparticles were stored in an ethanolic solution.

Sample SPION@MSN-Mal. 20 mg of the unfunctionalized iron oxide core – mesoporous silica shell nanoparticles (SPION@MSN) were washed 2x with toluene (2x 1.5 mL), redispersed in 10 mL of dry toluene and stirred in a flame-dried 25 mL round bottom flask under nitrogen. Then, 40 μL of N-((3-triethoxysilyl)propyl)maleimide was added, and the resulting mixture was heated to reflux overnight. The nanoparticles were collected by centrifugation (5 min at 16873 rcf), washed 2x with toluene (2x 1.5 mL) and redispersed in 2.5 mL of toluene.

Sample SPION@MSN-DA. 20 mg of SPION@MSN-Mal in 2.5 mL of toluene were stirred in a glass vial together with 80 mg of N-(furan-2-ylmethyl)adamantane-1-carboxamide for 3 days at 40 °C. The nanoparticles were collected by centrifugation in a cooled centrifuge (5 min at 20817 rcf and 18 °C), and washed 2x with toluene (2x 1.5 mL), 2x with ethanol (2x 1.5 mL) and 2x with water (2x 1.5 mL).

Sample SPION@MSN-CD. For loading the model drug into the nanoparticles, 1 mg of sample SPION@MSN-DA were dispersed in 1 mL of an aqueous fluorescein solution (1 mM) and kept on a shaker over night at room temperature. For capping, 15 mg of α -cyclodextrin was added to the solution, and shaking was continued for 1 d at room temperature. The nanoparticles were then collected by centrifugation in a cooled centrifuge (5 min at 20817 rcf and 18 °C), washed 5x with water (5x 1.5 mL), and redispersed in 250 μ L water.

Release experiments For the release experiments by conventional heating, 0.5 mg of nanoparticles suspended in 250 μ L water were added into a reservoir that was separated from an aqueous solution in a standard 1 cm fluorescence cuvette by a 14 kDa MWCO dialysis membrane (VWR). An emission scan (409.13 nm – 688.30 nm) was recorded every second, the intensity around the fluorescein emission maximum was integrated (500 nm – 550 nm) and averaged over 600 scans (corresponding to 10 minutes), and the results were plotted against time. For obtaining the spectral data of fluorescein fluorescence at different concentrations and temperatures, appropriate dilutions of fluorescein disodium salt in water were prepared and fluorescence emission data from 60 spectra were averaged. The obtained data were fitted with a linear regression model and used to calculate the amount of released fluorescein at different temperatures (see also Figure S 4-9).

In the superparamagnetic heating experiments at room temperature, 1 mg of nanoparticles was dispersed in 250 μ L water and added to a reservoir that was separated from an aqueous

solution (10 mL) in a 20 mL glass vial by a 14 kDa MWCO dialysis membrane. After monitoring the release every 15 minutes for 1 hour at room temperature, the sample was exposed to an AMF for 30 minutes, followed again by monitoring the release at room temperature for 30 minutes (plotted is the mean intensity of 3 individual measurements 0 min, 15 min and 30 min after the heating cycle). In total, five such heating/monitoring cycles were performed. For measuring fluorescein emission, a 2.5 mL sample was drawn from the vial, 60 emission scans were recorded from 409.13 nm – 688.30 nm at an exposure time of 1 second, the intensity around the fluorescein emission maximum was integrated (490 nm – 550 nm), the results were averaged, and the 2.5 mL sample was added back into the vial. Here, no correction was made to the emission intensity since the effect of temperature change of the bulk solution on fluorescein fluorescence was negligible.

The procedure for the superparamagnetic heating experiment at 0 °C was similar to the one described above. The only differences were that the sample was kept in an ice bath at 0 °C at all times, and that only three cycles with 30 minutes AMF exposure and 1 hour of monitoring time were carried out. Here, also no correction was made to the emission intensity since the temperature was always fixed at 0 °C for all measurements due to the ice bath.

4.5 References

1. M. W. Ambrogio, C. R. Thomas, Y.-L. Zhao, J. I. Zink and J. F. Stoddart, *Accounts of Chemical Research*, 2011, **44**, 903-913.
2. C. Argyo, V. Weiss, C. Bräuchle and T. Bein, *Chemistry of Materials*, 2014, **26**, 435-451.
3. Z. Li, J. C. Barnes, A. Bosoy, J. F. Stoddart and J. I. Zink, *Chemical Society reviews*, 2012, **41**, 2590-2605.
4. D. Tarn, C. E. Ashley, M. Xue, E. C. Carnes, J. I. Zink and C. J. Brinker, *Accounts of Chemical Research*, 2013, **46**, 792-801.
5. S.-H. Wu, C.-Y. Mou and H.-P. Lin, *Chemical Society reviews*, 2013, **42**, 3862-3875.
6. R. E. Rosensweig, *Proceedings of the 9th International Conference on Magnetic Fluids*, 2002, **252**, 370-374.
7. Q. A. P. a. J. C. a. S. K. J. a. J. Dobson, *Journal of Physics D: Applied Physics*, 2003, **36**, R167.
8. S. Laurent, D. Forge, M. Port, A. Roch, C. Robic, L. Vander Elst and R. N. Muller, *Chemical reviews*, 2008, **108**, 2064-2110.
9. Y. Wang and H. Gu, *Advanced materials*, 2015, **27**, 576-585.
10. J.-t. Jang, H. Nah, J.-H. Lee, S. H. Moon, M. G. Kim and J. Cheon, *Angewandte Chemie International Edition*, 2009, **48**, 1234-1238.
11. J. Dong and J. I. Zink, *ACS Nano*, 2014, **8**, 5199-5207.
12. C. R. Thomas, D. P. Ferris, J.-H. Lee, E. Choi, M. H. Cho, E. S. Kim, J. F. Stoddart, J.-S. Shin, J. Cheon and J. I. Zink, *Journal of the American Chemical Society*, 2010, **132**, 10623-10625.
13. N. Kuramoto, K. Hayashi and K. Nagai, *Journal of Polymer Science Part A: Polymer Chemistry*, 1994, **32**, 2501-2504.
14. A. M. Peterson, R. E. Jensen and G. R. Palmese, *ACS Applied Materials & Interfaces*, 2010, **2**, 1141-1149.
15. B. Rickborn, in *Organic Reactions*, John Wiley & Sons, Inc., 2004.
16. T. Engel and G. Kickelbick, *Chemistry of Materials*, 2013, **25**, 149-157.

17. T. T. T. N'Guyen, H. T. T. Duong, J. Basuki, V. Montembault, S. Pascual, C. Guibert, J. Fresnais, C. Boyer, M. R. Whittaker, T. P. Davis and L. Fontaine, *Angewandte Chemie International Edition*, 2013, **52**, 14152-14156.
18. A. B. S. Bakhtiari, D. Hsiao, G. Jin, B. D. Gates and N. R. Branda, *Angewandte Chemie International Edition*, 2009, **48**, 4166-4169.
19. S. Yamashita, H. Fukushima, Y. Niidome, T. Mori, Y. Katayama and T. Niidome, *Langmuir*, 2011, **27**, 14621-14626.
20. A. Baeza, E. Guisasola, E. Ruiz-Hernández and M. Vallet-Regí, *Chemistry of Materials*, 2012, **24**, 517-524.
21. I. Y. Galaev and B. Mattiasson, *Enzyme and Microbial Technology*, 1993, **15**, 354-366.
22. W. Guo, C. Yang, H. Lin and F. Qu, *Dalton transactions*, 2014, **43**, 18056-18065.
23. C. Liu, J. Guo, W. Yang, J. Hu, C. Wang and S. Fu, *Journal of Materials Chemistry*, 2009, **19**, 4764-4770.
24. T.-Y. Liu, S.-H. Hu, D.-M. Liu, S.-Y. Chen and I.-W. Chen, *Nano Today*, 2009, **4**, 52-65.
25. J. Dong, M. Xue and J. I. Zink, *Nanoscale*, 2013, **5**, 10300-10306.
26. M. W. Ambrogio, T. A. Pecorelli, K. Patel, N. M. Khashab, A. Trabolsi, H. A. Khatib, Y. Y. Botros, J. I. Zink and J. F. Stoddart, *Organic Letters*, 2010, **12**, 3304-3307.
27. T. M. Guardado-Alvarez, L. Sudha Devi, M. M. Russell, B. J. Schwartz and J. I. Zink, *Journal of the American Chemical Society*, 2013, **135**, 14000-14003.
28. K. Patel, S. Angelos, W. R. Dichtel, A. Coskun, Y.-W. Yang, J. I. Zink and J. F. Stoddart, *Journal of the American Chemical Society*, 2008, **130**, 2382-2383.
29. W. C. Cromwell, K. Bystrom and M. R. Eftink, *The Journal of Physical Chemistry*, 1985, **89**, 326-332.
30. M. R. Eftink, M. L. Andy, K. Bystrom, H. D. Perlmutter and D. S. Kristol, *Journal of the American Chemical Society*, 1989, **111**, 6765-6772.
31. D. Harries, D. C. Rau and V. A. Parsegian, *Journal of the American Chemical Society*, 2005, **127**, 2184-2190.
32. M. Xue, D. Cao, J. F. Stoddart and J. I. Zink, *Nanoscale*, 2012, **4**, 7569-7574.
33. J. Lu, M. Liong, J. I. Zink and F. Tamanoi, *Small*, 2007, **3**, 1341-1346.

34. H. Meng, M. Xue, T. Xia, Y.-L. Zhao, F. Tamanoi, J. F. Stoddart, J. I. Zink and A. E. Nel, *Journal of the American Chemical Society*, 2010, **132**, 12690-12697.
35. E. C. Aguiar, J. B. P. da Silva and M. N. Ramos, *MOLECULAR SPECTROSCOPY AND MOLECULAR STRUCTURE 2010 A Collection of Papers Presented at the XXXth European Congress on Molecular Spectroscopy, Florence, Italy, August 29 - September 3, 2010.*, 2011, **993**, 431-434.
36. W. L. F. Armarego and C. L. L. Chai, in *Purification of Laboratory Chemicals (Fifth Edition)*, ed. W. L. F. A. L. L. Chai, Butterworth-Heinemann, Burlington, 2003, pp. 500-577.
37. J.-t. Jang, H. Nah, J.-H. Lee, S. H. Moon, M. G. Kim and J. Cheon, *Angewandte Chemie International Edition*, 2009, **48**, 1234-1238.

4.6 Appendix

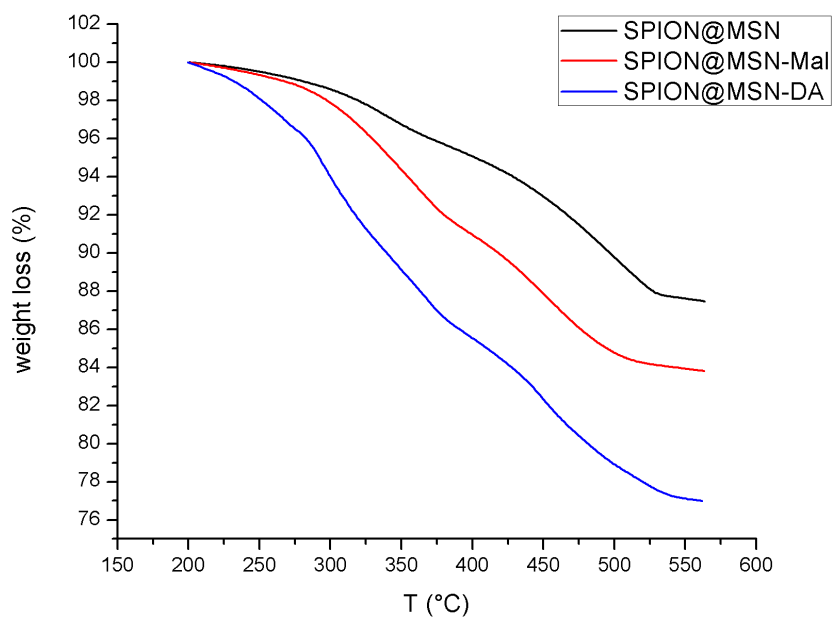


Figure S 4-1. Thermogravimetric analysis of samples SPION@MSN (black), SPION@MSN-Mal (red) and SPION@MSN-DA (blue).

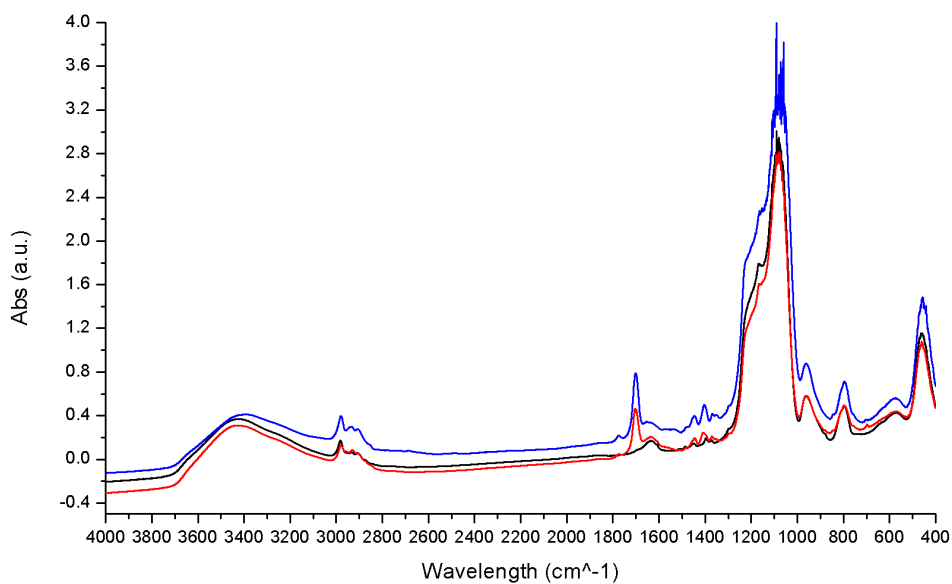


Figure S 4-2. Raw IR spectral data for samples SPION@MSN (black), SPION@MSN-Mal (red), and SPION@MSN-DA (blue).

4. A molecular nanocap activated by superparamagnetic heating for externally stimulated cargo release

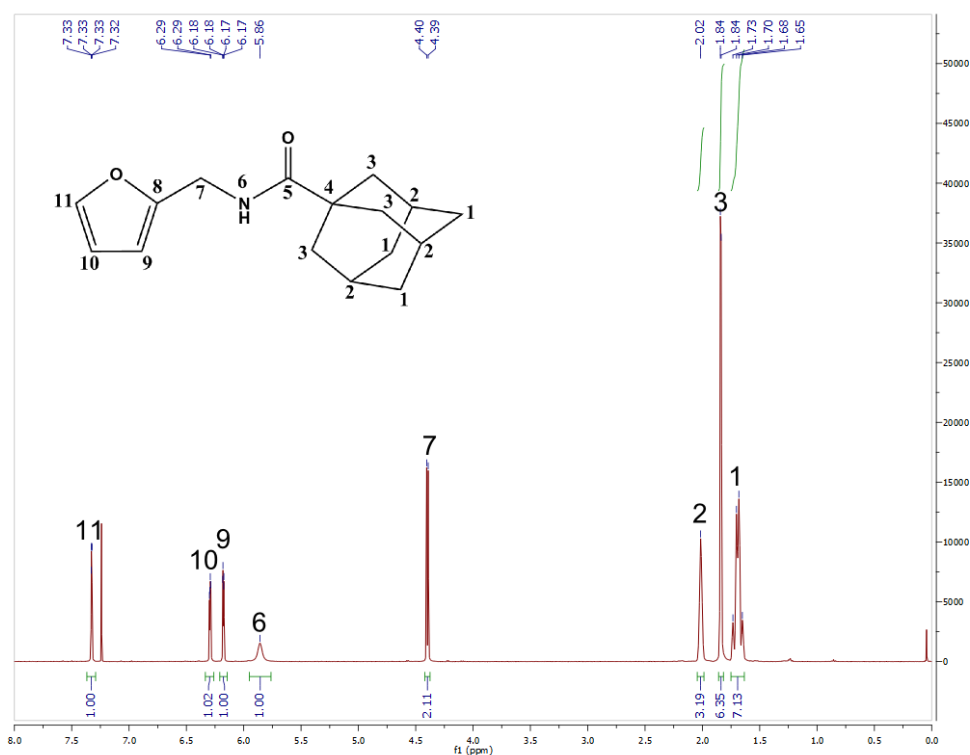


Figure S 4-3. ¹H NMR (CDCl₃, 25 °C) of N-(furan-2-ylmethyl)adamantane-1-carboxamide.

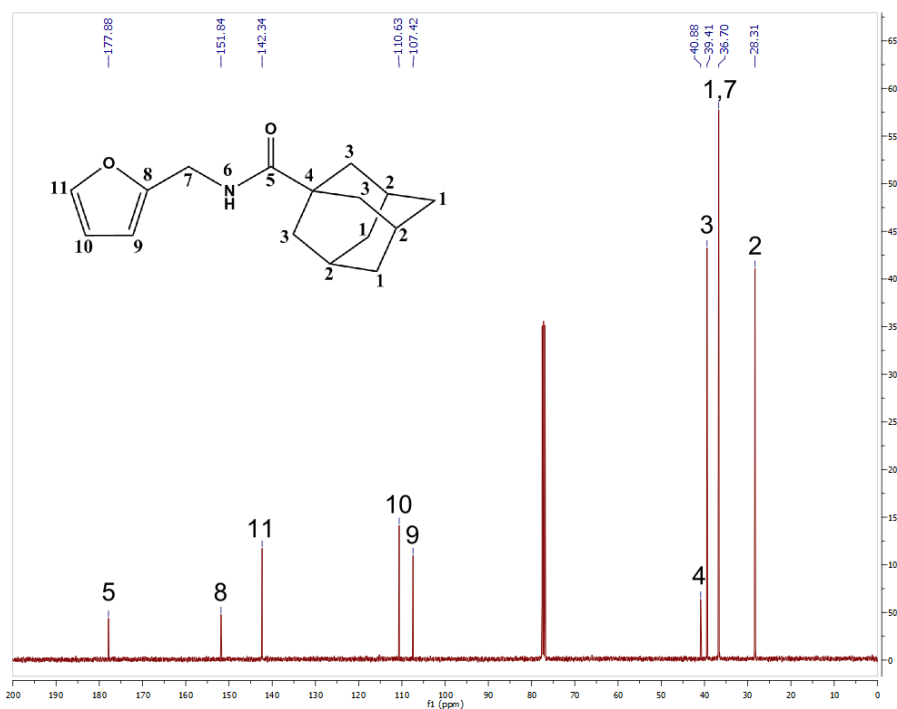


Figure S 4-4. ¹³C-NMR (CDCl₃, 25 °C) of N-(furan-2-ylmethyl)adamantane-1-carboxamide.

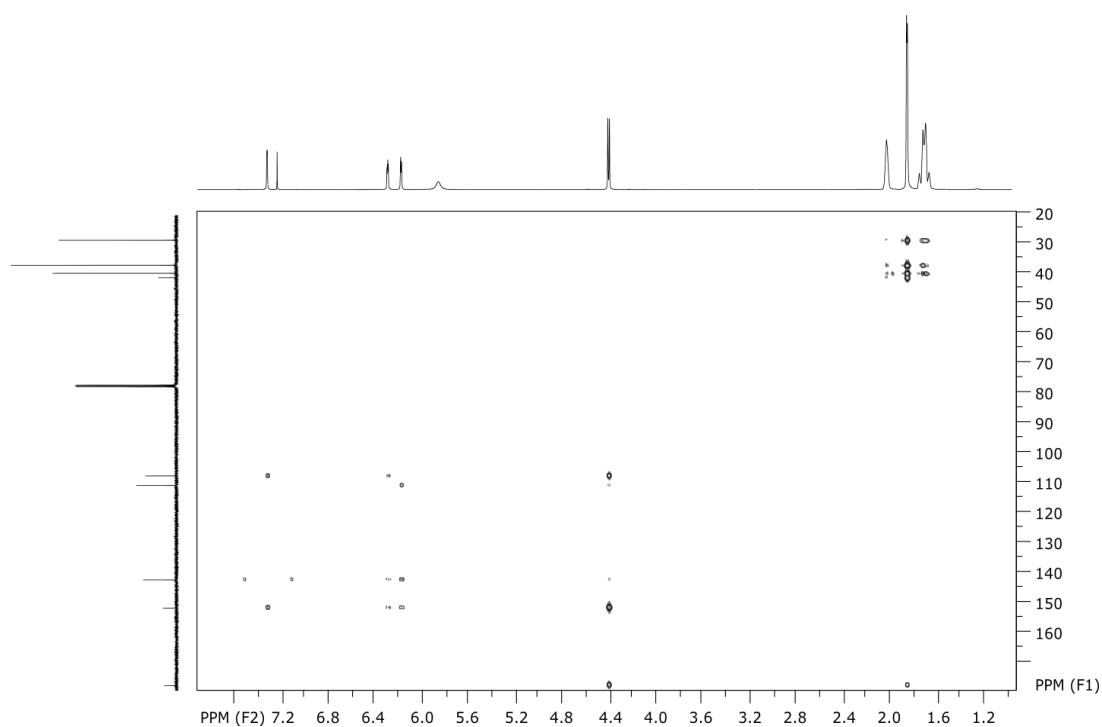


Figure S 4-5. ¹H-¹³C HMBC (CDCl₃, 25 °C) of N-(furan-2-ylmethyl)adamantane-1-carboxamide.

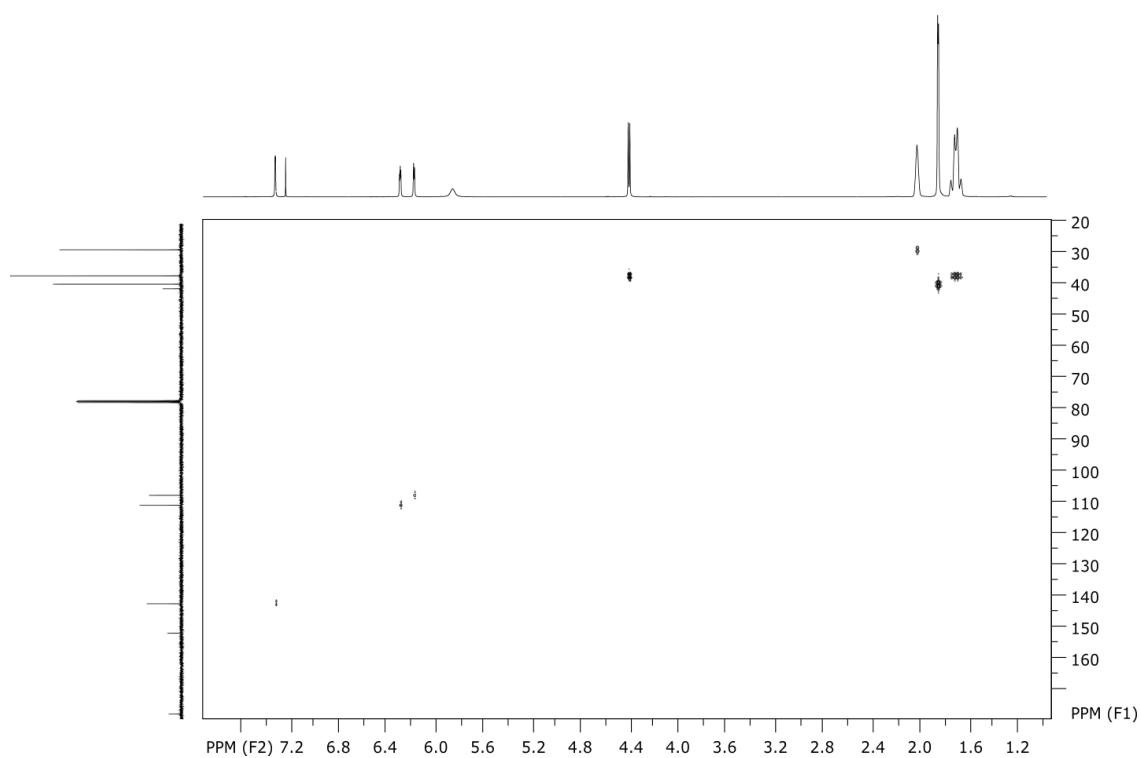


Figure S 4-6. ¹H-¹³C HMQC (CDCl₃, 25 °C) of N-(furan-2-ylmethyl)adamantane-1-carboxamide.

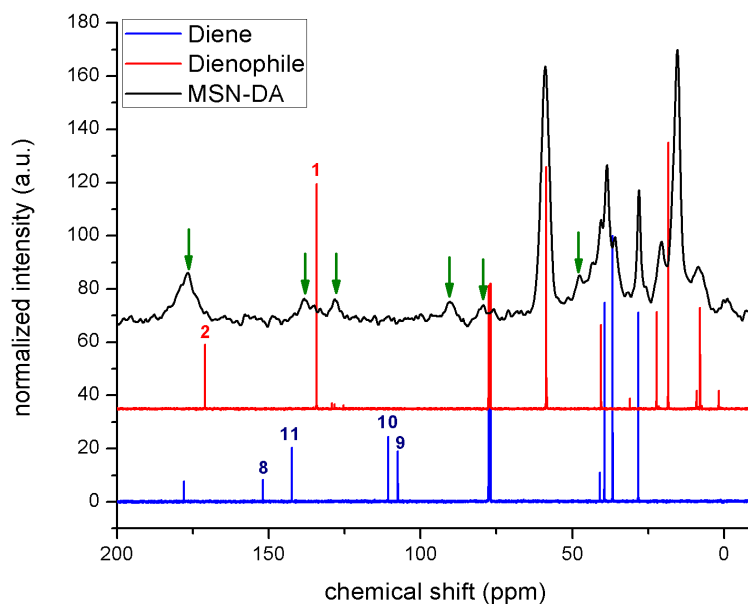


Figure S 4-7. ¹³C NMR data of the diene component (blue), the dienophile component (red) and the Diels-Alder cycloaddition product on the surface of the silica nanoparticles (black).

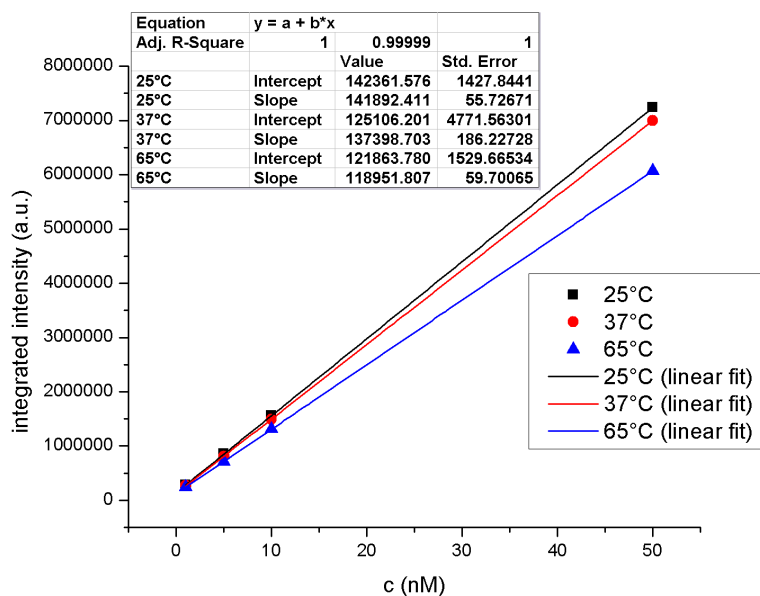


Figure S 4-8. Calibration curves for different fluorescein concentrations at 25 °C, 37 °C and 60 °C.

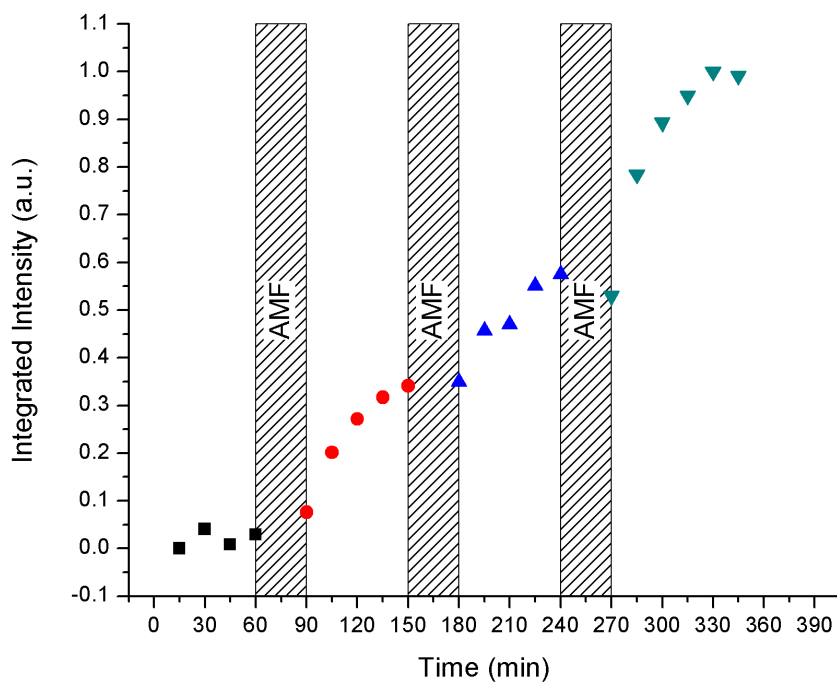


Figure S 4-9. Release experiments with superparamagnetic heating in an ice bath at 0 °C.

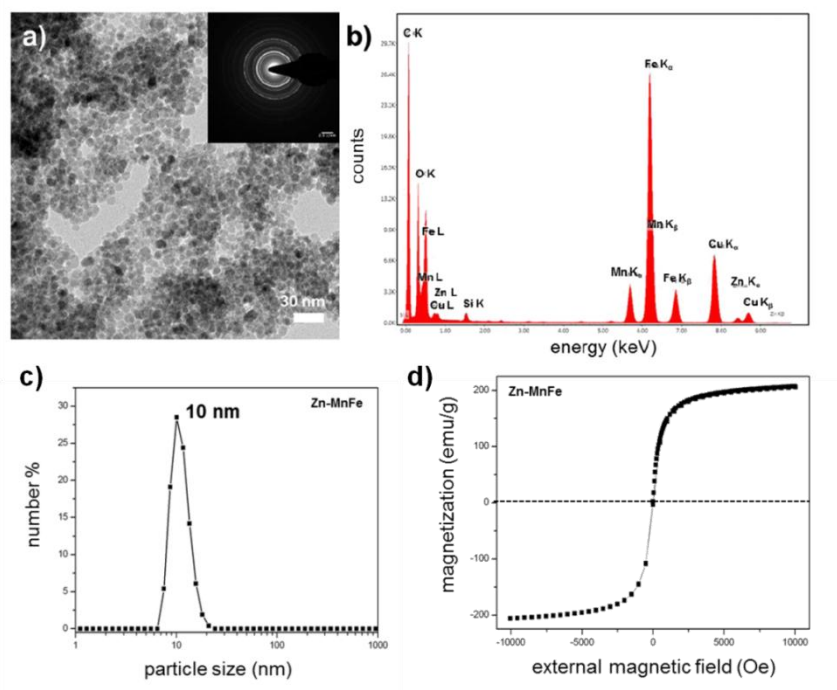


Figure S 4-10. Further characterization of zinc and manganese-doped iron oxide nanoparticles. (a) TEM image (inset: electron diffraction pattern). (b) EDX analysis. Cu and C are from the TEM grids. (c) Dynamic light scattering in CHCl_3 . The particle size is approximately 10 nm. (d) Field-dependent magnetization isotherms recorded at 300 K. The saturation magnetization is approximately 200 emu/g.

4. A molecular nanocap activated by superparamagnetic heating for externally stimulated cargo release

Property	SPION@MSN	SPION@MSN-DA
S _{BET} (m ² /g)	1034	859
d _{Pore} (NLDFT) (nm)	4.3	3.8
V _{tot} (NLDFT) (cc/g)	1.23	0.82
V _{mesopores} (NLDFT) (cc/g)	0.80	0.59
d _{Pore} (BJH) (nm)	3.0	2.8
V _{tot} (BJH) (cc/g)	1.48	0.97
V _{mesopores} (BJH) (cc/g)	1.03	0.73

Table 4-1. Nitrogen Sorption Data.

5 Genetically designed biomolecular capping system for mesoporous silica nanoparticles enables receptor-mediated cell uptake and controlled drug release

This chapter is based on the following publication:

Stefan Datz, Christian Argyo, Michael Gattner, Veronika Weiss, Korbinian Brunner, Johanna Bretzler, Constantin von Schirnding, Adriano Torrano, Fabio Spada, Milan Vrabel, Hanna Engelke, Christoph Bräuchle, Thomas Carell, and Thomas Bein, *Nanoscale* **2016**, *8*, 8101-8110.

Abstract

Effective and controlled drug delivery systems with on-demand release and targeting abilities have received enormous attention for biomedical applications. Here, we describe a novel enzyme-based cap system for mesoporous silica nanoparticles (MSNs) that is directly combined with a targeting ligand via bio-orthogonal click chemistry. The capping system is based on the pH-responsive binding of an aryl-sulfonamide-functionalized MSN and the enzyme carbonic anhydrase (CA). An unnatural amino acid (UAA) containing a norbornene moiety was genetically incorporated into CA. This UAA allowed for the site-specific bio-orthogonal attachment of even very sensitive targeting ligands such as folic acid and anandamide. This leads to specific receptor-mediated cell and stem cell uptake. We demonstrate the successful delivery and release of the chemotherapeutic agent Actinomycin D to KB cells. This novel nanocarrier concept provides a promising platform for the development of precisely controllable and highly modular theranostic systems.

5.1 Introduction

The development of effective systems for targeted drug delivery combined with *on demand* release behavior can be considered one of the grand challenges in nanoscience. In particular, porous nanocarriers with high drug loading capacity, immunological stealth behavior and tunable surface properties are promising candidates for biomedical applications such as cancer therapy and bioimaging.¹⁻⁵ Specifically, multifunctional mesoporous silica nanoparticles (MSNs) have great potential in drug delivery applications due to their attractive porosity parameters and the possibility to conjugate release mechanisms for diverse cargos^{6,7} including gold nanoparticles,^{8,9} iron oxide nanocrystals,¹⁰ bio-macromolecules,^{11,12} enzymes,¹³ and polymers.¹⁴ Control over a stimuli-responsive cargo release can be achieved via different trigger mechanisms such as redox reactions,¹⁵ pH changes,¹⁶ light-activation,^{6,17} or change in temperature.⁷ Drug delivery vehicles equipped with acid-sensitive capping mechanisms are highly desirable for acidified target environments such as the transition from early to late endosomes, tumors, or inflammatory tissues.

Here, we present genetically designed enzyme-capped MSNs that combine two important prerequisites for advances in drug delivery, namely stimuli-responsive drug release and specific cell targeting (Figure 5-1). Specifically, these pH-responsive MSNs consist of a capping structure based on carbonic anhydrase (CA). CA is a model enzyme abundant in humans and animals and generally catalyzes the hydration of carbon dioxide and the dehydration of bicarbonate.¹⁸ It is attached to the silica nanoparticle surface via aryl sulfonamide groups. As its natural inhibitor sulfonamide groups strongly bind to the active site of the CA. This enzyme-sulfonamide binding is reversible depending on the pH, where an acidic medium causes protonation of the sulfonamide, resulting in cleavage of the coordination bond and access to the porous system.¹⁹ The CA gatekeepers were used to

exploit the endosomal pH change as an internal cellular trigger and to gain control over the release of cargo molecules from the mesoporous system.

This stimuli-responsive capping system on MSNs was combined with cell targeting specificity via a bio-orthogonal click chemistry approach. Targeting ligands provide specific binding to certain cell membrane receptors allowing for an enhanced and distinctive cellular uptake of such modified nanocarriers. For example, various cell receptors are overexpressed on cancer cells, which can lead to a preferential receptor-mediated endocytosis of modified MSNs. For the attachment of such targeting ligands exclusively to the outer periphery of the enzyme gatekeepers, we exploited a recently developed method that takes advantage of the Pyrrolysine *amber suppression* system followed by bio-orthogonal copper-free click chemistry.²⁰⁻²² This system has already been utilized in applications such as optical gene control.²³ To the best of our knowledge, this is the first time the Pyrrolysine *amber suppression* system is used in a combination with porous nanocarriers for specific cell recognition and drug delivery. The incorporation of an unnatural amino acid (UAA) containing a norbornene moiety into CA provides a bio-orthogonal reaction pathway by covalently attaching tetrazine-modified targeting ligands.^{24, 25} It has recently been demonstrated that norbornene-tetrazine click chemistry is a favorable synthesis strategy over various other methods including thiol-maleimide reaction and amide formation due to extremely mild and biocompatible reaction conditions and higher selectivity.²⁶ Here, copper-free click chemistry of norbornene-modified human carbonic anhydrase II with targeting ligands was performed to prepare folate- and anandamide-modified multifunctional mesoporous silica nanocarriers.²⁷ The anandamide is, due the *cis*-configured double bonds, a particularly sensitive receptor ligand that requires extremely mild coupling conditions. The targeting system based on folate-modified silica nanocarriers was studied on KB cancer cells, which are known to overexpress the folate receptor FR- α .^{6, 28} The targeting system based on

5. Genetically designed biomolecular capping system for mesoporous silica nanoparticles enables receptor-mediated cell uptake and controlled drug release

anandamide-modified particles was tested on neural stem cells. The combination of on-demand release and specific receptor-mediated cell uptake properties within one multifunctional mesoporous silica nanocarrier system, containing biomolecular valves based on carbonic anhydrase, is anticipated to offer promising potential for controlled drug delivery applications including cancer therapy.

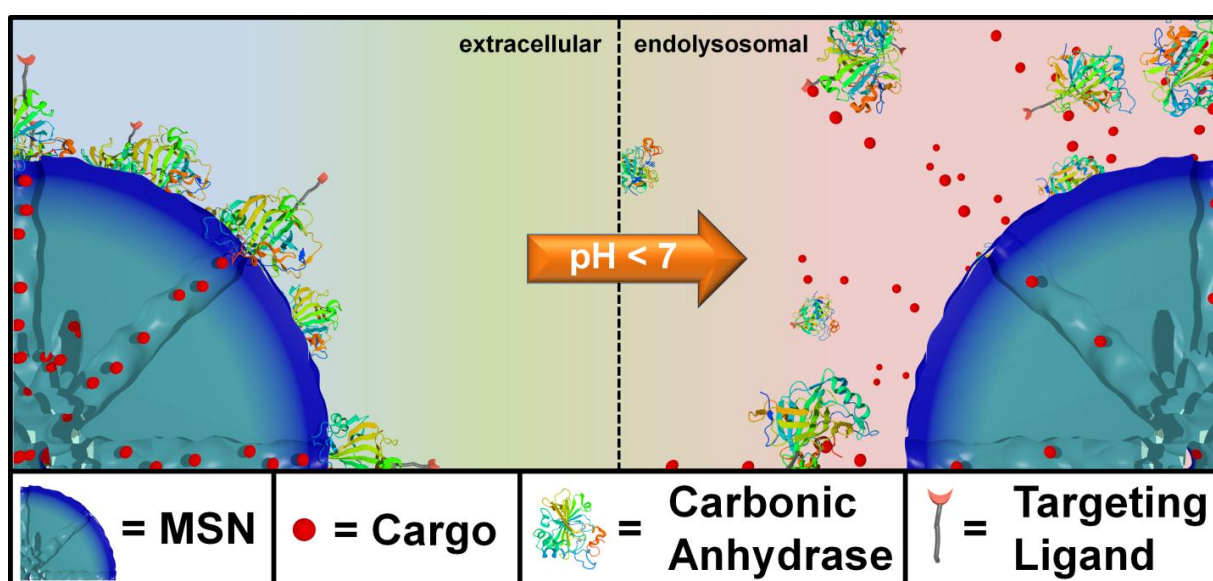


Figure 5-1. Schematic illustration of the genetically designed biomolecular pore gating system providing a pH-responsive drug release from mesoporous silica nanoparticles (MSNs). Aryl sulfonamide functionalized MSNs offer pH-dependent reversible attachment of the bulky enzyme carbonic anhydrase, which efficiently blocks the pore entrances to prevent premature cargo release. Furthermore, specific cancer cell targeting can be achieved via site-specific modification of a genetically incorporated norbornene amino acid in the biomolecular gatekeepers.

5.2 Results and Discussion

pH-Responsive MSNs with an average particle size of 150 nm (average pore diameter: 3.8 nm) containing biomolecular valves based on the enzyme carbonic anhydrase (CA, hydrodynamic diameter: 5.5 nm) were synthesized via a delayed co-condensation approach.³⁴ In a second step, benzene sulfonamide (phSA) groups were covalently attached to the silica nanoparticles via a short bifunctional crosslinker (maleimide-C₆-NHS) at mild reaction conditions (sample MSN-phSA). After cargo loading, the enzyme CA was added to the buffered particle solution (pH 7.4). The formation of the inhibitor-enzyme complex (phSA-CA) leads to a dense coating at the external particle surface (MSN-phSA-CA).

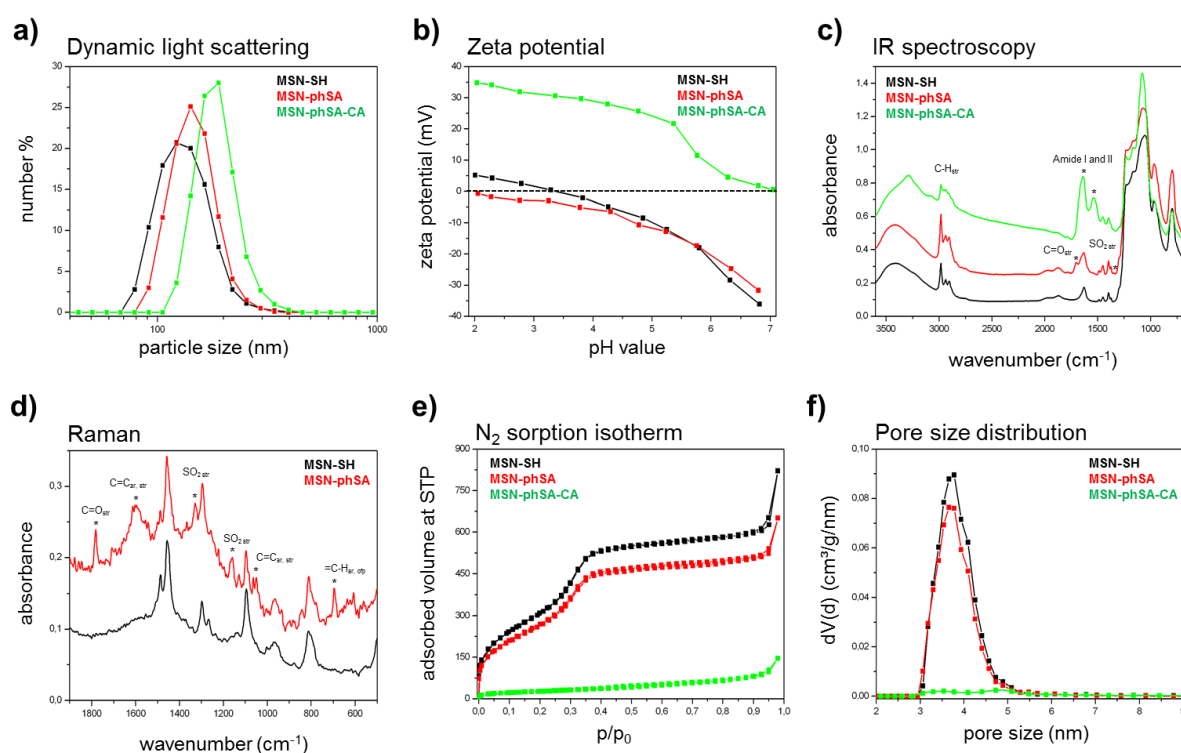


Figure 5-2. Characterization of multifunctional MSNs. a) Dynamic light scattering (DLS), b) zeta potential measurements, c) infrared (IR) spectroscopy data, d) Raman spectroscopy data, e) nitrogen sorption isotherms, and f) DFT pore size distribution of the MSNs. MSN-SH (black), MSN-phSA (red) and MSN-phSA-CA (green).

5. Genetically designed biomolecular capping system for mesoporous silica nanoparticles enables receptor-mediated cell uptake and controlled drug release

Dynamic light scattering (DLS) measurements showed the size distribution of the functionalized MSNs to be narrow and around 150 nm (Figure 5-2a), implying excellent colloidal stability after all functionalization steps. The surface charge of silica nanoparticles, measured as the zeta potential, changed due to the stepwise attachment of organic moieties (Figure 5-2b): The isoelectric point (IEP) of MSN-SH (pH 3.6) was shifted to a more acidic pH value (< 2) for MSNs containing the benzene sulfonamide groups on the outer surface. The tendency for sulfonamide groups to be protonated is relatively low due to the stabilizing resonance effect, which leads to the increase in negative surface charge (predominantly influenced by silanol content). After attachment of the carbonic anhydrase, a drastic increase of the zeta potential was observed resulting from amino acid residues that can be easily protonated - such as arginine, histidine and lysine - on the surface. IR data for all samples showed typical vibrational modes of the silica framework between 780 and 1300 cm^{-1} (Figure S 5-1c). MSNs containing the benzene sulfonamide groups showed additional modes for C=O stretching vibrations at 1700 and 1627 cm^{-1} and a peak of weak intensity at 1340 cm^{-1} , which belongs to the typical asymmetric SO_2 stretching vibration modes of the sulfonamide groups. For the sample MSN-phSA-CA, amide vibrations (Amide I: 1639 cm^{-1} , C=O stretching vibration; Amide II: 1535 cm^{-1} , N-H deformation and C-N stretching vibration) of high intensity were observed; these are typical for proteins. Raman spectroscopy provided data complementary to IR spectroscopy. In Figure 5-2d a more detailed view of the spectra for MSN-SH and MSN-phSA in the range between 1900 and 600 cm^{-1} is depicted and various additional bands (*) were observed for the benzene sulfonamide-functionalized particles. (data for MSN-phSA-CA not shown, for full range Raman spectra see Figure S4). Nitrogen sorption measurements show type IV isotherms for MSN-SH and MSN-phSA, confirming mesoporosity of the silica nanoparticles. Relatively high surface areas (up to 1200 m^2/g) and pore volumes (0.8 cm^3/g) were observed for MSN-SH and MSN-phSA (Table 5-1).

Sample	BET surface area (m ² /g)	Pore volume ^a (cm ³ /g)	DFT pore size ^b (nm)
MSN-SH	1170	0.83	3.8
MSN-phSA	1004	0.72	3.7
MSN-phSA-CA	99	0.07	-

Table 5-1. Porosity parameters of functionalized MSNs.

^aPore volume is calculated up to a pore size of 8 nm to remove the contribution of interparticle porosity.
^bDFT pore size refers to the peak maximum of the pore size distribution.

Importantly, the DFT pore size distribution (Figure 5-2f) was not affected by the attachment of the benzene sulfonamide linkers and no incorporation of organic groups inside the mesopores was observed. The attachment of the bulky enzyme carbonic anhydrase resulted in a drastic reduction of surface area and pore volume for sample MSN-phSA-CA. Thus, the carbonic anhydrase enzymes were able to efficiently block the mesopores even towards the access of nitrogen molecules. We observed no pore size distribution for MSN-phSA-CA in the range between 2 and 9 nm. This confirms the successful synthesis of carbonic anhydrase-coated MSNs via benzene sulfonamide linkers.

In order to investigate the pH-responsive removal of the bulky gatekeepers from the particles, *in vial* cargo release experiments were performed. We used a custom-made two-compartment system to analyze the time-based release of the fluorescent model cargo fluorescein.¹² After incorporation of fluorescein molecules into the mesoporous system, carbonic anhydrase was added to block the pore entrances. An efficient sealing of the pores and no premature release of the cargo was observed for the sample MSN-phSA-CA dispersed in HBSS buffer (pH 7.4) at 37 °C (Figure 5-3a, closed state, black curve). After 3 h the solution was exchanged and the particles were dispersed in citric-acid phosphate buffer (CAP buffer, pH 5.5). The change to acidic milieu, which simulates the acidification of endosomes, causes a significant increase in fluorescence intensity over time (open state, red curve). Furthermore, we could show the

5. Genetically designed biomolecular capping system for mesoporous silica nanoparticles enables receptor-mediated cell uptake and controlled drug release

long-term stability of the capping system for more than 16 hours in HBSS buffer and cell medium at pH 7.4 (Figure 5-3b). These *in vial* release experiments demonstrate efficient sealing of the pores with carbonic anhydrase acting as a bulky gatekeeper, preventing premature cargo release and allowing for release upon acid-induced detachment of the capping system.

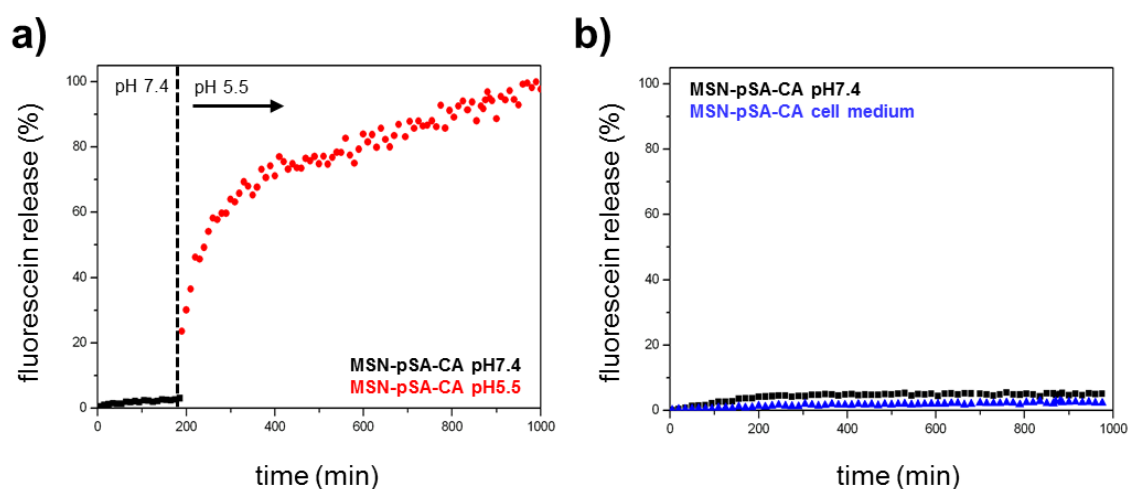


Figure 5-3. *In vial* release kinetics of fluorescein molecules from the enzyme-coated MSNs at different pH values. (a) Sample MSN-pSA-CA features no premature release of the fluorescent cargo molecules in HBSS buffer solution at pH 7.4 (closed state, black curve). After 3 h the medium was changed to slightly acidic milieu (CAP buffer, pH 5.5, red curve) resulting in a significant increase in fluorescence intensity. The gatekeepers are detached from the particle surface upon acidification, causing an efficient and precisely controllable release of fluorescein from the mesoporous system. (b) Long-term stability of the capping system was investigated in HBSS buffer (pH 7.4, black curve) and cell medium (blue curve). No unintended cargo release was observed within about 16 h.

The enzyme activity assay investigates the hydrolysis in TRIS-buffered solution of a chromogenic substrate (p-nitrophenyl acetate, NPA) in the presence of the enzyme, generating nitrophenol. UV-Vis spectroscopy is used to measure the resulting absorption maximum at 400 nm.

Figure 5-4 shows the resulting curve for the non-catalyzed (no carbonic anhydrase) reaction, which can be taken as baseline. The slight slope for this curve is due to the hydrolysis rate of

the pure substrate in aqueous solution in the absence of catalytic enzymes. In the presence of 100 nM enzyme (non-inhibited) the maximum conversion of the substrate can be obtained. A slight decrease in conversion efficiency can be observed upon addition of 50 μg of MSN-SH particles due to marginal reduction of enzyme activity in the presence of silica nanoparticles. We assume that this effect corresponds to minor unspecific attachment of the carbonic anhydrase to the silica nanoparticles causing blocking of the active sites to some extent. In comparison, the addition of inhibitor-containing particles (MSN-phSA) causes a significant decrease of the slope of the resulting curve. This proves a specific formation of the inhibitor-enzyme complex at the external surface of the silica nanoparticles. Thus we have shown conclusively that the sulfonamide-functionalized MSNs are able to bind the enzyme carbonic anhydrase. At neutral pH values, the enzyme is specifically attached to the sulfonamide-functionalized particle surface resulting in an inhibition of the enzyme's active site. This leads to a drastic decrease in enzyme activity.

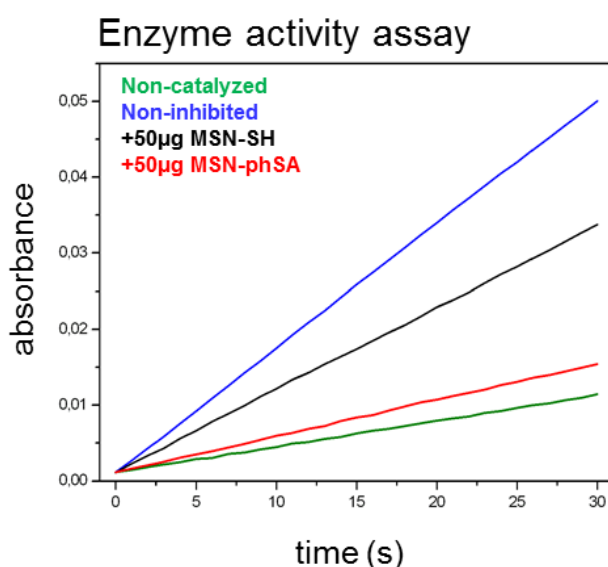


Figure 5-4. Enzyme activity assay of CA catalyzing the hydrolysis of the chromogenic substrate p-nitrophenyl acetate measured by UV-Vis spectroscopy (absorbance at 400 nm). Non-catalyzed (green) and non-inhibited (blue) reaction and after addition of MSN-SH (black) or MSN-phSA (red).

5. Genetically designed biomolecular capping system for mesoporous silica nanoparticles enables receptor-mediated cell uptake and controlled drug release

For efficient receptor-mediated cancer cell uptake and selective drug delivery a targeting ligand needs to be implemented. Since the particle surface is covered with bulky enzymes (CA), we aimed for the attachment of the targeting moieties directly to the outer periphery of the enzyme, in order to be accessible for cell receptors. For this approach to be successful, the site of targeting ligand attachment on the enzyme is of key importance. Ideally it should be positioned opposite of the binding site of the enzyme, to prevent blocking of the active site and thus leakage of the capping system. However, site-specific chemical modifications of proteins are highly challenging. Several methods, such as the reaction of thiol groups with maleimide or of lysine chains with activated esters, lack specificity. A more specific method is the incorporation of unnatural amino acids into the protein.^{20, 35, 36} Among others, the genetic incorporation of UAAs bearing side chains with alkyne,^{37, 38} trans-cyclooctene,³⁹ cyclooctyne⁴⁰ or norbornene^{20, 24} functionalities has been reported previously. Subsequently these residues can be modified specifically and bio-orthogonally, for example by reverse electron-demanding Diels-Alder reactions with tetrazines.^{25, 26, 39} The natural PylRS/tRNA_{Pyl} pair is perfectly suitable to genetically incorporate UAAs due to its orthogonality to common expression strains. Recently, a norbornene-containing Pyl analogue (Knorb) has been developed by some of us.^{20, 21} Here, the synthesis of norbornene-functionalized human carbonic anhydrase II (HCA) was accomplished similar to a previously described procedure yielding HCA H36Knorb.⁴¹ The correct position of the UAA was confirmed by tryptic digestion of the protein followed by HPLC-MS/MS analysis (see SI). HCA H36Knorb carrying norbornene on the opposite face of its phSA-binding site was bound to phSA-MSN and then treated with an excess of folate-PEG₂₀₀₀-tetrazine (Figure 5-5a) or anandamide-tetrazine. The excess of the tetrazine reagent could be easily removed by centrifugation of the nanoparticles followed by washing. The efficiency of the folate-targeting system was examined on KB-cells presenting either free or blocked FA-receptors (Figure 5-5). For

visualization, the cell membrane of the KB cells was stained with WGA488 (green), and the particles were labeled with Atto633 (red). In Figure 5-5 c-e we present the folic acid receptor blocked cells that were incubated with particles between 2 and 8 h. With increasing incubation time, only a few particles were internalized and unspecific cell uptake was observed only to a minor degree. In contrast, the cells with available folic acid receptor on their surface (Figure 5-5 f-h) exhibit a significant and increasing uptake behavior and a considerably higher degree of internalized particles. Thus we could confirm the successful application of bioorthogonal modification of a capping enzyme to act as targeting ligand. We also proved, that the here described genetically modified enzyme capping strategy can be used to attach even sensitive ligands like arachidonic acid via mild click-chemistry conditions e.g. for the site-specific targeting of neural stem cells and different cancer cells.³² We tested the anandamide-targeting system on neural stem cells and A431 cells. Neural stem cells have anandamide receptors and successfully internalized the anandamide-particles (see Appendix, Figure S 5-3). A431 cells (epidermoid carcinoma) are also known to overexpress the G-protein coupled cannabinoid-based receptors CB1 and CB2. These receptors can be attacked with anandamide-functionalized MSNs. Corresponding to the folate-based targeting experiment the cannabinoid receptors on the A431 cells were either blocked or free. After 3 h of incubation the receptor blocked cells internalized just a few anandamide-functionalized MSNs. In contrast, the amount of intracellular particles is clearly much larger in the case of non-blocked cannabinoid receptors (Figure S 5-4). The successful experiments with different cell lines and targeting ligands show that the investigated bioorthogonal attachment concept could be expanded on a variety of enzymes and ligands.

5. Genetically designed biomolecular capping system for mesoporous silica nanoparticles enables receptor-mediated cell uptake and controlled drug release

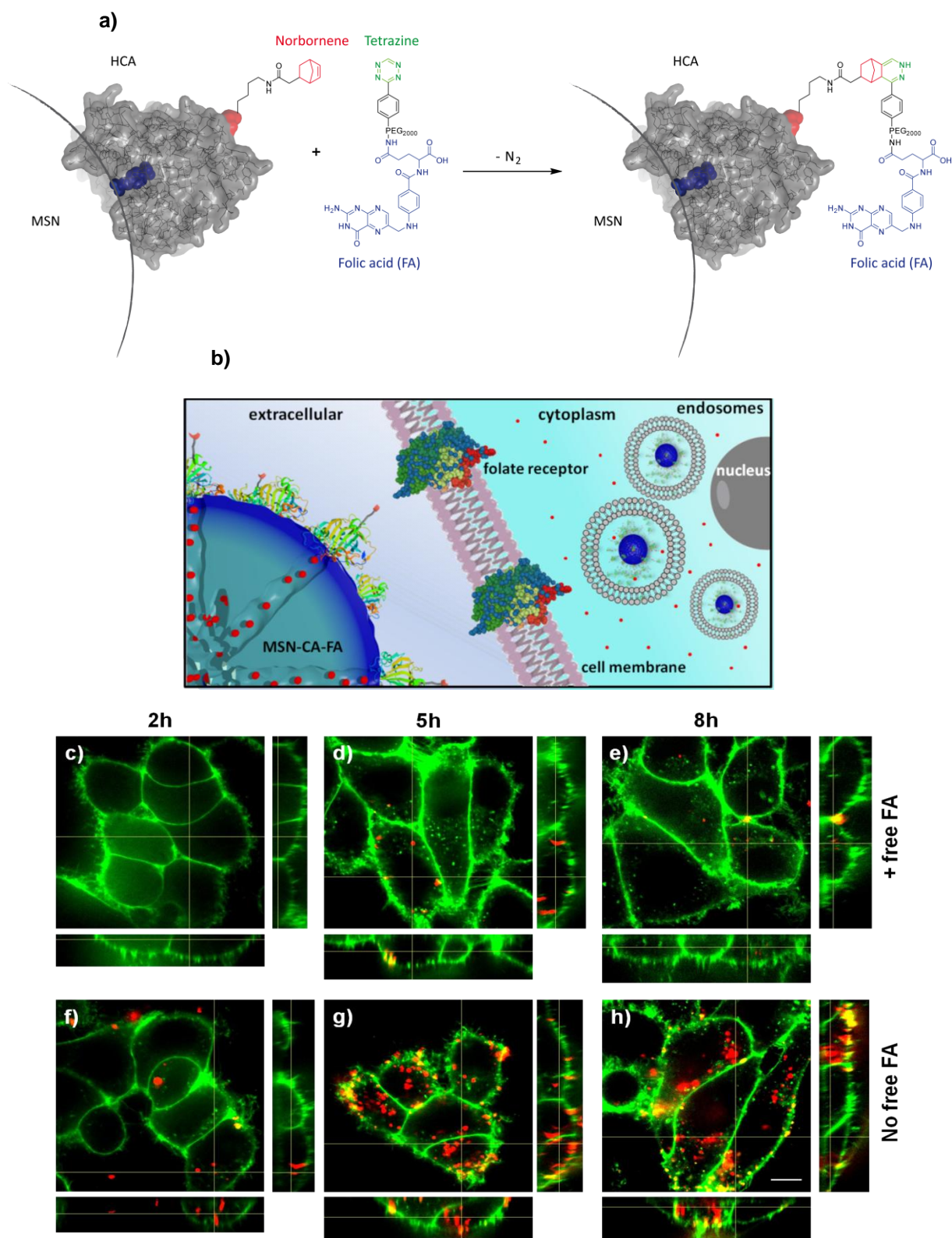


Figure 5-5. a) Norbornene-functionalized carbonic anhydrase (HCA H36Norb) with indicated functionalization site (red) and active site (blue) is able to react in a reversed-electron-demand Diels-Alder reaction with a folate-PEG2000-tetrazine derivative to give HCA-FA. b) Schematic receptor-mediated uptake of folate-functionalized MSN-CA nanoparticles. c-e) Nonspecific and f-h) receptor-mediated

endocytosis of MSN-phSA-CA-FA (red) by KB cells (WGA488 membrane staining, green). A specific receptor-mediated cell uptake was observed for MSN-phSA-CA-FA with KB cells (not pre-incubated with FA) after 5 and 8 h incubation at 37 °C (g/h). Incubation of MSN-phSA-CA-FA with FA-pre-incubated KB cells for 2, 5, 8 h at 37 °C showed only minor unspecific cellular uptake over all incubation times (c-e). The scale bar represents 10 μm .

Employing fluorescent live-cell imaging, we investigated the *in vitro* release behavior of encapsulated 4',6-diamidino-2-phenylindole (DAPI) in HeLa cancer cells. The molecular size of DAPI is similar to fluorescein. It was therefore expected to efficiently enter the mesoporous system of the silica nanoparticle. Due to its effective *turn-on* fluorescence upon intercalation into DNA double strands, DAPI is commonly used as nuclei counterstain in cell imaging (about 20 fold enhancement in fluorescence intensity).⁴² Since DAPI is cell membrane permeable, free fluorescent dye molecules are able to stain the nucleus within very short time periods (1-5 min), as described in several staining protocols.⁴³ After incorporation of DAPI into the mesoporous system of the silica nanocarriers, the pores were sealed by addition of carbonic anhydrase. The HeLa cells were incubated for a total time period of 24 h with the loaded particles, which were additionally labeled with Atto 633 dye (red), as depicted in Figure 5-6. After 7 h of incubation, MSNs were efficiently taken up by the cells and were found to be located in endosomes. Importantly, almost no staining of the nuclei with DAPI (blue) could be observed at this time point. Only after 15 h, blue fluorescence (even more intensive after 24 h) provided evidence of efficiently released DAPI from the MSNs. Control experiments in which the sample supernatant after particle separation (centrifugation) was added to the HeLa cells showed no significant nuclei staining even after 24 h (Figure 5-6d). These cell experiments prove a substantial time-dependent release of DAPI from the mesopores of our nanocarrier system and also show that no free dye molecules were present in the solution. We suggest that the observed delayed nuclei staining results from a cascaded release mechanism. First, acidification throughout the endosomal pathway to late endosomes

5. Genetically designed biomolecular capping system for mesoporous silica nanoparticles enables receptor-mediated cell uptake and controlled drug release

or endolysosomes is of key importance. Only the pH change to mildly acidic values (about 5.5) makes the detachment of the bulky gatekeepers from the MSN hosts possible. Subsequent opening of the pores leads to an efficient cargo release.

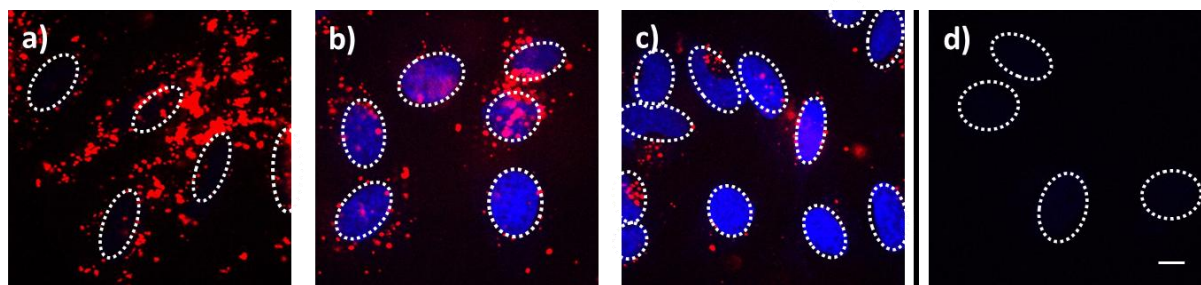


Figure 5-6. Fluorescence microscopy of HeLa cells incubated with MSN-phSA-CA nanoparticles loaded with DAPI and labeled with Atto 633 (red) after a) 7 h, b) 12 h and c) 24 h of incubation. The delayed nuclei staining with DAPI (blue) is caused by a time-dependent release of DAPI based on the need for an acidic environment. d) In a control experiment, the incubation with the supernatant solution (without MSNs) showed no staining of the nuclei with DAPI after 24 h, suggesting that no free DAPI molecules were present in the particle solution. The nuclei are indicated with dashed circles. The scale bar represents 10 μm .

Additional co-localization experiments showed the localization of CA-capped nanoparticles in acidic cell compartments after endocytosis (Figure S 5-2). To examine the ability of our newly developed MSN drug delivery system to transport chemotherapeutics and to affect cells with their cargo, we incorporated Actinomycin D (AmD), a cytostatic antibiotic, dissolved in DMSO. Free AmD is membrane permeable and induced an uncontrolled cell death within a few hours. MSN-phSA-CA provided intracellular AmD release and caused efficient cell death after 24 h. The delayed reaction demonstrates that AmD was delivered in a controlled manner via the particles and released only after acidification of the endosome and subsequent de-capping of the gate-keeper CA. In

Figure 5-7 cell death is visualized by a caspase 3/7 stain - a marker for apoptotic/dead cells. Control particles loaded with pure DMSO did not induce significant cell death at all, nor did the supernatant solution after particle separation via centrifugation (

Figure 5-7i-l). The results are in good accordance with dose-dependent cell viability studies (Figure S 5-5) where the AmD-loaded particles effectively killed HeLa cells after 24 h of incubation ($IC_{50,rel} = 8.3 \mu\text{g/mL}$). This experiment shows the great potential of the MSN-phSA-CA system to efficiently deliver chemotherapeutics to cancer cells. The pH-responsive genetically modified capping system provides the ability to act as a general platform for different targeting ligands and cargos.

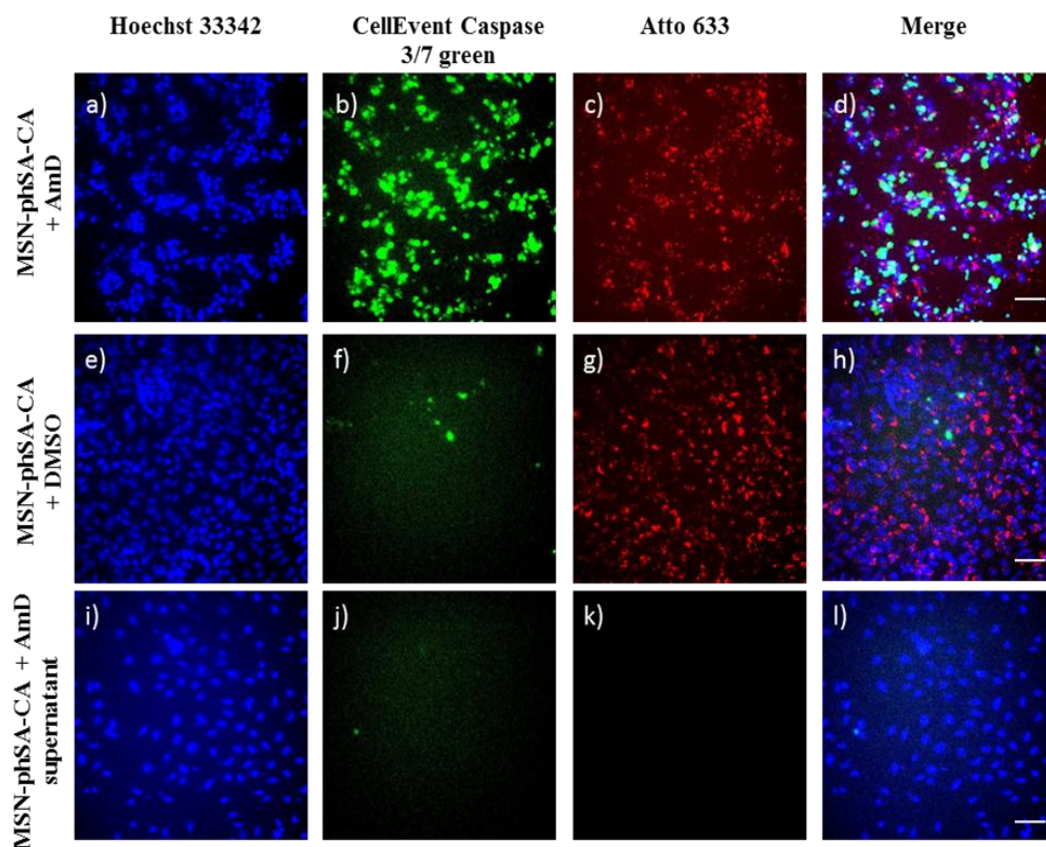


Figure 5-7. Representative fluorescence microscopy images of HeLa cells incubated with MSN-phSA-CA nanoparticles loaded with Actinomycin D (AmD; a-d) or DMSO (e-h) and labeled with Atto 633 (red) after 24 h of incubation. As a control, the supernatant of AmD loaded particles after particle separation was incubated with the cells (i-l). Cell nuclei were stained with Hoechst 33342 (blue). For live/dead

discrimination CellEvent caspase 3/7 (green) was used. Due to activation of caspase-3/7 in apoptotic cells, DNA can be stained after cleavage of the DNA-binding dye from a binding-inhibiting peptide. MSNs were efficiently taken up by cells (c/d and g/h). Cell death can only be observed for cells treated with AmD loaded MSN-phSA-CA after 24 h of incubation (increased DNA staining in green) (b). In contrast, nanoparticles loaded with DMSO or the sample supernatant do not induce significant apoptosis (almost no DNA-staining) (f and j). The scale bars represent 50 μm .

5.3 Conclusion

We conclude that the novel capping system concept based on pH-responsive detachment of carbonic anhydrase combined with folic acid as targeting ligand allows for highly controllable drug release from porous nanocarriers. Our drug delivery system provides an on-demand release mechanism shown by *in vial* and *in vitro* cargo release experiments. The multifunctional MSNs were efficiently endocytosed in cancer cells and could be located in acidic cell compartments where they released their cargo. Furthermore, the system has an on-board targeting mechanism as demonstrated in additional *in vitro* experiments. The targeting mechanism is attached at a specific site of the capping enzyme preventing interference with the closure mechanism. Our newly developed pH-responsive gatekeepers with genetically designed targeting functions provide a promising platform for the design of versatile and modular drug delivery systems.

5.4 Experimental Part

Materials. Tetraethyl orthosilicate (TEOS, Fluka, > 99 %), triethanolamine (TEA, Aldrich, 98 %), cetyltrimethylammonium chloride (CTAC, Fluka, 25 % in H₂O), (3-mercaptopropyl)-triethoxysilane (MPTES, Sigma Aldrich, > 80 %), 6-maleimidohexanoic acid N-hydroxysuccinimide ester (Fluka, > 98 %), bovine carbonic anhydrase (bCA, Sigma, > 95 %), 4-(2-aminoethyl)benzenesulfonic acid (Aldrich, 98 %), folic acid (FA, Sigma Aldrich, ≥ 97 %), 4,6-Diamidino-2-phenylindole dihydrochloride (DAPI, Sigma-Aldrich, ≥ 98 %), CellEvent™ Caspase-3/7 Green Detection Reagent (lifeTechnologies), Hoechst 33342, Trihydrochloride, Trihydrate (lifeTechnologies), Wheat Germ Agglutinin, Alexa Fluor® 488 Conjugate (lifeTechnologies), CellLight© Early Endosome-GFP, Late Endosome-GFP, and Lysosome-GFP, BacMam 2.0 (lifeTechnologies), Atto 633 maleimide (ATTO-TEC), ammonium nitrate (NH₄NO₃, Aldrich), ammonium fluoride (NH₄F, Aldrich), hydrochloric acid (37 %), fluorescein disodium salt dihydrate (Aldrich, 90 %), and Hank's balanced salt solution (HBSS-buffer, Sigma Aldrich) were used as received. Ethanol (EtOH, absolute, Aldrich), DMSO and dimethylformamide (DMF, dry, Aldrich) were used as solvent without further purification. Bidistilled water was obtained from a millipore system (Milli-Q Academic A10). Citric-acid phosphate buffer (CAP-buffer, pH 5.5) was freshly prepared by carefully mixing a certain amount of disodium hydrogen phosphate (Na₂HPO₄, 0.2 M in H₂O) and citric acid (0.2 M in H₂O) to adjust a pH value of 5.5. Subsequently, the solution was diluted with bidistilled H₂O to a total volume of 500 mL.

Characterization. DLS and zeta potential measurements were performed on a Malvern Zetasizer Nano instrument equipped with a 4 mW He-Ne-Laser (633 nm) and an avalanche photodiode detector. DLS measurements were directly recorded in diluted colloidal suspensions of the particles at a concentration of 1 mg/mL. Zeta potential measurements were

5. Genetically designed biomolecular capping system for mesoporous silica nanoparticles enables receptor-mediated cell uptake and controlled drug release

performed using the add-on Zetasizer titration system (MPT-2) based on diluted NaOH and HCl as titrants. For this purpose, 1 mg of the particles was diluted in 10 mL bi-distilled water. Thermogravimetric analyses (TGA) of the bulk extracted samples (approximately 10 mg) were recorded on a Netzsch STA 440 C TG/DSC. The measurements proceeded at a heating rate of 10 °C/min up to 900 °C in a stream of synthetic air of about 25 mL/min. Nitrogen sorption measurements were performed on a Quantachrome Instrument NOVA 4000e at -196 °C. Sample outgassing was performed for 12 hours at a vacuum of 10 mTorr at RT. Pore size and pore volume were calculated by a NLDFT equilibrium model of N₂ on silica, based on the desorption branch of the isotherms. In order to remove the contribution of the interparticle textural porosity, pore volumes were calculated only up to a pore size of 8 nm. A BET model was applied in the range of 0.05 – 0.20 p/p₀ to evaluate the specific surface area. Infrared spectra of dried sample powder were recorded on a ThermoScientific Nicolet iN10 IR-microscope in reflexion-absorption mode with a liquid-N₂ cooled MCT-A detector. Raman spectroscopy measurements were performed on a confocal LabRAM HR UV/VIS (HORIBA Jobin Yvon) Raman microscope (Olympus BX 41) with a SYMPHONY CCD detection system. Measurements were performed with a laser power of 10 mW at a wavelength of 633 nm (HeNe laser). Dried sample powder was directly measured on a coverslip. UV/VIS measurements were performed on a Perkin Elmer Lambda 1050 spectrophotometer equipped with a deuterium arc lamp (UV region) and a tungsten filament (visible range). The detector was an InGaAs integrating sphere. Fluorescence spectra were recorded on a PTI spectrofluorometer equipped with a xenon short arc lamp (UXL-75XE USHIO) and a photomultiplier detection system (model 810/814). The measurements were performed in HBSS buffer solution at 37 °C to simulate human body temperature. For time-based release experiments of fluorescein a custom made container consisting of a Teflon tube, a dialysis membrane (ROTH Visking type 8/32, MWCO 14,000 g/mol) and a fluorescence cuvette was

used. The excitation wavelength was set to $\lambda = 495$ nm for fluorescein-loaded MSNs. Emission scans (505 – 650 nm) were performed every 5 min. All slits were adjusted to 1.0 mm, bandwidth 8 nm). Mass spectra were recorded a *Thermo LTQ-Orbitrap XL*. For analytical HPLC separations of protein and peptide samples with subsequent MS a *Dionex Ultimate 3000 Nano* HPLC was used. Acetonitrile of LC-MS grade was purchased from *Carl Roth GmbH + Co. KG*. Water was purified by a Milli-Q Plus system from *Merck Millipore*.

Synthesis of thiol-functionalized MSNs (MSN-SH). A mixture of TEOS (1.92 g, 9.22 mol) and TEA (14.3 g, 95.6 mmol) was heated to 90 °C for 20 min under static conditions in a polypropylene reactor. Then, a preheated (60 °C) mixture of CTAC (2.41 mL, 1.83 mmol, 25 % in H₂O) and NH₄F (100 mg, 0.37 mmol) in bidistilled H₂O (21.7 g, 1.21 mol) was added and the resulting reaction mixture was stirred vigorously (700 rpm) for 30 min while cooling down to room temperature. Afterwards, TEOS (18.2 mg, 92 μmol) and MPTES (18.1 mg, 92 μmol) were premixed briefly before addition to the reaction mixture. The final reaction mixture was stirred over night at room temperature. After dilution with absolute ethanol (100 mL), the nanoparticles were collected by centrifugation (19,000 rpm, 43,146 rcf, 20 min) and redispersed in absolute ethanol. Template extraction was performed in an ethanolic solution of MSNs (100 mL) containing NH₄NO₃ (2 g) which was heated at reflux conditions (90 °C oil bath) for 45 min. This was followed by a second extraction step (90 mL absolute ethanol and 10 mL hydrochloric acid (37 %)) under reflux conditions for 45 min (the material was washed with absolute ethanol after each extraction step and collected by centrifugation); finally the particles were redispersed in absolute ethanol and stored as colloidal suspension.

Synthesis of sulfonamide-functionalized MSNs (MSN-phSA). For the covalent attachment of a sulfonamide derivative to the external particle surface, a thiol-reactive linker was synthesized. 6-maleimido-hexanoic acid *N*-hydroxysuccinimide ester (mal-C₆-NHS, 10 mg, 33 μmol) was dissolved in DMF (500 μL, dry) and was added to an ethanolic solution

5. Genetically designed biomolecular capping system for mesoporous silica nanoparticles enables receptor-mediated cell uptake and controlled drug release

(15 mL) containing 4-(2-aminoethyl)benzene sulfonamide (6.7 mg, 33 μmol). The resulting reaction mixture was stirred for 1 h at room temperature. Afterwards, thiol-functionalized silica nanoparticles (MSN-SH, 100 mg) in absolute ethanol (10 mL) were added and the mixture was stirred over night at room temperature. Subsequently, the particles were collected by centrifugation (19,000 rpm, 41,146 rcf, 20 min), washed twice with absolute ethanol and were finally redispersed in ethanol (15 mL) to obtain a colloidal suspension.

Cargo loading and particle capping. MSNs (MSN-phSA, 1 mg) were immersed in an aqueous solution of fluorescein (1 mL, 1 mM), DAPI (500 μL , 14.3 mM) or Actinomycin D (500 μL [14 v% DMSO], 140 μM) and stirred over night or for 1 h, respectively. After collection by centrifugation (14,000 rpm, 16,837 rcf, 4 min), the loaded particles were redispersed in a HBSS buffer solution (1 mL) containing carbonic anhydrase (1 mg) and the resulting mixture was allowed to react for 1 h at room temperature under static conditions. The particles were thoroughly washed with HBSS buffer (4 times), collected by centrifugation (5,000 rpm, 2,200 rcf, 4 min, 15 $^{\circ}\text{C}$), and finally redispersed in HBSS buffered solution.

Click chemistry of norbornene-containing hCA. MSNs (MSN-phSA, 0.5 mg) were immersed in 500 μL HBSS buffer solution and 0.5 mg norbornene-containing hCA were added. In the meantime, 2.5 μg tetrazin *p*-benzylamine (DMSO stock solution, 0.92 mg/mL) and 0.41 mg NHS-PEG₂₀₀₀-FA were mixed in 100 μL HBSS and stirred overnight in the dark at room temperature. The solutions were mixed afterwards and stirred for two hours, washed several times and redispersed in 1 mL HBSS buffer. Subsequently, 1 μL Atto633mal (DMF stock solution, 0.5 mg/mL) was added and the mixture was stirred for 1 hour. The particles were thoroughly washed with HBSS buffer (4 times), collected by centrifugation (5,000 rpm, 2,200 rcf, 4 min, 15 $^{\circ}\text{C}$), and finally redispersed in HBSS buffered solution.

Synthesis of Knorb. The norbornene containing amino acid Knorb was synthesized as described in Ref.²⁹

Mutagenesis of pACA_HCA H36amber. Adapted from Ref.³⁰ with permission from The Royal Society of Chemistry. The amber codon (TAG) was introduced into the expression vector pACA_HCA³¹ at position His36 of the human carbonic anhydrase II gene by blunt end site directed mutagenesis using the primers *forward HCA H36amber* and *reverse HCA H36amber* (see Table 5-2).

Name	Sequence
forward H36amber	HCA 5'phosph GTT GAC ATC GAC ACT TAG ACA GCC AAG TAT GAC
reverse H36amber	HCA 5'phosph AGG GGA CTG GCG CTC TCC CTT GG

Table 5-2. Sequences of the used primers for the generation of expression vector pACA_HCA H36amber. The introduced Amber codon is shown in bold.

Expression of norbornene-containing HCA. Adapted from Ref.³⁰ with permission from The Royal Society of Chemistry. The expression vector pACA_HCA H36 amber was transformed together with pACyc_pylRS Norb, 3xpylT²⁹ which contains the genes of the triple mutant of PylRS and three copies of *pylT* in *E. coli* BL21(DE3) cells (NEB). 1 L of LB medium containing 34 mg/L chloramphenicol, 100 mg/L carbenicillin and 2 mM norbornene amino acid Knorb was inoculated with 10 mL of an overnight culture. The cells were stirred at 37 °C until an OD₆₀₀ of 0.9. At this optical density 1 mM ZnSO₄ and 0.1 mM IPTG were added to induce the expression of the HCA H36amber gene. After further 10 h at 37 °C the cells were harvested and stored at -20 °C until further use. The harvested cells were resuspended in washing buffer (25 mM Tris; 50 mM Na₂SO₄; 50 mM NaClO₄; pH 8.8) and disrupted by French Press procedure. The supernatant of the centrifuged lysate was used for sulfonamide

5. Genetically designed biomolecular capping system for mesoporous silica nanoparticles enables receptor-mediated cell uptake and controlled drug release

affinity protein purification using an ÄKTA purifier system. The self-packed 3 mL column of *p*-Aminomethylbenzenesulfonamide-Agarose resin (Sigma-Aldrich, A0796) was equilibrated with washing buffer. After binding (0.75 mL/min) of the protein solution, the column was washed with 7 column volumes of washing buffer. HCA was eluted by lowering the pH by elution buffer (100 mM NaOAc; 200 mM NaClO₄; pH 5.6). The protein containing fractions were combined, analyzed by SDS-PAGE, dialyzed against water and lyophilized. Typical yields of the pure norbornene amino acid Knorb containing protein HCA H36Knorb were 20 mg/L expression medium.

Tryptic digestion and MS/MS of norbornene-containing HCA. Adapted from Ref. ³⁰ with permission from The Royal Society of Chemistry. The sequence of HCA II is shown in Table 5-3. Position His36 which was chosen for the incorporation of amino acid Knorb is shown in red. The peptide generated after tryptic digestion is emphasized in bold letters. Figure 5-8 shows the corresponding MS/MS spectrum. Table 5-4 shows the expected and identified MS/MS fragments of the relevant tryptic peptide.

Table 5-3. Amino acid sequence of HCA II.

10 20 30 40 50 60
MAHHWGYGKH NGPEHWHKDF PIAKGER**QSP V**DI**D**HTAKY DPSLKPLSVS YDQATSLRIL

70 80 90 100 110 120
NNGHAFNVEF DDSQDKAVLK GGPLDGTYRL IQFHFHWGSL DGQGSEHTVD KKKYAAELHL

130 140 150 160 170 180
VHWNTKYGDF CKAVQQPDGL AVLGIFLKVG SAKPGLQKVV DVLDSIKTKG KSADFTNFD

190 200 210 220 230 240
RGLLPESLDY WTPGSLTTP PLLESVTWIV LKEPISVSSE QVLKFRKLN NGEPEPEELM

250 260
VDNWRPAQPL KNRQIKASFK

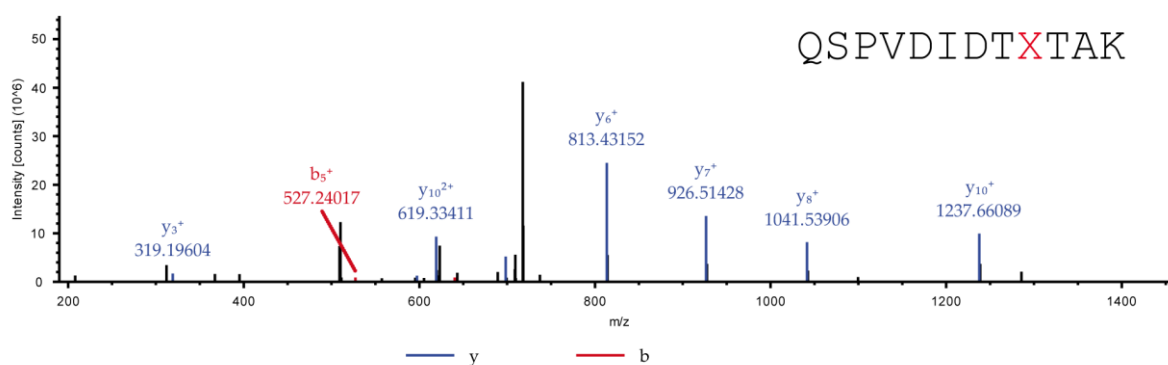


Figure 5-8. MS/MS spectrum of the tryptic peptide QSPVDIDTXTAK (X = 4). Parent ion: $[M+2H]2+_{calc.} = 726.8829$, $[M+2H]2+_{obs.} = 726.8807$ ($\Delta M = 3$ ppm).

#1	b ⁺	Seq.	y ⁺	#2
1	129.06586	Q		12
2	216.09789	S	1324.69949	11
3	313.15066	P	1237.66746	10
4	412.21908	V	1140.61469	9
5	527.24603	D	1041.54627	8
6	640.33010	I	926.51932	7
7	755.35705	D	813.43525	6
8	856.40473	T	698.40830	5
9	1134.56774	X	597.36062	4
10	1235.61542	T	319.19761	3
11	1306.65254	A	218.14993	2
12		K	147.11281	1

Table 5-4. Expected and identified MS/MS fragments of the tryptic peptide QSPVDIDTXTAK (X = Knorb). Identified fragments are shown in red for b ions and blue for y ions.

Synthesis of Anandamide-tetrazine. Chemicals were purchased from *Sigma-Aldrich*, *Fluka* or *Acros* and used without further purification. Solutions were concentrated *in vacuo* on a *Heidolph* rotary evaporator. The solvents were of reagent grade and purified by distillation.

5. Genetically designed biomolecular capping system for mesoporous silica nanoparticles enables receptor-mediated cell uptake and controlled drug release

Chromatographic purification of products was accomplished using flash column chromatography on *Merck Geduran Si 60* (40-63 μM) silica gel (normal phase). Thin layer chromatography (TLC) was performed on *Merck 60* (silica gel F254) plates. Visualization of the developed chromatogram was performed using fluorescence quenching or staining solutions. ^1H and ^{13}C NMR spectra were recorded in deuterated solvents on *Bruker ARX 300*, *Varian VXR400S*, *Varian Inova 400* and *Bruker AMX 600* spectrometers and calibrated to the residual solvent peak. Multiplicities are abbreviated as follows: s = singlet, d = doublet, t = triplet, q = quartet, m = multiplet, br. = broad. ESI spectra and high-resolution ESI spectra were obtained on the mass spectrometers *Thermo Finnigan LTQ FT-ICR*. IR measurements were performed on *Perkin Elmer Spectrum BX FT-IR* spectrometer (Perkin Elmer) with a diamond-ATR (Attenuated Total Reflection) setup. Repetencies are given in cm^{-1} . The intensities are abbreviated as follows: vs (very strong), s (strong), m (medium), w (weak), vw (very weak).

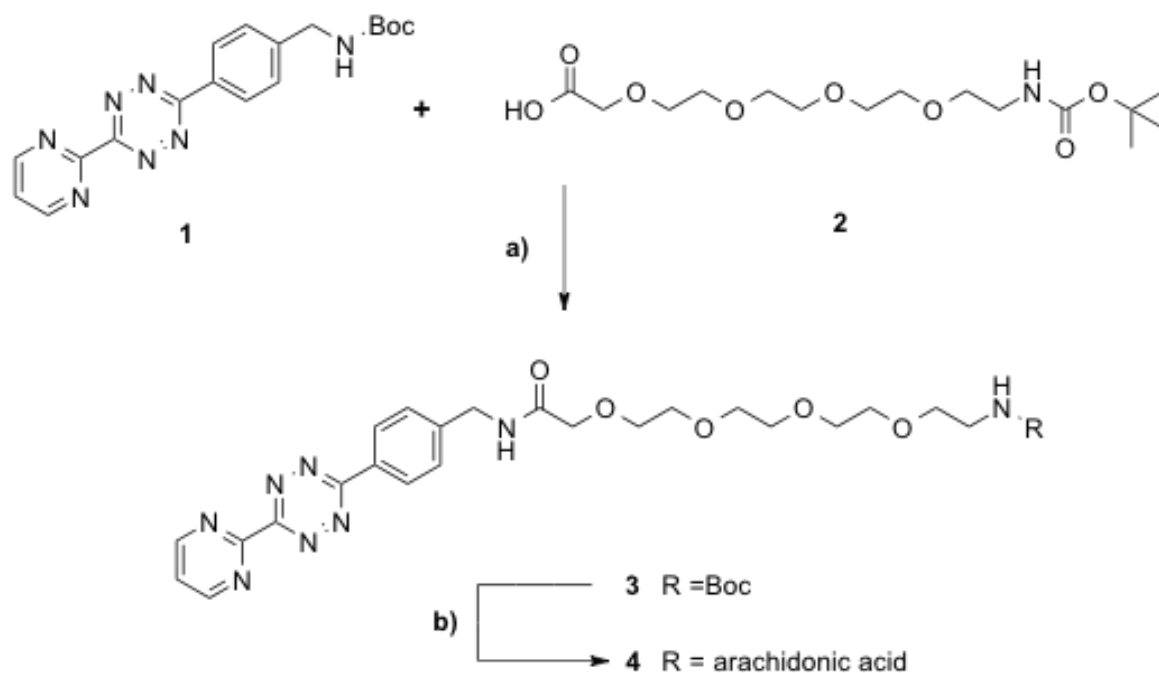
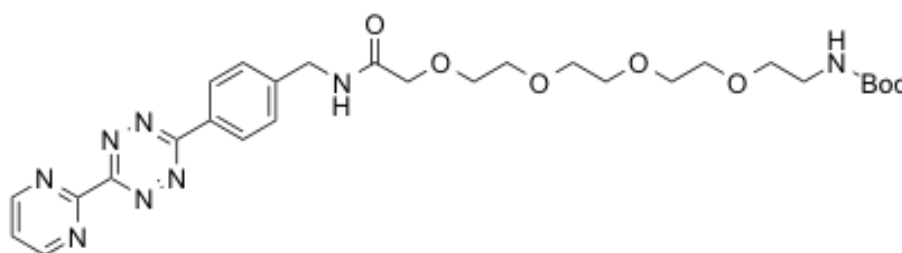


Figure 5-9. Synthesis of anandamide-tetrazine 4. a) 1. TFA, DCM, 0°C; 2. DIPEA, HATU, HOBt, DMF, RT, 42% b) 1. TFA, DCM, 0°C; 2. arachidonic acid, DIPEA, HATU, HOBt, RT, 46%.

tert-butyl (4-(6-(pyrimidin-2-yl)-1,2,4,5-tetrazin-3-yl)benzyl)carbamate (**1**) was synthesized according to the procedures described by Willems *et al.*

2,2-dimethyl-4-oxo-3,8,11,14,17-pentaoxa-5-azanonadecan-19-oic acid (**2**) was synthesized like from Shirude *et al* described.

tert-butyl (3-oxo-1-(4-(6-(pyrimidin-2-yl)-1,2,4,5-tetrazin-3-yl)phenyl)-5,8,11,14-tetraoxa-2-azahexadecan-16-yl)carbamate (**3**)



5. Genetically designed biomolecular capping system for mesoporous silica nanoparticles enables receptor-mediated cell uptake and controlled drug release

tert-butyl (4-(6-(pyrimidin-2-yl)-1,2,4,5-tetrazin-3-yl)benzyl)carbamate (1) (162 mg, 0.160 mmol) was dissolved in 6.4 mL DCM and cooled to 0°C before TFA (1.6 mL) were added. After 45 min the solvent was removed *in vacuo* and the resulting residue was used in the next reaction without further purification.

2,2-dimethyl-4-oxo-3,8,11,14,17-pentaoxa-5-azanonadecan-19-oic acid (2) (228 mg, 0.649 mmol, 2.5 eq.) was diluted in 3.77 mL dry DMF and HATU (119 mg, 0.312 mmol, 1.2 eq.), HOBt (102 mg, 0.780 mmol, 3 eq.) and finally DIPEA (0.192 mL, 0.780 mmol, 3 eq.) were added. After 10 min the deprotected tetrazinamine (0.068 mg, 0.260 mmol, 1 eq.) was added and the reaction was stirred over night at RT. The reaction was diluted with DCM and washed with water and brine before the combined organic phases were dried over MgSO₄ and the solvent was removed *in vacuo*. The residue was purified by column chromatography (silica, DCM/EtOAc/MeOH, 5:5:1) to obtain the **3** as violet oil (66.0 mg, 0.110 mmol, 42%).

R_f = 0.22 (CH₂Cl₂/EtOAc/MeOH, 5:5:1).

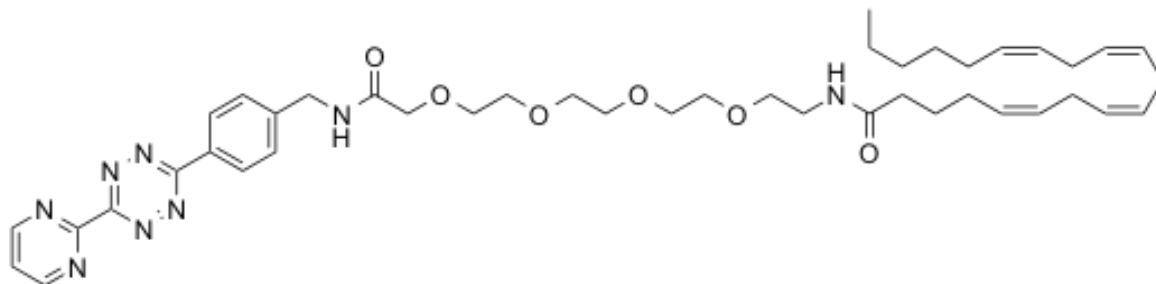
¹H-NMR (600 MHz, CDCl₃): δ [ppm] = 9.11 (d, ³J = 4.9 Hz, 2H, 2xC-H_{arom}), 8.68 (d, ³J = 8.4 Hz, 2H, 2xC₂-H_{arom}), 7.59 – 7.54 (m, 1H, C-H_{arom}), 4.61 (d, ³J = 6.2 Hz, 2H, Ar-CH₂-NH), 4.12 – 4.08 (m, 2H, C=O-CH₂-O), 3.73 – 3.50 (m, 14H, tetraethylene glycol 7x CH₂), 3.47 (t, ³J = 5.1 Hz, 2H, CH₂-NH), 1.40 (s, 9H, 3xCH₃-*t*Bu).

¹³C-NMR (150 MHz, CDCl₃): δ [ppm] = 164.57, 163.32, 159.82, 159.81, 158.62, 129.33, 128.77, 122.68, 70.62, 70.36 (Tetraethylenglykol 7 x CH₂), 42.76 (Ar-CH₂-NH), 28.64 (CH₃-*t*Bu).

HR-MS (ESI): [M+Na]⁺ calc.: 621.2755, found: 621.2763.

FT-IR (ATR, cm^{-1}): 3336 (br, w), 2921 (w), 1702 (m), 1676 (m), 1610 (m), 1563 (m), 1529 (m), 1434 (m), 1380 (vs), 1250 (m), 1144 (m), 1113 (m), 844 (s).

14-((5Z,8Z,11Z,14Z)-icosa-5,8,11,14-tetraenamido)-N-(4-(6-(pyrimidin-2-yl)-1,2,4,5-tetrazin-3-yl)benzyl)-3,6,9,12-tetraoxatetradecanamide (**4**)



tert-Butyl (3-oxo-1-(4-(6-(pyrimidin-2-yl)-1,2,4,5-tetrazin-3-yl)phenyl)-5,8,11,14-tetraoxa-2-azahexadecan-16-yl)carbamate (**3**) (66.0 mg, 0.1103 mmol) was dissolved in 1.15 mL DCM and 0.3 mL TFA was added. After 45 min the solvent was removed *in vacuo* and the resulting residue was used in the next step without further purification.

Arachidonic acid (54.6 μmol , 166 μmol , 1.5 eq.) was dissolved in 0.7 mL dry DMF and HATU (50.3 mg, 132 μmol , 1.2 eq.), HOBt (44.7 mg, 331 μmol , 3 eq.) and DIPEA (56.3 μL , 332 μmol , 3 eq.) were added. After 10 min the deprotected amine (55.0 mg, 110 μmol , 1 Äquiv.), dissolved in 0.6 mL dry DMF, was added and the reaction was stirred for 2 h at RT. The reaction was diluted with DCM and washed with saturated NH_4Cl -solution. After drying of the combined organic phases over MgSO_4 and removing of the solvent *in vacuo*, the residue was purified by column chromatography (silica, *i*Hex/EtOAc, 1:1 \rightarrow DCM/EtOAc/MeOH, 10:10:1). **4** was received as violet oil (39.6 mg, 50.6 μmol , 46%).

$R_f = 0.72$ ($\text{CH}_2\text{Cl}_2/\text{EtOAc}/\text{MeOH}$, 2:2:1).

5. Genetically designed biomolecular capping system for mesoporous silica nanoparticles enables receptor-mediated cell uptake and controlled drug release

¹H-NMR (600 MHz, CDCl₃): δ [ppm] = 9.11 (d, ³J = 4.8 Hz, 2H, C-H_{arom}), 8.67 (d, ³J = 8.4 Hz, 2H, 2xC3'-H_{arom}), 7.59 – 7.54 (m, 1H, C5-H_{arom}), 5.43 – 5.23 (m, 8H, 8xCH), 4.61 (d, ³J = 6.2 Hz, 2H, Ar-CH₂-NH), 4.11 – 4.02 (m, 2H, C=O-CH₂-O), 3.73 – 3.36 (m, 18H, tetraethylene glykole 8xCH₂, CH₂-NH), 2.82 – 2.72 (m, 6H, 3xC-H_{2arach}), 2.18 – 2.12 (m, 2H, CH_{2arach}), 2.09 – 1.99 (m, 4H, 2xC-H_{2arach}), 1.67 (q, ³J = 7.5 Hz, 2H, C-H_{2arach}), 1.37 – 1.20 (m, 6H, 3xC-H_{2arach}), 0.86 (t, J = 7.0 Hz, 3H, C-H_{3arach}).

¹³C-NMR (100 MHz, CDCl₃): δ [ppm] = 173.38, 170.64, 164.54, 163.27, 159.72 (C_q), 158.64 (2xC_{arom}), 129.35 (CH), 129.33 (2xC), 128.90, 128.81, 128.74, 128.43, 128.38, 128.06, 127.72 (7xCH), 126.95, 122.75 (C_{arom}), 71.30, 70.65, 70.60, 70.47, 70.34, 70.13 (Tetraethylenglykol 8xCH₂), 42.73 (CH₂-NH), 39.40, 36.21 (C_{arach}), 31.72 (C_{arach}), 29.92 (C_{arach}), 27.43 (C_{arach}), 26.91 (C_{arach}), 25.85 (C_{arach}), 25.83 (C_{arach}), 25.74 (C_{arach}), 22.79 (C_{arach}), 14.30 (C_{arach}).

HR-MS (ESI): [M+H]⁺ calc.: 785.4709, found: 785.4727.

FT-IR (ATR, cm⁻¹): 3311 (m), 2923 (s), 1555 (s), 1413 (s), 1103 (s).

Click chemistry of norbornene-containing hCA with anandamide tetrazine. MSNs (MSN-phSA, 0.5 mg) were loaded in 500 μL of calcein solution (1 mM) for 1 h. The loaded particles were collected by centrifugation (14,000 rpm, 16,837 rcf, 4 min) and 500 μL HBSS buffer solution was added. After addition of 0.5 mg norbornene-containing hCA the particles were redispersed and stirred for 1 h. Then, 5 μg anandamide tetrazine (DMSO stock solution, 2 mg/mL) were added and stirred for 1 h respectively. The particles were thoroughly washed with HBSS buffer (4 times), collected by centrifugation (5,000 rpm, 2,200 rcf, 4 min, 15 °C), and finally redispersed in 500 μL HBSS buffered solution.

Cell Culture. HeLa cells were grown in Dulbecco's modified Eagle's medium (DMEM):F12 (1:1) (lifeTechnologies) with Glutamax I medium and KB cells in folic acid deficient Roswell

Park Memorial Institute 1640 medium (RPMI 1640, lifeTechnologies), both supplemented with 10 % fetal bovine serum (FBS) at 37 °C in a 5 % CO₂ humidified atmosphere. The cells were seeded on collagen A-coated LabTek chambered cover glass (Nunc). For live cell imaging the cells were seeded 24 or 48 h before measuring, at a cell density of 2x10⁴ or 1x10⁴ cells/cm². The FGF-2 and EGF dependant neural stem cell line ENC1 was derived from E14 mouse embryonic stem cells and cultured as described.³² ENC1 cells were maintained in gelatine coated flasks and propagated in a 1:1 mixture of Knockout-DMEM (*Life Technologies*) and Ham's F-12 (*Sigma*) supplemented with 2 mM GlutaMAX-I (*Life Technologies*), 100 U/ml penicillin (*Sigma*), 100 mg/ml streptomycin (*Sigma*) 1% N2 and 20 ng/ml each of mouse recombinant FGF-2 and EGF (*Peprotech*). N2 supplement was produced in house as described, with the exception that Insulin was of human origin (*Sigma* I9278) instead of bovine. Stem cells were seeded on ibidi 8-well μ -slides.

***In vitro* Cargo Release.** Cells were incubated 7 – 24 h prior to the measurements at 37 °C under a 5% CO₂ humidified atmosphere. Shortly before imaging, the medium was replaced by CO₂-independent medium (Invitrogen). During the measurements all cells were kept on a heated microscope stage at 37 °C. The subsequent imaging was performed as described in the spinning disk confocal microscopy section.

Endosomal compartment staining. To stain the early/late endosome or the lysosome with GFP, commercially available CellLight© staining from lifeTechnologies was used . The cells were simultaneously incubated with MSNs and the BacMam 2.0 reagent. The concentration of the labeling reagent was chosen with 25 particles per cell (PCP) of the BacMam 2.0 reagent (cf. staining protocol ³³). For incubation, the cells stayed at 37 °C under 5% CO₂ humidified atmosphere for 21 – 24 h till the measurement.

5. Genetically designed biomolecular capping system for mesoporous silica nanoparticles enables receptor-mediated cell uptake and controlled drug release

Caspase-3/7 staining. For apoptosis detection commercially available CellEvent™ Caspase-3/7 Green Detection Reagent was used. A final concentration of 2.5 μM Caspase-3/7 reagent and 0.5 $\mu\text{g/mL}$ Hoechst 33342 were added to the cells for 30 min and imaging was performed without further washing steps.

Uptake studies. The functionality of the folic acid targeting ligand was evaluated in a receptor competition experiment. For this purpose, one part of the KB cells was pre-incubated with 3 mM folic acid, to block the receptors, for 2 h at 37 °C under a 5% CO_2 humidified atmosphere. Then the KB cells were incubated with particles for 2/5/8 h at 37 °C under a 5% CO_2 humidified atmosphere. For staining the cell membrane, the cells were incubated with a final concentration of 10 $\mu\text{g/mL}$ wheat germ agglutinin Alexa Fluor 488 conjugate for one minute. The cells were washed once with CO_2 -independent medium and imaged. For stem cell uptake studies cells were seeded the day prior to incubation. They were incubated for 2 h with free anandamide-tetrazine at a final concentration of 10 $\mu\text{g/mL}$. After 2 h 15 μg of particles were added and incubated for another 2 h. Then, the cells were washed 3x with medium containing growth factors and if preincubated free anandamide-tetrazine and incubated until imaging. Immediately before imaging, cells membranes were stained using cell mask deep red (lifetechnologies) and washed with medium.

Spinning disc confocal microscopy. Confocal microscopy for live-cell imaging was performed on a setup based on the Zeiss Cell Observer SD utilizing a Yokogawa spinning disk unit CSU-X1. The system was equipped with a 1.40 NA 100x Plan apochromat oil immersion objective or a 0.45 NA 10x air objective from Zeiss. For all experiments the exposure time was 0.1 s and z-stacks were recorded. DAPI and Hoechst 33342 were imaged with approximately 0,16 W/mm^2 of 405 nm, GFP was and the caspase-3/7 reagent were imaged with approximately 0.48 W/mm^2 of 488 nm excitation light. Atto 633 was excited

with 11 mW/mm^2 of 639 nm. In the excitation path a quad-edge dichroic beamsplitter (FF410/504/582/669-Di01-25x36, Semrock) was used. For two color detection of GFP/caspase-3/7 reagent or DAPI/Hoechst 33342 and Atto 633, a dichroic mirror (560 nm, Semrock) and band-pass filters 525/50 and 690/60 (both Semrock) were used in the detection path. Separate images for each fluorescence channel were acquired using two separate electron multiplier charge coupled device (EMCCD) cameras (Photometrics Evolve™).

5.5 References

1. Z. X. Li, J. C. Barnes, A. Bosoy, J. F. Stoddart and J. I. Zink, *Chem. Soc. Rev.*, 2012, **41**, 2590-2605.
2. J. L. Vivero-Escoto, I. I. Slowing, B. G. Trewyn and V. S. Y. Lin, *Small*, 2010, **6**, 1952-1967.
3. J. M. Rosenholm, V. Mamaeva, C. Sahlgren and M. Linden, *Nanomedicine*, 2012, **7**, 111-120.
4. C. Argyo, V. Weiss, C. Bräuchle and T. Bein, *Chemistry of Materials*, 2014, **26**, 435-451.
5. A. Ott, X. Yu, R. Hartmann, J. Rejman, A. Schutz, M. Ochs, W. J. Parak and S. Carregal-Romero, *Chemistry of Materials*, 2015, **27**, 1929-1942.
6. S. A. Mackowiak, A. Schmidt, V. Weiss, C. Argyo, C. von Schirnding, T. Bein and C. Bräuchle, *Nano Lett.*, 2013, **13**, 2576-2583.
7. A. Schlossbauer, S. Warncke, P. M. E. Gramlich, J. Kecht, A. Manetto, T. Carell and T. Bein, *Angew. Chem. Int. Ed.*, 2010, **49**, 4734-4737.
8. E. Aznar, L. Mondragon, J. V. Ros-Lis, F. Sancenon, M. Dolores Marcos, R. Martinez-Manez, J. Soto, E. Perez-Paya and P. Amoros, *Angew. Chem. Int. Ed.*, 2011, **50**, 11172-11175.
9. C.-Y. Lai, B. G. Trewyn, D. M. Jefthinija, K. Jefthinija, S. Xu, S. Jefthinija and V. S. Y. Lin, *J. Am. Chem. Soc.*, 2003, **125**, 4451-4459.
10. S. Giri, B. G. Trewyn, M. P. Stellmaker and V. S. Y. Lin, *Angew. Chem. Int. Ed.*, 2005, **44**, 5038-5044.
11. Z. Luo, K. Cai, Y. Hu, L. Zhao, P. Liu, L. Duan and W. Yang, *Angew. Chem. Int. Ed.*, 2011, **50**, 640-643.
12. A. Schlossbauer, J. Kecht and T. Bein, *Angew. Chem. Int. Ed.*, 2009, **48**, 3092-3095.
13. W. Zhao, H. Zhang, Q. He, Y. Li, J. Gu, L. Li, H. Li and J. Shi, *Chem. Commun.*, 2011, **47**, 9459-9461.
14. R. Liu, X. Zhao, T. Wu and P. Feng, *J. Am. Chem. Soc.*, 2008, **130**, 14418-+.
15. C. Wang, Z. Li, D. Cao, Y.-L. Zhao, J. W. Gaines, O. A. Bozdemir, M. W. Ambrogio, M. Frascioni, Y. Y. Botros, J. I. Zink and J. F. Stoddart, *Angew. Chem. Int. Ed.*, 2012, **51**, 5460-5465.

16. Q. Gan, X. Lu, Y. Yuan, J. Qian, H. Zhou, X. Lu, J. Shi and C. Liu, *Biomaterials*, 2011, **32**, 1932-1942.
17. S. Carregal-Romero, M. Ochs, P. Rivera-Gil, C. Ganas, A. M. Pavlov, G. B. Sukhorukov and W. J. Parak, *Journal of Controlled Release*, 2012, **159**, 120-127.
18. T. H. Maren, *Physiological Reviews*, 1967, **47**, 595-781.
19. P. W. Taylor, R. W. King and A. S. V. Burgin, *Biochemistry*, 1970, **9**, 3894-&.
20. E. Kaya, M. Vrabel, C. Deiml, S. Prill, V. S. Fluxa and T. Carell, *Angew. Chem. Int. Ed.*, 2012, **51**, 4466-4469.
21. S. Schneider, M. J. Gattner, M. Vrabel, V. Flügel, V. López-Carrillo, S. Prill and T. Carell, *ChemBioChem*, 2013, **14**, 2114-2118.
22. L. Davis and J. W. Chin, *Nat. Rev. Mol. Cell Biol.*, 2012, **13**, 168-182.
23. J. Hemphill, E. K. Borchardt, K. Brown, A. Asokan and A. Deiters, *J. Am. Chem. Soc.*, 2015, **137**, 5642-5645.
24. K. Lang, L. Davis, J. Torres-Kolbus, C. J. Chou, A. Deiters and J. W. Chin, *Nat. Chem.*, 2012, **4**, 298-304.
25. T. Plass, S. Milles, C. Koehler, J. Szymanski, R. Müller, M. Wiessler, C. Schultz and E. A. Lemke, *Angew. Chem. Int. Ed.*, 2012, **51**, 4166-4170.
26. M. Vrabel, P. Kölle, K. M. Brunner, M. J. Gattner, V. López-Carrillo, R. de Vivie-Riedle and T. Carell, *Chem. - Eur. J.*, 2013, **19**, 13309-13312.
27. J. Willibald, J. Harder, K. Sparrer, K.-K. Conzelmann and T. Carell, *J. Am. Chem. Soc.*, 2012, **134**, 12330-12333.
28. J. M. Rosenholm, A. Meinander, E. Peuhu, R. Niemi, J. E. Eriksson, C. Sahlgren and M. Linden, *ACS Nano*, 2009, **3**, 197-206.
29. E. Kaya, M. Vrabel, C. Deiml, S. Prill, V. S. Fluxa and T. Carell, *Angew Chem Int Ed Engl*, 2012, **51**, 4466-4469.
30. M. J. Gattner, M. Ehrlich and M. Vrabel, *Chem Commun (Camb)*, 2014, **50**, 12568-12571.
31. S. K. Nair, T. L. Calderone, D. W. Christianson and C. A. Fierke, *J Biol Chem*, 1991, **266**, 17320-17325.

5. Genetically designed biomolecular capping system for mesoporous silica nanoparticles enables receptor-mediated cell uptake and controlled drug release

32. K. Brunner, J. Harder, T. Halbach, J. Willibald, F. Spada, F. Gnerlich, K. Sparrer, A. Beil, L. Möckl, C. Bräuchle, K.-K. Conzelmann and T. Carell, *Angewandte Chemie International Edition*, 2015, **54**, 1946-1949.
33. <http://tools.lifetechnologies.com/content/sfs/manuals/mp10582.pdf>.
34. V. Cauda, A. Schlossbauer, J. Kecht, A. Zürner and T. Bein, *J. Am. Chem. Soc.*, 2009, **131**, 11361-11370.
35. K. Lang and J. W. Chin, *Chem. Rev.*, 2014, **114**, 4764-4806.
36. C. C. Liu and P. G. Schultz, *Annu. Rev. Biochem.*, 2010, **79**, 413-444.
37. T. Fekner, X. Li, M. M. Lee and M. K. Chan, *Angew. Chem. Int. Ed.*, 2009, **48**, 1633-1635.
38. E. Kaya, K. Gutsmedl, M. Vrabel, M. Muller, P. Thumbs and T. Carell, *ChemBioChem*, 2009, **10**, 2858-2861.
39. K. Lang, L. Davis, S. Wallace, M. Mahesh, D. J. Cox, M. L. Blackman, J. M. Fox and J. W. Chin, *J. Am. Chem. Soc.*, 2012, **134**, 10317-10320.
40. T. Plass, S. Milles, C. Koehler, C. Schultz and E. A. Lemke, *Angew. Chem. Int. Ed.*, 2011, **50**, 3878-3881.
41. M. J. Gattner, M. Ehrlich and M. Vrabel, *Chem. Commun.*, 2014, **50**, 12568-12571.
42. M. L. Barcellona, G. Cardiel and E. Gratton, *Biochem. Biophys. Res. Commun.*, 1990, **170**, 270-280.
43. <http://tools.lifetechnologies.com/content/sfs/manuals/mp01306.pdf>.

5.6 Appendix

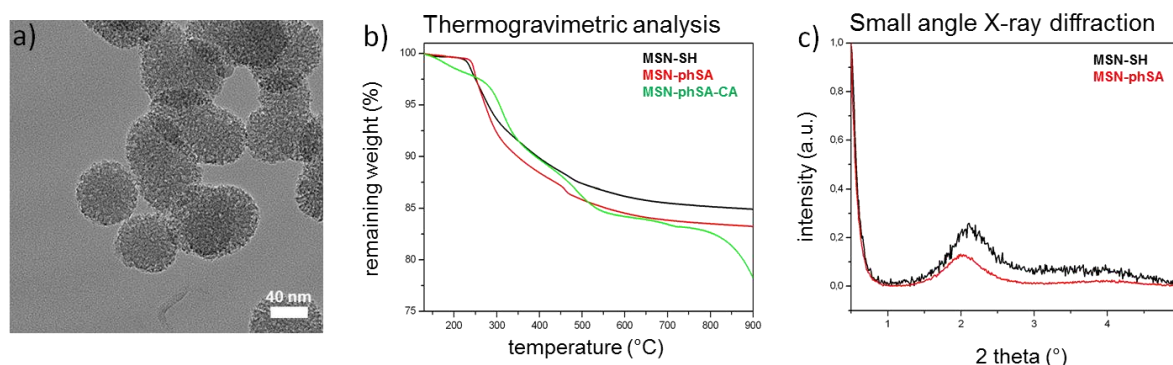


Figure S 5-1. a) Transmission electron micrograph of thiol-functionalized MSNs (MSN-SH). b) Small-angle X-ray diffraction pattern of MSN-SH (black) and MSN-phSA (red). c) Thermogravimetric analysis of MSN-SH (black), MSN-phSA (red), and MSN-phSA-CA (green).

TEM images of thiol-functionalized MSNs are depicted in Figure S 5-1 and display mostly spherically shaped particles with a radially disposed worm-like structure of the mesopores. The mesoporous structure is also confirmed by the first-order reflection of the mesoporous material observed with small-angle X-ray diffraction (XRD) (Figure S 5-1c). The amount of attached organic moieties on the MSNs was investigated by thermogravimetric analysis, showing an additional weight loss of about 14 % after attachment of CA (TGA, Figure S 5-1b). MSN-phSA particles show an additional weight loss of 3 % in the range between 130 and 900 °C due to the attachment of the benzene sulfonamide linker and enzyme-coated MSNs (MSN-phSA-CA) feature a relatively high additional weight loss compared to sample MSN-SH (+14 % at 900 °C). Apparently, degradation of the carbonized enzymes occurs only at very high temperatures, and is not even finished at 900 °C. This was already observed before for thermogravimetric analysis of enzyme-coated MSNs.

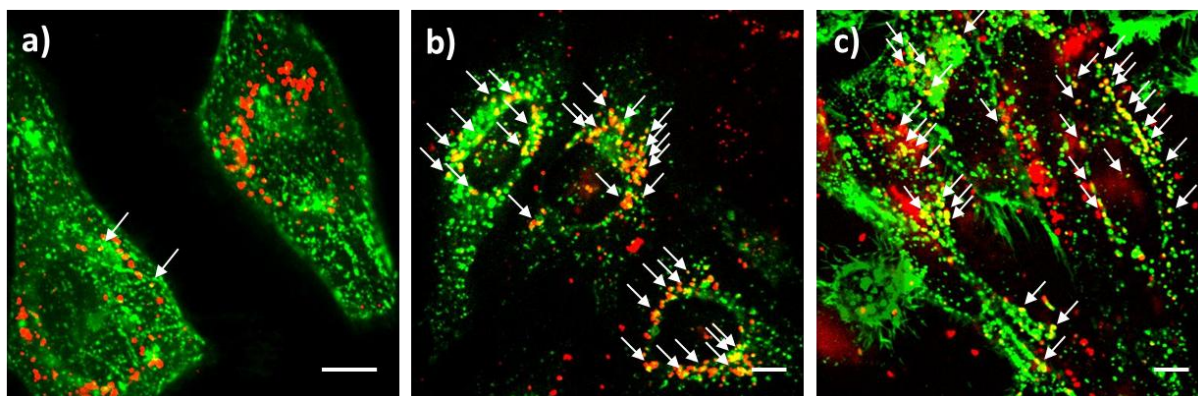


Figure S 5-2. Fluorescence microscopy of HeLa cells incubated with Atto 633-labeled MSN-phSA-CA (red) after a) 24 h on GFP-early endosome (green) tagged cells, b) 21 h incubation on GFP-late endosome (green) tagged cells, and c) 21 h on GFP-lysosome (green) tagged cells. Co-localization (yellow) could be primarily observed for late endosomes and lysosomes (indicated with arrows) suggesting that the multifunctional MSNs are located in acidic compartments after endocytosis. The scale bar represents 10 μm .

In order to verify the fate of our drug delivery vehicles ending up in acidic cell compartments, co-localization experiments with labeled MSNs and endosomes or lysosomes were performed. Simultaneous with particle incubation, the HeLa cells were transfected with a BacMam reagent in order to express different fusion-constructs of green fluorescent protein (GFP) and early/late endosome or lysosome markers, respectively. After 24 h of incubation with fluorescently labeled nanoparticles, almost no co-localization (yellow) between early endosomes and MSNs could be observed, as can be seen in Figure S 5-2a. In contrast, multiple yellow spots indicating co-localization between GFP (green) and MSNs (red) were clearly visible in the case of late endosomal and lysosomal staining after 21 h (Figure S 5-2b/c, denoted by arrows). This shows that the localization of our nanocarriers in an acidic compartment is crucial to initiate cargo release.

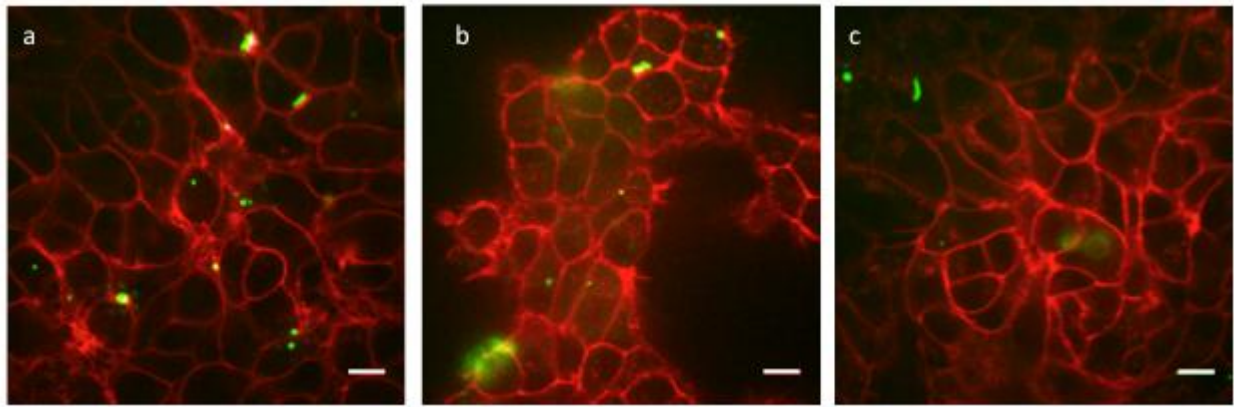


Figure S 5-3. Fluorescence microscopy of neural stem cells incubated with calcein-labeled MSN-phSA-CA (green) after 24h a) incubated with anandamide-targeted MSN-phSA-CA, b) pretreated with free anandamide-tetrazine and incubated with anandamide targeted MSN-phSA-CA afterwards c) incubated with control MSN-phSA-CA without anandamide. Cell membranes are stained with cell mask deep red. The scale bar represents 10 μm .

To test targeting of anandamide functionalized particles neural stem cells were treated with anandamide functionalized particles. As control, cells were pretreated with free anandamide-tetrazine and incubated with anandamide particles after 2 h of pretreatment. Another control was performed with control particles without anandamide functionalization. After two hours of particle incubation all cells were washed with medium. Already a few hours after incubation anandamide-particles were observed to stick to the cells in large amounts whereas particles without anandamide did not show this behavior. After 24h anandamide-targeted particles were successfully taken up into the cells. Cells that were incubated with control particles or preincubated with anandamide did not show as much particle uptake (Figure S 5-3).

5. Genetically designed biomolecular capping system for mesoporous silica nanoparticles enables receptor-mediated cell uptake and controlled drug release

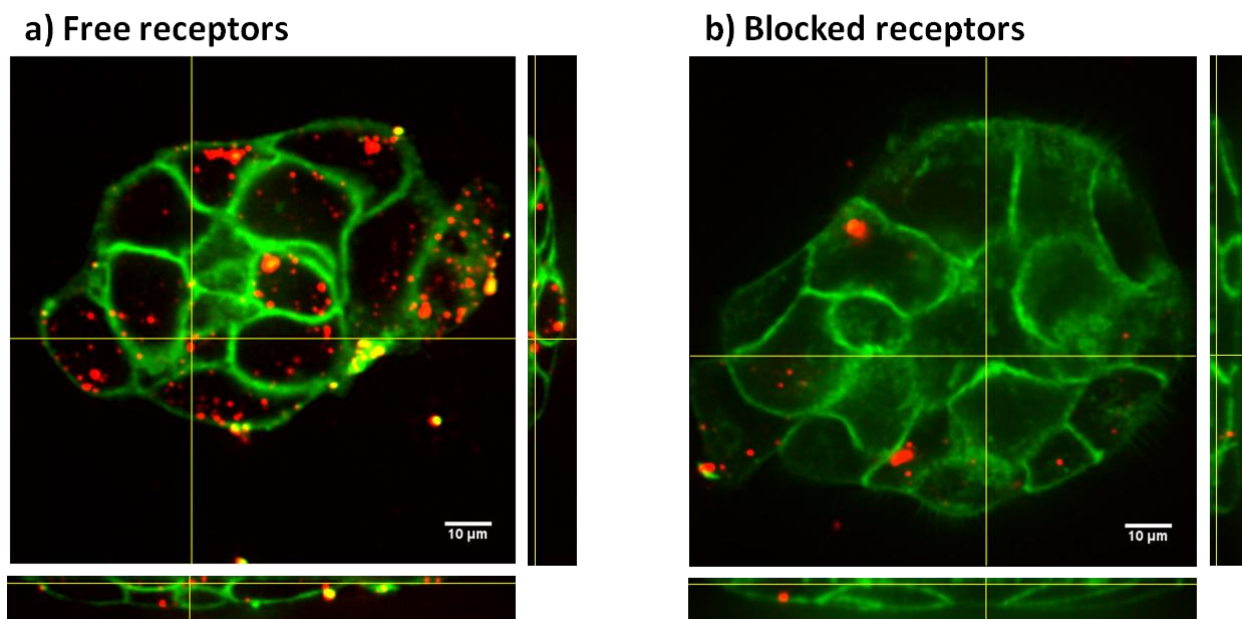


Figure S 5-4. Fluorescence microscopy of A431 cells incubated with Atto633-labeled MSN-phSA-CA (red) after 3h a) incubated with anandamide-targeted MSN-phSA-CA, b) pretreated with free inhibitors and incubated with anandamide targeted MSN-phSA-CA afterwards. Cell membranes are stained with CellMask orange (green).

To test the targeting of cannabinoid receptors with anandamide-functionalized particles on A431 cells, the receptors were either blocked or free corresponding to the folate-based experiments. The functionality was evaluated in a receptor competition experiment. For this purpose, one part of the A431 cells was pre-incubated with 10 μ L of an inhibitor mixture (1 mg/mL anandamide-tetrazine in DMSO, 1 mg/mL folic acid), to block the receptors, for 4 h at 37 °C under a 5% CO₂ humidified atmosphere. Then the A431 cells were incubated with 5 μ g MSN-phSA-CA-Anandamide particles for 3 h at 37 °C under a 5% CO₂ humidified atmosphere. For staining the cell membrane, the cells were incubated with CellMask orange (0.05%) for 1 min. The cells were washed three times with PBS, fresh medium was added and subsequently the cells were imaged. Clearly an enhanced receptor-mediated cell uptake can be seen when the cannabinoid receptors are available on the cell surface.

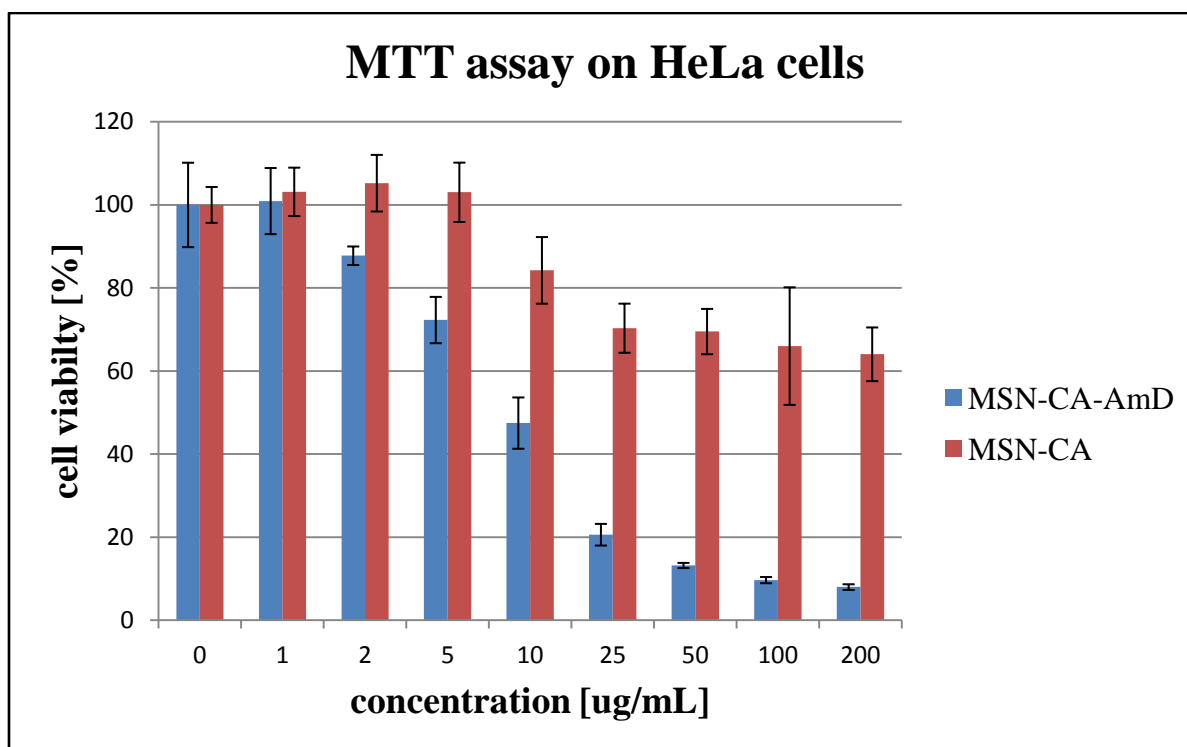


Figure S 5-5. MTT assay on HeLa cells with MSN-phSA-CA and MSN-phSA-CA+AmD (according to Figure 5). Incubation time was 24 h.

For MTT-Assays we seeded 5000 HeLa cells per well containing 100 μL of the respective medium and treated them with MSN-pHSA-CA and MSN-pHSA-CA+AmD 24h after seeding. After 24 h of incubation the cells were washed three times with PBS buffer. 100 μL of 3-(4,5-dimethylthiazol-2-yl)-2,5-diphenyltetrazolium bromide (MTT, 0.5 mg/mL in DMEM) was added to each well of the nanoparticle-treated cells and incubated for further 2 h. Unreacted MTT and medium were removed and the 96-well plates were stored at $-80\text{ }^{\circ}\text{C}$ for at least 1 h. Then, 100 μL DMSO was added to each well. The absorbance was read out by a Tecan plate reader. All studies were performed in triplicates.

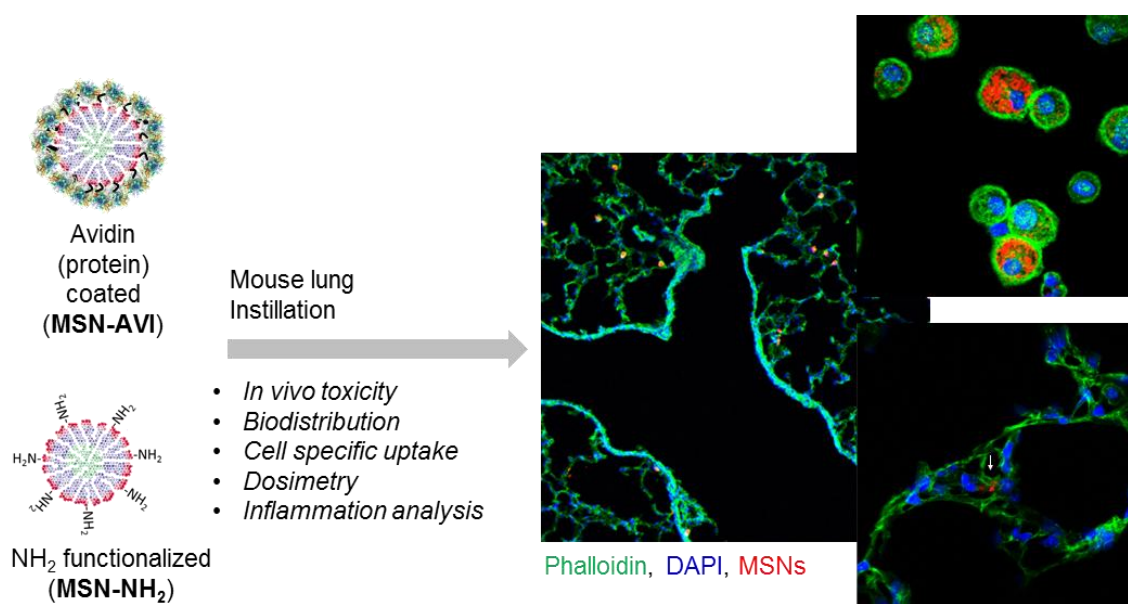
6 Applicability of avidin protein coated mesoporous silica nanoparticles as drug carriers in the lung

This chapter is based on the following publication:

Sabine van Rijt, Deniz Bölükbas, Christian Argyo, Karina Wipplinger, Mariam Naureen, Stefan Datz, Oliver Eickelberg, Silke Meiners, Thomas Bein, Otmar Schmid, Tobias Stöger, *Nanoscale*, **2016**, 8, 8058 – 8069.

Abstract

Mesoporous silica nanoparticles (MSNs) exhibit unique drug delivery properties and are thus considered as promising candidates for next generation nano-medicines. In particular, inhalation into the lungs represents a direct, non-invasive delivery route for treating lung disease. To assess MSN biocompatibility in the lung, we investigated the bioresponse of avidin-coated MSNs (MSN-AVI), as well as aminated (uncoated) MSNs, after direct application into the lungs of mice. We quantified MSN distribution, clearance rate, cell-specific uptake, and inflammatory responses to MSNs within one week after instillation. We show that amine-functionalized (MSN-NH₂) particles are not taken up by lung epithelial cells, but induced a prolonged inflammatory response in the lung and macrophage cell death. In contrast, MSN-AVI co-localized with alveolar epithelial type 1 and type 2 cells in the lung in the absence of sustained inflammatory responses or cell death, and showed preferential epithelial cell uptake in *in vitro* co-cultures. Further, MSN-AVI particles demonstrated uniform particle distribution in mouse lungs and slow clearance rates. Thus, we provide evidence that avidin functionalized MSN (MSN-AVI) have the potential to serve as versatile biocompatible drug carriers for lung-specific drug delivery.



The following experiments have been performed as a joint project: The nanoparticle synthesis, characterization and stabilization experiments were performed by Christian Argyo and Stefan Datz. The *in vitro* and *in vivo* studies were performed in the Comprehensive Penumology Center (CPC) in Munich. The study functions as the groundwork for the targeting experiments in the upcoming Chapter 7.

6.1 Introduction

In the past decades, the use of nanoparticles as inert carriers for therapeutic agents has revolutionized the field of drug delivery research. Several nanoscale drug delivery systems, especially non-functionalized particle formulations, have been approved by the FDA and European Medicines Agency for treatment of cancer.¹ Nanocarriers offer major improvements such as increased bio-availability of the incorporated agent, site specificity, and the ability to overcome multi-drug resistance.^{2, 3} Particularly, mesoporous silica nanoparticles (MSNs) are novel drug carriers with unique properties, such as high loading capacity with tunable pore

sizes and volumes for transport of a wide variety of cargo molecules.⁴ Importantly, these particles can be selectively functionalized at specific sites within their structure. For example, the particle core offers a site for covalent attachment of fluorescent dye molecules for particle tracking in biological studies.⁵ In addition, the surface of the MSNs can be selectively modified to introduce controlled drug release functions for optimized drug delivery.⁴ For example, in our recent work we developed mesoporous silica nanoparticles with protease-responsive avidin caps for controllable drug release in lung tumour areas.⁶ Due to the tight sealing of the mesopores by the avidin caps and the selective cleavage of these caps at high protease concentrations found in lung tumours, these drug carriers were able to efficiently release a combination of chemotherapeutic drugs *in vitro* and *ex vivo* (mouse and human) with high tumour-selectivity. Other interesting examples of functionalized MSNs that have shown *in vivo* effectiveness include MSNs functionalized with PEG chains,⁷ folic acid,⁸ or transferrin.⁹ Due to their unique properties, MSNs have been considered as promising candidates for next generation nano-medicines.¹⁰ However, before these carriers can be used in the clinic, their biocompatibility needs to be proven. Although MSNs are generally considered to be biocompatible, several reports suggest that their bioresponse is strongly affected by their size,¹¹ shape,¹² porosity,¹³ and surface chemistry.^{11, 14} In addition, the administration route has been found to play an important role for their biodistribution and bioresponse.¹⁵ Encouragingly, *in vivo* toxicity studies on different types of MSNs administered using several application routes, indicate that the use of these particles is safe for drug delivery purposes¹⁶⁻²⁰, however, not many of these studies deal with the applicability of MSNs directly in the lung.

Direct application of nanoparticles into the lung (i.e. inhalation therapy) would be beneficial for treatment of (chronic) lung diseases such as idiopathic pulmonary fibrosis (IPF), chronic

obstructive pulmonary disease (COPD) and asthma, as drugs are directly administered in the target organ. This is advantageous because high local doses at the site of disease (lung) can be accomplished allowing for high efficacy combined with low prevalence of side effects. Moreover, in contrast to oral administered delivery, inhaled drugs bypass the gastrointestinal tract and the liver, avoiding problems associated with drug degradation in these organs and/or stability in blood circulation. Moreover, pulmonary application of drugs presents a non-invasive route for systemic delivery of drugs, since the huge surface area of the alveolar lung epithelium (ca. 100 m²) presents an effective portal of entry into the blood stream. Many drug delivery materials such as polymers are commonly accepted as biocompatible for systemic applications, but some have shown to develop adverse cytotoxic and pro-inflammatory properties in the lungs and seem therefore not suited for direct application into the lung.²¹ Moreover, the inflammatory potential of nanoparticles is especially relevant for the treatment of inflammatory lung diseases such as COPD and asthma, as the additional inflammation caused by drug delivery particles could lead to worsening of the symptoms.

Here, we investigated the suitability of direct application of avidin-capped MSNs in the lung, namely their distribution, clearance rate, cell specific uptake, and the inflammatory response induced over the course of one-week time. For that purpose, single high doses (20 or 100 µg/mouse) of avidin-capped MSNs (MSN-AVI) were instilled in adult BALB/c mice, and their bioresponse after 1, 3, and 7 days was studied. To analyse the impact of the avidin protein coating, we also included non-protein coated MSNs containing propyl amines on the outer shell (MSN-NH₂) in the study. Labelling of the particle core with a fluorescent dye (ATTO 633) allowed for whole lung dosimetry as well as cell specific particle tracking in lung cryo-sections and cytopins of bronchoalveolar lavage fluid (BALF) recovered cells. Moreover, supporting studies using *in vitro* cell cultures were performed. This provided evidence that MSNs capped with avidin are significantly more biocompatible than amino

functionalized MSNs as proven by analyses of their inflammation and toxicity profiles, biodistribution, and cell specific internalization rates, and thus hold potential for use in future lung disease therapy.

6.2 Results and Discussion

Pulmonary inflammation analyses

In vivo inflammatory cell recruitment into the airspace was first assessed by BAL differential cell count. Total BAL cell numbers were not significantly different from sham control (PBS) at day 1, but increased at day 3 for 100 µg of MSN-AVI and at day 7 for 100 µg of MSN-NH₂ particles (Figure 6-1A). These changes are mainly related to the increases in macrophage numbers, which in general represent the majority of BAL leukocytes (Figure 6-1C). A particular severe inflammatory response was detected by the acute increase of polymorphonuclear neutrophils (PMNs): after 1 day of treatment with the high dose (100 µg) of MSN-NH₂ particles giving rise to 60% of total BAL cells (Figure 6-1B, Table 6-1). The same treatment with MSN-AVI particles also resulted in a distinct PMN influx into the airspace; however, comparatively less pronounced to what was observed for the MSN-NH₂ particles (33% of total BAL cells, Figure 6-1B). This almost 2 fold higher PMN influx into the alveolar airspace at day 1 after instillation for MSN-NH₂ compared to MSN-AVI particles indicates an improved biocompatibility of the MSN surface due to avidin capping. In addition, for both particle types, a time-dependent resolution of the neutrophilic inflammation was noted, but only for the MSN-AVI particles inflammation had completely resolved after 7 days (Figure 6-1B), further indicating improved biocompatibility for MSN-AVI.

In line with that, only MSN-NH₂ instillation resulted in macrophage accumulation in the airspace from day 3 to day 7 (Figure 6-1C, Table 6-1) as well as the formation of giant cells (multinucleated macrophages, Figure 6-1D, Table 6-1), both of which are signs for chronic inflammation and foreign body response.²⁷ Lymphocyte numbers remained below 2,000 (<0.5% of total BAL cells) for all conditions investigated (Figure S 6-3C).

6. Applicability of avidin protein coated mesoporous silica nanoparticles as drug carriers in the lung

		Instilled amount (µg)	PMN cell count x 10 ³ (%)	Macrophages cell count x 10 ³ (%)	Multinucleated macrophages cell count x 10 ³ (%)	Detected cytokines
1 d	HCC ^a	-	0.2 (0)	280 (100)	0.1 (0)	-
	PBS ^b	-	7.9 (1.6)	491 (98)	0.6 (0.1)	-
	MSN-AVI	20	9.2 (2)	444 (98)	0.1 (0)	-
	MSN-AVI	100	183 (33)	363 (66)	0.5 (0.1)	CXCL5, CXCL1
	MSN-NH ₂	100	326 (60)	131 (29)	0 (0)	CXCL5, CXCL1, CCL2, IL-1β, TNF-α
3 d	MSN-AVI	100	35 (5)	644 (95)	1.9 (0.3)	CXCL5, CXCL1
	MSN-NH ₂	100	65 (11)	511 (88)	3.4 (0.6)	CXCL5, CXCL1, TNF-α
7 d	MSN-AVI	100	2 (0.4)	581 (99)	0.9 (0.2)	CXCL5
	MSN-NH ₂	100	34 (4.3)	751 (95)	5.2 (0.7)	CXCL5

Table 6-1. Summary of the inflammatory effects of MSN-NH₂ and MSN-AVI in BAL at 1, 3 and 7 days after instillation. In addition, an overview of the collected cytokine parameters is given.

^a HCC= home cage control animals (non-treated mice)

^bPBS= 100 µL PBS instilled mice (vehicle/sham control)

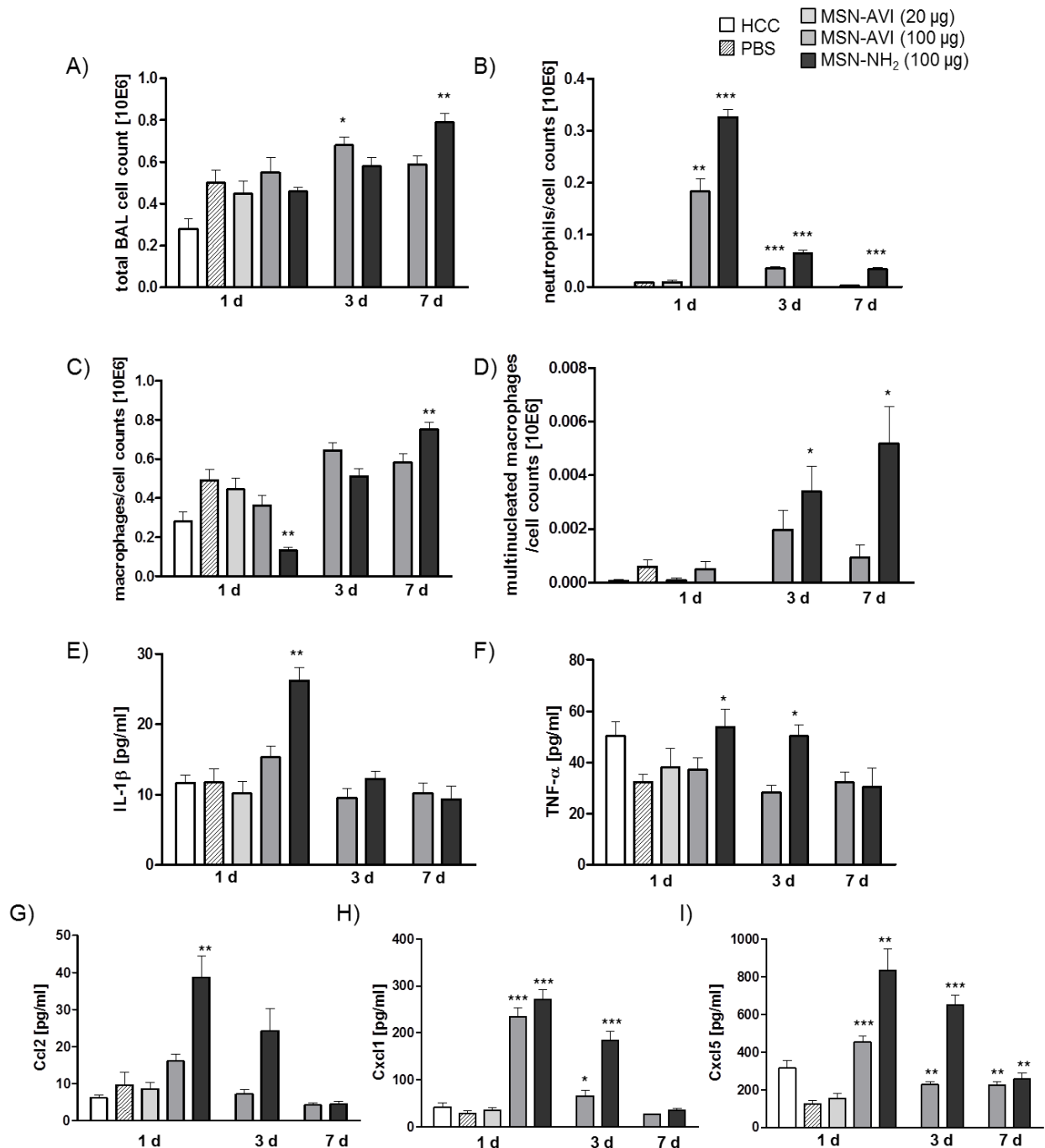


Figure 6-1. BAL cell analysis and cytokine release in BALF at three time points after MSN instillation into Balb/c mice. Bronchoalveolar lavage (BAL) cells were counted and dead cells were discriminated by Trypan blue staining; differentiation was analyzed by May-Grünwald staining. Total BAL cell count is shown in A, total neutrophil numbers in B, macrophage numbers in C, and multinucleated macrophages in D. Release of cytokines was measured in bronchoalveolar lavage fluid (BALF) for each animal in each group, interleukin-1 beta (IL-1β) is shown in E, TNF-α is shown in F, monocyte chemotactic protein 1 (CCL2) is shown in G, Cxcl1 is shown in H, and Cxcl5 is shown in I. Values are indicated as mean ± SD, n=6, asterisks represent significance compared to PBS control groups (100 µL PBS instilled animals) with *** p<0.001, ** p<0.01, * p<0.05. HCC = home cage control (non-treated animals).

Inflammation caused by MSN-NH₂ was further assessed on the molecular level by BALF cytokine profiling, assessing IL-1 β , and TNF- α as the major pro-inflammatory master cytokines, CCL2 as classical monocyte/macrophage and CXCL1 and CXCL5 as the most relevant neutrophil chemoattractants. Treatment with MSN-NH₂ caused the highest pro-inflammatory cytokine response; 1 day after treatment yielded high levels of all cytokines investigated (Figure 6-1 E-I). BALF levels of the two master cytokines for inflammation, IL-1 β and TNF α , were high during the acute phase after MSN-NH₂, but not after MSN-AVI treatment and returned to baseline levels by day 7 (Figure 6-1 E, F). Levels of chemokine CCL2, a monocyte attractant, correlated rather with PMN than macrophage numbers and were highest 1 day after MSN-NH₂ treatment (Figure 6-1G), where the lowest macrophage numbers were detected. This argues for significant macrophage cell death during the acute phase after MSN-NH₂ instillation, causing a depletion of the alveolar macrophage pool uncompensated by the high levels of the CCL2 monocyte/macrophage attractant. The concentrations of the functional murine IL-8 homologues, CXCL1 and -5 (Figure 6-1 H, I) correlated well with the number of BAL PMNs (Figure 6-1B) and showed accordingly higher levels for MSN-NH₂ than MSN-AVI treated lungs. Elevated levels of the epithelial derived CXCL5 at day 7 could be interpreted as a sign for prolonged epithelial pro-inflammatory response to MSN particles, however similar levels are observed for untreated controls at day 1, thus questioning a physiological relevance. No evidence for inflammation was detected at the lower dose of 20 μ g MSN-AVI per mouse, suggesting 1 mg/kg as a safe dose for pulmonary applications for this particle type.

The impact of the particle characteristics, agglomeration state, zeta-potential and specific surface area are of particular interest for the development of safe nanocarrier systems for pulmonary drug delivery. Recently, an indirect correlation between the agglomerate size of

instilled particles and the acute inflammatory response was described for different dispersions of nickel-oxide nanoparticles with size distributions ranging from 100 nm to 4 μm .²⁸ Based on their findings the authors argued that the reduced biologically accessible surface area of poorly dispersed suspensions might be limiting the bioactivity and toxicity of the instillation delivered nanoparticles. High zeta-potential of nanoparticle dispersions are generally appreciated for their enhanced stability, but have also been associated with increased toxicity and inflammation.^{29, 30} As opposed to this broad rule, we show an improved biocompatibility for MSN-AVI preparations characterized by low agglomerate size and even higher zeta-potential as compared to the MSN-NH₂ material. The particle surface of crystalline silica (i.e. quartz), is well known to induce lung inflammation (silicosis) upon inhalation. Toxicity has also been shown for some non-crystalline (amorphous) silica particles when applied directly in the lung, although highly dependent on size, surface and preparation route of the silica particles.³¹ The release of IL-1 β from pulmonary macrophages is described as a central mechanism triggering their toxicity in the lung.³² In agreement with the latter, the highest levels of IL-1 β release, and inflammatory cell accumulation were detected for MSN-NH₂ particles, where the silicate particle surface area is not coated and hidden by the basically charged glycoprotein, avidin. The observation of an increased inflammatory response for MSN-NH₂ compared to MSN-AVI particles suggests that the partially exposed silica surface of the MSN-NH₂ particles, but not the avidin protein covered surface, induces inflammation. The MSN-NH₂ particles have a large BET surface area of 1150 m²/g and a negative zeta potential of -30 mV, while MSN-AVI particles have a BET surface area of only 90 m²/g and a zeta potential of 30 mV (measured at pH = 7).⁶ This dramatic difference in accessible surface area and charge indicates that the avidin protein covers the surface of the MSN, thus significantly changing the surface characteristics of the particles. Further analysis of the MSN's incubated with isolated mouse lung alveolar lining fluid (BALF) revealed that MSN-

NH₂ particles form a significantly larger protein corona compared to MSN-AVI particles (Figure S 6-3D). This may be explained by the partially exposed silica surface of the MSN-NH₂ particles, compared to the already protein-coated MSN-AVI particles. This result highlights that MSN's coated with a protein corona do not behave similarly compared to MSN particles that have a protein coat that is covalently attached to the surface of the particle. Interestingly, when instilling 100 µL of MSN-NH₂ or non-functionalised MSNs (with hydroxyl groups on the surface; nonMSN) into mice, we observed that nonMSN cause significantly less acute inflammation (pulmonary PMNs influx) compared to MSN-NH₂ after 24 h (Table 6-1). Both particles have a large BET surface area arguing against surface area as major driver of toxicity in this case. It is possible that the amine groups are responsible for the increased inflammatory effect. Similarly, polystyrene particles with outer NH₂ groups have been reported to be more toxic than their hydroxyl counterparts.³⁶⁻³⁸ In addition to their differential functionalities, our observations may also be explained by the fact that MSN-NH₂ particles form larger agglomerates (about 1000 nm) compared to MSN-AVI and nonMSN particles (about 200 nm) after only a few hours in suspension (Figure S 6-3A). Large agglomerates (bigger than 400 nm) are more effectively phagocytized by macrophages than endocytosed by epithelial cells.³⁹ In addition, the formation of a larger protein corona on MSN-NH₂ particles compared to the MSN-AVI (Figure S 6-3) may also contribute to enhanced bio-activity and even to the observed increased macrophage particle uptake for the MSN-NH₂. Size-dependent nanoparticle uptake has been observed previously in lung macrophage and epithelial cells.⁴⁰ All in all, our data suggests that avidin protein modified MSNs are safe to use for lung application at 1mg/kg dose and induce a minor inflammatory response at 5mg/kg dose that completely resolved after 7 days.

Cytotoxicity analysis

The toxic effects of the two particle types in the mouse model were investigated with cytopins of bronchoalveolar lavage (BAL) cells and on lung cryo-sections (from non-lavaged mice) using immunofluorescence staining. For this approach, cells and tissues were stained with an apoptotic cell marker (cleaved caspase-3, green signal in Figure 6-2A). The MSNs, covalently labelled with ATTO 633 dye, could easily be recognised in both the cytopins and the cryo-sections (red signal in Figure 6-2A). Exposure to high doses of MSN-AVI particles did not cause any significant apoptotic toxicity in BAL cells, compared to the vehicle/sham control (PBS instilled mice) or the low dose of MSN-AVI (Figure 6-2A upper panel, controls are shown in Figure S 6-4). Significant apoptosis, however, could be observed for BAL cells exposed to MSN-NH₂ particles, which did not subside 7 days after exposure (Figure 6-2A lower panel). Neither particle type induced any distinguishable toxicity in lung cryo-sections of the lavaged lungs (Figure 6-2A, right panel). Furthermore, particle uptake and burden of the macrophages correlated with increased apoptosis marker staining (Figure 6-2B). Macrophage MSN particle internalization was confirmed with phalloidin staining in confocal microscopy, showing actin (green) encapsulated MSN agglomerates (Figure 6-2C). In addition, in *in vitro* exposure experiments of the three major cell types of the lung supported our *in vivo* observation; only for MSN-NH₂ showed significant cytotoxicity towards MH-S murine alveolar macrophage cells, whereas no effect was observed in murine lung epithelial (MLE-12) or fibroblast (CCL-206) cell lines at high doses for either material (Figure 6-2D). In line with that, also no structural changes of the alveolar microarchitecture could be observed in paraffin lung sections due to particle exposure (Figure S 6-4B).

6. Applicability of avidin protein coated mesoporous silica nanoparticles as drug carriers in the lung

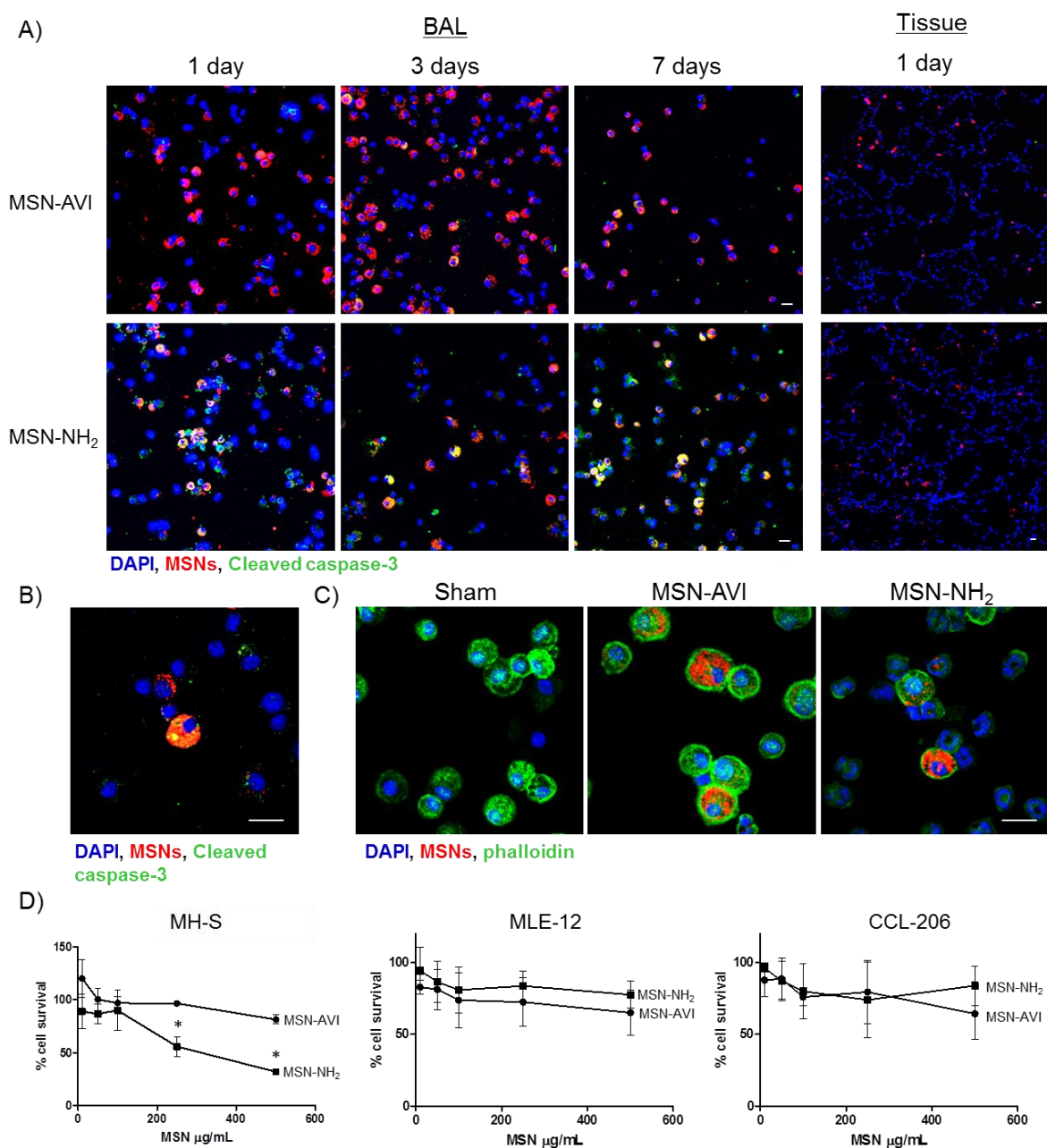


Figure 6-2. Cytotoxicity assessment of MSN-AVI and MSN-NH₂ particles. **A)** Toxicity of MSN-AVI or MSN-NH₂ particles in Balb/c mice after instillation with 100 μg for 1, 3, or 7 days, analyzed from cytopins of BAL cells (left) and lung cryo-slices (right). Cell nuclei are shown in blue (DAPI), ATTO 633 labelled MSNs are shown in red, and the apoptotic marker (cleaved caspase-3) is shown in green. **B)** Toxicity of MSN-NH₂ in Balb/c mice exposed to 100 μg for 7 days in cytopins of BAL recovered cells using a 63 x objective; high particle loading correlates with toxicity. The apoptotic marker (cleaved caspase-3) is shown in green. Yellow staining (in A and B) is due to overlap of MSNs (red) and apoptotic cells (green). **C)** MSN uptake in macrophages after 1 day exposure to, from left to right, 100 μL PBS, 100 μg MSN-AVI or MSN-NH₂ (cytoskeleton labelled with phalloidin, green), **D)** Cytotoxicity of MSN-AVI and MSN-NH₂ particles as determined by MTT assay in MH-S, MLE-12, and CCL-206 cells after 16 h of

exposure. Values are indicated as mean \pm SD, n=3, asterisks represent significance with * $p < 0.05$. Scale bar is 20 μm .

In accordance with our pulmonary inflammation analysis, the MSN-NH₂ particles appear to cause selective macrophage toxicity, but no toxicity in lung parenchyma or in epithelial and fibroblast cell lines. It seems therefore likely that a phagocytic uptake of the large MSN-NH₂ agglomerates is required to generate the cytotoxic response while non-professional phagocytes might be spared from the harmful effects of non-avidin coated MSNs. In summary, the nanoparticle coating appears to be crucial for their inflammatory and toxic response in the lung, where protein coating enhances biocompatibility.

Pulmonary dose and clearance of MSNs

The pulmonary dose of MSN-AVI particles at the three time points was determined by quantifying the fluorescent signal of the particles in three pulmonary compartments, namely homogenized lung tissue (after BAL), BAL fluid (BALF) and BAL cells. Using gravimetric analysis of the instillation wear prior and after instillation, we determined that $87.8 \pm 3.5 \mu\text{g}$ and $17.6 \pm 0.6 \mu\text{g}$ of the nominally applied 100 μg and 20 μg MSN dose was delivered to the lungs, respectively. It is important to note that while the absolute pulmonary dose (in μg) determines the toxicological (and pharmacological) response, the pulmonary clearance (removal) and biodistribution of particles is typically expressed in terms of relative dose, *i.e.* pulmonary dose normalized to applied dose (here: 87.8 or 17.6 μg). For the following, we refer to the pulmonary dose as the relative dose. As seen in Figure 6-3A, the pulmonary dose slowly decreased from 80.1% of the applied dose at day 1 to 55.5 % at day 7, indicating relatively slow clearance kinetics (for both 20 and 100 μg MSN doses), which can be attributed to macrophage clearance from the alveolar surface.³⁹ By fitting the measured total lung dose to an exponential function (relative dose = $0.851e^{-0.061t}$, where t represents time in

units of days), the alveolar clearance half time was determined as 8.7 days. During this period, the MSN dose decreased by 50% corresponding to an average clearance rate of 5.7 % per day. Consequently, we found a relatively high retention of MSN-AVI particles in pulmonary tissue at day 7 after instillation (56% of the applied dose). When extrapolating the exponential fit curve to $t = 0$ (time point of MSN application), one obtains a relative dose of 0.851, *i.e.* macrophage clearance can only account for 85.1% of the actually applied dose. The residual 14.9% can be attributed to a faster clearance mechanism known as mucociliary clearance from the bronchial region, which is typically completed within 1d after application.³⁹

The phagocytic clearance of MSNs was also studied on cytopins of BAL cells by counting the amount of MSN agglomerates larger than 1 μm (the smallest detectable cross sectional area) per nuclei on cytopins (*i.e.* the amount of $>1 \mu\text{m}$ MSN agglomerates over the total amount of counted nuclei per image). After 1 day, more agglomerates of MSN-AVI could be observed in the BAL compared to MSN-NH₂ (Figure 6-3C). The ratio of estimated MSN agglomerates per nuclei showed a transient increase at day 3 which declined again by day 7 after treatment (Figure 6-3D). The observed difference in clearance rate may be explained by the fact that at day 1 the number of macrophages in MSN-NH₂ treated lungs had declined to about one third of MSN-AVI treated mice due to the pronounced phagocyte toxicity of MSN-NH₂. However, the macrophage number recovered to similar levels of MSN-AVI treated mice at the later time points (Figure 6-1C).

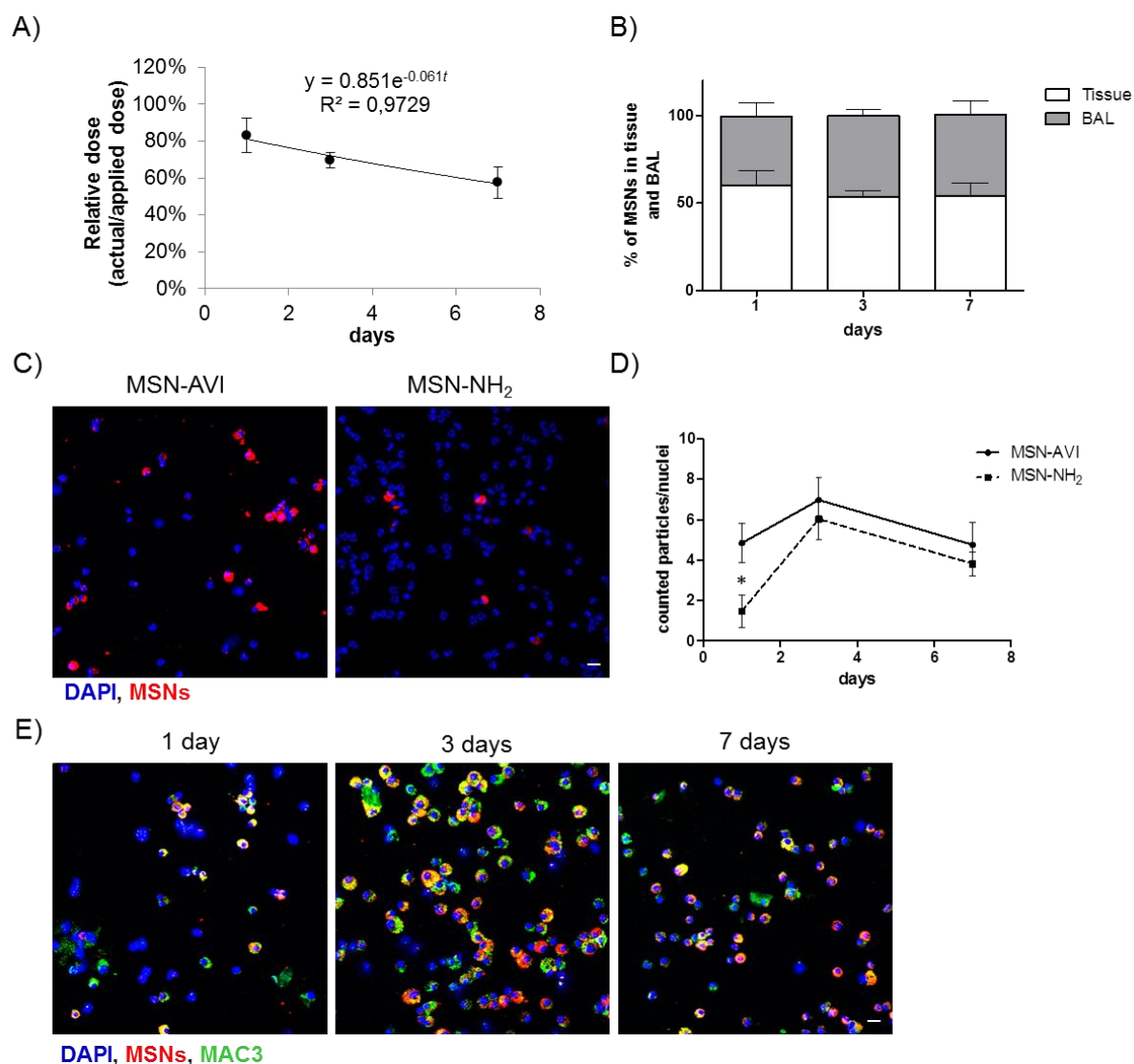


Figure 6-3. Pulmonary dose and clearance of MSNs in the lungs of Balb/c mice up to seven days after particle instillation. A) Temporal decrease of pulmonary dose (normalized to applied dose) and derived exponential clearance kinetics of MSN-AVI particles up to day 7 (n=3). B) MSN-AVI particle distribution in lung tissue and BAL over time (n=3). C) MSN-AVI and MSN-NH₂ particles (red) distribution in BAL cells (nuclei DAPI staining, blue) after 1 day. D) Quantification of particle clearance in BAL cells depicted as the number of MSN agglomerates (larger than 1 μ m) per counted nuclei (n=3 animals, 2 images per animal). E) MSN-AVI particles (red) in BAL recovered cells with macrophage marker co-staining (MAC3, green). Cell nuclei are shown in blue (DAPI), ATTO 633 labelled MSNs are shown in red. Scale bar is 20 μ m.

Particle uptake specifically by alveolar macrophages was confirmed, by counterstaining with a macrophage marker (MAC3, green channel). All detected MSN-AVI were found in macrophage marker positive cells with round nuclei, but not in

polymorphonuclear neutrophils, thus significant uptake by other BAL cells could be excluded (Figure 6-2E). The type A scavenger receptor MARCO (macrophage receptor with collagenous structure) has been described to function as an important receptor of alveolar macrophages mediating the interaction with unopsonized particles such as silica or bacteria.⁴¹ Since the expression of MARCO is restricted to subpopulations of tissue macrophages and particularly high in spleen marginal zone, resident peritoneal, and alveolar macrophages but is low in monocyte derived macrophages,⁴² the choice of cells studied is very important. Surface modification, such as by avidin might reduce the interaction of MSN particles with these scavenger receptors and thus effect a rapid phagocytosis and related clearance by alveolar macrophages. In summary, MSN-AVI particles showed the bimodal lung clearance kinetics (i.e. slow alveolar macrophage clearance, and fast mucociliary clearance from the bronchial region) which is typical for particle removal from the lungs.³⁹ The MSN-AVI had a slow clearance kinetics which is particularly promising for pulmonary therapy as it increases the residence time and hence the bioavailability of the encapsulated drugs.

Particle distribution in the lung

The distribution of MSNs in the lungs was assessed by preparing cryo-sections of (non-lavaged) lungs, which were analysed by immunofluorescence. ATTO 633 labelled MSNs could easily be detected by confocal microscopy on 14 μm thick lung cryo-sections (red channel, Figure 6-4A). The MSNs were distributed evenly over the tissue, also reaching the alveolar region of the lung. Furthermore, the nanoparticles showed widespread and significant accumulation in the lungs for at least 7 days, confirming our previous dosimetry findings (Figure 6-4A, Figure S 6-5).

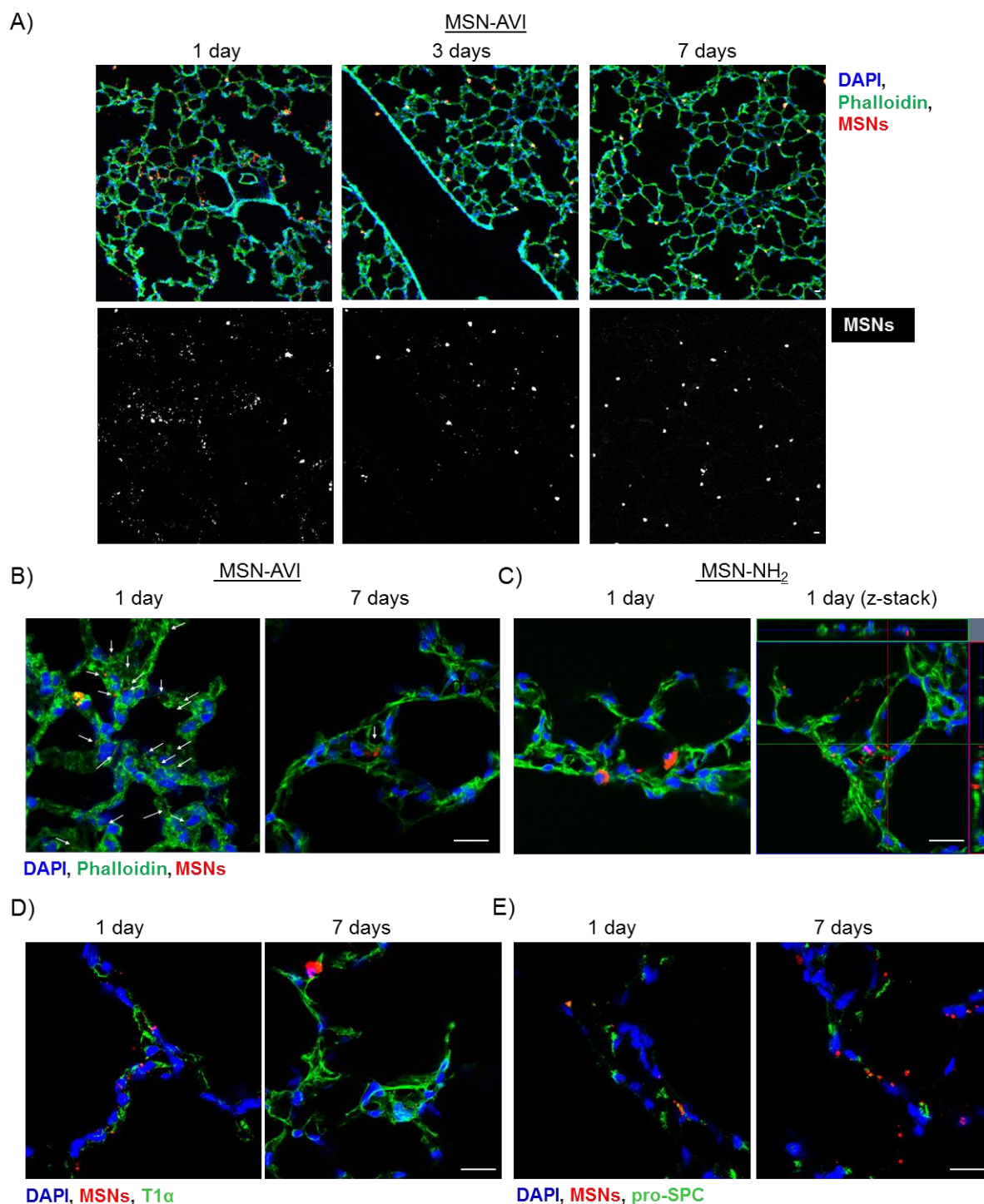


Figure 6-4. MSN distribution in mouse lungs up to 7 days after particle instillation. A) Lung cryo-slices of Balb/c mice exposed to 100 μ g MSN-AVI for 1, 3, or 7 days with phalloidin co-staining (upper panel) and the same images showing only MSNs (lower panel, MSNs are shown in white to increase the contrast). Lung cryo-slices of Balb/c mice exposed to B) 100 μ g MSN-AVI for 1 day (left) and 7 days (right)(arrowheads represent locations of MSN-AVI) and C) 100 μ g MSN-NH₂ for 1 day, D) 100 μ g MSN-AVI with epithelial cell type 1 co-staining (T1 α , green) for 1 day (left) and 7 days (right), and E) 100 μ g MSN-AVI with epithelial cell type 2 co-staining (pro-SPC, green) for 1 day (left) and 7 days (right). Cell

nuclei are shown in blue (DAPI), ATTO 633 labelled MSNs are shown in red. Images are representative images for n=4 animals. Scale bar is 20 μm .

After 1 day, many particle agglomerates could be observed, while after 3 and 7 days, fewer but bigger MSN-AVI agglomerates remained (Figure 6-4A lower panel). High magnification images indicated that a fraction of the MSN-AVI particles remained on the epithelium, evidence of which was still present after 7 days (Figure 6-4B, Figure S 6-5). In contrast, only limited evidence was obtained that MSN-NH₂ particles were taken up by epithelial cells. In fact, when investigating cryo-sections at higher magnifications, we mainly observed macrophage uptake of MSN-NH₂ particles (Figure 6-4C). Furthermore, z-stack images of non-phagocytized MSN-NH₂ particles revealed that these nanoparticles appear to associate with the tissue rather than being internalized into the cells (Figure 6-4C, right panel). Counterstaining the cryo-sections with epithelial type I and II cell markers, podoplanin (T1 α) and pro-surfactant associated protein C (Pro-SPC), respectively, revealed that MSN-AVI particles are internalized by epithelial lung cells (Figure 6-4D, E and Figure S 6-4) as confirmed by confocal z-stack imaging (Figure 6-5A). To investigate the cell specific uptake further, we prepared co-cultures of a murine alveolar macrophage cell line (MH-S) and an alveolar epithelial cell line (MLE-12) to study the fate of the particles in an *in vitro* model. Clearly distinguishable cell populations could be observed by fluorescence-activated cell sorting (FACS) analysis excluding leakage of the dye to the other cell type at the studied time-points (Figure S 6-7). Co-cultures indeed showed enhanced MSN-AVI particle uptake in epithelial cells compared to macrophage cell uptake (Figure 6-5B, left panel). In contrast, MSN-NH₂ particles showed almost exclusively uptake in macrophages in the same co-culture set-up (Figure 6-5B, right panel).

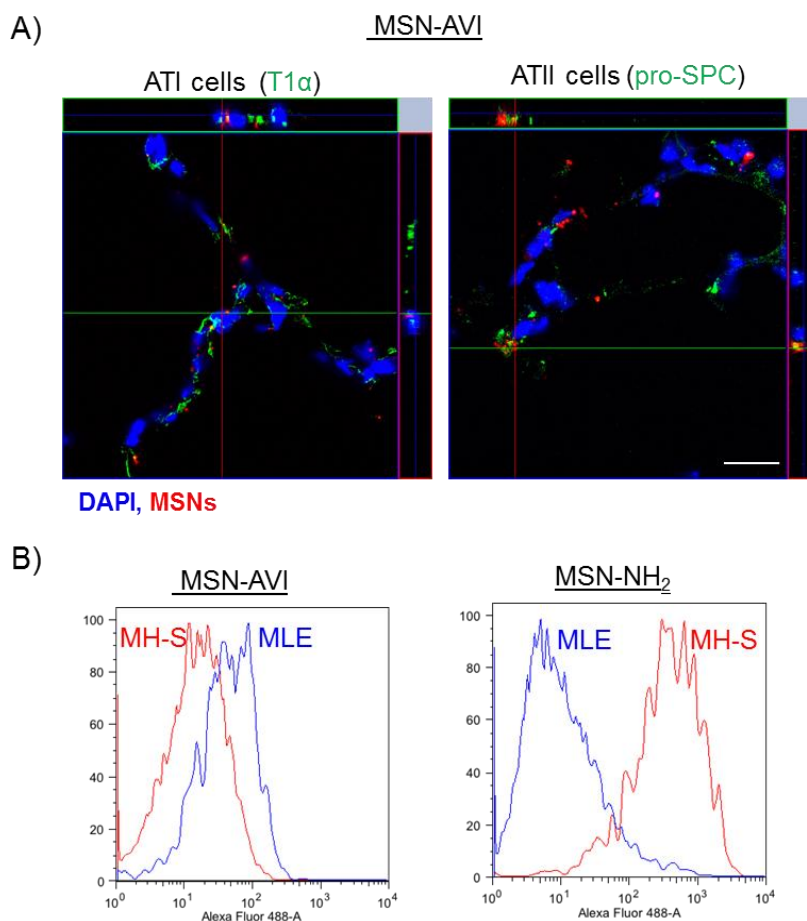


Figure 6-5. Cellular uptake comparison of MSN-AVI and MSN-NH₂. A) Z-stack images (63x objective) of cryo-slices of Balb/c mice exposed to MSN-AVI for 1 day after instillation, co-stained with alveolar epithelial cell type 1 (ATI) marker (T1 α , left image) and alveolar epithelial cell type 2 (ATII) marker (pro-SPC, right image) in green. DAPI staining in blue, scale bar is 20 μ m. B) Representative (of n=3) FACS histograms of co-cultures of MH-S and MLE-12 cells, showing differential cell uptake of MSN-AVI and MSN-NH₂ particles. MSN particles (labelled with Alexafluor 488) uptake could be quantified by gating MLE-12 DiD labelled cell population (630 nm) and non-labelled MH-S cell population.

In summary, cell type specific immunostainings revealed that MSN-NH₂ particles are preferentially internalized by macrophages *in vivo* and *in vitro* and that this leads to macrophage cytotoxicity. In contrast, MSN-AVI particles were - in addition to being phagocytically cleared by macrophages - also efficiently internalized by alveolar epithelial type 1 and type 2 cells, as investigated in lung tissue cryo-sections. Moreover, MSN-AVI also showed higher uptake in epithelial cells compared to macrophage cell uptake in an *in vitro* co-

culture model. Previous studies have shown that cellular uptake of MSNs is highly dependent on surface charge, surface modifications, and is cell type-specific.^{43,44} Furthermore, several *in vitro* studies have shown that the cell uptake of MSNs is cell-type-, dosage- and time-dependent.^{45, 46} Interestingly, it has been reported that amination of MSN particles prevents particle endocytosis in T-lymphocyte cells (Jurkat) and in a human neuroblast cell line.^{44,39} These findings highlight the importance of outer surface modifications and their interactions with different cell types, but also that avidin coating may be a good strategy to overcome issues related to macrophage uptake and particle toxicity.

6.3 Conclusion

In this study, we investigated the relevance of avidin-capped MSNs (MSN-AVI) for pulmonary therapy by looking at their pulmonary distribution, clearance rate, cell specific uptake, and induction of inflammatory response after direct (intratracheal) instillation in the lungs of mice. In a recent publication we showed that these particles are promising carriers for lung cancer therapy as they could release a combination of drugs efficiently and tumor-selectively in *in vitro* and in human and mouse *ex vivo* lung tissue.⁶ Since MSNs allow for multiple functionalizations, which have been found to be important for their bioresponse, we also included non-capped (only amino-functionalized; MSN-NH₂) particles in this study. We show that MSN avidin surface modification had an effect not only on toxicity, but also on cell specific uptake and tissue distribution in the lungs. In particular, non-capped (MSN-NH₂) particles were found to be cytotoxic to macrophages, caused an enhanced inflammatory response, and were hardly taken up by epithelial cells. In contrast, MSN-AVI particles co-localized with alveolar epithelial type 1 and type 2 cells in the lung tissue and showed preferential epithelial cell uptake in *in vitro* co-cultures. These findings, in combination with

the low surface specific toxicity, wide distribution of the particles in the mouse lungs and slow clearance rate is promising for the treatment of chronic lung diseases such as COPD, IPF, and lung cancer, where (alveolar) epithelial cells play an important role in the pathogenesis. Moreover, the inflammatory potential of drug delivery particles is most critical in inflammatory lung diseases such as asthma and COPD, due to additive effects leading to worsening of the symptoms. In this context, the observation that the dose of 1 mg/kg of MSN-AVI did not cause any detectable inflammatory response is particularly promising for treatment of these devastating lung diseases. Thus, we believe that avidin-coated MSNs offer potential for inhalative application as therapeutic drug carriers in chronic lung diseases. In addition, the finding that surface modifications greatly affect toxicity and cell type specific uptake highlights the importance of these types of studies for future development of nanomedicines.

6.4 Experimental Part

Materials. Core-shell functionalized MSNs containing thiol groups in the core and propyl amines on the shell (MSN-SH_{in}NH_{2,out}), avidin coated MSNs (MSN-AVI) and outer shell non-functionalised MSN particles (nonMSN) were synthesized as previously reported.^{5, 6} Characterisation of the MSN-SH_{in}NH_{2,out} and MSN-AVI can be found in the SI. Details on the synthesis and characterization of non-functionalised MSNs can be found in the SI. The MSNs suspended in bi-distilled water feature BET surface areas of 1150 m²/g (MSN-NH₂) and 90 m²/g (MSN-AVI), zeta-potentials of -30 mV (MSN-NH₂) and +30 mV (MSN-AVI) at pH 7.4, and diameter of 106±9 nm (MSN-NH₂) and 164±15 nm (MSN-AVI). The cores of the MSNs were covalently labelled with ATTO 633 dye and the outer surface contained either NH₂ groups (MSN-NH₂) or avidin protein (MSN-AVI) covalently attached to the MSNs through a peptide linker. Further details on the synthesis and characterization of the MSNs can be found in the supplementary details.

Cleaved caspase-3 antibody (Asp175) (Cell signaling, 9661), T1α antibody (R&D, AF3244), Pro-SPC antibody (Millipore, AB3786), MAC3 antibody (BD biosciences, BD 550292), were used as received. Bi-distilled water was obtained from a Millipore system (Milli-Q Academic A10). The mouse cell lines, MH-S (murine alveolar macrophages), MLE-12 (murine lung epithelial cells), and CCL-206 (murine lung fibroblasts) were obtained from ATCC (American Type Culture Collection, Manassas, USA). The MLE-12 cell line was maintained in RPMI 1640 medium (Gibco, Life Technologies); the MH-S cell line was maintained in RPMI 1640 medium supplemented with 1 mM Na-pyruvate, 10 mM HEPES, and 50 μM 2-ME (all AppliChem). The CCL-206 cell line was maintained in DMEM-F12 medium (Gibco, Life Technologies). All media were supplemented with 10% FBS (Biochrom) and 1%

penicillin/streptomycin (Life Technologies). All cells were grown at 37 °C in a sterile humidified atmosphere containing 5% CO₂.

Study design. The nanoparticles were instilled into Balb/c mice (20 or 100 µg) and after 1, 3, or 7 days the lungs were excised (n=10 per group). Characterisation of the MSN dispersion over time was performed to assess the agglomeration of the nanoparticles in cell culture medium (RPMI supplemented with FCS). MSN-NH₂ particles of 100 nm primary size agglomerated after 1 hour to form microparticles of about 1 µm, while MSN-AVI particles agglomerated to a much lesser extent (Figure S3A). It is important to note that the particles were instilled into the mouse lungs as a homogeneous mixture by vortexing before application (*i.e.* minimal agglomeration had taken place). Four lungs were directly prepared for cryo-slicing. An additional six mice were used for bronchoalveolar lavage (BAL); BAL fluid (BALF) was collected and separated into cells and supernatant by centrifugation. In addition, BAL recovered cells on cytopins were prepared for all mice for differential cell count. Furthermore, the lavaged lungs and the BAL were used for dosimetry analyses (see Figure S3B for a scheme of the experimental set-up).

MTT assay. The MTT assay was performed to assess cell viability after exposure to the MSNs *in vitro*. Briefly, 14 x 10³ MLE-12 cells/well and 7 x 10³ MH-S or CCL-206 cells/well were seeded in 96-well plates. 24 h after seeding, cells were exposed to 10, 50, 100, 250, or 500 µg/mL of MSN-NH₂ or MSN-AVI particles for 16 h. After treatment, 10 µL of freshly prepared solution of 5 mg thiazolyl blue tetrazolium bromide/mL PBS (Sigma) was added to each well, and the cells were incubated at 37 °C for 1 h. The supernatant was then aspirated, and the violet crystals were dissolved in 500 µL isopropanol + 0.1% Triton X-100 (both AppliChem). Absorbance was measured at 570 nm, using a Tristar LB 941 plate-reader (Berthold Technologies). Experiments were done in triplicate. Data analyses were performed in Prism GraphPad (version 5.0) software. All values are shown as mean with standard

deviation. For comparison of two groups, a one-way ANOVA was performed. A p-value lower than 0.05 was considered statistically significant.

Co-culture experiments. MLE-12 cells were labelled with VybrantDiD (Thermo Fisher Scientific, Germany) before they were seeded, according to the procedure described by Burguera *et al.*²² Briefly, MLE-12 cells were incubated for 20 min with 5 $\mu\text{L}/\text{mL}$ of VybrantDiD. The labelled cells were washed three times with their respective medium and 4 $\times 10^5$ cells/well were seeded in 6-well plates and incubated for 12 h. After incubation, 2 $\times 10^5$ MH-S cells/well were seeded in the same 6-well plates and incubated for 4 h. 50 $\mu\text{g}/\text{mL}$ MSN-AVI or MSN-NH₂ was added to the wells and the plate was incubated for 16 h. The cells were then trypsinised, washed three times with PBS, and finally suspended in 700 μL of PBS. Samples were then analysed by flow cytometry (BD LSRII). MSN uptake in the different cell types was quantified by gating the labelled MLE-12 cells and non-labelled MH-S cells using the APC-A channel (Figure S5), and analysing the particle signal (FITC channel) in each gated cell population.

Animal experiments. Animal experiments were carried out according to the German law of protection of animal life and were approved by an external review committee for laboratory animal care. 8-12 week-old female BALB/cAnNCrl mice (Charles River Laboratories, Sulzfeld, Germany) were intratracheally instilled, as described by Stoeger *et al.*²³ 1, 3, or 7 d post-instillation mice were sacrificed with an overdose of ketamine (188.3 mg/kg body weight) and xylazin hydrochloride solution (4.1 mg/kg body weight) (bela-pharm, Germany) and their blood was retro-orbitally collected for further investigation. The lungs of 6 mice were lavaged with PBS buffer (37 °C), as previously described.²⁴ Cyto-centrifuged slides of spun down lavaged cells were prepared for cell differentiation, after staining with *May-Grünwald* dye. For each mouse two slides were used for cell differentiation counting (200 cells/slide). Two additional sets of BAL cell cytopspins were frozen at -80°C for subsequent

confocal microscopy analyses. Lavaged lungs were then isolated and frozen for whole lung fluorescence analysis as described below. Four non-lavaged mice lungs from each group were excised and prepared for cryo-slicing and immunofluorescent staining.

Cytokine release. In this study, secretions of five cyto-/chemokines (IL-1 β , TNF- α , CXCL1, CXCL5, and CCL2) were investigated by ELISA analyses performed with the BAL (DuoSet ELISA, R&D Systems, Inc., Minneapolis, USA). The assay was performed as previously described.²⁵

Histological preparations. After treatments, four mice from each group were anaesthetised and sacrificed as aforementioned for histological analyses. Following intubation and diaphragm dissection, lungs were perfused via the right ventricle with sodium chloride solution (Braun Vet Care, Germany). Airways were filled with Neg-50TM frozen section medium (Fisher Scientific) at room temperature. Later, the tracheae were knotted, the lungs were excised and transferred into cryomolds (Thermo Scientific) loaded with Neg-50TM. Samples were left to freeze on dry ice and then stored at -80 °C. 14 μ m thick cryo-sections were sliced with the cryostat (Carl Zeiss Hyrax C 50) and placed on superfrost ultra plus adhesion slides (Thermo Scientific). Immunofluorescence stainings were performed as described below. For hematoxylin and eosin staining, the lungs were placed in 4% (w/v) paraformaldehyde and processed for paraffin embedding. The deparaffinised 3 μ m thick sections were stained with hematoxylin and eosin (both Carl Roth, Germany) subsequently, and dehydrated respectively in consecutively grading ethanol and xylene solutions (both AppliChem, Germany). Dried slides were mounted in entellan (Merck, Germany).

Immunofluorescence analyses. Lung cryo-sections or cytopins of BAL recovered cells were fixed with methanol 70 vol% solution for 10 min, washed with PBS, blocked with Roti®-ImmunoBlock (Carl Roth, Germany) for 1 h at room temperature, and incubated with primary antibody at 4 °C overnight. Afterwards, lung cryo-sections were washed with PBS,

incubated with Alexafluor 488 secondary antibody for 2 h at room temperature, again washed with PBS and finally stained with DAPI (Sigma-Aldrich). In case phalloidin staining (Life Technologies) was used, lung cryo-sections were incubated with a mixture of phalloidin and DAPI for 30 min at room temperature directly after the fixation and washing step. Stained lung cryo-sections were mounted using fluorescence mounting medium (DAKO, USA) and analysed using confocal microscopy (LSM710, Carl Zeiss, Germany).

Dosimetry. As the core of the MSNs was labelled with ATTO 633, both the BAL fluid and the lavaged lung tissue were analysed for MSN dosimetry based on quantitative fluorescence analysis at three time points (1d, 3d, 7d). While aliquots of the thawed supernatant of the centrifuged BAL could be sampled directly, an aliquot of the cell pellet of the BAL was resuspended in 200 μ L PBS, vortexed and further diluted with PBS to yield 1000 μ L of sample. The lavaged lung tissue was homogenized according to the following protocol. A defined volume of PBS (1200 μ L minus liquid content of the lung approximated by 1 mg of lung tissue corresponding to 1 μ L) was added to the tissue samples. The samples were mechanically homogenized with a high-performance disperser (T10 basic ULTRA-TURRAX®) at room temperature until no tissue pieces were visible anymore (ca. 3-5 min with short breaks to avoid undue heating of the samples). Residual tissue was rinsed off the disperser using 300 μ L of PBS. Samples were vortexed immediately prior to pipetting four 50 μ L aliquots (quadruple determination) from each of the samples in a black 96-well plate for quantitative fluorescence analysis with a standard multiwell plate reader (Tecan Safire 2; bandwidth of optical filters: 7 nm; excitation and emission wavelength: 630 nm and 650-670 nm (average of 650 nm, 660 nm and 670 nm), respectively). The fluorescence signals were related to the corresponding MSN mass using standard curves, which were prepared from the BAL and lung tissue of non-exposed mice according to the same protocol described above (cage control).

The dosimetric method presented here was validated using reference mice with a known pulmonary MSN dose as previously described.²⁶ In brief, these reference mice received 100 μ L of the MSN-AVI suspension via intratracheal instillation and were sacrificed immediately after the procedure to avoid dose bias due to partial clearance of the applied MSN-AVI particles from the lung. The actually instilled volume of the MSN-AVI suspension was determined for each mouse by gravimetric analysis of the instillation wear prior and after instillation.²⁶ The spectrophotometrically measured amount of MSN-AVI agreed with the applied amount of MSN-AVI within the expected experimental uncertainty of 15%. Finally, 7d-incubation of MSN-AVI particles in the supernatant of the BAL and subsequent centrifugation revealed that no detectable amount of the fluorescent tracer (ATTO 633) was leaking out of the MSN-AVI. This is a prerequisite for reliable pulmonary dosimetry based on fluorescence analysis.

Native gel (protein corona). To analyze the difference in protein corona formation with respect to the different functionalizations, we performed native PAGE after treating the MSNs with isolated mouse lungs alveolar lining fluid (BALF). 500 μ L of each MSN (-AVI or -NH₂ at a concentration of 1mg/mL) was centrifuged at 10,000 rpm and HBBS medium was removed, the pellet was resuspended in 500 μ L mouse BAL. 500 μ L of each MSN particle type in HBBS 1mg/mL was used as control. The samples were incubated at 37°C for 16 hours while gently shaking. After the incubation period, the samples were vortexed briefly followed by centrifugation at 18,000 rpm for 40 min at 15°C. The supernatant was removed and the remaining pellets were washed with PBS (centrifugation at 18,000 rpm for 40 min at 15°C after each wash). Finally, the pellet was dissolved in 50 μ L of PBS and run on a 10% native gel for 90 minutes at 100 V. The native gel was stained with page blueTM and the whole gel was imaged using a ChemiDoc imaging system (Bio-rad).

Statistics. All values are presented as mean \pm standard deviation (SD) of six animals per group (n=6), unless otherwise stated. Significant differences between two groups were evaluated by the unpaired two-tailed t-test with Welch's correction. Statistical analysis was performed using the program GraphPad Prism 5.0 (GraphPad Software, Inc., La Jolla, CA 92037, USA). Quantification of nanoparticles in cryo-sections or on BAL cytopins was conducted using the IMARISx64 software (version 7.6.4, Bitplane, Switzerland). A p-value lower than 0.05 was considered statistically significant.

6.5 References

1. C. M. Dawidczyk, C. Kim, J. H. Park, L. M. Russell, K. H. Lee, M. G. Pomper and P. C. Searson, *J control release*, 2014, **187**, 133-144.
2. C. A. Schutz, L. Juillerat-Jeanneret, H. Mueller, I. Lynch, M. Riediker and N. Consortium, *Nanomedicine*, 2013, **8**, 449-467.
3. S. H. van Rijt, T. Bein and S. Meiners, *Eur Respir J*, 2014, **44**, 765-774.
4. C. Argyo, V. Weiss, C. Bräuchle and T. Bein, *Chem. Mater.*, 2013, DOI: 10.1021/cm402592t.
5. V. Cauda, A. Schlossbauer, J. Kecht, A. Zurner and T. Bein, *J. Am. Chem. Soc.*, 2009, **131**, 11361-11370.
6. S. H. van Rijt, D. A. Bölükbas, C. Argyo, S. Datz, M. Lindner, O. Eickelberg, M. Koenigshoff, T. Bein and S. Meiners, *ACS Nano*, 2015.
7. H. K. Na, M. H. Kim, K. Park, S. R. Ryoo, K. E. Lee, H. Jeon, R. Ryoo, C. Hyeon and D. H. Min, *Small*, 2012, **8**, 1752-1761.
8. J. Lu, Z. Li, J. I. Zink and F. Tamanoi, *Nanomedicine: NBM*, 2012, **8**, 212-220.
9. H. Liu, T. Liu, X. Wu, L. Li, L. Tan, D. Chen and F. Tang, *Adv Mater*, 2012, **24**, 755-761.
10. Y. Chen, H. Chen and J. Shi, *Adv Mater*, 2013, **25**, 3144-3176.
11. Q. He, Z. Zhang, F. Gao, Y. Li and J. Shi, *Small*, 2011, **7**, 271-280.
12. X. Huang, L. Li, T. Liu, N. Hao, H. Liu, D. Chen and F. Tang, *ACS Nano*, 2011, **5**, 5390-5399.
13. Y. S. Lin and C. L. Haynes, *J. Am. Chem. Soc.*, 2010, **132**, 4834-4842.
14. Y. Zhao, X. Sun, G. Zhang, B. G. Trewyn, Slowing, II and V. S. Lin, *ACS Nano*, 2011, **5**, 1366-1375.
15. O. Taratula, O. B. Garbuzenko, A. M. Chen and T. Minko, *J Drug Target*, 2011, **19**, 900-914.
16. J. Lu, M. Liong, Z. Li, J. I. Zink and F. Tamanoi, *Small*, 2010, **6**, 1794-1805.
17. N. Kupferschmidt, X. Xia, R. H. Labrador, R. Atluri, L. Ballell and A. E. Garcia-Bennett, *Nanomedicine*, 2013, **8**, 57-64.
18. H. Vallhov, N. Kupferschmidt, S. Gabrielsson, S. Paulie, M. Stromme, A. E. Garcia-Bennett and A. Scheynius, *Small*, 2012, **8**, 2116-2124.
19. T. Yu, K. Greish, L. D. McGill, A. Ray and H. Ghandehari, *ACS Nano*, 2012, **6**, 2289-2301.

20. S. P. Hudson, R. F. Padera, R. Langer and D. S. Kohane, *Biomaterials*, 2008, **29**, 4045-4055.
21. A. Beyerle, A. Braun, A. Banerjee, N. Ercal, O. Eickelberg, T. H. Kissel and T. Stoeger, *Biomaterials*, 2011, **32**, 8694-8701.
22. E. F. Burguera, M. Bitar and A. Bruinink, *Eur cells mater*, 2010, **19**, 166-179.
23. T. Stoeger, C. Reinhard, S. Takenaka, A. Schroepel, E. Karg, B. Ritter, J. Heyder and H. Schulz, *Environ. Health Perspect.*, 2006, **114**, 328-333.
24. O. M. Merkel, A. Beyerle, D. Librizzi, A. Pfestroff, T. M. Behr, B. Sproat, P. J. Barth and T. Kissel, *Mol. Pharm.*, 2009, **6**, 1246-1260.
25. A. A. Gotz, A. Vidal-Puig, H. G. Rodel, M. H. de Angelis and T. Stoeger, *Part Fibre Toxicol.*, 2011, **8**, 28.
26. N. Barapatre, P. Symvoulidis, W. Moller, F. Prade, N. C. Deliolanis, S. Hertel, G. Winter, A. O. Yildirim, T. Stoeger, O. Eickelberg, V. Ntziachristos and O. Schmid, *J. Pharm. Biomed. Anal.*, 2015, **102**, 129-136.
27. J. M. Anderson, A. Rodriguez and D. T. Chang, *Semin Immunol* 2008, **20**, 86-100.
28. T. Sager, M. Wolfarth, M. Keane, D. Porter, V. Castranova and A. Holian, *Nanotoxicology*, 2015, DOI: 10.3109/17435390.2015.1025883, 1-11.
29. W. S. Cho, R. Duffin, F. Thielbeer, M. Bradley, I. L. Megson, W. Macnee, C. A. Poland, C. L. Tran and K. Donaldson, *Toxicol. Sci.*, 2012, **126**, 469-477.
30. M. Simko, D. Nosske and W. G. Kreyling, *Int J Environ Res Public Health* 2014, **11**, 4026-4048.
31. L. M. Costantini, R. M. Gilberti and D. A. Knecht, *PLoS One*, 2011, **6**, e14647.
32. W. J. Sandberg, M. Lag, J. A. Holme, B. Friede, M. Gualtieri, M. Kruszewski, P. E. Schwarze, T. Skuland and M. Refsnes, *Part Fibre Toxicol.*, 2012, **9**, 32.
33. O. Schmid, W. Moller, M. Semmler-Behnke, G. A. Ferron, E. Karg, J. Lipka, H. Schulz, W. G. Kreyling and T. Stoeger, *Biomarkers*, 2009, **14 Suppl 1**, 67-73.
34. T. Stoeger, O. Schmid, S. Takenaka and H. Schulz, *Environ. Health Perspect.*, 2007, **115**, A290-291; author reply A291-292.
35. V. Marzaioli, J. A. Aguilar-Pimentel, I. Weichenmeier, G. Luxenhofer, M. Wiemann, R. Landsiedel, W. Wohlleben, S. Eiden, M. Mempel, H. Behrendt,

- C. Schmidt-Weber, J. Gutermuth and F. Alessandrini, *Int J Nanomedicine*, 2014, **9**, 2815-2832.
36. S. Bhattacharjee, D. Ershov, K. Fytianos, J. van der Gucht, G. M. Alink, I. M. Rietjens, A. T. Marcelis and H. Zuilhof, *Part Fibre Toxicol.*, 2012, **9**, 11.
37. H. W. Chiu, T. Xia, Y. H. Lee, C. W. Chen, J. C. Tsai and Y. J. Wang, *Nanoscale*, 2015, **7**, 736-746.
38. P. Ruenraroengsak and T. D. Tetley, *Part Fibre Toxicol.*, 2015, **12**, 19.
39. W. G. Kreyling, M. Semmler-Behnke, S. Takenaka and W. Moller, *Acc. Chem. Res.*, 2013, **46**, 714-722.
40. D. A. Kuhn, D. Vanhecke, B. Michen, F. Blank, P. Gehr, A. Petri-Fink and B. Rothen-Rutishauser, *Beilstein J. Nanotechnol.*, 2014, **5**, 1625-1636.
41. M. S. Arredouani, A. Palecanda, H. Koziel, Y. C. Huang, A. Imrich, T. H. Sulahian, Y. Y. Ning, Z. Yang, T. Pikkarainen, M. Sankala, S. O. Vargas, M. Takeya, K. Tryggvason and L. Kobzik, *J. Immunol.*, 2005, **175**, 6058-6064.
42. S. Mukhopadhyay, Y. Chen, M. Sankala, L. Peiser, T. Pikkarainen, G. Kraal, K. Tryggvason and S. Gordon, *Eur. J. Immunol.*, 2006, **36**, 940-949.
43. T. H. Chung, S. H. Wu, M. Yao, C. W. Lu, Y. S. Lin, Y. Hung, C. Y. Mou, Y. C. Chen and D. M. Huang, *Biomaterials*, 2007, **28**, 2959-2966.
44. Z. Tao, B. B. Toms, J. Goodisman and T. Asefa, *Chem. Res. Toxicol.*, 2009, **22**, 1869-1880.
45. J. L. Vivero-Escoto, Slowing, II, B. G. Trewyn and V. S. Lin, *Small*, 2010, **6**, 1952-1967.
46. F. Tang, L. Li and D. Chen, *Adv. Mater.*, 2012, **24**, 1504-1534.

6.6 Appendix

Synthesis of MSN-SH_{core}-NH₂shell. Core-shell functionalized MSNs were synthesized using a similar method, as previously reported. In brief, a mixture of tetraethyl orthosilicate (TEOS, 1.63 g, 7.82 mmol), mercaptopropyl triethoxysilane (MPTES, 112 mg, 0.48 mmol) and triethanolamine (TEA, 14.3 g, 95.6 mmol) was heated under static conditions at 90 °C for 20 min in a polypropylene reactor. Then, a solution of cetyltrimethylammonium chloride (CTAC, 2.41 mL, 1.83 mmol, 25 wt% in H₂O) and ammonium fluoride (NH₄F, 100 mg, 2.70 mmol) in H₂O (21.7 g, 1.21 mmol) was preheated to 60 °C, and added to the TEOS solution rapidly. The reaction mixture was stirred vigorously (700 rpm) for 20 min while cooling down to room temperature. Subsequently, TEOS (138.2 mg, 0.922 mmol) was added in four equal increments every three minutes. After another 30 min of stirring at room temperature, TEOS (19.3 mg, 92.5 µmol) and aminopropyl triethoxysilane (APTES, 20.5 mg, 92.5 µmol) were added to the reaction. The resulting mixture was then allowed to stir at room temperature overnight. After addition of ethanol (100 mL), the MSNs were collected by centrifugation (19,000 rpm, 43,146 rcf, for 20 min) and re-dispersed in absolute ethanol. The template extraction was performed by heating the MSN suspension under reflux (90 °C, oil bath temperature) for 45 min in an ethanolic solution (100 mL) containing ammonium nitrate (NH₄NO₃, 2 g), followed by 45 min heating under reflux in a solution of concentrated hydrochloric acid (HCl, 10 mL) and absolute ethanol (90 mL). The mesoporous silica nanoparticles were collected by centrifugation and washed with absolute ethanol after each extraction step.

Heptapeptide functionalisation (MSN-HP). Bio-PLLMWSR (HP-biotin, 90.1 %, 5.0 mg, 4.0 µmol) was dissolved in 100 µL DMSO. The solution was diluted by addition of 400 µL H₂O. Then, EDC (0.8 mg, 5.2 µmol) was added, and the reaction mixture was stirred for

5 min at room temperature. Subsequently, sulfoNHS (1 mg, 5.0 μmol) was added, and the reaction mixture was stirred for another 5 min at room temperature. This mixture was added to a suspension containing 50 mg of $\text{MSN-NH}_{2,\text{OUT}}$ in a total volume of 8 mL (EtOH:H₂O 1:1). The resulting mixture was then allowed to stir at room temperature overnight. The MSNs were thoroughly washed by EtOH and H₂O (3 times) and finally collected by centrifugation (19,000 rpm, 43,146 rcf, 20 min). The HP-biotin functionalized MSNs were stored as colloidal suspension in absolute ethanol.

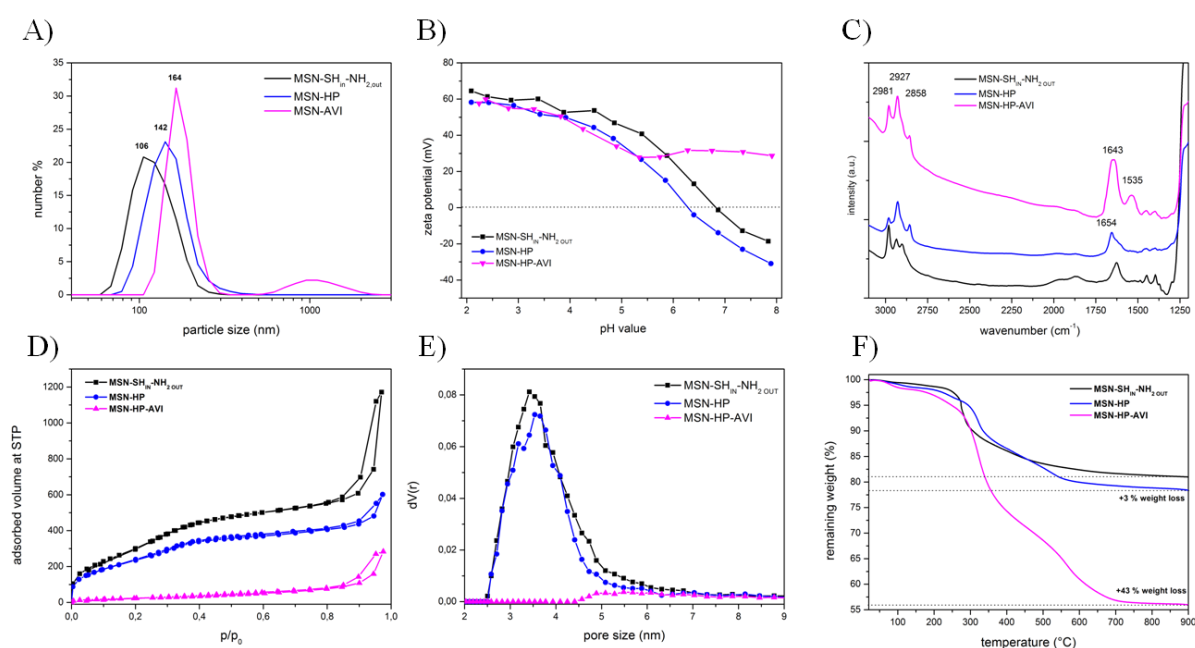


Figure S 6-1. Characterisation of $\text{MSN-SH}_{\text{in}}\text{-NH}_{2,\text{OUT}}$, MSN-HP and MSN-AVI particles A) DLS measurements of functionalised MSNs in ethanol. B) Zeta potential of the different functionalisation stages. C) A stepwise attachment of the peptide linker followed by the addition of avidin on the outer periphery can be visualised by infrared spectroscopy. D) Nitrogen sorption isotherms show mesoporous pore structure and huge surface areas for MSNs. E) After addition of avidin the pores are sealed and no pore size distribution is visible. F) Thermogravimetric analysis (TGA) data show increasing amount of organic residues in different functionalisation steps.

Avidin coating (MSN-AVI). 1 mg of MSN-HP (in 500 μL HBSS buffer) was added to 500 μL HBSS buffer containing 1 mg of avidin. The solution was mixed by 5 sec of vortexing and allowed to react for 30 min under static conditions at room temperature. The resulting

suspension was then centrifuged (5000 rpm, 2200 rcf, 4 min, 15 °C) and washed three times with HBSS buffer. The particles were finally re-dispersed in HBSS buffer and used *in vitro* and *in vivo* studies.

For Atto633 labeling, 1 mg MSNs in 1 mL ethanol were reacted with 1 uL Atto633Mal for 12 h. Afterwards the particles were washed three times with ethanol and resuspended in 1 mL HBSS buffer.

Synthesis of unfunctionalised MSNs (unMSN). In brief, a mixture of tetraethyl orthosilicate (TEOS, 1.92 g, 9.22 mmol) and triethanolamine (TEA, 14.3 g, 95.6 mmol) was heated under static conditions at 90 °C for 20 min in a polypropylene reactor. Then, a solution of cetyltrimethylammonium chloride (CTAC, 2.41 mL, 1.83 mmol, 25 wt% in H₂O) and ammonium fluoride (NH₄F, 100 mg, 2.70 mmol) in H₂O (21.7 g, 1.21 mmol) was preheated to 60 °C, and added to the TEOS solution rapidly. The reaction mixture was stirred vigorously (700 rpm) for 20 min while cooling down to room temperature. Subsequently, the resulting mixture was then allowed to stir at room temperature overnight. After addition of ethanol (100 mL), the MSNs were collected by centrifugation (19,000 rpm, 43,146 rcf, for 20 min) and re-dispersed in absolute ethanol. The template extraction was performed by heating the MSN suspension under reflux (90 °C, oil bath temperature) for 45 min in an ethanolic solution (100 mL) containing ammonium nitrate (NH₄NO₃, 2 g), followed by 45 min heating under reflux in a solution of concentrated hydrochloric acid (HCl, 10 mL) and absolute ethanol (90 mL). The unfunctionalized mesoporous silica nanoparticles were collected by centrifugation and washed with absolute ethanol after each extraction step.

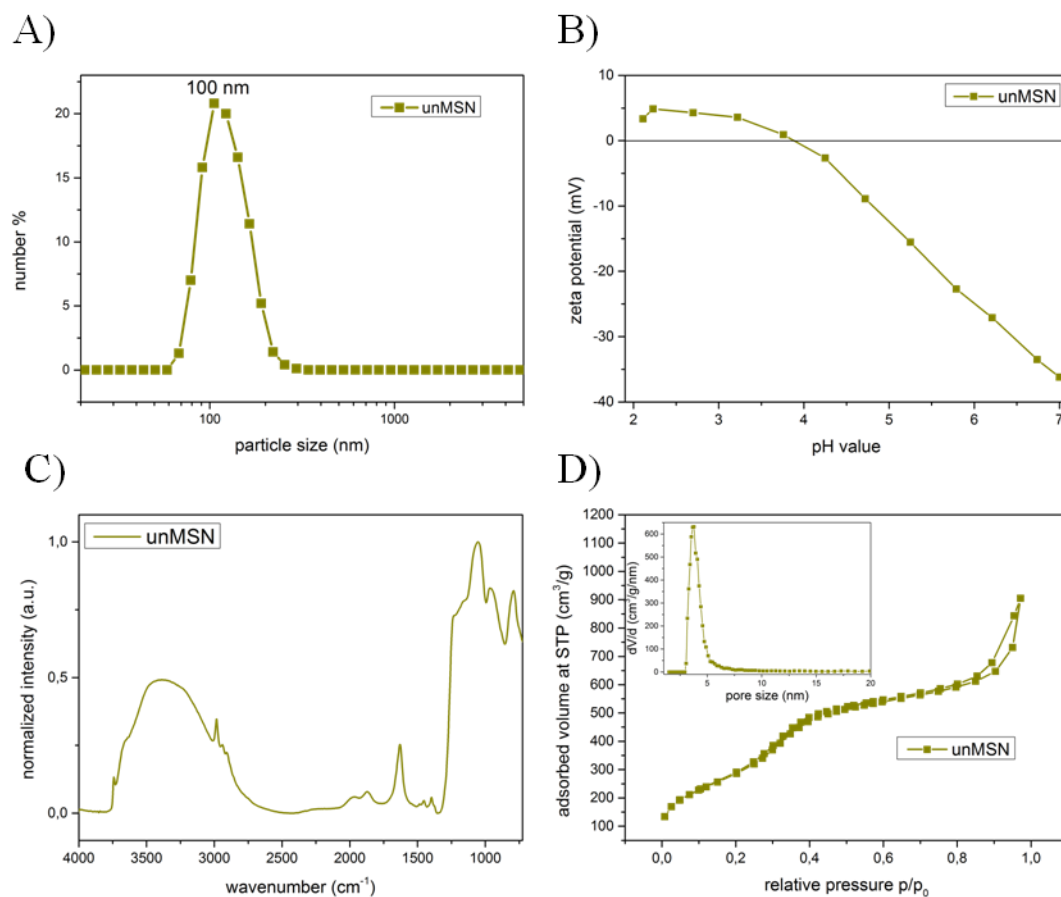


Figure S 6-2. A) DLS measurements of unfunctionalized MSNs (unMSN) in ethanol show a particle size of about 100 nm. B) Zeta potential of unMSN with an isoelectric point of 4. C) IR spectrum. D) Nitrogen sorption isotherms show mesoporous pore structure (pore size 3.7 nm) and huge surface areas (1050 m²/g) for unMSNs.

6. Applicability of avidin protein coated mesoporous silica nanoparticles as drug carriers in the lung

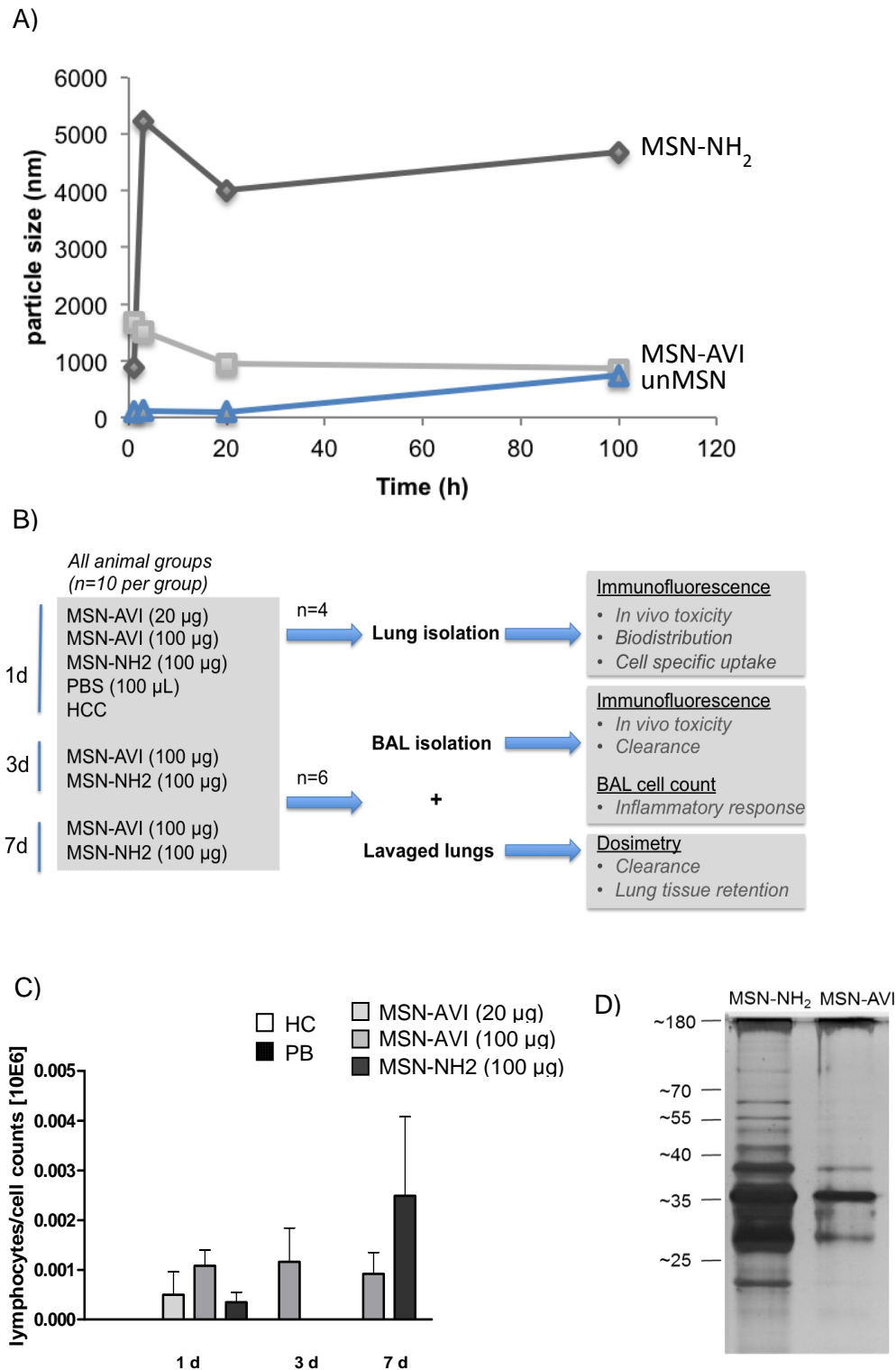


Figure S 6-3. A) DLS measurements of MSN-NH₂, unMSN and MSN-AVI suspensions over time. Data show that MSN-NH₂ particles suspended in cell culture buffer with 10% FCS, form larger agglomerates compared to MSN-AVI and unMSN in time. B) experimental set-up of animal work, C) Lymphocyte cell count in bronchoalveolar lavage (BAL). Lymphocyte counts are overall close to the detection limit (1% of

total BAL cells) and no significant changes ($p < 0.05$) have been observed between MSN treated and control mice ($n=6$). D) protein corona formation on MSN-AVI and MSN-NH₂: Native gel analysis of MSN-NH₂ and MSN-AVI incubated with mouse BALF fluid.

	N (mice)	Total cell count x 10 ⁶	Macrophage cell count x 10 ³	Multinucleated macrophages cell count x 10 ³	PMN cell count x 10 ³ (%)	Lymphocyte cell count x 10 ³ (%)
^a HCC	2	0.36 ± 0.00	356.2 ± 4.4	0.0 ± 0.0	0.0 ± 0.0 (0)	0.0 ± 0.0
^b PBS	6	0.29 ± 0.03	290.6 ± 29.5	0.0 ± 0.0	3.2 ± 1.6 (0)	0.0 ± 0.0
MSN-NH ₂	6	0.33 ± 0.03	135.0 ± 15.1	0.2 ± 0.1	191.5 ± 13.9 (59)	0.4 ± 0.2
unMSN	6	0.35 ± 0.03	308.7 ± 31.4	0.9 ± 0.4	37.33 ± 3.0 (11)	0.8 ± 0.2

Table 6-2. The inflammatory effects detected by BAL cell differentiation, 24 h after 100 µg of MSN-NH₂ or unMSN instillation, compared to 100 µL PBS (vehicle control) and HCC (home cage control) untreated animals.

^a HCC = home cage control animals (non-treated mice)

^b PBS = 100 µL PBS instilled mice (vehicle/sham control)

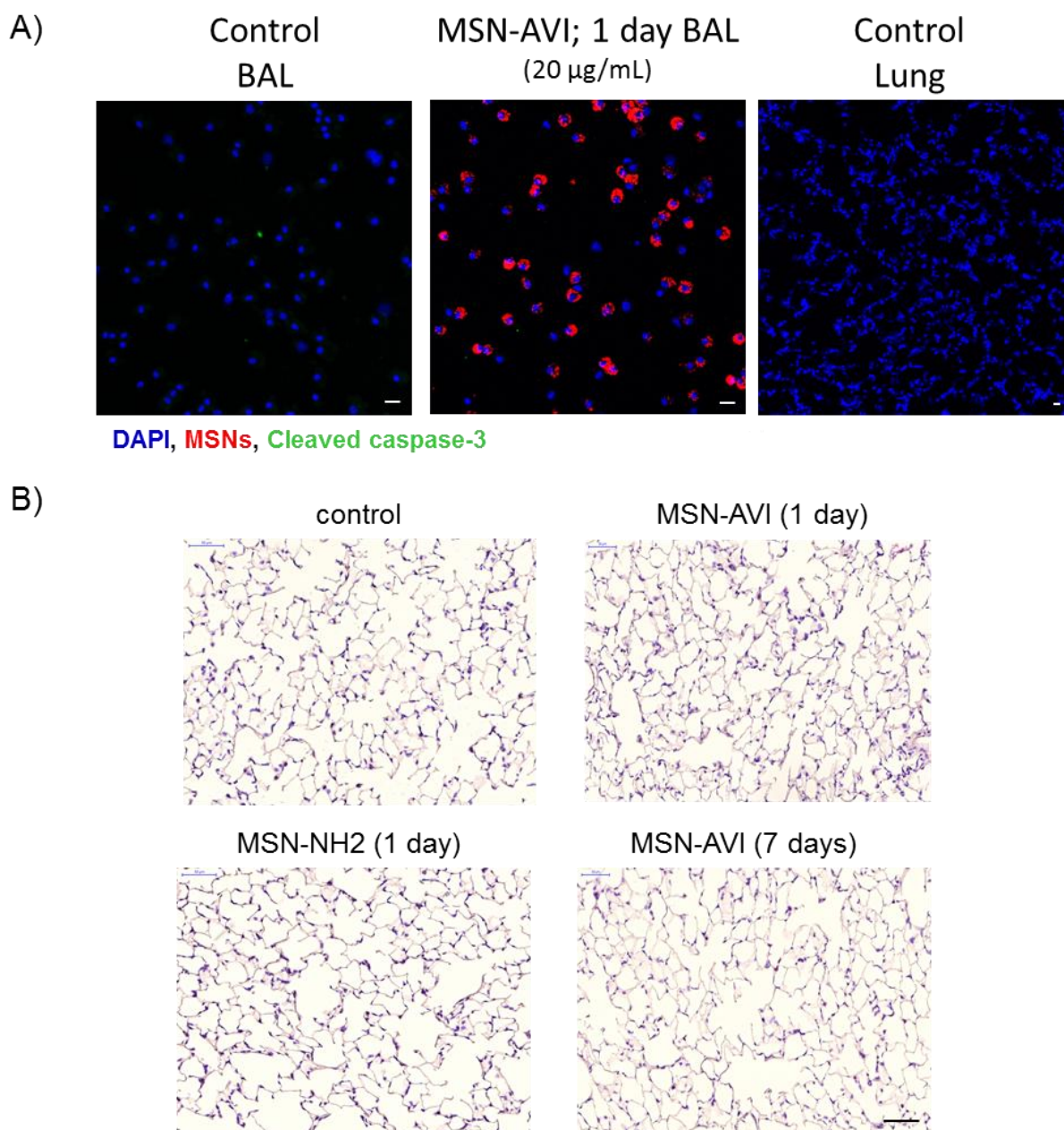


Figure S 6-4. A) Toxicity of BAL recovered cells of PBS control mice (left); MSN-AVI in Balb/c mice exposed to 20 μg for 1 day in BAL (middle) and lung tissue of PBS control mice (right). Cell nuclei are shown in blue (DAPI), ATTO 633 labeled MSNs are shown in red. Scale bar is 20 μm . B) Hematoxylin and eosin staining of lung sections from mice exposed to MSN-AVI or MSN-NH₂ particles for 1 or 7 days. Scale bar is 50 μm .

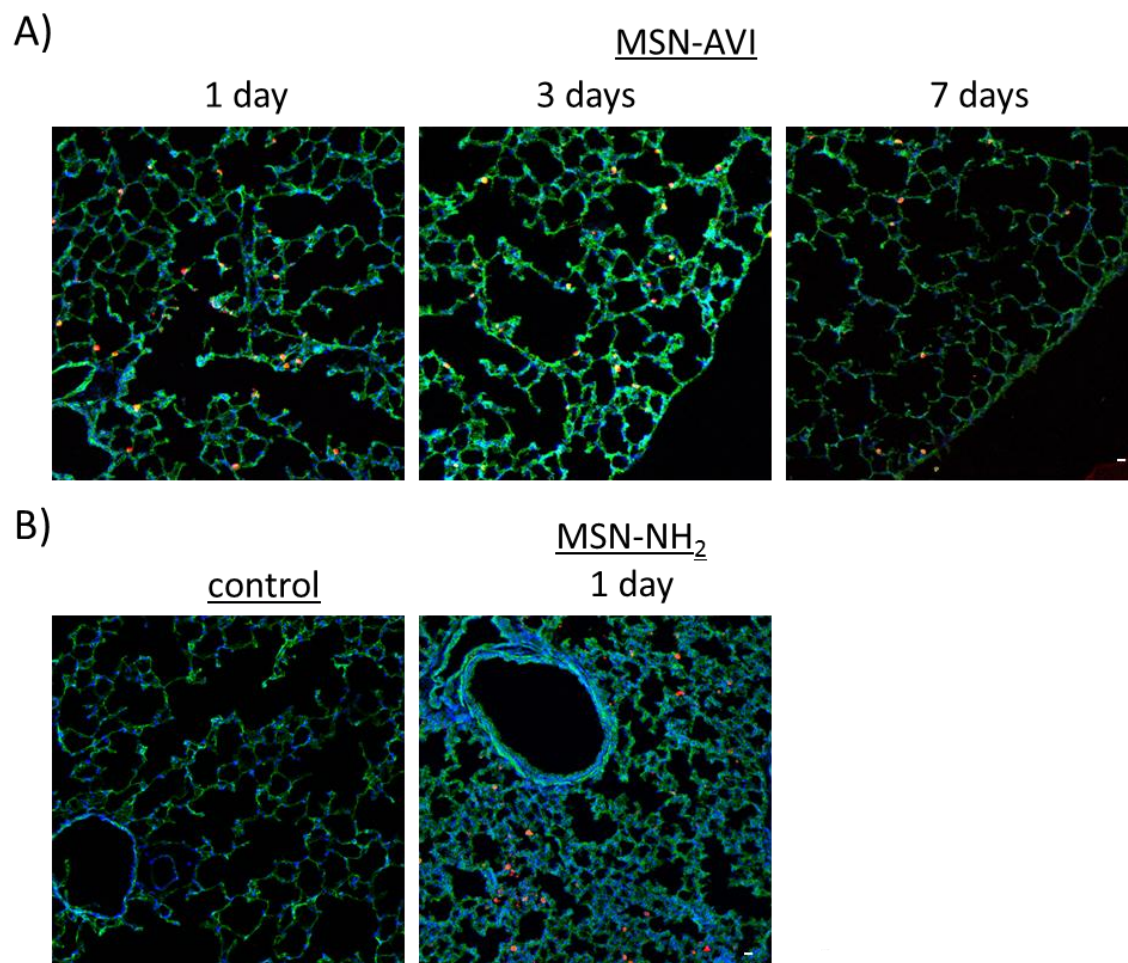


Figure S 6-5. Nanoparticle distribution in lung cryo-slices of Balb/c mice exposed to 100 μg MSN-AVI after 1, 3, and 7 days. B) PBS control and nanoparticle distribution in lung cryo-slices after 1 day exposure to 100 μg MSN-NH₂. Cell nuclei are shown in blue (DAPI), ATTO 633 labeled MSNs are shown in red, cell actin staining (phalloidin) is shown in green. Images are representative for n=4 animals. Scale bar is 20 μm .

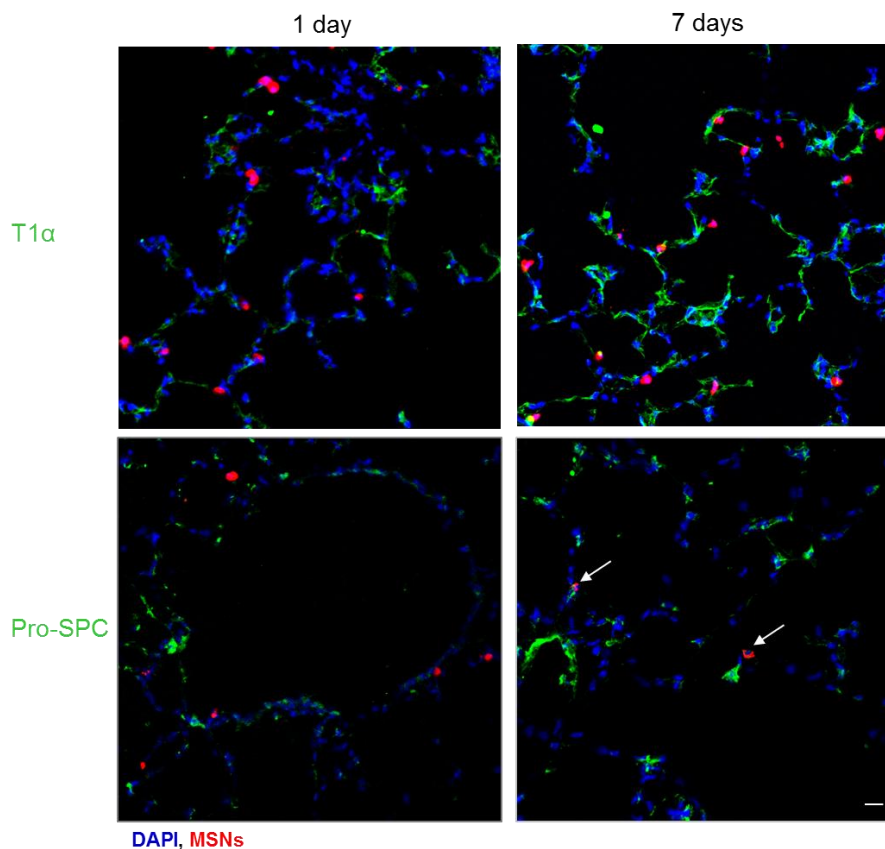


Figure S 6-6. Confocal microscopy images (20x objective) of cryo-slices of Balb/c mice exposed to MSN-AVI for 1 or 7 days, co-stained with alveolar epithelial cell type 1 marker (T1 α , green, top) or with alveolar epithelial cell type 2 marker (pro-SPC, green, bottom). Cell nuclei are shown in blue (DAPI) and ATTO 633 labeled MSNs are shown in red. Scale bar is 20 μ m.

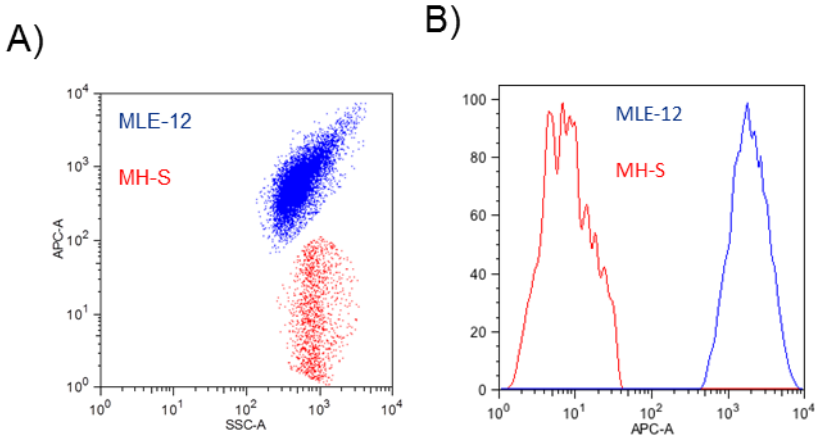


Figure S 6-7. DiD selective labeling of MLE-12 cells in a MLE-12/ MH-S co-culture set-up. A) dot plot of SSC against APC-A channel, B) histogram of co-culture in APC-A channel.

7 Cellular resolution is essential for validation of active targeting of nanoparticles *in vivo*

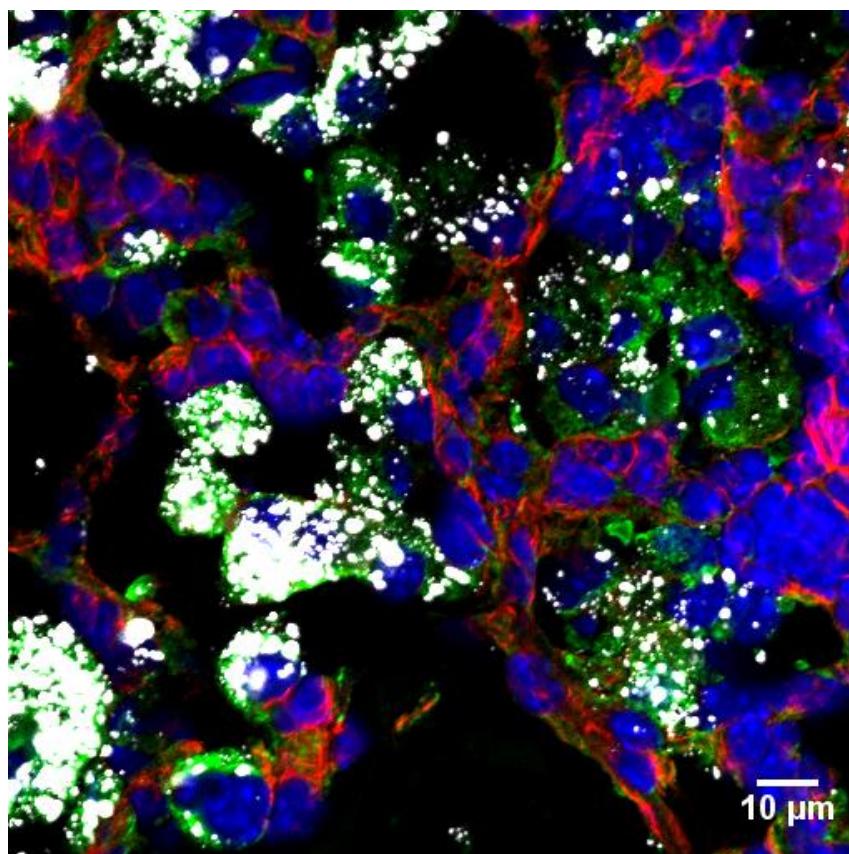
This chapter is based on the following publication:

Deniz Bölükbas, Stefan Datz, Charlotte Meyer-Schwickerath, Malamati Vreka, Lin Yang, Dorothée Gößl, Theodora Agalioti, Christian Argyo, Sabine van Rijt, Michael Lindner, Oliver Eickelberg, Tobias Stöger, Otmar Schmid, Georgios Stathopolous, Thomas Bein, Silke Meiners, 2017, *submitted*.

Abstract

Nanoparticle-based therapies hold great promise in targeted delivery of drugs. Targeting of tumors, for instance, involves functionalization of nanoparticles for receptors that are specific for cancer cells. Indeed, several cell types can be targeted in parallel by distinctly functionalized nanocarriers. Here, we investigated the targeting efficiencies of EGFR- or CCR2-targeted mesoporous silica nanoparticles (MSNs) *in vitro* and *in vivo* for lung cancer therapy with cellular resolution. Nanoparticles functionalized with the artificial peptides, GE11 or ECL1i for EGFR- or CCR2-targeting respectively, were specifically taken up by receptor overexpressing cell lines of the lung *in vitro*. Systemically applied GE11-functionalized nanoparticles, however, did not efficiently accumulate in EGFR-overexpressing flank tumors of mice, but were filtered out by the liver, regardless of their functionalization and tumor type. Moreover, both EGFR- or CCR2-functionalized MSNs, which were intratracheally administered to the lungs of Kras-mutant transgenic mice, did not preferentially target tumor cells, but were mainly taken up by resident alveolar macrophages in tumorous and also tumor-free regions of the lungs. Thus, not just regional but cellular

resolution is essential for validation of nanoparticle-based cell targeting. Novel strategies that overcome the effective natural defense against foreign materials are thus required to establish efficient cell-specific nanoparticle-mediated delivery of drugs for tumor therapy.



7.1 Introduction

The use of nanoparticles as therapeutic agents for cancer therapy has attracted great attention in the past decades ¹. In particular, nanoparticle-based active targeting of tumor cells has emerged as a potential therapeutic approach to increase drug doses within the tumor while reducing systemic toxicity ^{2,3}. Cell-specific targeting can be achieved by functionalization of nanoparticles with targeting ligands on their surface that bind to receptors that are specifically overexpressed on cancer cells. In this context, nanoparticles targeting the epidermal growth factor receptor (EGFR) have attracted notable attention ⁴. This receptor is overexpressed in

several types of cancers including breast carcinoma, colon carcinoma, and lung cancer^{5,6}. Nanoparticles are often functionalized with EGFR targeting ligands and designed to deliver either silencing agents against defined oncogenes or chemotherapeutic drugs⁴. These nanoparticles are then preferentially recognized and bound by the tumor cells overexpressing EGFR; then they are rapidly taken up into the cells by receptor-mediated endocytosis where the drug is released into the cytoplasm to specifically kill the tumor cells⁷. Receptor-mediated targeting via nanoparticles also offers the promise of targeting different types of cells at the same time. In particular, inflammatory immune cells such as tumor-associated macrophages have been identified as a major culprit supporting malignant and metastatic tumor growth^{8,9}. Accordingly, complementary targeting of tumor and tumor-associated immune cells has emerged as a novel approach for cancer therapy^{10,11}, yet has hardly been exploited for nanoparticle-mediated cell targeting^{12,13}. Such complementary targeting strategies require comprehensive validation of cell-specific targeting *in vivo* with cellular resolution. While many *in vivo* studies demonstrate effective targeting of tumor tissue and therapeutic efficiency of receptor-targeting nanoparticles in mouse tumor models¹⁴⁻¹⁶, most of these studies, however, lack proof of cell-specific targeting and nanoparticle-induced killing of tumor cells but rather show accumulation of nanoparticles in the target tissue¹⁷⁻²⁰. We here analyzed complementary targeting of tumor and tumor-associated immune cells by application of fluorescently labeled mesoporous silica nanoparticles (MSN) that had been coupled to EGFR- and C-C chemokine receptor type 2 (CCR2) -specific targeting ligands^{21,22} *in vitro* and *in vivo*. Cell-specific targeting efficiency of EGFR- and CCR2-ligand bound nanoparticles was validated using two distinct delivery strategies, *i.e.* systemic delivery via intravenous injection and local intratracheal delivery to the lung. This also allowed us to test targeting specificity of nanoparticles in two different biological environments which are known to form distinct protein coronas on nanoparticles that may influence receptor-mediated targeting²³⁻²⁸

Intriguingly, proven *in vitro* cellular targeting specificity of ligand-functionalized nanoparticles was severely hampered *in vivo* in two distinct tumor mouse models irrespective of particle delivery via the blood or the lung due to highly effective foreign body clearance mechanisms.

7.2 Results and Discussion

Complementary overexpression of EGFR and CCR2 in lung cancer

The EGF receptor is commonly overexpressed in non-small cell lung cancer (NSCLC) which correlates with poor prognosis of patients with NSCLC, a common devastating type of lung carcinoma with a mean 5-year survival of only 15%^{30,31}. CCR2 is a chemokine receptor that is specifically overexpressed in tumor-associated macrophages and promotes metastatic spread of tumor cells in preclinical cancer models including lung cancer³²⁻³⁶. For our complementary targeting approach, we first validated cell-type specific overexpression of EGFR and CCR2 in tumors of lung cancer patients. Pronounced overexpression of EGFR was observed in infiltrating nests of lung tumor cells, while CCR2 was strongly overexpressed in the surrounding stroma as depicted by immunohistopathological staining of the same patient material (Figure 7-1). These data validate the combined use of EGFR- and CCR2-specific targeting nanoparticles as a valid approach to obtain specific targeting of lung tumors and tumor-associated immune cells at the same time.

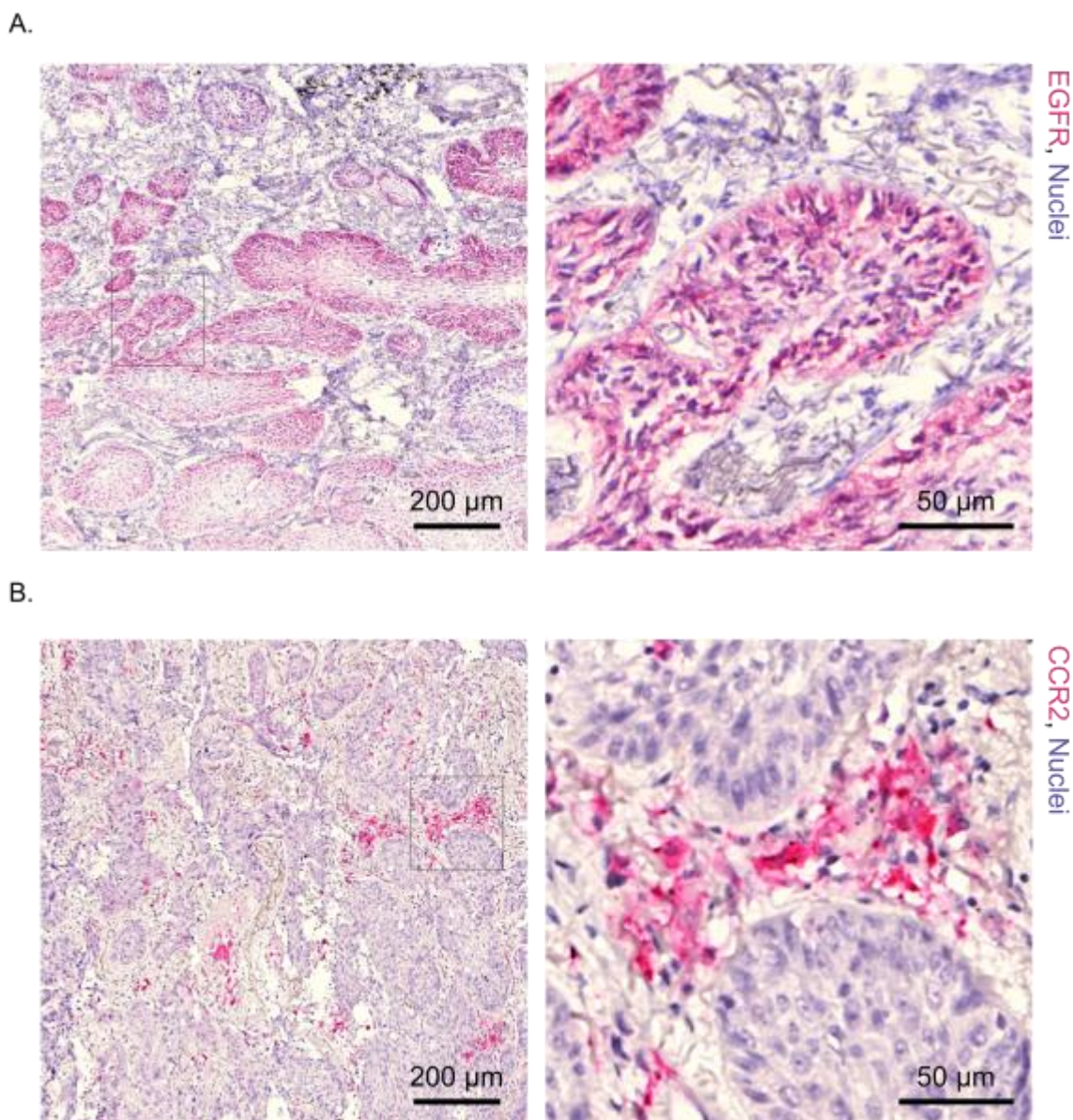


Figure 7-1. EGFR and CCR2 expression in non-small cell lung cancer (NSCLC). Immunohistochemical staining of (A) EGFR (pink) is observed in infiltrating tumor nests whereas (B) CCR2 (pink) mainly localizes to desmoplastic stroma of NSCLC tumors of the patient.

Synthesis and characterization of the mesoporous silica nanoparticles (MSNs)

Functionalized MSNs were synthesized according to previous reports, resulting in functionalization of the internal pore system with thiol groups and of the external particle surface with amino groups³⁷ (For details on the synthesis scheme and characterization of the particles see SI, Figure S 7-1). The additional core functionalization was used for covalent

attachment of fluorescent dyes for particle tracking in our *in vitro* and *in vivo* studies. The external surface of the MSNs was functionalized with a pH-cleavable linker system containing a biotin functionality on the outer periphery. The glycoprotein avidin was attached to the outer surface of the particles via noncovalent association with the biotin groups, thus acting as a bulky gatekeeper of the internal pore system. In our study, these MSN_{AVI} nanoparticles served as the non-targeting particle control. Different targeting ligands were attached to the outer surface of the avidin gatekeepers such as the natural ligand of the EGFR, *i.e.* EGF, an artificial ligand GE11, and the artificial CCR2 antagonist ECL1i referred to as particles MSN_{EGF}, MSN_{GE11}, and MSN_{ECL1i}, respectively (Figure S 7-1A)^{21,22,37}. All MSN types showed colloidal stability in aqueous and mucosal solutions (Figure S 7-1 I,J) and pH-responsive release behavior for independently manufactured batches as analyzed by release of propidium iodide as a model cargo (Figure S 7-1K). Additional comprehensive characterization of the MSN particle systems with thermogravimetric analysis, nitrogen sorption, zeta potential measurements, and IR spectroscopy can be found at the SI and confirmed successful synthesis of a pH-cleavable MSN system with different targeting ligands that was subsequently used for specific *in vitro* and *in vivo* cellular targeting experiments.

Receptor-mediated targeting of MSNs *in vitro*

We analyzed *in vitro* receptor-specific targeting of EGFR-abundant cells with fluorescently labeled functionalized MSNs in two human NSCLC cell lines that differ in their basal EGFR expression. EGFR is strongly overexpressed in A549 cells compared to H520 cells as determined by Western blot analysis (Figure 7-2A and Figure S 7-2). Of note, we always applied the nanoparticles in the presence of 10% FCS to allow for *in vitro* protein corona formation^{24,27}. Confocal microscopy revealed pronounced uptake of the targeted MSNs in

EGFR-abundant A549 cells. EGF receptor staining confirmed co-localization of the fluorescently labeled MSNs with EGFR, thus validating that the uptake was EGFR-mediated (Figure 7-2B). Importantly, the uptake was confirmed for different MSN particles presenting both the natural EGFR ligand, EGF, and the artificial ligand, GE11, using several independent batches of nanoparticle preparations. In contrast, EGFR-scarce H520 cells showed only a minor uptake of GE11-functionalized MSNs (Figure 7-2B and Figure S 7-2). In flow cytometry analysis, we observed significant increase in the uptake when the particles were EGFR-targeted with EGF or GE11 compared to non-targeted MSN_{AVI} particles (Figure 7-2C). Specificity of our CCR2-targeted MSNs was tested in the presence of serum in the mouse alveolar macrophage cell line MH-S, which expresses increased levels of CCR2 as determined by Western blot analysis (Figure S 7-3). Treatment of MH-S cells with CCR2-ligand functionalized and fluorescently labeled MSNs showed strong uptake of particles that co-localized with CCR2 staining indicating receptor-mediated uptake of these MSNs. In contrast, non-targeted MSN_{AVI} particles were only minimally taken up by MH-S cells (Figure 7-3A). In addition, the CCR2-scarce lung adenocarcinoma cell line A549 cells showed a much less pronounced uptake when compared to the MH-S cells, thus demonstrating CCR2-specific delivery of our CCR2-targeted MSNs (Figure S 7-3). Flow cytometry analysis confirmed the significant increase in uptake in MH-S cells upon CCR2-targeting with independent batches of particle preparations (Figure 7-3B).

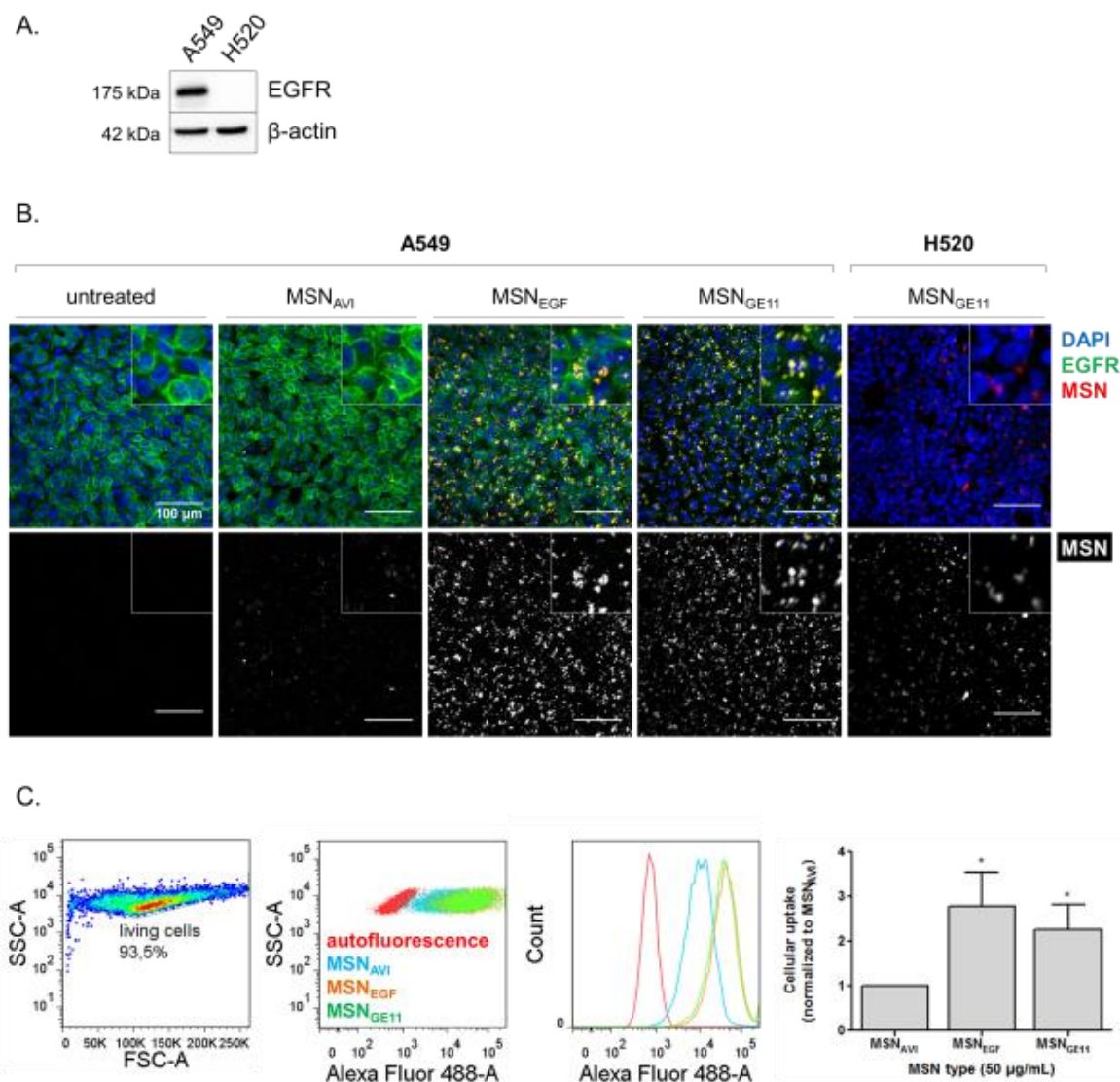


Figure 7-2. EGFR-specific uptake of MSNs *in vitro*. (A) Basal EGFR overexpression in A549 but not in H520 cells at the protein level, assessed by Western blot analysis. (B) EGFR-targeted *versus* non-targeted uptake of ATTO 633-labeled MSN_{AVI}, MSN_{EGF}, and MSN_{GE11} within 1 h by A549 cells compared to MSN_{GE11} uptake in H520 cells co-stained for EGFR by immunofluorescence, measured by confocal microscopy. Nuclear staining (DAPI) is shown in blue, EGFR staining in green and ATTO 633-labeled MSNs in red in the merged images, and in gray in the single channel for better resolution. (C) Quantification of the ATTO 488-labeled MSN_{AVI}, MSN_{EGF}, and MSN_{GE11} uptake within 1 h by A549 cells by flow cytometry analysis. After gating for the viable cells, medians of the histogram curves were obtained. Autofluorescence signals of the untreated cells were blanked from the treated cells. * indicates a significant increase in the uptake of MSN_{EGF} and MSN_{GE11} compared to MSN_{AVI} ($p < 0.05$). Values given are an average of six independent experiments using different particle preparations \pm SEM.

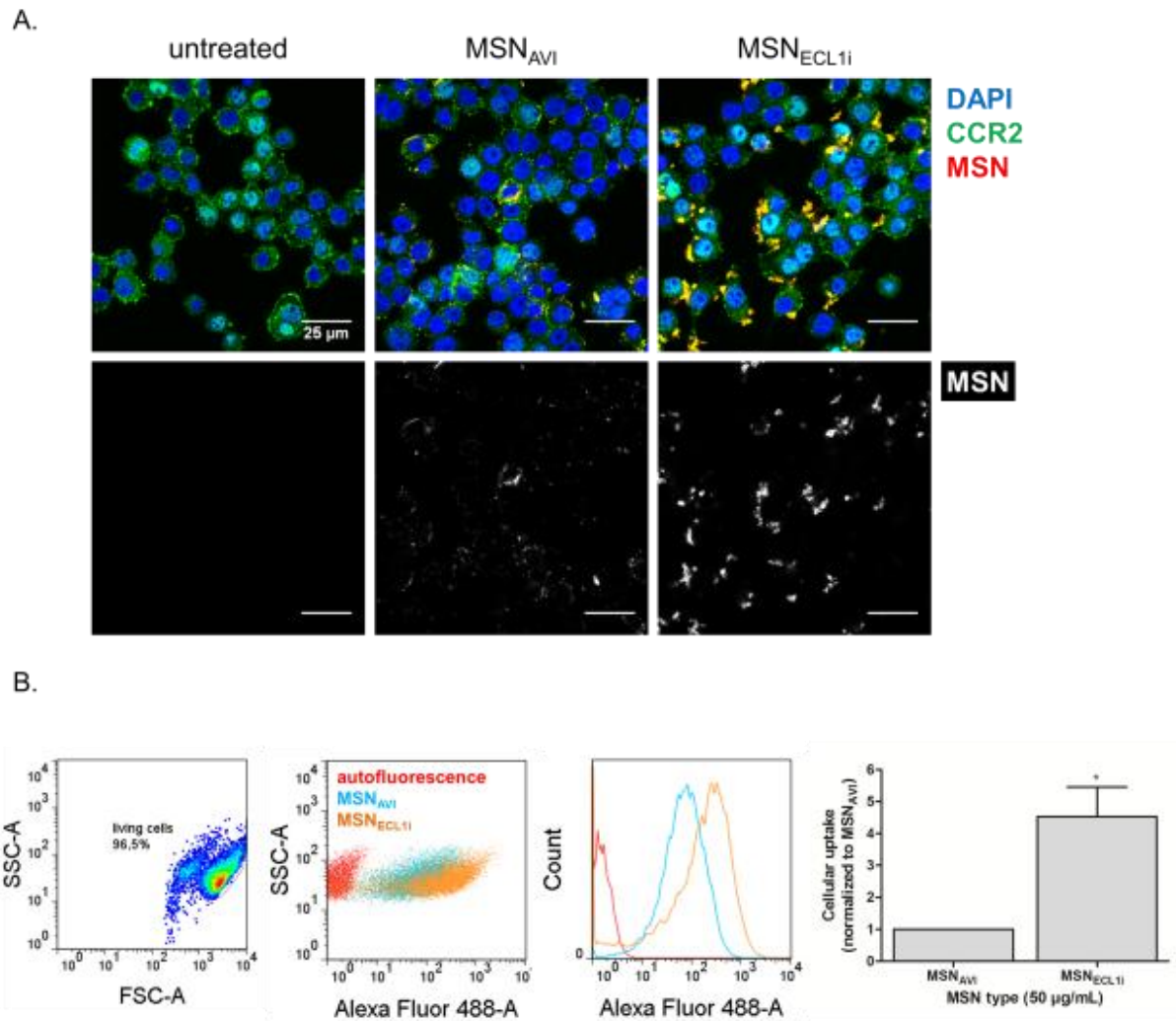


Figure 7-3. CCR2-specific uptake of MSNs *in vitro*. (A) CCR2-targeted *versus* non-targeted uptake of ATTO 633-labeled MSN_{AVI} and MSN_{ECL11} in one hour in MH-S cells immunofluorescently co-stained for CCR2, measured by confocal microscopy (B) Quantification of ATTO 488-labeled MSN_{AVI} and MSN_{ECL11} uptake within 1 h in MH-S cells by flow cytometry analysis. After gating for the viable cells, medians of the histogram curves were obtained. Autofluorescence signals of the untreated cells were blanked from the treated cells. * means a significant increase in the uptake of MSN_{ECL11} compared to MSN_{AVI} ($p < 0.05$). Values given are an average of four independent experiments using different particle preparations \pm SEM.

Systemic delivery of MSN_{GE11} versus MSN_{AVI} in mouse flank tumor models

In vivo, we first analyzed receptor-mediated targeting of the EGFR-functionalized nanoparticles in flank tumor bearing mouse models by systemic delivery via the bloodstream.

In the blood, nanoparticles are reported to be immediately coated with a distinct protein corona²⁵. EGFR-targeting specificity was assessed by using genetically engineered murine melanoma cells (B16F10), that express only low levels of EGFR (B16F10^{EGFR-}) and a derivative of these cells stably transfected to overexpress EGFR (B16F10^{EGFR+}) (Figure 7-4A). These cell lines were injected subcutaneously into the left and right flanks of a syngeneic and immunologically fully competent mouse strain (C57BL/6) for flank tumor formation.

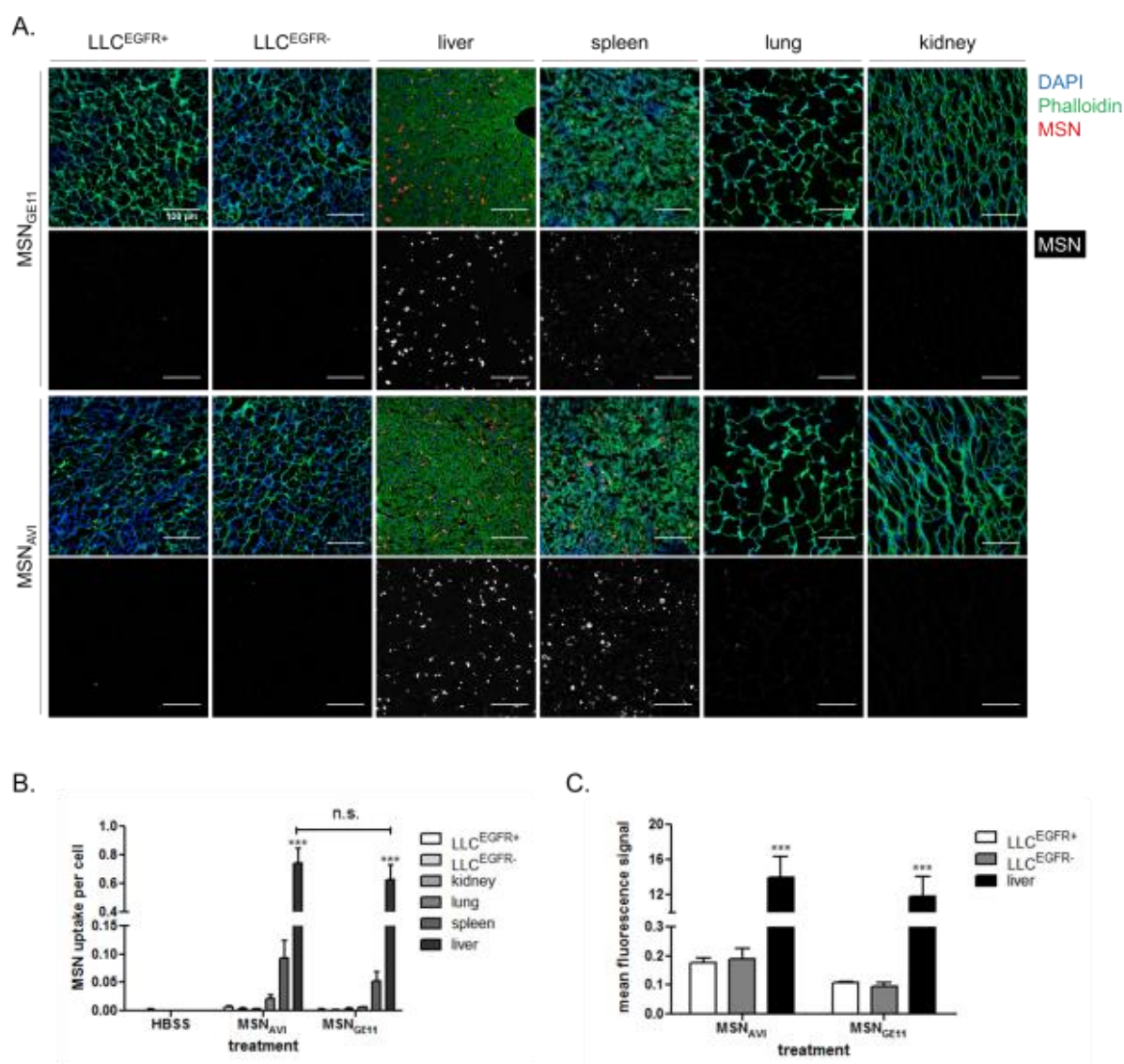


Figure 7-4. Biodistribution of EGFR- targeted versus non-targeted nanoparticles in mice with B16F10^{EGFR-} and B16F10^{EGFR+} syngeneic tumors. (A) Overexpression of EGFR protein in cDNA

transfected B16F10 cells in comparison to control vector transfected cells *in vitro* by Western blot analysis. (B) Histological analysis of the intravenously administered MSN_{AVI} and MSN_{GE11} biodistribution in the EGFR-abundant B16F10^{EGFR+} tumors, EGFR-scarce B16F10^{EGFR-} tumors, livers, spleens, lungs, and kidneys of the mice three days after treatment by means of confocal microscopy. Nuclear staining (DAPI) is shown in blue, actin staining (phalloidin) in green and ATTO 633-labeled MSNs in red in the merged image, and in gray in the single channel for improved resolution. To obtain reliable qualitative data on the distribution of the particles in these tissues, we analyzed 5 mice per group with 5 random sections and 3 images per section taken in a blinded manner. (C) Quantification of the MSN_{AVI} and MSN_{GE11} uptake per nuclei observed in histological analyses in B16F10^{EGFR-} and B16F10^{EGFR+} tumors, kidneys, lungs, spleens, and livers, respectively. In the HBSS control, animals only received HBSS buffer and no particles. *** indicates a significant increase in MSN uptake in the livers compared to the tumors ($p < 0.001$). Values given are averages \pm SEM of three different images/tissue sections per mouse in each group (n = 5 per MSN type).

In a complementary approach, genetically engineered murine Lewis lung carcinoma cells (LLC), which endogenously overexpresses EGFR (LLC^{EGFR+}) and a derivative of these cells in which EGFR had been knocked down via stable short-hairpin-mediated RNA silencing (LLC^{EGFR-}) were used (Figure S 7-4). With this approach, we are able to control for EGFR-specific targeting of our functionalized nanoparticles to tumor cells within the same mouse, as receptor-negative tumor cells serve as an internal control for receptor-specific targeting. This animal model thus allows for an unprecedented control of receptor-mediated targeting specificity. In both settings, cells grew to form tumors of similar size of 1-2 cm³ within two weeks with similar histology. ATTO 633-labeled EGFR-targeted nanoparticles were then systemically applied via retro-orbital intravenous injection and biodistribution of the particles was compared to labeled but non-targeted MSN_{AVI} particles by *in vivo* fluorescence imaging. Fluorescence signals were low and close to the detection limit of our near-infrared bioimaging system but indicated accumulation of nanoparticles in the liver (data not shown). We investigated the biodistribution of the systemically applied MSNs on the cellular level by comparative immunofluorescence analysis of the right and left flank tumors and of several internal organs. Both the targeted and non-targeted fluorescently-labeled MSNs were mainly localized in the liver and spleen with only little uptake into the flank tumors, lungs, and

kidneys (Figure 7-4B). Quantification of the immunofluorescence signal per cell nucleus confirmed that the delivery of the MSNs to the liver was much more effective than to other organs or tumors (Figure 7-4C). Importantly, we did not observe any difference in the uptake between EGFR overexpressing and EGFR-scarce B16F10 tumor cells. Very similar data were obtained with the second set of EGFR-abundant and -scarce LLC tumor cells (Figure S 7-4). Likewise, quantification of nanoparticle-derived fluorescence in tissue homogenates of flank tumors and the liver revealed pronounced accumulation of fluorescence signals in liver homogenates regardless of MSN functionalization in the LLC flank tumor model (Figure S 7-4).

Local intratracheal delivery of MSN_{GE11} and MSN_{ECL1i} in Kras-mutant transgenic mouse model

In order to assess the targeting specificity of our functionalized nanoparticles by a different delivery route and in the presence of a different biological environment, *i.e.* the lung lining fluid, we evaluated local delivery of targeted MSNs into the lungs via instillation using the Kras^{LA2} mouse model for lung cancer. In this mouse model, transgenic mice spontaneously develop lung tumors upon random activation of oncogenic Kras signaling, resulting in a more realistic tumor model than the inducible cancer models^{38,39}. As such, this mouse model closely resembles the onset of NSCLC in patients where activation of Kras has been shown to be the most prominent oncogenic driver mutation^{6,40}. Immunohistochemical staining for EGFR and CCR2 confirmed that the receptors are overexpressed in these lung tumors, thus validating the Kras^{LA2} lung tumor model as a suitable model for investigating EGFR- and CCR2-specific targeting via functionalized nanoparticles (Figure S 7-6). For *in vivo* evaluation of receptor-specific uptake of EGFR- and CCR2-targeted MSNs by tumor and tumor-associated immune cells, fluorescently labeled targeted (MSN_{GE11}, MSN_{ECL1i}) - and

7. Cellular resolution is essential for validation of active targeting of nanoparticles in vivo

non-targeted MSNs (MSN_{AVI}) were intratracheally instilled directly into the lungs of tumor-bearing Kras^{LA2} mice.

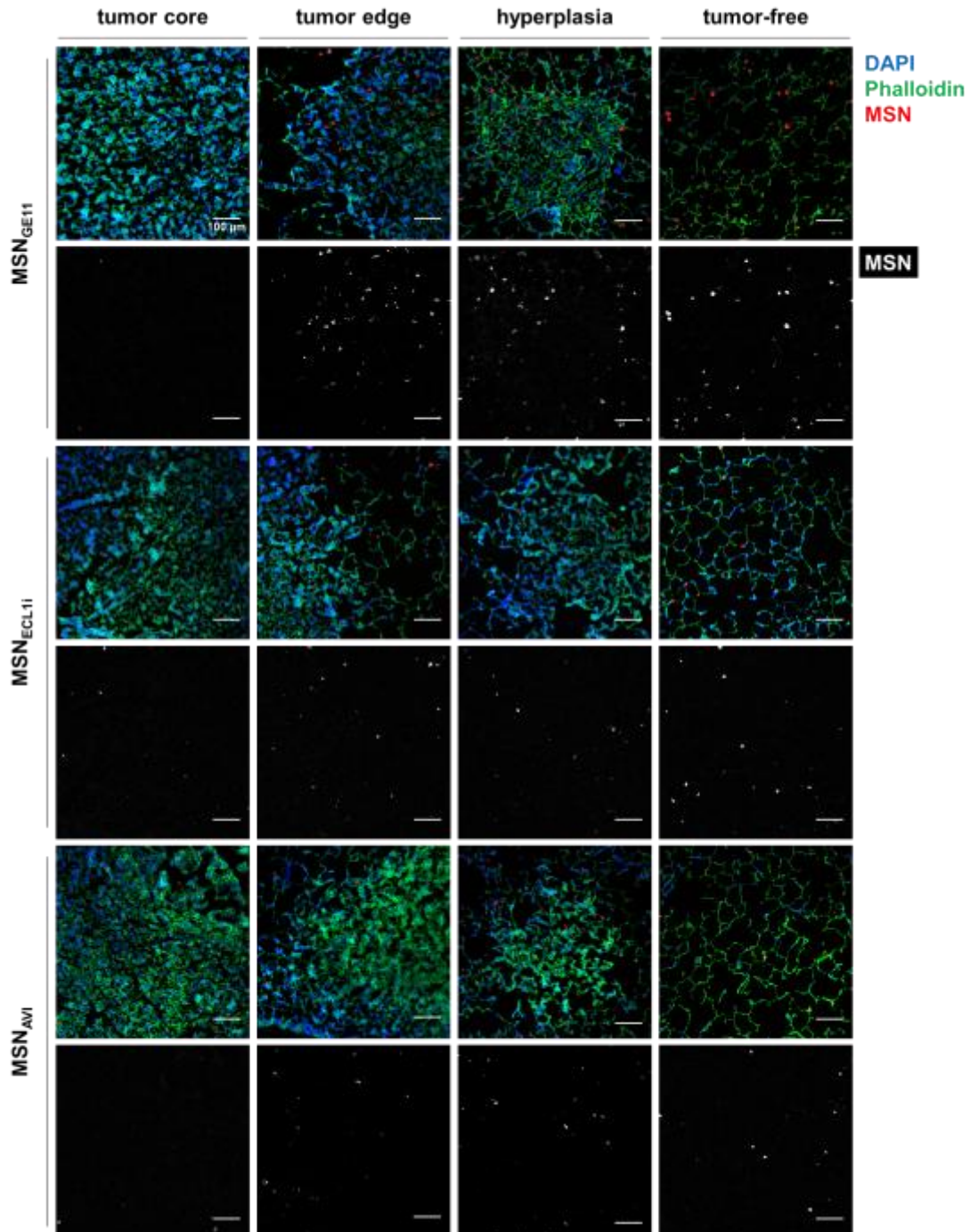


Figure 7-5. Cellular distribution of instilled nanoparticles in the lungs of Kras^{LA2} mutant mice. Histological analysis of ATTO 633-labeled MSN_{AVI} , MSN_{GE11} , and $\text{MSN}_{\text{ECL11}}$ uptake in solid tumor cores *versus* their edges, and in hyperplastic or in tumor-free regions of the tumorous lungs. Nuclear staining (DAPI) is shown in blue, actin staining (phalloidin) in green, and ATTO 633-labeled MSNs in red in the merged images, and in gray in the single channels for more clear observation. To obtain reliable

qualitative data on the distribution of the particles in these tissues, we analyzed five mice per group with five random sections and three images per section taken in a blinded manner. Images shown are representative for three different regions from each group of mice (n = 5 per MSN type).

The biodistribution of the fluorescently-labeled MSNs was evaluated three days after administration on the cellular level using confocal microscopy of the lung, liver, and spleen sections as described before. Translocation of MSNs to secondary organs was not detected⁴¹ (Figure S 7-7), instead MSNs were retained in the lungs of the $Kras^{LA2}$ mice (Figure 7-5). In the tumorous lungs, particle uptake was detected in smaller hyperplastic lesions of the lung but not in large and solid tumors, except for the edges of these tumors (Figure 7-5). Nanoparticles also localized to tumor-free lung tissue regardless of their functionalization (Figure 7-5). Importantly, we did not observe any difference in cellular uptake of EGFR-, CCR2-targeted nanoparticles, and non-targeted MSN_{AVI} particles on the cellular resolution level. Remarkably, the nanoparticles did accumulate in specific cells both in the tumor-free and in tumorous regions. Immunofluorescence staining with the macrophage marker CD68 identified these cells as alveolar macrophages (Figure S 7-8). These cells are specialized tissue-resident macrophages of the lung that colonize the alveolar surface and play an essential role in the pulmonary defense against particles and pathogens⁴². Of note, these cells stained also strongly positive for both EGFR and CCR2, in both the tumor-free and the tumorous lesions of $Kras^{LA2}$ tumor mice (Figure 7-6). Uptake of nanoparticles, however, was independent of the receptor expression as also the non-targeted MSN_{AVI} nanoparticles were efficiently taken up by EGFR- and CCR2-positive alveolar macrophages (Figure 7-6). Moreover, lung carcinoma cells that overexpressed both EGFR and CCR2 did not preferentially take up EGFR- and CCR2-targeted MSNs, respectively (Figure S 7-6 and Figure 7-6C&D). These data reveal disturbance of targeting specificity of functionalized nanoparticles in the lung.

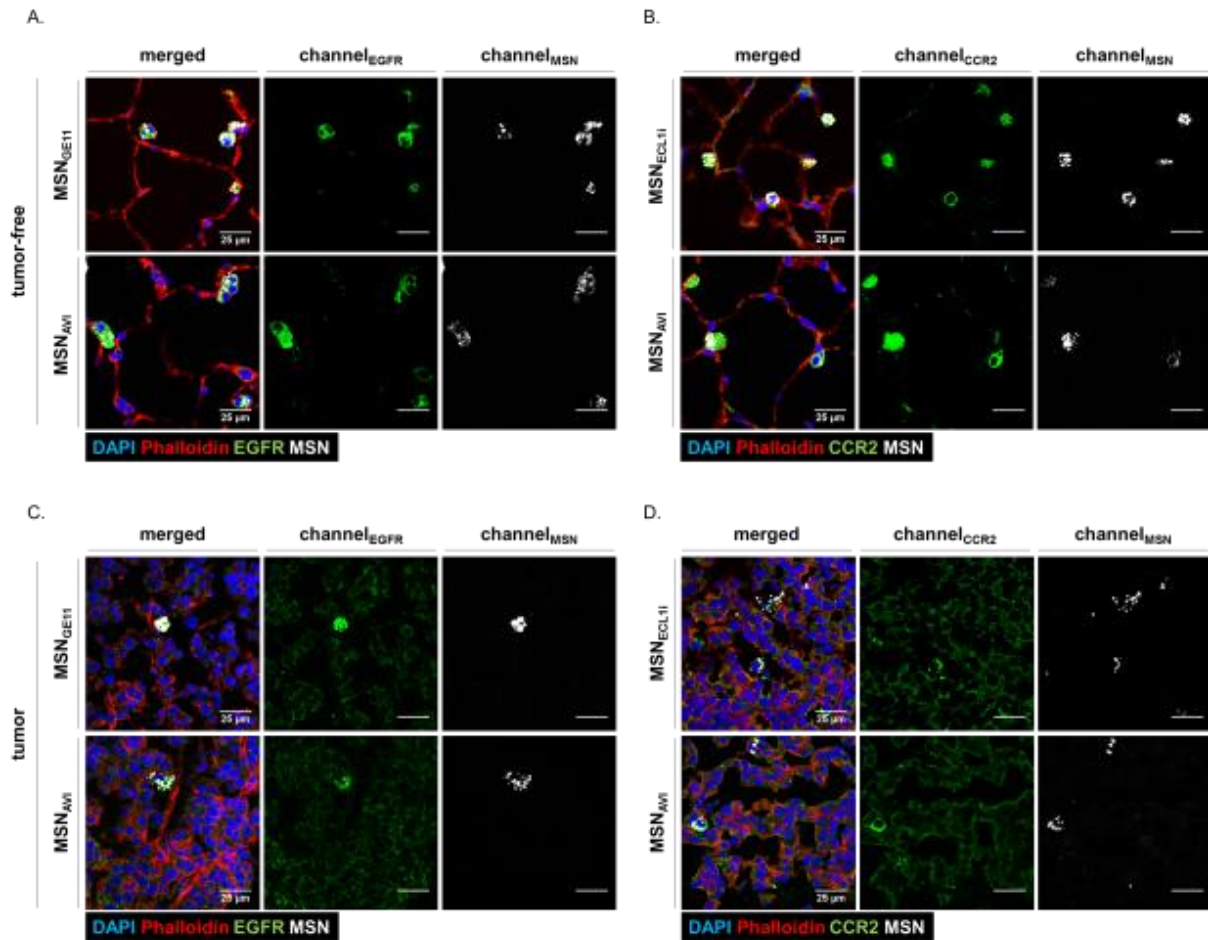


Figure 7-6. Nanoparticles localize to alveolar macrophages in $Kras^{LA2}$ mutant lungs. Immunofluorescence co-staining for (A) EGFR and (B) CCR2 in tumor-free regions compared to (C) EGFR and (D) CCR2 co-staining in tumor regions of the mutant lungs with lung cancer that had been treated with ATTO 633-labeled MSN_{AVI} versus MSN_{GE11} or MSN_{ECL11} . Nuclear staining (DAPI) is shown in blue, actin staining (phalloidin) in red, receptor staining (EGFR for A & C, CCR2 for B & D) in green, and ATTO 633-labeled MSNs in gray. Images shown are representative for three different regions from each group of mice ($n = 5$ per MSN type).

7.3 Conclusion

In conclusion, *in vitro* validated nanoparticle-mediated targeting of receptors on tumor and tumor-associated immune cells is strongly deprived *in vivo*. This failure in cellular targeting specificity is particularly obvious for the lung-delivered nanoparticles as the alveolar macrophages of the $Kras$ -mutant mice strongly overexpressed both EGFR and CCR2, but efficiently entrapped targeted as well as non-targeted nanoparticles to a similar extent.

Enhanced cell-specific uptake by macrophages of the lung compared to tumor cells would have escaped analysis if only particle uptake within the tissue would have been monitored as done previously¹⁷⁻²⁰. Similarly, analysis of cell-specific particle uptake in the flank tumor models also unambiguously revealed loss of cellular targeting specificity. Our data thus emphasize the need for analyzing cellular targeting specificities with cellular resolution also in the major target organs. This is particularly relevant when aiming for combination targeting of different cell populations with distinct ligand-functionalized nanoparticles.

These findings do not rule out that targeted nanoparticles have therapeutic effects in mouse tumor models as indicated by numerous studies using MSNs and other nanomaterials⁴³⁻⁴⁶. Our findings, however, indicate that these therapeutic effects may not always be due to a direct nanoparticle-mediated tumor killing but may also involve bystander effects such as cytotoxicity of tissue-resident phagocytic cells, immune-modulatory effects, and unspecific drug release from nanoparticles in the liver into the circulation. Some of these effects may have even been mitigated in previous studies due to the use of immunocompromised mice. As recently outlined by Wilhelm and Torrice^{47,48}, numbers of contradictory reports on *in vivo* tumor targeting efficiency of nanomedicines are on the rise and may explain the ineffective translation of nanomedicines into clinical practice. Our data also suggest that targeting specificity *in vivo* is probably not solely related to the shielding of ligand-receptor interactions on target cells by formation of a protein corona on the nanoparticles^{23,24} as cell-specific targeting was hampered in two distinct biological environments, i.e. the blood and the lung. Our own and other published data indicate that blood-derived serum and the lung lining fluid form distinct protein coronas on nanoparticles *in vitro* (Figure S 7-9)²³. Moreover, protein corona also forms rapidly in cell culture medium containing serum where receptor-mediated targeting was effective (Figure S 7-9). Taken together, our study argues in favor of a stringent validation of cell-specific targeting with cellular-resolution when using nanoparticle-based

targeting strategies. Moreover, closing the translational gap in nanomedicine calls first for physiologically relevant animal models, such as the Kras^{LA2} mice as used here which develop spontaneous lung tumors closely resembling the human situation, and second for rigorous biological testing of nanoparticles using state of the art molecular manipulation of cells and animals critically.

7.4 Experimental Part

Synthesis of the mesoporous silica nanoparticles (MSNs). The core-shell functionalized MSNs have been synthesized by a delayed co-condensation approach resulting in functionalization of the internal pore system with thiol groups and the external particle surface with amino groups. The additional core functionalization offers a site for covalent attachment of fluorescent dyes for particle tracking in *in vitro* and *in vivo* studies. The external amino functionalization was used to attach a linker system with avidin as the bulky gatekeeper. Subsequently, different targeting ligands were covalently attached on the outer periphery of the particles and the synthesized particle system was used for *in vitro* and *in vivo* uptake studies.

Cell culture. The human non-small-cell lung cancer cell lines, A549 and H520, and the mouse alveolar macrophage cell line; MH-S; were obtained from American Type Culture Collection. A549 cells were maintained in DMEM medium supplemented with 10% FBS and 1% Pen/Strep. H520 and MH-S cells were maintained in RPMI 1640 medium supplemented with 10% FBS and 1% Pen/Strep. MH-S cells were further supplemented with 1 mM sodium pyruvate, 10 mM HEPES, and 50 μ M β -mercaptoethanol (all AppliChem). All cells were grown at 37°C in a sterile humidified atmosphere containing 5% CO₂.

Animal models. *Syngeneic flank tumor models.* C57BL/6 mice were obtained from Jackson Laboratories (Bar Harbor) and were bred at the Center for Animal Models of Disease of the University of Patras. Experiments were approved a priori by the Veterinary Administration of the Prefecture of Western Greece, and were conducted according to Directive 2010/63/EU. Experimental mice were sex-, weight-, and age-matched. For induction of solid tumors, mice were anesthetized using isoflurane inhalation and received s.c. injections of 100 μ L PBS containing 0.5×10^6 LLC or B16F10 clones.

Transgenic lung cancer model. 129S/Sv-Kras^{tm3Tyj/J} (Kras^{LA2}) mutant mice were obtained from the Jackson Laboratory, USA, and cross-bred with FVB-NCrl WT females obtained from Charles River Laboratories, Germany, for over seven generations. Animals were kept in rooms maintained at constant temperature and humidity with a 12/12 h light/dark cycle and were allowed food and water *ad libitum*. Animal experiments were carried out according to the German law of protection of animal life and were approved by an external review committee for laboratory animal care.

In vivo biodistribution studies. *Intravenous application.* Two weeks after s.c. inoculation of EGFR-abundant and EGFR-scarce LLC and B16F10 tumor clones, 1 mg ATTO 633-labeled MSN_{AVI} or MSN_{GE11} was applied to each mouse retro-orbitally. The mice were sacrificed with an overdose of isoflurane three days after the administration.

Intratracheal application. 12 week-old Kras^{LA2} mutant mice were intratracheally instilled with ATTO 633-labeled targeted or non-targeted MSNs, as described by Stoeger *et al* ²⁹. Three days post-instillation, the mice were sacrificed with an overdose of ketamine (188.3 mg/kg) and xylazin hydrochloride (4.1 mg/kg) (bela-pharm). Lung lobes from each group (n=5 mice per group) were excised and prepared for cryoslicing.

Histological preparations and immunofluorescence imaging. For the intravenous systemic delivery experiment, internal organs as well as flank tumors were dissected and placed in 4% PFA overnight after which the suspension medium was exchanged to PBS. Representative parts of the organs were frozen in Tissue-Tek and kept at -80°C . For the intratracheal local delivery experiment, animals were sacrificed and the lungs were perfused via the right ventricle with NaCl solution. Airways were then filled with Tissue-Tek. Later, the lung lobes were separated, transferred into cryomolds, and covered with Tissue-Tek. Samples were left to freeze on dry ice and then stored at -80°C . For both experiments, $5\ \mu\text{m}$ thick cryo-sections were sliced with the cryostat (Zeiss Hyrax C 50) and placed on superfrost plus adhesion slides. Immediately before staining, all cryo-sections were fixed with 4% (w/v) PFA for 10 min, then washed with PBS, and permeabilized with 0.5% Triton-X. The sections were incubated with Roti-Block for 1 h at room temperature, and then incubated with the primary antibody at 4°C overnight; *i.e.* EGFR (Abcam, ab52894) and CCR2 (Novus Biologicals, NBP1-48338). Afterwards, the sections were washed with PBS, incubated with Alexa Fluor 488 secondary antibody for 1 h at room temperature. After another PBS wash, the sections were finally stained with DAPI. In case phalloidin staining was used, the sections were first incubated with phalloidin for 45 min and then with DAPI for 10 min at room temperature directly after the fixation and washing step. The sections were mounted using fluorescence mounting medium (DAKO) and analyzed using confocal microscopy (LSM710, Carl Zeiss). Quantification of the cellular uptake of the MSNs in the tissues was conducted using the IMARISx64 software (version 7.6.4, Bitplane).

7.5 References

1. Torchilin, V. P. Multifunctional, stimuli-sensitive nanoparticulate systems for drug delivery. *Nat. Rev. Drug Discov.* **13**, 813–827 (2014).
2. Peer, D. *et al.* Nanocarriers as an emerging platform for cancer therapy. *Nat. Nanotechnol.* **2**, 751–760 (2007).
3. Min, Y., Caster, J. M., Eblan, M. J. & Wang, A. Z. Clinical Translation of Nanomedicine. *Chem. Rev.* **115**, 11147–90 (2015).
4. Master, A. M. & Sen Gupta, A. EGF receptor-targeted nanocarriers for enhanced cancer treatment. *Nanomedicine (Lond).* **7**, 1895–906 (2012).
5. Normanno, N. *et al.* Epidermal growth factor receptor (EGFR) signaling in cancer. *Gene* **366**, 2–16 (2006).
6. Ciriello, G. *et al.* Emerging landscape of oncogenic signatures across human cancers. *Nat. Genet.* **45**, 1127–1133 (2013).
7. Mickler, F. M. *et al.* Tuning nanoparticle uptake: live-cell imaging reveals two distinct endocytosis mechanisms mediated by natural and artificial EGFR targeting ligand. *Nano Lett.* **12**, 3417–23 (2012).
8. Quail, D. F. & Joyce, J. A. Microenvironmental regulation of tumor progression and metastasis. *Nat. Med.* **19**, 1423–37 (2013).
9. McAllister, S. S. & Weinberg, R. A. The tumour-induced systemic environment as a critical regulator of cancer progression and metastasis. *Nat. Cell Biol.* **16**, 717–27 (2014).
10. Wolchok, J. & Chan, T. Cancer: Antitumour immunity gets a boost. *Nature* **515**, 496–498 (2014).
11. Sharma, P. & Allison, J. P. The future of immune checkpoint therapy. *Science (80-.).* **348**, 56–61 (2014).
12. Conde, J. *et al.* Dual targeted immunotherapy via in vivo delivery of biohybrid RNAi-peptide nanoparticles to tumour-associated macrophages and cancer cells. *Adv. Funct. Mater.* **25**, 4183–4194 (2015).
13. Shao, K. *et al.* Nanoparticle-Based Immunotherapy for Cancer. *ACS Nano* **9**, 16–30 (2015).
14. Patil, R. *et al.* MRI virtual biopsy and treatment of brain metastatic tumors with targeted nanobioconjugates: nanoclinic in the brain. *ACS Nano* **9**, 5594–608 (2015).

15. Lu, Y. *et al.* SiRNA delivered by EGFR-specific scFv sensitizes EGFR-TKI-resistant human lung cancer cells. *Biomaterials* **76**, 196–207 (2016).
16. Brinkman, A. M. *et al.* Aminoflavone-loaded EGFR-targeted unimolecular micelle nanoparticles exhibit anti-cancer effects in triple negative breast cancer. *Biomaterials* **101**, 20–31 (2016).
17. Nascimento, A. V. *et al.* Biodistribution and pharmacokinetics of Mad2 siRNA-loaded EGFR-targeted chitosan nanoparticles in cisplatin sensitive and resistant lung cancer models. *Nanomedicine (Lond)*. **11**, 767–781 (2016).
18. Taratula, O., Kuzmov, A., Shah, M., Garbuzenko, O. B. & Minko, T. Nanostructured lipid carriers as multifunctional nanomedicine platform for pulmonary co-delivery of anticancer drugs and siRNA. *J. Control. Release* **171**, 349–357 (2013).
19. Sadhukha, T., Wiedmann, T. S. & Panyam, J. Inhalable magnetic nanoparticles for targeted hyperthermia in lung cancer therapy. *Biomaterials* **34**, 5163–5171 (2013).
20. Bölükbas, D. A. & Meiners, S. Lung cancer nanomedicine: potentials and pitfalls. *Nanomedicine (Lond)*. **10**, 3203–12 (2015).
21. Li, Z. *et al.* Identification and characterization of a novel peptide ligand of epidermal growth factor receptor for targeted delivery of therapeutics. *FASEB J.* **19**, 1978–1985 (2005).
22. Auvynet, C. *et al.* ECL1i, d(LGTFLKC), a novel, small peptide that specifically inhibits CCL2-dependent migration. *FASEB J.* (2016). doi:10.1096/fj.201500116
23. Tenzer, S. *et al.* Rapid formation of plasma protein corona critically affects nanoparticle pathophysiology. *Nat. Nanotechnol.* **8**, 772–81 (2013).
24. Salvati, A. *et al.* Transferrin-functionalized nanoparticles lose their targeting capabilities when a biomolecule corona adsorbs on the surface. *Nat. Nanotechnol.* **8**, 137–43 (2013).
25. Hadjidemetriou, M. *et al.* In Vivo Biomolecule Corona around Blood-Circulating, Clinically Used and Antibody-Targeted Lipid Bilayer Nanoscale Vesicles. *ACS Nano* **9**, 8142–8156 (2015).
26. Raesch, S. S. *et al.* Proteomic and Lipidomic Analysis of Nanoparticle Corona upon Contact with Lung Surfactant Reveals Differences in Protein, but Not Lipid Composition. *ACS Nano* **9**, 11872–11885 (2015).

27. Mirshafiee, V., Mahmoudi, M., Lou, K., Cheng, J. & Kraft, M. L. Protein corona significantly reduces active targeting yield. *Chem. Commun. (Camb)*. **49**, 2557–9 (2013).
28. Pisani, C. *et al.* The timeline of corona formation around silica nanocarriers highlights the role of the protein interactome. *Nanoscale* (2016). doi:10.1039/c6nr04765c
29. Stoeger, T. *et al.* Instillation of six different ultrafine carbon particles indicates a surface area threshold dose for acute lung inflammation in mice. *Environ. Health Perspect.* **114**, 328–333 (2006).
30. Sharma, S. V, Bell, D. W., Settleman, J. & Haber, D. A. Epidermal growth factor receptor mutations in lung cancer. *Nat. Rev. Cancer* **7**, 169–181 (2007).
31. de Mello, R. A., Marques, D. S., Medeiros, R. & Araújo, A. M. Epidermal growth factor receptor and K-Ras in non-small cell lung cancer-molecular pathways involved and targeted therapies. *World J. Clin. Oncol.* **2**, 367–76 (2011).
32. Quatromoni, J. G. & Eruslanov, E. Tumor-associated macrophages: function, phenotype, and link to prognosis in human lung cancer. *Am. J. Transl. Res.* **4**, 376–89 (2012).
33. Schmall, A. *et al.* Macrophage and Cancer Cell Cross-talk via CCR2 and CX3CR1 Is a Fundamental Mechanism Driving Lung Cancer. *Am. J. Respir. Crit. Care Med.* **191**, 437–447 (2015).
34. Hiratsuka, S. *et al.* Primary tumours modulate innate immune signalling to create pre-metastatic vascular hyperpermeability foci. *Nat. Commun.* **4**, 1853 (2013).
35. Fritz, J. M. *et al.* Depletion of tumor-associated macrophages slows the growth of chemically induced mouse lung adenocarcinomas. *Front. Immunol.* **5**, 1–11 (2014).
36. Qian, B.-Z. *et al.* CCL2 recruits inflammatory monocytes to facilitate breast-tumour metastasis. *Nature* **475**, 222–5 (2011).
37. Cauda, V., Schlossbauer, A., Kecht, J., Zürner, A. & Bein, T. Multiple core-shell functionalized colloidal mesoporous silica nanoparticles. *J. Am. Chem. Soc.* **131**, 11361–11370 (2009).

38. Johnson, L. *et al.* Somatic activation of the K-ras oncogene causes early onset lung cancer in mice. *Nature* **410**, 1111–1116 (2001).
39. Zitvogel, L., Pitt, J. M., Daillère, R., Smyth, M. J. & Kroemer, G. Mouse models in oncoimmunology. *Nat. Rev. Cancer* **16**, 759–773 (2016).
40. Martin, P., Leighl, N. B., Tsao, M. S. & Shepherd, F. a. KRAS mutations as prognostic and predictive markers in non-small cell lung cancer. *J Thorac Oncol* **8**, 530–542 (2013).
41. Srinivasarao, M., Galliford, C. V. & Low, P. S. Principles in the design of ligand-targeted cancer therapeutics and imaging agents. *Nat. Rev. Drug Discov.* **14**, 1–17 (2015).
42. Lambrecht, B. N. Alveolar Macrophage in the Driver's Seat. *Immunity* **24**, 366–368 (2006).
43. Liu, X. *et al.* Irinotecan Delivery by Lipid-Coated Mesoporous Silica Nanoparticles Shows Improved Efficacy and Safety over Liposomes for Pancreatic Cancer. *ACS Nano* **10**, 2702–2715 (2016).
44. Meng, H. *et al.* Use of size and a copolymer design feature to improve the biodistribution and the enhanced permeability and retention effect of doxorubicin-loaded mesoporous silica nanoparticles in a murine xenograft tumor model. *ACS Nano* **5**, 4131–4144 (2011).
45. Wagner, E. Programmed drug delivery: nanosystems for tumor targeting. *Expert Opin. Biol. Ther.* **7**, 587–93 (2007).
46. Davis, M. E. *et al.* Evidence of RNAi in humans from systemically administered siRNA via targeted nanoparticles. *Nature* **464**, 1067–70 (2010).
47. Wilhelm, S. *et al.* Analysis of nanoparticle delivery to tumours. *Nat. Rev. Mater.* **1**, 16014 (2016).
48. Torrice, M. Does nanomedicine have a delivery problem? *ACS Cent. Sci.* **2**, 434–437 (2016).

7.6 Appendix

Materials. Tetraethyl orthosilicate (TEOS, Fluka, > 98%), triethanolamine (TEA, Aldrich, 98%), cetyltrimethylammonium chloride (CTAC, Fluka, 25% in H₂O), mercaptopropyl triethoxysilane (MPTES, Fluka, > 80%), aminopropyltriethoxysilane (APTES, Sigma Aldrich, 99%), ammonium fluoride (NH₄F, Fluka), ammonium nitrate (NH₄NO₃, Fluka), hydrochloric acid (HCl, 37%), oxalic acid dehydrate (Alfa, 98%), ECL(1) peptide (CKLFTGL, GenScript), GE11 peptide (YHWYGYTPQNVI, GenScript), recombinant EGF (Peprotech, 315-09), *N*-(3-dimethylaminopropyl)-*N*'-ethylcarbodiimide hydrochloride (EDC, Aldrich), *N*-hydroxysulfosuccinimide sodium salt (sulfoNHS, Aldrich), 3,9-bis(3-aminopropyl)-2,4,8,10-tetraoxaspiro-[5,5]-undecane (AK-linker), biotin (Aldrich), avidin from egg white (Merck, Calbiochem), ATTO 633-mal and ATTO 488-mal (ATTO-TEC), 2-iminothiolan hydrochloride (Aldrich, > 98%), O-[*N*-(6-maleimidohexanoyl)aminoethyl]-O'-[3-(*N*-succinimidylloxy)-3-oxopropyl] polyethylene glycol₃₀₀₀ (Aldrich), β -actin antibody (Cell Signaling), secondary Alexa fluor antibodies (Invitrogen), and phalloidin (Life Technologies), Tissue-Tek (Sakura), superfrost plus adhesion slides (Thermo Scientific), Entellan (Merck), Roti®-ImmunoBlock (Roti-Block, Carl Roth), penicillin/streptomycin (Pen/Strep, Life Technologies), fetal bovine serum (FBS, Biochrom), Triton-X (AppliChem), cOmplete protease inhibitor cocktail (Sigma-Aldrich), Pierce Silver Stain Kit (Thermo Scientific), and DAPI (Sigma-Aldrich) were used as received. Ethanol (Aldrich, absolute), sodium chloride (NaCl, Braun Vet Care), dimethylsulfoxide (DMSO, Aldrich), and DMEM, RPMI 1640, HBSS (Gibco, Life Technologies) were used as solutions without further purification. Ultrapure water was obtained from a Millipore system (Milli-Q Academic A10).

Human tissue. The stainings with human tissue were approved by the Ethics Committee of the Ludwig-Maximilians-University Munich, Germany (LMU, project no. 455-12). All samples were provided by the Asklepios Biobank for Lung Diseases, Gauting, Germany (project no. 333-10). Written informed consent was obtained from all subjects.

Immunohistochemistry. Lung tumor specimens from human and $Kras^{LA2}$ mutant mice were placed in 4% (w/v) paraformaldehyde (PFA) overnight at 4°C and processed for paraffin embedding. 3 µm thick paraffin sections were sliced with the microtome (Zeiss Hyrax M 55) and placed on superfrost plus adhesion slides. Deparaffinized sections were subjected to quenching of endogenous peroxidase activity using a mixture of methanol/H₂O₂ for 20 min, followed by antigen retrieval in a decloaking chamber. From this step on, the slides were washed with TBST (20 mM Tris, 0.8% NaCl, 0.02% Tween-20, pH 7.6 adjusted with HCl) after each incubation with the reagents throughout the procedure. The sections were incubated first with Rodent Block M (Zytomed Systems) for 30 min and then with the primary antibody, i.e., EGFR (Cell Signaling, D38B1 for human, Abcam, ab52894 for mouse), CCR2 (Novus Biologicals, NB110-55674), or IgG control for 1 h. The cuts were then incubated with Rabbit on Rodent AP-Polymer for 30 min, which was followed by Vulcan Fast Red AP substrate solution (both Biocare Medical) incubation for 10-15 min. Sections were counterstained with hematoxylin (Carl Roth) and dehydrated respectively in consecutively grading ethanol and xylene (both Appli-Chem) incubations. Dried slides were mounted in Entellan.

Synthesis of core-shell functionalized mesoporous silica nanoparticles (MSN-SH_{in}-NH_{2,out}). A mixture of tetraethyl orthosilicate (TEOS, 1.63 g, 7.82 mmol), mercaptopropyl triethoxysilane (MPTES, 112 mg, 0.48 mmol) and triethanolamine (TEA, 14.3 g, 95.6 mmol) was heated under static conditions at 90 °C for 20 min in a polypropylene reactor. Then, a solution of cetyltrimethylammonium chloride (CTAC, 2.41 mL, 1.83 mmol, 25 wt% in H₂O) and ammonium fluoride (NH₄F, 100 mg, 2.70 mmol) in H₂O (21.7 g, 1.21 mmol) was

preheated to 60 °C, and rapidly added to the TEOS solution. The reaction mixture was stirred vigorously (700 rpm) for 20 min while cooling down to room temperature. Subsequently, TEOS (138.2 mg, 0.922 mmol) was added in four equal increments every three minutes. After another 30 min of stirring at room temperature, TEOS (19.3 mg, 92.5 μmol) and aminopropyl triethoxysilane (APTES, 20.5 mg, 92.5 μmol) were added to the reaction. The resulting mixture was then allowed to stir at room temperature overnight. After addition of ethanol (100 mL), the MSNs were collected by centrifugation (7000 rcf, for 20 min) and re-dispersed in absolute ethanol. The template extraction was performed by heating the MSN suspension under reflux (90 °C, oil bath temperature) for 45 min in an ethanol solution (100 mL) containing ammonium nitrate (NH₄NO₃, 2 g), followed by 45 min heating under reflux in a mixture of concentrated hydrochloric acid (HCl, 10 mL) and absolute ethanol (90 mL). The mesoporous silica nanoparticles were collected by centrifugation and washed with absolute ethanol after each extraction step (SI Figure 1A(i)).

Synthesis of MSN_{COOH}. A large excess of oxalic acid (10 mg, 110 μmol) was dissolved in 2 mL water and activated with EDC (18 μL, 102 μmol) and a catalytic amount of sulfoNHS (1 mg) for 10 minutes at room temperature. The premixed solution was added dropwise to 100 mg MSN-SH_{in}-NH_{2,out} particles dissolved in 15 mL ethanol under vigorous stirring. The mixture was stirred at room temperature overnight. Afterwards the solution was centrifuged at 7000 rcf for 10 minutes, washed two times with ethanol and redispersed in 10 mL ethanol (SI Figure 1A(i)).

Synthesis of MSN_{AK}. 25 mg of MSN-COOH were diluted in 15 mL ethanol. Subsequently, 10 μL N-(3-dimethylaminopropyl)-N'-ethylcarbodiimide hydrochloride (EDC, 57 μmol) and 3.1 mg of N-hydroxysulfosuccinimide (sulfo-NHS, 14.3 μmol) were added and the mixture was stirred for 15 minutes at room temperature. A premixed solution containing of 3.5 mg

3,9-bis(3-aminopropyl)-2,4,8,10-tetraoxaspiro-[5,5]-undecane AK-Linker (13 μmol) in 3 mL of a 1/1 mixture ethanol/DMSO were added dropwise over a period of 10 minutes and the resulting solution was stirred over night at room temperature. The functionalized MSN_{AK} particles were separated by centrifugation (7000 rcf, 20 minutes), washed two times with ethanol and redispersed in 15 mL ethanol (SI Figure 1A(i)).

Synthesis of $\text{MSN}_{\text{Biotin}}$. A premixed solution of 1 mg biotin (4.1 μmol), 1 μL N-(3-dimethylaminopropyl)-N'-ethylcarbodiimide hydrochloride (EDC, 5.7 μmol) and 1.2 mg N-hydroxysulfosuccinimide (sulfo-NHS, 5.7 μmol) were added to 10 mg of MSN_{AK} particles in 5 mL ethanol and stirred overnight at room temperature. After centrifugation (7000 rcf, 20 minutes) and washing two times with ethanol, $\text{MSN}_{\text{Biotin}}$ particles were separated by centrifugation and redispersed in 5 mL ethanol (SI Figure 1A(i)).

Dye-labeling of $\text{MSN}_{\text{Biotin}}$. 1 mg $\text{MSN}_{\text{Biotin}}$ were diluted in 1 mL ethanol and 1 μL ATTO 633- or ATTO 488- maleimide (0.5 mg/mL in DMF) was added. The mixture was reacted for 12 h overnight in the dark. Afterwards the particles were centrifuged (7000 rcf, 5 min), washed twice with ethanol and resuspended in HBSS buffer to give a 1 mg/mL particle concentration (SI Figure 1A(ii)).

Synthesis of MSN_{AVI} . After centrifugation (14000 rpm, 4 minutes) the loaded or non-loaded residue ($\text{MSN}_{\text{Biotin}}$) was redispersed in a solution containing of 1 mg avidin from egg white in 1 mL HBSS buffer solution and stored for 1 h at room temperature in the dark without stirring. The resulting suspension was then centrifuged (5000 rcf, 4 minutes, cooled) and washed several times with buffer solution. Subsequently, the particles were finally redispersed in 1 mL of the corresponding buffer solution and used for the following experiments (SI Figure 1A(ii)).

Addition of the targeting ligands to synthesize MSN_{GE11}, MSN_{EGF}, and MSN_{ECL1i}. 1 mg of cargo-loaded and/or dye-labeled MSN_{AVI} particles were centrifuged (5000 rcf, 4 minutes, cooled) and redispersed in 500 μ L HBSS buffer solution. In the meantime, 50 μ L of the corresponding targeting ligand (GE11, EGF, ECL1i) dissolved in bi-distilled water (100 μ g/mL) were added to 200 μ L HBSS and 0.2 mg 2-iminothiolan hydrochloride (1.5 μ mol). The mixture was reacted for 1 h at room temperature without stirring. Subsequently, 0.3 mg of the hetero-bifunctional PEG-linker mal-PEG₃₀₀₀-NHS was added and the mixture was allowed to react for 1 h at room temperature. The activated PEG-targeting ligand was then added to the MSN_{AVI} particle solution, reacted for 1 h, centrifuged (5000 rcf, 4 minutes, cooled) and washed three times with HBSS. 1 mg of MSN_{GE11}, MSN_{EGF}, and MSN_{ECL1i} were redispersed in 1 mL HBSS, respectively (SI Figure 1A(iii)).

Characterization methods. Dynamic light scattering (DLS) and zeta potential measurements were performed on a Malvern Zetasizer-Nano instrument equipped with a 4 mW He-Ne laser (633 nm) and an avalanche photodiode detector. DLS measurements were directly recorded in diluted colloidal aqueous suspensions of the MSNs at a constant concentration of 0.5 mg/mL for all sample solutions. Zeta potential measurements were performed using the add-on Zetasizer titration system (MPT-2), based on diluted NaOH and HCl as titrants. For this purpose, 0.5 mg of the MSN sample was diluted in 10 mL bi-distilled water. Transmission electron microscopy (TEM) was performed at 300 kV on an FEI Titan 80-300 equipped with a field emission gun. For sample preparation, the colloidal solution of MSNs was diluted in absolute ethanol, and one drop of the suspension was then deposited on a copper grid sample holder. The solvent was allowed to evaporate. Thermogravimetric analyses (TGA) of the extracted bulk samples (approximately 10 mg) were recorded on a Netzsch STA 440 C TG/DSC. The measurements proceeded at a heating rate of 10 $^{\circ}$ C/min up to 900 $^{\circ}$ C, in a stream of synthetic air of about 25 mL/min. Nitrogen sorption measurements were performed

on a Quantachrome Instrument NOVA 4000e at $-196\text{ }^{\circ}\text{C}$. Sample outgassing was performed for 12 hours at a vacuum of 10 mTorr at $120\text{ }^{\circ}\text{C}$ or room temperature. Pore size and pore volume were calculated with an NLDFT equilibrium model of N_2 on silica, based on the desorption branch of the isotherms. In order to remove the contribution of the interparticle textural porosity, pore volumes were calculated only up to a pore size of 8 nm. A BET model was applied in the range of $0.05 - 0.20\text{ } p/p_0$ to evaluate the specific surface area. Infrared spectra were recorded on a ThermoScientific Nicolet iN10 IR-microscope in reflection-absorption mode with a liquid- N_2 cooled MCT-A detector. For time-based release experiments of propidium iodide, the loaded and avidin-capped particles were redispersed in the corresponding buffer solutions ($\text{pH} = 7$ and $\text{pH} = 5$) and stored at $37\text{ }^{\circ}\text{C}$ on a thermo shaker. After certain time-points (4 h, 24 h, 48 h) the particles were centrifuged (5000 rcf, 4 minutes, cooled) and the supernatant was measured on a UV/VIS Thermo Scientific NanoDrop 2000c system.

Characterization of the functionalized MSNs. The core-shell functionalized MSNs have been synthesized by a delayed co-condensation approach, resulting in functionalization of the internal pore system with thiol groups and the external particle surface with amino groups. The additional core functionalization offers a site for covalent attachment of fluorescent dyes for particle tracking, which is important for particle tracking in *in vitro* and *in vivo* studies. The synthesized core-shell functionalized MSNs reveal average sizes of about 100 nm as derived from transmission electron microscopy (TEM, SI Figure 1B). The TEM image shows a spherical particle shape and a worm-like pore structure. Nitrogen sorption measurements were performed to gain information about the porosity and the surface area of the functionalized MSNs. SI Figure 1D shows a typical type IV isotherm for the native core-shell functionalized $\text{MSN-SH}_{\text{in}}\text{-NH}_{2,\text{out}}$ with an inflection point at around $0.3\text{ } p/p_0$, indicating a mesoporous structure for these sample. Until the biotinylated stage ($\text{MSN}_{\text{Biotin}}$) the pore

structure remains accessible with surface areas of up to about 800 m²/g and a pore volume of 0.6 cm³/g. The narrow pore size distribution, with a maximum at around 3.6 nm, also confirmed an accessible porous system even after modification with the acetal and the biotin linkers (SI Figure 1D inset). Furthermore, nitrogen sorption isotherms showed a small hysteresis loop at around 0.9 p/p₀ for these two samples, which is attributed to interparticle textural porosity. A summary of the porosity parameters is given in SI Figure 1H. A drastic reduction in specific surface area and a loss in pore volume occurred for the MSNs containing the avidin capping (MSN_{AVI}). After the attachment of avidin to the silica nanoparticle surface, we obtained a type II isotherm and no visible pore size distribution, indicating successful sealing of the pores. Thermogravimetric analyses showed stepwise additional weight loss for the different samples (SI Figure 1E). The native core-shell functionalized MSNs reveal a weight loss of 17 % due to template residues and the organosilanes. Efficient attachment of the short organic linkers up to the biotinylated stage (MSN_{Biotin}) and the bulky protein avidin in the sample MSN_{AVI} (+ 5 % and + 65 % additional weight loss, respectively) was confirmed. To gain more information about the successful attachment of the different functional moieties FTIR-spectroscopy was used. The signals were normalized to the most intense absorbance of silica (SI Figure 1F). All of the synthesized samples show the characteristic silica stretching vibrations of the Si-O-Si network between 1000 and 1300 cm⁻¹. The two additional bands at 780 and 900 cm⁻¹ can be assigned to asymmetric stretching and bending vibrations of the Si-O-H groups. The biotinylated stage shows an intensive peak for the carbonyl stretching vibration at 1710 cm⁻¹ due to the different functional linker compounds attached on the surface. In the spectrum for the avidin-capped particle system, the typical broad amide vibrations (Amide I: C=O stretching vibration, Amide II: N-H deformation + C-N stretching vibration) can be seen in the region between 1500 and 1650 cm⁻¹. Also increasing intensities of C-H stretching vibrations at 2900 cm⁻¹ from the different

organic moieties are visible for the different functionalization stages. Therefore, a successful implementation of the biotin-functionalization as well as the avidin-capping can be concluded. The zeta potential measurements also correlate with the stepwise addition of the linkers and avidin as the bulky gatekeeper (SI Figure 1G). The shift of the isoelectric point towards 5.11 after carboxylic acid-functionalization can be explained with the attachment of negatively charged carboxylate groups. With addition of the AK-linker and biotin, the IEP shifts towards higher pH values. By adding the avidin capping, the outer surface is positively charged over the whole measured pH range because of the exceptional amount of cationic amino acids in the protein structure. The IEP is at 9.81, which is in good accordance to the literature value for avidin (9.99)¹. Dynamic light scattering (DLS) measurements in aqueous media revealed a mean particle size of 170 nm (SI Figure 1I) and good colloidal stability for all samples. This apparent difference in particle size, compared to TEM, is attributed to the involvement of the hydrodynamic diameter and weak transient agglomeration of a few nanoparticles during the DLS measurements. Importantly, a narrow particle size distribution and no significant agglomeration were observed after the complete synthesis functionalization steps. The sample MSN_{AVI}, as well as the samples with the different targeting ligands (MSN_{GE11}, MSN_{EGF}, MSN_{ECL11}) reveal nice colloidal stability in aqueous solution as well as in healthy and cancerous mucus conditions (SI Figure 1J). UV-VIS loading capacity measurements showed an average propidium iodide loading of 0.365 mg/mg MSNs. pH-responsive release of PI in different buffer solutions reveal an time-dependent release behavior with an average release of about 60 % after 48 h at pH 5 (SI Figure 1K).

Western blotting. A549, H520, and MH-S cells were lysed in RIPA buffer (50 mM Tris-HCl, pH 7.5, 150 mM NaCl, 1% NP-40, 0.5% sodium deoxycholate, 0.1% SDS) supplemented with protease inhibitor cocktail (Complete, Roche). Protein content was determined using the Pierce BCA protein assay kit (Thermo Scientific). For Western blot

analysis, equal amounts of protein were subjected to electrophoresis on 10% SDS-PAGE gels and blotted onto PVDF membranes (Bio-Rad). Membranes were treated with antibodies using standard Western blot techniques. The ECL Plus detection reagent (GE Healthcare) was used for chemiluminescent detection and the membranes were analyzed with the ChemiDoc XRS+ (Bio-Rad).

Immunocytofluorescence. A549, H520, and MH-S cells which were grown on coverslips were treated with ATTO 633-labeled nanoparticles for 1 h. Afterwards, the cells were washed three times with phosphate buffered saline (PBS), then once with NaCl (0.15 M, pH 3.0), and then three times with PBS. Cells were fixed with 70% ethanol and permeabilized with 0.1% Triton-X. After another PBS wash, cells were incubated with Roti-Block for 1 h at room temperature (RT). Afterwards, A549 and H520 cells were stained with EGFR antibody (Abcam, ab52894), whereas MH-S cells were stained with CCR2 antibody (Novus Biologicals, NB110-55674) overnight at 4°C. The following day, the cells were incubated with the Alexa Fluor secondary antibodies for 1 h at RT, washed with PBS, incubated with DAPI for 10 min for nuclear staining, and then mounted with fluorescent mounting medium (Dako).

Flow cytometry. 5×10^5 A549, H520, and MH-S cells were plated on 6 well plates and incubated overnight. The next day, the cells were treated with ATTO 488- or ATTO 633-labeled nanoparticles for 1 h. Afterwards, the cells were washed three times with PBS, once with NaCl (0.15 M, pH 3.0), and then three times with PBS again to create a final cell suspension. Samples were then analyzed by flow cytometry (BD LSR II). MSN uptake in different cell types was quantified by the median fluorescence signal collected in the Alexa Fluor 488 or 647 channels.

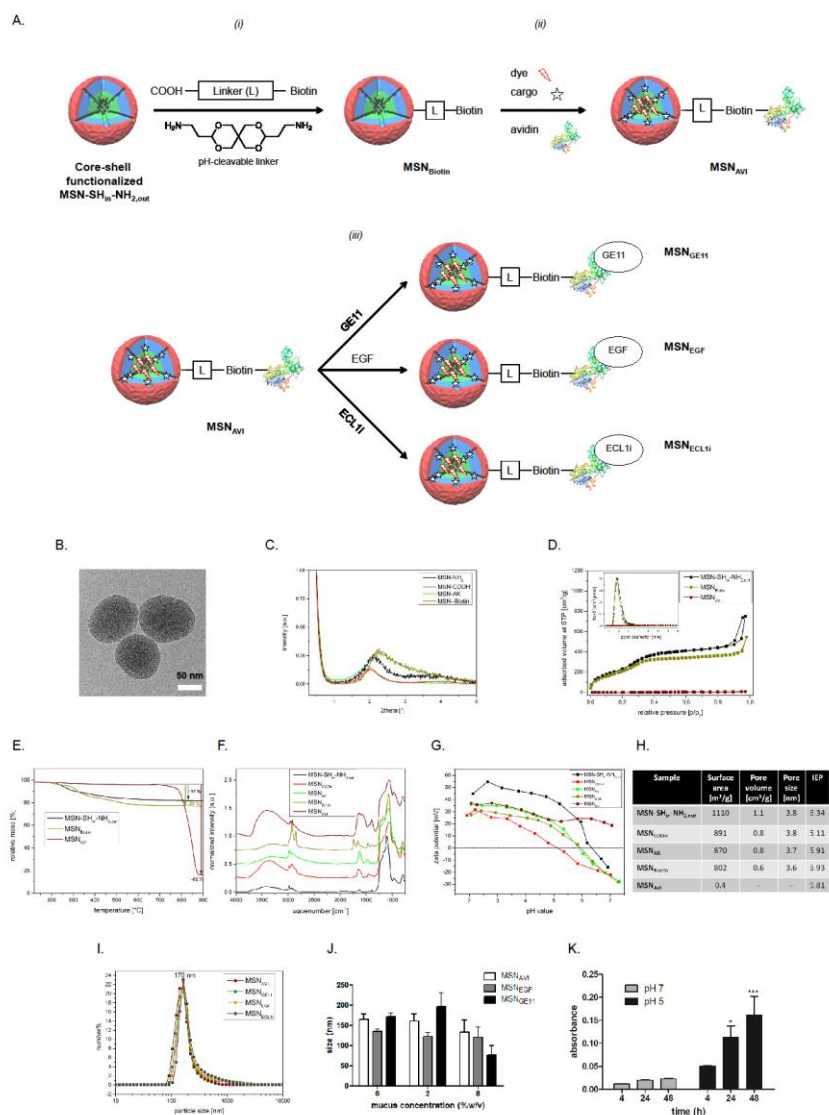
Genetic engineering for flank tumor models. C57BL/6 mouse Lewis lung carcinoma (LLC) and B16F10 skin melanoma cells were obtained from the NCI Tumor Repository (Frederick). For RNA interference, the following proprietary lentiviral shRNA pools were obtained from Santa Cruz Biotechnology (Palo Alto): random control shRNA (shC, sc-108080), GFP control (sc-108084), anti-EGFR-shRNA (sc-29302-V), and stable transfections of the LLC and B16F10 cells were generated.

Fluorescence dosimetry of MSNs in organ homogenates. The dose of fluorescence-labeled MSNs (ATTO 633) in the flank tumor and liver was determined with quantitative fluorescence analysis similar to the validated method described by Rijt et al.². Briefly, aliquots of the tissue were dried at low power setting in a microwave oven (SEVERIN, MW7803; 30% power; 270 Watt) until no change of tissue mass was observed anymore. Aliquots of dried tumor and liver tissue (ca. 10 mg) were diluted by 1:90 (w/v) and 1:60 with PBS, respectively (*i.e.* 1 mg of dried tissue was diluted by 89 and 59 μ L PBS, respectively). The diluted samples were mechanically homogenized with a high-performance disperser (T10 basic ULTRA-TURRAX®) at RT until no tissue pieces were visible anymore (ca. 3-5 min with short breaks to avoid undue heating of the samples). Residual tissue was rinsed off the disperser using 200 μ L of PBS. Samples were vortexed immediately prior to pipetting four 75 μ L aliquots (quadruple determination) from each of the samples into a black 96-well plate for quantitative fluorescence analysis with a standard multiwell plate reader (Tecan, Safire 2; excitation and emission wavelengths: 630 nm and 660 nm). The fluorescence signals were related to the corresponding MSN mass using standard curves, which were prepared from blank liver and flank tumor tissues of non-exposed mice spiked with known amount of MSN and processed according to the same protocol described above (cage control). The prerequisite for reliable dosimetry is that the homogenization and drying process does not destroy the fluorescence signal of MSN_{GE11} and MSN_{AVI}. This was proven by comparison of fluorescence

signals of homogenates from dried and non-dried samples as well as by adding MSN prior and after homogenization. For analysis of a potential enrichment of MSN_{GE11} over MSN_{AVI} in the tumor, the MSN concentration (MSN mass per mass of tissue) was calculated for both tumor and liver samples.

Characterization of protein corona on nanoparticles. 100 μ g MSN_{AVI} and MSN_{GE11} were shaken overnight (16 h) either in cell culture medium in the presence of 10% FCS, human serum, or murine lung lining fluid (diluted in 1 mL PBS containing cOmplete protease inhibitor cocktail) at room temperature. The suspension was centrifuged and the nanoparticles were resuspended in PBS three times (15,000 rpm, for 30 min, at 4°C). The proteins adsorbed on the pelleted nanoparticles were eluted by incubating them at 95°C for 5 min in Laemmli buffer. The suspension was centrifuged again and the supernatant was subjected to electrophoresis on 10% SDS-PAGE gels. Silver staining was conducted as described in the instructions manual of the Pierce Silver Stain Kit (Thermo Scientific). The gels were scanned with the ChemiDoc XRS+ (Bio-Rad).

7. Cellular resolution is essential for validation of active targeting of nanoparticles in vivo



SI Figure 1

Figure S 7-1. Synthesis scheme and characterization of pH-responsive mesoporous silica nanoparticles (MSNs) with different targeting ligands. (A) Delayed co-condensation process leads to different core (green, thiol groups) and shell (red, amino groups) functionalization of MSN-SH_{in}-NH_{2, out}. (i) In a three step modulation approach, first the amino groups were transformed into carboxy groups. EDC amidation with the pH-cleavable linker and subsequent addition of biotin leads to covalent attachment and results in MSN_{Biotin}. (ii) After cargo loading and covalent attachment of the dyes at the thiol groups in the inner pore system, avidin efficiently seals the mesopores and results in MSN_{AVI}. (iii) On the outer surface different targeting ligands were added (MSN_{GE11}, MSN_{EGF}, MSN_{ECL11}). Characterization of MSNs. (B) Transmission electron micrograph (TEM) of MSN-SH_{in}-NH_{2, out}. Scale bar = 50 nm. (C) Small-angle x-ray scattering (D) Nitrogen sorption isotherms of MSN-SH_{in}-NH_{2, out} (black), MSN_{Biotin} (green) and MSN_{AVI} (red) with

corresponding pore size distributions as inset. (E) Thermogravimetric analysis, (F) Infrared spectroscopy, (G) Zeta potential measurements, (H) Summary of sorption data and isoelectric points for the different functionalization stages, (I) Dynamic light scattering (DLS) of MSN_{AVI} (red), MSN_{GE11} (light green), MSN_{EGF} (orange) and MSN_{ECLi} (grey) in water. (J) Variance in size distribution in healthy (2%) versus cancerous (8%) mucus conditions. (K) Time-dependent pH-responsive percent release statistics at pH 7 and pH 5. * means a significant increase in the release of the cargo at pH 5 compared to pH 7 (** $p < 0.01$). Values given are an average of three independent experiments \pm SEM.

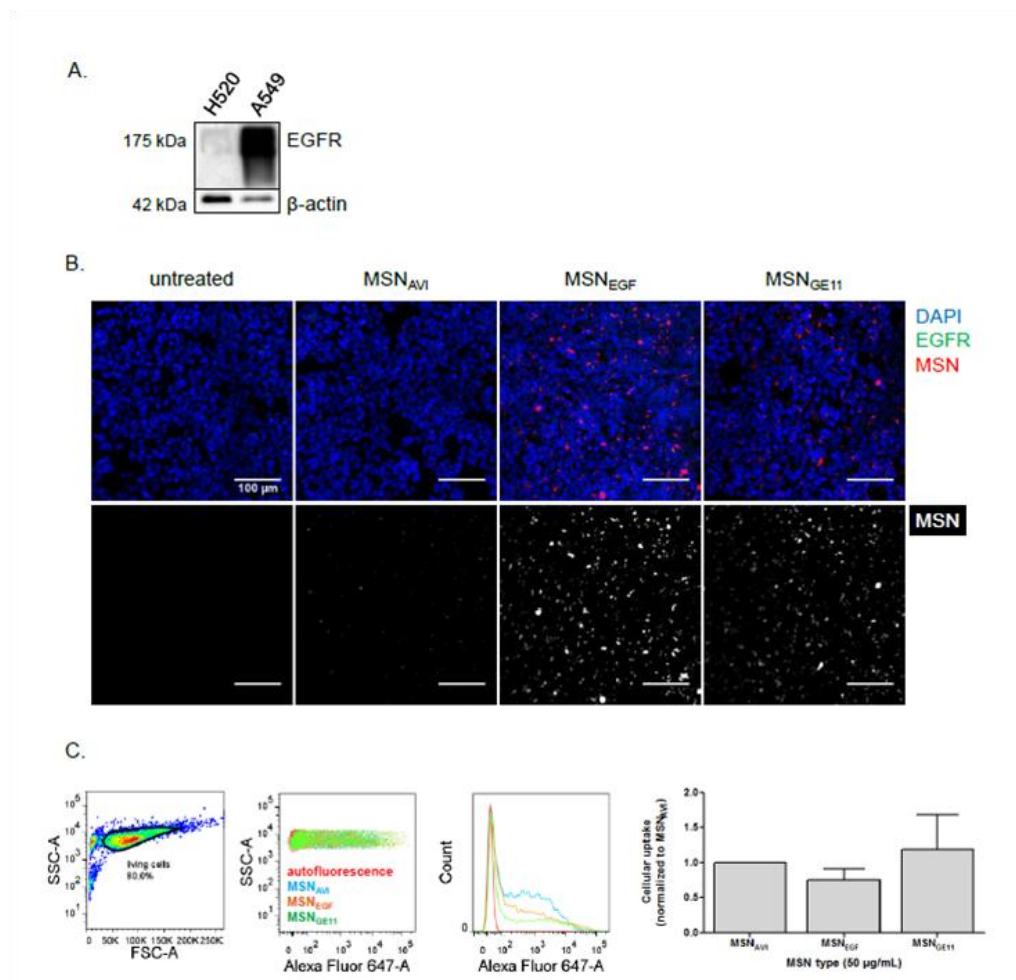


Figure S 7-2. EGFR-targeted MSN uptake in H520 cells *in vitro*. (A) Basal EGFR expression in A549 and in H520 cells at the protein level, assessed by Western blot analysis. (B) EGFR-targeted versus non-targeted uptake of ATTO 633-labeled MSN_{AVI} , MSN_{EGF} , and MSN_{GE11} in 1 h in EGFR-scarce H520 cells co-stained for EGFR by immunofluorescence, measured by confocal microscopy. Nuclear staining (DAPI) is shown in blue, EGFR staining in green, and ATTO 633-labeled MSNs in red in the merged image, and in gray in the single channel for improved resolution. Scale bar = 100 μ m. (C) Quantification of the ATTO 633-labeled MSN_{AVI} , MSN_{EGF} , and MSN_{GE11} uptake in 1 h in H520 cells by flow cytometry analysis. After gating for the viable cells, median fluorescence intensities from the histogram curves were obtained.

7. Cellular resolution is essential for validation of active targeting of nanoparticles *in vivo*

Autofluorescence signals of the untreated cells were blanked from the treated cells. Values given are an average of six independent experiments \pm SEM.

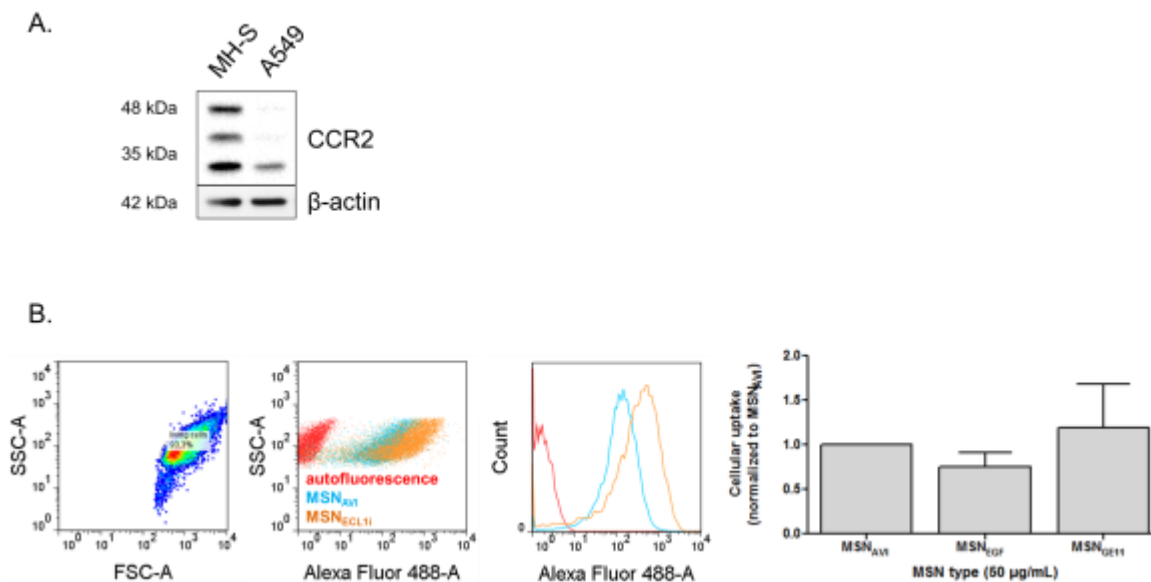


Figure S 7-3. CCR2-targeted MSNs uptake in A549 cells *in vitro*. (A) Basal CCR2 overexpression in MH-S cells *versus* A549 cells at the protein level, assessed by Western blot analysis. (B) Quantification of the ATTO 488- labeled MSN_{AVI} and MSN_{ECLI} uptake in 1 h in CCR2-scarce A549 cells by flow cytometry analysis. After gating for the viable cells, median fluorescence intensities from the histogram curves were obtained. Autofluorescence signals of the untreated cells were blanked from the treated cells. Values given are of a single experiment.

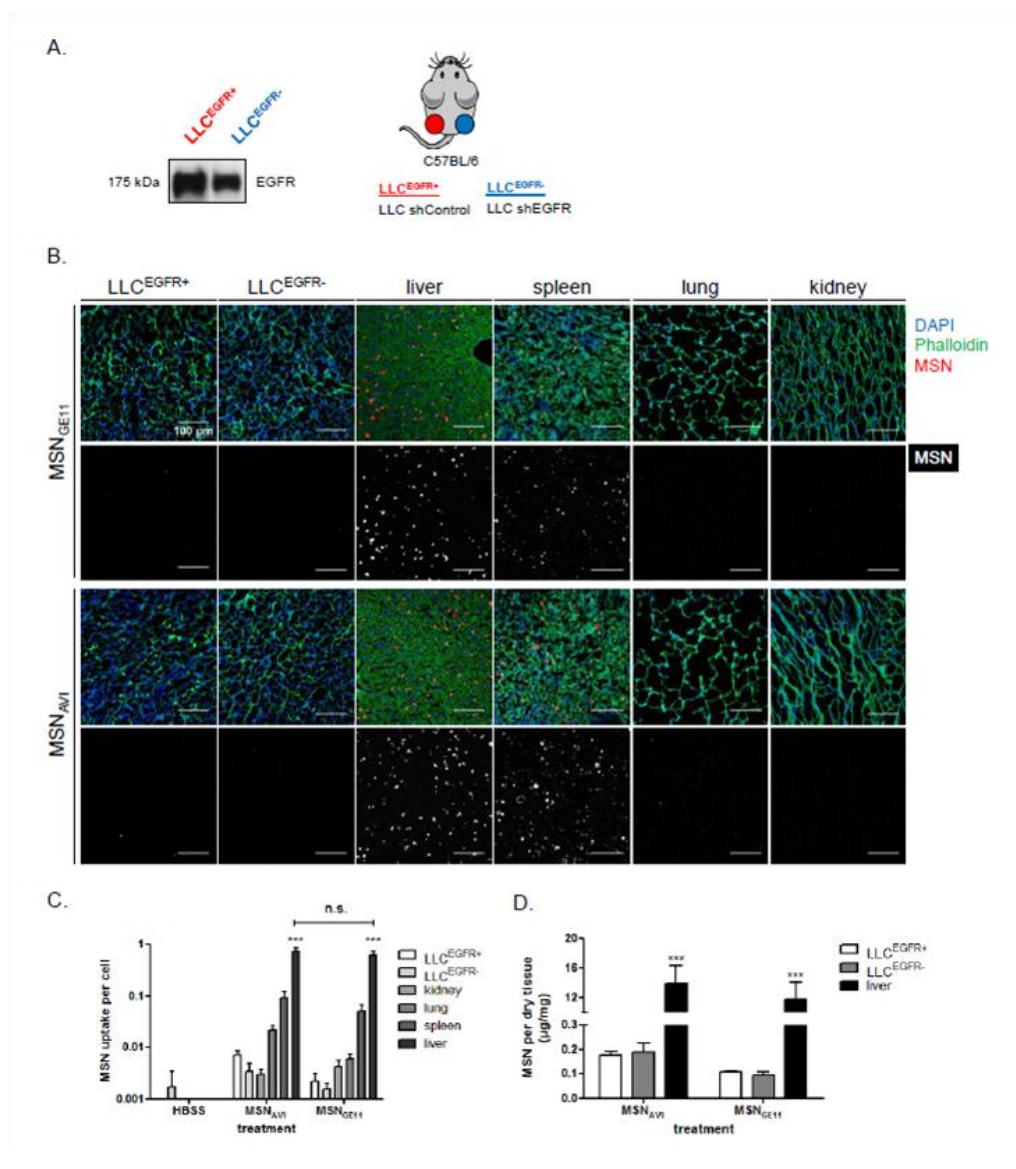


Figure S 7-4. Biodistribution of the EGFR-targeted versus non-targeted MSNs in mice bearing LLC^{EGFR+} versus LLC^{EGFR-} syngeneic flank tumors. (A) EGFR expression of genetically modified LLC clones at protein level shown by Western blot analysis, and schematic representation of the syngeneic double flank tumor-bearing mouse model that was generated by subcutaneous injection of the individual cell clones, respectively. (B) Histological analysis of the biodistribution of intravenously administered MSN_{AV1} and MSN_{GE11} in EGFR-abundant LLC^{EGFR+} and EGFR-scarce LLC^{EGFR-} tumors, livers, spleens, lungs, and kidneys of the mice by means of confocal microscopy. Nuclear staining (DAPI) is shown in blue, actin staining (phalloidin) in green and ATTO 633-labeled MSNs in red in the merged image, and in gray in the single channel for better resolution. Images shown are representative for three different regions from each mice (n = 5 mice treated). Scale bar = 100 μm. (C) Quantification of the MSN_{AV1} and MSN_{GE11} uptake per nuclei observed in histological analyses in LLC^{EGFR+} and LLC^{EGFR-} tumors, kidneys, lungs, spleens, and livers, respectively. (D) Quantitative dosimetric analyses of the MSN_{AV1} and MSN_{GE11} fluorescence achieved from the homogenates of LLC^{EGFR+} and LLC^{EGFR-} tumors versus livers of the treated mice. In the

7. Cellular resolution is essential for validation of active targeting of nanoparticles in vivo

HBSS control, animals only received HBSS buffer and no particles. *** means a significant increase in MSN uptake in the livers compared to the tumors ($p < 0.001$). Values given are average of three different images per each treated mice \pm SEM ($n = 5$ per MSN type).

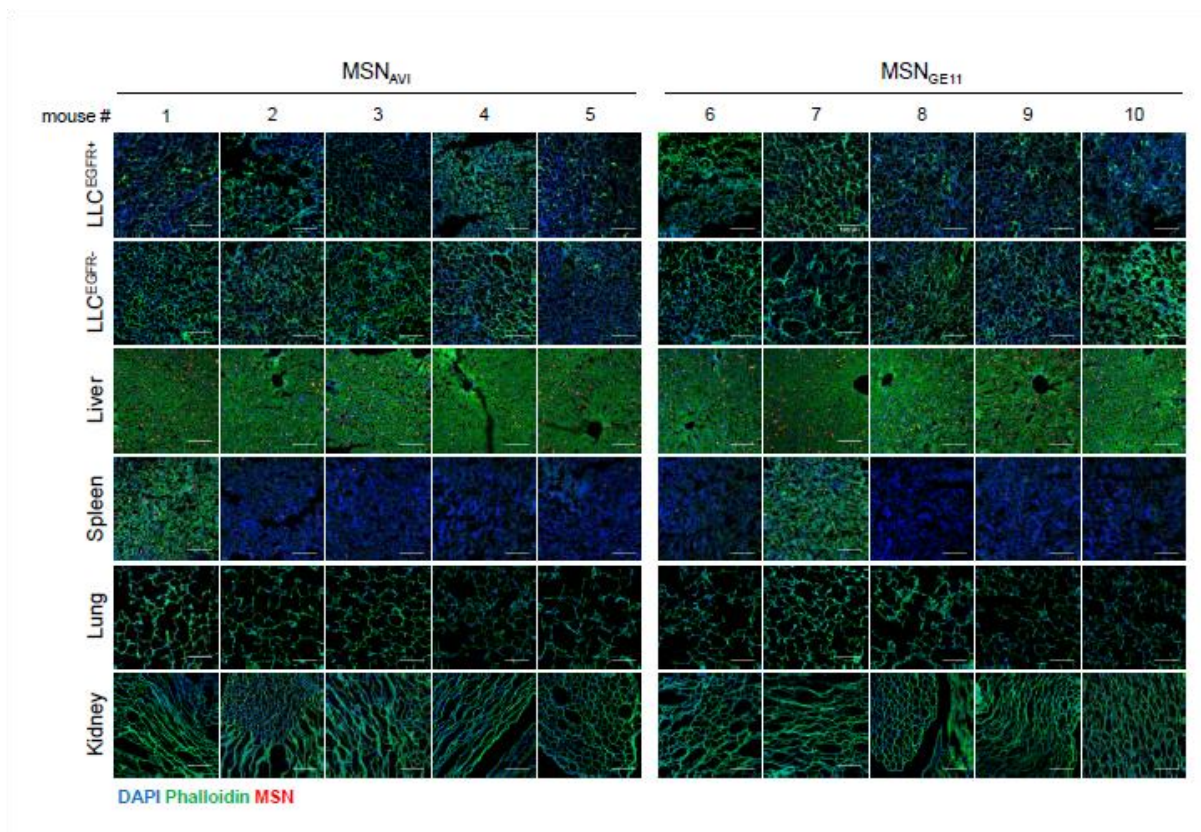


Figure S 7-5. Organ-specific biodistribution of EGFR- targeted versus non-targeted MSNs in mice bearing LLC^{EGFR+} versus LLC^{EGFR-} syngeneic flank tumors. Histological analysis of the biodistribution of retro-orbitally administered MSN_{AVI} and MSN_{GE11} in the EGFR-abundant LLC^{EGFR+} tumors, EGFR-scarce LLC^{EGFR-} tumors, livers, spleens, lungs, and kidneys of each of the treated mice by confocal microscopy. Nuclear staining (DAPI) is shown in blue, actin staining (phalloidin) in green, and ATTO 633-labeled MSNs in red. Images shown are representative for three different regions from each mice ($n = 5$ mice per MSN type). Scale bar = 100 μ m.

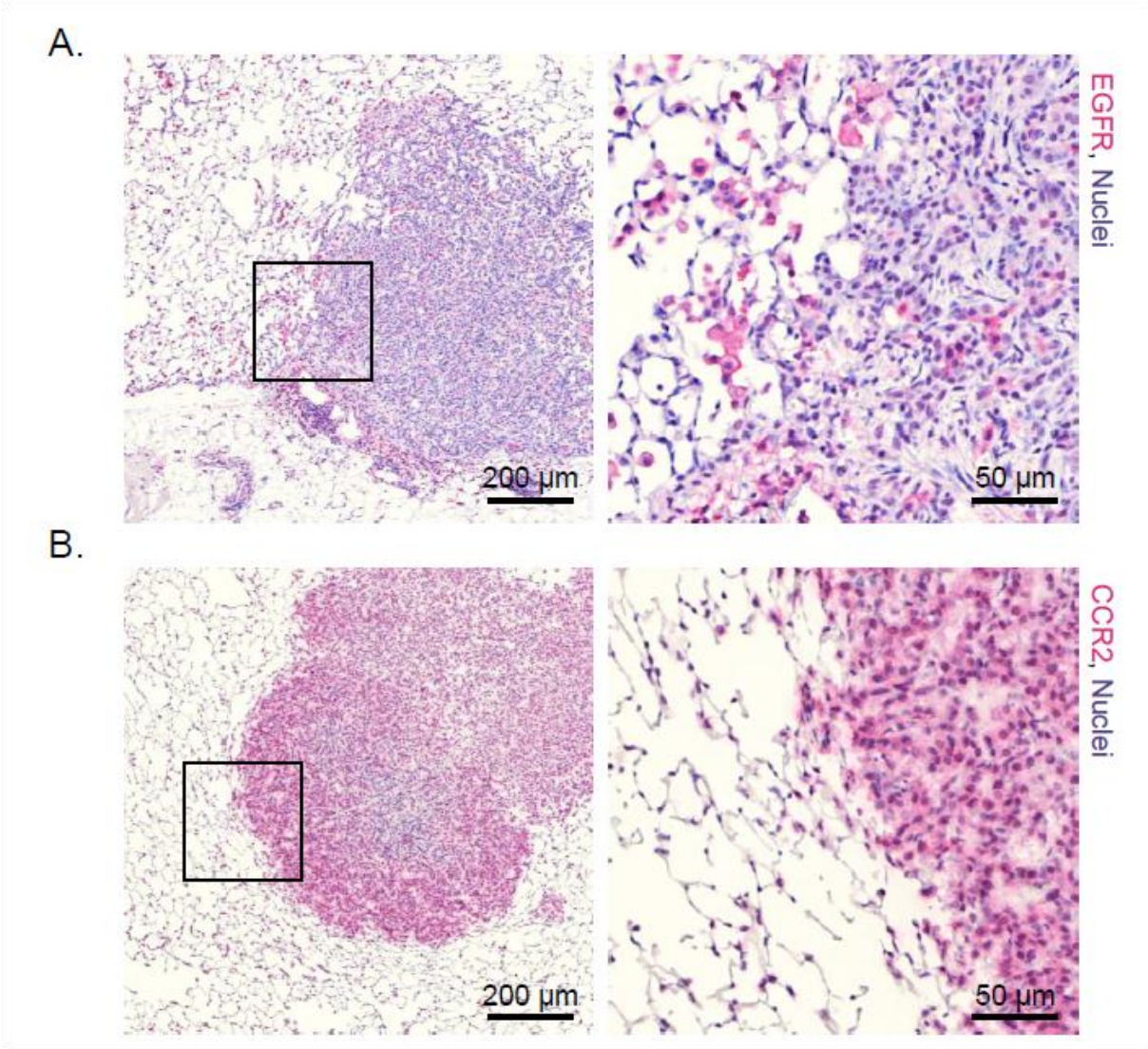


Figure S 7-6. EGFR and CCR2 expression in the lungs of $Kras^{LA2}$ transgenic mice with lung cancer. Immunohistochemical staining of (A) EGFR (pink) is overexpressed heterogeneously in tumor cells and immune cells whereas (B) CCR2 (pink) is overexpressed rather homogeneously in tumor cells and immune cells of the $Kras^{LA2}$ mutant mouse with lung cancer, respectively.

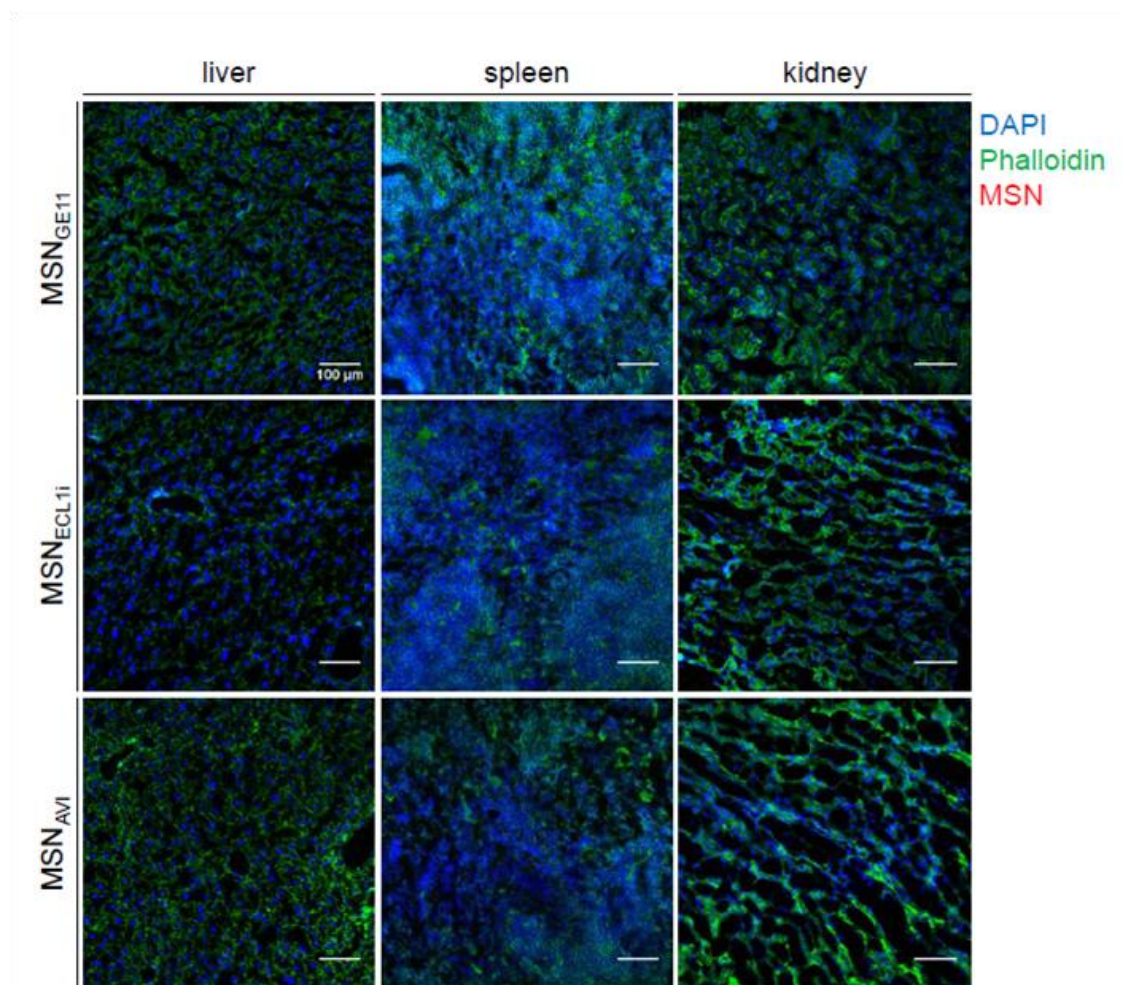


Figure S 7-7. Biodistribution of MSNs after local delivery to the lungs in major organs of $Kras^{LA2}$ mutant mice. Histological analysis of the biodistribution of ATTO 633-labeled MSN_{AVI} , MSN_{GE11} , and MSN_{ECL1i} in livers, spleens, and kidneys of the $Kras^{LA2}$ mutant mice three days after instillation. Nuclear staining (DAPI) is shown in blue, actin staining (phalloidin) in green, and ATTO 633-labeled MSNs in red. Images shown are representative for three different regions from each mice ($n = 5$ per MSN type). Scale bar = 100 μm .

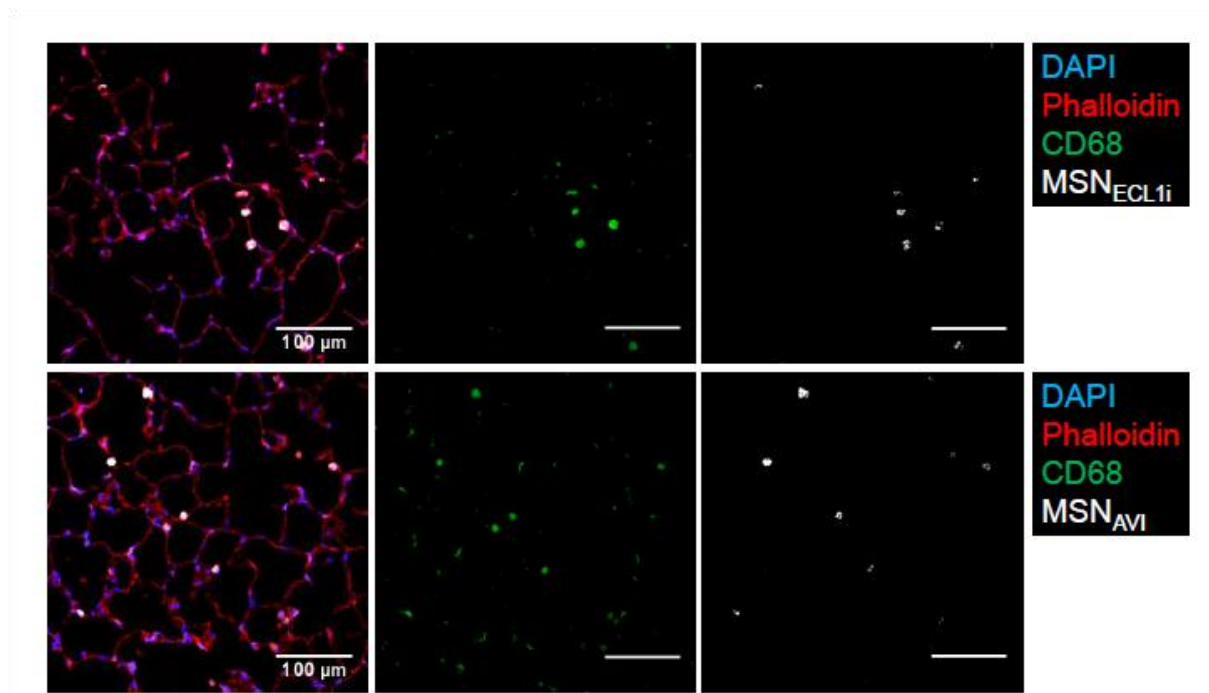


Figure S 7-8. CCR2-targeted and non-targeted MSNs accumulate in CD68 positive macrophages in $Kras^{LA2}$ mutant lungs. Immunofluorescence co-staining for the macrophage marker CD68 in tumor-free regions of the lungs of $Kras^{LA2}$ mice with ATTO 633-labeled MSNs. Nuclear staining (DAPI) is shown in blue, actin staining (phalloidin) in red, CD68 staining in green, and ATTO 633-labeled MSNs in gray. Images shown are representative for three different regions from each mice (n = 5 per MSN type). Scale bar = 100 μ m.

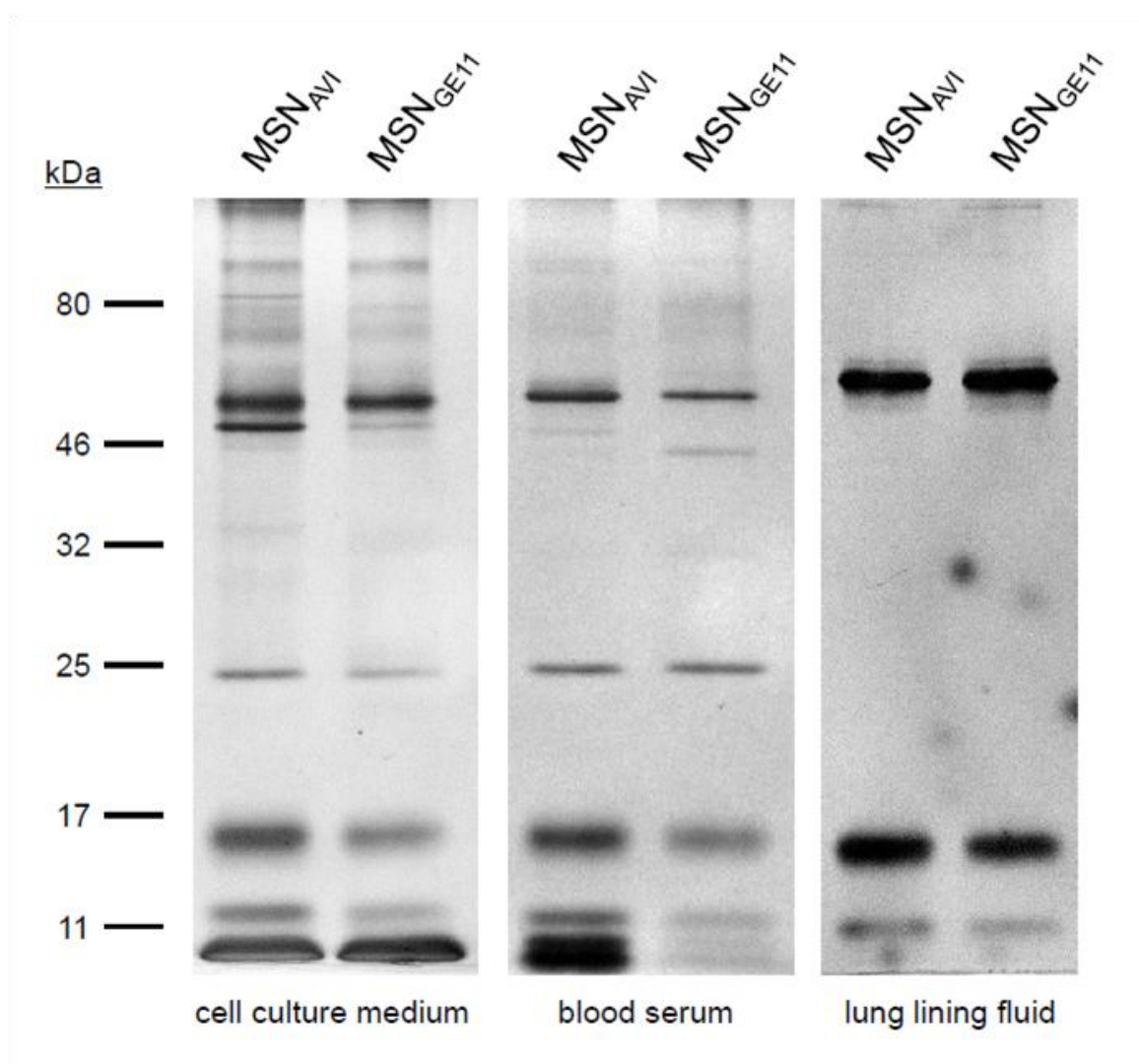


Figure S 7-9. Protein corona formation on the surface of the nanoparticles in distinct biological environments. Silver staining of the protein corona formed on the surface of MSN_{AVI} and MSN_{GE11} in cell culture medium with 10% FCS, human blood serum, and murine lung lining fluid, overnight.

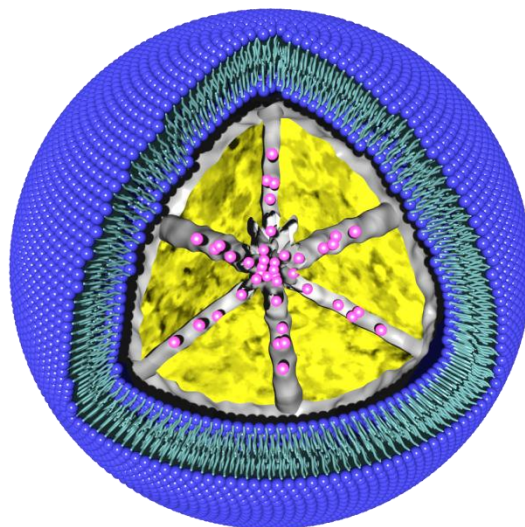
8 Lipid bilayer-coated curcumin-based mesoporous organosilica nanoparticles for cellular delivery

This chapter is based on the following publication:

Stefan Datz, Hanna Engelke, Constantin v. Schirnding, Linh Nguyen, Thomas Bein, *Microp. Mesop. Mater.* **2016**, 225, 371-377.

Abstract

Effective and controlled drug delivery systems with on-demand release abilities and biocompatible properties receive enormous attention for biomedical applications. Here, we describe a novel inorganic-organic hybrid material with a strikingly high organic content of almost 50 wt%. The colloidal periodic mesoporous organosilica (PMO) nanoparticles synthesized in this work consist entirely of curcumin and ethane derivatives serving as constituents that are crosslinked by siloxane bridges, without any added silica. These mesoporous curcumin nanoparticles (MCNs) exhibit very high surface areas (over 1000 m²/g), narrow particle size distribution (around 200 nm) and a strikingly high stability in simulated biological media. Additionally, the MCNs show high autofluorescence and were used as a cargo delivery system in live-cell experiments. A supported lipid bilayer (SLB) efficiently seals the pores and releases Rhodamin B as model cargo in HeLa cells. This novel nanocarrier concept provides a promising platform for the development of controllable and highly biocompatible theranostic systems.



8.1 Introduction

Periodic mesoporous organosilica (PMO) constitutes a new type of inorganic-organic porous hybrid material, which holds great promise in a variety of fields such as chemical sensing,¹⁻⁷ catalysis⁸⁻¹² and biomedical applications.¹³⁻¹⁵ Since the independent discovery of this new class of mesoporous materials in the groups of Inagaki, Stein and Ozin in 1999,¹⁶⁻¹⁸ PMO materials, synthesized by using bridged silsesquioxanes as precursors, have recently been prepared at the nanoscale.¹⁹⁻²¹ Different approaches were used to synthesize PMO nanoparticles with simple, low-molecular-weight organosilane bridging groups. In a sol-gel process using Pluronic P123 as the template, Landskron *et al.* synthesized rodlike nanoparticles with adjustable aspect ratios.²² Using cetyltrimethylammonium bromide (CTAB) as the micellar template and an ammonia-catalyzed sol-gel reaction, Huo *et al.* prepared highly ordered and dispersible PMO nanoparticles with methane, ethane, ethylene and benzene organic bridging groups within the pore walls.²³ In another approach the group of

Shi *et al.* used silica-etching chemistry to obtain hollow PMO nanoparticles that were used for nano-biomedical applications for the first time.²⁴

Recently, the group of Durand reported the synthesis of biodegradable PMO nanospheres and nanorods with a disulfide-containing organic bridging group. The morphology and size of these nanostructures was controlled by adjusting the ratio of bis(triethoxysilyl)ethane and bis(3-triethoxysilyl-propyl)-disulfide.²⁵ These mixed PMO nanospheres and rods were used as a biodegradable nanocarrier for doxorubicin in breast cancer cell lines. In the group of Kashab *et al.*, enzymatically degradable silsesquioxane nanoparticles were synthesized and used as fluorescent nanoprobe for *in vitro* imaging of cancer cells.²⁶ Zink and co-workers developed different light-activatable and pH-responsive hybrid materials for drug delivery applications.²⁷⁻²⁹ In these studies mostly low-molecular weight organic silsesquioxane bridging groups were incorporated into the pore walls of mesoporous nanostructures. Here, we report the synthesis of a PMO nanomaterial consisting of the biocompatible and large molecule curcumin and ethane organic moieties without the use of additional silica. Curcumin is a natural yellow-colored antioxidant compound extracted from *Curcuma longa* and has been used for centuries in its crude form as dietary supplement and in traditional Asian medicines.³⁰ Recently, it has been shown that curcumin exhibits an exceptionally large range of biomedical activity against diseases such as Alzheimer, Parkinson, Malaria and many more.³¹ In addition, it shows strong anti-inflammatory effects and has potential chemotherapeutic value as it inhibits cell proliferation and induces apoptosis in various cancer cell lines.³²⁻³⁵ However, its bioavailability is limited by its very low aqueous solubility.³⁶⁻³⁷ Many different approaches have been investigated to improve the bioavailability and biopharmaceutical properties such as incorporating curcumin into liposomes,³⁸⁻³⁹ polymeric nanoparticles⁴⁰⁻⁴², bioactive glasses⁴³ or amino acid conjugates.⁴⁴⁻⁴⁵ Various successful *in vitro*⁴⁶⁻⁴⁸ and *in vivo*⁴⁹⁻⁵¹ studies show the exceptional anticancer properties of curcumin

nanoformulations. Additionally, it is well tolerated by the human body up to 12 g/day in oral administration as shown in clinical studies, which shows great promise regarding the biocompatibility of curcumin-based nanosystems.⁵²

Here, we present the synthesis of PMO nanoparticles with curcumin being the main organic constituent of the organosilica framework. Importantly, the synthesis was achieved without the addition of tetraethyl orthosilicate (TEOS), which is often used in other PMO studies for framework stabilization. The nanoparticles obtained in this study exhibit good dispersibility and high porosity parameters, which hold promise for a variety of applications in drug delivery. Furthermore, the incorporated curcumin compounds cause significant fluorescence of the nanoparticles themselves, which implies that no additional dye is necessary to track the NPs in live-cell experiments. The mesoporous PMO nanoparticles were used as a cargo release system with a Supported Lipid Bilayer (SLB) serving as cap in various *in vitro* experiments.

8.2 Results and Discussion

The new nanomaterial was synthesized starting with the preparation of precursors. The synthesis of the precursor curcumin-IPTES was achieved following a previously described procedure.⁵ In this reaction, curcumin and 3-isocyanatopropyl-(triethoxy)silane (IPTES) form carbamate linkages under anhydrous basic conditions. The completion of the reaction can be monitored by infrared and UV-VIS spectroscopy in addition to NMR data shown in the experimental section. The UV-VIS spectrum (see SI, Figure S 8-1) shows a significant blue-shift in the absorption from 430 to 415 nm after addition of the electron-withdrawing carbamate-linked silyl groups next to the conjugated π -electron system of the curcumin compound. In the IR spectra, the completion of the reaction can be followed by the

disappearance of the characteristic isocyanate vibration at 2270 cm^{-1} and the increasing intensity of the C=O stretching vibration due to the carbamate linkage group absorbing at 1710 cm^{-1} . The synthesized precursor was then used in a carefully controlled sol-gel reaction to form mesoporous curcumin nanoparticles (MCNs). The synthesis was performed in a water-ethanol mixture with cetyltrimethylammonium bromide as the micellar template under slightly basic conditions (Figure 8-1). The addition of ethanol was crucial because of the low solubility of Curcumin-IPTES in aqueous solutions.

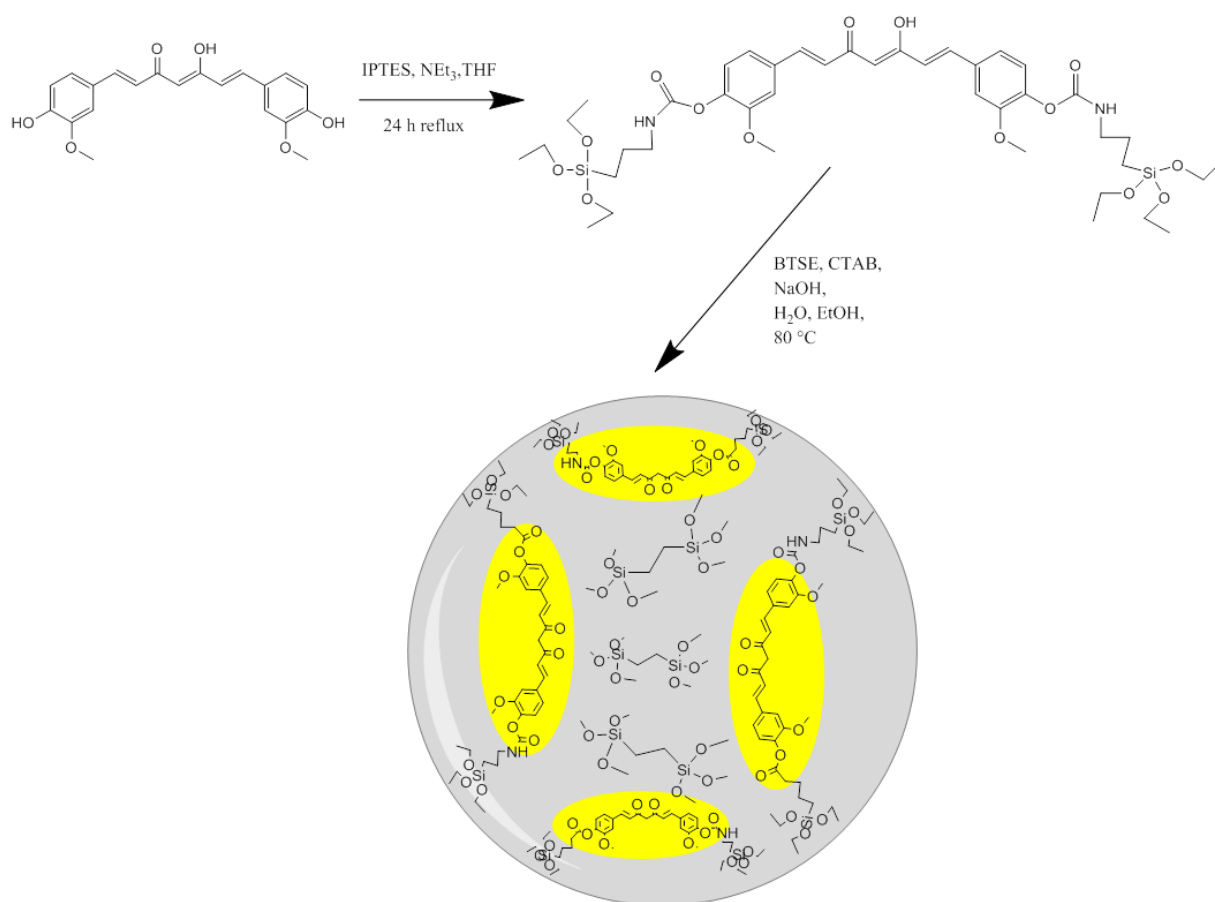


Figure 8-1. Schematic representation of the synthesis and the inorganic-organic hybrid composition of yellow-colored mesoporous curcumin nanoparticles (MCNs).

The template preparation, the catalyzed hydrolysis of Curcumin-IPTES and BTSE acting as the silica sources, and the nanoparticle formation was performed at $80\text{ }^\circ\text{C}$. After completion of the reaction the template was extracted in an ammonium nitrate containing ethanolic

8. Lipid bilayer-coated curcumin-based mesoporous organosilica nanoparticles for cellular delivery

solution followed by an additional extraction step with ethanol under reflux. After several washing steps and redispersion in absolute ethanol the synthesis resulted in a colloidal yellow suspension of MCNs (see SI, Figure S 8-3b).

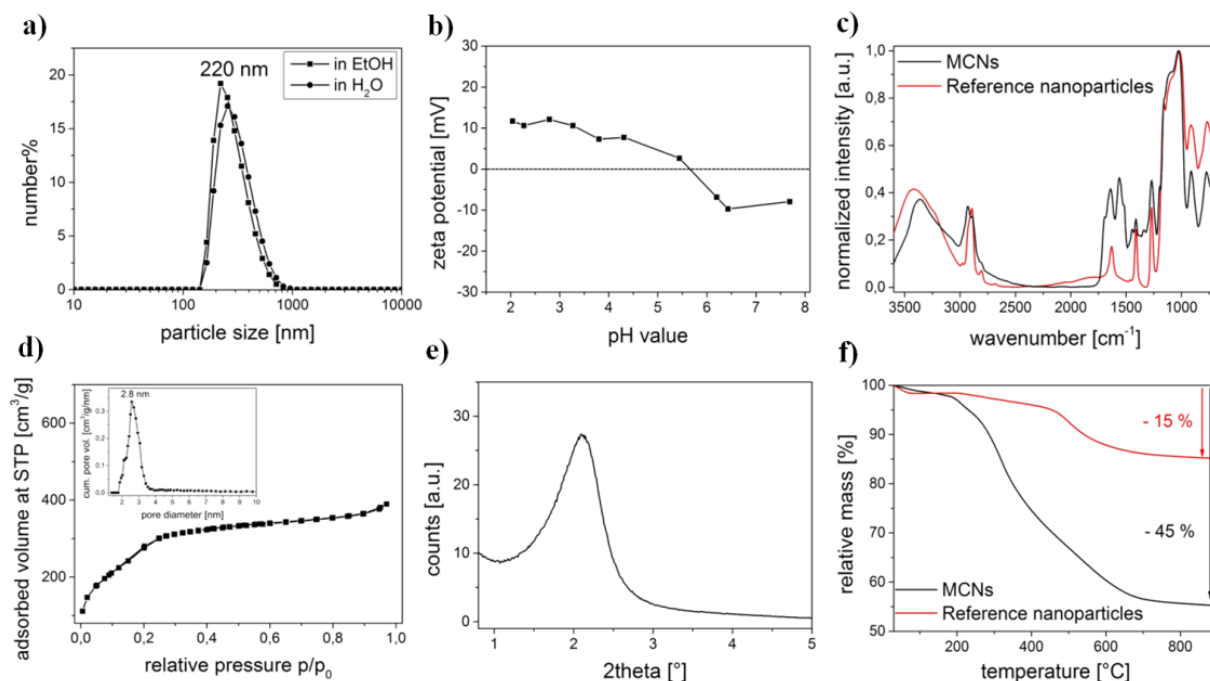


Figure 8-2. Characterization of the Curcumin PMO nanoparticle material. a) DLS measurements in ethanol and water, b) zeta potential measurement, c) infrared spectrum, d) nitrogen sorption isotherm and pore size distribution (inset), e) small-angle X-ray scattering (SAXS), f) thermogravimetric analysis of MCNs and reference nanoparticles without curcumin.

Dynamic light scattering (DLS) measurements showed a narrow size distribution of MCNs with a maximum around 220 nm (Figure 8-2a), implying excellent colloidal stability in ethanol and in water. Compared to silica particles, the zeta potential measurement of MCNs shows an increased isoelectric point at pH 5.5, which is due to the strongly reduced amount of negatively charged silanol groups on the surface of the nanoparticles, compared to common mesoporous silica nanoparticles (Figure 8-2b).⁵³ In order to investigate the total organic amount within the PMO framework, a reference PMO nanoparticle material was synthesized. These reference nanoparticles consist exclusively of ethane groups as the organic linker in the

PMO material. IR data for both types of samples depicted typical vibrational modes of the silica framework between 780 and 1300 cm^{-1} (Figure 8-2c). The shoulders at 1705 cm^{-1} and 1510 cm^{-1} in the MCN sample can be assigned to the stretching vibrations of C=O and N-H of the carbamate group, respectively. The peak at 1560 cm^{-1} is attributed to the secondary amine vibrational modes. The intensive signal at 1640 cm^{-1} is due to physisorbed water and can be seen in all spectra. The signals beyond 2800 cm^{-1} are assigned to C-H and N-H stretching vibrations of the incorporated organic moieties. Nitrogen sorption and small-angle X-ray scattering (SAXS) measurements were used to characterize the porosity parameters of the obtained nanoparticles. The nitrogen sorption data (Figure 8-2d) showed a type IV isotherm with a strikingly high calculated BET surface area of 1040 m^2/g and a narrow pore size distribution around 2.8 nm. The resulting pore volume is 0.55 cm^3/g . In SAXS measurements, only the first (100) reflex is observed, indicating a disordered worm-like pore structure of the mesopores in the nanoparticles (Figure 8-2e). Thermogravimetric analysis (TGA) data (Figure 8-2f) indicate a relative mass loss of 15 wt% up to 900 °C in the reference material consisting of a PMO with ethane groups but without curcumin. In comparison, the mixed PMO MCN nanoparticles containing curcumin and ethane organic bridging groups reveal a significantly enhanced mass loss of 45 wt% indicating the successful incorporation of curcumin into the silica framework. Raman spectroscopy and additional solid-state NMR spectra show specific signals for curcumin and ethane in the nanoparticle material as well (see SI, Figure S 8-3a and Figure S 8-4). The ^{29}Si -spectrum shows the presence of T-type signals between -45 and -70 ppm. The signals arising from the organic parts indicate that the organic linkers are completely included into the hybrid silica framework with a high degree of silanol condensation. Importantly, the absence of Q-type ^{29}Si -signals provides evidence that the Si-C bonds are stable under the applied synthetic conditions. Electron microscopy was used to investigate the morphology, pore structure and size distribution of MCNs.

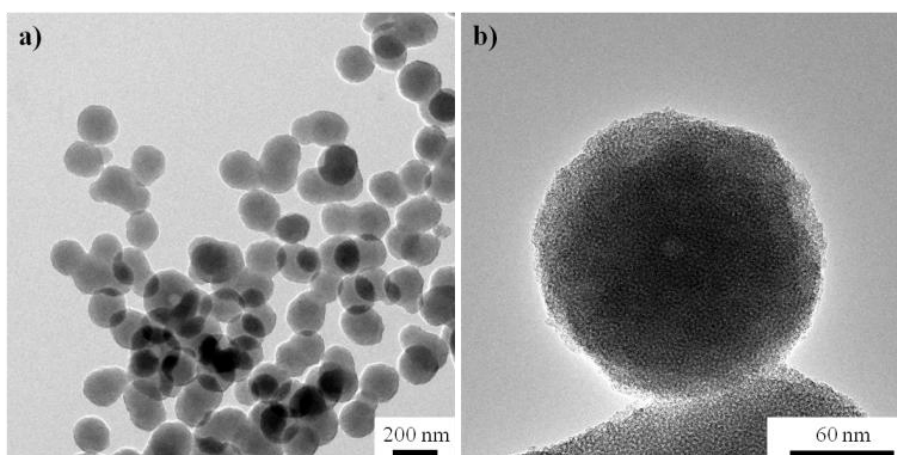


Figure 8-3. Transmission electron microscopy characterization of the MCNs.

TEM images of MCNs are depicted in Figure 8-3 and display spherically shaped particles with a very narrow particle size distribution. A radially disposed worm-like structure of the mesopores of MCNs can be seen in the STEM image (Figure S 8-5c). 2D Fourier transformation of the image (FFT, Figure S 8-5g) reveals a pore-to-pore distance of about 4.5 nm in good accordance to previously described sorption and SAXS measurements. The biological stability of MCNs was investigated in simulated body fluid (SBF) to gain insights regarding the reactivity of these particles in simulated biological media for future drug delivery applications. The long-term stability was investigated with nitrogen sorption, X-ray analysis, electron microscopy, and infrared spectroscopy. Strikingly, the particles were stable throughout the complete experimental time (up to 28 days) in SBF solution and showed no phase transition or crystallization behavior at all. In comparison, common mesoporous silica nanoparticles (MSNs) start to show degradation and formation of apatite-like structures after a few hours.⁵⁴ Figure 8-4 shows TEM images at the different time points of MCNs stored in SBF, where no morphology changes or increased agglomeration can be observed over the complete experimental time. The particles also retained their porosity during the process (Figure S 8-6).

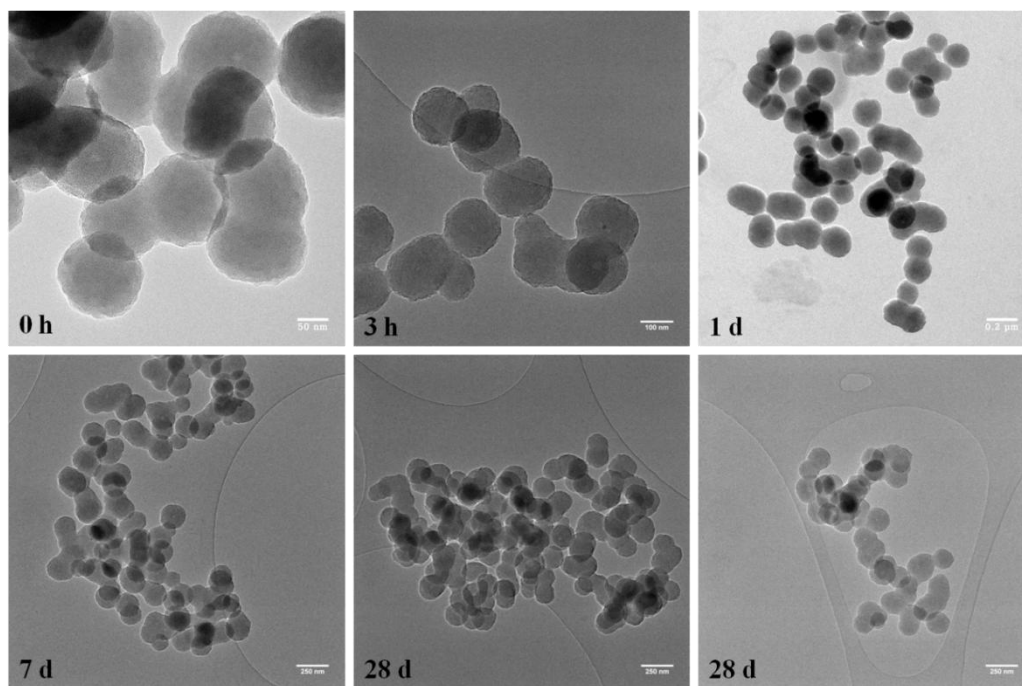


Figure 8-4. Transmission electron microscopy (TEM) images at different time points of MCNs in SBF (0 h, 3 h, 1 d, 7 d, 28 d) as part of the biodegradability test.

Our findings can be explained by the drastically decreased amount of reactive silanol groups and siloxane bridges on the surface of organosilica nanoparticles compared to classical silica-based MSNs. This feature is anticipated to make colloidal MCNs promising candidates for drug delivery applications in *in vivo* experiments where enhanced stability is desired.⁵⁵ The highly porous and colloidal MCN nanoparticles were also investigated in live-cell experiments. Cellular uptake of MCNs and the release of model cargos were investigated in HeLa cells. MCNs show significant autofluorescence with an excitation maximum at about 425 nm and an emission maximum at about 520 nm (Figure 8-5a). This key feature allows us to observe them in a fluorescence microscope without addition or attachment of further dyes. When coated with a lipid bilayer, colloidal curcumin nanoparticles are internalized with high efficiency by HeLa cells after 24 h of incubation and can be detected based on their autofluorescence (Figure 8-5b).

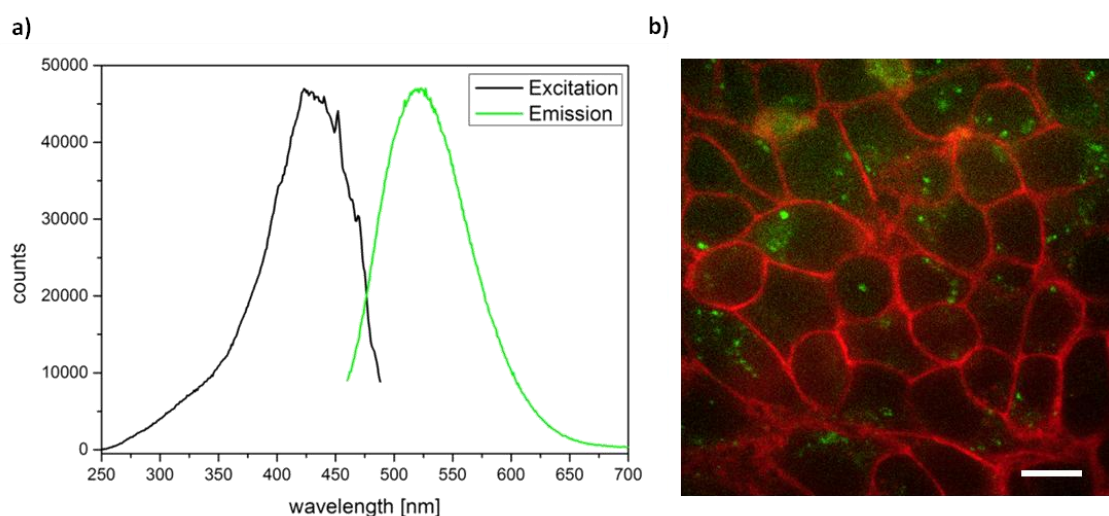


Figure 8-5. a) Fluorescence excitation and emission spectra of MCNs in PBS buffer. b) Cellular uptake of SLB-coated MCNs (green) after 24 h incubation on HeLa cells (red: WGA647 membrane staining); scale bar represents 10 μm .

The release behavior of cargo-loaded MCNs was investigated *in vitro*. Rhodamin B - a dye that stains mitochondria in cells - was chosen as a model cargo and the particles were sealed with a supported lipid bilayer (SLB). The SLB was produced in a modulated two-step approach employing first DOTAP only, followed by a DOTAP/DOPC mixture.⁵⁶ *In vial* release experiments show the effective closure of the porous system with the SLB. After incorporation of RhoB molecules into the mesopores, the SLB was used to block the pore entrances. An efficient sealing of the pores and almost no premature release of the cargo was observed, whereas upon addition of Triton-X the cargo was released within 48 h (Figure S 8-7). Additionally, the particles loaded with Rhodamin B and coated with the lipid layer were efficiently internalized by HeLa cells. After 24 h a slight release of Rhodamin B could be observed. Addition of chloroquine leads to an enhanced release after 48 h as shown in Figure 8-6.

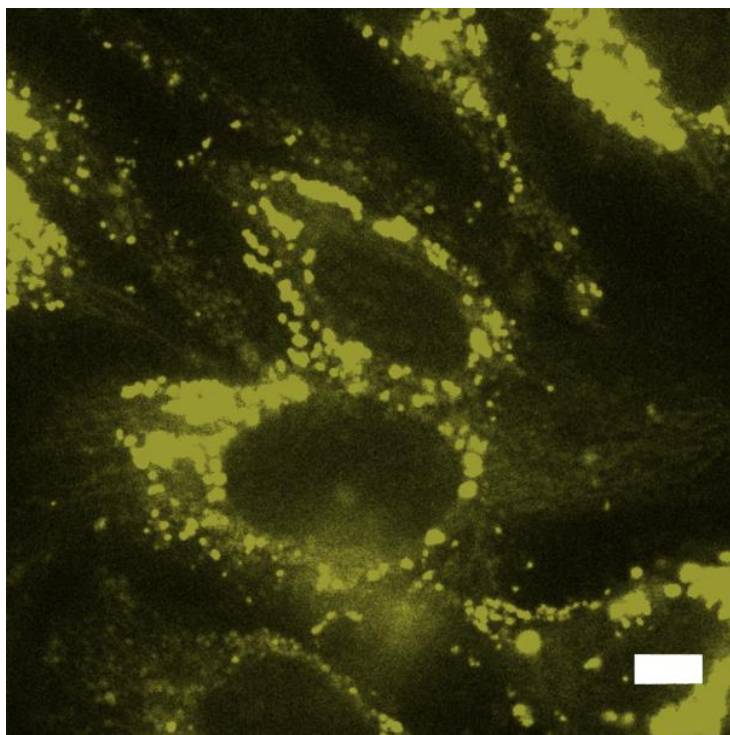


Figure 8-6. Rhodamin B-loaded MCNs in HeLa cells. Release can be observed after 48 h incubation and addition of chloroquine. Scale bar: 10 μm .

8.3 Conclusion

To conclude, we have developed new colloidal periodic mesoporous organosilica nanoparticles containing curcumin as organic component, with very high organic wall content. They are fluorescent, possess a large pore volume and surface area and show very high stability in simulated body fluid. When coated with a lipid layer they are successfully internalized by cells and can deliver and release Rhodamin B in those cells. Thus, they show great potential for future applications as drug delivery system.

8.4 Experimental Part

Materials and characterization techniques. Curcumin (60-70%), 3-isocyanatopropyl-(triethoxysilane) (IPTES), tetrahydrofuran (dry), triethylamine (97%), cetyl trimethylammonium bromide, ammonium nitrate, ammonium bicarbonate, Rhodamin B, calcein, sodium hydroxide, DMSO-*d*₆, dichloromethane, CDCl₃, methanol were purchased from Sigma Aldrich. Bis(triethoxysilyl)ethane (BTSE) was purchased from ABCR. DOPC (1,2-dioleoyl-*sn*-glycero-3-phosphocholine) and DOTAP (1,2-dioleoyl-3-trimethylammonium propane) were purchased from Avanti Polar Lipids. All chemicals were used as received without further purification. Doubly distilled water from a Millipore system (Milli-Q Academic A10) was used for all synthesis and purification steps. All samples were investigated with an FEI Titan 80-300 transmission electron microscope operating at 300 kV with a high-angle annular dark field detector. A droplet of the diluted MSN solution in absolute ethanol was dried on a carbon-coated copper grid. Dynamic light scattering (DLS) measurements were performed on a Malvern Zetasizer-Nano instrument equipped with a 4 mW He-Ne laser (633 nm) and an avalanche photodiode. The hydrodynamic radius of the particles was determined by dynamic light scattering in ethanolic suspension. For this purpose, 100 μ L of an ethanolic suspension of MSN (ca. 10 mg/mL) was diluted with 3 mL of ethanol prior to the measurement. Zeta potential measurements of the samples were performed on a Malvern Zetasizer-Nano instrument equipped with a 4 mW He-Ne laser (633 nm) and an avalanche photodiode. Zeta potential measurements were performed using the add-on Zetasizer titration system (MPT-2) based on diluted NaOH and HCl as titrants. For this purpose, 1 mg of the particles was diluted in 10 mL bi-distilled water. Nitrogen sorption measurements were performed on a Quantachrome Instruments NOVA 4000e. All samples (10 mg each) were heated to 100 °C for 12 h in vacuum (10 mTorr) to outgas the samples,

before nitrogen sorption was measured at 77 K. Pore size and pore volume were calculated with a NLDFT adsorption branch model of N₂ on silica, based on the adsorption branch of the isotherms. A BET model was applied in the range of 0.05 – 0.20 p/p₀ to evaluate the specific surface area of the samples. Centrifugation was performed using an Eppendorf centrifuge with an adapter for Falcon tubes or an Eppendorf centrifuge 5418 for small volumes. Raman spectra were recorded on a Jobin Yvon Horiba HR800 UV Raman microscope using a He-Ne laser emitting at $\lambda = 633$ nm with a laser power of 10 mW. IR measurements were performed on a Bruker Equinox 55 FTIR spectrometer in absorbance mode (spectra were background subtracted). UV-VIS spectra were recorded with a NanoDrop ND 1000 spectrometer. Usually, 2 μ L of sample were used and all presented spectra are background corrected for water absorption. Thermogravimetric analysis (TGA) of the samples (about 10 mg of dried nanoparticles) was performed on a Netzsch STA 440 Jupiter thermobalance with a heating rate of 10 K/min in a stream of synthetic air of about 25 mL/min. Cross-polarized ²⁹Si- and ¹³C-MAS NMR measurements were performed on a Bruker DSX Avance500 FT spectrometer (11.74 T) in a 4 mm ZrO₂ rotor. The spinning rate was 10 kHz and a total number of 256 scans were recorded. The used contact time was 2 ms and the recycle delay was 1 s.

Synthesis of Curcumin-Precursor. Curcumin ((1*E*,6*E*)-1,7-bis-(4-hydroxy-3-methoxyphenyl)-hepta-1,6-dien-3,5-dion, 2.00 g, 5.43 mmol, 1 eq.) was dissolved in 25 mL dry THF in a three-necked flask. Subsequently, 3-isocyanatopropyl(triethoxysilane) (5.37 g, 21.7 mmol, 4 eq.) and triethylamine (165 μ g, 1.63 mmol, 0.3 eq.) were added under stirring and the mixture was refluxed for 24 h at 85 °C in a nitrogen flow. After cooling down to room temperature, the sample was filtered and washed with ethyl acetate. The solvents were evaporated at reduced pressure and the sample was purified with column chromatography on silica gel with a solvent mixture containing 97 v% dichloromethane, 2 v% methanol and 1 v% triethylamine. The compound obtained (named Curcumin-IPTES) was dried under high

vacuum for 12 hours and used without further purification (yield: 2.29 g, 2.65 mmol, 49 %). $^1\text{H-NMR}$ (300 MHz, $\text{DMSO-}d_6$): δ [ppm] = 7.72 (t, 2H), 7.62 (d, 2H), 7.44 (s, 2H), 7.26 (d, 2H), 7.09 (d, 2H), 6.95 (d, 2H), 6.16 (s, 1H), 3.80 (s, 6H), 3.73 (qa, 18H), 1.45 (q, 6H), 1.12 (t, 27H), 0.55 (t, 6H). $^{13}\text{C-NMR}$ (400 MHz, CDCl_3): δ [ppm] = 183.14, 153.98, 152.00, 141.75, 140.10, 133.36, 124.00, 123.67, 121.10, 111.47, 101.68, 58.49, 51.92, 43.72, 23.61, 18.29, 9.20. MS (ESI): $[\text{M-H}]^-$ cal.: 861.36206, found: 861.36672.

Synthesis of mesoporous Curcumin-PMO nanoparticles (MCNs). In a two-step sol-gel reaction, cetyl trimethyl-ammonium bromide (CTAB, 0.96 mmol, 350 mg) was dissolved in a mixture containing 120 mL H_2O and 15 mL absolute ethanol in a 250 ml round bottom flask. Subsequently, 875 μL sodium hydroxide solution (2 M) was added and the mixture was stirred at 80 °C for 30 minutes. In a glass vessel, 400 mg Curcumin-IPTES (0.32 mmol) was mixed with 200 μL bis(triethoxysilyl)ethane (BTSE, 0.51 mmol) and 400 μL ethanol. This precursor solution was preheated to completely dissolve the compounds and afterwards quickly injected into the stirring aqueous template solution. The reaction was maintained for 90 minutes at 80 °C and 700 rpm. Extraction of the organic template was achieved by heating the ethanol-suspended (80 mg) sample under reflux at 90 °C for 1 h in a mixture of 2 g ammonium nitrate and 100 mL ethanol. Afterwards, the sample was centrifuged for 15 minutes at 7830 rpm (7197 rcf), redispersed in ethanol and heated under reflux at 90 °C in a solution of 100 mL ethanol for 45 minutes. After centrifugation, the particles were re-dispersed in 20 mL ethanol, resulting in a colloidal yellow suspension with a concentration of 4 mg/mL.

Synthesis of reference PMO nanoparticles. The reference PMO nanoparticles consisting exclusively of ethane organic bridging groups were synthesized in a similar two-step sol-gel approach as mentioned above. Cetyl trimethyl-ammonium bromide (CTAB, 0.96 mmol, 350

mg) was dissolved in a mixture containing 120 mL H₂O and 15 mL absolute ethanol in a 250 ml round bottom flask. Subsequently, 875 μ L sodium hydroxide solution (2 M) was added and the mixture was stirred at 80 °C for 30 minutes. 325 μ L bis(triethoxysilyl)ethane (BTSE, 0.83 mmol) and 400 μ L ethanol were mixed and quickly injected into the stirring aqueous template solution. The reaction was maintained for 90 minutes at 80 °C and 700 rpm. Extraction of the organic template was achieved by heating the ethanol-suspended (80 mg) sample under reflux at 90 °C for 1 h in a mixture of 2 g ammonium nitrate and 100 mL ethanol. Afterwards, the sample was centrifuged for 15 minutes at 7830 rpm (7197 rcf), redispersed in ethanol and heated under reflux at 90 °C in a solution of 100 mL ethanol for 45 minutes. After centrifugation, the particles were redispersed in 20 mL ethanol.

Degradation study in Simulated Body Fluid (SBF). To prepare the SBF buffer, the following reagents were dissolved in bi-distilled water and the solution was filled up to 1000 ml: 6.057 g NH₂C(CH₂OH)₃ (TRIS), 0.350 g NaHCO₃, 0.224 g KCl, 7.996 g NaCl, 0.228 g K₂HPO₄·3 H₂O, 0.305 g MgCl₂·6 H₂O, 0.278 CaCl₂, 0.071 g Na₂SO₄. The pH of the solution was adjusted to 7.4 at 37 °C with 1 M HCl.⁵⁵ 100 mg of as-synthesized Curcumin nanoparticles were centrifuged, washed with bi-distilled water and redispersed in 50 mL SBF buffer solution. The mixture was stored at 37 °C and at selected times, 10 mL of the solution containing nanoparticles was collected, centrifuged and washed with water for several times to remove deposited salts. The sample was then dried at 70 °C and used for further characterization. The collected supernatants were used for pH measurements. The selected times to collect the samples were 3 h, 1, 4, 7 and 28 days.

Lipid preparation. The following lipids were used: DOPC (1,2-dioleoyl-*sn*-glycero-3-phosphocholine, Avanti Polar Lipids), DOTAP (1,2-dioleoyl-3-trimethylammonium propane, Avanti Polar Lipids). The amount of 2.5 mg of the individual lipids was dissolved in a 1 mL mixture of 40 % vol absolute ethanol and 60 % vol MQ water (conc. 2.5 mg/mL).

Cargo loading and Supported Lipid Bilayer-capping (SLB). The amount of 0.5 mg of MCNs in ethanolic solution were centrifuged (4 min, 8609 rcf, at 15 °C) and redispersed in a 1000 µL loading mixture containing Rhodamin b (0.5 mM in water). The particles were centrifuged after 2 h of loading (4 min, 8609 rcf, at 15 °C), separated from the loading solution and 100 µL of the above DOTAP solution was added. Upon addition of 900 µL MQ water (pH adjusted to 9.4 with sodium hydroxide) the formation of the first SLB layer on the external surface of MCNs was induced. After centrifugation (4 min, 8609 rcf, at 15 °C) and redispersion in 100 µL of a 1:1 mixture of the above DOPC/DOTAP solutions, the formation of a second layer around the MCNs was induced by adding 900 µL HBSS buffer. For the *in vial* release experiments 10 µL of the detergent Triton-X were added to the loaded and capped MCNs in order to open the pores. The particles were centrifuged after 24 and 48 h and the supernatant was measured on the fluorescence spectrometer.

Cell culture. HeLa cells were grown in DMEM supplemented with 10 % FBS (lifetechnologies) at 37 °C in a humidified atmosphere containing 5 % CO₂. They were seeded into ibiTreat 8 well slides (ibidi GmbH) at concentrations of 5000 – 10 000 cells per well the day prior to treatment. For internalization as well as release studies 2 µg of particles were added per well. For internalization studies the cell membranes were stained immediately before imaging by addition of wheat germ agglutinin Alexa Fluor 647 conjugate (WGA 647, lifetechnologies) at a final concentration of 5 µg/mL and subsequent washing with DMEM medium.

Live cell imaging. Cells were imaged 24 or 48 h after incubation with particles on a spinning disc microscope (Zeiss Cell Observer SD utilizing a Yokogawa spinning disk unit CSU-X1). The objective was a 63x plan apochromat oil immersion objective (NA 1.4, Zeiss). The

exposure time was 0.1 s. For MCN imaging the excitation was 488 nm, for Rhodamin B 561 nm and for WGA 647 633 nm laser light.

8.5 References

1. Xiao, B.; Zhao, J.; Liu, X.; Wang, P.; Yang, Q., Synthesis of 1,10-phenanthroline functionalized periodic mesoporous organosilicas as metal ion-responsive sensors. *Microporous Mesoporous Mater.* **2014**, *199*, 1-6.
2. Rana, V. K.; Selvaraj, M.; Parambadath, S.; Chu, S.-W.; Park, S. S.; Mishra, S.; Singh, R. P.; Ha, C.-S., Heterocyclic tri-urea isocyanurate bridged groups modified periodic mesoporous organosilica synthesized for Fe(III) adsorption. *J. Solid State Chem.* **2012**, *194*, 392-399.
3. Qiu, X.; Han, S.; Hu, Y.; Gao, M.; Wang, H., Periodic mesoporous organosilicas for ultra-high selective copper(ii) detection and sensing mechanism. *J. Mater. Chem. A* **2014**, *2* (5), 1493-1501.
4. Nunes, S. C.; de Zea Bermudez, V.; Cybinska, J.; Sá Ferreira, R. A.; Legendziewicz, J.; Carlos, L. D.; Silva, M. M.; Smith, M. J.; Ostrovskii, D.; Rocha, J., Structure and photoluminescent features of di-amide cross-linked alkylene-siloxane hybrids. *J. Mater. Chem. A* **2005**, *15* (35-36), 3876.
5. Li, Y.; Auras, F.; Lobermann, F.; Doblinger, M.; Schuster, J.; Peter, L.; Trauner, D.; Bein, T., A photoactive porphyrin-based periodic mesoporous organosilica thin film. *J. Am. Chem. Soc.* **2013**, *135* (49), 18513-9.
6. Herault, D.; Cerveau, G.; Corriu, R. J.; Mehdi, A., New mesostructured organosilica with chiral sugar derived structures: nice host for gold nanoparticles stabilisation. *Dalton transactions* **2011**, *40* (2), 446-51.
7. Gao, M.; Han, S.; Qiu, X.; Wang, H., Biphenyl-bridged periodic mesoporous organosilicas: Synthesis and in situ charge-transfer properties. *Microporous Mesoporous Mater.* **2014**, *198*, 92-100.
8. Seki, T.; McEleney, K.; Crudden, C. M., Enantioselective catalysis with a chiral, phosphane-containing PMO material. *Chem. Comm.* **2012**, *48*, 6369.
9. Waki, M.; Maegawa, Y.; Hara, K.; Goto, Y.; Shirai, S.; Yamada, Y.; Mizoshita, N.; Tani, T.; Chun, W. J.; Muratsugu, S.; Tada, M.; Fukuoka, A.; Inagaki, S., A solid chelating ligand: periodic mesoporous organosilica containing 2,2'-bipyridine within the pore walls. *J. Am. Chem. Soc.* **2014**, *136* (10), 4003-11.

10. MacLean, M. W. A.; Wood, T. K.; Wu, G.; Lemieux, R. P.; Crudden, C. M., Chiral Periodic Mesoporous Organosilicas: Probing Chiral Induction in the Solid State. *Chem. Mater.* **2014**, *26* (20), 5852-5859.
11. De Canck, E.; Dosuna-Rodríguez, I.; Gaigneaux, E.; Van Der Voort, P., Periodic Mesoporous Organosilica Functionalized with Sulfonic Acid Groups as Acid Catalyst for Glycerol Acetylation. *Materials* **2013**, *6* (8), 3556-3570.
12. Corma, A.; Das, D.; Garcia, H.; Leyva, A., A periodic mesoporous organosilica containing a carbapalladacycle complex as heterogeneous catalyst for Suzuki cross-coupling. *J. Catal.* **2005**, *229* (2), 322-331.
13. Santha Moorthy, M.; Park, S.-S.; Fuping, D.; Hong, S.-H.; Selvaraj, M.; Ha, C.-S., Step-up synthesis of amidoxime-functionalised periodic mesoporous organosilicas with an amphoteric ligand in the framework for drug delivery. *J. Mater. Chem.* **2012**, *22* (18), 9100.
14. Parambadath, S.; Rana, V. K.; Zhao, D.; Ha, C.-S., N,N'-diureylenepiperazine-bridged periodic mesoporous organosilica for controlled drug delivery. *Microporous Mesoporous Mater.* **2011**, *141* (1-3), 94-101.
15. Parambadath, S.; Rana, V. K.; Moorthy, S.; Chu, S.-W.; Park, S.-K.; Lee, D.; Sung, G.; Ha, C.-S., Periodic mesoporous organosilicas with co-existence of diurea and sulfanilamide as an effective drug delivery carrier. *J. Solid State Chem.* **2011**, *184* (5), 1208-1215.
16. Brian J. Melde, B. T. H., Christopher F. Blanford, and Andreas Stein, Mesoporous Sieves with Unified Hybrid Inorganic/Organic Frameworks. *Chem. Mater.* **1999**, *11*, 3302-3308.
17. S. Inagaki, S. G., Y. Fukushima, T. Ohsuna, O. Terasaki, Novel Mesoporous Materials with a Uniform Distribution of Organic Groups and Inorganic Oxide in Their Frameworks. *J. Am. Chem. Soc.* **1999**, *121*, 9611-9614.
18. T. Asefas, M. J. M., N. Coombs, G. A. Ozin, Periodic mesoporous organosilicas with organic groups inside the channel walls. *Nature* **1999**, *402*, 867-871.
19. Rebbin, V.; Jakubowski, M.; Pötz, S.; Fröba, M., Synthesis and characterisation of spherical periodic mesoporous organosilicas (sph-PMOs)

- with variable pore diameters. *Microporous Mesoporous Mater.* **2004**, *72* (1-3), 99-104.
20. Mandal, M.; Kruk, M., Family of Single-Micelle-Templated Organosilica Hollow Nanospheres and Nanotubes Synthesized through Adjustment of Organosilica/Surfactant Ratio. *Chem. Mater.* **2012**, *24* (1), 123-132.
21. Croissant, J.; Cattoen, X.; Wong Chi Man, M.; Dieudonne, P.; Charnay, C.; Raehm, L.; Durand, J. O., One-Pot Construction of Multipodal Hybrid Periodic Mesoporous Organosilica Nanoparticles with Crystal-Like Architectures. *Adv. Mater.* **2014**, *27* (1), 145.
22. Mohanty, P.; Landskron, K., Simple systematic synthesis of periodic mesoporous organosilica nanoparticles with adjustable aspect ratios. *Nanoscale research letters* **2009**, *4* (12), 1524-9.
23. Guan, B.; Cui, Y.; Ren, Z.; Qiao, Z. A.; Wang, L.; Liu, Y.; Huo, Q., Highly ordered periodic mesoporous organosilica nanoparticles with controllable pore structures. *Nanoscale* **2012**, *4* (20), 6588-96.
24. Chen, Y.; Xu, P.; Chen, H.; Li, Y.; Bu, W.; Shu, Z.; Li, Y.; Zhang, J.; Zhang, L.; Pan, L.; Cui, X.; Hua, Z.; Wang, J.; Zhang, L.; Shi, J., Colloidal HPMO nanoparticles: silica-etching chemistry tailoring, topological transformation, and nano-biomedical applications. *Adv. Mater.* **2013**, *25* (22), 3100-5.
25. Croissant, J.; Cattoen, X.; Man, M. W.; Gallud, A.; Raehm, L.; Trens, P.; Maynadier, M.; Durand, J. O., Biodegradable ethylene-bis(propyl)disulfide-based periodic mesoporous organosilica nanorods and nanospheres for efficient in-vitro drug delivery. *Adv. Mater.* **2014**, *26* (35), 6174-80.
26. Fatieiev, Y.; Croissant, J.; Julfakyan, K.; Deng, L.; Anjum, D. H.; Khashab, N. M., Enzymatically Degradable Hybrid Organic-Inorganic Bridged Silsesquioxane Nanoparticles for In-Vitro Imaging. *Nanoscale* **2015**.
27. Croissant, J.; Maynadier, M.; Gallud, A.; Peindy N'Dongo, H.; Nyalosaso, J. L.; Derrien, G.; Charnay, C.; Durand, J.-O.; Raehm, L.; Serein-Spirau, F.; Cheminet, N.; Jarrosson, T.; Mongin, O.; Blanchard-Desce, M.; Gary-Bobo, M.; Garcia, M.; Lu, J.; Tamanoi, F.; Tarn, D.; Guardado-Alvarez, T. M.; Zink, J. I., Two-Photon-Triggered Drug Delivery in Cancer Cells Using Nanoimpellers. *Angewandte Chemie International Edition* **2013**, *52* (51), 13813-13817.
-

28. Croissant, J.; Chaix, A.; Mongin, O.; Wang, M.; Clément, S.; Raehm, L.; Durand, J.-O.; Hugues, V.; Blanchard-Desce, M.; Maynadier, M.; Gallud, A.; Gary-Bobo, M.; Garcia, M.; Lu, J.; Tamanoi, F.; Ferris, D. P.; Tarn, D.; Zink, J. I., Two-Photon-Triggered Drug Delivery via Fluorescent Nanovalves. *Small* **2014**, *10* (9), 1752-1755.
29. Théron, C.; Gallud, A.; Carcel, C.; Gary-Bobo, M.; Maynadier, M.; Garcia, M.; Lu, J.; Tamanoi, F.; Zink, J. I.; Wong Chi Man, M., Hybrid Mesoporous Silica Nanoparticles with pH-Operated and Complementary H-Bonding Caps as an Autonomous Drug-Delivery System. *Chemistry – A European Journal* **2014**, *20* (30), 9372-9380.
30. R. Sharma, A. G., W. Steward, Curcumin: the story so far. *Eur. J. Cancer* **2005**, *41* (41), 1955-1968.
31. O. Naksuriya, S. O., R. M. Schiffelers, W. E. Hennink, Curcumin nanoformulations: A review of pharmaceutical properties and preclinical studies and clinical data related to cancer treatment. *Biomaterials* **2014**, *35*, 3365-3383.
32. A. Duvoix, R. B., S. Delhalle, M. Schneckeburger, F. Morceau, E. Henry, Chemopreventive and therapeutic effects of curcumin. *Cancer Lett* **2005**, *223*, 181-190.
33. G. Bar-Sela, R. E., M. Schaffer, Curcumin as an anti-cancer agent. *Curr. Med. Chem.* **2010**, *17*, 190-197.
34. J. Ravindran, S. P., B. B. Aggarwal, Curcumin and cancer cells: how many ways can curry kill tumor cells selectively? *AAPS J* **2009**, *11*, 495-510.
35. S. Shishodia, M. M. C., Role of curcumin in cancer therapy. *Curr. Prob. Cancer* **2007**, *31*, 243-305.
36. B. T. Kurien, A. S., H. Matsumoto, R. H. Scofield, Improving the solubility and pharmacological efficacy of curcumin by heat treatment. *Assay Drug Dev. Tech.* **2007**, *5*, 567-576.
37. H. H. Tønnesen, M. M., T. Loftsson, Studies of curcumin and curcuminoids. *Int. J. Pharm.* **2002**, *244*, 127-135.
38. C. Li, Y. Z., T. Su, L. Feng, Y. Long, Z. Chen, Silica-coated flexible liposomes as a nanohybrid delivery system for enhanced oral bioavailability of curcumin. *Int. J. Nanomed.* **2011**, *7*, 5995-6002.

39. Y. L. Lin, Y. K. L., N. M. Tsai, J. H. Hsieh, C. H. Chen, C. M. Lin, A lipo-PEG-PEI complex for encapsulating curcumin that enhances its antitumor effects on curcumin-sensitive and curcumin-resistance cells. *Nanomed. Nanotechnol.* **2012**, *8*, 318-327.
40. J. Shaikh, D. A., V. Beniwal, D. Singh, M. Kumar, Nanoparticle encapsulation improves oral bioavailability of curcumin by at least 9-fold when compared to curcumin administered with piperine as absorption enhancer. *Eur. J. Pharm. Sci.* **2009**, *37*, 223-230.
41. M. M. Yallapu, B. K. G., M. Jaggi, S. C. Chauhan, Fabrication of curcumin encapsulated PLGA nanoparticles for improved therapeutic effects in metastatic cancer cells. *J. Colloid Interface Sci.* **2010**, *351*, 19-29.
42. S. Acharya, S. K. S., PLGA nanoparticles containing various anticancer agents and tumour delivery by EPR effect. *Adv. Drug Deliv. Rev.* **2011**, *63*, 170-183.
43. Shruti, S.; Salinas, A. J.; Ferrari, E.; Malavasi, G.; Lusvardi, G.; Doadrio, A. L.; Menabue, L.; Vallet-Regi, M., Curcumin release from cerium, gallium and zinc containing mesoporous bioactive glasses. *Microporous and Mesoporous Materials* **2013**, *180*, 92-101.
44. K. Parvathy, P. N., P. Srinivas, Curcumin-amino acid conjugates: synthesis, antioxidant and antimutagenic attributes. *Food Chem.* **201**, *120*, 523-530.
45. S. Manju, K. S., Conjugation of curcumin onto hyaluronic acid enhances its aqueous solubility and stability. *J. Colloid Interface Sci.* **2011**, *359*, 318-325.
46. S. Anuchapreeda, Y. F., S. Okonogi, H. Ichikawa, Preparation of lipid nanoemulsions incorporating curcumin for cancer therapy. *J. Nanotechnol.* **2012**, *41*, 1-11.
47. S. S. Dhule, P. P., T. Frazier, R. Walker, J. Feldman, G. Tan, Curcumin-loaded γ -cyclodextrin liposomal nanoparticles as delivery vehicles for osteosarcoma. *Nanomed. Nanotechnol.* **2012**, *8*, 440-451.
48. W. Wichitnithad, U. N., P. S. Callery, P. Rojsitthisak, Effects of different carboxylic ester spacers on chemical stability, release characteristics and anticancer activity of mon-PEGylated curcumin conjugates. *J. Pharm. Sci.* **2011**, *100*, 5206-5218.
49. L. Zhongfa, M. C., J. Wang, W. Chen, W. Yen, P. Fan-Havard, Enhancement of curcumin oral absorption and pharmacokinetics of curcuminoids and

- curcumin metabolites in mice. *Cancer Chemother. Pharmacol.* **2012**, *69*, 679-689.
50. P. Zou, L. H., A. Maitra, S. T. Stern, S. E. McNeil, Polymeric curcumin nanoparticle pharmacokinetics and metabolism in bile duct cannulated rats. *Mol. Pharm.* **2013**, *10*, 1977-1987.
51. Y. Gao, Z. L., M. Sun, H. Li, C. Guo, J. Cui, Preparation, characterization, pharmacokinetics and tissue distribution of curcumin nanosuspensions with TPGS as stabilizer. *Drug Dev. Ind. Pharm.* **2010**, *36*, 1225-1234.
52. S. Balaji, B. C., Toxicity prediction of compounds from turmeric. *Food Chem. Toxicol.* **2010**, *48*, 2951-2959.
53. Cauda, V.; Schlossbauer, A.; Kecht, J.; Zürner, A.; Bein, T., Multiple Core-Shell Functionalized Colloidal Mesoporous Silica Nanoparticles. *J. Am. Chem. Soc.* **2009**, *131* (32), 11361-11370.
54. Cauda, V.; Schlossbauer, A.; Bein, T., Bio-degradation study of colloidal mesoporous silica nanoparticles: Effect of surface functionalization with organo-silanes and poly(ethylene glycol). *Microporous Mesoporous Mater.* **2010**, *132* (1-2), 60-71.
55. Kokubo, T.; Takadama, H., How useful is SBF in predicting in vivo bone bioactivity? *Biomaterials* **2006**, *27* (15), 2907-2915.
56. Cauda, V.; Engelke, H.; Sauer, A.; Arcizet, D.; Brauchle, C.; Radler, J.; Bein, T., Colchicine-loaded lipid bilayer-coated 50 nm mesoporous nanoparticles efficiently induce microtubule depolymerization upon cell uptake. *Nano letters* **2010**, *10* (7), 2484-92.

8.6 Appendix

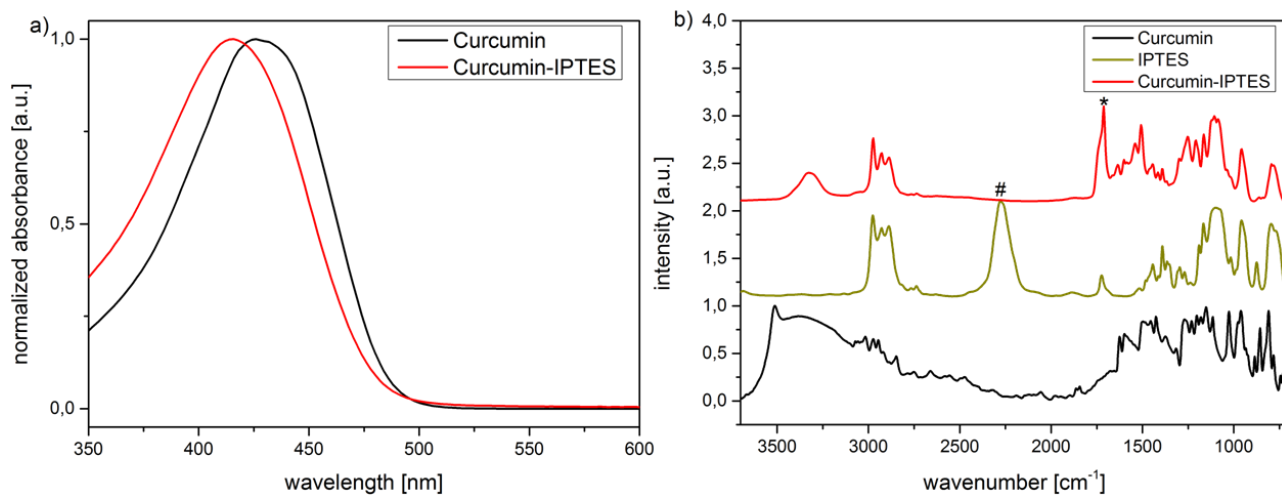


Figure S 8-1. UV-VIS absorption (a) and IR spectroscopy (b) data on the formation of the precursor.

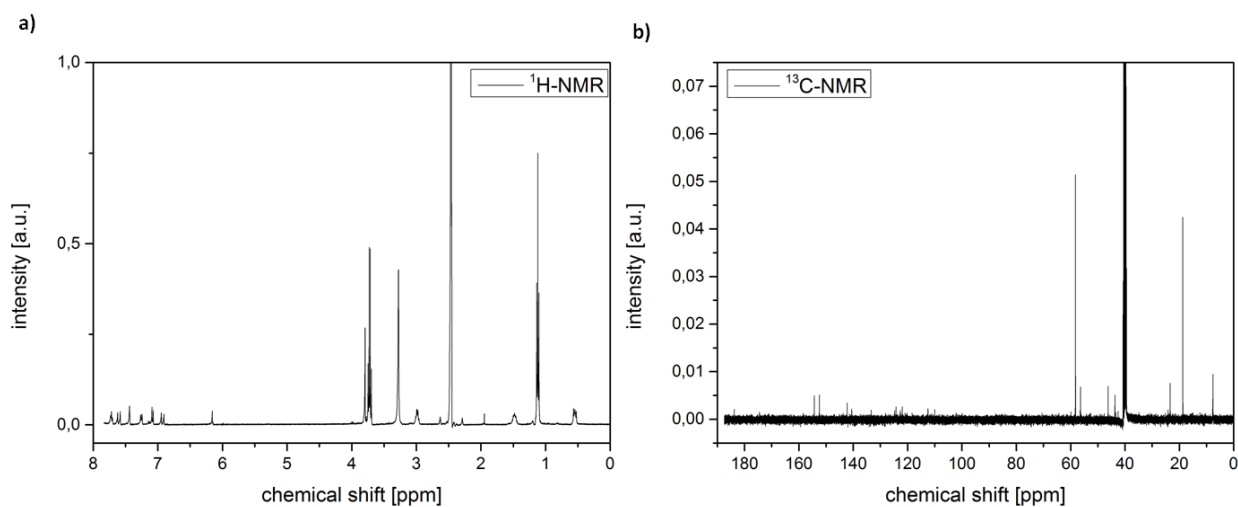


Figure S 8-2. ¹H-NMR (a) and ¹³C-NMR (b) data of the precursor Curcumin-IPTES.

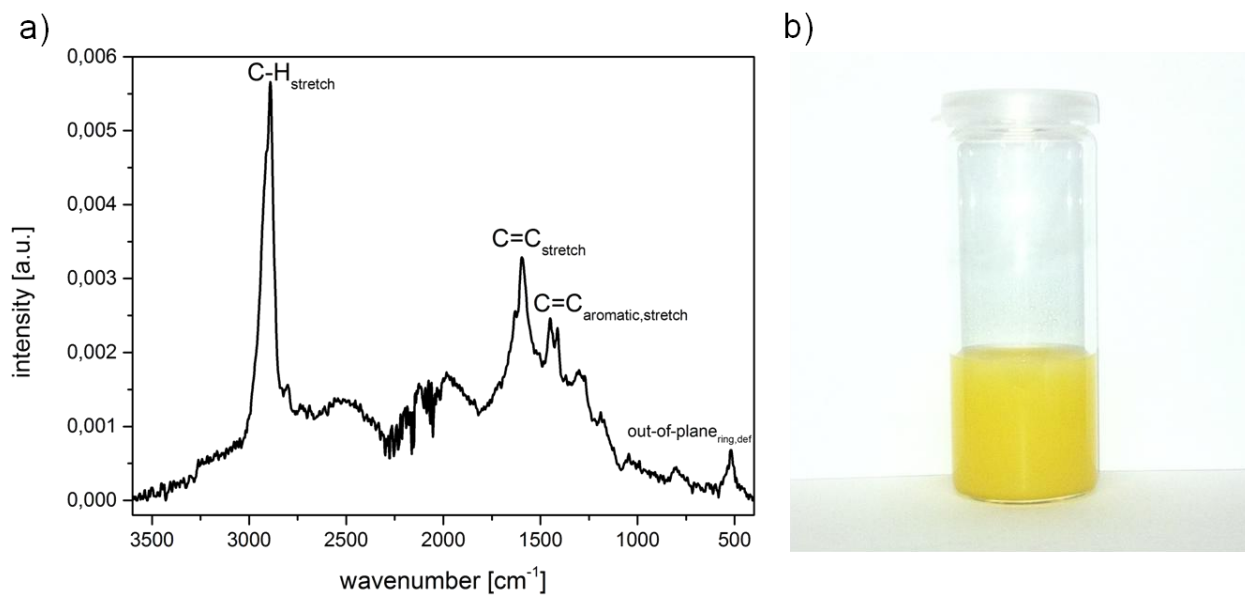


Figure S 8-3. Raman spectrum of MCNs (a), image of colloidal MCNs stored in ethanol (b).

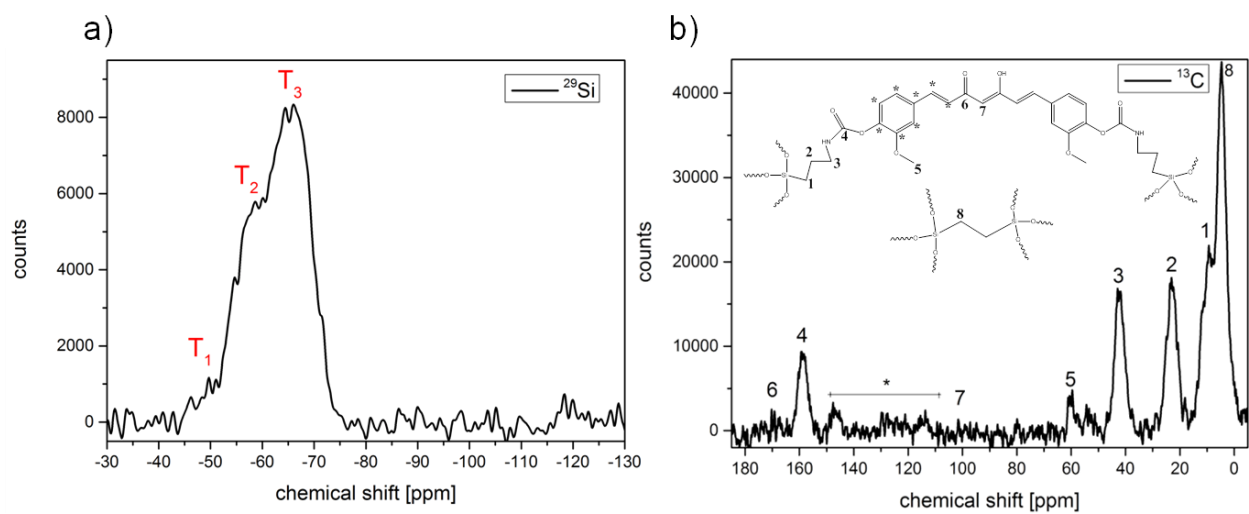


Figure S 8-4. ^{29}Si MAS ssNMR (a) and ^{13}C MAS ssNMR (b) of MCNs.

8. Lipid bilayer-coated curcumin-based mesoporous organosilica nanoparticles for cellular delivery

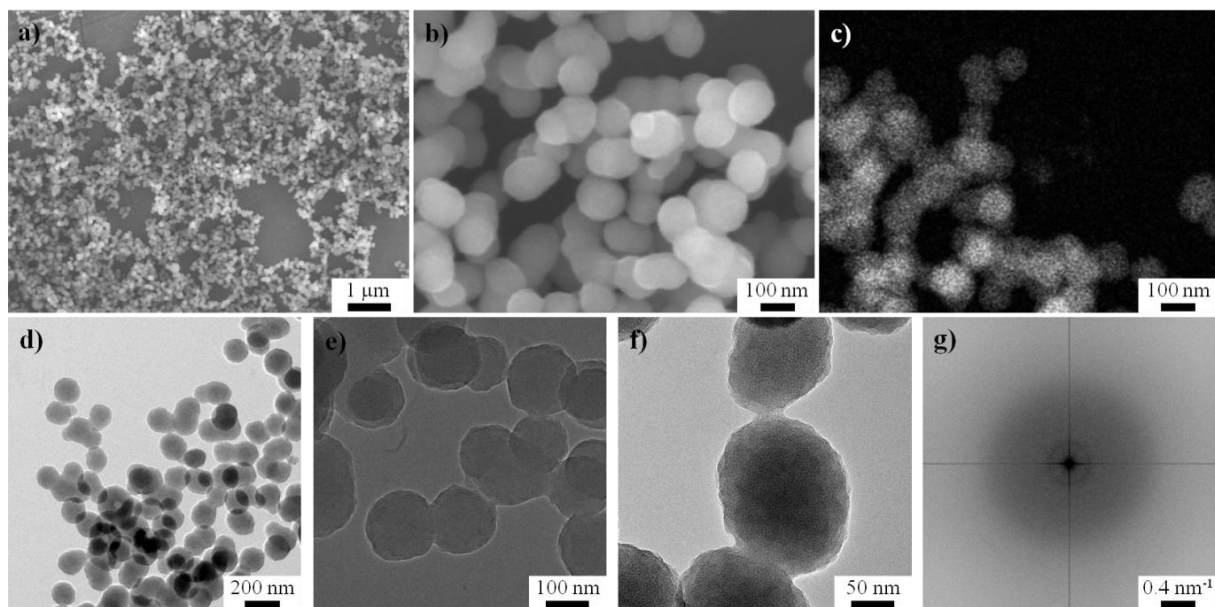


Figure S 8-5. Electron microscopy of MCNs. SEM images (a, b), STEM image (c), TEM images (d-f), FFT (g).

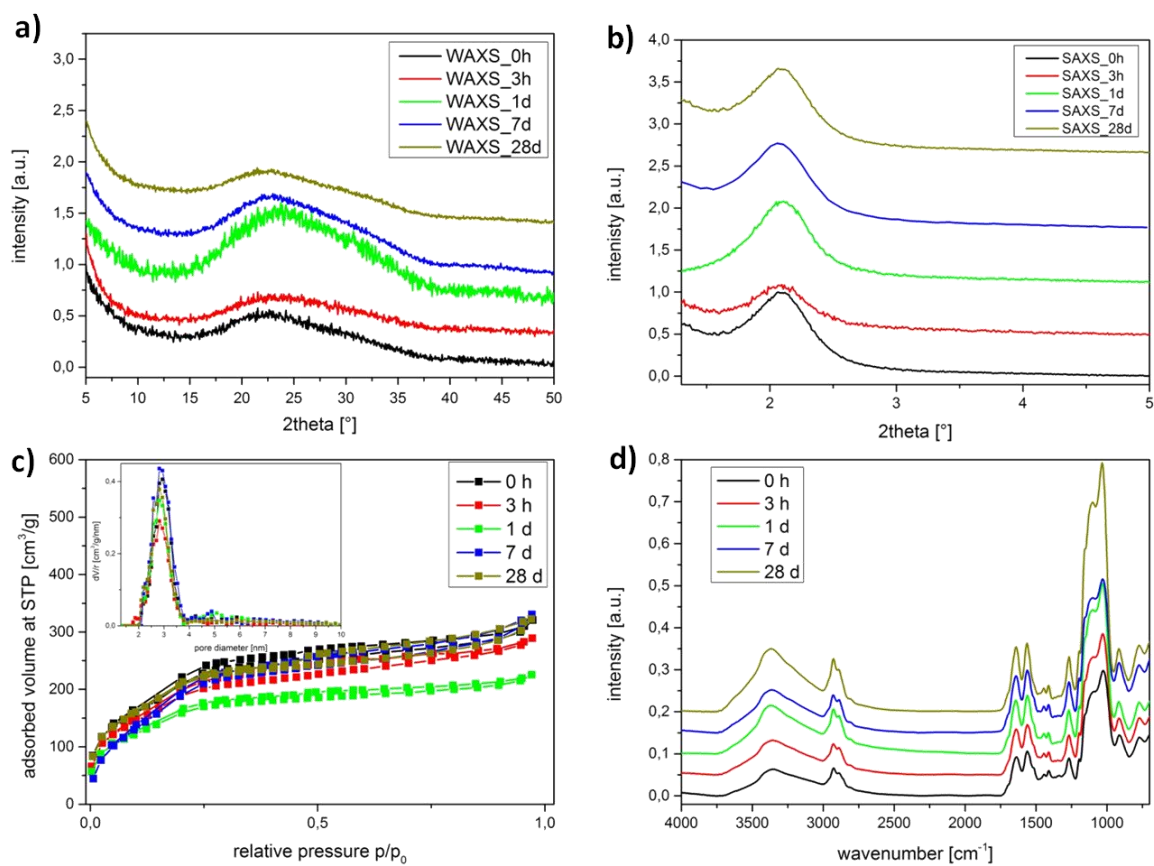


Figure S 8-6. Biostability study. Wide-angle X-ray scattering data (a, WAXS), small-angle X-ray scattering data (b, SAXS), nitrogen sorption isotherm (c, inset: pore size distribution), infrared spectroscopy (d).

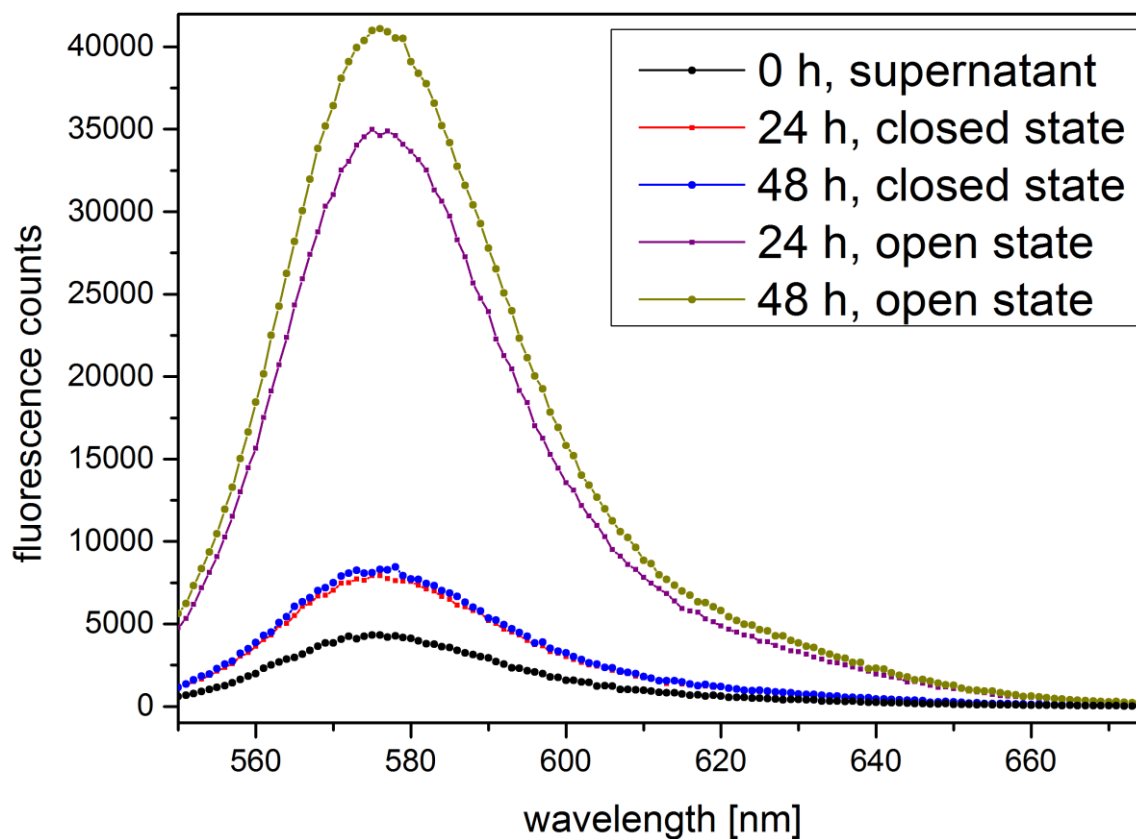


Figure S 8-7. *In vial* release experiment: Rhodamin B-loaded MCNs were sealed with SLB and measured in the closed and open state (opening of the lipid membrane was induced by adding the detergent Triton-X). Graphs show efficient sealing of the pore system and successful release of RhoB upon destruction of SLB within 48 h.

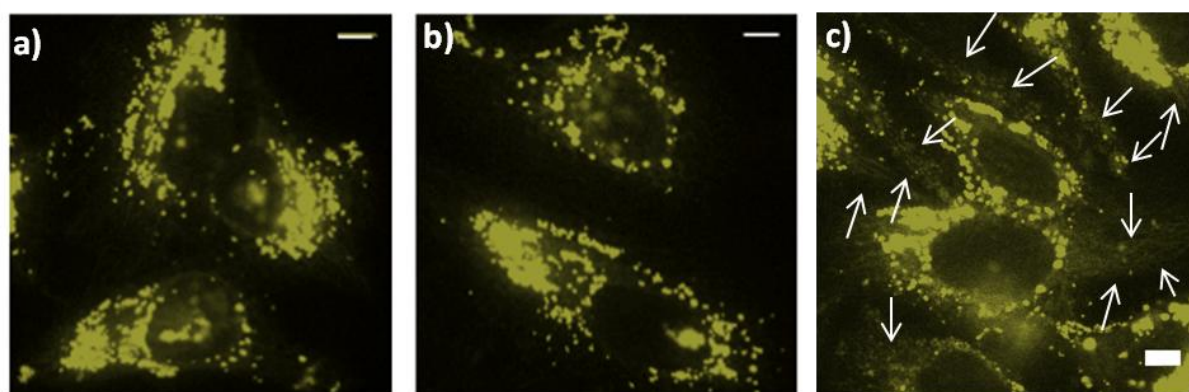


Figure S 8-8. Spinning disc micrographs of Rhodamin B loaded MCNs internalized by HeLa cells. After 24 h (a) and 48 h (b) only a slight release of Rhodamin B is visible. Upon addition of chloroquine release is significantly increased (indicated by white arrows) (c). Scale bar: 10 μm .

9 Biocompatible β -cyclodextrin nanoparticles as multifunctional carriers for cellular delivery

This chapter is based on the following work:

Stefan Datz, Bernhard Illes, Hanna Engelke, Thomas Bein, **2017**, *in preparation*.

Abstract

Nanoparticle-based biomedicine has received enormous attention for theranostic applications, as these systems are expected to overcome several drawbacks of conventional therapy. Herein, effective and controlled drug delivery systems with on-demand release abilities and biocompatible properties are used as a versatile and powerful class of nanocarriers. We report the synthesis of a novel biocompatible material, entirely consisting of covalently crosslinked organic molecules. Here, β -cyclodextrin structures were crosslinked with a rigid organic linker molecule to obtain small (~150 nm) and highly water-dispersable nanoparticles. The nanoparticles could be covalently labeled with dye molecules to effectively track them in *in vitro* cell experiments. Fast sugar-mediated cell-uptake kinetics was observed on HeLa cells, revealing particle uptake within less than an hour. Additionally, the particles could be loaded with different cargo molecules showing pH-responsive release behavior. Successful nuclei staining with Hoechst 33342 dye and effective cell killing with doxorubicin as cargo molecules were shown in live-cell experiments, respectively. This novel nanocarrier concept provides a promising platform for the development of controllable and highly biocompatible theranostic systems.

9.1 Introduction

Cancer therapy is currently shifting from a standardized systemic approach to a more personalized and specifically customized disease treatment. Such personalized treatments use multifunctional drugs in combination with carrier systems and are ideally based on molecular-level diagnosis.¹ After decades of research, the demand for innovative biocompatible nanomaterials for the transport of therapeutic agents is still growing. In particular, nanoparticle-based targeting of tumor cells has emerged as a potential therapeutic approach to release effective drug doses within the tumorous tissue.²⁻⁶ Because of the prolonged blood circulation time combined with nonspecific accumulation in tumors through the enhanced permeability and retention (EPR) effect, nanoparticles have been regarded as a suitable candidate in the pharmaceutical fields, especially for targeted and personalized cancer therapy. A number of different carrier systems have been investigated in the field of nanobiosciences with differing results in the last decade. Besides inorganic materials, such as mesoporous silica nanoparticles (MSNs),⁷⁻¹⁵ periodic mesoporous organosilica nanoparticles (PMOs),^{10, 16-20} or metal-based materials, e.g. Au-²¹⁻²³ or iron oxide nanoparticles,²⁴⁻²⁹ polymeric micelles,³⁰⁻³² lipids,³³⁻³⁵ and DNA origami are other examples for potential drug delivery systems used in fundamental biomedical research,³⁶⁻³⁸ However, some of these materials have certain drawbacks, e.g. polymeric micelles and lipids often need specific formulations for different cargos, and may face stability issues. Besides small magnetic iron-oxide based materials, none of the other larger solid nanoparticles, such as silica materials, have reached clinical trials, partially due to concerns about the unknown fate of these particles in the human organism.³⁹ In obvious contrast to the ever-growing number of sophisticated nanoparticle-based cell-targeting strategies that effectively target tumor cells *in vitro*, only few studies showed successful tumor-cell specific targeting and controlled cancer cell killing *in vivo*. Even fewer nanoformulations have found their way into clinical studies and

practice.⁴⁰ Ligand-assisted targeting of cancer cells with nanoparticles *in vivo* through specific receptor-mediated uptake can be limited due to protein corona formation.⁴¹ Therefore, there is a rapidly growing interest in new nanomaterials which can overcome some of the aforementioned limitations. Sugar-based materials are promising candidates since cancer cells are known to have a faster glycolysis metabolism that selectively leads to an increased glucose uptake compared to healthy cells.⁴²⁻⁴⁵ In the following work, a novel biocompatible multifunctional nanomaterials class consisting of cross-linked β -cyclodextrin molecules is presented. Cyclodextrins (CDs) are a family of cyclic oligosaccharides composed of six, seven, or eight D(+)-glucose units linked by α -1,4-linkages, which are named α -, β -, and γ -CD, respectively.⁴⁶ These different oligosaccharides are frequently used in the medical field because of their biocompatibility and their low toxicity.⁴⁷⁻⁵⁰ CDs have a hydrophilic exterior and a hydrophobic cavity inside the oligosaccharide rings that can be used to encapsulate different kinds of guest and cargo molecules.⁵¹⁻⁵⁴ This encapsulation is based on supramolecular host-guest interactions such as hydrogen bonding, van-der-Waals forces or hydrophobic interactions, and is used in various application fields including biomedicine, catalysis, environmental protection and separation processes.⁵⁵ Although the use of different CDs in the medical field has been documented for decades, their application is still rather limited due to significant synthetic challenges, demanding the development of more specific and controllable CD-containing nanoparticles. Until now, a variety of supramolecular nanoparticles (SNPs) with CD-building blocks have been investigated. However, SNPs are particles in which different building blocks are brought together by non-covalent interactions resulting in controlled larger assemblies.⁵⁶ The assembly is either based on electrostatic interactions or host-guest interactions.^{57, 58} The non-covalent interactions limit their use for drug delivery applications, since they might degrade easily before they reach their target and any new guest molecule that is incorporated or loaded into the particle needs to be optimized

regarding its interactions with the particle structure. Thus, a covalently crosslinked CD nanoparticle is viewed as an enabling concept that could facilitate a breakthrough for drug delivery applications. Recently, different approaches were used to prepare covalently crosslinked CD molecule-containing materials. One is defined by crosslinking α -CD-polyethyleneglycol (PEG) inclusion complexes by using epichlorohydrin. The nanomaterial was obtained after extracting the PEG chains that penetrated the hydrophobic cavity.⁵⁹ In another approach, Dichtel *et al.* polymerized β -CD in a nucleophilic aromatic substitution reaction with tetrafluoro terephthalonitrile and obtained mesoporous bulk material that was used to rapidly remove organic micropollutants from waste water.⁶⁰ However, no nanoparticles of covalently crosslinked CD molecules were obtained yet. In the following work, we combined these different approaches to crosslink β -CD-PEG inclusion complexes with rigid aromatic groups providing for the first time small, dispersible and thermally stable nanoparticles. These NPs can be covalently labeled with dye molecules exploiting simple click-chemistry to track them effectively in *in vitro* cell experiments. β -CD NPs were taken up by cancer cells very rapidly and could efficiently release different cargo molecules. This novel and biocompatible nanocarrier concept provides a promising platform for the development of controllable and efficient theranostic systems.

9.2 Results and Discussion

Highly dispersible and thermally stable β -CD NPs for possible drug delivery applications were derived from a carefully controlled nucleophilic aromatic substitution reaction with tetrafluoroterephthalonitrile (TFTN, see Figure 9-1A).

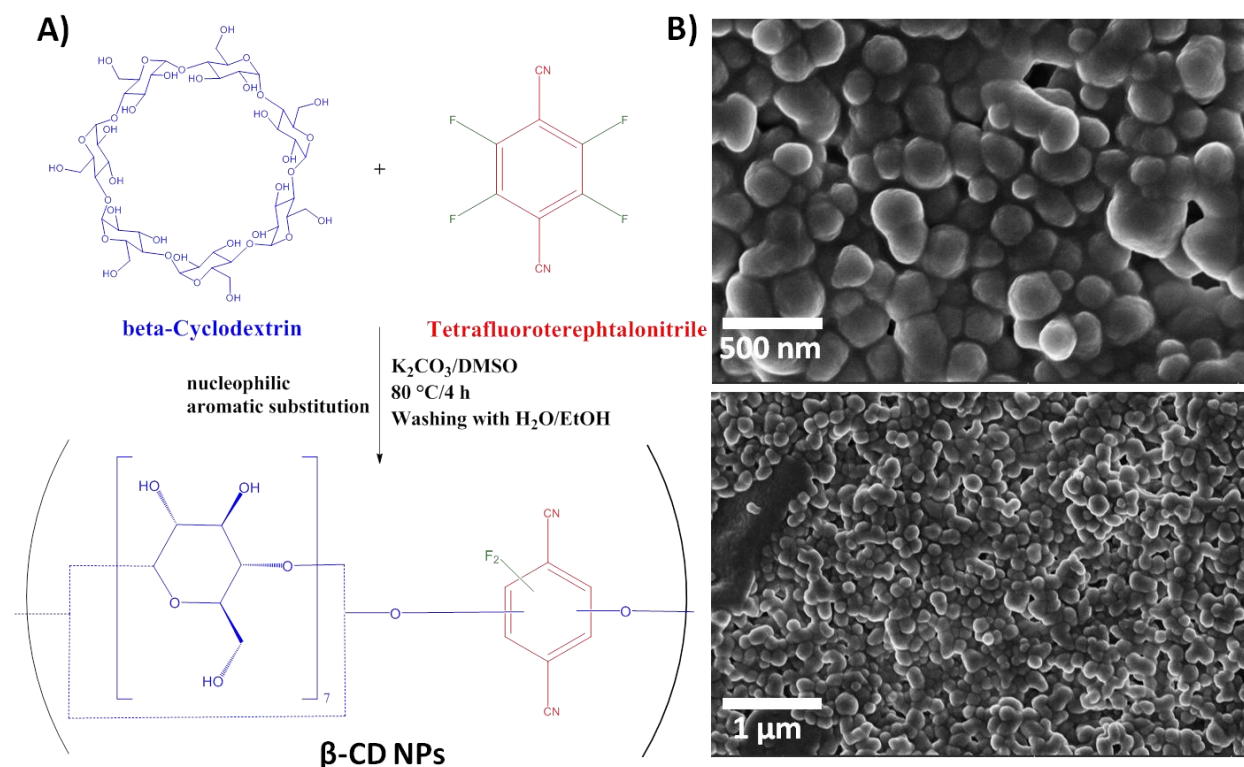


Figure 9-1: Synthesis scheme of β -CD NPs following a nucleophilic aromatic substitution reaction with TFTN (A), SEM images of β -CD NPs showing spherical particles with a narrow particle size distribution (B).

Since cyclodextrins (CDs) are known to form inclusion complexes with certain linear polymer chains such as poly(ethylene glycol) (PEG), this approach was used to create self-assembled aggregates of CD nanostructures.⁶¹ By modifying previously described synthesis procedures, these polyrotaxane structures were reacted with the rigid aromatic linker TFTN to form small and water-dispersible spherical nanoparticles. In this work, the β -CD-PEG inclusion complexes self-assembled with the help of CTAB surfactant into spherical nanostructures and were subsequently polymerized and cross-linked with TFTN in a suspension of K_2CO_3 in dimethylsulfoxide (DMSO) at $80\text{ }^\circ C$. Several washing steps were essential to remove the excess of precursors and salt and the included PEG chains, resulting in a pale yellow suspension of β -CD NPs with a yield of 25%. As can be seen in the scanning electron

microscopy (SEM) images in Figure 9-1B the obtained nanoparticles exhibit diameters of 150 to 200 nm with a narrow particle size distribution. Additional transmission electron microscopy (TEM) images can be found in the supporting information. Further characterization of the obtained nanomaterial is shown in Figure 9-2. Dynamic light scattering (DLS, Figure 9-2A) measurements reveal a high colloidal stability with hydrodynamic particle diameters of about 180 nm in water, rendering the obtained β -CD NPs useful for cellular delivery applications. Because of their exceptional colloidal stability without agglomeration in aqueous solutions, no additional hydrophilic coating such as PEGylation is necessary to use them in biotheranostics.⁶² Infrared spectroscopy (Figure 9-2B) was used to follow the formation of β -CD NPs with TFTN as the rigid organic crosslinker. The strong signal (a) at 1035 cm^{-1} corresponds to characteristic $\text{R}_3\text{C-OH}$ stretching vibrations due to the oligosaccharide rings of the incorporated β -cyclodextrin compounds. Signal (b) at 1260 cm^{-1} is due to saturated aliphatic C-O-C ether vibrations of the sugar rings and newly formed asymmetric alkyl-aryl-ether $=\text{C-O-C}$ vibrations of the crosslinked material. The aromatic system of TFTN incorporated into the nanostructure of β -CD NPs is also confirmed by the signals (c) corresponding to aromatic $-\text{C}=\text{C}-$ stretching vibrations and (d) corresponding to the strong nitrile vibration. The very broad band (e) around 3200 cm^{-1} is attributed to O-H absorption of the incorporated oligosaccharide building blocks. Additional solid-state nuclear magnetic resonance (ssNMR) characterization reveals the presence of both TFTN and β -cyclodextrin in the crosslinked material (see SI). Figure 9-2C displays nitrogen sorption experiments of freeze-dried β -CD NPs and reveals an isotherm with a calculated specific Brunauer-Emmett-Teller (BET) surface area of about $140\text{ m}^2/\text{g}$. The pore size distribution (inset) shows different pore sizes ranging from 1 to 6.5 nm comprising the majority of the accessible pore volume of $0.26\text{ cm}^3/\text{g}$. Thermogravimetric analysis (TGA) of β -CD NPs (Figure 9-2D) indicates the presence of a thermally stable material up to $285\text{ }^\circ\text{C}$ and a

complete mass loss of almost 100 % up to 900 °C. Zeta potential measurements show that the nanoparticles have a negative surface charge of about -35 mV at pH 7 due to the free hydroxyl groups of the oligosaccharide compounds. This zeta potential is comparable to other nanocarriers such as unfunctionalized mesoporous silica nanoparticles.⁶³

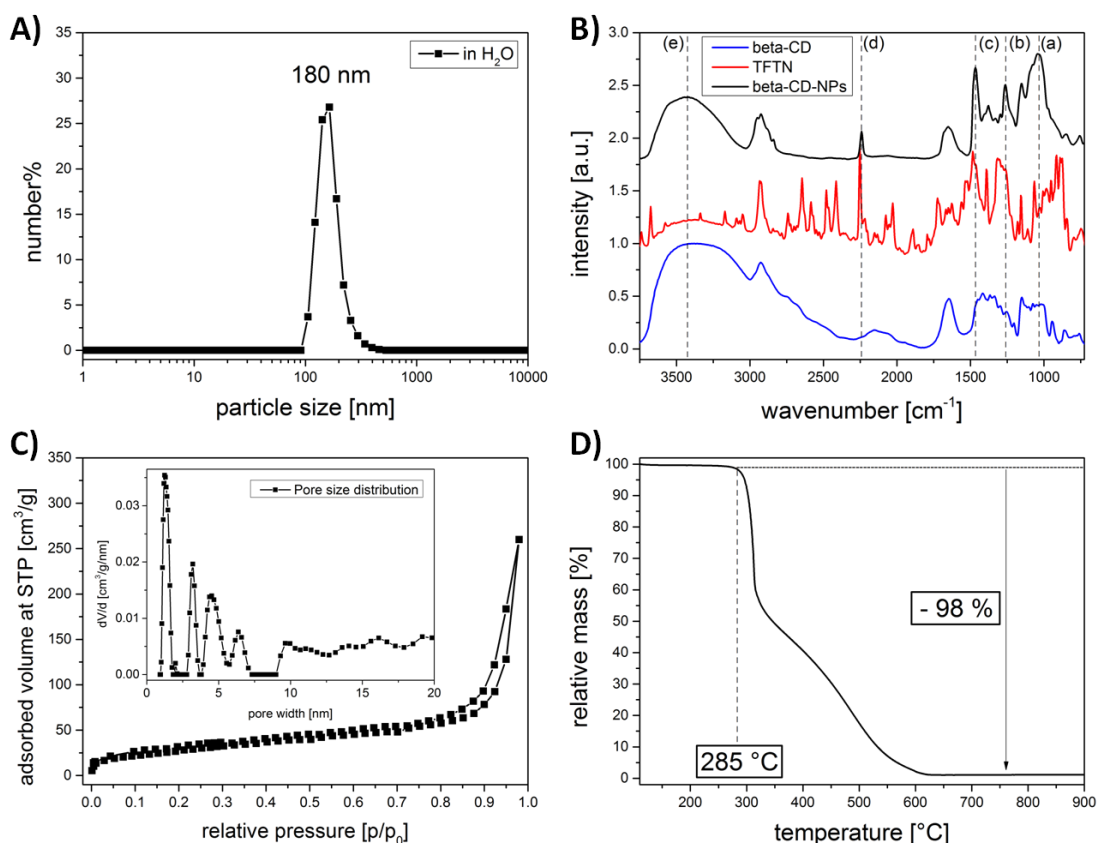


Figure 9-2: Characterization of β -CD NPs. A) Dynamic light scattering (DLS) revealing hydrodynamic particle diameters of about 180 nm in aqueous solution. B) Infrared spectroscopy data of β -CD (blue), TFTN (red) and β -CD NPs (black) with characteristic vibrations. Spectra were normalized and shifted for clarity by 0.75 a.u. along the y-axis. C) Nitrogen sorption isotherm and pore size distribution (inset) of β -CD NPs. D) Thermogravimetric analysis (TGA) up to 900 °C of β -CD NPs.

With this size and zeta potential as well as their porosity maintained even in the dry state, the particles reveal promising properties for drug delivery purposes. Therefore, the synthesized nanoparticles were subsequently used for *in vitro* drug delivery experiments. First, the cell uptake kinetics of rhodamine-labeled β -CD nanoparticles was studied on HeLa cells. To

obtain labeled nanoparticles, the free nitrile groups of the incorporated organic crosslinker can be used to covalently attach specific dye molecules. Here, the fluorescent tetramethylrhodamine (TAMRA) azide was used under mild reaction conditions in a zinc-catalyzed formation of a tetrazole-ring with the free nitrile groups of β -CD nanoparticles.⁶⁴ The formation of the compound was followed with IR spectroscopy (see SI). After several washing steps the particles were used for *in vitro* experiments.

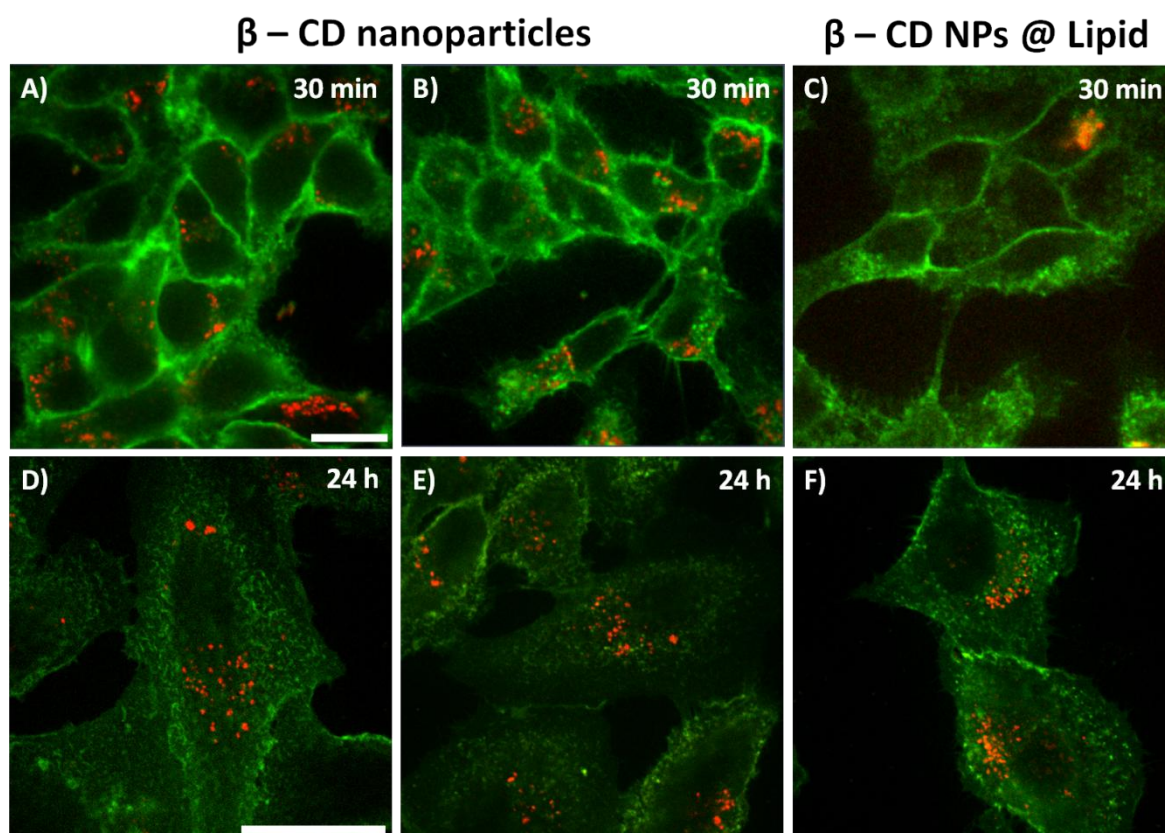


Figure 9-3: Upper panel: *In vitro* cell uptake of rhodamine-labeled β -CD nanoparticles (red) without additional coating (A, B) and with lipid coating (C) after 30 min of incubation on WGA-stained HeLa cells (green). The blurry red spot in C) results from an accumulation of particles on top of the cells. Lower panel: *In vitro* cell uptake of rhodamine-labeled β -CD nanoparticles (red) without additional coating (D, E) and with lipid coating (F) after 24 h of incubation on WGA-stained HeLa cells (green). Scale bar represents 10 μ m, respectively.

The upper panel of Figure 9-3 shows representative confocal microscopy images of particle uptake by HeLa cells after just 30 min of incubation. The red-fluorescent material was

efficiently internalized by cancer cells - even after very short incubation times of 30 minutes (Figure 9-3 A, B). Compared to the uptake of other nanomaterials, the internalization was very fast, possibly due to the oligosaccharide nature of the particles and sugar-receptor mediated endocytosis.^{65, 66} As a reference experiment, the particles were coated with a lipid bilayer in order to compare cell uptake kinetics with as-synthesized β -CD nanoparticles (see Figure 9-3 C and F). After 30 min, exclusively uncoated β -CD nanoparticles were taken up by HeLa cells, whereas after 24 h of incubation both particle types are internalized. The experiment leads us to the assumption that the oligosaccharides are effectively taken up via sugar receptors and that the oligosaccharides can be shielded by the lipid coating resulting in slower cell uptake compared to the sugar-receptor mediated endocytosis of the uncoated particles. This suggests that an additional surface coating for as-synthesized β -CD nanoparticles is counterproductive for cellular uptake.

In order to obtain more insights into the endocytosis pathway of β -CD nanoparticles, an *in vitro* competition experiment was performed. For this purpose, prior to the particle incubation the sugar receptors on the external cell surface of HeLa cells were saturated by adding concentrated aqueous solutions of different mono- and oligosaccharides, namely D-glucose, D-L-arabinose, 2-deoxy-D-glucose and β -cyclodextrin (see SI, Figure S 9-3). In all cases the particle uptake was hindered when the receptors were blocked, confirming our hypothesis that the endocytosis of β -CD nanoparticles is mediated via a specific sugar-receptor mediated cell uptake.

Next, the drug delivery and release properties of β -CD nanoparticles were evaluated by the loading and release of different guest molecules, namely Hoechst 33342 as nuclei staining dye and doxorubicin as model chemotherapeutic agent. Rhodamine-labeled β -CD NPs were loaded with Hoechst 33342 or doxorubicin and subsequently used for *in vitro* release

experiments. The inclusion capability of the β -CD nanoparticles was evaluated by the loading and release of different guest molecules. Using the porous β -CD cavities that were liberated from the inclusion of PEG, the β -CD nanoparticles could be loaded with either Hoechst 33342 as a nuclei staining dye or with doxorubicin as a chemotherapeutic agent, respectively. First, we studied loading and release of Hoechst 33342. Strikingly, the benzimidazole-containing compound is effectively loaded and efficiently released after particle endocytosis due to the acidification in the lysosomal compartments that destroys the hydrophobic interaction of Hoechst 33342 and the particle cavities (Figure 9-4).^{67, 68} Since Hoechst 33342 is membrane-permeable, it is able to penetrate the lysosomal membrane and to efficiently stain the nuclei of HeLa cells within very short time periods of less than 10 minutes.

As a reference experiment the used particle solution was centrifuged after 2 h and the supernatant was incubated on HeLa cells. No nuclei staining could be observed. Since Hoechst 33342 is a live cell stain, any molecules in the solution would have stained the nuclei. The absence of any staining resulting from the supernatant demonstrates that no cargo molecules were released prematurely and that the *in vitro* nuclei staining is due to the acidification of nanoparticles in the endosomal compartments that triggers the release of the dye. This rapid and efficient delivery and release of Hoechst 33342 as model cargo suggests that the newly synthesized particles can serve as a promising drug delivery platform with controlled release mechanism.

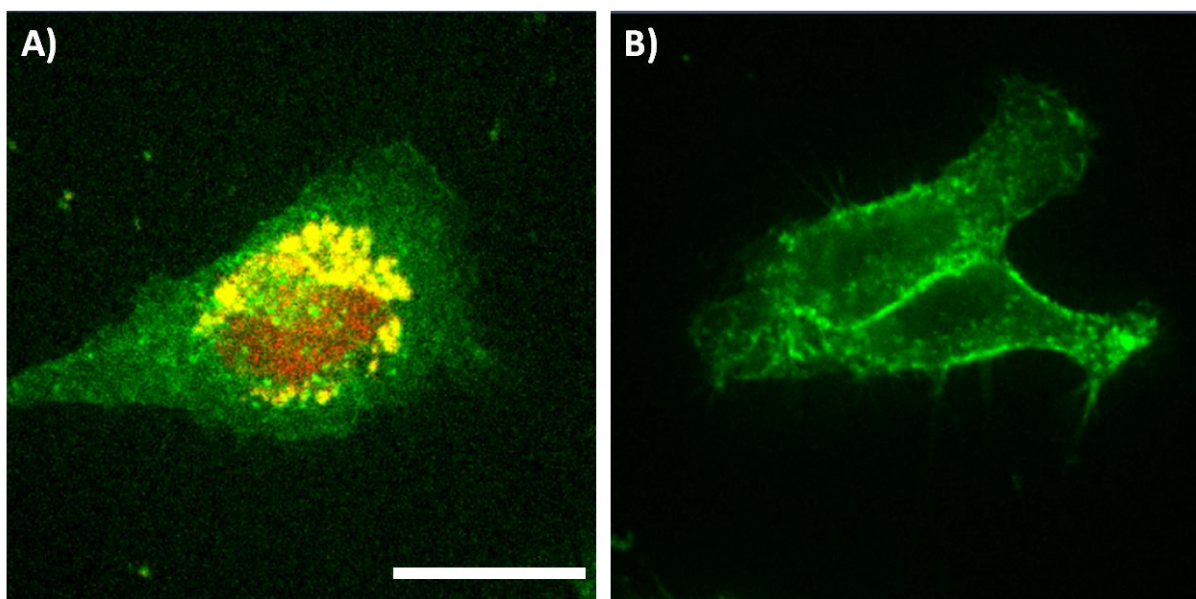


Figure 9-4: *In vitro* Hoechst 33342 release on HeLa cells. A) Rhodamin-labelled β -CD NPs (yellow) released Hoechst 33342 nuclei staining (red) on WGA-stained HeLa cells (green) after just 2 h of incubation time. B) As a control experiment the supernatant of centrifuged particles (after 2 h) was added to HeLa cells showing no nuclei staining, i.e. no premature release of cargo molecules. Scale bar represents 10 μ m.

In order to investigate the ability of our newly developed drug delivery system to transport and release chemotherapeutics and to affect cancer cells with their cargo, we replaced the model cargo Hoechst 33342 with doxorubicin (DOX), a classic cytostatic agent. DOX is known to form inclusion complexes based on hydrophobic interactions with β -cyclodextrin structures similarly to Hoechst 33342 and should therefore exhibit a similar loading and release behavior. Additionally, it should reveal a pH-responsive release behavior due to enhanced solubility when protonated.⁶⁹⁻⁷¹ Hence, the effect of particles containing DOX on HeLa cells was investigated. Free DOX is membrane-permeable and is able to induce an uncontrolled cell death within a few hours. Thus, we expected it to escape from the endosomal membrane when released from the particle in the lysosome and to subsequently induce cell death within a few hours after endosomal escape.

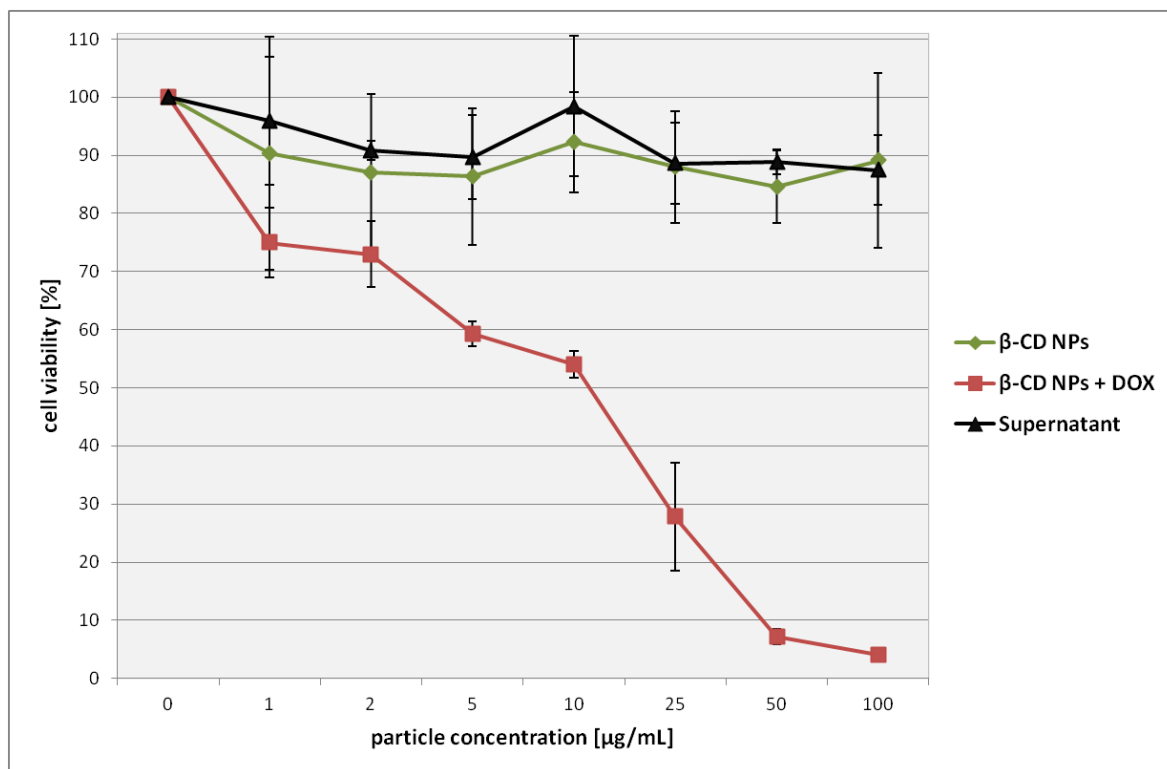


Figure 9-5: Dose-dependent cell-viability study on HeLa cells after 24 h of incubation with β -CD NPs, DOX-loaded β -CD NPs and the supernatant after centrifugation as a reference.

Indeed, our newly developed β -CD NPs provided intracellular DOX release and caused efficient cell death after 24 h of incubation with a calculated IC_{50} value of 7.23 $\mu\text{g/mL}$ for the DOX-loaded β -CD particles. In addition, the nanoparticles exhibited an exceptionally high DOX-loading capacity of up to 40 wt% (see SI, Figure S 9-4). The dose-dependent cell viability assay demonstrates that DOX was delivered in a controlled manner via the particles and released only after endosomal acidification. In contrast, as-synthesized β -CD NPs without any cargo show good biocompatibility in the dose-dependent cell viability studies (Figure 9-5). As a control experiment the DOX-loaded nanoparticles were centrifuged after 24 h storage and the respective amount of supernatant was incubated on HeLa cells. This control revealed good biocompatibility, i.e. no prematurely released cargo molecules were present. This experiment shows the great potential of β -CD NPs to efficiently deliver chemotherapeutics to cancer cells without premature release. The newly developed

biocompatible carrier system provides the ability to act as a general platform for cellular delivery applications with exceptionally fast cell uptake kinetics.

9.3 Conclusion

To conclude, we have developed a novel nanomaterial consisting of covalently crosslinked β -cyclodextrin molecules as the main organic component. The obtained nanoparticles are small (~150 nm) and highly dispersible in aqueous solutions. They exhibit very fast cell uptake kinetics due to sugar-receptor mediated endocytosis and can be covalently labeled with dye molecules to effectively track them in *in vitro* experiments. Furthermore, the porous cavities of the particles can be loaded with different cargo molecules, which are subsequently released in the endosomal cell compartments due to acidification. This triggered release mechanism allows us to show efficient nuclei staining with Hoechst 33342 dye and effective cancer cell killing with doxorubicin as cargos, respectively. Thus, the nanoparticles show great potential for future applications as a biocompatible drug carrier system.

9.4 Experimental Part

Materials. β -cyclodextrin (97 %, Sigma Aldrich), tetrafluoroterephthalonitrile (TFTN, 98 %, Alfa Aesar), polyethylene glycol 2000 (PEG2000, BioUltra, Sigma Aldrich), potassium carbonate (K_2CO_3 , 99.5 %, Grüssing GmbH), tetramethylrhodamine 5-carboxamido-(6-azidohexanyl) (TAMRA azide, Base click), doxorubicin hydrochloride (98 % HPLC, Sigma Aldrich), D-glucose (Sigma Aldrich), D-L-arabinose (Sigma Aldrich), 2-deoxy-D-glucose (Sigma Aldrich), Hoechst 33342 trihydrochloride (ThermoFisher Scientific), cetyl trimethylammonium bromide (Sigma Aldrich), wheat germ agglutinin, Alexa Fluor® 488 conjugate (lifeTechnologies), Dulbecco's modified Eagle's medium (DMEM) (lifeTechnologies), Hank's balanced salt solution (HBSS-buffer, Sigma Aldrich) were used as received. Ethanol (EtOH, absolute, Aldrich), hydrochloric acid (1 M, Bernd Kraft), dimethylsulfoxide (DMSO, anhydrous, >99.9 %, Sigma Aldrich) and dimethylformamide (DMF, >99.9 %, anhydrous, Sigma Aldrich) were used as solvents without further purification. Bidistilled water was obtained from a millipore system (Milli-Q Academic A10).

Characterization. DLS and zeta potential measurements were performed on a Malvern Zetasizer Nano instrument equipped with a 4 mW He-Ne-Laser (633 nm) and an avalanche photodiode detector. DLS measurements were directly recorded in diluted colloidal suspensions of the particles at a concentration of 1 mg/mL. Zeta potential measurements were performed using the add-on Zetasizer titration system (MPT-2) based on diluted NaOH and HCl as titrants. For this purpose, 1 mg of the particles was diluted in 10 mL bi-distilled water. Thermogravimetric analyses (TGA) of the bulk-extracted samples (approximately 10 mg) were recorded on a Netzsch STA 440 C TG/DSC. The measurements proceeded at a heating rate of 10 °C/min up to 900 °C in a stream of synthetic air of about 25 mL/min. Nitrogen sorption measurements were performed on a Quantachrome Instrument NOVA 4000e at -196 °C. Sample outgassing was performed for 12 hours at a vacuum of 10 mTorr at 120 °C.

Pore size and pore volume were calculated by a QSDFT equilibrium model of N₂ on carbon, based on the adsorption and desorption branch of the isotherms. A BET model was applied in the range of 0.05 – 0.20 p/p₀ to evaluate the specific surface area. Infrared spectra of dried sample powder were recorded on a ThermoScientific Nicolet iN10 IR-microscope in reflection-absorption mode with a liquid-N₂ cooled MCT-A detector. Cross-polarized ¹³C-MAS NMR measurements were performed on a Bruker DSX Avance500 FT spectrometer (11.74 T) in a 4 mm ZrO₂ rotor. The spinning rate was 10 kHz and a total number of 256 scans was recorded. The used contact time was 2 ms and the recycle delay was 1 s. Scanning electron microscopy (SEM) was performed on a FEI Helios instrument at an acceleration voltage of 2.5 kV. For this purpose the samples were put on an adhesive graphite film and sputtered twice with carbon with a BALTEC MED 020 Coating System. Transmission electron microscopy (TEM) data were obtained with a FEI Titan Themis 60–300 microscope at an acceleration voltage of 80 kV.

Synthesis of β-CD NPs. In a 40 mL polypropylene reactor, 400 mg β-cyclodextrin (0.35 mmol), 200 mg tetrafluoroterephthalonitrile (TFTN, 1.00 mmol), 600 mg K₂CO₃ (4.34 mmol), 50 mg polyethylene glycol (PEG₂₀₀₀) and 50 mg cetyltrimethylammonium bromide (CTAB, 0.14 mmol) were mixed with 15 mL anhydrous DMSO. The mixture was sonicated (15 min) and subsequently stirred at 900 rpm and 80 °C for 3 h. The orange suspension was cooled to room temperature and 15 mL bidistilled water and 15 mL hydrochloric acid (1 M) were slowly added to the reaction mixture. After centrifugation for 15 minutes at 7830 rpm (7197 rcf) the isolated light yellow solid was washed extensively with water (2 x 40 mL), HCl (1 M, 2 x 40 mL) and ethanol (2 x 40 mL) followed by centrifugation steps (15 min, 7197 rcf), respectively. Finally, the pale yellow powder was dispersed in 10 mL bidistilled water and used for further characterization (150 mg, 25 % yield).

Rhodamine-labelling of β -CD NPs. 1 mg of β -CD NPs in ethanolic solution were mixed with 2 μ L TAMRA-azide (2 mg/mL in anhydrous DMF) and a catalytic amount of zinc(II) acetate dihydrate. The mixture was shaken at 37 °C for 12 h and afterwards washed extensively with ethanol and water (centrifugation steps: 14,000 rpm, 16,837 rcf, 4 min) until no fluorescence could be detected in the supernatant. Finally, the particles were redispersed in 1 mL H₂O and used for *in vitro* uptake experiments.

Cargo loading of β -CD NPs. An aqueous solution of 1 mg/mL β -CD NPs was centrifuged (14,000 rpm, 16,837 rcf, 4 min), washed once with 500 μ L HBSS buffer and redispersed again in a mixture containing 500 μ L HBSS buffer with either 5 μ L doxorubicin hydrochloride (100 mg/mL in DMSO) or 500 μ L Hoechst 33342 (10 mg/mL in water), respectively. The nanoparticles were incubated for 3 h and subsequently washed extensively with HBSS buffer (14,000 rpm, 16,837 rcf, 4 min) until no fluorescence could be detected in the supernatant. Finally, the loaded nanoparticles were redispersed in 1 mL HBSS buffer and used for further *in vitro* release experiments. As a reference sample the particles were centrifuged (14,000 rpm, 16,837 rcf, 4 min) after certain time points and the corresponding amount of supernatant was used on HeLa cells.

Lipid preparation. The following lipids were used: DOPC (1,2-dioleoyl-*sn*-glycero-3-phosphocholine, Avanti Polar Lipids), DOTAP (1,2-dioleoyl-3-trimethylammonium propane, Avanti Polar Lipids). The amount of 2.5 mg of the individual lipids was dissolved in a 1 mL mixture of 40 % vol absolute ethanol and 60 % vol MQ water (conc. 2.5 mg/mL). The amount of 1 mg of nanoparticles in aqueous solution was centrifuged (4 min, 8609 rcf, at 15 °C) and redispersed in 100 μ L of the above DOTAP solution. Upon addition of 900 μ L MQ water (pH adjusted to 9.4 with sodium hydroxide) the formation of the first SLB layer on the external surface of the nanoparticles was induced. After centrifugation (4 min, 8609 rcf, at 15 °C) and

redispersion in 100 μL of a 1:1 mixture of the above DOPC/DOTAP solutions, the formation of a second layer around the nanoparticles was induced by adding 900 μL HBSS buffer.

Cell Culture. HeLa cells were grown in Dulbecco's modified Eagle's medium (DMEM) (Life Technologies) supplemented with 10 % fetal bovine serum (FBS) and incubated at 37 °C under a 5 % CO_2 humidified atmosphere. For live cell imaging the cells were seeded on ibidi 8-well μ -slides 24 h before adding particles, at a cell density of 5000 cells per well.

Uptake studies and *in vitro* Cargo release. The cells were incubated with 2 μL or 5 μL of a 1 mg/mL β -CD NPs solution for 0.5 – 24 h prior to the measurements at 37 °C under a 5% CO_2 humidified atmosphere. During the measurements all cells were kept on a heated microscope stage at 37 °C under a 5% CO_2 humidified atmosphere. For imaging, the cells were stained with 1 μL of a WGA solution and were incubated for 2-5 min at 37°C in a 5% CO_2 humidified atmosphere and then washed twice with DMEM. In addition to the uptake studies, the supernatant of the stock solution was similarly investigated for fluorescence and nucleus staining. The subsequent imaging was performed as described in the spinning disk confocal microscopy section.

Spinning disc confocal microscopy. Confocal microscopy for live-cell imaging was performed on a setup based on the Zeiss Cell Observer SD utilizing a Yokogawa spinning disk unit CSU-X1. The system was equipped with a 1.40 NA 63x Plan apochromat oil immersion objective from Zeiss. For all experiments the exposure time was 0.2 s and z-stacks were recorded. Hoechst 33342 was imaged with light at 405 nm and a power density of approximately 0.16 W/mm^2 , WGA was imaged at 488 nm with approximately 0.48 W/mm^2 , and Rhodamin was excited at 561 nm with 11 mW/mm^2 . In the excitation path a quad-edge dichroic beamsplitter (FF410/504/582/669-Di01-25x36, Semrock) was used. Separate images

for each fluorescence channel were acquired using two separate electron multiplier charge coupled device (EMCCD) cameras (PhotometricsEvolveTM).

Cell viability studies. For MTT-Assays we seeded 5000 HeLa cells per well containing 100 μ L of high glucose DMEM medium and treated them with particles 24 h after seeding. After 24 h of incubation the cells were washed twice with HBSS buffer. 100 μ L of 3-(4,5-dimethylthiazol-2-yl)-2,5-diphenyltetrazolium bromide (MTT, 0.5 mg/mL in DMEM) was added to each well of the nanoparticle-treated cells and incubated for further 2 h. Unreacted MTT and medium were removed and the 96-well plates were stored at -80 °C for at least 1 h. Then, 100 μ L DMSO was added to each well. The absorbance was read out by a Tecan plate reader at 590 nm with a reference wavelength of 630 nm. All studies were performed in triplicates. The IC₅₀ and the standard mean deviations were calculated using the Origin 9.0 software.

9.5 References

1. R. Kojima, D. Aubel and M. Fussenegger, *Current Opinion in Chemical Biology*, 2015, **28**, 29-38.
2. C. Argyo, V. Weiss, C. Bräuchle and T. Bein, *Chemistry of Materials*, 2014, **26**, 435-451.
3. M. W. Ambrogio, C. R. Thomas, Y.-L. Zhao, J. I. Zink and J. F. Stoddart, *Accounts of Chemical Research*, 2011, **44**, 903-913.
4. Y. Wang, Q. Zhao, N. Han, L. Bai, J. Li, J. Liu, E. Che, L. Hu, Q. Zhang, T. Jiang and S. Wang, *Nanomedicine: Nanotechnology, Biology and Medicine*, 2015, **11**, 313-327.
5. S. Singh, V. K. Pandey, R. P. Tewari and V. Agarwal, *Nanoparticle Based Drug Delivery System: Advantages and Applications*, 2011.
6. R. Singh and J. W. Lillard, *Experimental and molecular pathology*, 2009, **86**, 215-223.
7. V. Cauda, H. Engelke, A. Sauer, D. Arcizet, C. Brauchle, J. Radler and T. Bein, *Nano letters*, 2010, **10**, 2484-2492.
8. S. A. Mackowiak, A. Schmidt, V. Weiss, C. Argyo, C. von Schirnding, T. Bein and C. Bräuchle, *Nano letters*, 2013, **13**, 2576-2583.
9. S. Niedermayer, V. Weiss, A. Herrmann, A. Schmidt, S. Datz, K. Muller, E. Wagner, T. Bein and C. Brauchle, *Nanoscale*, 2015, **7**, 7953-7964.
10. J. Croissant, A. Chaix, O. Mongin, M. Wang, S. Clément, L. Raehm, J.-O. Durand, V. Hugues, M. Blanchard-Desce, M. Maynadier, A. Gallud, M. Gary-Bobo, M. Garcia, J. Lu, F. Tamanoi, D. P. Ferris, D. Tarn and J. I. Zink, *Small*, 2014, **10**, 1752-1755.
11. B. Rühle, P. Saint-Cricq and J. I. Zink, *ChemPhysChem*, 2016, **17**, 1769-1779.
12. S. H. van Rijt, D. A. Bölükbas, C. Argyo, S. Datz, M. Lindner, O. Eickelberg, M. Königshoff, T. Bein and S. Meiners, *ACS Nano*, 2015, **9**, 2377-2389.
13. Y. Zhao, J. L. Vivero-Escoto, I. I. Slowing, B. G. Trewyn and V. S. Y. Lin, *Expert Opinion on Drug Delivery*, 2010, **7**, 1013-1029.
14. Q. Zheng, Y. Hao, P. Ye, L. Guo, H. Wu, Q. Guo, J. Jiang, F. Fu and G. Chen, *Journal of Materials Chemistry B*, 2013, **1**, 1644-1648.

15. S. Datz, C. Argyo, M. Gattner, V. Weiss, K. Brunner, J. Bretzler, C. von Schirnding, A. A. Torrano, F. Spada, M. Vrabel, H. Engelke, C. Brauchle, T. Carell and T. Bein, *Nanoscale*, 2016, **8**, 8101-8110.
16. J. Croissant, X. Cattoen, M. W. Man, A. Gallud, L. Raehm, P. Trens, M. Maynadier and J. O. Durand, *Adv. Mater.*, 2014, **26**, 6174-6180.
17. J. G. Croissant, S. Picard, D. Aggad, M. Klausen, C. Mauriello Jimenez, M. Maynadier, O. Mongin, G. Clermont, E. Genin, X. Cattoen, M. Wong Chi Man, L. Raehm, M. Garcia, M. Gary-Bobo, M. Blanchard-Desce and J.-O. Durand, *Journal of Materials Chemistry B*, 2016, **4**, 5567-5574.
18. J. Croissant, M. Maynadier, A. Gallud, H. Peindy N'Dongo, J. L. Nyalosaso, G. Derrien, C. Charnay, J.-O. Durand, L. Raehm, F. Serein-Spirau, N. Cheminet, T. Jarrosson, O. Mongin, M. Blanchard-Desce, M. Gary-Bobo, M. Garcia, J. Lu, F. Tamanoi, D. Tarn, T. M. Guardado-Alvarez and J. I. Zink, *Angewandte Chemie International Edition*, 2013, **52**, 13813-13817.
19. C. Mauriello-Jimenez, N. Knezevic, Y. Galan-Rubio, S. Szunerits, R. Boukherroub, F. Teodorescu, J. G. Croissant, O. Hocine, M. Seric, L. Raehm, V. Stojanovic, D. Aggad, M. Maynadier, M. Garcia, M. Gary-Bobo and J.-O. Durand, *Journal of Materials Chemistry B*, 2016, DOI: 10.1039/C6TB01915C.
20. S. Datz, H. Engelke, C. v. Schirnding, L. Nguyen and T. Bein, *Microporous and Mesoporous Materials*, 2016, **225**, 371-377.
21. G. Ajnai, A. Chiu, T. Kan, C.-C. Cheng, T.-H. Tsai and J. Chang, *Journal of Experimental & Clinical Medicine*, 2014, **6**, 172-178.
22. R. Arvizo, R. Bhattacharya and P. Mukherjee, *Expert opinion on drug delivery*, 2010, **7**, 753-763.
23. E. C. Dreaden, L. A. Austin, M. A. Mackey and M. A. El-Sayed, *Therapeutic delivery*, 2012, **3**, 457-478.
24. A. Baeza, E. Guisasola, E. Ruiz-Hernández and M. Vallet-Regí, *Chemistry of Materials*, 2012, **24**, 517-524.
25. Q. A. P. a. J. C. a. S. K. J. a. J. Dobson, *Journal of Physics D: Applied Physics*, 2003, **36**, R167.
26. W. Guo, C. Yang, H. Lin and F. Qu, *Dalton transactions*, 2014, **43**, 18056-18065.
27. S. Laurent, D. Forge, M. Port, A. Roch, C. Robic, L. Vander Elst and R. N. Muller, *Chemical reviews*, 2008, **108**, 2064-2110.

28. T. T. T. N'Guyen, H. T. T. Duong, J. Basuki, V. Montembault, S. Pascual, C. Guibert, J. Fresnais, C. Boyer, M. R. Whittaker, T. P. Davis and L. Fontaine, *Angewandte Chemie International Edition*, 2013, **52**, 14152-14156.
29. B. Ruhle, S. Datz, C. Argyo, T. Bein and J. I. Zink, *Chemical communications*, 2016, **52**, 1843-1846.
30. A. Kumari, S. K. Yadav and S. C. Yadav, *Colloids and Surfaces B: Biointerfaces*, 2010, **75**, 1-18.
31. W. B. Liechty, D. R. Kryscio, B. V. Slaughter and N. A. Peppas, *Annual review of chemical and biomolecular engineering*, 2010, **1**, 149-173.
32. K. S. Soppimath, T. M. Aminabhavi, A. R. Kulkarni and W. E. Rudzinski, *Journal of Controlled Release*, 2001, **70**, 1-20.
33. S. Kalepu, M. Manthina and V. Padavala, *Acta Pharmaceutica Sinica B*, 2013, **3**, 361-372.
34. A. Puri, K. Loomis, B. Smith, J.-H. Lee, A. Yavlovich, E. Heldman and R. Blumenthal, *Critical reviews in therapeutic drug carrier systems*, 2009, **26**, 523-580.
35. H. Shrestha, R. Bala and S. Arora, *Journal of Pharmaceutics*, 2014, **2014**, 10.
36. R. Ranjbar and M. S. Hafezi-Moghadam, *Electronic Physician*, 2016, **8**, 1857-1864.
37. P. W. K. Rothmund, *Nature*, 2006, **440**, 297-302.
38. Q. Zhang, Q. Jiang, N. Li, L. Dai, Q. Liu, L. Song, J. Wang, Y. Li, J. Tian, B. Ding and Y. Du, *ACS Nano*, 2014, **8**, 6633-6643.
39. S. Hedgire, S. McDermott and M. Harisinghani, in *Nanomedicine-Basic and Clinical Applications in Diagnostics and Therapy*, Karger Publishers, 2011, vol. 2, pp. 96-105.
40. T. Lammers, F. Kiessling, W. E. Hennink and G. Storm, *Journal of controlled release*, 2012, **161**, 175-187.
41. A. Salvati, A. S. Pitek, M. P. Monopoli, K. Prapainop, F. B. Bombelli, D. R. Hristov, P. M. Kelly, C. Åberg, E. Mahon and K. A. Dawson, *Nature nanotechnology*, 2013, **8**, 137-143.
42. R. A. Gatenby and R. J. Gillies, *Nature Reviews Cancer*, 2004, **4**, 891-899.
43. R. A. Cairns, I. S. Harris and T. W. Mak, *Nature Reviews Cancer*, 2011, **11**, 85-95.

44. P. P. Hsu and D. M. Sabatini, *Cell*, 2008, **134**, 703-707.
45. R. J. DeBerardinis, J. J. Lum, G. Hatzivassiliou and C. B. Thompson, *Cell metabolism*, 2008, **7**, 11-20.
46. J. Szejtli, *Chemical reviews*, 1998, **98**, 1743-1754.
47. F. Acartürk and N. Çelebi, *Cyclodextrins in pharmaceuticals, cosmetics, and biomedicine: current and future industrial applications*, 2011, 45-64.
48. H. Arima, K. Motoyama and T. Irie, *Cyclodextrins in pharmaceuticals, cosmetics, and biomedicine: Current and future industrial applications*, 2011, 91-122.
49. E. Bilensoy, *Cyclodextrins in pharmaceuticals, cosmetics, and biomedicine: current and future industrial applications*, John Wiley & Sons, 2011.
50. A. A. Hincal, H. Eroğlu and E. Bilensoy, *Cyclodextrins in Pharmaceuticals, Cosmetics, and Biomedicine: Current and Future Industrial Applications*, 2011, 123-130.
51. T. Auletta, M. R. de Jong, A. Mulder, F. C. J. M. van Veggel, J. Huskens, D. N. Reinhoudt, S. Zou, S. Zapotoczny, H. Schönherr, G. J. Vancso and L. Kuipers, *Journal of the American Chemical Society*, 2004, **126**, 1577-1584.
52. W. C. Cromwell, K. Bystrom and M. R. Eftink, *The Journal of Physical Chemistry*, 1985, **89**, 326-332.
53. M. R. Eftink, M. L. Andy, K. Bystrom, H. D. Perlmutter and D. S. Kristol, *Journal of the American Chemical Society*, 1989, **111**, 6765-6772.
54. B. V. K. J. Schmidt, M. Hetzer, H. Ritter and C. Barner-Kowollik, *Progress in Polymer Science*, 2014, **39**, 235-249.
55. E. M. Del Valle, *Process biochemistry*, 2004, **39**, 1033-1046.
56. L. G. Suárez, W. Verboom and J. Huskens, *Chemical communications*, 2014, **50**, 7280-7282.
57. S. Yu, Y. Zhang, X. Wang, X. Zhen, Z. Zhang, W. Wu and X. Jiang, *Angewandte Chemie International Edition*, 2013, **52**, 7272-7277.
58. M. E. Davis, *Molecular pharmaceuticals*, 2009, **6**, 659-668.
59. W. Zhu, K. Zhang, Y. Chen and F. Xi, *Langmuir*, 2013, **29**, 5939-5943.
60. A. Alsaiee, B. J. Smith, L. Xiao, Y. Ling, D. E. Helbling and W. R. Dichtel, *Nature*, 2015.
61. G. Wenz, B.-H. Han and A. Müller, *Chemical reviews*, 2006, **106**, 782-817.

62. J. V. Jokerst, T. Lobovkina, R. N. Zare and S. S. Gambhir, *Nanomedicine (London, England)*, 2011, **6**, 715-728.
63. A. L. B. de Barros, K. S. de Oliveira Ferraz, T. C. S. Dantas, G. F. Andrade, V. N. Cardoso and E. M. B. d. Sousa, *Materials Science and Engineering: C*, 2015, **56**, 181-188.
64. S. Vorona, T. Artamonova, Y. Zevatskii and L. Myznikov, *Synthesis*, 2014, **46**, 781-786.
65. A. Moore, R. Weissleder and A. Bogdanov, *Journal of Magnetic Resonance Imaging*, 1997, **7**, 1140-1145.
66. F. Osaki, T. Kanamori, S. Sando, T. Sera and Y. Aoyama, *Journal of the American Chemical Society*, 2004, **126**, 6520-6521.
67. M. Xue, X. Zhong, Z. Shaposhnik, Y. Qu, F. Tamanoi, X. Duan and J. I. Zink, *Journal of the American Chemical Society*, 2011, **133**, 8798-8801.
68. H. Meng, M. Xue, T. Xia, Y.-L. Zhao, F. Tamanoi, J. F. Stoddart, J. I. Zink and A. E. Nel, *Journal of the American Chemical Society*, 2010, **132**, 12690-12697.
69. L. Lu, X. Shao, Y. Jiao and C. Zhou, *Journal of Applied Polymer Science*, 2014, **131**, n/a-n/a.
70. L. Y. Qiu, R. J. Wang, C. Zheng, Y. Jin and L. Q. Jin, *Nanomedicine*, 2010, **5**, 193-208.
71. T. Yousef and N. Hassan, *Journal of Inclusion Phenomena and Macrocyclic Chemistry*, 2016, DOI: 10.1007/s10847-016-0682-4, 1-11.

9.6 Appendix

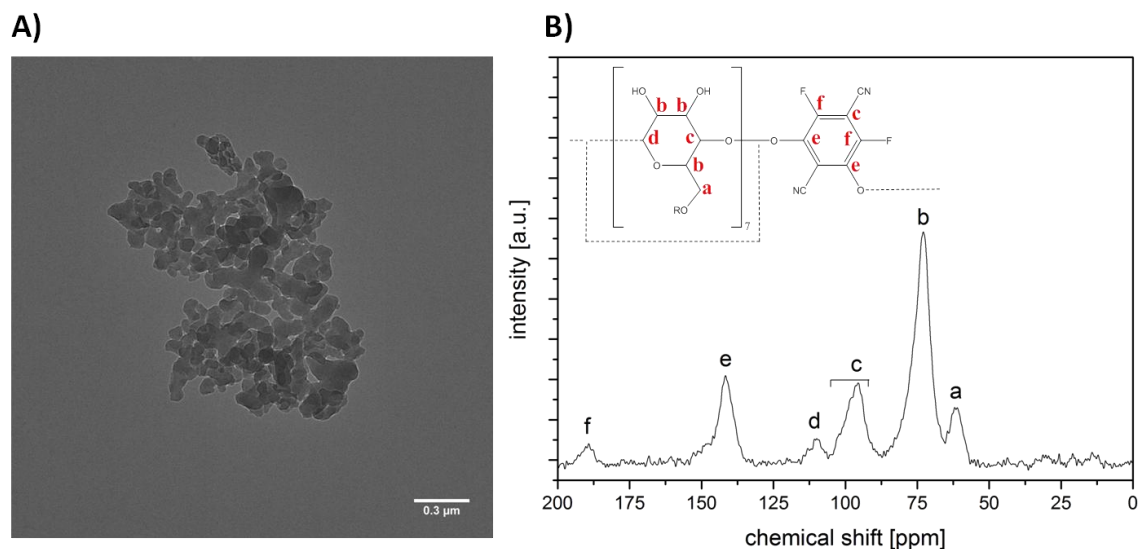


Figure S 9-1: A) Transmission electron microscopy (TEM) image of β -CD NPs revealing a particle size distribution of around 100-200 nm. B) ^{13}C -MAS solid-state nuclear magnetic resonance (ssNMR) spectrum of β -CD NPs indicating the successful incorporation of the oligosaccharide compounds and the rigid organic linker into the crosslinked material.

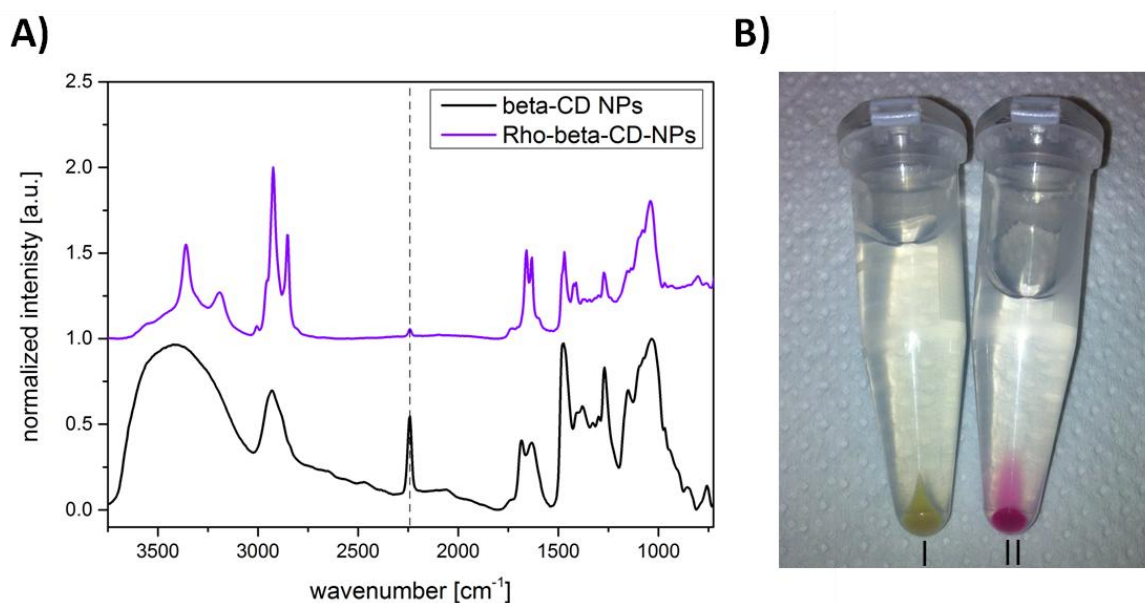


Figure S 9-2: A) IR spectroscopy data of as-synthesized β -CD NPs (black) and rhodamine-labeled nanoparticles (violet). The successful attachment can be followed by the vanishing nitrile stretching vibration at 2245 cm^{-1} due to the covalent binding of the dye's azide groups to form tetrazole rings in a 1,3-dipolar cycloaddition. Spectra were normalized and shifted for clarity by 1.0 along the y-axis. B)

Photograph of 1 mg of as-synthesized pale yellow β -CD NPs (I) and pink labeled Rho- β -CD NPs (II) in water after centrifugation, respectively.

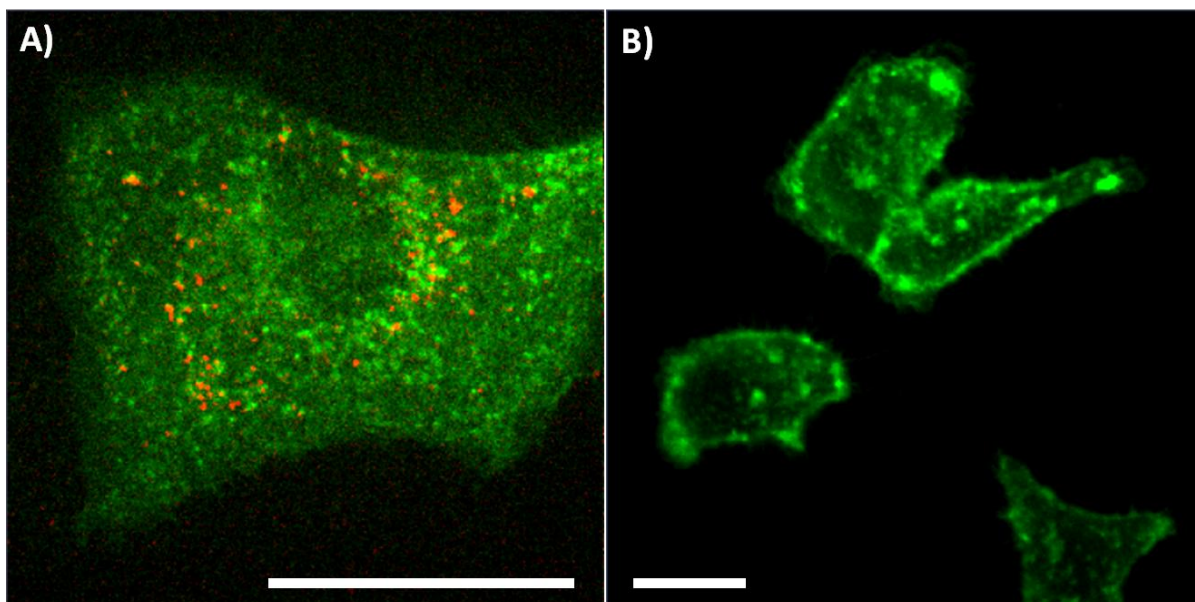


Figure S 9-3. Fluorescence microscopy of HeLa cells incubated with rhodamine-labeled β -CD NPs (red) after 30 min (A), or pretreated with free inhibitors (e.g. β -cyclodextrin) for 30 min and incubated with rhodamine-labeled β -CD NPs for 30 min afterwards (B). Cell membranes are stained with WGA (green). Scale bars represent 10 μ m each.

To test the targeting of sugar receptors with β -CD nanoparticles on HeLa cells, the receptors were either blocked or free. The functionality was evaluated in a receptor competition experiment. For this purpose, one part of the HeLa cells was pre-incubated with 5 μ L of an inhibitor solution (10 mM aqueous solutions of D-glucose, D-L-arabinose, 2-deoxy-D-glucose or β -cyclodextrin, respectively), to block the receptors, for 30 min at 37 $^{\circ}$ C under a 5% CO₂ humidified atmosphere. Then the HeLa cells were incubated with 5 μ g of rhodamine-labeled β -CD-NPs for 30 min at 37 $^{\circ}$ C under a 5% CO₂ humidified atmosphere. For staining the cell membrane, the cells were incubated with WGA for 2 min. The cells were washed three times with PBS, fresh medium was added and subsequently the cells were imaged. Clearly an

enhanced sugar receptor-mediated cell uptake can be seen when the sugar receptors are available on the cell surface (A) compared to blocked receptors (B).

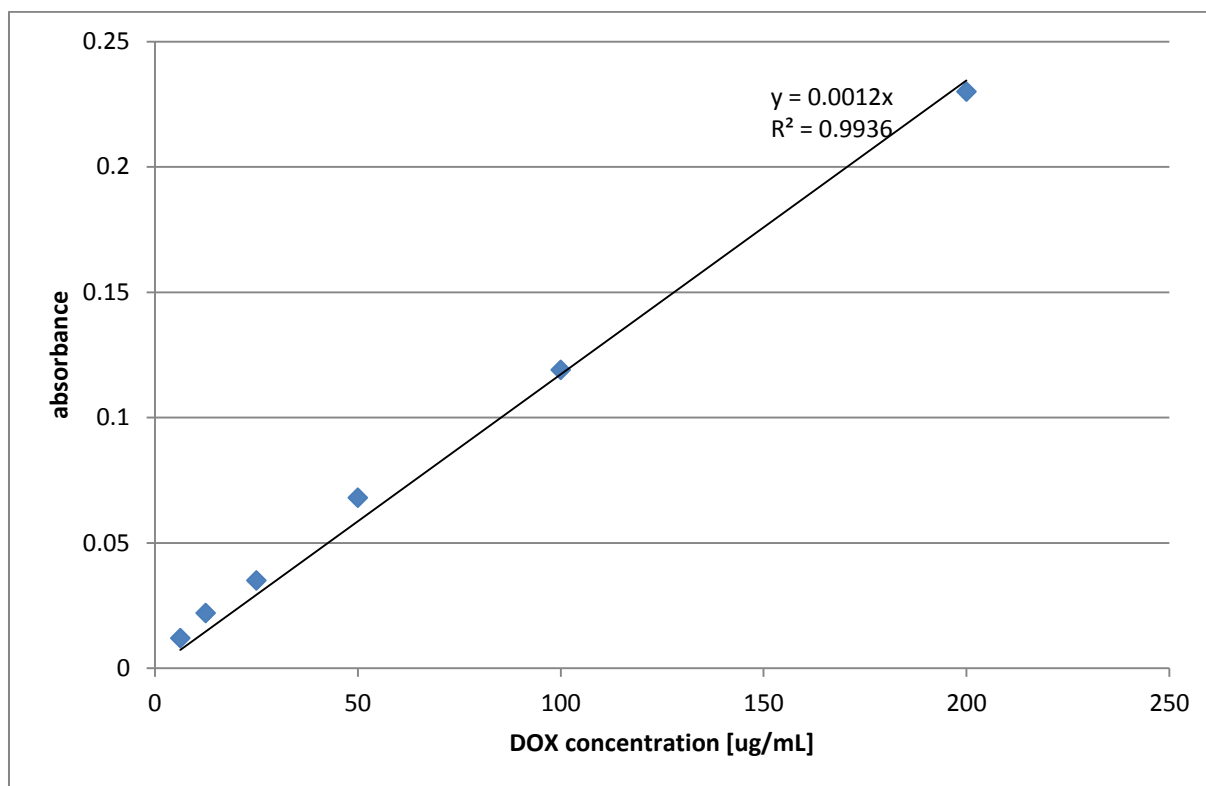


Figure S 9-4: Calibration curve for doxorubicin loading capacity measured at 500 nm.

The concentration of the DOX loading solution was 1 mg/mL with 1 mg nanoparticles. After several washing steps the supernatants were collected and revealed an added-up absorbance of 0.698. By using the linear regression fit of the calibration curve this leads to a DOX content of 580 $\mu\text{g/mL}$ in the collected supernatants. Therefore, the total amount of loaded DOX was 420 μg per mg nanoparticles leading to a loading capacity of 42 wt%.

10 Conclusions and Outlook

The focus of this thesis was the development of different stimuli-responsive capping systems for multifunctional mesoporous silica nanoparticles. Additionally, toxicity and targeting studies were performed with MSNs *in vitro* and *in vivo*. As a highlight, two new innovative nanoparticle materials were developed and applied in cellular delivery applications.

In the first three chapters capping systems on MSNs responding to different external or internal stimuli were synthesized and investigated for drug delivery applications. An enzyme-responsive capping system based on a matrix metalloproteinase 9 (MMP9) specific linker molecules was developed to obtain tightly capped MSNs. MMP9 is overexpressed in tumors and known to enhance the metastatic potency of malignant cells, and has been associated with poor prognosis of lung cancer. The used MSNs are tightly capped by avidin molecules via MMP9 sequence-specific linkers to allow for site-selective drug delivery in high MMP9-expressing tumor areas. This study shows the feasibility of MMP9 mediated drug release in human lung tissue and in an advanced mouse model (Kras mutant mice) that closely reflects the human pathophysiology. Moreover, our novel drug delivery system using MMP9 responsive MSN particles could be used to effectively deliver a combination of two drugs, bortezomib and cisplatin, in a stimuli-controlled manner, and potentiate a synergistic effect selectively to (metastatic) tumors in mouse and human *ex vivo* tissue slices.

Another capping system developed in this thesis is based on the externally applied magnetic heating stimulus. This new concept of a molecular nanocap based on a retro-Diels Alder reaction and activated through superparamagnetic heating adds to the toolbox of externally controllable, thermally triggered nano-valves. We envision that changing the electronic properties of the diene and dienophile component in the Diels Alder reaction should allow for

further fine-tuning of the release properties of such nanovalves. Actuation through an alternating magnetic field has the advantage of deep tissue penetration and non-invasiveness, making these nanovalves interesting candidates for future applications in drug delivery.

In a third approach, a pH-responsive capping system was developed for internally triggered cargo release in addition to specific bioorthogonal targeting experiments. The novel capping system concept based on pH-responsive detachment of carbonic anhydrase combined with folic acid as targeting ligand allows for highly controllable drug release from porous nanocarriers. The drug delivery system provides an on-demand release mechanism shown by *in vivo* and *in vitro* cargo release experiments. The multifunctional MSNs were efficiently endocytosed in cancer cells and could be located in acidic cell compartments where they released their cargo. Furthermore, the system has an on-board targeting mechanism as demonstrated in additional *in vitro* experiments. The targeting mechanism is attached at a specific site of the capping enzyme, preventing interference with the closure mechanism. These newly developed pH-responsive gatekeepers with genetically designed targeting functions provide a promising platform for the design of versatile and modular drug delivery systems.

In the following chapter, we investigated the relevance of avidin-capped MSNs (MSN-AVI) for pulmonary therapy by looking at their pulmonary distribution, clearance rate, cell specific uptake, and induction of inflammatory response after direct (intratracheal) instillation in the lungs of mice. Since MSNs allow for multiple functionalizations, which have been found to be important for their bioresponse, we also included non-capped (only amino-functionalized; MSN-NH₂) particles in this study. We showed that MSN avidin surface modification had an effect not only on toxicity, but also on cell specific uptake and tissue distribution in the lungs. Specifically, non-capped (MSN-NH₂) particles were found to be cytotoxic to macrophages, caused an enhanced inflammatory response, and were hardly taken up by epithelial cells. In

contrast, MSN-AVI particles co-localized with alveolar epithelial type 1 and type 2 cells in the lung tissue and showed preferential epithelial cell uptake in *in vitro* co-cultures. These findings, in combination with the low surface-specific toxicity, wide distribution of the particles in the mouse lungs and slow clearance rate is promising for the treatment of chronic lung diseases such as COPD (chronic obstructive pulmonary disease), IPF (idiopathic pulmonary fibrosis), and lung cancer, where (alveolar) epithelial cells play an important role in the pathogenesis. Moreover, the inflammatory potential of drug delivery particles is most critical in inflammatory lung diseases such as asthma and COPD, due to additive effects leading to worsening of the symptoms. In this context, the observation that the dose of 1 mg/kg of MSN-AVI did not cause any detectable inflammatory response is particularly promising for treatment of these devastating lung diseases. Thus, we believe that avidin-coated MSNs offer potential for inhalative application as therapeutic drug carriers in chronic lung diseases. In addition, the finding that surface modifications greatly affect toxicity and cell type specific uptake highlights the importance of these types of studies for future development of nanomedicines. These toxicity data were the fundamental basis for the following application of MSNs in specific receptor-mediated targeting studies.

In chapter 7, we investigated the targeting efficiencies of EGFR- or CCR2-targeted mesoporous silica nanoparticles (MSNs) *in vitro* and *in vivo* for lung cancer therapy with cellular resolution. Notably, *in vitro* validated nanoparticle-mediated targeting of receptors on tumor and tumor-associated immune cells is strongly deprived *in vivo*. This failure in cellular targeting specificity is particularly obvious for the lung-delivered nanoparticles as the alveolar macrophages of the Kras-mutant mice strongly overexpressed both EGFR and CCR2, but efficiently entrapped targeted as well as non-targeted nanoparticles to a similar extent. Enhanced cell-specific uptake by macrophages of the lung compared to tumor cells would have escaped analysis if only particle uptake within the tissue would have been monitored as

done previously. Similarly, analysis of cell-specific particle uptake in flank tumor models also unambiguously revealed loss of cellular targeting specificity. Our data thus emphasize the need for analyzing cellular targeting specificities with cellular resolution also in the major target organs. This is particularly relevant when aiming for combination targeting of different cell populations with distinct ligand-functionalized nanoparticles. Our findings, however, indicate that these therapeutic effects may not always be due to a direct nanoparticle-mediated tumor killing but may also involve bystander effects such as cytotoxicity of tissue-resident phagocytic cells, immune-modulatory effects, or unspecific drug release from nanoparticles in the liver into the circulation. Our own and other published data indicate that blood-derived serum and the lung lining fluid form distinct protein coronas on nanoparticles *in vitro*. Moreover, protein corona also forms rapidly in cell culture medium containing serum where receptor-mediated targeting was effective. Taken together, our study argues in favor of a stringent validation of cell-specific targeting with cellular-resolution when using nanoparticle-based targeting strategies. Moreover, closing the translational gap in nanomedicine calls first for physiologically relevant animal models, such as the Kras^{LA2} mice as used here which develop spontaneous lung tumors closely resembling the human situation, and second for rigorous biological testing of nanoparticles using state of the art molecular manipulation of cells and animals critically.

Two different novel nanomaterials for drug delivery were successfully synthesized, with reduced silica-content and completely without silica. In chapter 8, we report the development of new colloidal periodic mesoporous organosilica nanoparticles containing curcumin as the main organic component, with very high organic wall content. They are fluorescent, possess a large pore volume and surface area and show very high stability in simulated body fluid. When coated with a lipid layer they are successfully internalized by cells and can deliver and release Rhodamin B in those cells. Thus, they show great potential for future applications as

drug delivery system. Additionally, we have developed a novel nanomaterial consisting of crosslinked β -cyclodextrin molecules as the main organic component. The obtained nanoparticles are small (~150 nm) and highly dispersible in aqueous solutions. They exhibit very fast cell uptake kinetics due to sugar-receptor mediated endocytosis and can be covalently labeled with dye molecules to effectively track them in *in vitro* experiments. Furthermore, the porous cavities of the particles could be loaded with different cargo molecules, which were subsequently released in the endosomal cell compartments due to acidification. This triggered release mechanism allowed us to show efficient nuclei staining with Hoechst 33342 and effective cancer cell killing with doxorubicin acting as cargo, respectively. Thus, the nanoparticles show great potential for future applications as a biocompatible drug delivery system.

In conclusion, we have developed novel synthesis and application strategies for the production of multifunctional mesoporous silica nanoparticles. These were successfully used as stimuli-responsive carrier systems in drug delivery applications *in vitro*, *ex vivo* and *in vivo*. Additional toxicity studies and targeting experiments showed the great potential as well as specific challenges of these nanosystems. To overcome some of these challenges, two new novel nanomaterials were successfully synthesized and applied as carrier systems in cellular delivery investigations.

11 Curriculum Vitae

Personal Information

Name: Datz Stefan
Address: An der Tuchbleiche 20
81927 München, Germany
Phone: + 49 (0) 176 20296340
E-Mail: stefan.datz@gmx.de
Date of birth: October 05, 1987
Place of birth: Traunstein
Nationality: German

Education

January 2014 – present PhD student in the group of Prof. Thomas Bein
Ludwig-Maximilians-University, Munich
September 2011 – September 2013 Master Studies in Chemistry
Ludwig-Maximilians-University, Munich
Master of Science (M.Sc., Grade: 1.1)
October 2008 – August 2011 Bachelor Studies in Chemistry and Biochemistry
Ludwig-Maximilians-University, Munich
Bachelor of Science (B. Sc., Grade: 1.6)
September 1998 – June 2007 Chiemgau-Gymnasium, Traunstein
General qualification for university entrance
(Grade: 2.2)

Research Internship

October 2014 – November 2014 Research internship in the group of Prof. Dr. Jeffrey I. Zink at the University of California, Los Angeles

Work Experience

September/October 2015 Hendlhacker in the Augustiner tent at the Oktoberfest
January 2011 – May 2016 Salesperson in Fischer' Früchte (fruits, vegetables, wine)

June 2012 - May 2016 Event-Teamer at COMMUNICO GmbH
July 2009 – September 2010 Working Student Bosch & Siemens Hausgeräte GmbH
August 2007 – April 2008 Alternative service at Malteser Hilfsdienst e.V.

Awards and Scholarships

„Preis der Dr. Klaus Römer-Stiftung“ for outstanding master studies 2014

Bavaria California Technology Center scholarship 2014

1. Place *Hands-on-Experimente-Wettbewerb* at the NIM Nanoday 2014

Presentation award at the International Symposium on Nanobiotechnology, Los Angeles, 2016

Travel Scholarship of the Gesellschaft Deutscher Chemiker for Presentation at the 14th ESCDD, 2016

Member of the Nanosystems Initiative Munich Graduate Program (2014-2017)

Computer Skills

MS Office, ChemDraw, Origin, ImageJ, Web

Languages

German: native speaker

English: business fluent

French: basic skills

Other Activities

Since January 2014 Scientific executive for Fluorescence spectroscopy, Raman and Infrared spectroscopy, Nitrogen Sorption, Cell biology, Laboratory and safety manager

Since January 2014 Supervision of practical courses in inorganic and physical chemistry, Supervision of interns, master students and exchange students of the Nanosystems Initiative Munich (NIM) Summer Research Program (SRP)

Commitment

private tutor in chemistry, tennis and skiing instructor

Hobbies

soccer, surfing, tennis, skiing, reading, travelling

12 Publications and Presentations

12.1 Publications

1.) Protease-mediated release of chemotherapeutics from mesoporous silica nanoparticles to ex vivo human and mouse lung tumors

S. H. van Rijt, D. A. Bölükbas, C. Argyo, S. Datz, M. Lindner, O. Eickelberg, M. Königshoff, T. Bein, and S. Meiners, *ACS Nano* **2015**, *9*, 2377.

2.) Multifunctional polymer-capped mesoporous silica nanoparticles for pH-responsive targeted drug delivery

S. Niedermayer, V. Weiss, A. Hermann, A. Schmidt, S. Datz, K. Müller, E. Wagner, T. Bein, C. Bräuchle, *Nanoscale* **2015**, *7*, 7953.

3.) Lipid-Bilayer Coated Curcumin-based Mesoporous Organosilica Nanoparticles for Cellular Delivery

S. Datz, H. Engelke, C. v. Schirnding, L. Nguyen, T. Bein, *Micropor. Mesopor. Mater.* **2016**, *225*, 371.

4.) A molecular nanocap activated by superparamagnetic heating for externally stimulated cargo release

B. Rühle, S. Datz, C. Argyo, T. Bein, J. I. Zink, *Chem. Comm.* **2016**, *52*, 1843.

5.) Genetically designed biomolecular capping system for mesoporous silica nanoparticles enables receptor-mediated cell uptake and controlled drug release

S. Datz, C. Argyo, M. Gattner, V. Weiss, K. Brunner, J. Bretzler, C. v. Schirnding, H. Engelke, F. Spada, M. Vrabel, C. Bräuchle, T. Carell, T. Bein, *Nanoscale* **2016**, *8*, 8101.

6.) From Highly Crystalline to Outer Surface-Functionalized Covalent Organic Frameworks – A Modulation Approach

M. Calik, T. Sick, M. Dogru, M. Döblinger, S. Datz, H. Budde, A. Hartschuh, F. Auras, T. Bein, *J. Am. Chem. Soc.* **2016**, *138*, 1234.

7.) Applicability of avidin protein coated mesoporous silica nanoparticles as drug carriers in the lung

S. H. van Rijt, D. A. Bölükbas, C. Argyo, K. Wipplinger, M. Naureen, S. Datz, O. Eickelberg, S. Meiners, T. Bein, O. Schmidt, T. Stöger, *Nanoscale* **2016**, *8*, 8058.

8.) Dendronized mesoporous silica nanoparticles provide an internal endosomal escape mechanism for successful cytosolic drug release

V. Weiss, C. Argyo, A. A. Torrano, C. Strobel, S. A. Mackowiak, A. Schmidt, S. Datz, T. Gattenmeier, I. Hilger, C. Bräuchle, T. Bein, *Micropor. Mesopor. Mater.* **2016**, *227*, 242.

9.) Chemical Twinning of Salt and Metal in the Subnitridometalates $\text{Ba}_{23}\text{Na}_{11}(\text{MN}_4)_4$ with $M = \text{V}, \text{Nb}, \text{Ta}$

M. Wörsching, F. Tambornino, S. Datz, C. Hoch, *Angew. Chem.* **2016**, *55*, 10868.

10.) Cellular resolution is essential for validation of active targeting of nanoparticles in vivo

Deniz Bölükbas, Stefan Datz, Charlotte Meyer-Schwickerath, Malamati Vreka, Lin Yang, Dorothee Gößl, Theodora Agalioti, Christian Argyo, Sabine van Rijt, Michael Lindner, Oliver Eickelberg, Tobias Stöger, Otmar Schmid, Georgios Stathopolous, Thomas Bein, Silke Meiners, *submitted* **2017**.

11.) Biocompatible β -cyclodextrin nanoparticles as multifunctional carriers for cellular delivery

Stefan Datz, Bernhard Illes, Hanna Engelke, Thomas Bein, *manuscript in preparation* **2017**.

12.2 Presentations

1.) Multifunctional polymer-capped mesoporous silica nanoparticles for pH-responsive targeted drug delivery

SFB749 Workshop, *Dynamics and Inclusion Chemistry in Mesoporous Host Systems*, **2014**, Venice, Italy.

2.) Genetically designed biomolecular capping system for mesoporous silica nanoparticles enables receptor-mediated cell uptake and controlled drug release

113. Bunsentagung, *Physical Chemistry on the Nanometer Scale*, **2014**, Hamburg, Germany.

3.) Genetically designed biomolecular capping system for mesoporous silica nanoparticles enables receptor-mediated cell uptake and controlled drug release

6th International FEZA Conference, *Porous Systems: From Novel Materials to Sustainable Solutions*, **2014**, Leipzig, Germany.

4.) Genetically designed biomolecular capping system for mesoporous silica nanoparticles enables receptor-mediated cell uptake and controlled drug release

International Symposium on Nanobiotechnology, *NanoMedicine from discovery to clinical reality: therapeutics, delivery and imaging*, **2016**, California Nanosystems Institute, Los Angeles, USA.

5.) Lipid-Bilayer Coated Curcumin-based Mesoporous Organosilica Nanoparticles for Cellular Delivery

28. Deutsche Zeolith-Tagung, **2016**, Justus-Liebig-Universität, Gießen, Germany.

6.) Genetically designed biomolecular capping system for mesoporous silica nanoparticles enables receptor-mediated cell uptake and controlled drug release

14th European Symposium on Controlled Drug Delivery, **2016**, Egmond aan Zee, Netherlands.

7.) Lipid-Bilayer Coated Curcumin-based Mesoporous Organosilica Nanoparticles for Cellular Delivery

Nanosystems Initiative Munich Summer Retreat **2016**, Hersching, Germany.

8.) Genetically designed biomolecular capping system for mesoporous silica nanoparticles enables receptor-mediated cell uptake and controlled drug release

Center for Nanoscience Workshop, *Nanoscale Matter: Novel Concepts and Functions* **2016**, Venice, Italy.

9.) In vitro tumor targeting of functionalized nanoparticles does not predict in vivo behaviour

29. Deutsche Zeolith-Tagung, **2017**, Dechema-Haus, Frankfurt a.M., Germany.